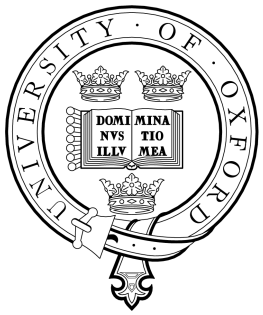

Magnetic Field Effects in Chemical Systems

by

Christopher T. Rodgers

A thesis submitted in partial fulfilment of the requirements
for the degree of Doctor of Philosophy

Hilary Term 2007

University of Oxford

Physical & Theoretical Chemistry Laboratory
and
St John's College

Abstract

Magnetic Field Effects in Chemical Systems

Christopher T. Rodgers

Physical & Theoretical Chemistry Laboratory and St John's College

Abstract of a thesis submitted for the degree of Doctor of Philosophy

Hilary Term 2007

Magnetic fields influence the rate and/or yield of chemical reactions that proceed via spin correlated radical pair intermediates. The field of spin chemistry centres around the study of such magnetic field effects (MFEs). This thesis is particularly concerned with the effects of the weak magnetic fields $B_0 \sim 1\,\mathrm{mT}$ relevant in the ongoing debates on the mechanism by which animals sense the geomagnetic field and on the putative health effects of environmental electromagnetic fields. Relatively few previous studies have dealt with such weak magnetic fields. This thesis presents several new theoretical tools and applies them to interpret experimental measurements.

- Chapter 1 surveys the development and theory of spin chemistry.
- Chapter 2 introduces the use of Tikhonov and Maximum Entropy Regularisation methods as a new means of analysing MARY field effect data. These are applied to recover details of the diffusive motion of reacting pyrene and N,N-dimethylaniline radicals.
- Chapter 3 gives a fresh derivation and appraisal of an approximate, semiclassical approach to MFEs. Monte Carlo calculations allow the elucidation of several "rules of thumb" for interpreting MFE data.
- Chapter 4 discusses recent optically-detected zero-field EPR measurements, adapting the γ–`COMPUTE` algorithm from solid state NMR for their interpretation.
- Chapter 5 explores the role of RF polarisation in producing MFEs. The breakdown in weak fields of the familiar rotating frame approximation is analysed.
- Chapter 6 reviews current knowledge and landmark experiments in the area of animal magnetoreception. The origins of the sensitivity of European robins *Erithacus rubecula* to the Earth's magnetic field are given particular attention.
- In Chapter 7, Schulten and Ritz's hypothesis that avian magnetoreception is founded on a radical pair mechanism (RPM) reaction is appraised through calculations in model systems.
- Chapter 8 introduces quantitative methods of analysing anisotropic magnetic field effects using spherical harmonics.
- Chapter 9 considers recent observations that European robins may sometimes be disoriented by minuscule RF fields. These are shown to be consistent with magnetoreception via a radical pair with no (effective) magnetic nuclei in one of the radicals.

Acknowledgements

This thesis would not have been possible without the help, support and encouragement of many others for which I am most grateful.

Peter Hore and Chris Timmel: Thank you for welcoming me as a member of your research groups and for many years of patient supervision, encouragement, ideas and funding. Thank you particularly giving me the freedom to develop as a scientist.

Stuart Norman, Philipp Kukura, Kevin Henbest and Chris Wedge: Thank you for supplying all the experimental data in Chapter 2–5 and for many useful discussions. Thank you for allowing me to watch your experiments and answering my frequent questions. Chris, I thank you especially for your help in proof reading this thesis.

Nicola Wagner-Rundell: It's been a pleasure to have you as a "partner in crime" since our arrival as Part II students. Thanks for your good company and food. I wish you and Ben every happiness in your married life.

Ilya Kuprov: Thank you for your readiness to share ideas and for help when I've been stuck. It was fun doing the SCM2005 and ESR2007 conference IT together. Thank you also for taking me to Magdalen for dinner!

Iain Day, Paul McKeating and Anthony O'Dea: Thanks for helping me to get started as a Part II student in Peter's group and for tea time banter.

Martin Goez: Thank you for your company at tea, for your gentle advice and encouragement and for some excellent concerts.

Pete Biggs: Thank you for keeping all of our computers working and for treating this "user" with courtesy and respect.

Thorsten Ritz, Henrik Mouritsen, Roswitha Wiltschko and Nikita Lukzen: Thank you for several interesting discussions.

Caroline: You are a beautiful fiancée. Thanks for your encouragement and prayers as I wrote this thesis. Thank you for so many happy times together. I'm looking forward to being "Dr & Dr Rodgers" soon!

Dad, Mum and Tim: Thank you for your love, support, encouragement and prayers.

Leonard, David, Jonathan and Steve: Thank you for your encouragement and prayers. Thank you particularly for making 8SPC such a happy place to live.

I thank God for His grace towards me and for making such an interesting world to study. This thesis is dedicated to Him.

Contents

Chapter 1

Introduction

1.1 Spin chemistry

Magnetic fields can alter the rate, yield or product distribution of chemical reactions [1, 2]. Amazingly, fields of only $\sim 40\,\mu\mathrm{T}$, which are comparable to that of the Earth, produce demonstrable effects on the reaction of certain molecules [3]. This exquisite sensitivity arises even though the interaction between molecules and these weak magnetic fields has an energy much smaller than the average thermal energy $k_\mathrm{B}T$. Figure 1.1 shows photographs of another, visually striking demonstration of chemical effects caused by a magnetic field. These phenomena, as we shall see later, arise through a detailed interplay of diffusion, reaction and quantum mechanical effects on the electron and nuclear spins of the species involved.

Spin chemistry is an area of research centred around the influence of electron and nuclear spins on chemical reactivity. It encompasses research into chemically-induced polarisation effects in NMR and EPR spectroscopy, *i.e.* CIDNP and CIDEP respectively, and into chemical magnetic field effects (MFEs), with which this thesis is concerned.

Apart from a few scattered reports, which were often unreproducible or lacked a theoretical interpretation, the first convincing chemical magnetic field effects were observed in the late 1960s by Johnson for the triplet-exciton annihilation luminescence of anthracene crystals [6, 7]. These experimental results were interpreted by Merrifield using a spin Hamiltonian approach [8].

Similar ideas emerged in the context of radiolysis, where the impact of high energy particles creates radical ions which subsequently react with one another. Brocklehurst noted that electron spin is conserved during chemical reactions. Furthermore, in the hydrocarbon glasses used as a medium for radiolysis experiments, he estimated that electron spin relaxation would be relatively slow. Taking these ideas together, he predicted that the yield of recombination reactions between radical ions produced by radiolysis would show magnetic field effects [9–11].

Also in the 1960s, several workers observed anomalous lineshapes and enhanced signal intensities in the EPR spectra of radical reaction intermediates and later in the NMR spectra of the products of radical reactions [12]. These effects were dubbed chemically induced dynamic electron (or nuclear) polarisation (CIDEP or CIDNP) respectively. They were interpreted independently by Kaptein and Oosterhoff [13] and by Closs [14] in terms of the radical pair mechanism (RPM) described below.

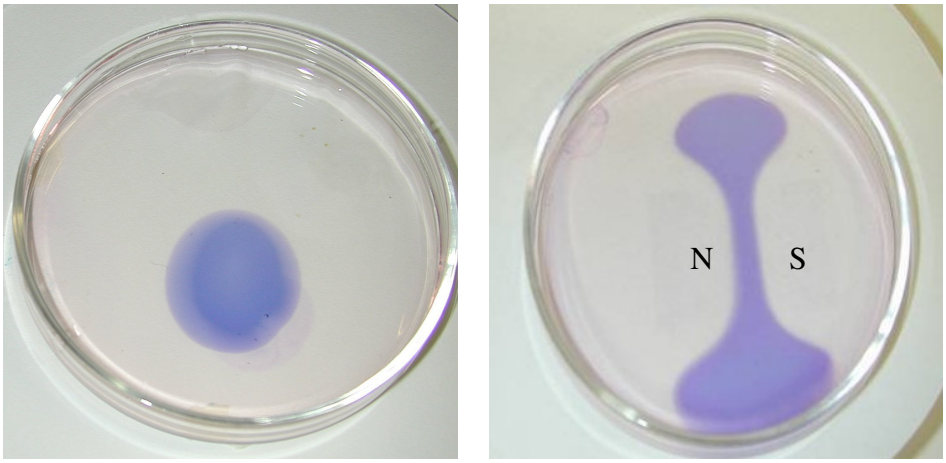

(a) Reaction at ambient conditions where only the geomagnetic field is present

(b) A permanent horseshoe magnet, whose poles are denoted N and S, is placed under the sample

$$\underset{\text{pale pink}}{Co^{II}EDTA^{2-}} + \tfrac{1}{2}\,H_2O_2 \xrightarrow{OH^-} \underset{\text{blue}}{Co^{III}EDTA^{-}} + OH^-$$

Figure 1.1: A visually striking demonstration that magnetic fields truly are able to influence chemical reactions comes from the autocatalytic oxidation of $Co^{II}EDTA^{2-}$ by hydrogen peroxide. Pale pink $Co^{II}EDTA^{2-}$ solution is placed in a Petri dish and reaction is initiated by placing a drop of NaOH at the centre of the dish. Photograph (a) shows the behaviour in ambient fields: a blue region of $Co^{III}EDTA^{-}$ develops at the centre of the dish and grows outwards evenly until reaction is complete and the whole dish is blue. In contrast, (b) is a photograph taken shortly after initiation when a permanent horseshoe magnet has been placed under the Petri dish. The blue region of $Co^{III}EDTA^{-}$ avoids the poles of the magnet as it expands. Photographs were supplied by Timmel. The mechanism of this MFE has been studied in detail using magnetic resonance imaging [4, 5].

The RPM was soon applied to the interpretation of chemical magnetic field effects by Lawler and Evans [15]. This introduction of the RPM in the late 1960s marks the birth of spin chemistry.

The field grew rapidly in the following years. In the early 1970s, the triplet mechanism (TM) was introduced to explain entirely emissive CIDEP signals by Wan in Canada [16] and by Atkins and McLauchlan in Oxford [17]. Soon, Pedersen and Freed published a series of papers in which they developed a detailed theory for CIDEP [18–23]. A similarly detailed theory of chemical magnetic field effects via the RPM arose a few years later in the 1970s with particular contributions from Brocklehurst [10, 11] and Schulten [24–29]. By this stage, spin chemistry was burgeoning with input from research groups in Japan, Russia, Western Europe and the United States.

Today spin chemistry is a well established branch of physical chemistry. For example, in 2005 the most recent Spin Chemistry Meeting, held in Oxford, was attended by some 138 delegates from 16 countries [30]. The methods of CIDNP and CIDEP have been developed and applied widely [31, 32]. Chemical magnetic field effects have formed the basis of a variety of reaction yield detected magnetic resonance techniques [33–38]. These have been applied to study reactions in solids, liquids and in heterogeneous media such as micelles. The literature on magnetic field effects is too

extensive for us to give a comprehensive review here. Instead, for further information, the reader is encouraged to refer to one of the following review articles [1, 39–43] or books [2, 44–46]. The comprehensive review by Steiner and Ulrich [1] and the textbook by Hayashi [2] are particularly recommended.

1.2 Applications of spin chemistry

1.2.1 Chemical physics

Studies of chemical MFEs and related phenomena have provided a good deal of insight into basic chemical physics. A good example of this contribution is in the theory of the diffusive motion of molecules. The magnitude and features of CIDNP, CIDEP and chemical magnetic field effects depend critically on the diffusive motion of the radical pair. Adrian [47–50] and Pedersen and Freed [18–23, 51] introduced in some detail the concept of a radical pair making diffusive excursions to separations beyond those where exchange dominates the RP spin evolution before either separating for ever to form freely diffusing "F-pairs" or re-encountering one-another and perhaps reacting. The close agreement, in strong magnetic fields, of experiment and calculations made according to their model validates these concepts.

More recently, Pedersen has shown how to incorporate treatments of diffusion in many different media in strong magnetic fields into a unified theory based on appropriate Green's functions [52]. He has used this formalism to interpret experiments measuring the effect of viscosity on the hydrogen abstraction reaction of 4-methoxybenzophenone with thiophenol [53]. Other workers have studied RP reactions in micelles [54–58] or in more esoteric systems such as carbon nanotubes [59] where the diffusive motion of radicals is quite different to that in isotropic solution. Accurate simulation of such experiments depends on a sound physical model of diffusion and is a good test of the theory. In Chapter 2, we introduce new methods to analyse MFE data for the reaction between pyrene and N,N-dimethylaniline in order to extract details of the radicals' diffusive motion.

Another aspect of chemical physics in which magnetic field effect studies have contributed to our understanding is electron site exchange ("hopping"). Grampp and coworkers made measurements of reaction yield as a function of magnetic field strength, an experiment known as magnetically altered reaction yield (MARY) spectroscopy, for several donor-acceptor systems that react via radical ion pair intermediates. From these data, they were able to extract rate constants for the electron self-exchange processes that occur as the radical ions transfer electrons to or from closed shell, neutral solvent molecules [60–62].

Finally, RP reactions may be subjected simultaneously to static magnetic fields and to microwaves or to radio waves. A number of magnetic resonance experiments are based around this idea. Examples include reaction yield detected magnetic resonance (RYDMR) which involves microwave irradiation in static fields of around 1 T and the optically detected zero-field EPR experiment developed in Oxford that we describe in Chapter 4 where weaker fields $B_0 \leq 20\,\mathrm{mT}$ and MHz RF fields are used. RYDMR has been used to probe the reactions occurring during photosynthesis [63–65] and more recently to study the electron-hole recombination in organic light emitting diodes [66].

(a) Suggestions that EMFs from electricity transmission lines and mobile telephones cause leukaemia have caused controversy in recent years [68–72].

(b) The European robin (*Erithacus rubecula*) was shown to possess a magnetic compass sense in 1966 [73]. This work was later published in English [74].

Figure 1.2: Spin chemistry has made important contributions to research on the biological effects of magnetic fields.

The field of "spintronics" may offer many exciting physical and technological applications for similar experiments in the future [67].

1.2.2 Biological relevance

Spin chemistry, particularly the study of MFEs, has also made significant contributions in the life sciences. We have been particularly interested in two of these contributions, illustrated in Figure 1.2. This thesis is motivated by a desire to lay firm theoretical, physico-chemical foundations upon which discussion of the biological effects of magnetic fields may be grounded.

First, environmental electromagnetic fields are alleged to have effects on human health. Examples include fears that mobile telephones [71] and electricity transmission lines [70] might cause cancer, particularly childhood leukaemia. Anthropogenic EMFs are ubiquitous, invisible, colourless, odourless and tasteless, making claims that they pose a hazard to health apt to cause widespread concern. Hence, many epidemiological studies have attempted to assess the validity of these charges [68–72]. Controversy in this area is increased further by many dubious claims that magnets or magnetic fields possess healing qualities [75]. In the words of Atkins, "the study of the effect of magnetic fields on chemical reactions has long been a romping ground for charlatans" [76].

Yet, the stakes in the debate on EMFs are very real. To be over-cautious in setting legal limits for exposure to EMFs may do more harm than good. One example is the recent EU directive on electromagnetic fields which "in its present form ... severely hinders the clinical use of MRI and also threatens research in this field" [77]. There is a need for basic scientific research to understand the physical mechanisms by which environmental EMFs interact with living tissue, particularly with the human body [78]. Without this understanding, it is almost impossible to design appropriate epidemiological studies, or to set evidence-based exposure limits. As the only established mechanism by which weak magnetic fields may influence chemical reactions, studies of the radical pair mechanism and associated chemical magnetic field effects make an important contribution to this debate [41, 79, 80].

The second biological application of spin chemistry is in the field of animal navigation. Many animals have a magnetic sense which enables them to use the Earth's magnetic field as a "map" or "compass" in order to find their way as they migrate. A review of the literature on animal magnetoreception is given in Chapter 6. Experiments in migratory birds, especially the European robin *Erithacus rubecula*, suggest that their magnetic sense is perhaps based on a chemical magnetic field effect in a radical pair reaction occurring in the retina. In Chapters 7–9, we take up this RPM hypothesis, performing a number of detailed modelling studies in order to assess whether it is consistent with results from behavioural experiments on robins.

1.2.3 Weak magnetic fields

The other theme that unites the work described in the following chapters is a focus on the chemical effects of weak magnetic fields [43]. By weak, we mean magnetic fields whose electron Zeeman interaction energy is comparable to or smaller than the energy of the hyperfine interaction between electron and nuclear spins. For typical organic radicals, this means that we are chiefly concerned with $B_0 \sim 1\,\mathrm{mT}$ magnetic fields.

The spin chemistry of weak magnetic fields is interesting because of its relevance to the biological applications discussed above and also because many of the simplifying assumptions and approximations associated with work at high fields $B_0 \sim 1\,\mathrm{T}$ no longer apply. In Chapters 2–5, we analyse and interpret theoretically results from several experiments performed by other members of the Oxford group. We tackle the breakdown in weak fields of the established high-field EPR selection rules and of the rotating frame approximation in Chapters 4 and 5. Other workers are pursuing similar objectives, for example in the study of modified photosynthetic reaction centres [81] and MFEs in enzyme reactions [82, 83].

In conclusion, this thesis is concerned with spin chemistry in the weak fields that are relevant to biological applications. We are particularly concerned to explore and develop a sound theoretical basis for chemical magnetic field effects in weak magnetic fields. We are also interested in developing spectroscopic techniques that employ weak magnetic fields and in the physico-chemical information that they yield about the diffusive and other processes occurring during RPM reactions in liquids.

1.3 Essential theoretical background

Having discussed the context and motivation for the work presented in this thesis, we conclude by introducing a few elements of theoretical background that are necessary to understand the work that follows. There is insufficient space to give a detailed account of some of these topics, but the interested reader is encouraged to consult the literature. The book by Hayashi [2] is particularly recommended as an introduction to spin chemistry, whilst those by Ernst [84], Slichter [85] and Levitt [86] give good accounts of the relevant theoretical aspects of magnetic resonance.

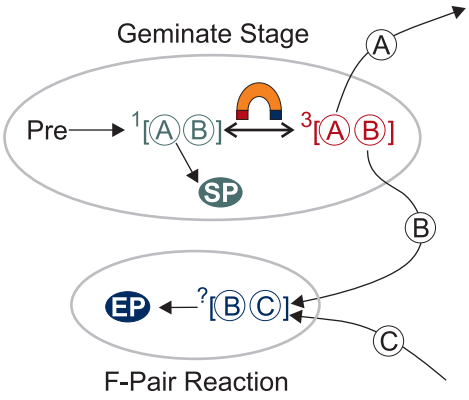

Figure 1.3: Schematic depiction of the radical pair mechanism in liquids.

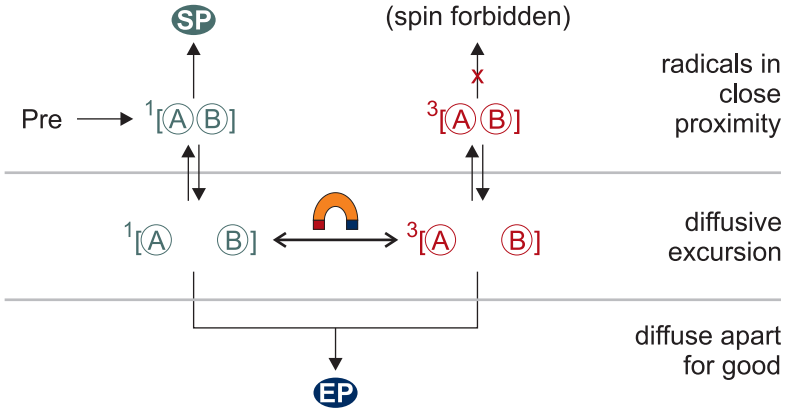

Figure 1.4: Expanded schematic depiction of reactions during the geminate phase which are part of the radical pair mechanism in liquids.

1.4 Radical Pair Mechanism

The radical pair mechanism (RPM) [13, 14, 87] provides the mechanistic basis for our interpretation of magnetic field effects in chemical systems. A generic scheme for reactions occurring in the liquid phase is given in Figure 1.3. Further details of the critical geminate stage where magnetic fields arise are given in Figure 1.4. The essential features are as follows:

- The precursor or precursors (Pre) react to form two radicals (A and B) whose electron spins are correlated. We refer to these radicals as a spin-correlated radical pair (SCRP) or radical pair (RP) for short. For example, when UV light is shone onto a solution of pyrene (Py) and N,N-dimethylaniline (DMA) photochemically-induced electron transfer occurs between Py and DMA precursors to give $Py^{\bullet-}$ and $DMA^{\bullet+}$ radical ions. Since the precursors, Py and DMA, are closed-shell $S = 0$ molecules, and since spin is conserved during electron transfer, the radical ions are generated exclusively in a mutual singlet $S = 0$ spin state. They are described as a singlet radical (ion) pair. Other means of generating RPs include hydrogen abstraction, which often occurs after excitation in micellar systems, and homolytic bond breaking.

- Immediately after their creation, the radicals (A and B) are trapped in very close

proximity inside the same solvent cage. The processes occurring during this "geminate stage[1]" are depicted in Figure 1.4.

- For the first $\sim 500\,\text{ps}$ after their creation, the radicals are caught in very close proximity by a "cage" of surrounding solvent molecules. They collide frequently with one another during this first "encounter". A proportion of the RPs react during these frequent collisions. This is known as "primary geminate recombination".

- The extent of primary geminate recombination is not affected by magnetic fields. Indeed, for Py and DMA in fields $B_0 < 20\,\text{mT}$ there are no magnetic field effects for approximately 2 ns as we show experimentally in Chapter 2. Primary geminate recombination contributes a constant background signal in MFE experiments, which is often suppressed using modulation and phase sensitive detection techniques. Hence, in our analysis of MFEs, we are normally quite free to ignore such fast-reacting RPs.

- Some RPs, however, do not react in the very first instants after RP creation. These separate somewhat and diffuse in the surrounding liquid. They are said to make a diffusive excursion.

- During these diffusive excursions, the exchange interaction between electron spins that was very large when the radicals were in close proximity is much less significant. Instead, the RP spin state evolves (between overall singlet and triplet states) under the influence of molecular hyperfine interactions and, crucially, under the influence of any applied magnetic field.

- After a diffusive excursion, RPs may either separate for good, whence they react ultimately to form escape products (EP), or they may move back into close proximity, which is known as a re-encounter.

- During a re-encounter the radicals are once more held within a solvent cage and undergo frequent collisions, which afford them opportunity to react with one another. Such reactions are known as "secondary geminate recombination". Whether the radicals react or not during a re-encounter depends on the spin evolution during the preceding diffusive excursion. For example, in the reaction between Py and DMA, spin is conserved during the back electron transfer reaction to form an exciplex. This means that the radicals may only undergo back electron transfer during a re-encounter when the RP is in an overall singlet spin state. We refer to such products as the "singlet product" (SP). RPs in a triplet state can do nothing other than to separate once more.

The key feature of the RPM is the spin evolution between singlet and triplet states during diffusive excursions in the geminate stage. In weak magnetic fields, this is driven primarily by the hyperfine interaction. Externally applied magnetic fields affect the rate and extent of this spin evolution and hence they may affect the yield of

[1]The definitions of various terminology for chemical kinetics that we use here are those recommended by IUPAC [88, 89]. There is some variation in terminology amongst the spin chemistry community.

secondary geminate recombination products, *i.e.* the yield of SP. Since this is an activationless kinetic effect, even weak magnetic fields whose interaction energies are far less than the thermal energy $k_{\mathrm{B}}T$ may cause significant changes in the yield of singlet products.

1.5 Spin evolution

Chemical MFEs arising from the RPM depend critically on the manner in which the overall RP spin state evolves during diffusive excursions in the geminate stage. They derive from a detailed interplay of the interactions of the unpaired electron spins and of the diffusional motion of the radicals. We discuss first the electron spin evolution.

The unpaired electron spins and their selective reactivity are inherently quantum mechanical. In full generality, we ought to describe them by a wavefunction $\Psi(\boldsymbol{r}_i, \boldsymbol{s}_i, t)$ evolving under the influence of a Hamiltonian $\hat{H}(t)$, where $\boldsymbol{r}_i$ and $\boldsymbol{s}_i$ are the spatial and spin coordinates of the i^{th} electron. Of course, the unpaired electrons would interact with all the other, paired, electrons in each radical giving rise to electron correlation effects. Solving the Schrödinger equation for a radical pair described at this level of detail would be a formidable undertaking. Even after making the Born-Oppenheimer approximation, we would need to complete a full time-dependent quantum chemical calculation for every diffusive step. It is doubtful whether, even with contemporary computing hardware, such a calculation would be feasible for any radicals of chemical interest.

1.5.1 Spin Hamiltonian

Fortunately, it is not necessary to work in such generality. As in so much of science, the key to developing a useful theory of MFEs is to keep things as simple as possible, making as many simplifying assumptions as are permitted by experimental data. The first, and most essential, approximation that we make is to treat the time evolution of the electron spin and spatial coordinates separately. We do this by converting the full Hamiltonian into a spin Hamiltonian, which contains a number of empirical parameters, and the full wavefunction into a wavefunction containing only spin variables [90, 91]. The spin Hamiltonian approach is ubiquitous in magnetic resonance. Fortunately for us, this means that the form of the contributions to the spin Hamiltonian arising from different magnetic interactions is already well known (see [86, ch7] and [92, p434ff]). Indeed, modern quantum chemical methods are able to calculate accurately many of the spin Hamiltonian parameters that we require.

1.5.2 Vector operators

Many contributions to the RP spin Hamiltonian are most elegantly expressed using the notation of vector operators. We pause briefly to show how this notation applies to the operators for an electron spin.

The bulk magnetisation of a sample of electron spins is a quantum mechanical observable or expectation value. In some circumstances, e.g. when discussing Stern-Gerlach experiments, the uncertainty principle and the Einstein-Podolsky-Rosenberg paradox, it is most helpful to talk in terms of the separate observables $S_x = \langle \hat{S}_{\mathrm{x}} \rangle$,

$S_y = \langle \hat{S}_\mathrm{y} \rangle$ and $S_z = \langle \hat{S}_\mathrm{z} \rangle$ that describe the components of the bulk magnetisation along the x-, y- and z-axes respectively.

The notation is simplified by defining an electron spin *vector operator*

$$\hat{\boldsymbol{S}} = \hat{S}_\mathrm{x}\boldsymbol{i} + \hat{S}_\mathrm{y}\boldsymbol{j} + \hat{S}_\mathrm{z}\boldsymbol{k} \tag{1.1}$$

where $\boldsymbol{i}$, $\boldsymbol{j}$ and $\boldsymbol{k}$ are unit vectors along the x-, y- and z-axes respectively. The expectation value of this vector operator is the electron spin magnetisation *vector*

$$\left\langle \hat{\boldsymbol{S}} \right\rangle = \langle \hat{S}_\mathrm{x} \rangle \boldsymbol{i} + \langle \hat{S}_\mathrm{y} \rangle \boldsymbol{j} + \langle \hat{S}_\mathrm{z} \rangle \boldsymbol{k}. \tag{1.2}$$

Vector operators provide a compact notation. For example, the singlet projection operator may be defined as

$$\hat{P}^\mathrm{S} = \frac{1}{4} - \hat{\boldsymbol{S}}^\mathrm{A} \cdot \hat{\boldsymbol{S}}^\mathrm{B}, \tag{1.3}$$

where A and B label two electron spins and where the dot product "$\cdot$" between vector operators is to be interpreted as

$$\hat{\boldsymbol{S}}^\mathrm{A} \cdot \hat{\boldsymbol{S}}^\mathrm{B} = \hat{S}_\mathrm{Ax}\hat{S}_\mathrm{Bx} + \hat{S}_\mathrm{Ay}\hat{S}_\mathrm{By} + \hat{S}_\mathrm{Az}\hat{S}_\mathrm{Bz} \tag{1.4}$$

which is itself another operator.

Finally, if we choose a set of basis functions, it is, of course, possible to write vector operators in the Hilbert space matrix formalism. For example, the electron spin vector operator is proportional to

$$\hat{\boldsymbol{S}} = \begin{pmatrix} 0 & 1/2 \\ 1/2 & 0 \end{pmatrix} \boldsymbol{i} + \begin{pmatrix} 0 & -\mathrm{i}/2 \\ \mathrm{i}/2 & 0 \end{pmatrix} \boldsymbol{j} + \begin{pmatrix} 1/2 & 0 \\ 0 & -1/2 \end{pmatrix} \boldsymbol{k} \tag{1.5}$$

in the eigenbasis of $\hat{S}_\mathrm{z}$.

1.5.3 Zeeman interaction

In a rotationally symmetric potential, such as in an atom, the Zeeman interaction between an electron and a magnetic field is [93]

$$\hat{H}_\mathrm{Z} = \mu_\mathrm{B} \left(\hat{\boldsymbol{L}} + g_\mathrm{e} \hat{\boldsymbol{S}} \right) \cdot \boldsymbol{B}, \tag{1.6}$$

where μ_B is the Bohr magneton, $\hat{\boldsymbol{L}}$ is the electron orbital angular momentum vector operator, g_e is the free electron g-factor, and $\boldsymbol{B}$ is the magnetic field vector. The values of μ_B and g_e are given in Appendix D.

In a molecule, the electric potential field is no longer rotationally symmetric. As a consequence, there are complicated interactions between the electrons, which are responsible for spin–orbit coupling. In molecules, we introduce the tensor g to account for these complexities. For a particular molecule in a particular electronic state, the Zeeman interaction may therefore be written [93]

$$\hat{H}_\mathrm{Z} = \mu_\mathrm{B} \hat{\boldsymbol{S}} \cdot \mathrm{g} \cdot \boldsymbol{B}. \tag{1.7}$$

The g-tensor is often determined empirically from EPR spectra. Alternatively, modern density functional theory (DFT) methods allow reasonably accurate calculation of the g-tensor for molecules as large as a small protein [94, 95].

For the small organic molecules and weak fields that we consider in this thesis, it is reasonable to assume that the g-tensor is that of a free electron. Hence

$$\hat{H}_{\mathrm{Z}} = g_{\mathrm{e}}\mu_{\mathrm{B}}\hat{\boldsymbol{S}}\cdot\boldsymbol{B} = -\gamma_{\mathrm{e}}\hbar\hat{\boldsymbol{S}}\cdot\boldsymbol{B}, \tag{1.8}$$

where we have introduced the electron magnetogyric ratio $\gamma_{\mathrm{e}} = -|g_{\mathrm{e}}|\,\mu_{\mathrm{B}}/\hbar$. Finally, if we write the Hamiltonian in angular frequency units as is done throughout the body of this thesis, then

$$\hat{H}_{\mathrm{Z}} = -\gamma_{\mathrm{e}}\hat{\boldsymbol{S}}\cdot\boldsymbol{B}. \tag{1.9}$$

The nuclei in a RP also experience Zeeman interactions with the applied magnetic field, but these are negligible because nuclear magnetogyric ratios (see Appendix D) are many times smaller than that of the electron and because we will only be concerned with weak applied fields where the nuclear Zeeman interaction is much weaker than the hyperfine interaction.

1.5.4 Zeeman resonance

If we define the z-axis to lie along the magnetic field orientation so that $\boldsymbol{B} = B_0\boldsymbol{k}$, then to first order, the Zeeman energy for an electron spin eigenstate $\hat{S}_{\mathrm{z}}|m_{\mathrm{s}}\rangle = m_{\mathrm{s}}\hbar|m_{\mathrm{s}}\rangle$ is

$$E_{\mathrm{Z}} = -\gamma_{\mathrm{e}}\hbar m_{\mathrm{s}}B_0. \tag{1.10}$$

The selection rule for transitions between these states is that $\Delta m_{\mathrm{s}} = \pm 1$. This transition is therefore in resonance with photons of frequency ν_{rf} where

$$h\nu_{\mathrm{rf}} = \Delta E_{\mathrm{Z}} = |\gamma_{\mathrm{e}}|\,\hbar B_0 \tag{1.11}$$

and hence a Zeeman resonance might be expected for radio frequencies

$$\nu_{\mathrm{rf}} = \frac{|\gamma_{\mathrm{e}}|}{2\pi}B_0 = \left(28.025\,\mathrm{MHz\,mT^{-1}}\right)\times B_0 \tag{1.12}$$

or equivalently at field strengths

$$B_0 = \frac{2\pi}{|\gamma_{\mathrm{e}}|}\nu_{\mathrm{rf}} = \left(35.682\,\mu\mathrm{T\,MHz^{-1}}\right)\times \nu_{\mathrm{rf}}. \tag{1.13}$$

1.5.5 Hyperfine interaction

The Zeeman interaction couples the unpaired electron spin of a radical with an external applied magnetic field. In contrast, the hyperfine interaction couples the unpaired electron spin with the internal magnetic field from the spins of magnetic $I > 0$ nuclei in the radical. The hyperfine interaction is made up of two contributions [92, p438ff].

The first of these is the direct dipolar interaction between the magnetic moments of the unpaired electron and the nucleus in question. When MFEs are measured in

isotropic liquid phases, as is the case in Chapters 2–5, this dipolar interaction is averaged to zero by rapid tumbling of the radicals. In the solid state or in oriented media, these dipolar contributions make the hyperfine interaction anisotropic. We discuss this point in Chapter 7. The anisotropic part of the hyperfine interaction may be calculated from the electron density in the singly occupied molecular orbital (SOMO), which may itself be calculated using DFT.

The other contribution to the hyperfine interaction is known as the Fermi contact interaction. It is caused by the magnetic interaction of the electron and nuclear spins when the electron is *within* the nucleus. As such, it is proportional to the s-orbital character of the SOMO around the nucleus in question. The Fermi contact interaction is isotropic; it does not depend on the orientation of the electron or nuclear spins with respect to the molecule, but only on their relative orientation. We describe the Fermi contact interaction by the spin Hamiltonian

$$\hat{H}_{\mathrm{HFI}} = a_{i\mathrm{N}} \hat{\boldsymbol{S}}^{\mathrm{N}} \cdot \hat{\boldsymbol{I}}_i \tag{1.14}$$

where $a_{i\mathrm{N}}$ is the isotropic hyperfine coupling constant for interaction between an electron $\hat{\boldsymbol{S}}^{\mathrm{N}}$ and nuclear spin $\hat{\boldsymbol{I}}_i$. Hyperfine coupling constants for the radicals studied in this thesis are tabulated in Appendix A.

1.5.6 Exchange interaction

We normally think of the radicals in a RP as separate entities. Within each radical, Coulombic forces between the electrons and the nuclei determine the radical's geometry and electronic structure. These, in turn, produce contributions to the radical spin Hamiltonian characterised by the g-tensor and hyperfine tensors.

However, this picture is incomplete. For a full treatment, we ought also to include the Coulombic interactions between all the nuclei and electrons on one radical with those on the other radical. Figures 1.5 and 1.6 illustrate these effects for a radical pair comprising two hydrogen atoms $\mathrm{H}^{\bullet}$, *i.e.* for a streched H_2 molecule.

- As the hydrogen atoms are brought together, their electronic wavefunctions begin to overlap. The interaction between the atomic wavefunctions produces bonding $1\sigma_{\mathrm{g}}$ and anti-bonding $2\sigma_{\mathrm{u}}^{*}$ molecular orbitals (one-electron molecular wavefunctions) as shown in Figure 1.5.

- According to the orbital approximation, the n-electron wavefunction for the RP as a whole is given as a symmetrised product of these one-electron molecular orbitals.

- The lowest energy state (n-electron wavefunction) arises when both electrons occupy the $1\sigma_{\mathrm{g}}$ MO. According to the Pauli principle, this is only possible when the electron spins are paired to give a ${}^{1}\Sigma_{\mathrm{g}}^{+}$ state.

- The next state arises when one electron is promoted to the $2\sigma_{\mathrm{u}}^{*}$ MO. This time, the Pauli principle permits ${}^{3}\Sigma_{\mathrm{u}}^{+}$ and ${}^{1}\Sigma_{\mathrm{u}}^{+}$ states.

- According to Hund's rules, the ${}^{3}\Sigma_{\mathrm{u}}^{+}$ state is the lower in energy.

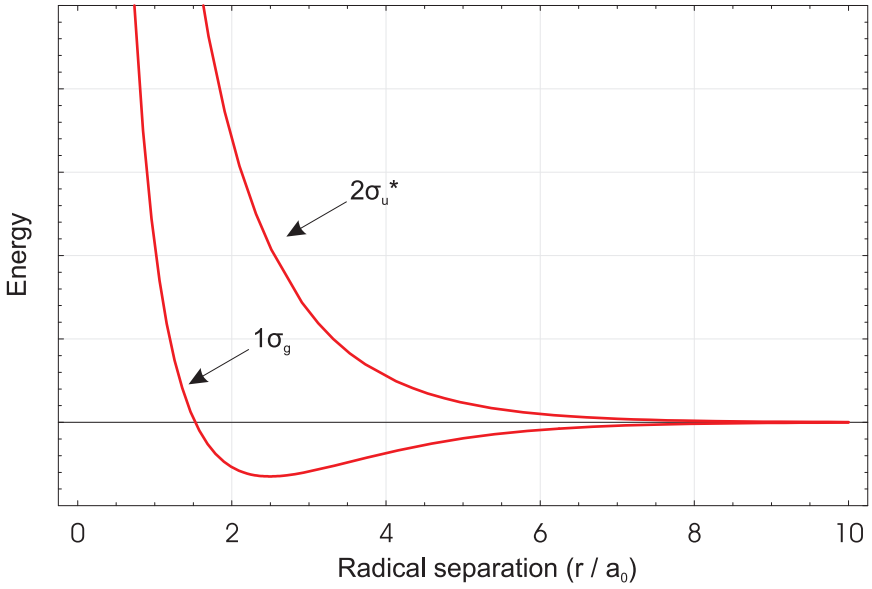

Figure 1.5: First two LCAO molecular orbital energies for the hydrogen molecular ion H_2^+ as a function of internuclear separation [96, p420]. These are a first approximation to the molecular orbital energies of the neutral hydrogen molecule H_2, neglecting shielding effects.

- Figure 1.6 shows the energies of the ${}^1\Sigma_g^+$ ground state (labelled "S" for singlet) and the ${}^3\Sigma_u^+$ first excited state (labelled "T" for triplet). The energy difference between these states, denoted $J(r)$, depends on the radical separation r.

To describe the spin evolution of a RP where the radicals approach closely enough for inter-radical electron correlation and bonding effects to set in, we use the Heisenberg-Dirac-van Vleck (HDVV) spin Hamiltonian [97]

$$\hat{H}_{\text{ex}} = -J\hat{\boldsymbol{S}}_{\text{A}} \cdot \hat{\boldsymbol{S}}_{\text{B}}. \tag{1.15}$$

The empirical parameter J is chosen so that the HDVV eigenstates have the same energy separation as the ground and first excited states when the Schrödinger equation is solved for the "molecule" comprising both radicals taken together. For a RP, this means that J is the difference in energy between the lowest energy singlet and triplet states.

It is a formidable task to calculate J for radicals in solution. Quantum chemically, this is equivalent to calculating the energy levels in a loosely bound "molecule" comprising the radicals A and B together with any solvent molecules in proximity. The solvent molecules can be particularly significant because they can mediate the interaction between the unpaired electrons on each radical in a process known as superexchange. Nevertheless, the availability of modern configuration interaction (CI) *ab initio* and DFT methods running on modern computer hardware is beginning to make such calculations feasible [97]. The first comparison of DFT calculations with experimental measurements of *intermolecular J* values was made in solid state lophyl radical pairs in 2001 by Abe [98].

In spin chemistry, the exchange interaction is normally assumed to decrease exponentially with increasing RP separation and to be independent of the orientation of the

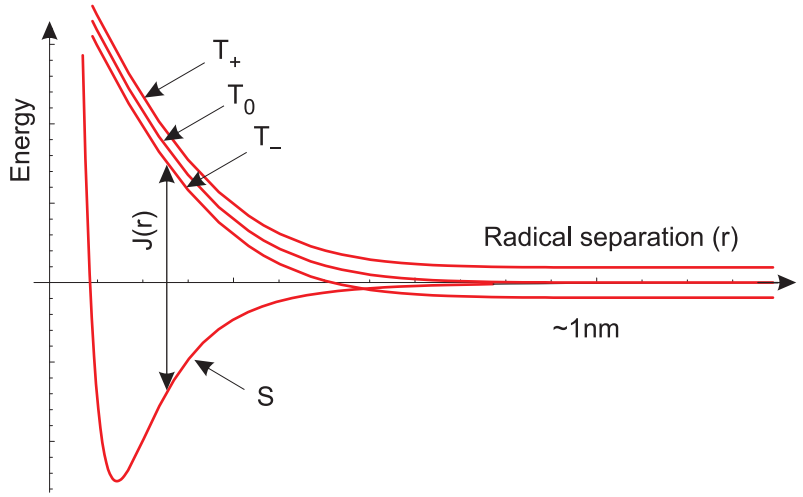

Figure 1.6: Approximate energies for the ground ($^1\Sigma_g^+$ "S") and first excited ($^3\Sigma_u^+$ "T") states of a pair of hydrogen atoms as a function of internuclear separation r. When r is short, the hydrogen atoms are bonded and should best be thought of as an H_2 molecule. At long separations, we could better describe this system as a $[H^\bullet\ H^\bullet]$ radical pair. The separation between S and T_0 states is labelled $J(r)$. The $T_\pm$ and T_0 states are split apart due to the Zeeman interaction.

radicals and of the solvent [87]. In other words

$$J(r) \approx J_0 \mathrm{e}^{-r/r_J} \tag{1.16}$$

where the magnitude $J_0 \sim 2 \times 10^{17}\,\mathrm{rad\,s^{-1}}$, r is the inter-radical separation and $r_J \sim 50\,\mathrm{pm}$ is a range parameter. In 2005, Sinks studied exchange in a series of related electron transfer triad molecules using a combination of MFE measurements and DFT calculations [99]. Unfortunately, it was only possible to determine J values in two of these molecules. Further work may soon enable the accuracy of equation (1.16) to be assessed.

In RP reactions, exchange acts to prevent singlet–triplet interconversion. Hence, whenever the radicals are close enough that exchange dominates the RP spin Hamiltonian no magnetic field effects may arise. For example, exchange suspends RP spin evolution during each diffusive encounter as discussed in §1.4.

1.5.7 Dipolar interaction

Each unpaired electron spin also experiences a magnetic field from the other unpaired electron. These dipolar interactions may be described by the Hamiltonian [84]

$$\hat{H}_\mathrm{D} = \frac{\mu_0 \mu_\mathrm{B}^2 g_\mathrm{A} g_\mathrm{B}}{4\pi\hbar^2 r^3} \left[\hat{\boldsymbol{S}}_\mathrm{A} \cdot \hat{\boldsymbol{S}}_\mathrm{B} - \frac{3}{r^2} (\hat{\boldsymbol{S}}_\mathrm{A} \cdot \boldsymbol{r})(\hat{\boldsymbol{S}}_\mathrm{B} \cdot \boldsymbol{r}) \right] \tag{1.17}$$

in angular frequency units where g_i are the electron g-factors for each radical and $\hat{\boldsymbol{S}}$ are the electron spin vector operators. Equation 1.17 is, strictly speaking, only valid for point dipoles separated by a vector $\boldsymbol{r}$. In real molecules, $\boldsymbol{r}$ is closely approximated by the vector between the "centres" of the SOMOs on each radical. Simple algebraic

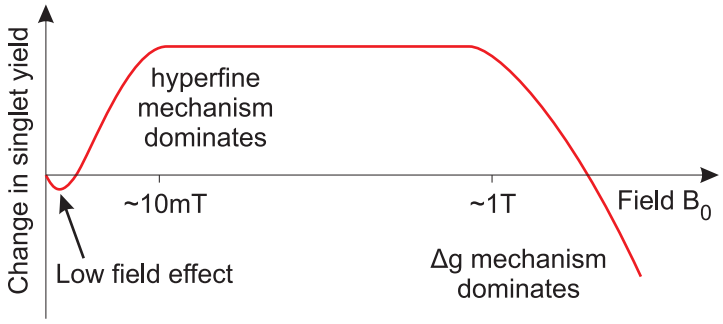

Figure 1.7: Typical magnetic field effects in organic RPs from zero field up to a few Tesla.

manipulations allow equation (1.17) to be written

$$\hat{H}_{\mathrm{D}} = \hat{\boldsymbol{S}}_{\mathrm{A}} \cdot \mathsf{D} \cdot \hat{\boldsymbol{S}}_{\mathrm{B}} \tag{1.18}$$

in terms of the dipolar tensor D. At high field, diffusive motion of one radical around the other causes the dipolar interaction to average to zero. In weak fields, the situation is more complicated. Detailed calculations show that at weak fields, the dipolar interaction acts to suppress magnetic field effects [100].

1.5.8 Summary

This thesis considers magnetic field effects on the RP reactions between various organic radicals. The data presented in later chapters were taken in fields $B_0 < 50\,\mathrm{mT}$. At these field strengths, the singlet–triplet interconversion responsible for magnetic field effects is governed primarily by the isotropic electron Zeeman and the hyperfine interactions. This is known as the hyperfine mechanism. At higher fields, the situation is rather different. There, singlet–triplet interconversion arises for the most part because of small differences in the g-tensors of the two radicals, in what is known as the Δg-mechanism. Figure 1.7 summarises this change in mechanism.

1.6 Diffusion

We saw in §1.4 that magnetic field effects on reactions proceeding via the RPM arise because an applied magnetic field alters the extent of singlet–triplet interconversion during each diffusive excursion of a RP. The rate and extent of singlet–triplet interconversion may be calculated by solving the Schrödinger equation (or equivalently the Liouville-von Neumann equation) for an appropriate spin Hamiltonian containing the terms outlined above. In other words, we may calculate the probability that the RP is in a singlet state $\left\langle \hat{P}^{\mathrm{S}} \right\rangle (t)$ at a time t after the end of the primary geminate encounter, *i.e.* after the radicals have separated to a point where the exchange interaction no longer quenches singlet–triplet interconversion.

Following Noyes [101], we describe the diffusion controlled aspects of the RPM in terms of a re-encounter probability distribution $f(t)$. For a pair of radicals that were created together and have subsequently diffused apart, $f(t)\,\mathrm{d}t$ is the probability that the same radicals next encounter one another between times t and $t + \mathrm{d}t$. If subsequent

re-encounters are important, one may also define $f_n(t)$ analogously as the probability distribution for an n$^{\text{th}}$ re-encounter at time t.

Since only RPs in a singlet spin state are able to react during a re-encounter, the probability of reaction is $\left\langle \hat{P}^{\mathrm{S}} \right\rangle (t) f(t)\,\mathrm{d}t$. Hence, the yield of singlet product ("singlet yield" Φ_{S}) from first re-encounters is

$$\Phi_{\mathrm{S}} = \int_0^\infty \left\langle \hat{P}^{\mathrm{S}} \right\rangle (t) f(t)\,\mathrm{d}t. \tag{1.19}$$

It is often assumed that after a first re-encounter, radicals either react or diffuse apart for ever.

In the analysis of magnetic field effects and other spin chemical effects, two functional forms of $f(t)$ are used widely. The "exponential model" [13, 15, 79] takes

$$f(t) = k\mathrm{e}^{-kt} \tag{1.20}$$

where k is a phenomenological rate constant. The "diffusion model" introduced by Adrian [47–49], assumes that the radicals diffuse in a random flight during each excursion. After some algebra, this assumption gives a re-encounter probability

$$f(t) = \frac{R_\sigma (R_0 - R_\sigma)}{R_0} \left(\frac{1}{4\pi D t} \right)^{\frac{3}{2}} \exp\left(-\frac{(R_0 - R_\sigma)^2}{4Dt} \right) \tag{1.21}$$

where R_σ is the distance at which the radicals may react to form products, R_0 is the separation of the radicals as they are created (*i.e.* as they leave the strong exchange region) and D is the mutual diffusion coefficient for the two radicals. We discuss the role of diffusion in RP reactions in Chapter 2, showing that it is possible to extract an empirical re-encounter probability distribution $f(t)$ directly from experimental magnetic field effect measurements.

1.7 Other effects

Our treatment of RP reactions produces good qualitative results quickly by considering separately the spin evolution and diffusion of radicals. Yet, in some circumstances, it is important to allow connections between the RP spin evolution, diffusion and reaction. For instance, the exchange and dipolar interactions vary strongly as a function of inter-radical separation. This means that, at the end of a diffusive excursion, the RP spin state can depend in detail on the path that the radicals took. In other instances, second and subsequent re-encounters are significant. These effects may be modelled by treating the exchange and dipolar interactions as stochastic perturbations to the RP spin Hamiltonian. Product yields may then be found using a stochastic Liouville equation [102, 103], albeit at a cost of more time- and memory-intensive calculation. Furthermore, stochastic processes are responsible for non-coherent relaxation of RP spin states towards thermal equilibrium. At present, relaxation in the weak magnetic fields with which we are concerned is only poorly understood. Indeed, it is a topic of ongoing research by Wagner-Rundell [104].

Formula	SI units	Angular frequency units
$E = \hbar\omega$	$1\,\mathrm{rad\,s^{-1}} = \hbar\,\mathrm{J}$	
	$\approx 1.05 \times 10^{-34}\,\mathrm{J}$	
$E = h\nu$	$1\,\mathrm{Hz} = h\,\mathrm{J}$	$1\,\mathrm{Hz} = 2\pi\,\mathrm{rad\,s^{-1}}$
	$\approx 6.63 \times 10^{-34}\,\mathrm{J}$	$\approx 6.28\,\mathrm{rad\,s^{-1}}$
	$1\,\mathrm{MHz} = 10^6 h\,\mathrm{J}$	$1\,\mathrm{MHz} = 2\pi \times 10^6\,\mathrm{rad\,s^{-1}}$
	$\approx 6.63 \times 10^{-28}\,\mathrm{J}$	$\approx 6.28 \times 10^6\,\mathrm{rad\,s^{-1}}$
$\Delta E = g_e \mu_\mathrm{B} B$ [a]	$1\,\mathrm{T} = g_e \mu_\mathrm{B}\,\mathrm{J}$	$1\,\mathrm{T} = -\gamma_\mathrm{e}\,\mathrm{rad\,s^{-1}}$
	$\approx 1.86 \times 10^{-23}\,\mathrm{J}$	$\approx 1.76 \times 10^{11}\,\mathrm{rad\,s^{-1}}$
	$1\,\mathrm{mT} = g_e \mu_\mathrm{B} \times 10^{-3}\,\mathrm{J}$	$1\,\mathrm{mT} = -\gamma_\mathrm{e} \times 10^{-3}\,\mathrm{rad\,s^{-1}}$
	$\approx 1.86 \times 10^{-26}\,\mathrm{J}$	$\approx 1.76 \times 10^8\,\mathrm{rad\,s^{-1}}$
		$\approx 2.8 \times 10^7 \times 2\pi\,\mathrm{rad\,s^{-1}}$

[a] This is the vacuum Zeeman energy for an electron in the given field.

Table 1.1: Units of energy: relationships between magnetic resonance units and the International System of Units (SI). Accurate values for physical constants are given in Appendix D.

1.8 Angular frequency units

Best practice, as recommended by IUPAC, calls for the expression of all physical quantities using the International System of Units (SI). Nevertheless, as is conventional in the magnetic resonance community, we write the radical pair spin Hamiltonian in angular frequency units for brevity. RP energy levels are also therefore frequently given in angular frequency units. It is also common amongst the magnetic resonance community, although not recommended and indeed not strictly correct, to express energies in units of magnetic field strength. To avoid confusion, we show briefly how such units may be related to the normal International System of Units (SI). The conversion factors are summarised in Table 1.1.

Chapter 2

Re-encounter distributions from experiment

2.1 Introduction

Magnetic fields can alter the rates and yields of chemical reactions that proceed via spin-correlated radical pair intermediates and so provide information on the structures, dynamics, kinetics and reactivity of free radicals [1, 2, 40, 41, 87]. Chemical magnetosensitivity via the radical pair mechanism (RPM) requires the following sequence of events: first, creation of a pair of radicals, with correlated electron spins, in a pure singlet (S) or pure triplet (T) state; second, coherent evolution of the radical pair between the near-degenerate S and T spin states; and third, reaction of the S and T radical pairs to form different products (or the same product at different rates). It is during the second of these steps that the magnetic field acts — via the electron Zeeman interaction — altering the extent and frequency of singlet–triplet interconversion and hence the relative yields of reaction products and/or the lifetime of the radical pair. RPM magnetic field effects are thus kinetic in origin and may be detected for magnetic fields with Zeeman energies much smaller than the average thermal energy per molecule, $k_{\mathrm{B}}T$.

As the only well-established mechanism by which non-ionising electromagnetic radiation can affect chemical processes, the RPM has featured in debates on the possible adverse health effects of the very weak fields emitted by electrical equipment and power transmission lines [68–70, 72, 78, 79] and has been proposed as a mechanism for the magnetic compass sense of migratory birds [105–107]. In both cases, the magnetic fields involved are weaker than 1 mT such that, for typical organic free radicals, the magnetic electron-nuclear hyperfine interactions in the radical pair are larger than the electron Zeeman interactions. Such systems may demonstrate a "low field effect" (LFE) [10, 108–113], which leads to a decrease in the fraction of singlet-born radical pairs that recombine via the S state (and, conversely, an increase for triplet-born pairs). When present, the LFE dominates the response to magnetic fields that are weaker than the hyperfine interactions. As the magnetic field strength is increased, the LFE gradually gives way to the "conventional" magnetic field effect (MFE) on the relative product yields and/or radical pair lifetime. This change occurs as the Zeeman interaction energy increases and comes to dominate the hyperfine interactions; it can be understood in terms of the detailed interplay of the two types of magnetic interac-

tion and their effects on singlet–triplet interconversion [1, 108]. The MFE has a phase that is opposite to that of the LFE, *i.e.* an increase in S-product yield for a singlet-born radical pair.

Traditionally, two approaches have been taken to quantify MFE data. One is based on the observation that most MFE responses are approximately sigmoidal. The principal variation observed for different radical pairs may therefore be quantified by measuring the zero-field and high-field (saturation) values of the product yield and hence the magnetic field strength, $B_{1/2}$, corresponding to a product yield mid-way between these limits. This approach is discussed in greater detail in Chapter 3. The other approach involves fitting computer simulations of the magnetic field response to experimental data using a set of magnetic interaction parameters (g-tensors, hyperfine couplings, etc.) and a model for the diffusive motion of the radicals. This procedure is most successful when the majority of the parameters are independently known, e.g. g-values and hyperfine coupling constants from EPR or ENDOR spectra or from *ab initio* calculations.

In this chapter, we introduce a novel approach for interpreting LFE and MFE data. To determine more clearly the roles played by spin dynamics and diffusional motion, the effect of an applied magnetic field on the radical ion pair $\left[\mathrm{Py}^{\bullet-}\ \mathrm{DMA}^{\bullet+}\right]$ formed in the photochemical reaction of pyrene (Py) with N,N-dimethylaniline (DMA), whose structures are shown in Figure 2.6, in a viscous solvent has been measured by Norman and Henbest [114]. The exciplex fluorescence produced by this reaction is strong and allows sensitive measurements of the MARY spectrum, that is of singlet product yield as a function of field strength. To allow reliable separation of spin and motion effects, data were recorded for combinations of fully protonated or fully deuterated reactants (Py-h_{10}, Py-d_{10}, DMA-h_{11}, DMA-d_{11}) to obtain four isotopomeric radical pairs. It seems reasonable to suppose that deuteration has little effect on the diffusive motion of the radicals or on their reactivity, but that it will dramatically alter the hyperfine interactions and thus the singlet–triplet interconversion, principally via the 6.5-fold difference in the magnetic moments of ^{1}H and ^{2}H nuclei. Using Tikhonov and maximum entropy regularisation techniques, we show that it is possible to extract detailed information about the diffusive motion of the radicals directly from this experimental data.

A simple way of modelling these diffusive trajectories, introduced by Noyes [101], is in terms of a re-encounter probability distribution $f(t)$. Now, at the instant of their creation, the two radicals that comprise a geminate pair are usually sufficiently close to one another that their mutual exchange interaction is large enough to lock the pair into its initial S or T state [100]. Only when the radicals have separated to a point where the exchange is comparable to the hyperfine and Zeeman interactions (typically 1.0–1.5 nm), can singlet–triplet interconversion start. For the magnetic field to affect the product yield, the radicals have then to diffuse back together ("re-encounter") in order to be able to recombine in a spin-selective fashion, usually from the S state. We assume that the radical pair spin Hamiltonian does not depend substantially on the inter-radical separation during the course of this diffusive excursion. We also assume that each radical pair undergoes only a single re-encounter at which time the radicals either react to form a singlet product, or separate permanently to form triplet (escape)

products. This means that the probability of reaction to form a singlet product is simply

$$\Phi_{\mathrm{S}}(B) = \int_0^\infty \left\langle \hat{P}^{\mathrm{S}} \right\rangle (B,t) f(t)\,\mathrm{d}t \tag{2.1}$$

where $\hat{P}^{\mathrm{S}}$ is the singlet projection operator for the unpaired electron spins in the RP and hence $\left\langle \hat{P}^{\mathrm{S}} \right\rangle (B,t)$ is the probability that the RP will be found in a singlet state for a given magnetic field strength B at a time t measured from the instant of radical pair creation. Finally, $f(t)$ is the probability that the radicals re-encounter at that time.

In model-fitting approaches to magnetic field effects and related phenomena, two functional forms of $f(t)$ have been widely used. The first of these is the "exponential model" [13, 15, 79] which assumes that

$$f(t) = k\mathrm{e}^{-kt} \tag{2.2}$$

where k is a phenomenological rate constant. Alternatively, treating the motion of the radicals as a random walk, one arrives at the "diffusion model" [47–49] in which

$$f(t) = \frac{R_\sigma(R_0 - R_\sigma)}{R_0}\left(\frac{1}{4\pi D t}\right)^{\frac{3}{2}} \exp\left(-\frac{(R_0 - R_\sigma)^2}{4Dt}\right) \tag{2.3}$$

where R_σ is the distance at which the radicals may react to form products, R_0 is the separation of the radicals as they are created and D is the mutual diffusion coefficient for the two radicals. In contrast, our approach here is to extract an empirical $f(t)$ directly from experimental magnetic field effect measurements.

In order to solve equation (2.1) and extract the desired empirical re-encounter distribution, we must possess an accurate knowledge of the singlet probability $\left\langle \hat{P}^{\mathrm{S}} \right\rangle (B,t)$ at all relevant field strengths and times. In other words, we must be in a position to solve accurately the "forward" problem of finding the singlet yield when the re-encounter distribution is known. Calculation of accurate singlet yields is straightforward in simple model radical pairs that have only a limited number of hyperfine couplings, but becomes rapidly more difficult as the number of hyperfine couplings increases. In order to model the spin evolution in radicals such as $\mathrm{Py}^{\bullet-}$ and $\mathrm{DMA}^{\bullet+}$ which have many hyperfine couplings, we will need to make careful use of simplifying factorisations and approximations. In the early parts of this chapter, we therefore discuss methods for calculating product yields in realistic radical pairs. The remainder of the chapter is addressed to the development and evaluation of two methods for solving the "inverse" problem of finding the empirical re-encounter distribution given a set of isotopomer MARY spectra.

2.2 Singlet yield in multinuclear radical pairs

We describe in this section an efficient method for calculating the product yield of a radical pair reaction in the presence of a static magnetic field. This approach will be used throughout this thesis as the standard method for calculating product yields in systems which are not subject to time dependent magnetic fields.

We begin by considering a Hamiltonian of the form

$$\hat{H} = \hat{H}^{\mathrm{A}} + \hat{H}^{\mathrm{B}} \tag{2.4}$$

where $\hat{H}^{\mathrm{N}}$ contains a combination of spin operators which act only on the unpaired electronic and nuclear spins of radical N. Assuming a Hamiltonian of this form allows a dramatic decrease in the computational resources required for calculation in a realistic radical pair, as will become apparent below.

Physically, we have neglected all inter-radical interactions, such as the exchange and dipolar interactions between the unpaired electron spins. The exchange interaction is strongly dependent upon the radical separation, which means that in order to rigorously calculate its effects one must work from the Stochastic Liouville Equation. This would greatly increase the computational effort involved and also, unfortunately, mean that diffusion and the spin-dynamics of the system would be inextricably linked. However, it is often a good approximation to assume that the exchange interaction acts primarily to "freeze" singlet–triplet interconversion whilst the radicals are in close proximity but has negligible effects during a diffusive excursion. For radical pairs in solution, the effects of the dipolar interaction are averaged out by diffusive translational motions of the radicals around one-another [100]. In the solid state, the dipolar interaction may be neglected provided that the correlated radicals are sufficiently separated, perhaps as a result of sequential electron transfer in forming the radical pair.

For solution-phase radical pairs, such as $\left[\mathrm{Py}^{\bullet-}\ \mathrm{DMA}^{\bullet+}\right]$ which is discussed later in this chapter, only a few interactions need to be included in the Hamiltonian. Notably, anisotropic interactions are averaged by molecular tumbling in solution; spin relaxation is insignificant during the short $\left[\mathrm{Py}^{\bullet-}\ \mathrm{DMA}^{\bullet+}\right]$ lifetime; g-value differences between the two radicals are negligible at the fields of interest here; and the nuclear Zeeman interaction is also negligible at these fields. Thus, we consider a model system Hamiltonian (in angular frequency units) containing only terms for the isotropic electron–nuclear hyperfine interaction and the isotropic electron Zeeman interaction:

$$\hat{H}^{\mathrm{N}} = \sum_i a_{i\mathrm{N}}\, \hat{\boldsymbol{I}}_{i\mathrm{N}} \cdot \hat{\boldsymbol{S}}_{\mathrm{N}} - \gamma_{\mathrm{e}} B \hat{S}_{\mathrm{Nz}}, \tag{2.5}$$

in which $\hat{S}_{\mathrm{N}}$ is the unpaired electron spin vector operator, $a_{i\mathrm{N}}$ is the isotropic hyperfine coupling constant for nuclear spin $\hat{\boldsymbol{I}}_{i\mathrm{N}}$, γ_{e} is the electron magnetogyric ratio and B is the applied magnetic field, which is taken to lie along the z-axis for convenience. The dot product "$\cdot$" is defined in §1.5.2.

2.2.1 Time domain

According to equation (2.1), the singlet yield in a RP depends on its spin evolution, expressed in terms of the singlet probability $\left\langle \hat{P}^{\mathrm{S}} \right\rangle (B,t)$. For simplicity of exposition, we confine our attention to radical pairs which are created in and recombine from a singlet state. Working in the density matrix formalism, we write the singlet probability as

$$\left\langle \hat{P}^{\mathrm{S}} \right\rangle = \mathrm{Tr}\left[\hat{\rho}(t)\hat{P}^{\mathrm{S}}\right]. \tag{2.6}$$

The density matrix evolves from its initial singlet state under the influence of the Hamiltonian as

$$\hat{\rho}(t) = U\hat{\rho}(0)U^{\dagger} = \frac{1}{M} U\hat{P}^{\mathrm{S}}U^{\dagger} \tag{2.7}$$

where M is the number of nuclear spin states and the propagator $U = \mathrm{e}^{-\mathrm{i}\hat{H}t}$. Using the fact that $\hat{P}^{\mathrm{S}} \equiv \frac{1}{4}\mathbb{1} - \hat{\boldsymbol{S}}_{\mathrm{A}} \cdot \hat{\boldsymbol{S}}_{\mathrm{B}}$, we begin to separate the calculation onto the two individual radicals. Thus, following Till [115, 116], we write

$$\begin{aligned}\left\langle \hat{P}^{\mathrm{S}} \right\rangle &= \frac{1}{M} \mathrm{Tr}\left[U \left(\frac{1}{4}\hat{\mathbb{1}} - \hat{\boldsymbol{S}}_{\mathrm{A}} \cdot \hat{\boldsymbol{S}}_{\mathrm{B}} \right) U^{\dagger} \left(\frac{1}{4}\hat{\mathbb{1}} - \hat{\boldsymbol{S}}_{\mathrm{A}} \cdot \hat{\boldsymbol{S}}_{\mathrm{B}} \right) \right] \\ &= \frac{1}{M} \left\{ \frac{1}{16} \mathrm{Tr}\left[\hat{\mathbb{1}}\right] - \frac{1}{2} \mathrm{Tr}\left[\hat{\boldsymbol{S}}_{\mathrm{A}} \cdot \hat{\boldsymbol{S}}_{\mathrm{B}} \right] + \mathrm{Tr}\left[U \left(\hat{\boldsymbol{S}}_{\mathrm{A}} \cdot \hat{\boldsymbol{S}}_{\mathrm{B}} \right) U^{\dagger} \left(\hat{\boldsymbol{S}}_{\mathrm{A}} \cdot \hat{\boldsymbol{S}}_{\mathrm{B}} \right) \right] \right\}. \end{aligned} \tag{2.8}$$

Considering these three terms separately, we make the following simplifications:

- These operators are defined in a product basis set which includes the nuclear spins (giving M possible states) and the two unpaired electrons (giving four possible states). Therefore

$$\mathrm{Tr}\left[\hat{\mathbb{1}}\right] = 4M \tag{2.9}$$

- Since the spin operators $\hat{\boldsymbol{S}}_{x,y,z}$ all have zero trace and since addition and the Kronecker product are distributive

$$\mathrm{Tr}\left[\hat{\boldsymbol{S}}_{\mathrm{A}} \cdot \hat{\boldsymbol{S}}_{\mathrm{B}} \right] = \sum_{p=x,y,z} \mathrm{Tr}\left[\hat{S}_{\mathrm{A}p} \hat{S}_{\mathrm{B}p} \right] = \sum_{p=x,y,z} \mathrm{Tr}\left[\hat{S}_{\mathrm{A}p} \right] \mathrm{Tr}\left[\hat{S}_{\mathrm{B}p} \right] = 0 \tag{2.10}$$

- Since all "A" operators commute with all "B" operators, then $U = U^{\mathrm{A}} U^{\mathrm{B}}$ where $U^{\mathrm{N}} = \mathrm{e}^{-\mathrm{i}\hat{H}^{\mathrm{N}}t}$ and

$$\mathrm{Tr}\left[U \left(\hat{\boldsymbol{S}}_{\mathrm{A}} \cdot \hat{\boldsymbol{S}}_{\mathrm{B}} \right) U^{\dagger} \left(\hat{\boldsymbol{S}}_{\mathrm{A}} \cdot \hat{\boldsymbol{S}}_{\mathrm{B}} \right) \right] = \sum_{p,q=x,y,z} \mathrm{Tr}\left[(U^{\mathrm{A}} \hat{S}_{\mathrm{A}q} U^{\mathrm{A}\dagger} \hat{S}_{\mathrm{A}p}) (U^{\mathrm{B}} \hat{S}_{\mathrm{B}q} U^{\mathrm{B}\dagger} \hat{S}_{\mathrm{B}p}) \right] \tag{2.11}$$

Separating the trace into terms on each radical and by cyclic permutation, we define

$$R^{\mathrm{N}}_{pq}(t) = \mathrm{Tr}\left[\hat{S}_{\mathrm{N}p} \mathrm{e}^{-\mathrm{i}\hat{H}^{\mathrm{N}}t} \hat{S}_{\mathrm{N}q} \mathrm{e}^{\mathrm{i}\hat{H}^{\mathrm{N}}t} \right]. \tag{2.12}$$

as a compact notation for the bracketed terms in equation (2.11). Substituting into equation (2.8) gives

$$\left\langle \hat{P}^{\mathrm{S}} \right\rangle (t) = \frac{1}{4} + \frac{1}{M} \sum_{p,q=x,y,z} R^{\mathrm{A}}_{pq}(t) R^{\mathrm{B}}_{pq}(t). \tag{2.13}$$

We may expose the time-dependence of the $R^{\mathrm{N}}_{pq}(t)$ more clearly by transforming to the eigenbasis of the Hamiltonian. We define

$$\tilde{H} = V^{\dagger} \hat{H} V \tag{2.14}$$

where V is the unitary matrix of eigenvectors of $\hat{H}$ and $\tilde{H}$ is the real, diagonal matrix of eigenvalues of $\hat{H}$. Similarly, we define

$$\tilde{S}_{\mathrm{N}p} = V^{\dagger} \hat{S}_{\mathrm{N}p} V \qquad \text{where } p = x, y, z. \tag{2.15}$$

Thus, we may write (2.12) as

$$R^{\mathrm{N}}_{pq}(t) = \mathrm{Tr}\left[\tilde{S}_{\mathrm{N}p}\mathrm{e}^{-\mathrm{i}\tilde{H}^{\mathrm{N}}t}\tilde{S}_{\mathrm{N}q}\mathrm{e}^{\mathrm{i}\tilde{H}^{\mathrm{N}}t}\right] = \sum_{m,n}\mathrm{e}^{\mathrm{i}\omega^{\mathrm{N}}_{mn}t}(\tilde{S}_{\mathrm{N}p})_{mn}(\tilde{S}_{\mathrm{N}q})_{nm} \tag{2.16}$$

where $\omega^{\mathrm{N}}_{mn} = \tilde{H}^{\mathrm{N}}_{mm} - \tilde{H}^{\mathrm{N}}_{nn}$. Substituting this expression into equation (2.13) gives

$$\left\langle \hat{P}^{\mathrm{S}} \right\rangle (t) = \frac{1}{4} + \sum_{p,q=x,y,z}\frac{1}{M}\left[\sum_{m,n}\mathrm{e}^{\mathrm{i}\omega^{\mathrm{A}}_{mn}t}(\tilde{S}_{\mathrm{A}p})_{mn}(\tilde{S}_{\mathrm{A}q})_{nm}\right]\left[\sum_{s,r}\mathrm{e}^{\mathrm{i}\omega^{\mathrm{B}}_{sr}t}(\tilde{S}_{\mathrm{B}p})_{sr}(\tilde{S}_{\mathrm{B}q})_{rs}\right]. \tag{2.17}$$

This formula keeps the sum on radical A (over m,n) and that on radical B (over s,r) separate, allowing an efficient evaluation of the singlet probability at a given moment.

2.2.2 Frequency domain

Often, we wish ultimately to evaluate singlet yields. This can, in principle, be achieved by numerical integration of equation (2.1) using singlet probabilities calculated in the time domain with equation (2.17). However, such a procedure is rather inefficient and will give results whose accuracy is limited by the numerical integration scheme. A better solution is often to work in the frequency domain. As shown in §B.4, the singlet yield is given by

$$\Phi_{\mathrm{S}}(B) = \int_{-\infty}^{\infty}\left\langle \hat{P}^{\mathrm{S}} \right\rangle (B,\omega)F(\omega)^{*}\,\mathrm{d}\omega \tag{2.18}$$

where $\left\langle \hat{P}^{\mathrm{S}} \right\rangle (B,\omega)$ and $F(\omega)$ are Fourier transforms of $\left\langle \hat{P}^{\mathrm{S}} \right\rangle (B,t)$ and $f(t)$ respectively. For a given re-encounter probability distribution, we need only to evaluate the Fourier transform of equation (2.13):

$$\left\langle \hat{P}^{\mathrm{S}} \right\rangle (B,\omega) = \sqrt{\frac{1}{2\pi}}\int_{-\infty}^{\infty}\left[\frac{1}{4} + \frac{1}{M}\sum_{p,q=x,y,z}R^{\mathrm{A}}_{pq}(t)R^{\mathrm{B}}_{pq}(t)\right]\mathrm{e}^{\mathrm{i}\omega t}\,\mathrm{d}t. \tag{2.19}$$

Using equations (B.17) and (B.20), we simplify this to give

$$\left\langle \hat{P}^{\mathrm{S}} \right\rangle (B,\omega) = \frac{\sqrt{2\pi}}{4}\delta(\omega) + \frac{1}{M\sqrt{2\pi}}\sum_{p,q=x,y,z}R^{\mathrm{A}}_{pq}(\omega)\star R^{\mathrm{B}}_{pq}(\omega) \tag{2.20}$$

where $\star$ denotes convolution and, by equation (B.20),

$$R^{\mathrm{N}}_{pq}(\omega) = \sqrt{2\pi}\sum_{m,n}(\tilde{S}_{\mathrm{N}p})_{mn}(\tilde{S}_{\mathrm{N}q})_{nm}\delta(\omega+\omega^{\mathrm{N}}_{nm}). \tag{2.21}$$

Exact evaluation

Having derived a frequency domain expression for the singlet yield, we consider how this might best be implemented in a computer program. It is easy to show that the convolution of two delta functions

$$a_0\delta(x+x_0)\star a_1\delta(x+x_1) = a_0a_1\delta(x+x_0+x_1) \tag{2.22}$$

is also a Delta function. Therefore, equation (2.20) may be expanded to give the singlet probability as a sum of delta functions

$$\left\langle \hat{P}^{\mathrm{S}} \right\rangle (B,\omega) = \sum_k \alpha_k(B)\delta(\omega+\omega_k(B)) \tag{2.23}$$

with various amplitudes α_k and frequencies ω_k. Substituting into equation (2.18) and noting, as shown in Appendix B, that $F(\omega) = F(-\omega)^*$, the singlet yield is

$$\begin{aligned}\Phi_{\mathrm{S}}(B) &= \int_{-\infty}^{\infty} \left[\sum_k \alpha_k(B)\delta(\omega+\omega_k(B))\right] F(\omega)^* \,\mathrm{d}\omega \\ &= \sum_k \alpha_k(B) F(\omega_k(B)).\end{aligned} \tag{2.24}$$

This formula provides the basis for an efficient computer algorithm:

- Calculate the $(\tilde{S}_{\mathrm{N}p})_{mn}$ and ω^{N}_{mn} matrices in each radical.
- Combine elements from radicals A and B using equations (2.20) and (2.22). This gives one amplitude

  $$\alpha_k = \frac{\sqrt{2\pi}}{M} \sum_{p,q} (\tilde{S}_{\mathrm{A}p})_{mn} (\tilde{S}_{\mathrm{A}q})_{nm} (\tilde{S}_{\mathrm{B}p})_{sr} (\tilde{S}_{\mathrm{B}q})_{rs} \tag{2.25}$$

  and one frequency

  $$\omega_k = \omega^{\mathrm{A}}_{nm} + \omega^{\mathrm{B}}_{rs} \tag{2.26}$$

  for every combination of m,n,s,r. There is also a contribution with $\alpha_0 = \frac{\sqrt{2\pi}}{4}$ and $\omega_0 = 0$. (N.B. it was found that the overall performance of this calculation could be increased by a factor of 10–15 times by rewriting this central combination step in `C` whilst keeping all other code in `Matlab` [117].)
- For any given re-encounter distribution $f(t)$, the singlet yield is then given trivially by equation (2.24). Significantly, this means that singlet yields can be calculated for several different rate constants k in virtually the same time as for a single rate constant.

Approximate evaluation

The algorithm above is very appealing for radical pairs with fewer than four spin-½ nuclei per radical. However, as the number of magnetic nuclei increases further, the second step becomes very slow. This is because the number of combinations of m,n,s,r grows as $M_{\mathrm{A}}^2 M_{\mathrm{B}}^2$ where M_{N} is the number of nuclear spin states in radical N. Often, it is not necessary to calculate the singlet yield to machine precision. In such cases, the poor scaling may be improved dramatically at the cost of a small approximation.

In each of the nine $R^{\mathrm{N}}_{pq}(\omega)$ given in equation (2.21), we combine terms which have a similar frequency, approximating them with a single delta function. This binning procedure is illustrated schematically in Figure 2.1. The approximate $R^{\mathrm{N}}_{pq}(\omega)$ have a fixed number of frequency components. Therefore, the convolution step now takes a

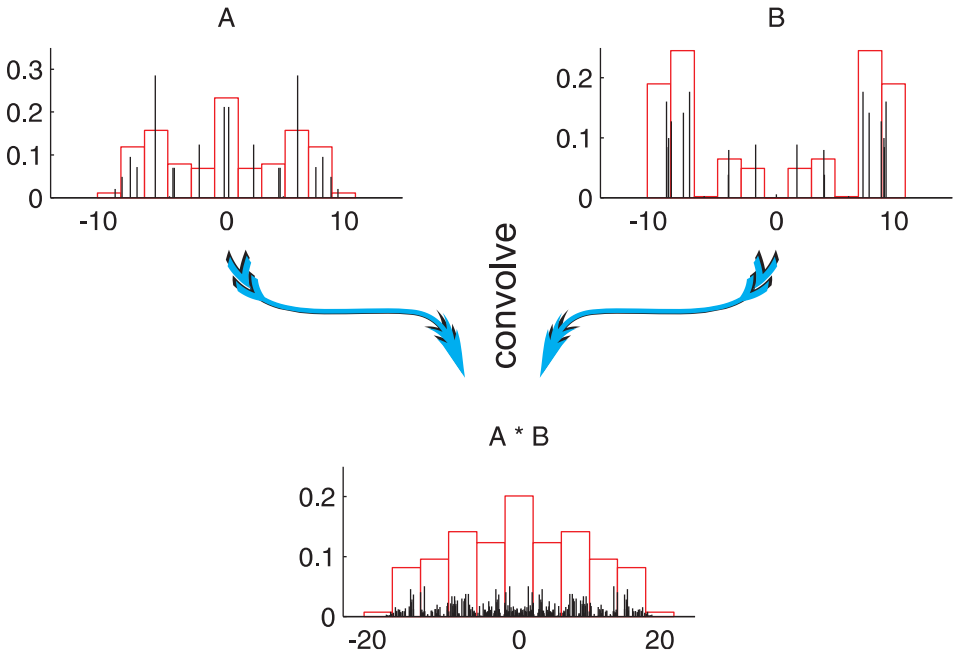

Figure 2.1: Schematic of the binning procedure. The black vertical lines represent delta function whose amplitude is given by the height of the line. The red histogram represents a very coarse set of bins.

constant time, independent of the size of the radical pair spin system. The algorithm scales as $k_{\mathrm{A}}M_{\mathrm{A}}^2 + k_{\mathrm{B}}M_{\mathrm{B}}^2$, where k_{A} and k_{B} are constants. For radical pairs with many nuclei, this improvement in the scaling may give an enormous increase in performance.

For re-encounter distributions with a continuous Fourier transform $F(\omega)$, we know that

$$\lim_{\delta\omega\to 0} F(\omega+\delta\omega) = F(\omega). \tag{2.27}$$

Consider the worst case for binning, where all the delta functions in $R_{pq}^{\mathrm{N}}(\omega)$ lie at the edge of a bin. After convolution, the frequency error $\delta\omega$ will be one bin-width. Therefore, according to equations (2.24) and (2.27), we may calculate the singlet yield for all time to any desired accuracy by choosing a sufficient number of bins. This frequency domain binning algorithm gives the best of both worlds. Just like the time domain formula, equation (2.17), it scales well as the number of nuclei is increased, but it also avoids, when singlet yields are to be calculated, numerical integration of equation (2.1). The integration step is instead done analytically when finding $F(\omega)$.

2.2.3 Comments on the R_{pq}^{N}

Symmetry constraints

In systems with isotropic hyperfine coupling constants, it may be shown that [118]

$$\begin{aligned} R_{xx}^{\mathrm{N}} &= R_{yy}^{\mathrm{N}} \\ R_{xy}^{\mathrm{N}} &= -R_{yx}^{\mathrm{N}} \\ R_{xz}^{\mathrm{N}} &= R_{yz}^{\mathrm{N}} = R_{zx}^{\mathrm{N}} = R_{zy}^{\mathrm{N}} = 0. \end{aligned} \tag{2.28}$$

Therefore, one need only deal with three of the nine p,q, increasing the efficiency of calculation.

Physical interpretation of the R^{N}_{pq}

The derivation above uses the "Schrödinger picture" [119]. This formalism attaches all time-dependence to the wave function (to the density matrix here) with operators for observables being time independent. Therefore, we consider

$$R^{\mathrm{N}}_{pq}(t) = \mathrm{Tr}[\underbrace{\hat{S}_{\mathrm{N}p}}_{\hat{\Omega}}\underbrace{\mathrm{e}^{-\mathrm{i}\hat{H}^{\mathrm{N}}t}\hat{S}_{\mathrm{N}q}\mathrm{e}^{\mathrm{i}\hat{H}^{\mathrm{N}}t}}_{\hat{\rho}(t)}]. \tag{2.29}$$

In the Schrödinger picture, R^{N}_{pq} gives the expectation value that a system which starts out as in a pure $\hat{S}_{\mathrm{N}q}$ state is found in the state $\hat{S}_{\mathrm{N}p}$ at time t.

We may equally well adopt the "Heisenberg picture", in which the operators are time-dependent and the wave function (or density matrix) does not depend on time. Making a cyclic permutation of the trace, we consider

$$R^{\mathrm{N}}_{pq}(t) = \mathrm{Tr}[\underbrace{\mathrm{e}^{\mathrm{i}\hat{H}^{\mathrm{N}}t}\hat{S}_{\mathrm{N}p}\mathrm{e}^{-\mathrm{i}\hat{H}^{\mathrm{N}}t}}_{\hat{S}_{\mathrm{N}p}(t)}\underbrace{\hat{S}_{\mathrm{N}q}}_{\hat{S}_{\mathrm{N}q}(0)}]. \tag{2.30}$$

In the Heisenberg picture, R^{N}_{pq} allows the spin operators at time t to be written in terms of those at time zero. In other words,

$$\hat{S}_{\mathrm{N}p}(t) = \sum_q R^{\mathrm{N}}_{pq}(t)\hat{S}_{\mathrm{N}q}(0). \tag{2.31}$$

The R^{N}_{pq}(t) may aptly be termed "spin correlation tensors" [27] in the Heisenberg picture.

Magnetically equivalent nuclei

Many radical pairs of chemical interest contain magnetically equivalent nuclei. For the Hamiltonian in equation (2.5), nuclei in the same radical, with the same spin quantum number and the same hyperfine coupling constant are magnetically equivalent. When present, this equivalence may be utilised to increase substantially the efficiency of calculation, as illustrated in the following example.

Consider a radical pair with two equivalent spin-½ nuclei on radical A. The radical pair Hamiltonian contains hyperfine and Zeeman interaction terms

$$\hat{H} = \hat{H}_{\mathrm{HFI}} + \hat{H}_{\mathrm{Z}}. \tag{2.32}$$

The hyperfine interaction $\hat{H}_{\mathrm{HFI}} = a\left(\hat{\boldsymbol{S}}_{\mathrm{A}}\cdot\hat{\boldsymbol{I}}_1 + \hat{\boldsymbol{S}}_{\mathrm{A}}\cdot\hat{\boldsymbol{I}}_2\right)$. We may write this schematically in the product basis as

$$\hat{H}_{\mathrm{HFI}}/a = \hat{\boldsymbol{S}}_{\mathrm{A}}\cdot\hat{\boldsymbol{I}}_1 + \hat{\boldsymbol{S}}_{\mathrm{A}}\cdot\hat{\boldsymbol{I}}_2 = \begin{matrix}|\tfrac{1}{2},+\tfrac{1}{2};\tfrac{1}{2},+\tfrac{1}{2}\rangle\\ |\tfrac{1}{2},+\tfrac{1}{2};\tfrac{1}{2},-\tfrac{1}{2}\rangle\\ |\tfrac{1}{2},-\tfrac{1}{2};\tfrac{1}{2},+\tfrac{1}{2}\rangle\\ |\tfrac{1}{2},-\tfrac{1}{2};\tfrac{1}{2},-\tfrac{1}{2}\rangle\end{matrix}\begin{bmatrix}\boxed{\cdot\,\cdot} & \boxed{\cdot\,\cdot} & \boxed{\cdot\,\cdot} & \boxed{\cdot\,\cdot}\\ \boxed{\cdot\,\cdot} & \boxed{\cdot\,\cdot} & \boxed{\cdot\,\cdot} & \boxed{\cdot\,\cdot}\\ \boxed{\cdot\,\cdot} & \boxed{\cdot\,\cdot} & \boxed{\cdot\,\cdot} & \boxed{\cdot\,\cdot}\\ \boxed{\cdot\,\cdot} & \boxed{\cdot\,\cdot} & \boxed{\cdot\,\cdot} & \boxed{\cdot\,\cdot}\end{bmatrix} \tag{2.33}$$

where the basis states are given in the form $|I_1, m_{I1}; I_2, m_{I2}; m_{S1}; m_{S2}\rangle$. We use a condensed notation in which $\boxed{::}$ denotes a set of potentially non-zero matrix elements which share a common nuclear spin state. Notice that in the product basis, this operator is generally a *dense* matrix. Yet, we may factorise

$$\hat{H}_{\mathrm{HFI}}/a = \hat{\boldsymbol{S}}_{\mathrm{A}} \cdot \hat{\boldsymbol{I}}_1 + \hat{\boldsymbol{S}}_{\mathrm{A}} \cdot \hat{\boldsymbol{I}}_2 = \hat{\boldsymbol{S}}_{\mathrm{A}} \cdot \left(\hat{\boldsymbol{I}}_1 + \hat{\boldsymbol{I}}_2\right) = \hat{\boldsymbol{S}}_{\mathrm{A}} \cdot \hat{\boldsymbol{I}}_{\mathrm{tot}} \tag{2.34}$$

where we introduce the total (coupled) nuclear spin $\hat{\boldsymbol{I}}_{\mathrm{tot}} = \hat{\boldsymbol{I}}_1 + \hat{\boldsymbol{I}}_2$. The natural basis states for such an expression are $|I_1, I_2; I_{\mathrm{tot}}, m_{\mathrm{Itot}}; m_{S1}; m_{S2}\rangle$. These are related to the uncoupled states by the familiar Clebsch-Gordan series [120–122]. When coupling two angular momenta, the Clebsch-Gordan series gives non-zero terms only when $I_{\mathrm{tot}} = I_1 + I_2, I_1 + I_2 - 1, \ldots, |I_1 - I_2|$. Here, we find that $I_{\mathrm{tot}} = 1$ or 0. This gives rise to three nuclear spin basis states when $I_{\mathrm{tot}} = 1$ and one when $I_{\mathrm{tot}} = 0$. The total number of basis states is therefore the same as in the uncoupled representation. Working in the coupled basis

$$\hat{H}_{\mathrm{HFI}}/a = \hat{\boldsymbol{S}}_{\mathrm{A}} \cdot \hat{\boldsymbol{I}}_{\mathrm{tot}} = \begin{matrix} |\frac{1}{2},\frac{1}{2};1,+1\rangle \\ |\frac{1}{2},\frac{1}{2};1,0\rangle \\ |\frac{1}{2},\frac{1}{2};1,-1\rangle \\ |\frac{1}{2},\frac{1}{2};0,0\rangle \end{matrix} \begin{bmatrix} \boxed{::} & \boxed{::} & \boxed{::} & 0 \\ \boxed{::} & \boxed{::} & \boxed{::} & 0 \\ \boxed{::} & \boxed{::} & \boxed{::} & 0 \\ 0 & 0 & 0 & \boxed{::} \end{bmatrix}. \tag{2.35}$$

We see that the matrix now has a block structure; each block corresponds to a particular total nuclear spin quantum number I_{tot}. Since the electron Zeeman term $\hat{H}_{\mathrm{Z}}$ does not depend on nuclear spin, the full Hamiltonian, equation (2.32), has the same block structure.

As an aside, it is easy to see that multiplication of matrices M_1 and M_2 which have the same block structure preserves this structure in the result M. Furthermore, each resulting block in M is equal to the product of blocks in M_1 and M_2. Schematically:

$$\left[\begin{array}{c|c} A_1 & \\ \hline & B_1 \end{array}\right] \left[\begin{array}{c|c} A_2 & \\ \hline & B_2 \end{array}\right] = \left[\begin{array}{c|c} A_1 A_2 & \\ \hline & B_1 B_2 \end{array}\right]. \tag{2.36}$$

Now, to see how the coupled basis facilitates calculation, we substitute equation (2.35) into equations (2.6) and (2.7). Writing the matrices involved schematically, and subsuming the factor of M into one of the singlet projection operators, the singlet

probability in our radical pair is

$$\left\langle \hat{P}^{\mathrm{S}} \right\rangle = \mathrm{Tr}\left[\frac{1}{M} U \hat{P}^{\mathrm{S}} U^{\dagger} \hat{P}^{\mathrm{S}}\right] =$$

$$\mathrm{Tr}\left[\begin{bmatrix} \boxed{::} & \boxed{::} & \boxed{::} & 0 \\ \boxed{::} & \boxed{::} & \boxed{::} & 0 \\ \boxed{::} & \boxed{::} & \boxed{::} & 0 \\ 0 & 0 & 0 & \boxed{::} \end{bmatrix} \begin{bmatrix} \boxed{::} & 0 & 0 & 0 \\ 0 & \boxed{::} & 0 & 0 \\ 0 & 0 & \boxed{::} & 0 \\ 0 & 0 & 0 & \boxed{::} \end{bmatrix} \begin{bmatrix} \boxed{::} & \boxed{::} & \boxed{::} & 0 \\ \boxed{::} & \boxed{::} & \boxed{::} & 0 \\ \boxed{::} & \boxed{::} & \boxed{::} & 0 \\ 0 & 0 & 0 & \boxed{::} \end{bmatrix} \begin{bmatrix} \boxed{::} & 0 & 0 & 0 \\ 0 & \boxed{::} & 0 & 0 \\ 0 & 0 & \boxed{::} & 0 \\ 0 & 0 & 0 & \boxed{::} \end{bmatrix}\right]$$

$$= \mathrm{Tr}\left[\begin{bmatrix} \boxed{::} & \boxed{::} & \boxed{::} & 0 \\ \boxed{::} & \boxed{::} & \boxed{::} & 0 \\ \boxed{::} & \boxed{::} & \boxed{::} & 0 \\ 0 & 0 & 0 & \boxed{::} \end{bmatrix}\right]. \quad (2.37)$$

This calculation may be simplified by considering each block individually. For example, in this radical pair

$$\left\langle \hat{P}^{\mathrm{S}} \right\rangle = \frac{1}{M}\left\{ \underbrace{\mathrm{Tr}\left[U \hat{P}^{\mathrm{S}} U^{\dagger} \hat{P}^{\mathrm{S}}\right]}_{I_{\mathrm{tot}}=1} + \underbrace{\mathrm{Tr}\left[U \hat{P}^{\mathrm{S}} U^{\dagger} \hat{P}^{\mathrm{S}}\right]}_{I_{\mathrm{tot}}=0} \right\}. \quad (2.38)$$

We obtain the singlet probability as the sum of contributions from two radical pairs, each having a single "effective nucleus" of spin 0 or spin 1.

In practice, a group of magnetically equivalent nuclei may contain more than two members, and each nucleus need not be spin-½. Such cases are treated by the following coupling scheme

$$\begin{aligned} I_1 \;\&\; I_2 &\rightarrow I_{12} \\ I_{12} \;\&\; I_3 &\rightarrow I_{123} \\ I_{123} \;\&\; I_4 &\rightarrow I_{1234}, \quad \text{etc.} \end{aligned} \quad (2.39)$$

This scheme is unique because all the nuclei are equivalent. The resulting I_{tot} blocks are found by successive application of the Clebsch-Gordan series. For example, in a system of three spins-½

$$\begin{aligned} I_{12} &= \frac{1}{2} + \frac{1}{2}, \ldots, \left|\frac{1}{2} - \frac{1}{2}\right| = 1 \text{ or } 0 \\ I_{\mathrm{tot}} = I_{123} &= \left(1 + \frac{1}{2}, \ldots, \left|1 - \frac{1}{2}\right|\right) \text{ or } \left(0 + \frac{1}{2}, \ldots, \left|0 - \frac{1}{2}\right|\right) = \frac{3}{2} \text{ or } \frac{1}{2} \text{ (twice).} \end{aligned} \quad (2.40)$$

Treating magnetically equivalent nuclei in this manner allows substantial savings in memory usage and CPU time when calculating the singlet yield. The same approach is applicable to calculation of the R^{N}_{pq}.

2.3 Differentiation

Until now, we have concentrated our attention on calculating the singlet product yield Φ_S. A chemical magnetic field effect arises when the singlet yield depends on applied field strength. Practically, however, it can be difficult to detect the — often small — changes in singlet yield at different magnetic field strengths. This is particularly challenging when experiments are conducted in the low field region, using fields of a few millitesla.

Modulation methods are often employed to overcome these limitations. In essence, modulated detection involves adding a small oscillatory contribution to the magnetic field which causes any field-dependent quantity to oscillate at the same frequency. Using a lock-in amplifier [123, 124], it is possible to extract the oscillatory part of the measured signal (e.g. exciplex fluorescence) by phase sensitive detection. Such a procedure greatly improves the signal-to-noise ratio in MFE measurements.

Another effect of modulated detection is that we no longer measure the singlet yield, but, for small modulation amplitudes, we measure the first derivative of singlet yield with respect to magnetic field $\mathrm{d}\Phi_S(B)/\mathrm{d}B$. Hence, it is important to consider how to calculate such derivatives.

2.3.1 Numerical differentiation

The simplest approach to differentiating $\Phi_S(B)$ uses the definition of the derivative

$$\Phi'_S(B) = \frac{\mathrm{d}\Phi_S}{\mathrm{d}B} = \lim_{\delta B \to 0} \frac{\Phi_S(B+\delta B) - \Phi_S(B)}{\delta B}, \tag{2.41}$$

taking some suitably small numeric value for δB. We must choose δB to be small enough that the limit converges, but it must not be so small that rounding errors come to dominate the numerator $\Phi_S(B+\delta B) - \Phi_S(B)$.

2.3.2 Finite differences

The method of finite differences is also widely used for performing numerical differentiation. We begin by evaluating $\Phi_S(B_k)$ at a selection of field strengths B_k. The field strengths B_k are often arranged in a regularly spaced grid. Finite differences formulae approximate the derivative by

$$\Phi'_S(B_j) = \ldots + w_{-1}\Phi_S(B_{j-1}) + w_0\Phi_S(B_j) + w_1\Phi_S(B_{j+1}) + \ldots \tag{2.42}$$

The weights w_k are determined once for a particular finite difference scheme. Typically, this is done by finding a polynomial which interpolates some neighbouring $\Phi_S(B_k)$, differentiating the polynomial and evaluating its derivative at B_k. Fornberg [125] explains this procedure in detail. The convergence properties of a finite differences scheme depend on the number of points used for interpolation and on the type of grid. The order of convergence may be calculated easily by inspection of the error terms in a Taylor series expansion using a computer algebra system such as `Maple` [126] or `Mathematica` [127].

A particularly useful feature of finite differences approximations is that they may be written in matrix form. If we consider the singlet yield values to be components of a vector $\boldsymbol{s}$, where $s_k = \Phi_S(B_k)$, and do likewise for the derivative $s'_k = \Phi'_S(B_k)$, then

$$s'_j = \sum_k D_{jk} s_k. \tag{2.43}$$

In other words

$$\boldsymbol{s}' = \mathsf{D}\boldsymbol{s} \tag{2.44}$$

where D is a banded matrix containing the weights w.

2.3.3 Analytical approach

Instead of making numerical approximations to the derivative, we may differentiate analytically one of the formulae in §2.2. Evaluating the resulting expression numerically would give the singlet yield derivative directly. The only non-standard step in such a differentiation arises because the singlet yield depends on the eigenvalues and eigenvectors of the Hamiltonian.

2.3.4 Analytic derivatives of matrix-valued functions

Many physical systems are described by a matrix A. Often, this matrix may be written as a matrix-valued function $\mathsf{A}(\rho)$ of one or more scalar parameters ρ. To give a concrete example, the radical pair spin systems discussed above are described by the Hamiltonian $\hat{H}$. Equations 2.4 and 2.5 define a matrix-valued function $\hat{H}(B, a_{1A}, \ldots)$ for the Hamiltonian in terms of scalar parameters such as the field strength B. The problem of differentiating the eigenvalues and eigenvectors of such matrices $\mathsf{A}(\rho)$ with respect to their parameter ρ has been tackled by several workers [128–134]. We thank Andrew for his advice [135] and outline here the approach of Andrew and Tan [128].

No degenerate eigenvalues

We begin by considering a matrix $\mathsf{A}(\rho)$ that has no degenerate eigenvalues. By definition, the i^{th} eigenvalue $\lambda_i(\rho)$ and its corresponding eigenvector $\boldsymbol{x}_i(\rho)$ satisfy

$$\mathsf{A}(\rho)\boldsymbol{x}_i(\rho) = \lambda_i(\rho)\boldsymbol{x}_i(\rho). \tag{2.45}$$

For simplicity, we require that A be Hermitian, that $\rho \in \mathbb{R}$ and that A is analytic throughout some open interval I_0 containing the point ρ_0 at which we wish to determine the derivatives. Andrew and Tan show [128] that in order to fully define the eigenvectors, we must make a further restriction, in this case choosing "orthogonally constrained" eigenvectors, which satisfy

$$\boldsymbol{x}_i^\dagger(\rho_0)\boldsymbol{x}_i(\rho) = 1. \tag{2.46}$$

Such eigenvectors are unique up to a phase factor. Differentiating (2.45) gives

$$\mathsf{A}'(\rho)\boldsymbol{x}_i(\rho) + \mathsf{A}(\rho)\boldsymbol{x}'_i(\rho) = \lambda'_i(\rho)\boldsymbol{x}_i(\rho) + \lambda_i(\rho)\boldsymbol{x}'_i(\rho) \tag{2.47}$$

where $'$ denotes the derivative with respect to the parameter ρ. Premultiplying by $\boldsymbol{x}_i^\dagger(\rho_0)$ we find that

$$\boldsymbol{x}_i^\dagger(\rho_0)\mathsf{A}'(\rho)\boldsymbol{x}_i(\rho)+\boldsymbol{x}_i^\dagger(\rho_0)\mathsf{A}(\rho)\boldsymbol{x}_i'(\rho)=\lambda_i'(\rho)\boldsymbol{x}_i^\dagger(\rho_0)\boldsymbol{x}_i(\rho)+\lambda_i(\rho)\boldsymbol{x}_i^\dagger(\rho_0)\boldsymbol{x}_i'(\rho). \tag{2.48}$$

This may be further simplified using equation (2.46), its derivative ($\boldsymbol{x}_i^\dagger(\rho_0)\boldsymbol{x}_i'(\rho)=0$) and the Hermiticity of $\mathsf{A}(\rho)$ to give

$$\boldsymbol{x}_i^\dagger(\rho_0)\mathsf{A}'(\rho)\boldsymbol{x}_i(\rho)+\left[\mathsf{A}(\rho)\boldsymbol{x}_i(\rho_0)\right]^\dagger\boldsymbol{x}_i'(\rho)=\lambda_i'(\rho). \tag{2.49}$$

Setting $\rho=\rho_0$ and substituting the bracketed expression with equation (2.45) gives

$$\begin{aligned}\lambda_i'(\rho_0)&=\boldsymbol{x}_i^\dagger(\rho_0)\mathsf{A}'(\rho_0)\boldsymbol{x}_i(\rho_0)+\lambda_i^*(\rho_0)\boldsymbol{x}_i^\dagger(\rho_0)\boldsymbol{x}_i'(\rho_0)\\&=\boldsymbol{x}_i^\dagger(\rho_0)\mathsf{A}'(\rho_0)\boldsymbol{x}_i(\rho_0)\end{aligned} \tag{2.50}$$

which is the desired eigenvalue derivative. In order to extract the eigenvector derivative, we rearrange equation (2.47) to give

$$\left[\mathsf{A}(\rho)-\lambda_i(\rho)\mathsf{I}\right]\boldsymbol{x}_i'(\rho)=\left[\lambda_i'(\rho)\mathsf{I}-\mathsf{A}'(\rho)\right]\boldsymbol{x}_i(\rho). \tag{2.51}$$

Since all other quantities are known, this equation may be solved for $\boldsymbol{x}_i'(\rho_0)$ using, for example, the `Matlab` "\" command.

Degenerate eigenvalues

When the i^{th} eigenvalue is r-fold degenerate at ρ_0, matters are somewhat more complicated. Instead of equation (2.45), one must consider

$$\mathsf{A}(\rho)\mathsf{X}_i(\rho)=\mathsf{X}_i(\rho)\Lambda_i(\rho) \tag{2.52}$$

where $\mathsf{X}_i(\rho)$ is an $n\times r$ matrix whose columns are the r eigenvectors in this degenerate set and $\Lambda_i=\lambda_i\mathsf{I}$. By analogous considerations, we arrive at

$$\Lambda_i'(\rho_0)=\mathsf{X}_i^\dagger(\rho_0)\mathsf{A}'(\rho_0)\mathsf{X}_i(\rho_0). \tag{2.53}$$

When the eigenvalues of $\mathsf{A}(\rho_0)$ are degenerate, numerical routines for solving equation (2.52) at ρ_0 will in fact give $\hat{\mathsf{X}}$ where

$$\mathsf{X}_i(\rho_0)=\hat{\mathsf{X}}\mathsf{C}_0 \tag{2.54}$$

where C_0 is an unknown $r\times r$ unitary matrix which accounts for the fact that the numerical routine may choose an arbitrary linear combination of the degenerate eigenvectors at ρ_0. These are indeed eigenvectors at ρ_0, but they are likely to be very different from the almost-degenerate eigenvectors when ρ is close to ρ_0. Thus, $\hat{\mathsf{X}}$ gives another (essentially random) basis set for the vector space spanned by the degenerate eigenvalues. We cannot take the derivative through the point ρ_0 without untangling the proper eigenvectors there.

Hence, in order to evaluate the eigenvalue derivatives, we first solve equation (2.52) numerically at $\rho=\rho_0$ to give $\Lambda_i(\rho_0)$ and $\hat{\mathsf{X}}$. We then form the matrix M_1, defined as

$$\mathsf{M}_1=\hat{\mathsf{X}}_i^\dagger(\rho_0)\mathsf{A}'(\rho_0)\hat{\mathsf{X}}_i(\rho_0). \tag{2.55}$$

Now, substituting the definition of $\hat{\mathsf{X}}$ from equation (2.54) and by equation (2.53)

$$\mathsf{M}_1 = \mathsf{C}_0 \left[\mathsf{X}_i^\dagger(\rho_0)\mathsf{A}'(\rho_0)\mathsf{X}_i(\rho_0)\right] \mathsf{C}_0^\dagger \tag{2.56}$$

$$= \mathsf{C}_0 \Lambda_i'(\rho_0)\mathsf{C}_0^\dagger. \tag{2.57}$$

This is another $r \times r$ eigenvalue problem, which we solve numerically to give $\Lambda_i'(\rho_0)$ and a set of eigenvectors C_0. Providing that the $\lambda_i'(\rho_0)$ are distinct (*i.e.* $m = 1$ in Andrew and Tan's notation), then C_0 is uniquely defined and we may find the true eigenvectors $\mathsf{X}_i(\rho_0)$ using equation (2.54).

Finally, we form an equation analogous to equation (2.51)

$$[\mathsf{A}(\rho) - \lambda_i(\rho)\mathsf{I}]\, \mathsf{X}_i'(\rho) = \mathsf{X}_i(\rho)\Lambda_i'(\rho) - \mathsf{A}'(\rho)\mathsf{X}_i(\rho), \tag{2.58}$$

which we solve for $\mathsf{X}_i'(\rho_0)$ using, for example, the `Matlab` "\" command.

In real systems, it is possible that the $\lambda_i'(\rho_0)$ are not all distinct. Such cases require some technical extensions to the algorithm presented here. These are discussed by Andrew and Tan and incorporated into their "Algorithm 1" [128], which we use henceforth.

Simple test case

Consider the matrix-valued function $\mathsf{A}(\rho)$ given by

$$\mathsf{A}(\rho) = \begin{pmatrix} \cos(\rho) & \sin(\rho) & 0 \\ -\sin(\rho) & \cos(\rho) & 0 \\ 0 & 0 & 1 \end{pmatrix} \begin{pmatrix} 4-\rho^2 & 0 & 0 \\ 0 & 10 & 0 \\ 0 & 0 & 3\rho \end{pmatrix} \begin{pmatrix} \cos(\rho) & -\sin(\rho) & 0 \\ \sin(\rho) & \cos(\rho) & 0 \\ 0 & 0 & 1 \end{pmatrix}. \tag{2.59}$$

It is easy to see that the eigenvalues of A are $4-\rho^2$, 10 and 3ρ, while the eigenvectors are the columns of the first matrix (up to a phase factor). The derivatives with respect to ρ of the eigenvalues are therefore -2ρ, 0 and 3, and those of the eigenvectors have components 0, $\pm\cos(\rho)$ and $-\sin(\rho)$. Figure 2.2 shows the output of Algorithm 1 plotted on these analytic solutions. There is clearly excellent agreement.

2.3.5 One-proton radical pair

Symbolic test case

Using a symbolic manipulation package such as `Mathematica`, it is straightforward to obtain the following expression for the singlet yield in a radical pair with a single spin-½ magnetic nucleus:

$$\Phi_{\mathrm{S}}(\tilde{\omega}_0, \tilde{k}) = \frac{\begin{bmatrix} 4\left(32\tilde{k}^4 + 12\tilde{k}^2 + 1\right)\tilde{\omega}_0^6 + \left(384\tilde{k}^6 + 304\tilde{k}^4 + 84\tilde{k}^2 + 3\right)\tilde{\omega}_0^4 \\ +16\tilde{k}^2\left(24\tilde{k}^6 + 37\tilde{k}^4 + 16\tilde{k}^2 + 2\right)\tilde{\omega}_0^2 + 16\tilde{k}^4\left(\tilde{k}^2+1\right)^2\left(8\tilde{k}^2+5\right) \end{bmatrix}}{\begin{bmatrix} 8\left(\tilde{k}^2 + \tilde{\omega}_0^2 + 1\right)\left(4\tilde{k}^4 + 4((\tilde{\omega}_0 - 1)\tilde{\omega}_0 + 1)\tilde{k}^2 + \tilde{\omega}_0^2\right) \\ \times\left(4\tilde{k}^4 + 4\left(\tilde{\omega}_0^2 + \tilde{\omega}_0 + 1\right)\tilde{k}^2 + \tilde{\omega}_0^2\right) \end{bmatrix}} \tag{2.60}$$

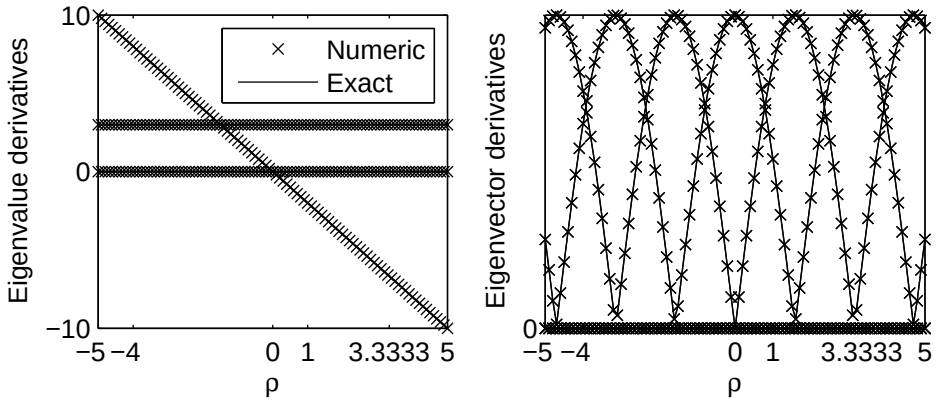

Figure 2.2: Comparison of the derivatives of the eigenvalues and eigenvectors of $\mathsf{A}(\rho)$ defined in equation (2.59). Exact, analytical solutions are shown as lines. Numerical solutions from Algorithm 1 are shown as crosses. Notice the good behaviour when eigenvalue degeneracies occur (at $\rho = -4$, 1 and $10/3$). Left: First derivative with respect to ρ of the eigenvalues of $\mathsf{A}(\rho)$. Right: Absolute values of each component of the eigenvector derivatives with respect to ρ. The absolute value is plotted to mitigate the effects of the arbitrary phase factors in the numerical solutions.

where $\tilde{\omega}_0 = \omega_0/a = -\gamma_e B/a$ and $\tilde{k} = k/a$ are dimensionless forms of the magnetic field strength and exponential model rate constant respectively, and a is the hyperfine coupling constant. When a value for the scaled rate constant $\tilde{k}$ is specified, this expression simplifies to give a compact form that is useful for testing other algorithms against.

Equation 2.60 may also be differentiated symbolically to give the singlet yield derivative that we seek to calculate numerically. When $\tilde{k} = 1/10$, we find that

$$\frac{\mathrm{d}\Phi_\mathrm{S}}{\mathrm{d}\tilde{\omega}_0} = \frac{20000\tilde{\omega}_0 \begin{bmatrix} 5330650000000\tilde{\omega}_0^8 + 67788500000\tilde{\omega}_0^6 \\ -404431016250\tilde{\omega}_0^4 - 32814321775\tilde{\omega}_0^2 - 650119931 \end{bmatrix}}{\left(676000000\tilde{\omega}_0^6 + 734280000\tilde{\omega}_0^4 + 53055300\tilde{\omega}_0^2 + 1030301\right)^2}. \quad (2.61)$$

Numerical calculation of singlet yield derivative

In order to calculate the singlet yield derivative in a simple radical pair, we proceed as follows. To begin, we write the singlet probability as

$$\left\langle \hat{P}^\mathrm{S} \right\rangle = \mathrm{Tr}\left[\frac{1}{M} \mathrm{e}^{-\mathrm{i}\hat{H}t} \hat{P}^\mathrm{S} \mathrm{e}^{\mathrm{i}\hat{H}t} \hat{P}^\mathrm{S}\right] = \mathrm{Tr}\left[\frac{1}{M} \mathrm{e}^{-\mathrm{i}\tilde{H}t} \hat{P}^\mathrm{ST} \mathrm{e}^{\mathrm{i}\tilde{H}t} \hat{P}^\mathrm{ST}\right] \quad (2.62)$$

where $\tilde{H} = V^\dagger \hat{H} V$ is the diagonal matrix of eigenvalues of $\hat{H}$, V is the matrix of eigenvectors and $\hat{P}^\mathrm{ST} = V^\dagger \hat{P}^\mathrm{S} V$. Expanding the trace, we therefore write

$$\left\langle \hat{P}^\mathrm{S} \right\rangle = \frac{1}{M} \sum_{m,n} \left| \hat{P}^\mathrm{ST}_{mn} \right|^2 \mathrm{e}^{\mathrm{i}\omega_{mn}t} \quad (2.63)$$

where $\omega_{mn} = \tilde{H}_{mm} - \tilde{H}_{nn}$. In other words, using equations (2.18) and (B.20) and flattening the matrix of frequencies $\omega_{mn} \to \omega_k$, we may write the singlet yield in terms of

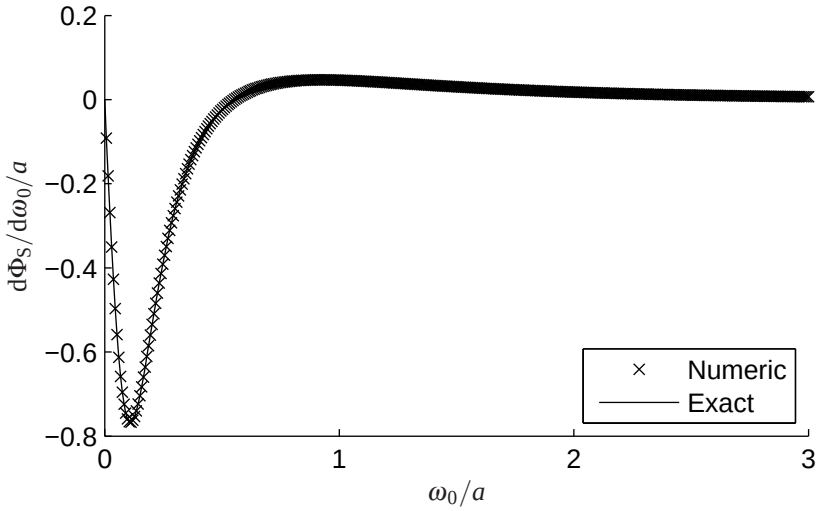

Figure 2.3: Singlet yield derivative in a radical pair with hyperfine coupling constant a to a single spin-½ nucleus, using the exponential model with rate constant $k = a/10$. Numerical results (crosses) were obtained from equation (2.66) using Andrew and Tan's Algorithm 1 [128]. The exact singlet yield derivative (line) is given by equation (2.61).

amplitudes

$$\alpha_k = \frac{\sqrt{2\pi}}{M} \left|\hat{P}_k^{\mathrm{ST}}\right|^2 \tag{2.64}$$

and the Fourier transform of the re-encounter distribution $F(\omega)$:

$$\Phi_\mathrm{S}(\omega_0) = \sum_k \alpha_k(\omega_0) F(\omega_k(\omega_0)). \tag{2.65}$$

This expression is equivalent to equation (2.24).

Now, denoting differentiation with respect to ω_0 by $'$ we write

$$\Phi_\mathrm{S}' = \sum_k \alpha_k'(\omega_0) F(\omega_k(\omega_0)) + \alpha_k(\omega_0)\omega_k'(\omega_0) F'(\omega_k(\omega_0)). \tag{2.66}$$

This expression may be evaluated numerically by using Algorithm 1 to compute $\alpha_k'(\omega_0)$ and $\omega_k'(\omega_0)$. Figure 2.3 compares the singlet yield derivative calculated using Algorithm 1 and equation (2.66) with the symbolic expression in equation (2.61). There is excellent agreement.

2.3.6 Multinuclear radical pairs

Exact evaluation

Multinuclear radical pairs could be treated using the above method. However, it is more efficient to factorise the Hamiltonian into terms on each radical as described in §2.2. The singlet yield derivative is still given by equation (2.66), but the amplitudes

α_k and frequencies ω_k are now calculated according to equations (2.25) and (2.26). Flattening the indices $nm \to k^{\mathrm{A}}$ and $rs \to k^{\mathrm{B}}$ we therefore write

$$\alpha_k = \frac{\sqrt{2\pi}}{M} \sum_{p,q} \alpha^{\mathrm{A}}_{k^{\mathrm{A}}}(p,q,\omega_0)\alpha^{\mathrm{B}}_{k^{\mathrm{B}}}(p,q,\omega_0) \tag{2.67}$$

$$\omega_k = \omega^{\mathrm{A}}_{k^{\mathrm{A}}}(\omega_0) + \omega^{\mathrm{B}}_{k^{\mathrm{B}}}(\omega_0). \tag{2.68}$$

Their derivatives are therefore

$$\alpha'_k = \frac{\sqrt{2\pi}}{M} \sum_{p,q} \begin{bmatrix} \left(\alpha^{\mathrm{A}}_{k^{\mathrm{A}}}\right)'(p,q,\omega_0)\alpha^{\mathrm{B}}_{k^{\mathrm{B}}}(p,q,\omega_0) \\ +\alpha^{\mathrm{A}}_{k^{\mathrm{A}}}(p,q,\omega_0)\left(\alpha^{\mathrm{B}}_{k^{\mathrm{B}}}\right)'(p,q,\omega_0) \end{bmatrix} \tag{2.69}$$

and

$$\omega'_k = \left(\omega^{\mathrm{A}}_{k^{\mathrm{A}}}\right)' + \left(\omega^{\mathrm{B}}_{k^{\mathrm{B}}}\right)' \tag{2.70}$$

with one k for every combination of m,n,s,r. There is also a contribution with $\alpha_0 = \frac{\sqrt{2\pi}}{4}$, $\alpha'_0 = 0$ and $\omega_0 = \omega'_0 = 0$. Calculations were performed using this algorithm in `Matlab`. The results agree to machine precision with those obtained by numerical differentiation.

Approximate evaluation

When calculating singlet yields, a frequency domain binning procedure was found to improve performance dramatically in large radical pairs. We outline a similar frequency domain binning procedure for the singlet yield derivatives.

The central idea is to gather together terms on each radical whose frequencies are close to a bin centre frequency $\bar{\omega}^{\mathrm{N}}_{j^{\mathrm{N}}}$. For the j^{N}-th bin, we consider contributions to the singlet yield only from terms in the sum over k that satisfy

$$\omega^{\mathrm{N}}_{k^{\mathrm{N}}} \approx \bar{\omega}^{\mathrm{N}}_{j^{\mathrm{N}}}. \tag{2.71}$$

The contribution to the singlet yield derivative from bin j^{A} on radical A and bin j^{B} on radical B is

$$\left(\Phi'_{\mathrm{S}}\right)_{j^{\mathrm{A}}j^{\mathrm{B}}} \approx \frac{\sqrt{2\pi}}{M} \sum_{p,q} \begin{bmatrix} \left\{\sum_{k^{\mathrm{A}}} \left(\alpha^{\mathrm{A}}_{k^{\mathrm{A}}}\right)'\right\}\left\{\sum_{k^{\mathrm{B}}} \alpha^{\mathrm{B}}_{k^{\mathrm{B}}}\right\} F(\bar{\omega}^{\mathrm{A}}_{j^{\mathrm{A}}} + \bar{\omega}^{\mathrm{B}}_{j^{\mathrm{B}}}) \\ +\left\{\sum_{k^{\mathrm{A}}} \alpha^{\mathrm{A}}_{k^{\mathrm{A}}}\right\}\left\{\sum_{k^{\mathrm{B}}} \left(\alpha^{\mathrm{B}}_{k^{\mathrm{B}}}\right)'\right\} F(\bar{\omega}^{\mathrm{A}}_{j^{\mathrm{A}}} + \bar{\omega}^{\mathrm{B}}_{j^{\mathrm{B}}}) \\ +\left\{\sum_{k^{\mathrm{A}}} \alpha^{\mathrm{A}}_{k^{\mathrm{A}}}\left(\omega^{\mathrm{A}}_{k^{\mathrm{A}}}\right)'\right\}\left\{\sum_{k^{\mathrm{B}}} \alpha^{\mathrm{B}}_{k^{\mathrm{B}}}\right\} F'(\bar{\omega}^{\mathrm{A}}_{j^{\mathrm{A}}} + \bar{\omega}^{\mathrm{B}}_{j^{\mathrm{B}}}) \\ +\left\{\sum_{k^{\mathrm{A}}} \alpha^{\mathrm{A}}_{k^{\mathrm{A}}}\right\}\left\{\sum_{k^{\mathrm{B}}} \alpha^{\mathrm{B}}_{k^{\mathrm{B}}}\left(\omega^{\mathrm{B}}_{k^{\mathrm{B}}}\right)'\right\} F'(\bar{\omega}^{\mathrm{A}}_{j^{\mathrm{A}}} + \bar{\omega}^{\mathrm{B}}_{j^{\mathrm{B}}}) \end{bmatrix}. \tag{2.72}$$

The frequency domain binning algorithm may be summarised thus:

1. On radical A, select a bin j^{A}.

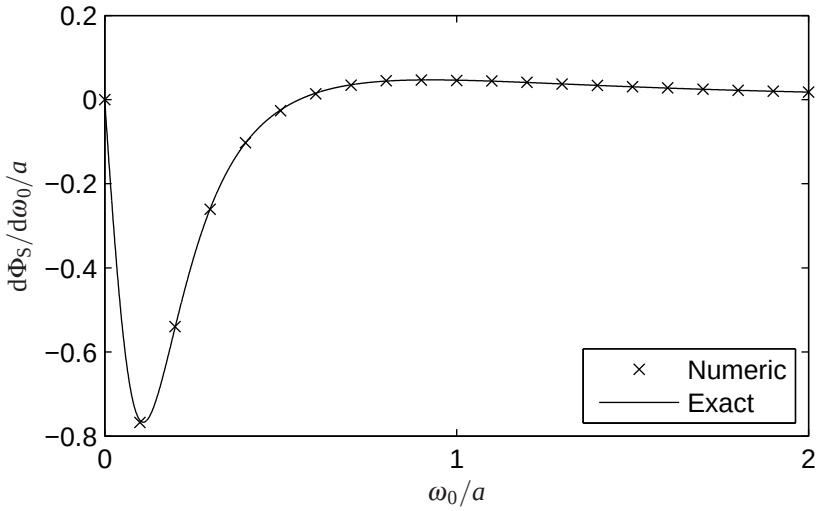

Figure 2.4: Singlet yield derivative in a radical pair with hyperfine coupling constant a to a single spin-½ nucleus, using the exponential model with rate constant $k = a/10$. Numerical results (crosses) were obtained using the frequency domain binning algorithm described in the text. The total number of bins was 8001, with automatic selection of an appropriate number of bins on each radical. Calculation required 23 s on a 3 GHz Pentium IV machine. The exact singlet yield derivative (line) is given by equation (2.61).

2. Evaluate the sums $\left\{\sum_{k^A} \alpha_{k^A}^A\right\}$, $\left\{\sum_{k^A} \left(\alpha_{k^A}^A\right)'\right\}$ and $\left\{\sum_{k^A} \alpha_{k^A}^A \left(\omega_{k^A}^A\right)'\right\}$ for each p and q to give 27 numbers for the chosen bin.

3. Repeat steps 1–2 for the other bins on radical A.

4. Repeat steps 1–3 for radical B.

5. Combine the binned quantities from the two radicals, calculating the contribution to the singlet yield derivative for each combination of bins (j^A on radical A and j^B on radical B) according to equation (2.72).

6. Sum these contributions to give the singlet yield derivative.

This algorithm allows rapid calculation of $d\Phi_S(B)/d\omega_0$ given the Fourier transform of the re-encounter probability $F(\omega)$ and its derivative $F'(\omega)$. Figure 2.4 compares values of the singlet yield derivative calculated using this algorithm with those from equation (2.61). Good convergence to the true singlet yield derivative is seen. Currently, `Matlab` code is used to combine the binned quantities from the two radicals. It is expected that the overall performance could be enhanced by a factor of 10–15 times by rewriting this key step in `C`, just as was found for the binning algorithm in §2.2.2.

2.4 Experimental methods

A simplified reaction scheme for the photo-induced electron transfer reaction between Py and DMA is shown in Figure 2.5. Both S and T pairs can diffuse out of the geminate solvent cage to form free radicals, but only S pairs can recombine to produce a

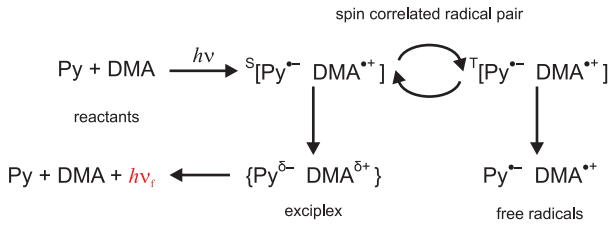

Figure 2.5: Essential steps in the photo-induced reaction of pyrene (Py) and N,N-dimethylaniline (DMA) via the radical pair state $\left[\mathrm{Py}^{\bullet-}\ \mathrm{DMA}^{\bullet+}\right]$ which is responsible for the magnetic field-sensitivity of the exciplex fluorescence. $h\nu$ signifies the incoming ultraviolet radiation and $h\nu_{\mathrm{f}}$ the observed exciplex fluorescence. The structures of Py and DMA are shown in Figure 2.6. See [136], [137, p430], [138, p77] and references therein for further details.

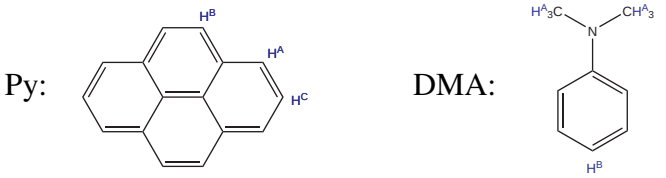

Figure 2.6: Structure of pyrene (Py) and N,N-dimethylaniline (DMA).

fluorescent exciplex. An applied magnetic field modifies the singlet–triplet interconversion, alters the fraction of radical pairs that form exciplexes and hence changes the fluorescence intensity.

Experiments were performed by Norman [139] using apparatus based upon that of Hamilton [140]. Singlet $\left[\mathrm{Py}^{\bullet-}\ \mathrm{DMA}^{\bullet+}\right]$ radical ion pairs were generated by continuous UV irradiation using a 350 W Xe arc lamp (Oriel 66011) with a power supply (Oriel 68811) which delivered approximately constant light intensity across the 300–800 nm range. The light was passed through a water filter to remove the infrared components, through a UV short-pass filter (Andover 345FG01-50; 50% cut-off at 345 nm) and then directed to the sample via a liquid-filled light guide. The fluorescence was collected at 90° to the incident beam, filtered (548 nm filter; 100 nm bandwidth) and transmitted via a light guide to a photomultiplier tube (Hamamatsu R928 mounted on a Hamamatsu C6271 high voltage power supply unit). A variable resistor allowed manual adjustment of the bias voltage across the photomultiplier, whose output was sent to an analogue lock-in amplifier (Stanford Research Systems SR510) which was connected to a personal computer and controlled using `LabVIEW` software [141].

One output from the lock-in amplifier was used to drive the power supply for the static-field coils, generating 0.0–0.6 A, corresponding to a maximum field of 26 mT. A second set of coils was fed with both fixed and audio frequency currents, the latter under the control of the lock-in amplifier; the former was manually controlled and provided a static field of up to 8 mT anti-parallel to that produced by the static-field coils. The amplitude of the 379 Hz audio frequency field modulation was adjustable in the range 0–2 mT; the resulting modulations in the exciplex fluorescence were detected as described above. The net applied field is the sum of the contributions from the two sets of coils and was typically swept from -3 mT to $+23$ mT, with a modulation amplitude of 1.5 mT. The modulation technique results in a signal that is proportional

Isotopomer combination	**hh**	**hd**	**dh**	**dd**
Experimental LFE depth / a.u.	0.15	-	1.54	0.35
Experimental $B_{½}$/mT	6	4	7	4
Calculated $\tilde{a}_{\mathrm{DMA}}/\tilde{a}_{\mathrm{Py}}$	3.2	1.8	12.9	7.3
Calculated $B_{½}$/mT	5.0	2.8	5.6	3.0

Table 2.1: Empirical magnetic field effect parameters and effective hyperfine coupling constants for $\left[\mathrm{Py}^{\bullet-}\ \mathrm{DMA}^{\bullet+}\right]$ radical pairs. Quantities in the bottom two rows were calculated using the hyperfine data from Table 2.2 and equations (3.32) and (3.58).

to the first derivative of the exciplex fluorescence intensity with respect to the strength of the applied magnetic field.

Magnetic field effects were measured for solutions of 1.0 mM pyrene (Py-h_{10} or Py-d_{10}) and 20 mM N,N-dimethylaniline (DMA-h_{11} or DMA-d_{11}) in a 1:4 mixture of dimethylformamide (DMF) and tetrahydrofuran (THF). Samples were sonicated for 30 minutes to aid dissolution of the pyrene and to ensure good mixing. De-oxygenation by bubbling with nitrogen was found to have an insignificant effect on the measured signal strength and shape. The data presented for the four isotopomeric mixtures were each averages of three separate measurements on three 3 ml samples. As far as possible, experimental conditions for the isotopomer combinations were identical; the relative amplitudes of the four data sets are therefore significant. Chemicals and solvents were used as received: Py-h_{10} (Aldrich; 98%), Py-d_{10} (Cambridge Isotope Laboratories, Inc; 98%), DMA-h_{11} (Fluka; $> 99.5\%$), DMA-d_{11} (Cambridge Isotope Laboratories, Inc; $> 98\%$), THF (Sigma-Aldrich; 99.5+%, spectrophotometric grade) and DMF (Sigma-Aldrich; $\geq 99.8\%$, ACS reagent, spectrophotometric grade).

2.5 Experimental results

The dependence of the intensity of the modulated fluorescence on the strength of the applied magnetic field ($-3 < B < 23$ mT) is shown in Figure 2.7 for the four $\left[\mathrm{Py}^{\bullet-}\ \mathrm{DMA}^{\bullet+}\right]$ isotopomers. For brevity, we will refer to the four isotopomer combinations as "**hh**" $\left[\text{Py-h}_{10}^{\bullet-}\ \text{DMA-h}_{11}^{\bullet+}\right]$, "**hd**" $\left[\text{Py-h}_{10}^{\bullet-}\ \text{DMA-d}_{11}^{\bullet+}\right]$, "**dh**" $\left[\text{Py-d}_{10}^{\bullet-}\ \text{DMA-h}_{11}^{\bullet+}\right]$, and "**dd**" $\left[\text{Py-d}_{10}^{\bullet-}\ \text{DMA-d}_{11}^{\bullet+}\right]$. The use of field modulation and the consequent detection of the field-derivative of the fluorescence intensity mean that the data should be anti-symmetric around $B = 0$ mT, as is indeed observed.

Several features are immediately obvious. All four data sets have broadly similar amplitudes; all except **hd** show a LFE — the negative-going region between 0 and ~ 1 mT; and all four show saturation behaviour at magnetic fields greater than about 20 mT. Such observations are common to a great many magnetic field effect measurements [10, 57, 108–111, 113] and have motivated the use of empirical parameters for their qualitative analysis. The pertinent parameters are the LFE depth, defined here as the integral over the negative-going region of the data around zero field, and the half-saturation field $B_{½}$ [142], defined as the magnetic field at which the integrated signal reaches exactly one-half of the integral from $B = 0$ mT to $B = \infty$. Table 2.1 gives the values of these parameters measured from the data in Figure 2.7.

Table 2.2 presents the three largest hyperfine coupling constants $a_{i\mathrm{N}}$ and the effec-

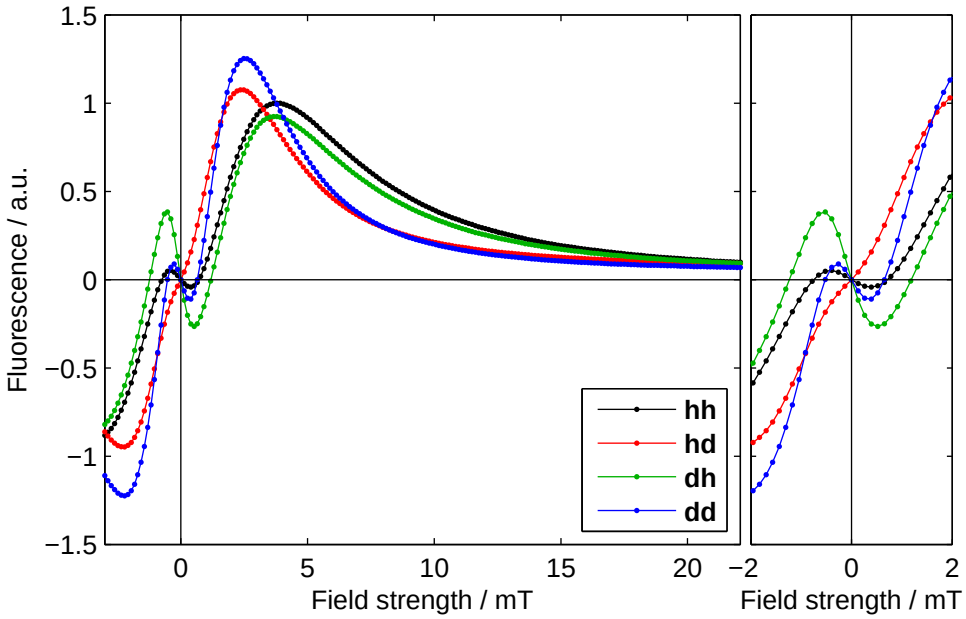

Figure 2.7: First-derivative magnetic field effect on the photochemical reaction of pyrene and N,N-dimethylaniline detected as the intensity of the modulated fluorescence of the exciplex formed from the singlet $\left[\mathrm{Py}^{\bullet-}\ \mathrm{DMA}^{\bullet+}\right]$ radical pair. Data are shown for the four isotopomeric radical pairs described in the text: **hh** (black), **hd** (red), **dh** (green) and **dd** (blue). The panel on the right is an enlargement of the low field region. In both panels, the experimental data points (filled circles) are linked by lines to guide the eye.

Species N	a_{1N}/mT	a_{2N}/mT	a_{3N}/mT	$\tilde{a}_N$/mT[a]
Py-$h_{10}^{\cdot-}$ [143, 145]	0.481 (4H)	0.212 (4H)	0.103 (2H)	1.061
Py-$d_{10}^{\cdot-}$ [b]	0.074 (4D)	0.033 (4D)	0.016 (2D)	0.267
DMA-$h_{11}^{\cdot+}$ [144, 145]	1.180 (6H)	1.100 (1N)	0.520 (1H)	3.443
DMA-$d_{11}^{\cdot+}$ [b]	0.181 (6D)	1.100 (1N)	0.080 (1D)	1.941

[a] Effective hyperfine coupling constants are calculated using equation (3.32).
[b] The ^{2}H couplings were obtained using $a_{\text{deuterated}}/a_{\text{protonated}} = \gamma_D/\gamma_H = 0.1535$.

Table 2.2: Hyperfine coupling constants in Py and DMA radicals. Hyperfine coupling constants are listed for the three groups of equivalent nuclei in each radical that have the largest couplings. H, D and N indicate ^{1}H, ^{2}H and ^{14}N. The number of equivalent nuclei in each group is given in parentheses.

tive coupling constants ($\tilde{a}_{Py}$ and $\tilde{a}_{DMA}$) for each of the four radicals [143, 144]. These values were used to determine the ratio of effective coupling constants and the value of $B_{1/2}$, using equation (3.58), for each radical pair (Table 1). Comparing these calculated values with the corresponding experimental results (also in Table 1), it is clear that the empirical parameters for the four radical pairs are consistent with a series of "rules of thumb" that will be outlined in Chapter 3. Specifically, the measured LFE depth increases as the two effective hyperfine couplings become more disparate and the measured $B_{1/2}$ corresponds reasonably well to the Weller formula, equation (3.58).

Returning to Table 2.1, the agreement between the calculated effective hyperfine couplings and the empirical field effect parameters implies that the differences in the observed field effect curves shown in Figure 2.7 arise from changes in the spin dynamics via the isotope effect on the ^{1}H/^{2}H hyperfine interactions. However, it cannot be ruled out at this stage that the observed variations in LFE depth and $B_{1/2}$ arise from differences in the recombination rates of the isotopomeric radical pairs due, for example, to an isotope effect on the electron transfer rates. We therefore proceed to a detailed quantitative analysis of the data in Figure 2.7 in order to find an empirical re-encounter probability distribution $f(t)$.

2.6 Discretisation

As explained earlier, the experimental fluorescence data in Figure 2.7 may be interpreted, through the RPM, as being proportional to $\Phi'_S(B)$. In order to find the empirical re-encounter distribution that we seek, we must solve the following integral equation

$$\Phi'_S(B) = \int_0^\infty \left\langle \hat{P}^S \right\rangle'(B,t) f(t)\,\mathrm{d}t. \tag{2.73}$$

where $\left\langle \hat{P}^S \right\rangle(B,t)$ is the probability that the radical pair will be found in a singlet state for a given magnetic field strength B at a time t after the instant of radical pair creation, and where the prime $'$ indicates differentiation with respect to field strength, and $f(t)$ is the probability [101] that the radicals re-encounter at time t.

We use the approximate frequency domain algorithm from §2.2.2, with hyperfine coupling constants taken from Table 2.2, to calculate a set of amplitudes α_k and fre-

quencies ω_k such that the singlet yield is given by equation (2.24)

$$\Phi_S(B) = \sum_k \alpha_k(B) F(\omega_k(B)).$$

We proceed by discretising equation (2.24) over a set of regularly-spaced field strengths B_j; the frequencies ω_k are also regularly spaced because of the binning procedure. Provided that we have taken enough frequency samples, $F(\omega)$ will be piecewise constant around each sample ω_k. Therefore we write

$$\boldsymbol{s} = \mathsf{A}\boldsymbol{F} \tag{2.74}$$

where the vector of singlet yield has elements $s_j = \Phi_S(B_j)$, the singlet probability becomes a matrix with elements $A_{jk} = \alpha_k(B_j)$ and the Fourier transform of the re-encounter probability is sampled to give a vector with elements $F_k = F(\omega_k)$. The field strengths are chosen to cover the range of experimental data, which, for ease of analysis, are interpolated at a resolution of 0.1 mT within this interval.

The experimental data are proportional to the derivative of singlet yield with respect to magnetic field strength. We differentiate equation (2.74) approximately by premultiplying by a differentiation matrix D giving

$$\boldsymbol{s}' = \mathsf{D}\boldsymbol{s} = \mathsf{DA}\boldsymbol{F}. \tag{2.75}$$

In this work, D is a fourth order finite differences matrix, calculated using Fornberg's method (see §2.3.2 and [125]). The appropriate one-sided finite differences approximations are used for the terminal points, making use of the symmetry $\Phi_S(B) = \Phi_S(-B)$.

Finally, to allow us to use our physical intuition in respect of the time-domain re-encounter probability $\boldsymbol{f}$, we convert $\boldsymbol{F}$ back into the time domain using the appropriate inverse discrete Fourier transform, shown here by the matrix $\mathscr{F}^{-1}$

$$\begin{aligned}\boldsymbol{s}' &= [\mathsf{DA}\mathscr{F}]\left[\mathscr{F}^{-1}\boldsymbol{F}\right] \\ &= \mathsf{R}\boldsymbol{f}.\end{aligned} \tag{2.76}$$

In practice, the matrix R is evaluated as a column-wise fast Fourier transform of DA, whilst a row-wise FFT would suffice to convert $\boldsymbol{F}$ into $\boldsymbol{f}$.

In preliminary work, we calculated the spin evolution in the $\left[\mathrm{Py}^{\bullet-}\ \mathrm{DMA}^{\bullet+}\right]$ radical pair using a variety of different frequency domain binning resolutions and included different numbers of hyperfine coupling constants. Each case was evaluated by plotting the singlet yield derivative determined using $f(t) = k\mathrm{e}^{-kt}$ for the re-encounter probability distribution [10].

It was found that the three groups of equivalent nuclei with the largest hyperfine couplings on each radical (Table 2.2) could be included within a reasonable computation time. In order to obtain singlet-yield derivative curves that were converged to plotting accuracy for magnetic fields in the range 0–20 mT we found that the number of bins should not be less than $\sim 25\,000$. In the following, 25 001 bins were used so as to have one centred at zero frequency. Although this calculation of the matrix R is lengthy, it need only be performed once for any given radical pair and set of magnetic field values.

Thus, R has dimension $201 \times 25\,001$ corresponding, via equation (2.76), to 201 data points and 25 001 samples of $f(t)$, which are evenly distributed over times $t = 0 \rightarrow 5000\pi$ ns. However, in work with both synthetic and experimental data, we found no reasonable solution for $f(t)$ that had significant amplitude beyond 100 ns. In order to improve the speed of data analysis, we assume that $f(t) = 0 \; \forall \; t \geq 80\pi$ ns. When applied to equation (2.76), this assumption amounts to truncating $\boldsymbol{f}$ after 400 elements and deleting all but the first 400 columns of R. Results obtained using the regularisation methods described below with both the full R and the reduced R are almost indistinguishable. The reduced R has consequently been used in all the reconstructions presented below.

2.7 Need for regularisation

From the form of equation (2.76) it would appear that we are very near to finding the empirical re-encounter probability distribution that we seek. However, there are 25 001 (or 400 in the simplified case) values of $f(t)$ in $\boldsymbol{f}$ which must be determined from 201 experimental data points in $\boldsymbol{s'}$. Such under-determined problems are very common and linear solvers (e.g. the "\" solver built into `Matlab`) are designed to find an optimal solution in a least squares sense, namely

$$\boldsymbol{f}_{LS} = \underset{\boldsymbol{f}}{\operatorname{argmin}} \left\| \mathsf{R}\boldsymbol{f} - \boldsymbol{s'} \right\|_2 . \tag{2.77}$$

Unfortunately, when this solution $\boldsymbol{f}_{LS}$ is examined, it is found to be both highly oscillatory and dominated by numerical noise. The problem is not just under-determined; it is ill-posed. In other words, the recovered solutions $\boldsymbol{f}_{LS}$ are very sensitive to errors in the data $\boldsymbol{s'}$ and in the matrix R — to the extent that rounding errors accumulated while the linear solver runs are enough to render the recovered $\boldsymbol{f}_{LS}$ meaningless. The ill-posed nature of the problem manifests itself in other ways too. For example, we initially attempted to invert the continuous form of this problem — equation (2.73) — by choosing a model functional form for $f(t)$ and fitting a set of parameters. Yet, because the problem is ill-posed, there were a great many local minima amongst the parameters and it proved impossible to optimise the model $f(t)$ properly.

Fortunately, such ill-posed, under-determined problems occur frequently throughout the physical sciences and powerful "regularisation methods" have been developed for their solution [146–150]. There is even a journal "Inverse Problems" which contains a wealth of further examples. At the heart of all these methods is the use of some *a priori* restriction on the set of allowable solutions in order to select a desirable solution from amongst those consistent with the data. Consistency is determined using a suitable statistical test together with an estimate of the noise or uncertainty in the data. Regularisation allows a balance to be struck between doggedly reproducing every detail of the experimental data — including errors — and producing plausible solutions. Hansen gives a very readable, unified account of many such methods in [150]; he also provides an extensive set of `Matlab` implementations in [151]. Using his `Matlab` toolkit, we have been able to apply a substantial number of regularisation methods to this problem, although we only discuss two here. These two regularisation methods are first tested using synthetic data and then applied to the experimentally determined magnetic field effect data.

2.8 Tikhonov regularisation

Tikhonov regularisation is one of the simplest and best known linear regularisation methods [152, 153]. We introduce two measures of the quality of a solution: the residual norm $\|\mathsf{R}\boldsymbol{f} - \boldsymbol{s'}\|_2$ measures the failure of the solution to reproduce the data, whilst the solution norm $\|\mathsf{L}\boldsymbol{f}\|_2$ measures the deviation of the solution from some expected form (typically based on physical insight). The Tikhonov solution is

$$\boldsymbol{f}_T = \underset{\boldsymbol{f}}{\operatorname{argmin}} \left\{ \left\|\mathsf{R}\boldsymbol{f} - \boldsymbol{s'}\right\|_2 + \lambda \left\|\mathsf{L}\boldsymbol{f}\right\|_2 \right\}. \tag{2.78}$$

The regularisation parameter λ allows us to choose how rigidly to enforce our prior knowledge on the solution. A very large value of λ produces a solution which has very little connection to the data but which will conform to our prior knowledge, whilst a very small value of λ will not produce sufficient damping of the troublesome oscillatory components and will therefore give way to noisy solutions. In the limit $\lambda \to 0$, equation (2.78) tends to equation (2.77) and the Tikhonov solution $\boldsymbol{f_T}$ tends to the least squares solution $\boldsymbol{f}_{LS}$. We choose an optimal value for λ using the "L-curve" method [150, 154, 155].

The regularisation matrix L is chosen to select the unwanted components in a solution, which are then penalised by the second term in equation (2.78). In this work, we have used either L equal to the identity matrix, which tends to reduce the recovered $f(t)$ to zero wherever possible or L equal to a second derivative finite-differences matrix D_2, which tends to produce smooth $f(t)$ by penalising regions with large changes in gradient. Both choices will penalise the highly oscillatory behaviour seen in the unregularised solutions.

In addition to these preferences for non-oscillatory solutions, we know that $f(t)$ must be non-negative because it is a probability distribution. It would seem sensible to solve equation (2.78) subject to the constraint that $\boldsymbol{f} \geq 0$. It may be shown [150] that equation (2.78) can be solved by finding the constrained least squares solution to the following normal equation:

$$\left[\mathsf{R}^\dagger\mathsf{R} + \lambda^2\mathsf{L}^\dagger\mathsf{L}\right]\boldsymbol{f_T} = \mathsf{R}^\dagger\boldsymbol{s'} \qquad : \boldsymbol{f_T} \geq 0. \tag{2.79}$$

In the following work, we solved the unconstrained problem in equation (2.78) using the `tikhonov` code in Hansen's `Matlab` toolbox [151]. For the constrained problem in equation (2.79) we used the fast non-negative least squares (FNNLS) algorithm proposed by Bro and Jong [156], which is a more efficient implementation of the classic NNLS algorithm of Lawson and Hansen [157]. Again, calculations were performed in `Matlab`.

2.8.1 Appraisal using synthetic data

Given the difficulty of obtaining reliable solutions to equation (2.76) and given the plethora of regularisation methods available, we must have some means of evaluating their effectiveness. In this work, we used "synthetic data" for this test. The procedure is as follows:

- We choose some re-encounter probability distribution $f(t)$. In our tests, we used, amongst others, re-encounter probability distributions from the well-known exponential [10] and diffusion [47–49] models of radical pair kinetics.
- We then sample $f(t)$ to give $\boldsymbol{f}$.
- Using equation (2.76) in the forward sense, we calculate a set of clean synthetic data corresponding to the chosen $f(t)$.
- We then add normally-distributed random noise, with standard deviation σ_{add}, to the clean synthetic data.
- The noisy synthetic data $\boldsymbol{s}'$ are now passed as input to the chosen regularisation method to give a regularised solution $\boldsymbol{f_R}$.
- The regularised solution $\boldsymbol{f_R}$ and the original, true re-encounter probability distribution vector $\boldsymbol{f}$ are compared.

Applying this procedure to a variety of $f(t)$, we are able to chose optimal regularisation parameters which should allow accurate reconstruction of the empirical re-encounter probability $f(t)$ from the experimental data. Significantly, we may avoid the two pitfalls of regularisation methods: under-regularisation, when the solution will show excessive noise; and over-regularisation, when the solution will not bear a strong resemblance to the chosen $f(t)$.

Choice of λ

Following conventional practice, we choose an optimal value for λ using the L-curve technique [154]. Figure 2.8 shows an example of an L-curve obtained during Tikhonov regularisation for the **hd** isotopomer combination using synthetic data created with an exponential model $f(t)$, with added Gaussian noise of standard noise deviation $\sigma_{\text{add}} = 0.02$. The L-curve provides a simple visual method of choosing the optimal value of λ, showing the trade-off between regularisation, which pushes the solution towards one which fits our prior knowledge, and the need to fit the experimental data. On the right hand side, there are three sets of subfigures. In the top pair, we see the case of under-regularisation, where the value of λ is too small and the solution is therefore dominated by numerical noise even though the fit to the data is exemplary; this situation corresponds to the top-left end of the L-curve. At the other extreme lies the bottom pair, where λ is much too large and the solution $f(t)$ is virtually zero everywhere in order to minimise the solution norm, yet the fit to the data is dire; this over-regularised solution corresponds to the bottom-right end of the L-curve. In between these extremes, near the elbow of the L-curve, we strike a balance. This central region gives the optimal λ, which fits well with the synthetic data and which reproduces the true $f(t)$. This is shown in the middle pair of subfigures.

Choice of L and least squares algorithm

Figure 2.9 shows a selection of Tikhonov reconstructions, each with optimal λ. The figures differ in the choice of solution norm $\mathsf{L} = \mathsf{I}$ (identity matrix) or $\mathsf{L} = \mathsf{D}_2$, where D_2 is a finite-differences approximation to the second-derivative operator (see §2.3.2)

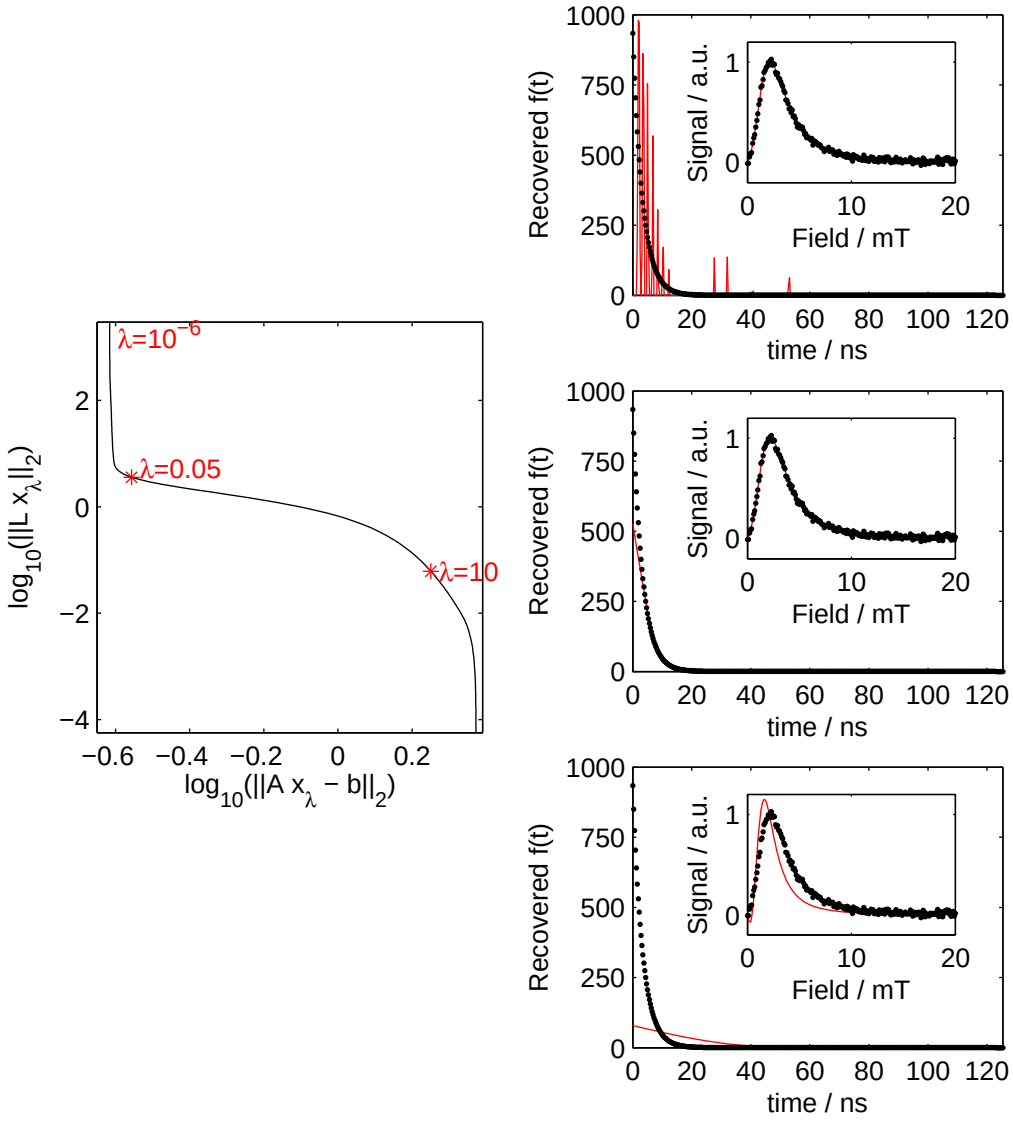

Figure 2.8: L-curve (left) for exponential model synthetic data in **hd**. Hyperfine couplings are given in Table 2.2 and the rate constant $k = 3 \times 10^8\,\mathrm{s}^{-1}$. The figures on the right show the Tikhonov reconstruction of $f(t)$ in red with the exact $f(t)$ in black. Inset into each figure are the synthetic data in black and the Tikhonov fit in red. Together the figures show under-regularisation (top $\lambda = 10^{-6}$), over-regularisation (bottom $\lambda = 10$) and optimal regularisation (centre $\lambda = 0.05$).

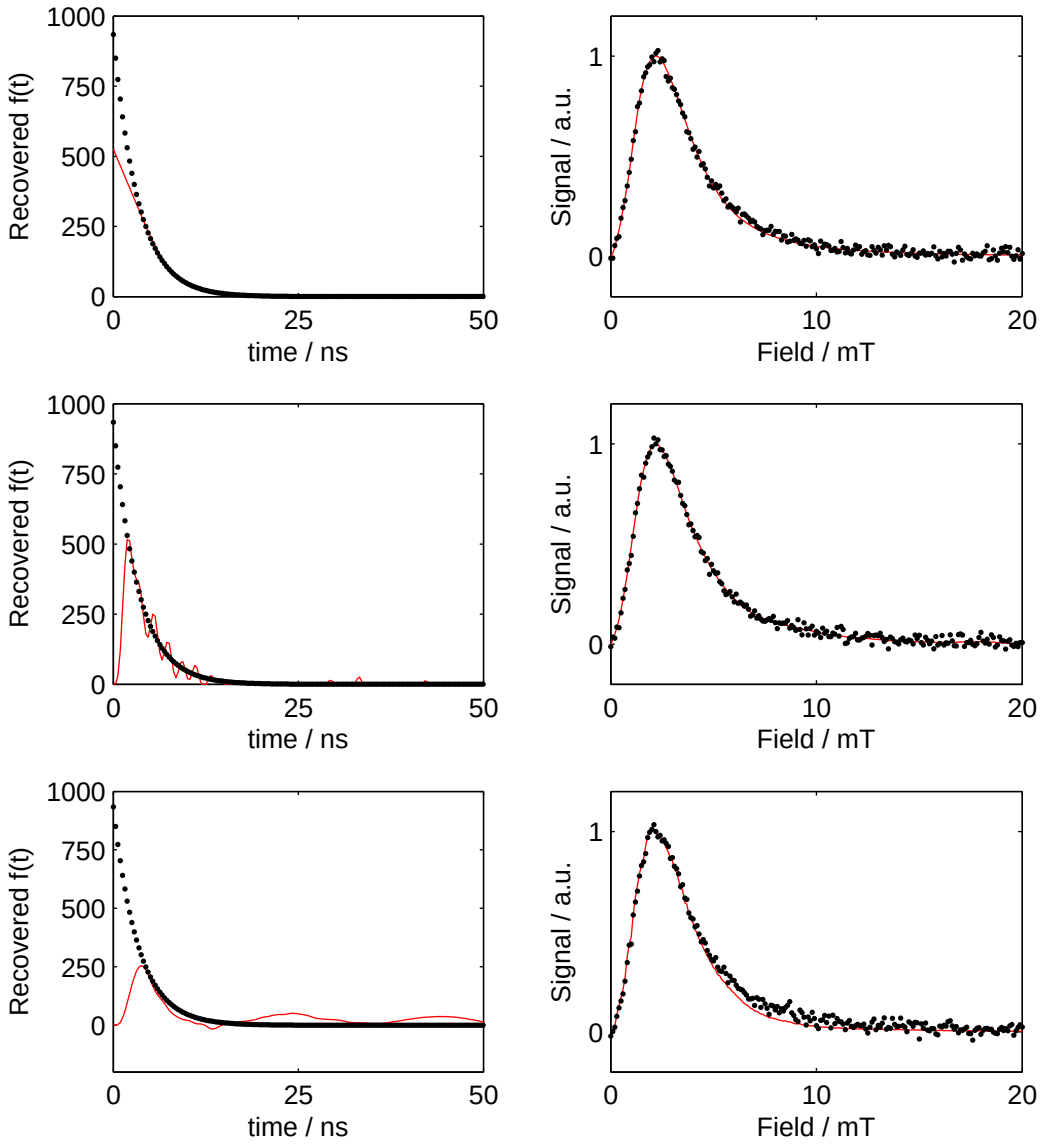

Figure 2.9: Three sets of Tikhonov reconstructions from synthetic data calculated using an exponential model ($k = 3 \times 10^8\,\mathrm{s}^{-1}$) in **hd**. The hyperfine coupling data were taken from Table 2.2. The L-curve method was used to choose an optimal value of λ in each plot. The recovered $f(t)$ were essentially zero outside the range shown. Top: $\mathrm{L} = \mathrm{D}_2$ and using FNNLS [156]. Middle: $\mathrm{L} = \mathrm{I}$ and using FNNLS. Bottom: $\mathrm{L} = \mathrm{I}$ and using Hansen's SVD-based Tikhonov method [151]. Notice that the best reconstruction arises when we enforce non-negative values for $f(t)$ and when we use $\mathrm{L} = \mathrm{D}_2$ which penalises oscillatory solutions.

and in whether $f(t)$ is constrained to be non-negative. Using a solution norm $\mathsf{L} = \mathsf{I}$ will pull the solution $f(t)$ towards zero wherever the data do not provide sufficient evidence for a non-zero value. Physically, this is not a particularly natural choice. Instead, we choose to prefer smooth solutions or, in other words, ones with a small second derivative. We do this by setting $\mathsf{L} = \mathsf{D}_2$. Figure 2.9 shows that this choice of solution norm produces better reconstructions. The figure also shows the importance of constraining $f(t)$ to be non-negative by using the FNNLS algorithm [156].

Although not shown here, Tikhonov regularisation methods were also tested against other model re-encounter probabilities $f(t)$ such as the diffusion model [47–49], or a single Gaussian peak centred at a chosen time. In each case, choosing L to approximate the second derivative operator was found to give the best reconstruction. Together, these results suggest that Tikhonov regularisation is capable of recovering the re-encounter probability $f(t)$ from the experimental data when $\mathsf{L} = \mathsf{D}_2$ and when the FNNLS algorithm is used to guarantee a non-negative solution.

2.9 Maximum entropy regularisation

An alternative, non-linear, Bayesian regularisation method is known as the maximum entropy method (often abbreviated as MEM or MaxEnt) [158–162]. In its classic form, the algorithm aims to recover, from amongst all the solutions consistent with the experimental data, the most probable or maximum likelihood solution $\boldsymbol{f}_{\mathrm{ME}}$. As before, consistency means that $\mathsf{R}\boldsymbol{f}_{\mathrm{ME}} \approx \boldsymbol{s}'$ as measured by an appropriate statistic. In practice, this maximum likelihood solution is determined by maximising the entropy

$$S = -\sum_k \left(\frac{(f_{\mathrm{ME}})_k}{b}\right) \ln\left(\frac{(f_{\mathrm{ME}})_k}{b}\right) \tag{2.80}$$

subject to a chi-squared test

$$\chi^2_{\mathrm{target}} \geq \chi^2 = \sum_k \left[(\mathsf{R}\boldsymbol{f}_{\mathrm{ME}})_k - s'_k\right]^2 / \sigma^2 \tag{2.81}$$

where b is a baseline parameter and σ is (an estimate of) the standard deviation of the experimental noise and χ^2_{target} is equal to the number of data points in $\boldsymbol{s}'$ (201 here) [158, 162].

In this formulation, the baseline factor b is the principal regularisation variable. If the data do not constrain the solution at a particular point, then the maximum entropy method will choose $(f_{\mathrm{ME}})_k = \tilde{f}_{\mathrm{ME}} = b\,\mathrm{e}^{-1}$ for the re-encounter probability there. When the solution is constrained by the data, b governs the relative penalty for increasing f at that point. For a re-encounter probability value $(f_{\mathrm{ME}})_k > b\exp(-1)$, the entropy penalty will increase more rapidly the smaller b. Thus, smaller values of b will pull the baseline down more aggressively and give sharper peaks, whilst larger values of b will result in broader peaks and a higher baseline. The choice of the optimal value of b is discussed below.

In this work, we use an algorithm described by Skilling and Bryan [163] to solve the non-linear constrained optimisation problem defined by equations (2.76), (2.80) and (2.81). This algorithm uses a suitable subspace of search directions based on the entropy S and the constraint χ^2 with a metric for optimisation based on the entropy S.

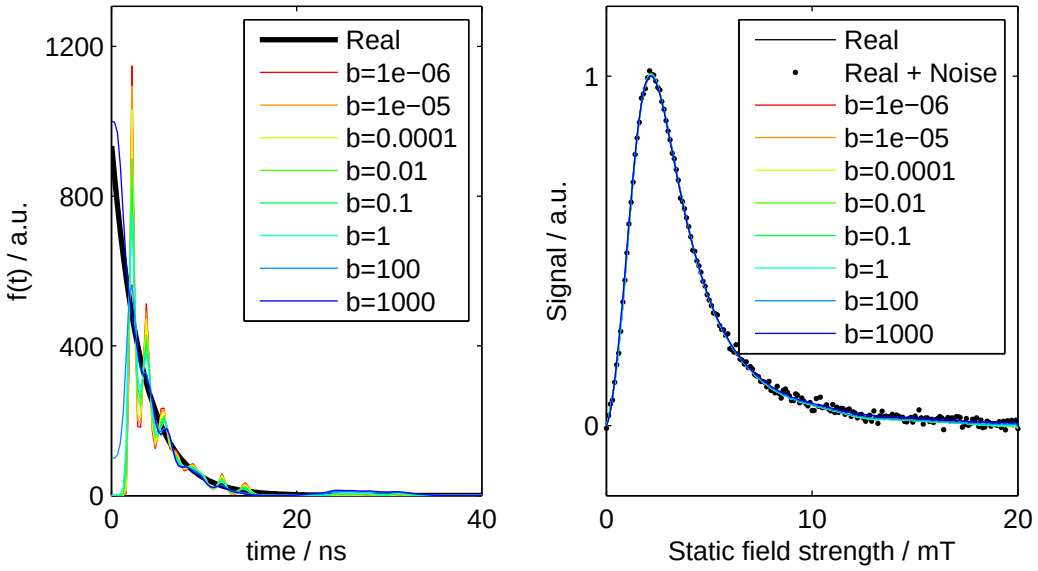

Figure 2.10: Maximum entropy reconstructions of $f(t)$ in the **hd** isotopomer (hyperfine data were taken from Table 2.2). Synthetic data were generated using the exponential model ($k = 3 \times 10^8\,\mathrm{s}^{-1}$) shown in black with normally-distributed random noise added ($\sigma_{\mathrm{add}} = 0.01$). The maximum entropy noise estimate $\sigma = 0.01$. The different reconstructions show how the parameter b influences $f(0)$ and also the oscillations in the recovered $f(t)$. Notice that the fit to the experimental data (right) is exemplary in each case. This illustrates the ill-posed nature of this problem; many f(t) are consistent with the data.

All calculations shown were performed in `Matlab`, based on original `Fortran` code kindly supplied by G. J. Daniell (University of Southampton).

2.9.1 Appraisal using synthetic data

When using the maximum entropy method for regularisation, we must also choose two parameters: the baseline parameter b and an estimate of the noise σ present in the recorded signal. We use synthetic data, following the procedure detailed in §2.8.1, to investigate the most appropriate choices of these parameters for recovering $f(t)$.

Choice of baseline parameter b

Figure 2.10 shows a series of maximum entropy reconstructions with different values of the baseline parameter b. We see that the overall shape of the re-encounter probability $f(t)$ is recovered for a wide range of b values. However, we may also note that increasing the value of the baseline parameter b decreases the tendency of the maximum entropy method to produce sharp peaks. Whilst sharp peaks are desirable when reconstructing overlapping spectral features - for example, in NMR spectra - they do not make good physical sense in this context and therefore we will tend to choose larger values of b than have typically been used to process NMR data [158, 164].

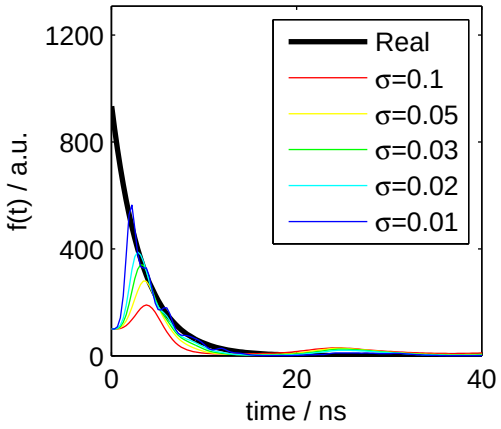

Figure 2.11: Maximum entropy reconstructions of $f(t)$ in the **hd** isotopomer (hyperfine data were taken from Table 2.2). Synthetic data were generated using the exponential model ($k = 3 \times 10^8\,\mathrm{s}^{-1}$) shown in black with normally-distributed random noise added ($\sigma_{\mathrm{add}} = 0.01$). The maximum entropy parameter $b = 100$ in all cases. The different reconstructions show how the estimated noise standard deviation σ influences the recovered $f(t)$. The maximum entropy method was found not to converge for $\sigma < 0.01$ (*i.e.* when $\sigma < \sigma_{\mathrm{add}}$).

Choice of noise estimate σ

Figure 2.11 shows another series of maximum entropy reconstructions from the same system, where we set $b = 100$ and explore the effects of altering the noise estimate σ. Clearly, the quality of the recovered $f(t)$ improves as the noise estimate approaches the true noise level σ_{add}. Notably, $f(t)$ is recovered properly at earlier times as σ is reduced. On the other hand, attempts to use a noise estimate σ smaller than the true noise level ($\sigma_{\mathrm{add}} = 0.01$) resulted in the method failing to converge. In light of these results, we adopt a pragmatic approach when analysing the experimental data and choose the lowest value of σ at which the maximum entropy solution converges within 1000 iterations.

Figure 2.12 summarises the results of a large series of maximum entropy calculations on this same set of synthetic data. For each converged solution, we plot a point whose co-ordinates indicate the errors in fitting the synthetic data and the errors in recovering the true $f(t)$. This figure supports the argument above that a value of $b \sim 100$–1000 and the smallest possible noise estimate σ are close to being optimal. Other analogous calculations were performed for synthetic data from the diffusion model and for a re-encounter probability having the form of a single Gaussian peak. The results in these cases support the same conclusion.

2.10 Results

Having established that the two regularisation methods are able to recover the re-encounter probability $f(t)$ from a variety of synthetic data, we proceed to apply them to the experimental data shown in Figure 2.7. In both cases, the regularisation parameters were chosen after a careful evaluation using the synthetic data (discussed above).

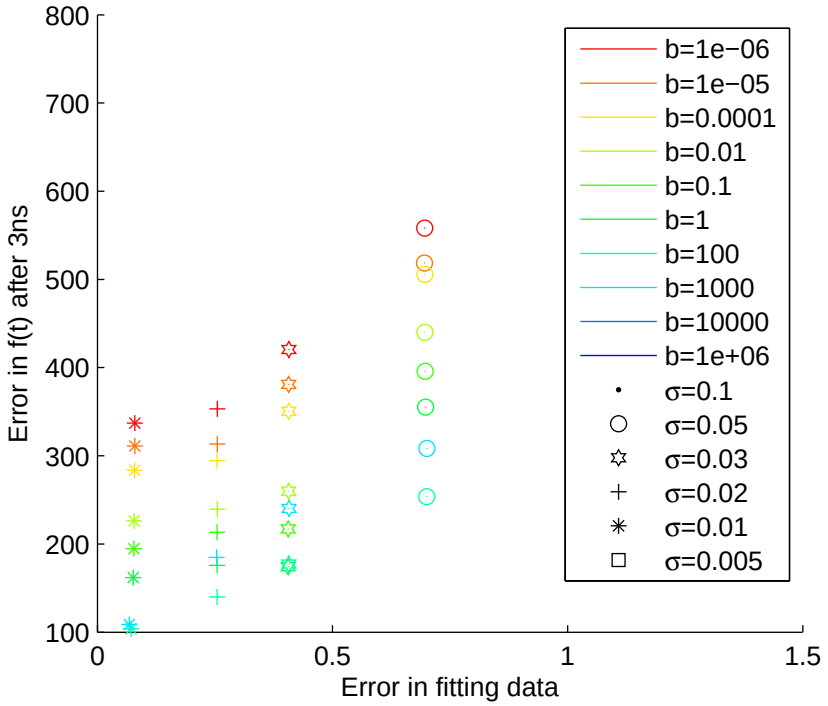

Figure 2.12: Summary of several maximum entropy reconstructions of $f(t)$ in the **hd** isotopomer. Synthetic data were generated using an exponential model $f(t)$ with normally-distributed random noise added ($\sigma_{\text{add}} = 0.01$). Reconstructions were attempted with a variety of b and σ values. For each converged reconstruction, we plot a point showing the residual norm in recovering $f(t)$ *vs.* the norm of the deviations from the synthetic data. Notice that the best results are when σ matches the true noise standard deviation and with a reasonably large value of b. Underestimating σ or choosing an excessive b causes the maximum entropy method not to converge. Overestimating σ or using a small b gives rise to a suboptimal reconstruction.

Tikhonov regularisation was applied to the data for each isotopomer combination taken separately. We obtained the most satisfactory results by using $\mathsf{L} = \mathsf{D}_2$ for the solution seminorm, which discourages oscillations in the recovered $f(t)$; by constraining $f(t) \geq 0$ using the FNNLS algorithm; and by choosing λ using the L-curve method. The results are given in Figure 2.13A and discussed below.

Maximum entropy regularisation was also applied to each isotopomer combination taken separately. Figure 2.13B shows the recovered $f(t)$, which is discussed below. One difference between the tests using synthetic data and the analysis of the experimental data was the choice of noise standard deviation estimate σ. In order to obtain convergence with the experimental data, it was necessary to increase σ slightly from the value estimated by inspection of the raw data at fields higher than the saturation value. This discrepancy might arise because of the use of a lock-in amplifier, which causes the noise to be correlated somewhat between neighbouring data points — something that is not included in our maximum entropy treatment. It could also arise from the neglect of some of the small hyperfine couplings or other interactions. Nevertheless, evaluation with synthetic data shows that increasing the noise estimate slightly has only a small effect on the recovered $f(t)$. Hence, this point should not concern us further.

The $f(t)$ distributions for the four isotopomer combinations (Figures 2.13A and B) are strikingly similar to one another for values of t greater than 2 ns. To test whether they are truly equivalent, we attempted to recover a single $f(t)$ by processing all four isotopomer combination data sets simultaneously. Very satisfactory fits to the data were obtained by allowing a modest constant scaling of each data set relative to **hh**. Physically, this corresponds to dropping our assumption of exactly identical experimental conditions (e.g. concentrations, light intensity, detector performance, sample temperature) for the four isotopomer combinations. The combined analysis was accomplished by wrapping an outer non-linear least squares minimisation routine around the Tikhonov regularisation code. In the outer routine, the relative intensities of the data sets are varied in order to minimise the residual norm. This process was repeated for each value of λ in order to construct an L-curve from which the optimal λ was obtained, giving the result presented in Figure 2.13C.

Before interpreting the re-encounter probability distributions in Figure 2.13, two technical points need to be mentioned. First, we observed that the data for the **dd** isotopomer were somewhat more difficult to analyse than those from the other isotopomer combinations. This is reflected in the slightly higher maximum entropy noise estimate required for the **dd** analysis in Figure 2.13B. During our evaluation with synthetic data, it was also found to be more difficult to reconstruct $f(t)$ from the **dd** isotopomer combination. Since these difficulties arise even with synthetic data, they are not caused by deficiencies in the theoretical model, nor by experimental difficulties. Instead, it seems that the particular hyperfine coupling constants in the **dd** isotopomer combination create an inversion problem that is even more severely ill-posed than those for the other isotopomer combinations. Second, there are noticeable residual oscillations in the $f(t)$ functions obtained by all three methods (Figure 2.13). These are almost certainly spurious since their positions and amplitudes depend on the choice of regularisation parameter (b for maximum entropy and λ for Tikhonov regularisation). They demonstrate one of the fundamental tendencies of ill-posed problems, which tend to introduce unphysical oscillations into the solution when even very tiny amounts of noise are present

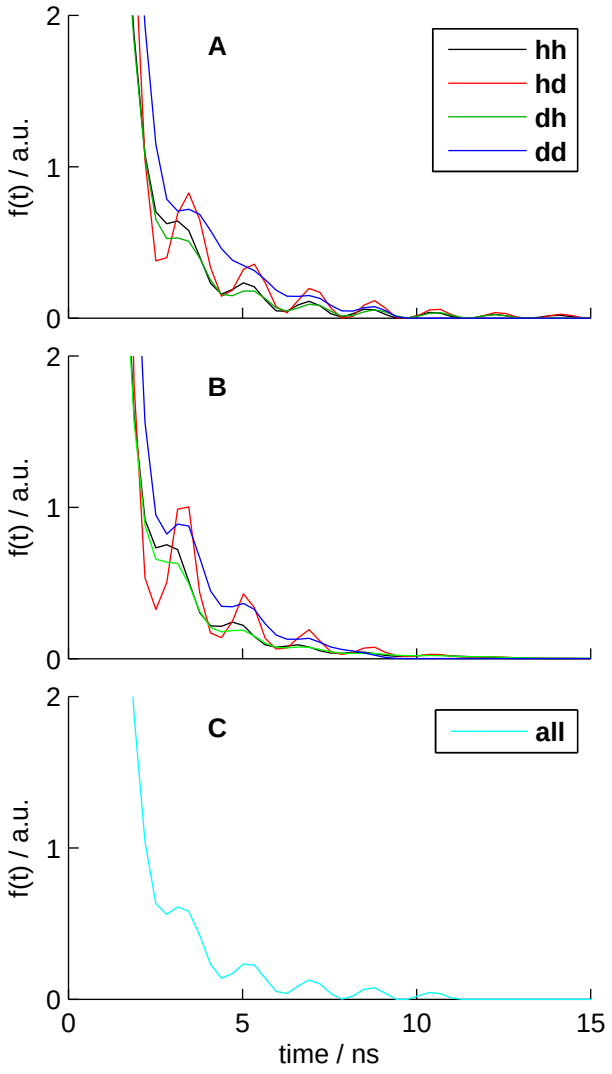

Figure 2.13: Best recovered $f(t)$ for: (A) Tikhonov regularisation; and (B) maximum entropy regularisation for each of the four isotopomer combinations. (C) Tikhonov regularisation recovery of a single $f(t)$ to fit all four isotopomer combinations simultaneously. For (C), the experimental data for each isotopomer combination were scaled as part of the regularisation procedure. The optimal scaling factors were: **hh** 1.00 (*i.e.* not rescaled), **hd** 0.73, **dh** 1.08, **dd** 0.59. In all cases, the fits to the experimental data were exemplary. The fits for case (A) are shown in Figure 2.14 with an illustrative L-curve in Figure 2.15; the fits for case (B) are shown in Figure 2.16; and those for case (C) are shown in Figure 2.17.

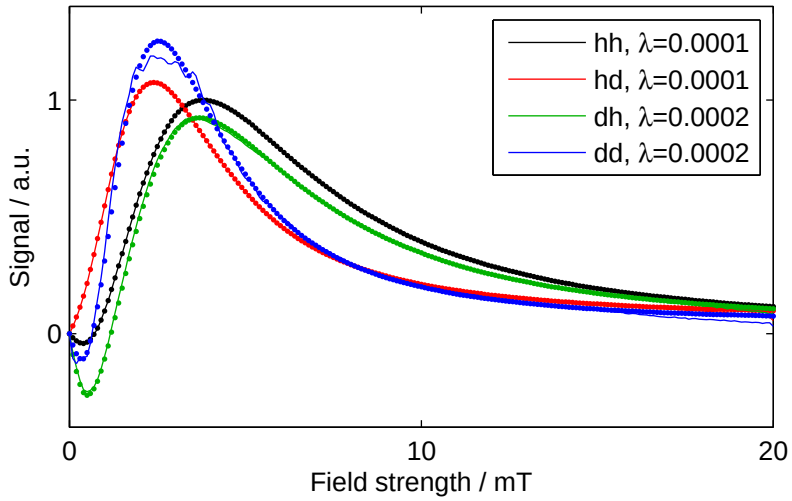

Figure 2.14: Fits (lines) to the experimental data (dots) for Tikhonov regularisation corresponding to the recovered $f(t)$ in Figure 2.13A. Optimal values of the regularisation parameter λ, chosen according to the L-curve method, are given in the legend for each isotopomer combination.

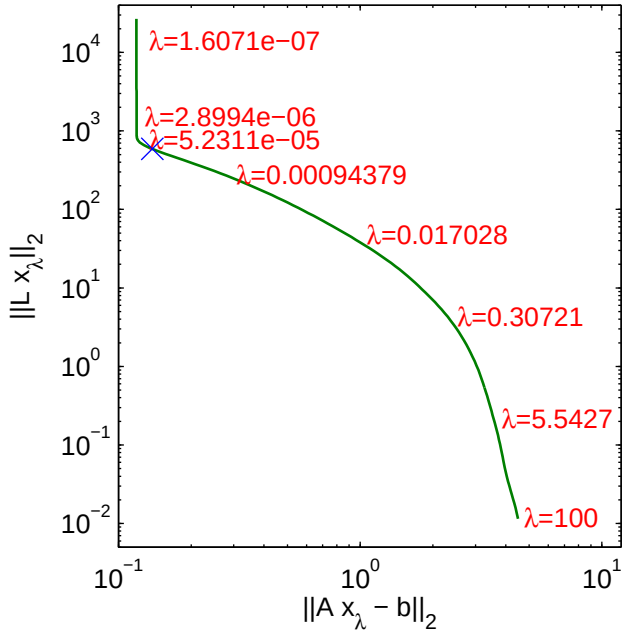

Figure 2.15: Illustrative L-curve showing the trade off between solution and residual norm for Tikhonov regularisation in the **dh** isotopomer pair with different choices of the regularisation parameter λ. The optimal value of λ, indicated with a blue cross, is just below and to the right of the "L". This L-curve corresponds to the green curve in Figures 2.13A and 2.14.

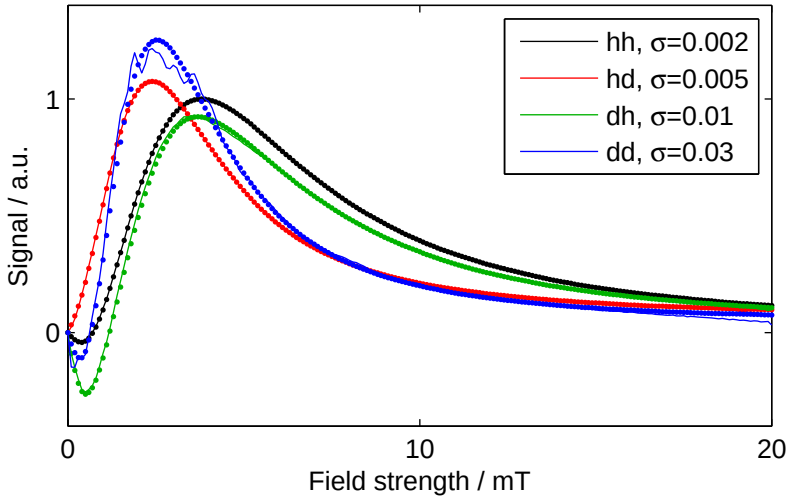

Figure 2.16: Best fits to the experimental data using maximum entropy regularisation. The maximum entropy noise estimates σ for each isotopomer combination are given in the legend. These were chosen to be as small as possible, as described in the text. Notice that the fits are exemplary, except for a small region in the **dd** isotopomer around $3\,$mT which is discussed in the text. This figure complements Figure 2.13B.

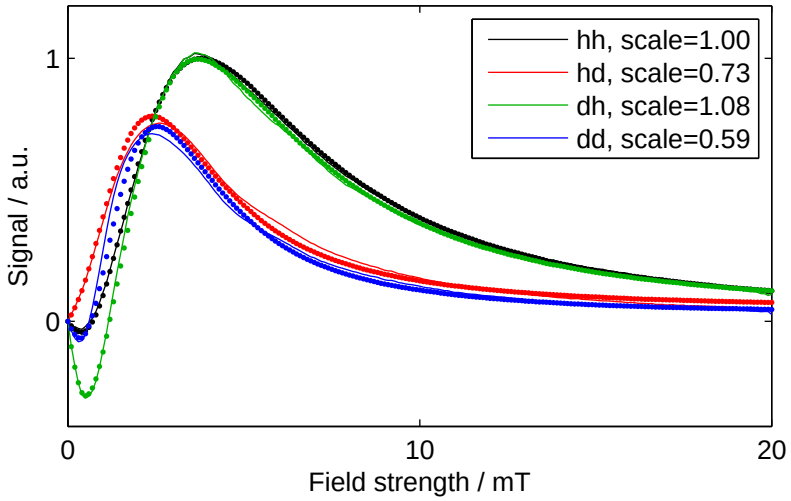

Figure 2.17: Best fits to the experimental data using Tikhonov regularisation applied to all four data sets simultaneously in order to produce a single re-encounter probability $f(t)$. The regularisation parameter $\lambda = 0.0002$ was chosen using the L-curve method. The experimental data were multiplied by optimised values of "scale" before using Tikhonov regularisation. Notice that the fit is exemplary, except for small deviations in the **dd** isotopomer curve. This figure complements Figure 2.13C.

in the data [150]. Thus, attempts to solve equation (2.77) in a least squares sense (not shown) gave "solutions" with such wild oscillations that any physically meaningful information on the re-encounter probability was completely obscured. Regularisation methods dramatically improve this situation and allow many of the oscillations to be eliminated. Nevertheless, there are fundamental limits to the information contained in experimental data such as those in Figure 2.13. We should not expect to achieve a perfect suppression of oscillatory artefacts in an ill-posed problem.

2.11 Discussion

The re-encounter probability distributions $f(t)$ for the four isotopomer combinations are remarkably similar to one another for times longer than $\sim 2\,\mathrm{ns}$. This can be seen in Figures 2.13A and B, and is perhaps most powerfully demonstrated by Figure 2.13C, where a single $f(t)$ was recovered from data for all four isotopomeric reactions simultaneously. The close fit to the experimental data (see Figures 2.14–2.17) provides direct evidence that diffusion and reaction kinetics in these aromatic radical ion pairs are changed very little by perdeuteration. Isotopic substitution is clearly an effective means of modifying the hyperfine interactions and hence the extent and efficiency of singlet–triplet interconversion in a radical pair reaction without disturbing other parameters; this bodes well for future studies.

We also note the strong resemblance of the $f(t)$ distributions recovered from the Tikhonov (Figure 2.13A) and maximum entropy (Figure 2.13B) methods. The former is a linear regularisation method, while the latter is non-linear. That these two disparate techniques yield the same re-encounter probability distributions (for $t > 2\,\mathrm{ns}$) significantly strengthens our confidence that the $f(t)$ shown above are to be believed. It seems quite implausible that two independent methods should both fail in the same manner. This confidence is increased still further by the robust behaviour of the two approaches when working with synthetic data.

Although the re-encounter probabilities obtained from Tikhonov and maximum entropy regularisation are rather similar, there are substantial differences in the first 2 ns (not shown in Figure 2.13). The Tikhonov $f(t)$ is essentially linear in t for $t < 2\,\mathrm{ns}$ with a large negative gradient. The $f(t)$ from maximum entropy, however, tends to the value of the baseline parameter b as $t \to 0\,\mathrm{ns}$. This contrasting behaviour is expected if $f(t)$ is not constrained by the experimental data during the first 2 ns, *i.e.* if the re-encounters that occur during the first 2 ns make little contribution to $\mathrm{d}\Phi_S(B)/\mathrm{d}B$. In such a situation, as discussed in connection with equations (2.78) and (2.79), the use of $\mathsf{L} = \mathsf{D}_2$ in Tikhonov regularisation disfavours oscillations and so will produce an $f(t)$ with vanishing second derivative; meanwhile, the form of the expression for S, in equation (2.80), causes the maximum entropy reconstruction to be pulled strongly towards the value of the baseline parameter b.

Figure 2.18 demonstrates qualitatively that the experimental data do not constrain $f(t)$ at short times. The figure is produced by calculating the singlet probability in the **hd** isotopomer for 201 magnetic fields between 0 and 20 mT and at many times during the first 50 ns. From these data, we find the standard deviation of the singlet probabilities at different field strengths for a given time. This standard deviation is plotted to give a qualitative measure of the extent to which the singlet probability depends on magnetic field strength in the **hd** isotopomer during the first 50 ns. Accord-

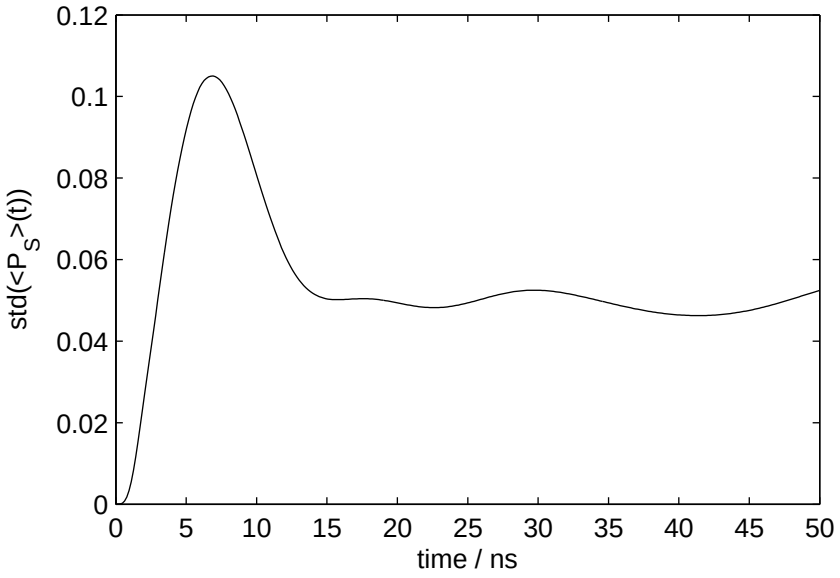

Figure 2.18: Standard deviation of the singlet probability in **hd** at each of the 201 field points plotted as a function of time. Notice that in the first few nanoseconds after radical pair creation there is very little change in spin evolution at different static field strengths. This means that the experiment is insensitive to $f(t)$ at short times. The standard deviation remains roughly constant around 0.05 at times greater than 15 ns.

ing to equation (2.73), the experimental data are the sum over time of contributions $\left\langle \hat{P}^{\mathrm{S}} \right\rangle'(B,t) f(t)$. When the standard deviation of singlet probabilities is small, so must be $\left\langle \hat{P}^{\mathrm{S}} \right\rangle'(B,t)$ and the contribution to the data will be largely independent of $f(t)$ at that time. Hence, Figure 2.18 gives a qualitative measure of the extent to which $f(t)$ is constrained by the experimental data. It is clear, therefore, that the contribution to the singlet yield during the period $0 < t < 2\,\mathrm{ns}$ is almost independent of the magnetic field strength and thus, the data do not constrain $f(t)$ at these short times.

This argument sheds light on the interpretation of the $f(t)$ distributions recovered from the magnetic field effect data. The results in Figure 2.13 do not represent the total distributions of re-encounter probabilities, but rather the distributions of the re-encounters *that are important for the formation of a magnetic field effect*. It is evident from Figure 2.13 that these re-encounters occur principally between about 2 and 10 ns. The large number of re-encounters that are expected to take place during the first 2 ns are unimportant because 2 ns is too short a time to allow significant spin-evolution of the radical pair under the Zeeman interaction. For applied magnetic fields in the range $0 < B < 20\,\mathrm{mT}$, the electron Zeeman interaction has a maximum frequency of $\sim 560\,\mathrm{MHz}$, whose reciprocal is $\sim 2\,\mathrm{ns}$. Since $\mathrm{d}\Phi_{\mathrm{S}}(B)/\mathrm{d}B$ is expected to have its maximum value at $B \approx B_{½} \approx 5\,\mathrm{mT} \approx 140\,\mathrm{MHz}$, we can anticipate that the optimum time for re-encounters will be approximately $(1/140)\,\mathrm{MHz} \approx 7\,\mathrm{ns}$, as found in the recovered $f(t)$ functions in Figure 2.13.

We may speculate on a further aspect of the interpretation of the $f(t)$ distributions in Figure 2.13. Hitherto we have chosen to ignore the exchange interaction between the two radicals — certainly a good approximation when the radical–radical separation is large (> 1.0–$1.5\,\mathrm{nm}$). However, when the radicals are close enough that the exchange

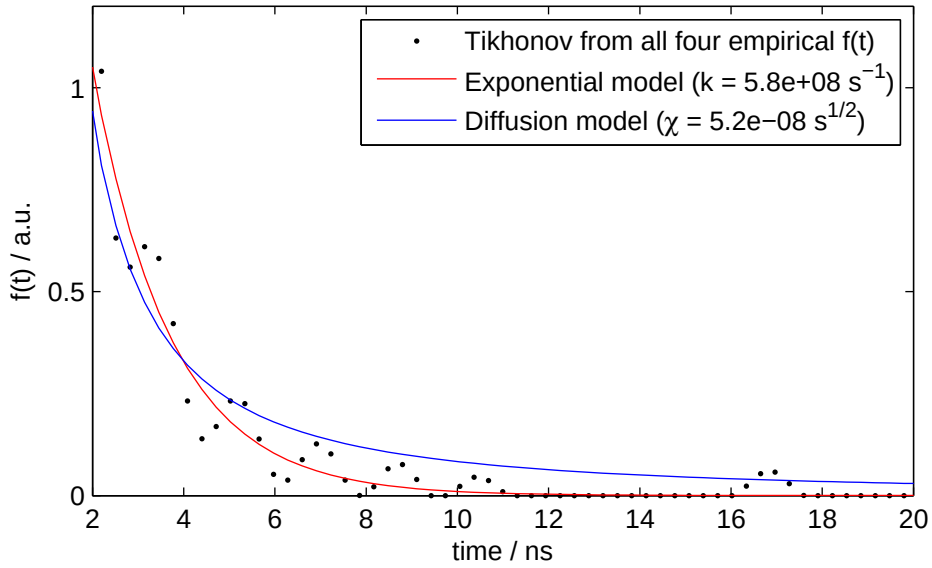

Figure 2.19: Analysis of Tikhonov regularisation $f(t)$ from Figure 2.13C (black points). We fit the recovered $f(t)$ to the exponential and diffusion models for times $t > 2$ ns. It is clear that the Tikhonov regularised $f(t)$ is close to that predicted by the exponential model (k is the rate constant). The diffusion model gives a rather poorer fit ($\chi = (R_0 - R_\sigma)/\sqrt{2D}$, where R_0 is the initial radical separation, R_σ is the separation at which reaction occurs and D is the mutual diffusion coefficient).

dominates the hyperfine and Zeeman interactions, all singlet–triplet interconversion ceases and the pair is locked into a singlet or triplet eigenstate. We may therefore think of an "exchange zone" of radical–radical separations (extending out to 1.0–1.5 nm) in which there is no dependence of the radical pair spin evolution on the applied magnetic field. Thus, during a diffusive trajectory, singlet–triplet interconversion can be considered to start only when the radicals leave the exchange zone and to stop as soon as they re-enter it. Any radical pair that re-enters in a singlet state remains in a singlet state until it either recombines or diffuses apart again. Thus, the recovered $f(t)$ may be regarded as giving information on the trajectories that are important for the generation of the magnetic field effect, *i.e.* those that spend 2–10 ns outside the exchange zone. The fact that all the $f(t)$ distributions in Figure 2.13 have a very low amplitude beyond 10 ns simply reflects the low probability that the radicals return to the exchange zone after such a time.

Finally, Figure 2.19 shows that the decaying $f(t)$ distribution ($t > 2$ ns) in Figure 2.13 resembles that assumed in the traditional exponential model [10] (with a best-fit rate constant $k = 5.8 \times 10^8\,\mathrm{s}^{-1}$). The agreement with the diffusion model [48] is less satisfactory principally because the predicted $t^{-3/2}$ dependence seriously overestimates the extent of the "tail" of the $f(t)$ distribution after about 6 ns. The exponential model, in spite of its apparent crudity, evidently captures the general behaviour of the re-encounters on which the magnetic field effects depend. Our data therefore support the use of such empirical diffusion models for the calculation of magnetic field effects.

2.12 Conclusions

To conclude, we have interpreted experimental data on the effects of applied magnetic fields ($\leq 23\,\mathrm{mT}$) on the spin-selective recombination of isotopomeric $\left[\mathrm{Py}^{\bullet-}\ \mathrm{DMA}^{\bullet+}\right]$ radical pairs [114]. Qualitatively, the experimental $B_{1/2}$ values agree well with predictions based on the Weller equation and the known hyperfine coupling constants, and the amplitude of the LFE correlates well with the ratio of effective hyperfine couplings, $\tilde{a}_{\mathrm{DMA}}/\tilde{a}_{\mathrm{Py}}$. Using an efficient method for calculating the spin evolution of radical pairs containing a total of 18 spin-½ and spin-1 nuclear spins, we have inverted the magnetic field effect data to obtain the radical re-encounter probability distribution $f(t)$ — a highly ill-posed and under-determined problem — by means of Tikhonov and maximum entropy regularisation methods. The resulting $f(t)$ functions are very similar for the four isotopomeric radical pairs and have significant amplitude between 2 and 10 ns after the creation of the geminate radical pair. This interval reflects the timescale of re-encounters that are important for generating the magnetic field response.

Chapter 3

Empirical parameters for MARY spectra

3.1 Introduction

Certain chemical reactions are known whose product yields vary as a function of applied magnetic field strength. Amongst these, the most thoroughly studied are those proceeding via spin correlated radical pairs [1, 2, 87]. Such reactions occur in a wide variety of systems, although we focus our attention in this chapter on reactions in isotropic, homogeneous liquid phases. A typical example would be the photo-induced reaction between pyrene (Py) and N,N-dimethylaniline (DMA), whose structures are shown in Figure 2.6, dissolved in a 1:4 mixture of dimethylformamide (DMF) and tetrahydrofuran (THF) [114, 139]. A schematic reaction scheme is given in Figure 3.1, which shows that one product is a fluorescent exciplex. The balance between the formation of this fluorescent exciplex and of other products is found to depend critically on the presence of a magnetic field. One can therefore perform a variety of experiments varying magnetic field parameters (strength, orientation, frequency) whilst monitoring the exciplex fluorescence. This is the basis of the magnetic field effect on reaction yield (MARY) experiment in which reaction yield is measured as a function of applied static magnetic field strength.

This chapter aims primarily to investigate the gross features of such MARY spectra. We introduce a small number of empirical parameters which characterise qualitatively the shape of a MARY spectrum. These parameters include measurements of the magnetic field required to saturate a field effect, as well as the depth and position of any low field effect (LFE) feature which may be present. As part of this survey, we show that the rate of radical pair re-encounter is critical to the qualitative features of a MARY spectrum. It is suggested that some long standing apparently contradictory statements in the literature regarding the circumstances in which a strong LFE may be observed may be reconciled since they refer to different limiting kinetic regimes.

In order to perform such an investigation, we need appropriate theoretical methods. Therefore, this chapter also aims to develop and evaluate two such methods. We provide a fresh derivation of the semiclassical approximation (SCA) [27, 28], in order to emphasise its close connections with our quantum mechanical calculations. Although the SCA is of long standing in the literature, it appears to have been tested and reworked only very rarely, and then only to extend the SCA to interpret RP reactions

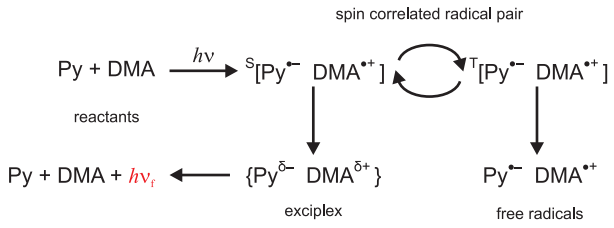

Figure 3.1: Essential steps in the photoinduced reaction of pyrene (Py) and N,N-dimethylaniline (DMA), whose structures are given in Figure 2.6, via the radical pair intermediate $\left[\mathrm{Py}^{\bullet-}\ \mathrm{DMA}^{\bullet+}\right]$ which is responsible for the magnetic field-sensitivity of the exciplex fluorescence. $h\nu$ signifies the incoming ultraviolet radiation and $h\nu_{\mathrm{f}}$ the observed exciplex fluorescence.

involving degenerate electron exchange[1]. We introduce a second method of calculation, based on Monte Carlo statistical averaging in a suitable ensemble of radical pairs. This method is used to evaluate the reliability of the SCA for a variety of parameters. The method is also used to develop a series of "rules of thumb" for predicting the qualitative feature of MARY spectra.

3.2 Model

The radical pair mechanism (RPM) [13, 14, 87] provides the mechanistic basis for our interpretation of magnetic field effects in the reaction of Py and DMA. The essential features are summarised in §1.4. The key feature of the RPM is the spin-evolution between singlet and triplet states during diffusive excursions of the geminate radical pair.

Experimentally, the reaction between Py and DMA is followed by measuring the fluorescence of the exciplex that is in rapid equilibrium with the singlet RP. Therefore, in order to model these data, the central quantity that we wish to calculate is the yield of singlet product, or "singlet yield" Φ_{S} for short.

Using the formalism of Noyes [101], described more fully in §1.6, the singlet yield may be written as

$$\Phi_{\mathrm{S}}(B) = \int_0^\infty \left\langle \hat{P}^{\mathrm{S}} \right\rangle (B,t) f(t)\,\mathrm{d}t \tag{3.1}$$

where $\hat{P}^{\mathrm{S}}$ is the RP unpaired electron singlet projection operator, and hence $\left\langle \hat{P}^{\mathrm{S}} \right\rangle (B,t)$ is the probability that the radical pair will be found in a singlet state for a given magnetic field strength B and a time t, and where $f(t)$ is the probability distribution for first re-encounters. For simplicity, we use assume that this re-encounter distribution has the form

$$f(t) = k\mathrm{e}^{-kt}, \tag{3.2}$$

where k is a first-order rate constant. This is known in the literature as the "exponential model" [13, 15, 79]. We can therefore predict the RP singlet yield, and hence the observed fluorescence intensity, using equation (3.1) providing that we know how the RP

[1] The author used ISI Web of Science to locate and study all the 49 papers that have cited refs [27, 28].

spin state evolves — *i.e.* providing that we know the time-dependent singlet probability $\left\langle \hat{P}^{\mathrm{S}} \right\rangle (B,t)$.

3.3 Semi-classical approximation

The semi-classical approximation introduced by Knapp, Schulten and Wolynes [27, 28] attempts to calculate MFEs in RP reactions without becoming embroiled in laborious full quantum mechanical calculations of the RP spin evolution. When first introduced, it was especially significant because digital computers of the era lacked the RAM and processing power to which we have become accustomed. As we will see shortly, the semi-classical approximation may be derived by assuming that each nuclear spin behaves as a classical magnetic dipole — in other words, that nuclear spin is not quantised. We then assume that in any given radical, the unpaired electron spin precesses around the resultant vector formed from the applied magnetic field and from each nuclear spin magnetic dipole. Using a result from polymer statistical physics, we integrate over all possible orientations of the nuclear spins to give an ensemble average electron spin evolution. Finally, treating the electron spins quantum mechanically, and using a formula analogous to equation (3.6) we arrive at a new closed-form expression for the time-dependent singlet probability $\left\langle \hat{P}^{\mathrm{S}} \right\rangle$. This may be substituted into equation (3.1) to give the singlet yield as a function of applied magnetic field strength.

3.3.1 Recap of density matrix approach

In order to emphasise its close relationship with the SCA, we give here a brief resumé of the density matrix approach to singlet yield calculations that we take elsewhere in this thesis. In the density matrix approach, we assume that the only significant interactions are the isotropic hyperfine interaction between the electron and nuclear spins in each radical and the isotropic Zeeman interaction of the electron spins with the applied magnetic field.[2] Thus, we write the spin Hamiltonian of the radical pair — composed of radicals "A" and "B" — as

$$\hat{H} = \hat{H}^{\mathrm{A}} + \hat{H}^{\mathrm{B}} \quad \text{where} \quad \hat{H}^{\mathrm{N}} = \sum_i a_{i\mathrm{N}} \hat{\boldsymbol{S}}_{\mathrm{N}} \cdot \hat{\boldsymbol{I}}_{i\mathrm{N}} - \gamma_{\mathrm{e}} B \hat{S}_{\mathrm{Nz}}, \tag{3.3}$$

in which $a_{i\mathrm{N}}$ are the isotropic hyperfine coupling constants between the unpaired electron on radical N and a magnetic nucleus i, $\hat{\boldsymbol{S}}$ and $\hat{\boldsymbol{I}}$ are the electron and nuclear spin operators respectively, γ_{e} is the electron magnetogyric ratio whose value is given in Appendix D and where the field is applied along the z-axis. We use angular frequency units for the Hamiltonian.

In terms of a time-dependent density matrix $\hat{\rho}(t)$, the singlet probability is

$$\left\langle \hat{P}^{\mathrm{S}} \right\rangle = \mathrm{Tr}\left[\hat{\rho}(t)\hat{P}^{\mathrm{S}}\right] \tag{3.4}$$

[2] Anisotropic interactions are averaged by molecular tumbling in solution; spin relaxation is insignificant during the short $\left[\mathrm{Py}^{\bullet-}\ \mathrm{DMA}^{\bullet+}\right]$ radical pair lifetime; g-value differences between the two radicals are negligible at the fields of interest here; and the nuclear Zeeman interaction is also negligible at these fields.

where $\hat{P}^{\mathrm{S}}$ is the RP singlet projection operator. The density matrix evolves from its initial singlet state under the influence of the Hamiltonian as

$$\hat{\rho}(t) = U\hat{\rho}(0)U^{\dagger} = U\frac{1}{M}\hat{P}^{\mathrm{S}}U^{\dagger} \tag{3.5}$$

where M is the number of nuclear spin states and the propagator U is defined as $U = \mathrm{e}^{-\mathrm{i}\hat{H}t}$. Then, noticing that $\hat{P}^{\mathrm{S}} \equiv \frac{1}{4}\mathbb{1} - \hat{\boldsymbol{S}}_{\mathrm{A}} \cdot \hat{\boldsymbol{S}}_{\mathrm{B}}$ we separate the calculation onto the two individual radicals. After some manipulations, following [115, 116], we write

$$\left\langle \hat{P}^{\mathrm{S}} \right\rangle (t) = \frac{1}{4} + \frac{1}{M} \sum_{p,q=x,y,z} R^{\mathrm{A}}_{pq}(t) R^{\mathrm{B}}_{pq}(t) \tag{3.6}$$

in which

$$R^{\mathrm{N}}_{pq}(t) = \mathrm{Tr}\left[\hat{S}_{\mathrm{N}p}\mathrm{e}^{-\mathrm{i}\hat{H}^{\mathrm{N}}t}\hat{S}_{\mathrm{N}q}\mathrm{e}^{\mathrm{i}\hat{H}^{\mathrm{N}}t}\right]. \tag{3.7}$$

The singlet yield calculated in this manner is exact (given the basic assumptions outlined previously). However, there is a serious problem with this technique: as the number of hyperfine couplings included in the calculation is increased, the dimensions of the Hamiltonian rise exponentially. Therefore, the amount of memory and computational effort required to calculate the singlet yield grows exponentially as more hyperfine couplings are incorporated. Since chemically realistic radicals tend to have many (inequivalent) hyperfine couplings, we are often unable to calculate using this method without further approximation. Often, we simply neglect all but the largest few hyperfine couplings in order to complete a calculation in a reasonable amount of time. This approximation can cause noticeable disagreement between simulated and experimental MFEs. An example would be the zero-field anomalies in MARY-ν spectra discussed in Chapter 4.

3.3.2 Single radical pair

Having reminded ourselves of the well-established density matrix spin-factorisation approach to calculating the singlet yield in radical pairs with a realistic number of magnetic nuclei, we now turn to the semi-classical approximation. In the following pages, we will see the simplifying approximations that embody this technique.

Consider a single radical pair composed of radicals "A" and "B". If we assume that the nuclear spins behave as unquantised, classical dipoles we may rewrite the Hamiltonian as

$$\hat{H} = \hat{H}^{\mathrm{A}} + \hat{H}^{\mathrm{B}} \quad \text{where} \quad \hat{H}^{\mathrm{N}} = \sum_i a_{i\mathrm{N}}\hat{\boldsymbol{S}}_{\mathrm{N}} \cdot \boldsymbol{I}_i(t) - \gamma_{\mathrm{e}}B\hat{S}_{\mathrm{Nz}}. \tag{3.8}$$

This Hamiltonian differs from that in equation (3.3) in two ways: we have replaced nuclear spin operators $\hat{\boldsymbol{I}}_{i\mathrm{N}}$ with classical vectors $\boldsymbol{I}_i$ and therefore the new Hamiltonian has dimensions of only 4×4 because the nuclear spin is no longer included in the basis states. Writing the magnetic field $\boldsymbol{B} = B\boldsymbol{k}$ where $\boldsymbol{k}$ is the unit vector along the z-axis, we may collect terms to give

$$\hat{H}^{\mathrm{N}} = \hat{\boldsymbol{S}}_{\mathrm{N}} \cdot \left[\sum_i a_{i\mathrm{N}}\boldsymbol{I}_i(t) - \gamma_{\mathrm{e}}B\boldsymbol{k}\right]. \tag{3.9}$$

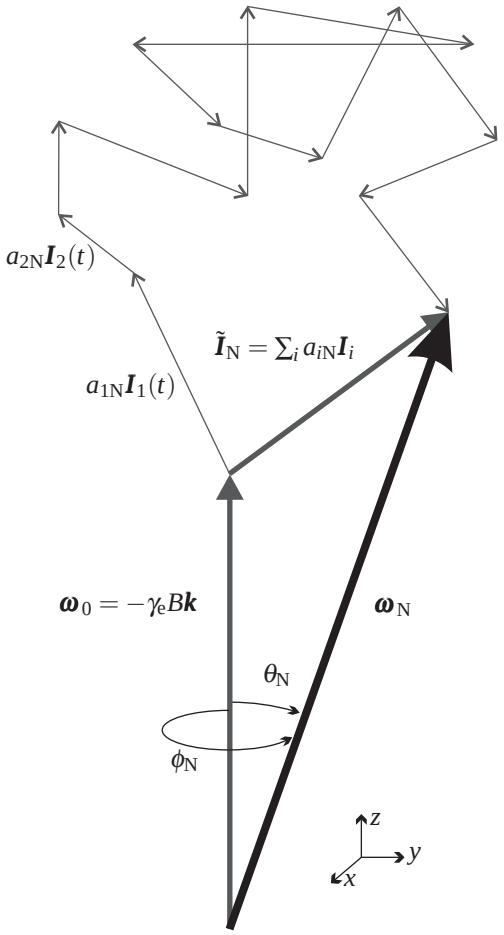

Figure 3.2: Schematic of the angular momenta in one radical (N = A or B) according to the semi-classical approximation. The hyperfine and Zeeman interactions sum to give a "resultant effective field" $\boldsymbol{\omega}_\mathrm{N}$. The electron spin undergoes Larmor precession about $\boldsymbol{\omega}_\mathrm{N}$.

We assume further that the bracketed resultant vector is time-independent; for brevity we denote it $\boldsymbol{\omega}_\mathrm{N}$. Thus, the electron spin in each radical will precess around a "resultant effective field" given by $\boldsymbol{\omega}_\mathrm{N}$ according to the Hamiltonian

$$\hat{H}^\mathrm{N} = \hat{\boldsymbol{S}}_\mathrm{N} \cdot \boldsymbol{\omega}_\mathrm{N} \tag{3.10}$$

where $\boldsymbol{\omega}_\mathrm{N} = \tilde{\boldsymbol{I}}_\mathrm{N} + \boldsymbol{\omega}_0$, $\tilde{\boldsymbol{I}}_\mathrm{N} = \sum_i a_{i\mathrm{N}}\boldsymbol{I}_i$ and $\boldsymbol{\omega}_0 = -\gamma_\mathrm{e}B\boldsymbol{k}$. This equation is summarised in Figure 3.2.

Using the new Hamiltonian defined in equation (3.10), we follow the same working as in the quantum case to write the singlet probability in a particular radical pair according to equation (3.6) as

$$\left\langle \hat{P}^\mathrm{S} \right\rangle_1 (t; \boldsymbol{\omega}_\mathrm{A}, \boldsymbol{\omega}_\mathrm{B}) = \frac{1}{4} + \sum_{p,q=x,y,z} R^\mathrm{A}_{pq}(t; \boldsymbol{\omega}_\mathrm{A}) R^\mathrm{B}_{pq}(t; \boldsymbol{\omega}_\mathrm{B}). \tag{3.11}$$

This result is almost that which we require, but not quite. In the quantum treatment, the trace in equation (3.7) covers all possible nuclear spin states because we have incorporated the nuclear spins into our basis states. This trace, therefore, generates

the ensemble average across all possible nuclear spin states. In contrast, the SCA Hamiltonian given in equation (3.10) includes only the electron spins in its basis states. The average in equation (3.11) applies only for a single configuration of the nuclear spins; this is denoted by the subscript "1". In order to complete our calculation, we must take the ensemble average of the singlet probability across all possible nuclear spin configurations as a separate step.

3.3.3 Ensemble averaging

At room temperature and magnetic fields $\lesssim 1\,\mathrm{T}$, the nuclear Zeeman interaction is much weaker than the thermal energy $k_\mathrm{B}T$ and therefore all nuclear spin states are equally probable. In terms of the vector model outlined in Figure 3.2, this means that each nuclear spin vector $a_{i\mathrm{N}}\boldsymbol{I}_i$ has a fixed length $a_{i\mathrm{N}}\sqrt{I_i(I_i+1)}$ but that its orientation is random. We are concerned to find the distribution of end-to-end vectors $\tilde{\boldsymbol{I}}_\mathrm{N}$ and hence the distribution of "resultant effective fields" $\boldsymbol{\omega}_\mathrm{N}$, which controls the spin evolution in each radical.

Fortunately, this distribution of nuclear spin vectors is exactly equivalent to the distribution of polymer segments in the well-known random flight model of polymer physics. In his classic text, Flory gives the following expression for the distribution of end-to-end vectors in a random flight as the number of segments tends to infinity [165, chapter VIII, eq 35]

$$\lim_{n\to\infty} W(\boldsymbol{r}) = \left(\frac{3}{2\pi n l^2}\right)^{\frac{3}{2}} \exp\left(\frac{-3r^2}{2nl^2}\right), \tag{3.12}$$

where n is the number of segments, $\boldsymbol{r}$ is the end-to-end vector, $W(\boldsymbol{r})$ is the probability of finding a polymer amongst the ensemble with end-to-end vector between $\boldsymbol{r}$ and $\boldsymbol{r}+\delta\boldsymbol{r}$, and l^2 is the average square segment length. We make several replacements to adapt Flory's notation to that used in this chapter:

$$nl^2 \to \sum_i a_{i\mathrm{N}}^2 I_i(I_i+1), \qquad \boldsymbol{r} \to \tilde{\boldsymbol{I}}_\mathrm{N} \quad \text{and} \quad r \to \tilde{I}_\mathrm{N}.$$

Thus, the distribution of hyperfine effective fields becomes

$$\lim_{n\to\infty} W(\tilde{\boldsymbol{I}}_\mathrm{N}) = \left(\frac{1}{4\pi}\,\tau_\mathrm{N}^2\right)^{\frac{3}{2}} \exp\left(\frac{-\tilde{I}_\mathrm{N}^2}{4}\,\tau_\mathrm{N}^2\right). \tag{3.13}$$

where

$$\tau_\mathrm{N}^2 = \frac{6}{\sum_i a_{i\mathrm{N}}^2 I_i(I_i+1)} \tag{3.14}$$

encapsulates the hyperfine couplings and nuclear spin quantum numbers in the radical.

Using the cosine rule on the bold triangle in Figure 3.2, we know that $\tilde{I}_\mathrm{N}^2 = \omega_0^2 + \omega_\mathrm{N}^2 - 2\omega_0\omega_\mathrm{N}\cos\theta_\mathrm{N}$ and hence

$$\lim_{n\to\infty} \tilde{W}(\boldsymbol{\omega}_\mathrm{N};\omega_0) = \left(\frac{1}{4\pi}\,\tau_\mathrm{N}^2\right)^{\frac{3}{2}} \exp\left(\frac{-(\omega_0^2+\omega_\mathrm{N}^2-2\omega_0\omega_\mathrm{N}\cos\theta_\mathrm{N})\tau_\mathrm{N}^2}{4}\right). \tag{3.15}$$

Using this distribution for the nuclei on each radical, we may average the singlet probability over all nuclear spin configurations of the radical pair to give the full ensemble average

$$\begin{aligned}\left\langle \hat{P}^{\mathrm{S}} \right\rangle (t;\omega_0) &= \iint \left\langle \hat{P}^{\mathrm{S}} \right\rangle_1 (t;\boldsymbol{\omega}_{\mathrm{A}},\boldsymbol{\omega}_{\mathrm{B}}) \tilde{W}(\boldsymbol{\omega}_{\mathrm{A}}) \tilde{W}(\boldsymbol{\omega}_{\mathrm{B}}) \,\mathrm{d}\boldsymbol{\omega}_{\mathrm{A}} \,\mathrm{d}\boldsymbol{\omega}_{\mathrm{B}} \\ &= \frac{1}{4} + \sum_{p,q=x,y,z} \tilde{R}^{\mathrm{A}}_{pq}(t) \tilde{R}^{\mathrm{B}}_{pq}(t) \end{aligned} \tag{3.16}$$

where

$$\tilde{R}^{\mathrm{N}}_{pq}(t) = \int R^{\mathrm{N}}_{pq}(t;\boldsymbol{\omega}_{\mathrm{N}}) \tilde{W}(\boldsymbol{\omega}_{\mathrm{N}}) \,\mathrm{d}\boldsymbol{\omega}_{\mathrm{N}} \tag{3.17}$$

and where the integrals with respect to $\boldsymbol{\omega}_{\mathrm{N}}$ are taken over all space.

3.3.4 Explicit form of the R_{pq}'s

This integral is most easily evaluated by writing the resultant effective field $\boldsymbol{\omega}_{\mathrm{N}}$ in spherical polar co-ordinates: $(\theta_{\mathrm{N}}, \phi_{\mathrm{N}}, \omega_{\mathrm{N}})$ where θ_{N} is the polar angle from the z-axis, ϕ_{N} is the azimuthal angle anti-clockwise from the x-axis and ω_{N} is the magnitude of the resultant effective field.

In these polar co-ordinates, the Hamiltonian in equation (3.10) becomes

$$\hat{H}^{\mathrm{N}} = \frac{\omega_{\mathrm{N}}}{2} \begin{pmatrix} \cos\theta_{\mathrm{N}} & \mathrm{e}^{-\mathrm{i}\phi_{\mathrm{N}}} \sin\theta_{\mathrm{N}} \\ \mathrm{e}^{\mathrm{i}\phi_{\mathrm{N}}} \sin\theta_{\mathrm{N}} & -\cos\theta_{\mathrm{N}} \end{pmatrix} \tag{3.18}$$

and thus the propagator is given by

$$U^{\mathrm{N}} = \mathrm{e}^{-\mathrm{i}\hat{H}^{\mathrm{N}}t} = \begin{pmatrix} \upsilon_{\mathrm{N}} & \mathrm{i}\chi^*_{\mathrm{N}} w_{\mathrm{N}} \\ \mathrm{i}\chi_{\mathrm{N}} w^*_{\mathrm{N}} & \upsilon^*_{\mathrm{N}} \end{pmatrix} \tag{3.19}$$

in which

$$\upsilon_{\mathrm{N}} = \cos(\omega_{\mathrm{N}} t/2) - \mathrm{i}\cos(\theta_{\mathrm{N}}) \sin(\omega_{\mathrm{N}} t/2), \tag{3.20}$$

$$\chi_{\mathrm{N}} = \mathrm{e}^{\mathrm{i}\phi_{\mathrm{N}}} \tag{3.21}$$

$$\text{and} \quad w_{\mathrm{N}} = -\sin(\omega_{\mathrm{N}} t/2) \sin(\theta_{\mathrm{N}}). \tag{3.22}$$

Substituting equation (3.7) into equation (3.17), making the change of variable $y_{\mathrm{N}} = \cos\theta_{\mathrm{N}}$ and writing explicitly the spherical polar volume element

$$\mathrm{d}\boldsymbol{\omega}_{\mathrm{N}} = \omega^2_{\mathrm{N}} \,\mathrm{d}y_{\mathrm{N}} \,\mathrm{d}\phi_{\mathrm{N}} \,\mathrm{d}\omega_{\mathrm{N}} \tag{3.23}$$

gives

$$\tilde{R}^{\mathrm{N}}_{pq}(t) = \int_0^{\infty} \int_{-1}^{1} \tilde{\tilde{R}}^{\mathrm{N}}_{pq}(t) \tilde{W}(\boldsymbol{\omega}_{\mathrm{N}}) \omega^2_{\mathrm{N}} \,\mathrm{d}y_{\mathrm{N}} \,\mathrm{d}\omega_{\mathrm{N}} \tag{3.24}$$

in which we have written separately the integral with respect to ϕ_{N}

$$\tilde{\tilde{R}}^{\mathrm{N}}_{pq}(t) = \int_0^{2\pi} \mathrm{Tr}\left[\hat{S}_{\mathrm{N}p} \begin{pmatrix} \upsilon_{\mathrm{N}} & \mathrm{i}\chi^*_{\mathrm{N}} w_{\mathrm{N}} \\ \mathrm{i}\chi_{\mathrm{N}} w^*_{\mathrm{N}} & \upsilon^*_{\mathrm{N}} \end{pmatrix} \hat{S}_{\mathrm{N}q} \begin{pmatrix} \upsilon^*_{\mathrm{N}} & -\mathrm{i}\chi^*_{\mathrm{N}} w_{\mathrm{N}} \\ -\mathrm{i}\chi_{\mathrm{N}} w^*_{\mathrm{N}} & \upsilon_{\mathrm{N}} \end{pmatrix} \right] \mathrm{d}\phi_{\mathrm{N}}. \tag{3.25}$$

Despite the somewhat complex appearance of this expression, it may be quickly evaluated using a computer algebra system (CAS) such as `Mathematica` to give

$$\begin{aligned}\tilde{\tilde{R}}^{\mathrm{N}}_{xx} &= \tilde{\tilde{R}}^{\mathrm{N}}_{yy} = \frac{\pi}{2}\left(1 - y_{\mathrm{N}}^2 + \cos\omega_{\mathrm{N}}t + y_{\mathrm{N}}^2\cos\omega_{\mathrm{N}}t\right)\\ \tilde{\tilde{R}}^{\mathrm{N}}_{yx} &= -\tilde{\tilde{R}}^{\mathrm{N}}_{xy} = \pi y_{\mathrm{N}}\sin\omega_{\mathrm{N}}t\\ \tilde{\tilde{R}}^{\mathrm{N}}_{zz} &= \pi\left(y_{\mathrm{N}}^2 + \cos\omega_{\mathrm{N}}t - y_{\mathrm{N}}^2\cos\omega_{\mathrm{N}}t\right)\end{aligned} \tag{3.26}$$

with the other $\tilde{\tilde{R}}^{\mathrm{N}}_{pq}$ being zero.

Substituting these values for $\tilde{\tilde{R}}^{\mathrm{N}}_{pq}$ into equation (3.17) gives the $\tilde{R}^{\mathrm{N}}_{pq}$ values that we need. (N.B. In practice, these integrals are sufficiently involved that `Mathematica` could only handle them if each term in the $\tilde{\tilde{R}}^{\mathrm{N}}_{pq}$ is integrated separately, summing the results afterwards.) The $\tilde{R}^{\mathrm{N}}_{pq}$ values are quite bulky. The most compact is

$$\tilde{R}^{\mathrm{N}}_{yx} = -\tilde{R}^{\mathrm{N}}_{xy} = \frac{\mathrm{e}^{-t^2/\tau_{\mathrm{N}}^2}\left(2t\omega_0\cos(t\omega_0) + \left(\tau_{\mathrm{N}}^2\omega_0^2 - 2\right)\sin(t\omega_0)\right)}{2\tau_{\mathrm{N}}^2\omega_0^2}. \tag{3.27}$$

Finally, substituting the $\tilde{R}^{\mathrm{N}}_{pq}$ values into equation (3.16) gives an expression for the ensemble average singlet probability according to the semi-classical approximation

$$\begin{aligned}\left\langle \hat{P}^{\mathrm{S}}\right\rangle = \frac{1}{4} +& \\ &\frac{\left[\begin{array}{l}\left(\begin{array}{l}\tau_{\mathrm{A}}\omega_0\left(\tau_{\mathrm{A}}^2\omega_0^2 + 4\mathrm{e}^{-\frac{t^2}{\tau_{\mathrm{A}}^2}}\cos(t\omega_0) - 4\right) + \\ 2\mathrm{e}^{-\frac{1}{4}\tau_{\mathrm{A}}^2\omega_0^2}\sqrt{\pi}\left(-\mathrm{i}\,\mathrm{erf}\left(\frac{t}{\tau_{\mathrm{A}}} - \frac{\mathrm{i}\tau_{\mathrm{A}}\omega_0}{2}\right) + \mathrm{i}\,\mathrm{erf}\left(\frac{t}{\tau_{\mathrm{A}}} + \frac{\mathrm{i}\tau_{\mathrm{A}}\omega_0}{2}\right) + 2\,\mathrm{erfi}\left(\frac{\tau_{\mathrm{A}}\omega_0}{2}\right)\right)\end{array}\right)\\ \times\left(\begin{array}{l}\tau_{\mathrm{B}}\omega_0\left(\tau_{\mathrm{B}}^2\omega_0^2 + 4\mathrm{e}^{-\frac{t^2}{\tau_{\mathrm{B}}^2}}\cos(t\omega_0) - 4\right) + \\ 2\mathrm{e}^{-\frac{1}{4}\tau_{\mathrm{B}}^2\omega_0^2}\sqrt{\pi}\left(-\mathrm{i}\,\mathrm{erf}\left(\frac{t}{\tau_{\mathrm{B}}} - \frac{\mathrm{i}\tau_{\mathrm{B}}\omega_0}{2}\right) + \mathrm{i}\,\mathrm{erf}\left(\frac{t}{\tau_{\mathrm{B}}} + \frac{\mathrm{i}\tau_{\mathrm{B}}\omega_0}{2}\right) + 2\,\mathrm{erfi}\left(\frac{\tau_{\mathrm{B}}\omega_0}{2}\right)\right)\end{array}\right)\end{array}\right]}{4\tau_{\mathrm{A}}^3\tau_{\mathrm{B}}^3\omega_0^6} + \\ &\frac{\left[\begin{array}{l}\mathrm{e}^{-\frac{t^2}{\tau_{\mathrm{A}}^2}-\frac{t^2}{\tau_{\mathrm{B}}^2}}\left(2t\omega_0\cos(t\omega_0) + \left(\tau_{\mathrm{A}}^2\omega_0^2 - 2\right)\sin(t\omega_0)\right)\\ \times\left(2t\omega_0\cos(t\omega_0) + \left(\tau_{\mathrm{B}}^2\omega_0^2 - 2\right)\sin(t\omega_0)\right)\end{array}\right]}{2\tau_{\mathrm{A}}^2\tau_{\mathrm{B}}^2\omega_0^4} + \\ &\frac{\left[\begin{array}{l}\left(\begin{array}{l}\mathrm{i}\mathrm{e}^{-\frac{1}{4}\tau_{\mathrm{A}}^2\omega_0^2}\sqrt{\pi}\left(\mathrm{erf}\left(\frac{t}{\tau_{\mathrm{A}}} - \frac{\mathrm{i}\tau_{\mathrm{A}}\omega_0}{2}\right) + \mathrm{erfc}\left(\frac{t}{\tau_{\mathrm{A}}} + \frac{\mathrm{i}\tau_{\mathrm{A}}\omega_0}{2}\right) + 2\mathrm{i}\,\mathrm{erfi}\left(\frac{\tau_{\mathrm{A}}\omega_0}{2}\right) - 1\right)\\ +\tau_{\mathrm{A}}\omega_0\left(\mathrm{e}^{-\frac{t^2}{\tau_{\mathrm{A}}^2}}\left(\left(\tau_{\mathrm{A}}^2\omega_0^2 - 2\right)\cos(t\omega_0) - 2t\omega_0\sin(t\omega_0)\right) + 2\right)\end{array}\right)\\ \times\left(\begin{array}{l}\mathrm{i}\mathrm{e}^{-\frac{1}{4}\tau_{\mathrm{B}}^2\omega_0^2}\sqrt{\pi}\left(\mathrm{erf}\left(\frac{t}{\tau_{\mathrm{B}}} - \frac{\mathrm{i}\tau_{\mathrm{B}}\omega_0}{2}\right) + \mathrm{erfc}\left(\frac{t}{\tau_{\mathrm{B}}} + \frac{\mathrm{i}\tau_{\mathrm{B}}\omega_0}{2}\right) + 2\mathrm{i}\,\mathrm{erfi}\left(\frac{\tau_{\mathrm{B}}\omega_0}{2}\right) - 1\right)\\ +\tau_{\mathrm{B}}\omega_0\left(\mathrm{e}^{-\frac{t^2}{\tau_{\mathrm{B}}^2}}\left(\left(\tau_{\mathrm{B}}^2\omega_0^2 - 2\right)\cos(t\omega_0) - 2t\omega_0\sin(t\omega_0)\right) + 2\right)\end{array}\right)\end{array}\right]}{2\tau_{\mathrm{A}}^3\tau_{\mathrm{B}}^3\omega_0^6}.\end{aligned} \tag{3.28}$$

This expression for the singlet probability is in closed form, unlike those derived by Knapp and Schulten [28]. It allows us to calculate the singlet probability as a function of time in any radical pair given the static field strength $B_0 = -\omega_0/\gamma_{\mathrm{e}}$ and the hyperfine coupling constants, which determine τ_{A} and τ_{B}.

3.3.5 No static field

Equation (3.28) contains $\omega_0 = -\gamma_e B_0$ in the denominator of some terms. This will cause problems when there is no static field present, because as the formula is written we would divide by zero, which is not a defined operation. This difficulty is easily overcome by taking the limit as $\omega_0 \to 0$ to give the following expression for the zero field singlet probability:

$$\left\langle \hat{P}^{\mathrm{S}} \right\rangle = \frac{\mathrm{e}^{-t^2\left(\frac{1}{\tau_{\mathrm{B}}^2}+\frac{1}{\tau_{\mathrm{A}}^2}\right)} \left[\begin{array}{l} 8t^4 - 2\left(\left(2+\mathrm{e}^{\frac{t^2}{\tau_{\mathrm{A}}^2}}\right)\tau_{\mathrm{A}}^2 + \left(2+\mathrm{e}^{\frac{t^2}{\tau_{\mathrm{B}}^2}}\right)\tau_{\mathrm{B}}^2\right)t^2 \\ +\left(2+\mathrm{e}^{\frac{t^2}{\tau_{\mathrm{A}}^2}}+2\mathrm{e}^{t^2\left(\frac{1}{\tau_{\mathrm{B}}^2}+\frac{1}{\tau_{\mathrm{A}}^2}\right)}+\mathrm{e}^{\frac{t^2}{\tau_{\mathrm{B}}^2}}\right)\tau_{\mathrm{A}}^2\tau_{\mathrm{B}}^2 \end{array} \right]}{6\tau_{\mathrm{A}}^2\tau_{\mathrm{B}}^2}. \tag{3.29}$$

This expression is identically equal to that given, after a different derivation, by Schulten and Wolynes in their opening paper [27].

3.3.6 No magnetic nuclei on one radical

Molin, Stass and coworkers examined the special case of radical pairs which have hyperfine couplings on only one radical [110]. Such "n–0" radical pairs are of practical interest since they were found to exhibit strong LFEs. We may adapt equation (3.28) to the case of an "n-0" radical pair by taking the limit as $\tilde{a}_{\mathrm{B}} \to 0$, or equivalently as $\tau_{\mathrm{B}} \to \infty$. Evaluation of the limit in `Mathematica` gives

$$\begin{aligned} \left\langle \hat{P}^{\mathrm{S}} \right\rangle = & \frac{\mathrm{e}^{-\frac{t^2}{\tau_{\mathrm{A}}^2}}\left(1+\mathrm{e}^{\frac{t^2}{\tau_{\mathrm{A}}^2}}\right)\tau_{\mathrm{A}}\omega_0\left(\tau_{\mathrm{A}}^2\omega_0^2+2\cos(t\omega_0)-2\right)}{2\tau_{\mathrm{A}}^3\omega_0^3} \\ & + \frac{\mathrm{i}\mathrm{e}^{-\frac{1}{4}\tau_{\mathrm{A}}^2\omega_0^2}\sqrt{\pi}(\cos(t\omega_0)-1)\left[\begin{array}{l} \mathrm{erf}\left(\frac{t}{\tau_{\mathrm{A}}}-\frac{\mathrm{i}\tau_{\mathrm{A}}\omega_0}{2}\right) \\ +\mathrm{erfc}\left(\frac{t}{\tau_{\mathrm{A}}}+\frac{\mathrm{i}\tau_{\mathrm{A}}\omega_0}{2}\right) \\ +2\mathrm{i}\,\mathrm{erfi}\left(\frac{\tau_{\mathrm{A}}\omega_0}{2}\right)-1 \end{array} \right]}{2\tau_{\mathrm{A}}^3\omega_0^3} \end{aligned} \tag{3.30}$$

in an "n–0" radical pair. This expression is clearly substantially simpler than that for an "m–n" radical pair. In the zero field limit, the singlet probability in an "n–0" RP simplifies still further to

$$\left\langle \hat{P}^{\mathrm{S}} \right\rangle = \frac{1}{2}\left[\mathrm{e}^{-\frac{t^2}{\tau_{\mathrm{A}}^2}}\left(1-\frac{2t^2}{\tau_{\mathrm{A}}^2}\right)+1\right]. \tag{3.31}$$

3.3.7 Effective HFC

We may also phrase the semi-classical approximation in terms of effective hyperfine coupling constants

$$\tilde{a}_{\mathrm{N}}^2 = \frac{4}{3}\sum_i a_{i\mathrm{N}}^2 I_i(I_i+1) \tag{3.32}$$

$$\implies \tilde{a}_{\mathrm{N}} = \frac{2\sqrt{2}}{\tau_{\mathrm{N}}}. \tag{3.33}$$

This effective HFC constant is defined such that the Zeeman energy levels of a one-proton radical pair are preserved. The reader should take heed that there are several definitions of the effective hyperfine coupling constant in the literature, which differ in the choice of numerical prefactor.

3.3.8 Appraisal of semi-classical singlet probability

The singlet probability is determined solely by the effective HFC on each radical within the semi-classical approximation. Not only that, but this dependence can be written in closed form, *viz.* equation (3.28). Importantly, the time taken to evaluate this singlet probability does not depend on the number of magnetic nuclei in the radical pair — in stark contrast to the exponential growth in calculation time for the exact quantum calculation. Also, since there are so few parameters, it is feasible to derive general trends which should hold true for any radical pair. However, these benefits of the semi-classical approximation may only be realised if its predictions are close to reality. In this section, we critically analyse the performance of the SCA by comparison with exact quantum calculations in a fairly large spin system: pyrene and DMA.

Figure 3.3(a) shows triplet probability as a function of time in a radical pair with 18 magnetic nuclei. The hyperfine couplings have been chosen to match those used by Knapp & Schulten [28] for calculations in a $\left[\mathrm{Py}^{\bullet-}\ \mathrm{DMA}^{\bullet+}\right]$ radical pair (their Figure 1). The effective hyperfine coupling constants, given by equation (3.32), are 1.1 mT on radical A and 3.7 mT on radical B. Calculations were performed at four static field strengths, chosen to include fields smaller than, comparable to and greater than the effective hyperfine couplings. It should be noted that these hyperfine coupling constants are somewhat different to those given in Table 2.2, which we have used for $\left[\mathrm{Py}^{\bullet-}\ \mathrm{DMA}^{\bullet+}\right]$ elsewhere in this thesis. It is not clear how discrepancy arises — perhaps the two measurements were made in a different solvent, or at different temperatures.

Inspection of the figures reveals broad agreement of the SCA and QM results, which is quantified in Figure 3.3(b) as a plot of the percentage error in the SCA triplet yields relative to the QM values. This agreement is rather good — within 1% — during the first 5 ns for all four field strengths. This is comparable to the timescale of hyperfine-induced spin evolution in radical A given by $1/(-\gamma_{\mathrm{e}} \times 1.11\,\mathrm{mT}) = 5.0\,\mathrm{ns}$. For the 15 mT static field, the agreement is better than 3% at all times. These observations will become something of a theme: the SCA performs best at short times (*i.e.* in RPs with rapid re-encounter kinetics) or at high static field strengths.

Sadly, agreement is not always so good. At field strengths comparable to the hyperfine couplings, we see errors of more than 5% in the triplet yield. Such errors

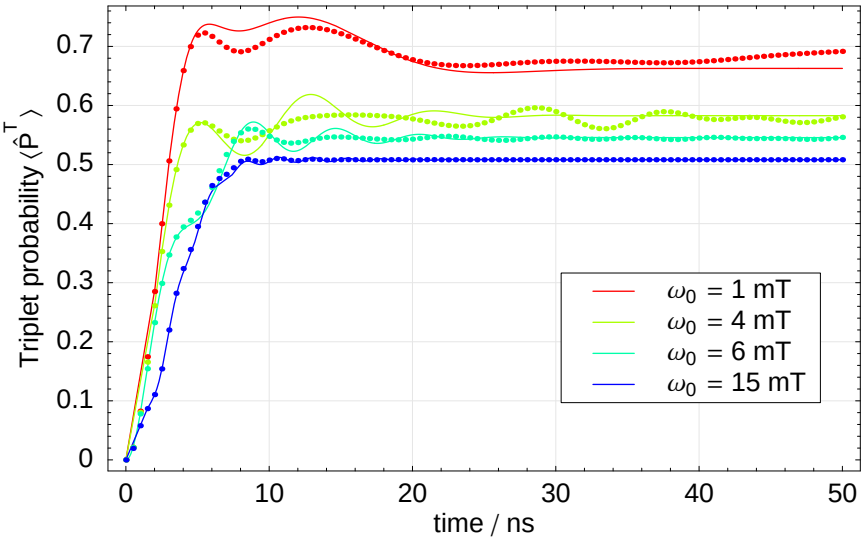

(a) Comparison of triplet probabilities calculated according to the SCA (solid lines) with those obtained from an exact quantum calculation in the time domain (points) in a radical pair with 18 magnetic nuclei.

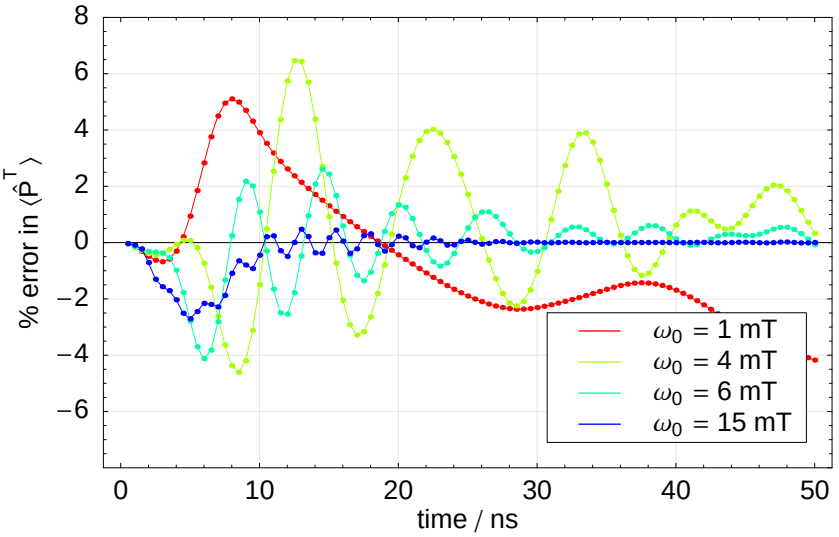

(b) Discrepancy between the SCA and the exact QM calculation in Figure 3.3(a) expressed as a percentage of the exact QM results. We omit the point at $t = 0$ because, since the RP is born in a singlet state, the triplet probability is identically zero at this time; the percentage error in these points would involve division by zero and is therefore undefined.

Figure 3.3: Comparison of triplet probabilities ($\langle \hat{P}^{\mathrm{T}} \rangle(t) = 1 - \langle \hat{P}^{\mathrm{S}} \rangle(t)$) calculated according to the semi-classical approximation using equation (3.28) with the results of an exact quantum mechanical calculation in the time domain (see §2.2.1). The hyperfine coupling constants were $4 \times 0.23\,\mathrm{mT}$ ($I = 1/2$) and $4 \times 0.52\,\mathrm{mT}$ ($I = 1/2$) on radical A; and $6 \times 1.20\,\mathrm{mT}$ ($I = 1/2$), $1 \times 1.20\,\mathrm{mT}$ ($I = 1$) and $3 \times 0.625\,\mathrm{mT}$ ($I = 1/2$) on radical B. The effective hyperfine constants were thus $1.1\,\mathrm{mT}$ on radical A and $3.7\,\mathrm{mT}$ on radical B. These values were chosen to match those used by Knapp and Schulten in their Figure 1 [28]. Static field strengths were chosen to include values comparable to and greater than the effective hyperfine constants.

are substantially greater than the experimental error in modern field effect measurements. Finally, it is immediately apparent that the SCA underestimates the oscillations present in the triplet probability. Physically, these oscillations are caused by coherent spin evolution in the radical pair. Obviously, the SCA cannot reproduce such coherent evolution because it is founded on the assumption that the nuclear spins behave classically. At longer times, this may be a significant failing.

On a separate note, it is fruitful to compare Figure 3.3(a) with Figure 1 from [28]. Despite the presence of a number of errors in Knapp & Schulten's original derivation, we agree to within plotting accuracy on the triplet yield in this $\left[\mathrm{Py}^{\bullet-}\ \mathrm{DMA}^{\bullet+}\right]$ radical pair. This is an encouraging result. Nevertheless, the derivation given in this chapter seems preferable to that of Knapp & Schulten, not least because we are able to give an expression in closed form for the SCA singlet probability.

3.3.9 Singlet yield

Our focus in this chapter is predicting, perhaps qualitatively, MARY spectra. A MARY spectrum shows the variation in singlet yield (on the y-axis) as a function of static magnetic field strength (on the x-axis). We must, therefore, continue our SCA derivation to give singlet yields instead of singlet probabilities.

Equation (3.1) allows us to calculate the singlet yield from the singlet probability, which we know by equation (3.28), and the probability $f(t)$ that the radicals will re-encounter at time t. As is common in work on magnetic field effects, we adopt a simple model for the re-encounter probability: the exponential model, $f(t) = k\mathrm{e}^{-kt}$, where k is a rate constant. Hence,

$$\Phi_{\mathrm{S}}(B) = k\int_0^\infty \mathrm{e}^{-kt}\left\langle \hat{P}^{\mathrm{S}}\right\rangle(B,t)\,\mathrm{d}t. \tag{3.34}$$

Having obtained equation (3.28) using the `Mathematica` computer algebra system, we attempted to evaluate this integral using `Mathematica` again. Yet, despite allowing two weeks of processing time on a 3 GHz Pentium IV machine, `Mathematica` failed to evaluate this expression. Attempts to simplify the problem by expanding out all the brackets in equation (3.28) and then integrating term-by-term were also unsuccessful. Out of 160 terms to be integrated, there remained 35 distinct integrals which `Mathematica` would not evaluate.

Since the straightforward approaches to performing this integral in `Mathematica` fail, we must consider other options. One possibility, which we have not yet explored, is to use another CAS such as `Maple` to tackle the 35 unevaluated integrals. Since there is no general algorithm for performing integration, CASs use large sets of heuristics and tables of integrals when integrating. Therefore, it is quite possible to find problems that can be solved in one CAS but not in another.

The other approach is to tackle, either in whole or in part, the integral numerically. The following results were obtained using the generic `NIntegrate` function provided by `Mathematica`. This approach allowed us to explore the SCA over a wide range of parameters even though `NIntegrate` is not robust enough to be used without manual inspection of the results. It is important to note that the singlet yield at zero-field must be evaluated separately, using equation (3.29) for the singlet probability in equation (3.34). This is necessary to avoid division by zero.

If one wished to use the SCA for modelling or curve-fitting then a more robust, more computationally efficient numerical algorithm would need to be developed. A promising candidate is a form of Gauss-Laguerre quadrature [166, Gauss-Laguerre Quadrature]. Two packages of `Matlab` routines that are likely to be suitable for performing the Gauss-Laguerre quadrature are `QUADRULE` [167] and `galag` [168]. Another approach would be to make power series or asymptotic expansions of the integrands in the 35 unevaluated integrals. These series approximants could then be symbolically integrated to give an approximate form for the singlet probability. If the series could be made to converge rapidly, this technique could be very efficient.

Finally, although the singlet yield for the general "m–n" radical pair could not be found analytically, it is quite straightforward to perform the integration in equation (3.34) for an "n–0" radical pair. The resulting closed form expression for the singlet yield is reasonably compact. It may also be differentiated analytically in order to locate stationary points in the MARY spectrum. Such analysis suggests that the SCA always predicts an LFE, although this is often vanishingly small. This conclusion differs from that of Stass *et al.* who evaluated the SCA singlet yield in an "n–0" RP numerically [110, Figure 1] and concluded that an LFE only emerges when $\tilde{a} \gg \sqrt{2}k$ (*i.e.* [110, eq. 8] rewritten in our notation).

3.3.10 Appraisal of semi-classical singlet yield

Figure 3.4 shows MARY spectra for the $\left[\mathrm{Py}^{\bullet-}\ \mathrm{DMA}^{\bullet+}\right]$ radical pair, where we have used hyperfine coupling data from [28] in order to allow a comparison with the triplet probability curves in Figure 3.3. The top subfigure shows MARY spectra for a variety of different rate constants, calculated using both the SCA and by means of a frequency domain quantum mechanical calculation. The lower subfigure makes the comparison more explicit, giving the percentage error in the SCA singlet yield as compared to the quantum calculation result.

For rapid re-encounter kinetics, where[3] $k \geq 5\,\mathrm{mT}$, there is a strikingly good agreement of the SCA and QM singlet yields. For these rate constants, the SCA remains well within 1% of the true singlet yield value over the whole MARY spectrum. Also, the SCA works well at higher field strengths. For static fields $B_0 \geq 3\,\mathrm{mT}$, the SCA is within 1% of the correct value except for the curve with the slowest kinetics, $k = 0.1\,\mathrm{mT}$. However, in the low field effect region — $B_0 < 2\,\mathrm{mT}$ — the semi-classical approximation often deviates by a few percent from the true singlet yield. Furthermore, it is clear that for slow re-encounter kinetics, the SCA fails to capture even the qualitative shape of the MARY spectrum in this LFE region.

Thus, in the particular case of a $\left[\mathrm{Py}^{\bullet-}\ \mathrm{DMA}^{\bullet+}\right]$ radical pair using hyperfine data from [28], the SCA performs well at higher static field strengths and for faster re-encounter kinetics. It performs less well at weak fields or with slow re-encounter kinetics. Comparison with Figure 3.3 shows that these trends are to be expected, since the singlet (or triplet) probability is approximated best at higher static field strengths and during the first few ns. Since the LFE is intimately connected with changes in the selection rules and coherent spin evolution as the symmetry at zero field is broken by the application of a magnetic field, it seems quite reasonable that the SCA should have difficulty reproducing accurately its features.

[3] The use of magnetic field units for rate constants and energies is explained in §1.8.

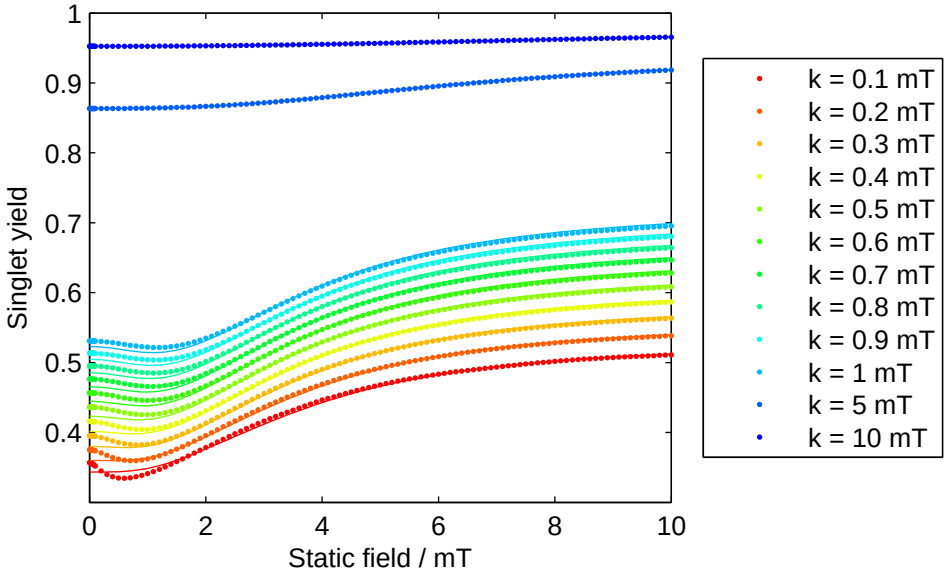

(a) Comparison of singlet yields calculated according to the SCA (solid lines) with those obtained from a quantum calculation (points).

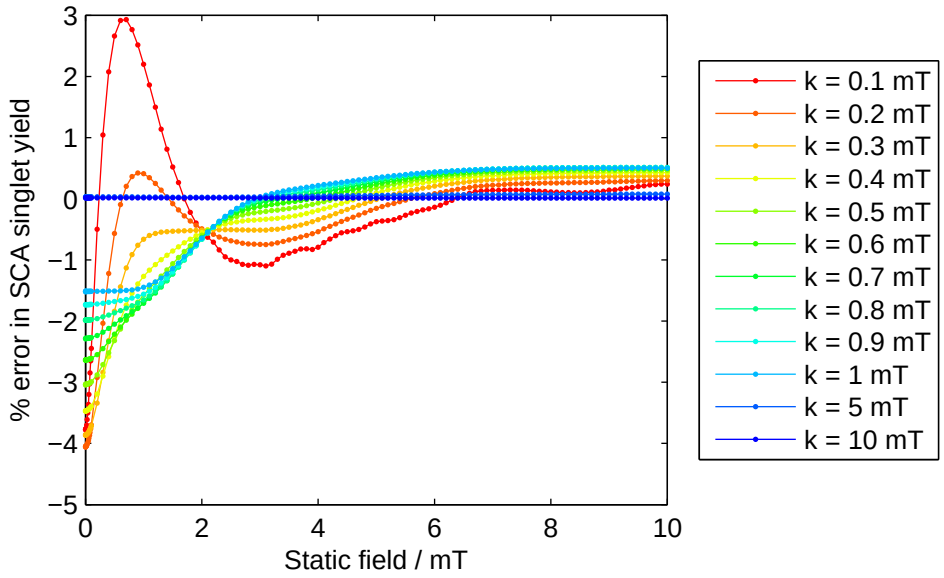

(b) Difference between the SCA and QM calculated singlet yield (above) as a percentage of the QM results.

Figure 3.4: Comparison of singlet yields calculated according to the semi-classical approximation with those calculated quantum mechanically. In both calculations, the hyperfine coupling constants were $4 \times 0.23\,\text{mT}$ $(I = 1/2)$ and $4 \times 0.52\,\text{mT}$ $(I = 1/2)$ on radical A; and $6 \times 1.20\,\text{mT}$ $(I = 1/2)$, $1 \times 1.20\,\text{mT}$ $(I = 1)$ and $3 \times 0.625\,\text{mT}$ $(I = 1/2)$ on radical B. The effective hyperfine constants were thus $1.1\,\text{mT}$ on radical A and $3.7\,\text{mT}$ on radical B. These values were chosen to match those used by Knapp and Schulten in their Figure 1 [28]. The exponential model $f(t) = k\mathrm{e}^{-kt}$ was used for the re-encounter probability. The quantum mechanical calculations were performed in the frequency domain (see §2.2.2), with 10^4 bins at angular frequencies up to $5 \times 10^9\,\text{s}^{-1}$. This is a sufficient number of bins for convergence to plotting accuracy.

3.4 Quantum mechanical Monte Carlo method

The semi-classical approximation allows the singlet probability in a radical pair to be written in terms of a very few parameters at the price of introducing additional assumptions about the spin evolution. As such, it represents a theory-first or assumptions-first approach to extracting the central model parameters. It is also fruitful to approach matters from the opposite direction using a quantum mechanical Monte Carlo (QMMC) technique.

Instead of making new physical assumptions, we begin by calculating the MARY spectra for each member of a large ensemble of radical pairs, using the exact frequency domain binning algorithm described in §2.2.2. The hyperfine coupling constants are chosen at random for any particular radical pair. The calculated MARY spectra are then analysed by another computer program in order to measure empirical parameters such as the depth of the low field effect minimum. Across the whole ensemble, these parameters will take on values according to some probability distribution, providing that enough MARY spectra have been calculated to minimise fluctuations. Then, the problem becomes a matter of analysing the probability distributions, often graphically, to determine the most important, controlling combination of variables for each empirical parameter. For example, we may pose questions such as: does the low field effect depth vary with the ratio of the effective hyperfine couplings on each radical? A Monte Carlo approach will not explain *why* a parameter is controlled by particular variables, but neither does it need such knowledge (in the form of physical assumptions) to be provided in advance.

3.4.1 Systematic testing of SCA singlet yield convergence

Figure 3.4 compared singlet yields calculated according to the SCA with those from an exact quantum mechanical calculation in a particular radical pair. Such a comparison is interesting to make, but it leaves two important questions unanswered. First, the SCA uses an asymptotic limiting expression for the probability distribution of end-to-end distances in a random flight polymer. According to Flory, "departures from the Gaussian formula become appreciable for [chains of] less than 20–50 bonds" [165]. It is important to test whether and how quickly exact quantum calculations converge to the SCA result as the number of magnetic nuclei is increased. Second, such a test uses only a single set of hyperfine couplings. It is important to calculate in a large ensemble of radicals with random hyperfine couplings in order to see how much deviation there is between MARY spectra having the same effective hyperfine couplings. It is possible that the SCA captures the mean response well, but that there is large scope for variations in a particular radical pair. On the other hand, it may be that almost all MARY spectra with a particular combination of effective hyperfine couplings are essentially identical, with only occasional, rare outliers. We quantify these situations by measuring the standard deviation of the singlet yields across the different members of the ensemble.

Figure 3.5 presents selected results from a series of calculations designed to answer these questions. The black lines in each subfigure show the singlet yield according to the SCA in a radical pair with effective hyperfine couplings $\tilde{a}_A = \tilde{a}_B = 0.2\,\mathrm{mT}$. Subfigures (a) – (c) are calculated with an exponential model rate constant k that is

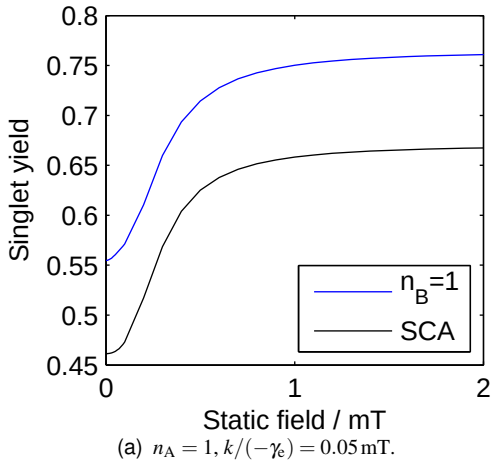

(a) $n_A = 1, k/(-\gamma_e) = 0.05\,\text{mT}$.

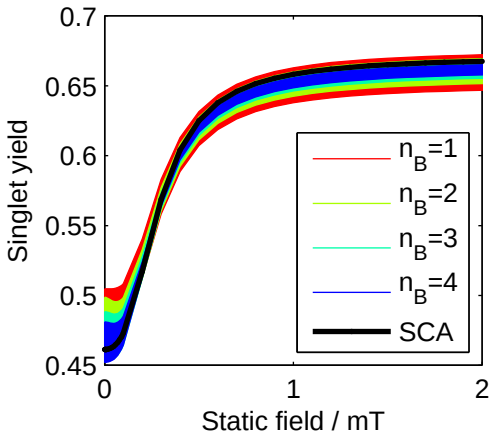

(b) Random hyperfine coupling constants, $n_A = 5$, $k/(-\gamma_e) = 0.05\,\text{mT}$. Line widths are $\pm$ one standard deviation in singlet yield.

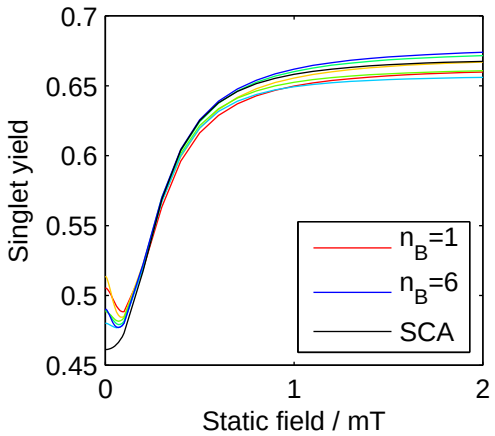

(c) Identical hyperfine coupling constants, $n_A = 6$, $k/(-\gamma_e) = 0.05\,\text{mT}$. The legend omits lines with $2 \leq n_B \leq 5$ so as not to obscure the results.

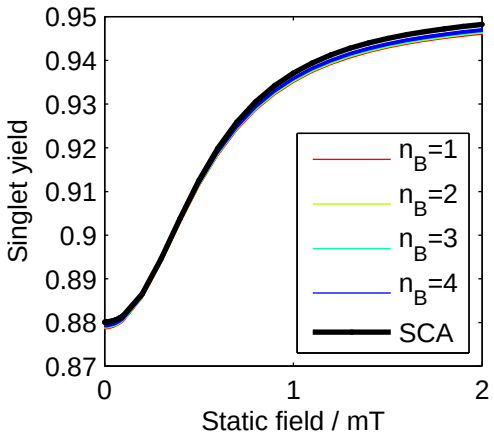

(d) Random hyperfine coupling constants, $n_A = 5$, $k/(-\gamma_e) = 0.40\,\text{mT}$. Line widths are $\pm$ one standard deviation in singlet yield.

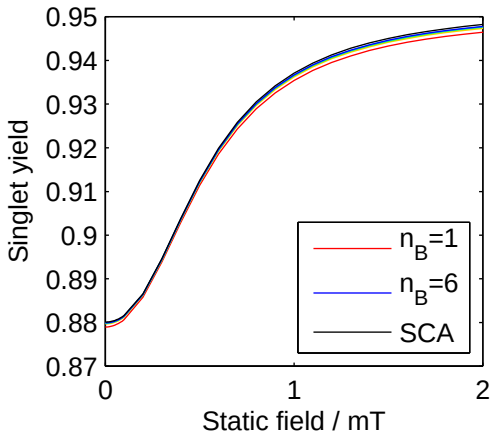

(e) Identical hyperfine coupling constants, $n_A = 6$, $k/(-\gamma_e) = 0.40\,\text{mT}$. The legend omits lines with $2 \leq n_B \leq 5$ so as not to obscure the results.

Figure 3.5: Effect of the number of magnetic nuclei on the agreement between singlet yields calculated according to the SCA (black line) and those from quantum mechanical calculations in the frequency domain. In all cases, hyperfine coupling constants were chosen such that the effective hyperfine coupling constants $\tilde{a}_A = \tilde{a}_B = 0.2\,\text{mT}$. The number of magnetic nuclei on radical N is denoted n_N. The hyperfine coupling constants in each calculation were chosen as described in the main text.

smaller than the effective hyperfine couplings $\tilde{a}$, whilst Subfigures (d) and (e) have a rate constant that is larger. Although calculations were performed with static fields up to 10 mT in each case, the singlet yields do not vary substantially after 2 mT and we have therefore shown only the low field region of each MARY spectrum.

Figure 3.5(a) compares the SCA singlet yield with that obtained in a radical pair having only two hyperfine couplings of 0.2 mT, one on each radical. Clearly, there is rather poor agreement between the SCA and this special case. This is not surprising, since the random flight end-to-end distance distribution formula is a very poor approximation to the true distribution when there is only one segment (HFC).

We now proceed to build up the number of hyperfine couplings in each radical, whilst keeping the effective HFC constant. The quickest way to do this is to have a single group of equivalent nuclei on each radical, altering the hyperfine couplings for this group appropriately as the number of nuclei increases. Figures 3.5(c) and 3.5(e) show the results of this approach. It is clear that the SCA is rather poor at low rate constants, e.g. in Figure 3.5(c), where at high static field strengths, convergence of the quantum mechanical singlet yield to the SCA result clearly does not occur rapidly with increasing number of magnetic nuclei. The situation is worse still in the low field effect region, where even for a RP with six nuclei on each radical, the SCA does not agree even qualitatively with the shape of the LFE minimum. At higher values of the rate constant, e.g. in Figure 3.5(e), the agreement is much more satisfactory and would probably be within the bounds of experimental error.

A more realistic approach to building up the number of magnetic nuclei assigns different hyperfine coupling constants to each nucleus. These hyperfine coupling constants must be chosen such that the effective hyperfine coupling constant remains fixed, at a value of 0.2 mT in this case. To achieve this, we choose each hyperfine coupling constant from an independent normal distribution with zero mean and unit standard deviation

$$P(a_{i\mathrm{N}}) = \sqrt{\frac{1}{2\pi}} \exp\left(-\frac{a_{i\mathrm{N}}^2}{2}\right). \tag{3.35}$$

Thus, the joint probability distribution for the values of n hyperfine coupling constants in a radical together is

$$P(a_{1\mathrm{N}}, \ldots, a_{n\mathrm{N}}) = (2\pi)^{-n/2} \exp\left(-\frac{a_{1\mathrm{N}}^2}{2}\right) \cdots \exp\left(-\frac{a_{n\mathrm{N}}^2}{2}\right) \tag{3.36}$$

$$= (2\pi)^{-n/2} \exp\left(-\frac{a_{1\mathrm{N}}^2 + \cdots + a_{n\mathrm{N}}^2}{2}\right). \tag{3.37}$$

If we choose to use only spin-½ nuclei, then by equation (3.32)

$$P(a_{1\mathrm{N}}, \ldots, a_{n\mathrm{N}}) = (2\pi)^{-n/2} \exp\left(-\frac{\tilde{a}_{\mathrm{N}}^2}{2}\right). \tag{3.38}$$

The joint probability distribution depends only on the effective hyperfine coupling constant and not on any of the individual hyperfine coupling constants. In geometrical terms, if we consider the individual hyperfine coupling constants as components of a vector, then the vectors picked in this manner will be spherically distributed in orientation and have a normal distribution of lengths. As a final step, we may normalise the

vectors (individual hyperfine coupling constants) to give a set of vectors of constant length (the chosen effective hyperfine coupling constant) but random orientation. This algorithm is known to be an efficient means of picking a point on the surface of an n-dimensional hypersphere S_{n-1}.

Figures 3.5(b) and 3.5(d) summarise the MARY spectra calculated in several ensembles of radical pairs. The 1 000 members of each ensemble have n_A hyperfine couplings on radical A and n_B on radical B. These coupling constants are chosen by means of the hypersphere point picking algorithm described above such that the effective hyperfine coupling constants $\tilde{a}_A = \tilde{a}_B = 0.2\,\text{mT}$. All nuclei are taken as spins-½ and there are no equivalent hyperfine couplings, except accidentally. The 1 000 different calculated MARY spectra in each ensemble are summarised by plotting a line that is centred on the mean singlet yield in the ensemble and which extends above and below the mean by one standard deviation.

At low rate constants, e.g. in Figure 3.5(b), we see that there is quite a substantial variation in singlet yield between members of the $n_A = 5$, $n_B = 1$ ensemble. The SCA singlet yield falls within one standard deviation of the mean, but may not be of huge predictive value because the singlet yield is clearly rather sensitive to the details of the hyperfine coupling constants in the radical pair and not merely to the effective hyperfine coupling constants. However, as we add additional magnetic nuclei to radical B, the situation improves. The $n_A = 5$, $n_B = 4$ ensemble shows agreement within about one percent between the mean singlet yield and the SCA singlet yield. Nevertheless, the low field effect minimum clearly differs qualitatively in shape between members of the ensemble. It is not determined particularly well by the effective hyperfine coupling constants, and hence neither is it predicted particularly well by the SCA at low values of the exponential model rate constant.

In contrast, at higher rate constants, e.g. in Figure 3.5(d), the SCA singlet yield agrees to within 1% with the mean values from all four ensembles presented in the figure. The only criticism here is that the SCA systematically overestimates the singlet yield at high static field strengths and also in the LFE region. Unfortunately, it was not possible to continue these calculations adding further magnetic nuclei because of limited computing resources. It is possible that, for larger spin systems, convergence to the SCA would become better still.

In answer to our initial questions, it would appear that radical pairs with five or six inequivalent magnetic nuclei in each partner show close agreement to the SCA, providing that the exponential model rate constant is greater than the effective hyperfine coupling constants in the radicals. Furthermore, in this "high" rate constant regime, there is little deviation between the MARY spectra in each ensemble; the effective hyperfine coupling constant is a good predictor of the MARY spectrum. However, at "low" values of the rate constant, the MARY spectra depend to a greater extent on the individual hyperfine coupling constants.

3.5 High field, many nuclei limit

As noted in our discussion of Figure 3.3, the SCA can be rather accurate when the static magnetic field strength is greater than the hyperfine couplings. In this section, we show how to calculate quantum mechanically the high-field limiting singlet yield in a radical pair containing a large number of magnetic nuclei. It will transpire that

this quantum mechanical calculation gives the same formula for the high-field singlet yield as does the SCA.

Consider a radical pair containing n_{A} spins-½ on radical A and n_{B} spins-½ on radical B. The hyperfine coupling constants for the nuclei on radical A are all a_{A} and those on radical B are all a_{B}. In the high-field limit, we are free to make the so-called secular approximation, where we neglect all the off-diagonal terms — which arise only from the hyperfine interaction — in the Hamiltonian. The secular Hamiltonian may therefore be written

$$\hat{H} = \hat{H}^{\mathrm{A}} + \hat{H}^{\mathrm{B}} \quad \text{where} \quad \hat{H}^{\mathrm{N}} = \sum_i a_{\mathrm{N}} \hat{S}_{\mathrm{Nz}} \hat{I}_{\mathrm{iz}} + \omega_0 \hat{S}_{\mathrm{Nz}}. \tag{3.39}$$

In the product basis, this Hamiltonian only has non-zero elements on the diagonal. Each element will take the form

$$\hat{H}^{\mathrm{N}}_{kk} = \frac{1}{2}\left[\pm\omega_0 + \frac{1}{2}\sum_i \pm a_{\mathrm{N}}\right] \tag{3.40}$$

where each combination of $\pm$ gives rise to an element kk. Substituting into equation (3.7) and then using equation (3.6) gives the high field singlet probability

$$\left\langle \hat{P}^{\mathrm{S}} \right\rangle (t) = \frac{1}{2} + \frac{1}{2}\left[\cos\left(a_{\mathrm{A}}t/2\right)^{n_{\mathrm{A}}} \times \cos\left(a_{\mathrm{B}}t/2\right)^{n_{\mathrm{B}}}\right]. \tag{3.41}$$

Each of the cosine powers may be expanded e.g.

$$\begin{aligned}
\cos\left(a_{\mathrm{A}}t/2\right)^3 &= \frac{1}{2^3}\begin{bmatrix}
\cos\left(\{+a_{\mathrm{A}}+a_{\mathrm{A}}+a_{\mathrm{A}}\}t/2\right)+ \\
\cos\left(\{+a_{\mathrm{A}}+a_{\mathrm{A}}-a_{\mathrm{A}}\}t/2\right)+ \\
\cos\left(\{+a_{\mathrm{A}}-a_{\mathrm{A}}+a_{\mathrm{A}}\}t/2\right)+ \\
\cos\left(\{+a_{\mathrm{A}}-a_{\mathrm{A}}-a_{\mathrm{A}}\}t/2\right)+ \\
\cos\left(\{-a_{\mathrm{A}}+a_{\mathrm{A}}+a_{\mathrm{A}}\}t/2\right)+ \\
\cos\left(\{-a_{\mathrm{A}}+a_{\mathrm{A}}-a_{\mathrm{A}}\}t/2\right)+ \\
\cos\left(\{-a_{\mathrm{A}}-a_{\mathrm{A}}+a_{\mathrm{A}}\}t/2\right)+ \\
\cos\left(\{-a_{\mathrm{A}}-a_{\mathrm{A}}-a_{\mathrm{A}}\}t/2\right)
\end{bmatrix} \\
&= \frac{1}{2^3}\left[\cos\left(3a_{\mathrm{A}}t/2\right) + 3\cos\left(a_{\mathrm{A}}t/2\right) + 3\cos\left(-a_{\mathrm{A}}t/2\right) + \cos\left(-3a_{\mathrm{A}}t/2\right)\right]
\end{aligned} \tag{3.42}$$

which is clearly a binomial series. Using Stirling's approximation, it may be shown that this binomial probability distribution tends to a Gaussian distribution for very large numbers of magnetic nuclei [166, Binomial Distribution]. Hence, in the limit of a very large number of nuclei, the probability distribution for different frequency factors (e.g. "$3/2$" in the first term of equation (3.42)) is given by

$$P(x) = \sqrt{\frac{2}{\pi n_{\mathrm{N}}}}\,\exp\left(\frac{-2x^2}{n_{\mathrm{N}}}\right) \tag{3.43}$$

and hence the large n limiting singlet probability is

$$\left\langle \hat{P}^{\mathrm{S}} \right\rangle (t) = \frac{1}{2} + \frac{1}{2}\left[\int_{-\infty}^{\infty} \cos\left(x a_{\mathrm{A}} t\right) P(x)\,\mathrm{d}x \times \int_{-\infty}^{\infty} \cos\left(x a_{\mathrm{B}} t\right) P(x)\,\mathrm{d}x\right] \tag{3.44}$$

$$= \frac{1}{2} + \frac{1}{2}\exp\left(-\frac{1}{8}\left\{a_{\mathrm{A}}^2 n_{\mathrm{A}} + a_{\mathrm{B}}^2 n_{\mathrm{B}}\right\} t^2\right). \tag{3.45}$$

We may identify $a_{\mathrm{N}}^2 n_{\mathrm{N}} = \tilde{a}_{\mathrm{N}}^2$, the effective hyperfine coupling constant in radical N.

We note also that in the limit of a large number of nuclei, the saturation value for the singlet yield

$$\Phi_{\mathrm{S}} = \frac{1}{2} + \frac{k_* \sqrt{\pi}}{2} \exp\left(k_*^2\right) \operatorname{erfc}\left(k_*\right) \qquad \text{where } k_* = \frac{k\sqrt{2}}{\tilde{a}_{\mathrm{RP}}} \tag{3.46}$$

depends only on the exponential model rate constant k and the overall *radical pair* effective hyperfine coupling constant

$$\tilde{a}_{\mathrm{RP}} = \sqrt{\tilde{a}_{\mathrm{A}}^2 + \tilde{a}_{\mathrm{B}}^2}. \tag{3.47}$$

This provides a theoretical justification for the importance of $\tilde{a}_{\mathrm{RP}}$, which is better known as an experimental parameter.

In their 1978 paper, Schulten and Wolynes give an expression for the semiclassical approximate triplet probability in the limit of high magnetic field strength [27, eq (33)]:

$$\left\langle \hat{P}^{\mathrm{T}} \right\rangle (t) = \frac{1}{2} \left[1 - \exp\left(-t^2/\tau_{\mathrm{A}}^2\right) \exp\left(-t^2/\tau_{\mathrm{B}}^2\right) \right] \tag{3.48}$$

Rewriting this expression in terms of effective hyperfine coupling constants using equation (3.33) and noting that $\left\langle \hat{P}^{\mathrm{S}} \right\rangle (t) = 1 - \left\langle \hat{P}^{\mathrm{T}} \right\rangle (t)$ we find that

$$\left\langle \hat{P}^{\mathrm{S}} \right\rangle (t) = \frac{1}{2} \left[1 + \exp\left(-\frac{1}{8} \left\{ \tilde{a}_{\mathrm{A}}^2 + \tilde{a}_{\mathrm{B}}^2 \right\} t^2 \right) \right] \tag{3.49}$$

which is clearly identical to the result obtained using the secular approximation and the large n limiting form of the binomial distribution.

3.6 Validity of the SCA

These tests of the semi-classical approximation show that it is sometimes accurate to within 1% when calculating singlet yields. It is most accurate at high static field strengths and also in systems with rapid re-encounter kinetics. Conversely, in the LFE region and in systems with slow re-encounter kinetics, the SCA can fail to reproduce even qualitatively the true MARY spectrum. These observations are quite consistent with our remarks in connection with Figure 3.3 where we found that the triplet (and hence also the singlet) probability was most accurate at short times, or at high field strengths.

That the SCA sometimes comes very close to the true singlet probabilities, and hence singlet yields, is rather surprising when one considers its origins. It is not physical to expect that the nuclear spins behave classically. In addition, detailed calculations of the spin evolution in a radical pair using the product operator formalism show that the nuclear spins evolve substantially during a radical pair's lifetime. This is at variance with the assumption of a fixed, time-independent resultant nuclear spin vector $\tilde{\boldsymbol{I}}_{\mathrm{N}}$ in the SCA. Furthermore, as shown in Figure 3.5, the SCA improves quite rapidly as we increase the number of magnetic nuclei in each radical. For a "5–4" radical pair, the agreement is already fair. This convergence occurs despite the use of an asymptotic

random flight probability distribution — equation (3.12) — that is not expected to be accurate until there are "20–50 bonds [*i.e.* nuclei]" [165].

In a manner of thinking, the SCA replaces a problem of coherent spin evolution in the radical pair with one of inhomogeneous line broadening or dephasing caused by variations in the "resultant effective field" $\boldsymbol{\omega}_{\mathrm{N}}$ formed from the applied magnetic field and the electron–nuclear hyperfine magnetic fields. This viewpoint fits naturally with the failure of the SCA to reproduce (coherent) oscillations in the singlet, or triplet, probability at long times as was seen in Figure 3.3.

A full explanation for the quality of the SCA remains elusive. On the one hand, it rests on rather shaky physical assumptions, yet on the other hand it clearly reproduces the exact quantum calculations quite adequately at high fields and at short times. Some encouragement may be taken from a comparison of the quantum mechanical high field, many nuclei limiting singlet probability with that predicted by the SCA. As shown above in §3.5, the SCA gives identical results to a quantum mechanical calculation in this limit. At short times, it seems likely that the short time approximation (STA) introduced by Haberkorn [169] would agree with the SCA. The STA is derived by time dependent perturbation theory, treating the hyperfine interactions as perturbations of the Zeeman interaction. It is encouraging that the STA also predicts singlet probabilities that depend on the effective hyperfine coupling constants in the two radicals. In summary. it seems likely that the SCA formula performs as well as it does because it is an extrapolation from more rigorous quantum mechanical limits. It could be fruitful to study the breakdown of these limiting cases in the hope of arriving at a more physically sound, quantum mechanical approximate calculation scheme for singlet yields which retained the computational advantages of the SCA.

3.7 Empirical parameters

Having outlined two methods for the calculation of MARY spectra in radical pairs possessing several magnetic nuclei, we proceed to the major objective of this chapter. Figure 3.6 shows a MARY spectrum for a simple radical pair. Although the details of the spectrum will change substantially in different radical pairs and when the recombination kinetics differ, it is known that many MARY spectra resemble one-another qualitatively. As a result of this resemblance, a MARY spectrum may be qualitatively characterised by the positions of a small number of features, which are marked in the figure and described below.

$\Phi_{\mathrm{S}}(\infty)$: The limiting (saturation) value of the singlet yield as the magnetic field strength is increased to around 100 mT. In reality, the singlet yield will begin to change again at higher field strengths as other mechanisms for singlet–triplet interconversion, such as the Δg mechanism, become operative. We do not consider these high field mechanisms in this chapter.

$B_{1/2}$: The magnetic field strength at which the singlet yield is half way between its value at zero-field $\Phi_{\mathrm{S}}(0)$ and that in the high field limit $\Phi_{\mathrm{S}}(\infty)$.

B_{LFE}: In many MARY spectra, there is an initial decrease in singlet yield upon application of fields smaller than ~ 1 mT, *i.e.* the low field effect (LFE). The magnetic

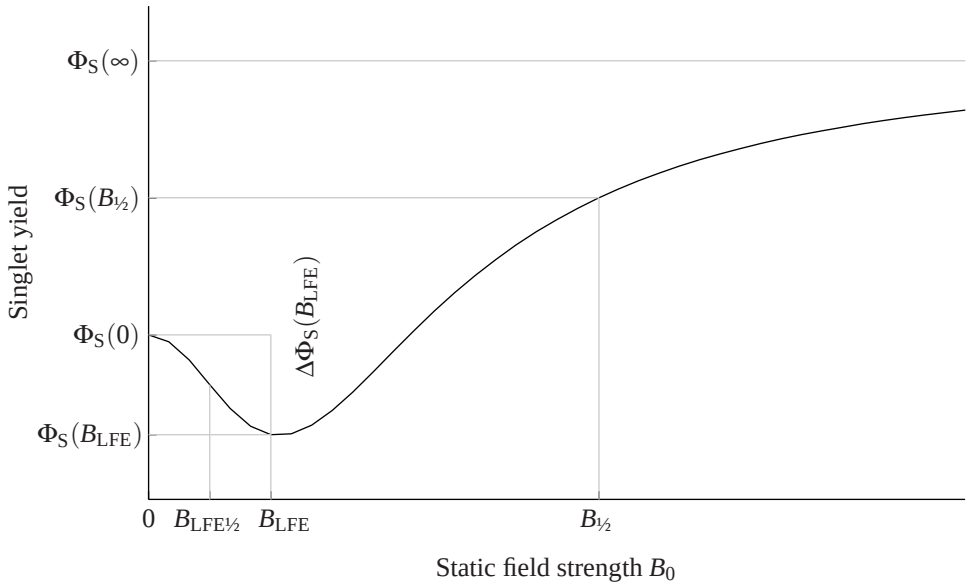

Figure 3.6: MARY spectrum for a one-proton radical pair marked with the principal empirical parameters to be discussed in the text.

field corresponding to the minimum singlet yield in the LFE region $\Phi_S(B_{LFE})$ is termed B_{LFE}.

$B_{LFE½}$: The magnetic field required to produce one half of the drop in singlet yield found at B_{LFE}.

$\Delta\Phi_S(B_{LFE})$: The LFE depth is the change in singlet yield between zero field and the LFE minimum.

We apply the SCA and QMMC methods to radical pairs with a wide range of hyperfine couplings and exponential model rate constants in order to elucidate the factors controlling these features.

MARY spectra were calculated according to the SCA in `Mathematica` using the built-in numerical integration function `NIntegrate`. The singlet yield was calculated at field strengths between 0 and 10 mT with more closely-spaced field strengths below 0.1 mT; exponential model rate constants were taken between 0.05 and 10 mT; and effective hyperfine coupling constants were taken between 0.001 and 10 mT. The combination of rate constants and effective HFCs gave 405 distinct MARY spectra. As discussed in §3.3.9, the numerical integration of the SCA expression for singlet probability is challenging. This was evidenced by a failure to converge adequately in 30 of the MARY spectra (7.4%). It is not believed that these failures have any significant effect on the trends discussed below.

MARY spectra were also calculated in an ensemble of 12 737 radical pairs using the QMMC method described in §3.4. Each member of the ensemble had six random hyperfine couplings to spin-½ nuclei — three on each radical. These hyperfine couplings were chosen such that the effective HFCs on each radical were uniformly distributed between 0 and 1.5 mT. After selection of the HFCs, MARY spectra were calculated for each member of the ensemble at 1 000 field strengths varying logarithmically between 10^{-11} and 10 mT and at zero field. Exponential model rate constants were taken

between 10^{-2} and $10^{12}\,\mathrm{s}^{-1}$, which covers the typical experimental values and several orders of magnitude either side. In total, the QMMC calculation involved more than 300 000 000 singlet yield calculations. We are indebted to the Oxford Supercomputing Centre for providing the necessary computational resources.

3.8 Empirical parameters: LFE depth

The first experimental feature that we consider is the LFE depth $\Delta\Phi_{\mathrm{S}}(B_{\mathrm{LFE}})$. The origins of the LFE have been investigated previously with a combination of theory and experiment [10, 108, 110, 140]. The LFE is particularly important to discussions on the possible adverse health effects of non-ionising radiation from mobile phones and power lines [68–70, 72, 78, 79] and to the question of biological magnetoreception [105–107], since in each case the magnetic fields involved are weaker than about 1 mT and thus fall within the realm of the LFE.

Molin, Stass and coworkers investigated experimentally the LFE in a variety of radical pairs subjected to X-ray irradiation in the non-polar solvent squalene [110, 170]. They present two significant rules of thumb for the presence of a LFE with significant depth: (i) "for a radical pair containing a great number of non-equivalent nuclei in both of the partners the effect of interference [*i.e.* the LFE] is rather weak and vanishes in the semiclassical limit", and (ii) "[a] minor inversion [*i.e.* an LFE] is to be observed for radical pairs with a few groups of equivalent nuclei". In contrast, Timmel developed expressions for the limiting LFE depth as $k \to 0$ using perturbation theory [108]. In this limit, essentially any radical pair shows a marked LFE. We address this apparent discrepancy here.

Figure 3.8 shows the variation of LFE depth with effective HFC extracted from the QMMC MARY spectra for three different exponential model rate constants. We plot both the mean LFE depth for members of the ensemble having effective HFCs within each rectangle and also their standard deviation. In the limit of slow recombination kinetics, when $k \ll -\tilde{a}_{\mathrm{A,B}}/\gamma_{\mathrm{e}} \sim 10^8\,\mathrm{s}^{-1}$, the LFE depth is virtually independent of the hyperfine couplings (Figures 3.8(a) and 3.8(b)) as reported by Timmel [108]. For intermediate kinetics, when $k \sim -\tilde{a}_{\mathrm{A,B}}/\gamma_{\mathrm{e}} \sim 10^8\,\mathrm{s}^{-1}$, the LFE depth is rather small unless $\tilde{a}_{\mathrm{A}} \gg \tilde{a}_{\mathrm{B}}$ or vice-versa (Figures 3.8(c)–3.8(f)). However, when $\tilde{a}_{\mathrm{A}} \gg \tilde{a}_{\mathrm{B}}$ we also find the largest standard deviation in the LFE depth. Hence, for rate constants comparable to the effective HFCs, radical pairs with dominant HFCs on one partner may, but need not necessarily, show a deep LFE. Finally, for rapid kinetics, when $k \gg -\tilde{a}_{\mathrm{A,B}}/\gamma_{\mathrm{e}} \sim 10^8\,\mathrm{s}^{-1}$, a LFE is not seen and the field effect curve increases monotonically to the $\Phi_{\mathrm{S}}(\infty)$ value.

The SCA results presented in Figure 3.7 are in broad agreement with those discussed above. Although the SCA may well not be accurate in the LFE region, it is worth examining the trends that it predicts. Not least, this is worthwhile because the SCA has been used in the literature for interpretation of LFEs; comparison of Figures 3.8 and 3.7 gives an idea of how accurate such statements from the literature might be. Once again, at intermediate values of the rate constant, we find that a substantial LFE occurs in radical pairs where the HFCs on one radical dominate, *i.e.* $\tilde{a}_{\mathrm{A}} \gg \tilde{a}_{\mathrm{B}}$ or vice-versa (Figure 3.7(a)). At high values of the rate constant, the LFE tends to disappear (Figure 3.7(b)) as before. These limits on the rate constant may be made clearer by plotting LFE depth $\Delta\Phi_{\mathrm{S}}(B_{\mathrm{LFE}})$ against rate constant k for a selection of ef-

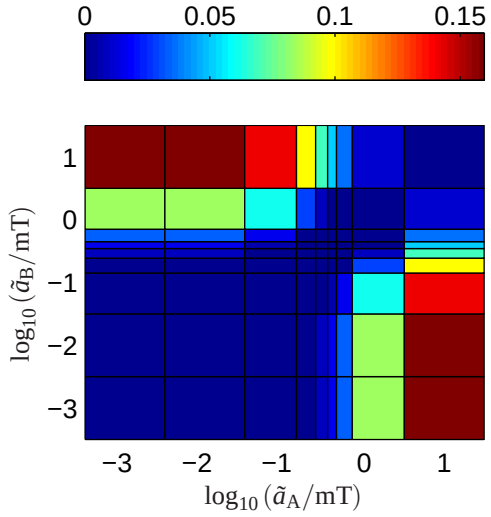

(a) $k = 0.20\,\mathrm{mT}$. LFE depth varies between 0 and 0.16.

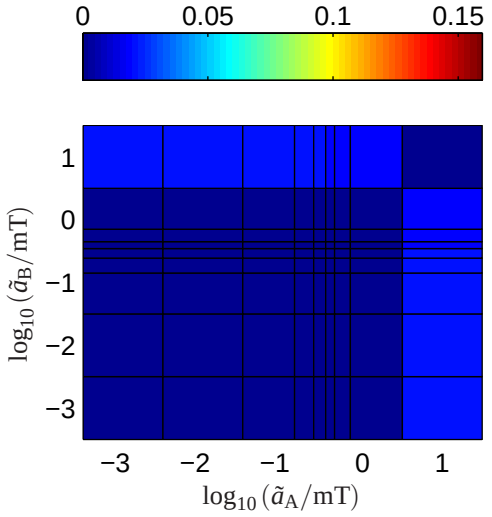

(b) $k = 5.00\,\mathrm{mT}$. LFE depth varies between 0 and 0.02.

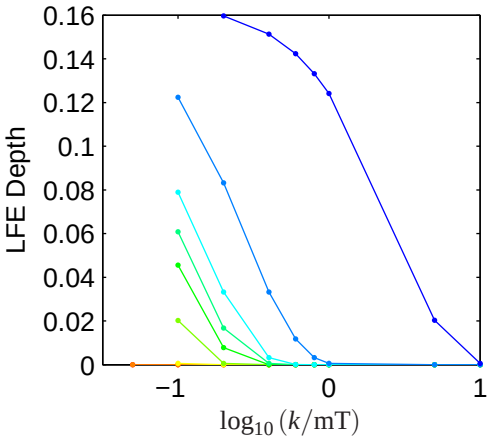

(c) $\tilde{a}_B = 0.001\,\mathrm{mT}$. Line colour indicates $\tilde{a}_A$ (see legend).

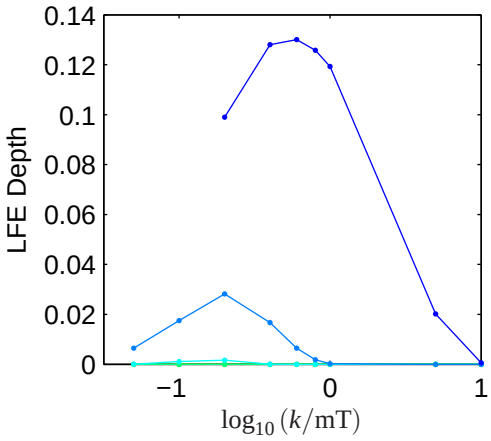

(d) $\tilde{a}_B = 0.2\,\mathrm{mT}$. Line colour indicates $\tilde{a}_A$ (see legend).

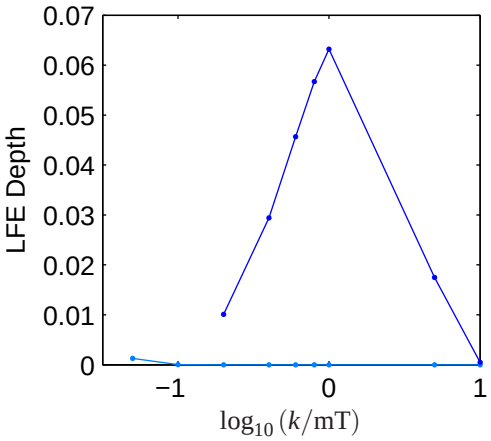

(e) $\tilde{a}_B = 1\,\mathrm{mT}$. Line colour indicates $\tilde{a}_A$ (see legend).

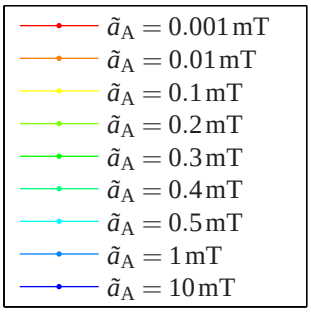

Figure 3.7: LFE depth $\Delta\Phi_S(B_{LFE})$ according to the SCA. Calculations were performed across all plausible values of the re-encounter rate constant k and effective hyperfine coupling constants $\tilde{a}_{A,B}$. (a–b): Each rectangle shows the LFE depth for the effective HFCs at its centre. 227 of the 405 MARY spectra showed no LFE, recorded here as $\Delta\Phi_S(B_{LFE}) = 0$. (c–e): The dependence of LFE depth on rate constant k. There is one line per choice of $\tilde{a}_{A,B}$. Some points are missing because 30 of the 405 MARY spectra did not converge satisfactorily.

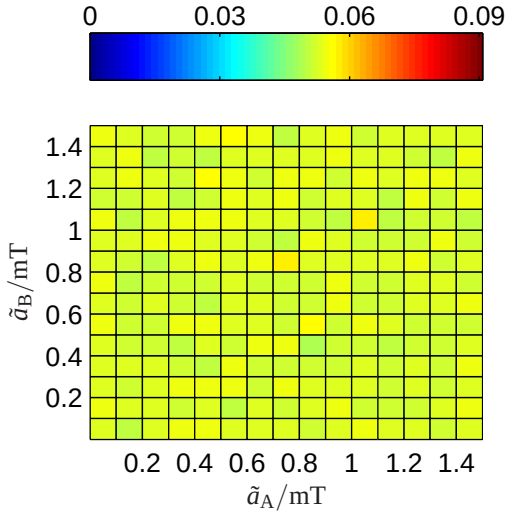

(a) Mean LFE depth when $k = 0.01\,\mathrm{s}^{-1}$. Values range between 0.05 and 0.06.

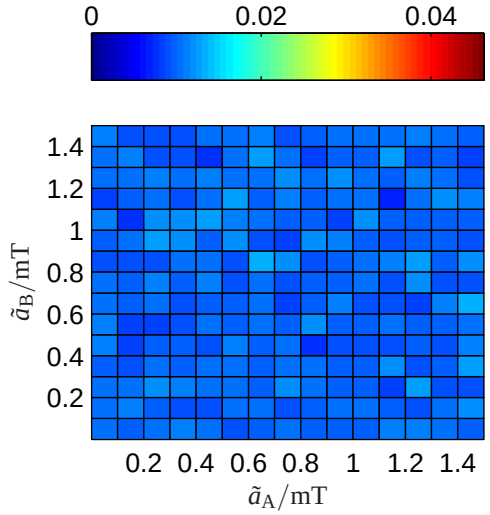

(b) Standard deviation in LFE depth when $k = 0.01\,\mathrm{s}^{-1}$. Values range between 0.01 and 0.01.

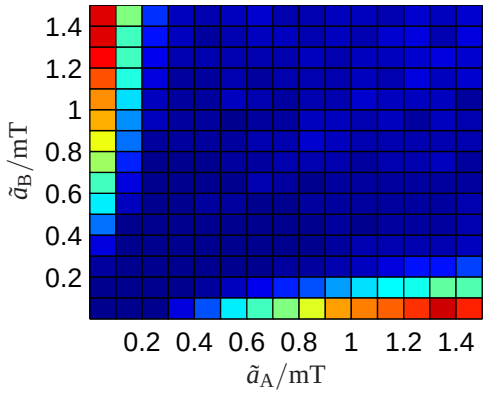

(c) Mean LFE depth when $k = 3 \times 10^7\,\mathrm{s}^{-1}$. Values range between 0.00 and 0.08.

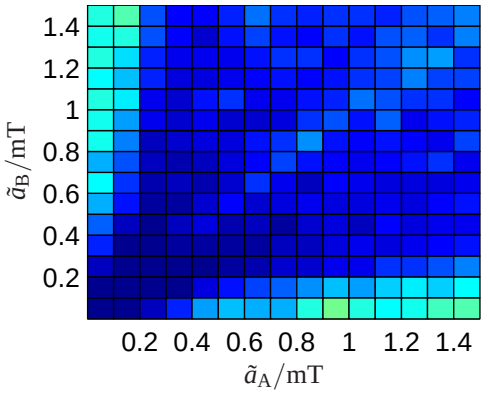

(d) Standard deviation in LFE depth when $k = 3 \times 10^7\,\mathrm{s}^{-1}$. Values range between 0.00 and 0.02.

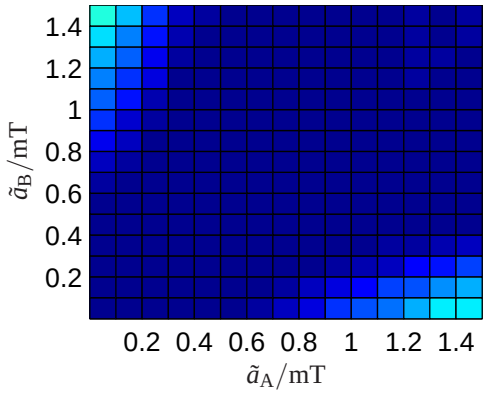

(e) Mean LFE depth when $k = 8 \times 10^7\,\mathrm{s}^{-1}$. Values range between 0.00 and 0.04.

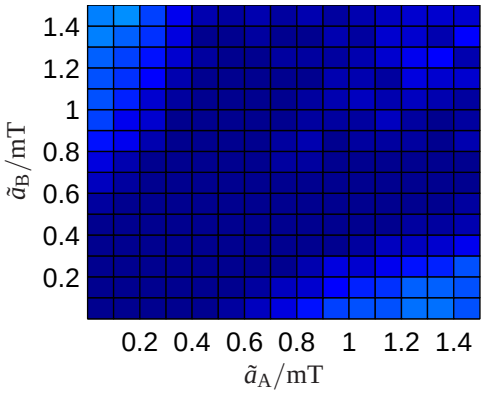

(f) Standard deviation in LFE depth when $k = 8 \times 10^7\,\mathrm{s}^{-1}$. Values range between 0.00 and 0.01.

Figure 3.8: LFE depth $\Delta\Phi_S(B_{\mathrm{LFE}})$ according to QMMC calculations in an ensemble of 12 737 radical pairs. The colour of each rectangle summarises the results from those members of the ensemble having effective HFCs which fall within it. We plot the mean LFE depth in each cell on the left and the standard deviations on the right. Rate constants k were selected to be less than and comparable to the effective HFCs. Calculations with $k > 5 \times 10^8\,\mathrm{s}^{-1}$ showed no LFE at all and are therefore not presented.

fective HFCs (Figures 3.7(c)–3.7(e)). In general, it would appear that even when one radical has dominant HFCs, the rate constant must fall approximately within the range $\tilde{a}_{\mathrm{B}} < k < \tilde{a}_{\mathrm{A}}/2$ where $\tilde{a}_{\mathrm{B}}$ is the smaller of the two effective HFCs. It seems likely that this condition arises because of the need to allow sufficient dephasing to occur within the re-encounter timescale in order to observe a LFE in the SCA.

3.9 Empirical parameters: LFE position

3.9.1 B_{LFE}

The LFE is clearly characterised not just by its depth, but also by the field strength at which it occurs in a given radical pair. The simplest way to quantify this LFE position is to measure the magnetic field, B_{LFE}, at which the singlet yield takes its minimum value. Figure 3.9 summarises the behaviour of B_{LFE} in an ensemble of 12 737 radical pairs as a function of the effective HFCs and using three different rate constants. We plot the mean of $\log_{10}(B_{\mathrm{LFE}}/\,\mathrm{mT})$ in the left column and the standard deviations on the right.

For slow kinetics, when $k \ll -\tilde{a}_{\mathrm{A,B}}/\gamma_{\mathrm{e}}$, the LFE minimum field B_{LFE} varies little as the effective HFC changes. It would appear that the LFE minimum position shifts to higher magnetic fields when both $\tilde{a}_{\mathrm{A}}$ and $\tilde{a}_{\mathrm{B}}$ are large. The standard deviations are small in this limit, showing that the LFE minimum field does not depend on the individual hyperfine couplings.

However, the situation becomes much more complicated for faster kinetics. Inspecting Figures 3.9(c)–3.9(f), one can see that there are regions of very high standard deviation when $\tilde{a}_{\mathrm{A}} \approx \tilde{a}_{\mathrm{B}}$. In these regions, the LFE minimum field position depends critically upon the individual hyperfine couplings in the system and is not well described by the effective HFCs. As a rule of thumb, it would appear that such complex behaviour occurs when $\frac{10}{-\gamma_{\mathrm{e}}}k > \tilde{a}_{\mathrm{A}} \sim \tilde{a}_{\mathrm{B}}$. In contrast, when $\tilde{a}_{\mathrm{A}} \gg \tilde{a}_{\mathrm{B}}$ (or vice-versa), we see LFE minimum field positions which are of the order of 1 mT and which have small standard deviations. These minima are clearly in the hyperfine dominated region of the MARY spectrum.

Finally, for rapid kinetics, when $k \gg -\tilde{a}_{\mathrm{A,B}}/\gamma_{\mathrm{e}}$ we do not see any LFE; the MARY spectra increase monotonically with field strength.

3.9.2 $B_{\mathrm{LFE}½}$

An alternative measure of the LFE position is given by $B_{\mathrm{LFE}½}$, the static field strength required to reduce the singlet yield half way to its value at the LFE minimum. Figure 3.10 summarises the behaviour of $B_{\mathrm{LFE}½}$ in our ensemble of radical pairs. The most notable feature is that $B_{\mathrm{LFE}½}$ is proportional to the rate constant k in the limit of slow recombination and that it hardly depends on the hyperfine couplings at all.

Figure 3.11 shows the same effect, this time plotting MARY spectra for one member of the ensemble at a selection of different rate constants. This figure is plotted with a logarithmic scale for the field strength. It is easy to see that for small rate constants k, the LFE develops in two approximately sigmoidal steps whose centres bear a simple relationship to k.

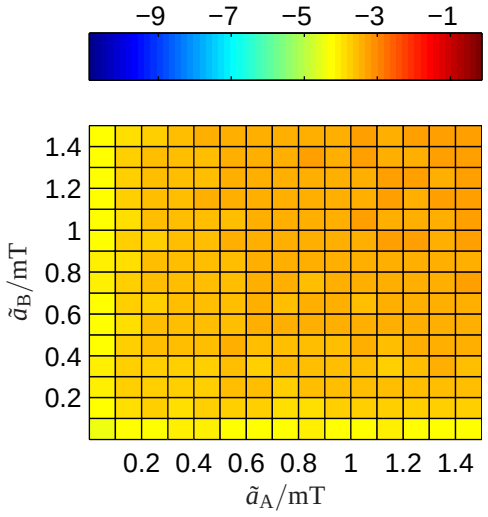

(a) Mean of $\log_{10}(B_{\mathrm{LFE}}/\mathrm{mT})$ when $k = 0.01\,\mathrm{s}^{-1}$. Values range between -4.40 and -3.23.

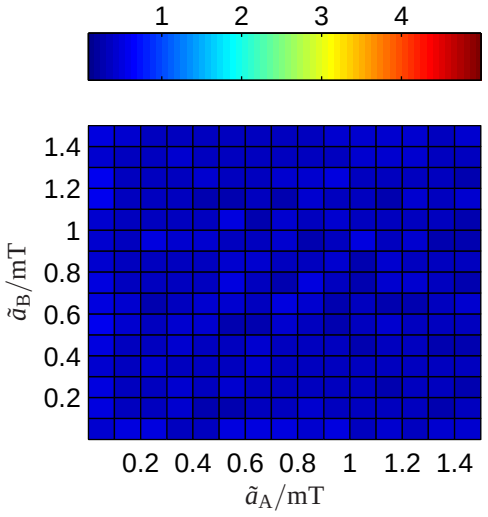

(b) Standard deviation of $\log_{10}(B_{\mathrm{LFE}}/\mathrm{mT})$ when $k = 0.01\,\mathrm{s}^{-1}$. Values range between 0.24 and 0.57.

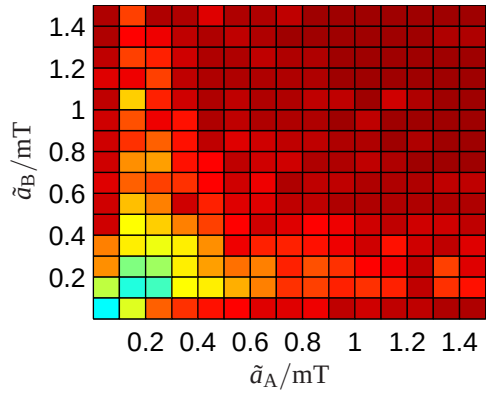

(c) Mean of $\log_{10}(B_{\mathrm{LFE}}/\mathrm{mT})$ when $k = 5 \times 10^6\,\mathrm{s}^{-1}$. Values range between -6.99 and -0.50.

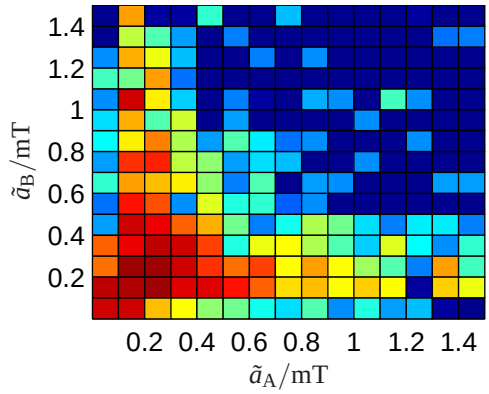

(d) Standard deviation of $\log_{10}(B_{\mathrm{LFE}}/\mathrm{mT})$ when $k = 5 \times 10^6\,\mathrm{s}^{-1}$. Values range between 0.08 and 4.82.

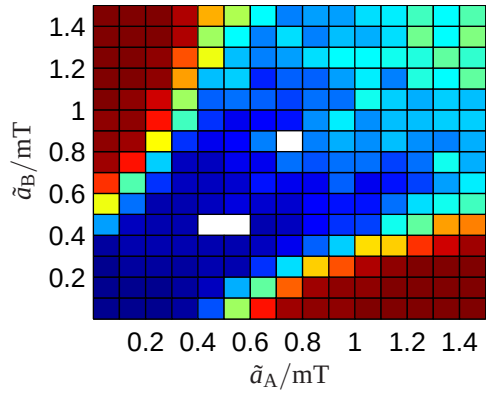

(e) Mean of $\log_{10}(B_{\mathrm{LFE}}/\mathrm{mT})$ when $k = 8 \times 10^7\,\mathrm{s}^{-1}$. Values range between $-\infty$ (*i.e.* no LFE) and -0.14.

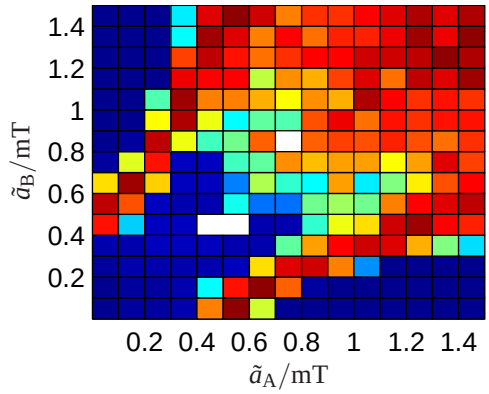

(f) Standard deviation of $\log_{10}(B_{\mathrm{LFE}}/\mathrm{mT})$ when $k = 8 \times 10^7\,\mathrm{s}^{-1}$. Values range between 0.08 and 4.89.

Figure 3.9: LFE minimum field B_{LFE} according to QMMC calculations in 12 737 radical pairs. The colour of each rectangle summarises the results from those members of the ensemble having effective HFCs which fall within it. We plot the mean of $\log_{10}(B_{\mathrm{LFE}}/\mathrm{mT})$ in each cell on the left and the standard deviations on the right. Rate constants k were selected to be less than and comparable to the effective HFCs. Calculations with $k > 5 \times 10^8\,\mathrm{s}^{-1}$ showed no LFE at all and are therefore not presented.

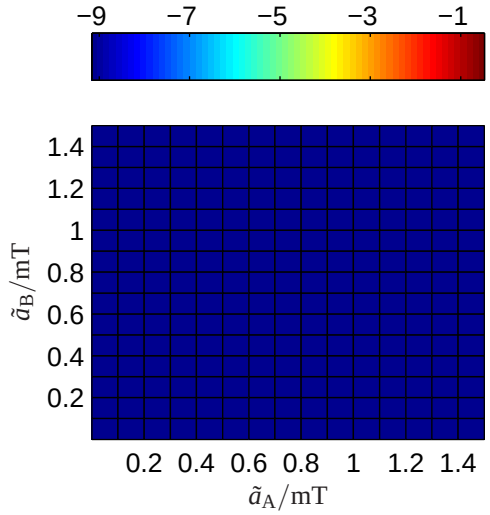

(a) Mean of $\log_{10}(B_{\mathrm{LFE}½}/\mathrm{mT})$ when $k = 0.01\,\mathrm{s}^{-1}$. Values range between -9.16 and -9.04.

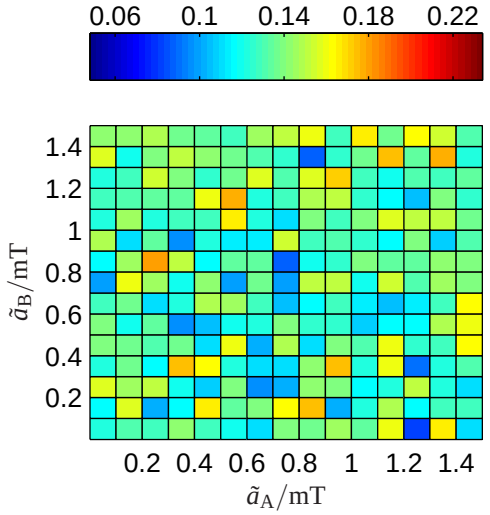

(b) Standard deviation of $\log_{10}(B_{\mathrm{LFE}½}/\mathrm{mT})$ when $k = 0.01\,\mathrm{s}^{-1}$. Values range between 0.08 and 0.18.

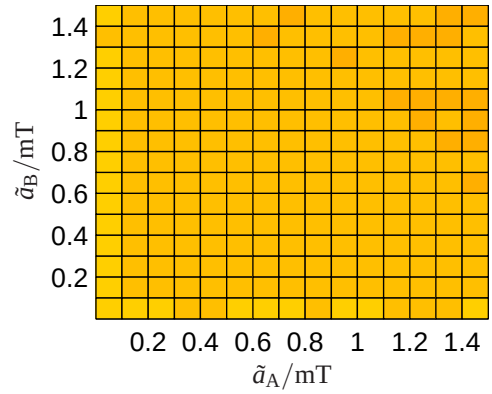

(c) Mean of $\log_{10}(B_{\mathrm{LFE}½}/\mathrm{mT})$ when $k = 10^4\,\mathrm{s}^{-1}$. Values range between -3.40 and -3.16.

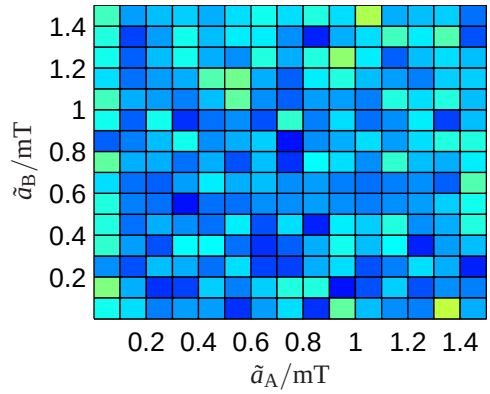

(d) Standard deviation of $\log_{10}(B_{\mathrm{LFE}½}/\mathrm{mT})$ when $k = 10^4\,\mathrm{s}^{-1}$. Values range between 0.07 and 0.15.

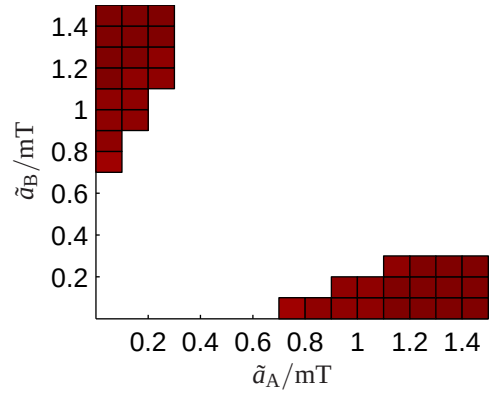

(e) Mean of $\log_{10}(B_{\mathrm{LFE}½}/\mathrm{mT})$ when $k = 8^7\,\mathrm{s}^{-1}$. Values range between -0.86 and -0.49. White regions mean that $B_{\mathrm{LFE}½}$ values could not always be found.

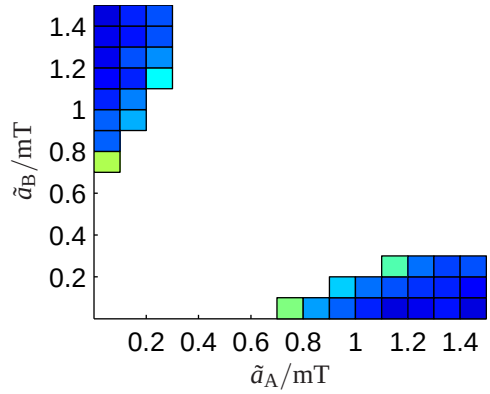

(f) Standard deviation of $\log_{10}(B_{\mathrm{LFE}½}/\mathrm{mT})$ when $k = 8^7\,\mathrm{s}^{-1}$. Values range between 0.06 and 0.15. White regions mean that $B_{\mathrm{LFE}½}$ values could not always be found.

Figure 3.10: LFE half-onset field $B_{\mathrm{LFE}½}$ according to QMMC calculations in 12737 radical pairs. The colour of each rectangle summarises the results from those members of the ensemble having effective HFCs which fall within it. We plot the mean of $\log_{10}(B_{\mathrm{LFE}½}/\mathrm{mT})$ in each cell on the left and the standard deviations on the right. Rate constants k were selected to be less than and comparable to the effective HFCs. Calculations with $k > 5\times10^8\,\mathrm{s}^{-1}$ showed no LFE at all and are therefore not presented.

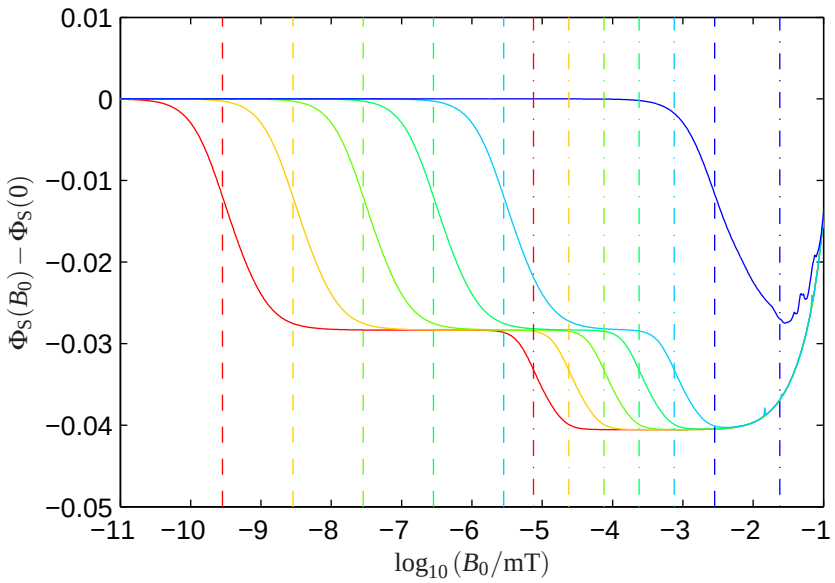

Figure 3.11: Low field region of the MARY spectrum in one radical pair from the QMMC ensemble. Note the logarithmic field axis. Lines are plotted for rate constants k =0.01, 0.1, 1, 10, 100 and 10^5 s^{-1}. Dashed vertical lines are drawn in at $B_0 = -5k/\gamma_e$. Dot-dashed vertical lines are drawn in at $(B_0)^2 = -k/\gamma_e$.

Perturbation theory provides a simple rationalisation for this effect. Consider the Hamiltonian for a radical pair

$$\hat{H} = \hat{H}^{(0)} + \hat{H}^{(1)}$$

where

$$\hat{H}^{(0)} = \sum_i a_{i\mathrm{A}}\,\hat{\boldsymbol{S}}_\mathrm{A}\cdot\hat{\boldsymbol{I}}_{i\mathrm{A}} + \sum_i a_{i\mathrm{B}}\,\hat{\boldsymbol{S}}_\mathrm{B}\cdot\hat{\boldsymbol{I}}_{i\mathrm{B}} \quad \text{and}$$

$$\hat{H}^{(1)} = -\gamma_e B\left(\hat{S}_{\mathrm{Az}} + \hat{S}_{\mathrm{Bz}}\right). \tag{3.50}$$

Ignoring complications arising from degenerate states, for a zero-field eigenstate $\hat{H}^{(0)}\,|m\rangle = E_m^{(0)}\,|m\rangle$, the first order correction to the energy is given by [92]

$$\Delta E_m^{(1)} = \langle m|\,\hat{H}^{(1)}\,|m\rangle \tag{3.51}$$

$$= -\gamma_e B\,\langle m|\,\hat{S}_{\mathrm{Az}} + \hat{S}_{\mathrm{Bz}}\,|m\rangle = -\gamma_e B\,(c_1)_m \tag{3.52}$$

and the second order correction by

$$\Delta E_m^{(2)} = \sum_{s\neq m} \frac{\langle m|\,H^{(1)}\,|s\rangle\,\langle s|\,H^{(1)}\,|m\rangle}{E_m - E_s} \tag{3.53}$$

$$= (\gamma_e B)^2 \sum_{s\neq m} \frac{\left[\langle m|\,\hat{S}_{\mathrm{Az}} + \hat{S}_{\mathrm{Bz}}\,|s\rangle\right]^2}{E_m - E_s} = (\gamma_e B)^2\,(c_2)_m\,. \tag{3.54}$$

To second order the energy of state $|m\rangle$ is therefore

$$E_m = E_m^{(0)} + \Delta E_m^{(1)} + \Delta E_m^{(2)}. \tag{3.55}$$

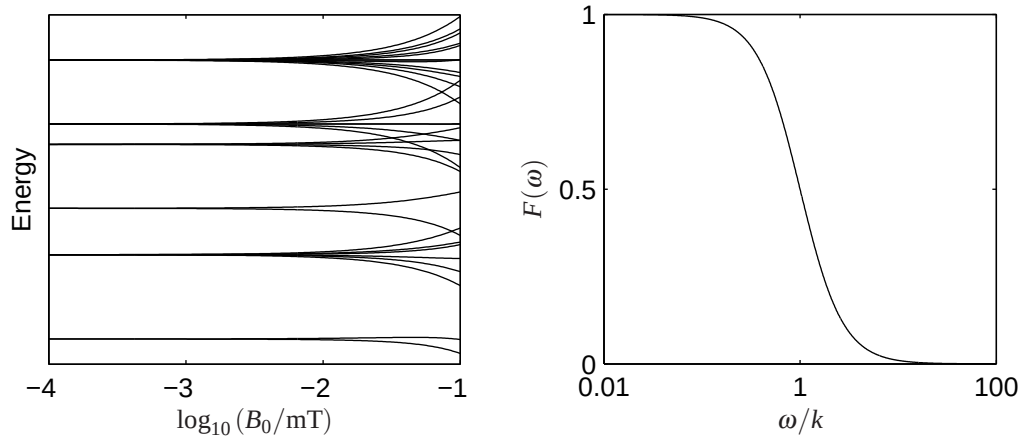

Figure 3.12: Left: Energy levels in a radical pair with two hyperfine couplings on one radical and one on the other. Notice the gradual lifting of zero-field degeneracies until fields of $\sim 0.1\,\mathrm{mT}$ when level crossings and other complications arise. Right: Plot of the Lorentzian function defined by equation (3.56) on a logarithmic ω-axis. Note the sigmoidal lineshape.

These perturbations in the energy levels can be seen clearly on the left of Figure 3.12. In the region $B_0 < 2\,\mathrm{mT}$, the perturbations act to split apart states which were degenerate at zero field. At higher field strengths, the Zeeman interaction becomes comparable in energy to the hyperfine interaction and our perturbation treatment breaks down.

Now, we know from our frequency domain derivation (see §2.2.2) that the singlet yield is given as a weighted sum of functions of energy splittings $\omega_{mn} = E_m - E_n$

$$\Phi_{\mathrm{S}}(B) = \sum_{m,n} a_{mn} F(\omega_{mn}) \quad \text{where} \quad F(\omega) = \frac{1}{1 + \left(\frac{\omega}{k}\right)^2}. \tag{3.56}$$

(We have eliminated the imaginary part of $F(\omega)$ from this expression because of symmetry in the amplitudes a_{mn}.) The function $F(\omega)$ is plotted on a logarithmic field axis on the right of Figure 3.12. Notice that when $\omega \ll k$, $F(\omega) \approx 1$ and that when $\omega \gg k$, $F(\omega) \approx 0$.

Consider a radical pair with rate constant k that is much smaller than the zero-field energy splittings. Thus, at zero field, the singlet yield will be given by

$$\Phi_{\mathrm{S}}(B) = \sum_{\substack{m,n \\ \text{degenerate}}} a_{mn} F(0) = \sum_{\substack{m,n \\ \text{degenerate}}} a_{mn}. \tag{3.57}$$

Now, as we move away from zero field, the Zeeman interaction splits apart eigenstates that were degenerate. It turns out that for the important energy levels $\langle m|\hat{S}_{\mathrm{Nz}}|m\rangle \sim 1$ and so $c_1 \sim 1$. The zero-field energy gaps are of the order of the hyperfine couplings, so $c_2 \sim \frac{1}{-\gamma_{\mathrm{e}} \times 1\,\mathrm{mT}}$. Thus when first order perturbations dominate $\omega_{mn} \sim -\gamma_{\mathrm{e}} B$. Plotting the field axis logarithmically, these energy splitting will therefore be responsible for a sigmoidal feature when $k \sim -\gamma_{\mathrm{e}} B$. Similarly, when second order perturbations dominate $\omega_{mn} \sim \gamma_{\mathrm{e}}^2 B^2 \frac{1}{-\gamma_{\mathrm{e}} \times 1\,\mathrm{mT}}$. Hence, if we measure B in mT, we will see a sigmoidal feature in the singlet yield when $k \sim -\gamma_{\mathrm{e}} B^2$.

3.10 Empirical parameters: $B_{1/2}$

The final empirical parameter that we consider is $B_{1/2}$, the magnetic field required to produce half of the saturation field effect. This parameter was introduced by Weller [142]. Weller measured $B_{1/2}$ values in a number of chemical systems and, supported by some musings on its theoretical plausibility, proposed the following formula[4] for the estimation of $B_{1/2}$ from the effective hyperfine couplings

$$B_{1/2} \approx \sqrt{3}\frac{\tilde{a}_{\mathrm{A}}^2 + \tilde{a}_{\mathrm{B}}^2}{\tilde{a}_{\mathrm{A}} + \tilde{a}_{\mathrm{B}}}. \tag{3.58}$$

Measurements of $B_{1/2}$ have proved useful for more quantitative analysis, for example in the work by Justinek and coworkers on electron self-exchange rates [60–62].

Figure 3.13 presents a selection of results from a QMMC calculation in an ensemble of 12737 radical pairs. The saturation singlet yield $\Phi_{\mathrm{S}}(\infty)$ was calculated in each radical using the high field limit (*i.e.* the secular approximation), following working analogous to that in §3.5. This gave the singlet yield corresponding to $B_{1/2}$: $\Phi_{\mathrm{S}}(B_{1/2}) = \frac{1}{2}[\Phi_{\mathrm{S}}(0) + \Phi_{\mathrm{S}}(\infty)]$. Thence, $B_{1/2}$ was determined by interpolation of the calculated MARY spectrum.

Figures 3.13(a) and 3.13(b) show the mean and standard deviation of $B_{1/2}$ as a function of effective HFC. It is clear that the situation where the effective HFC on one radical dominates (e.g. $\tilde{a}_{\mathrm{A}} \gg \tilde{a}_{\mathrm{B}}$) allows — but does not require — a large value for $B_{1/2}$.

In order to test further the reliability of Weller's empirical formula, equation (3.58), Figures 3.13(c)–3.13(f) show scatter plots of the actual calculated $B_{1/2}$ value versus the $B_{1/2}$ value predicted using Weller's formula. Each point in the plots represents one member of the QMMC ensemble of radical pairs. It is immediately obvious that there is frequently a sizeable scatter in the figures.

When the rate constant is smaller than the effective HFCs (Figure 3.13(c)), we see that the Weller formula provides something of an upper bound for the true $B_{1/2}$. The Weller formula may overestimate $B_{1/2}$ by around a factor of two. Quite by chance, such a situation was encountered experimentally in the Oxford group around the time that these calculations were performed.

When the rate constant is similar to the effective HFCs (Figures 3.13(d) and 3.13(e)), we see that the Weller formula and the calculated $B_{1/2}$ values correlate reasonably well. The Weller formula clearly captures the average behaviour of the exact $B_{1/2}$ values. Nevertheless, there is a scatter of $\pm 30\%$, and in some cases the exact $B_{1/2}$ value significantly exceeded Weller's predictions. At intermediate rate constants, the Weller formula is thus only a useful rule of thumb for predicting the $B_{1/2}$ value.

Finally, when the rate constant is significantly faster than the effective HFCs, the Weller formula gives a dramatic underestimate of the $B_{1/2}$ value.

3.11 Conclusions

In this chapter, we have explored the qualitative shape of MARY spectra, as expressed by a small number of experimental features. To this end, two methods were introduced

[4] Weller's original definition was posed in terms of RMS hyperfine couplings not effective hyperfine couplings and thus had a "2" where we give "$\sqrt{3}$".

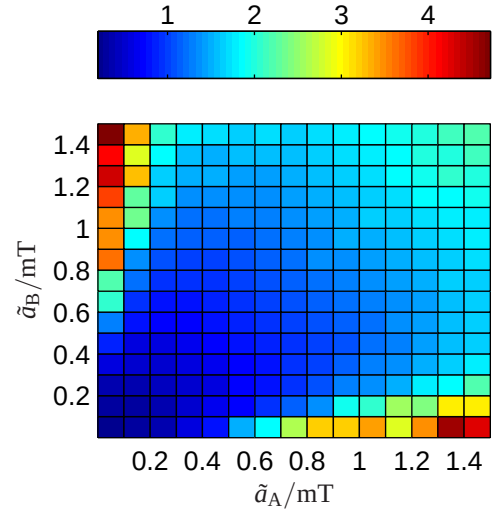

(a) Mean value of $B_{1/2}$/ mT when $k = 3 \times 10^7\,\mathrm{s}^{-1}$.

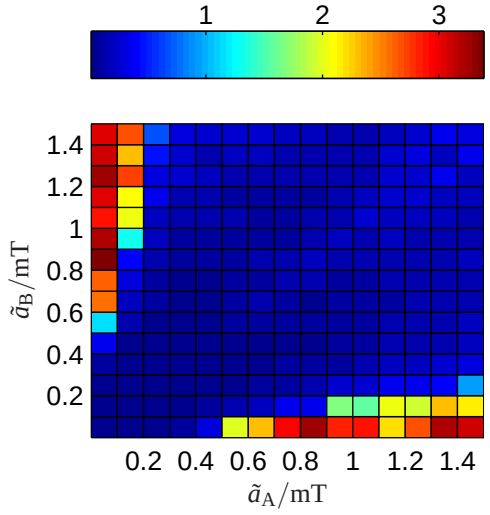

(b) Standard deviation in $B_{1/2}$/ mT when $k = 3 \times 10^7\,\mathrm{s}^{-1}$.

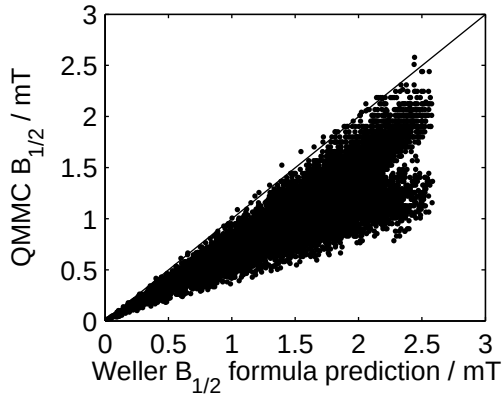

(c) QMMC $B_{1/2}$ *vs.* equation (3.58) when $k = 0.01\,\mathrm{s}^{-1}$.

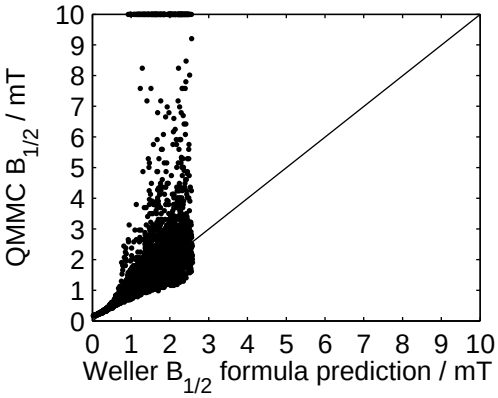

(d) QMMC $B_{1/2}$ *vs.* equation (3.58) when $k = 3 \times 10^7\,\mathrm{s}^{-1}$.

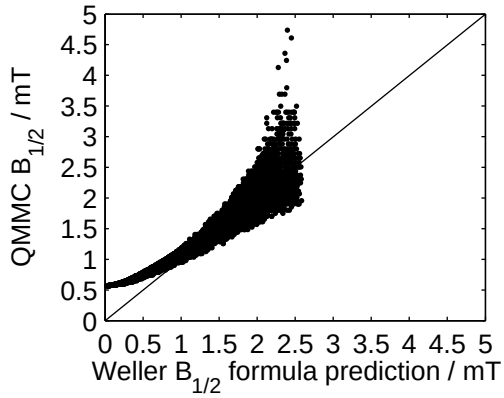

(e) QMMC $B_{1/2}$ *vs.* equation (3.58) when $k = 10^8\,\mathrm{s}^{-1}$.

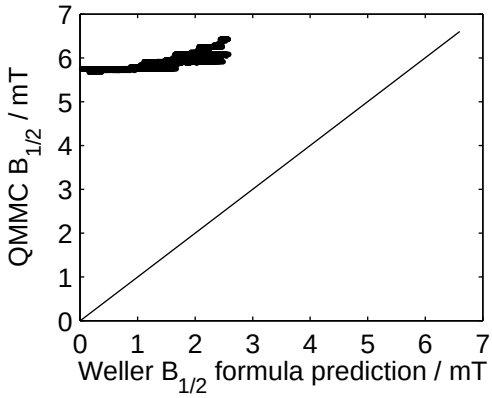

(f) QMMC $B_{1/2}$ *vs.* equation (3.58) when $k = 10^{11}\,\mathrm{s}^{-1}$.

Figure 3.13: Half-saturation field $B_{1/2}$ according to QMMC calculations in 12 737 radical pairs (see text for details). (a–b): The colour of each rectangle summarises the results from those members of the ensemble having effective HFCs which fall within it. We plot the mean $B_{1/2}$/ mT in each cell on the left and the standard deviations on the right. (c–f): Each point represents one radical pair from the ensemble. Were the Weller formula — given in equation (3.58) — perfect, all points would lie on the diagonal line. Rate constants were chosen to be smaller than (c), comparable to (a–b,d–e) and larger than (f) the effective HFCs.

for the characterisation of typical MARY spectra: the semiclassical approximation (SCA) and a quantum mechanical Monte Carlo method (QMMC).

Concerning the SCA, we gave a new derivation, working in the Schrödinger picture and emphasising the close connections with the quantum mechanical density matrix used earlier in this thesis. We were able to give an expression in closed form for the SCA singlet probability. Limiting variants of this expression were found for the case of zero static field, radical pairs with no hyperfine couplings on one partner and in the limit of high static field. These SCA results were verified by comparison with the literature and with results from the QMMC method. It was shown that the SCA expression for singlet yield is identical to that calculated quantum mechanically in the limit of high field, in a radical pair with a large number of nuclei. It was suggested that this agreement explains the success of the SCA despite the unphysical assumptions underlying its derivation. However, at low fields the SCA was found to give poor agreement with quantum mechanical calculations. In particular, the SCA is not well suited for calculations of the low field effect.

The QMMC method, that is quantum mechanical calculation of MARY spectra in a suitable ensemble of radical pairs, proved to be a powerful approach. The QMMC results provided a means of critically evaluating the SCA singlet yield. Furthermore, they allowed a series of "rules of thumb" to be elucidated for the qualitative experimental features in MARY spectra. Perhaps the most significant result of these QMMC calculations is that these rules of thumb differ markedly for rate constants which are smaller than, comparable to or larger than the effective hyperfine couplings in a radical pair. It was suggested that these differences account for the existence in the literature of different predictions about the presence of a LFE.

3.12 Suggestions for future work

The magnetic sense of many birds and other migratory animals is a subject of considerable interest at this time. One of the leading hypothesis for the mechanistic basis of this sense is that detection of the Earth's field occurs in a sensory organ using radical pair chemistry at its core. [105] A much fuller discussion of this field is given later in this thesis, but we note here that modelling of these problems requires calculations of the singlet yield in large radical pairs containing many anisotropic hyperfine couplings. Since current quantum mechanical calculations scale exponentially with the number of magnetic nuclei, it is extremely challenging to calculate the singlet yield in such radical pairs. It could be possible to develop a version of the SCA suitable for use with anisotropic hyperfine couplings. Such a calculation would begin by performing many times a numerical anisotropic random flight in order to obtain a numerical distribution for the "resultant effective field" $\boldsymbol{\omega}$. Expanding this distribution in terms of spherical harmonics and using the result in place of equation (3.15) would allow evaluation of the singlet probability and thence the singlet yield in such a radical pair.

The SCA performs better than one would expect, given the unphysical nature of its underlying assumptions. If the reasons for its success could be elucidated, it might be possible to incorporate them into an approximate quantum mechanical method of calculation. As discussed above, there is an urgent need for efficient quantum mechanical methods of calculating singlet yield in the presence of weak magnetic fields and for the large spin systems found in biologically relevant radical pairs.

The QMMC approach is quite general. It provides important insight into the mean values of experimental features, allowing the statement of certain rules of thumb. Significantly, via the standard deviation, it also gives insight into the likelihood of these rules being broken. It would be useful to apply the same statistical approach to the calculation of singlet yields in systems subject to radio frequency fields and also to anisotropic systems in order to develop similar rules of thumb there. Such calculations could require significantly more computational resources than those in this chapter and will therefore require some care.

Chapter 4

Optically detected low field EPR

4.1 Introduction

Radical pairs (RPs) are important reaction intermediates in a wide range of photolytic, thermal and radiolytic processes [1, 2]. Their electron spin-dependent reactivity and magnetic interactions give rise to magnetic polarisation phenomena observable by nuclear magnetic resonance (NMR) and electron paramagnetic resonance (EPR) spectroscopies [12, 31, 171]. Radical pairs also form the basis of the only well established mechanism — the Radical Pair Mechanism — by which magnetic fields are known to influence the rates and yields of chemical reactions [41]. These phenomena have been widely exploited to provide detailed insight into free radical chemistry and physics [40], photosynthetic energy conversion [65], the structure and folding of proteins [32], and enzyme kinetics [39, 82, 83].

In Chapters 2 and 3, we discussed the manner in which the yield of a radical pair reaction may depend on the strength of an applied static magnetic field. This magnetic field effect (MFE) formed the basis of the magnetically altered reaction yield (MARY) experiment. Using as an illustrative example a set of measurements in the $\left[\mathrm{Py}^{\bullet-}\ \mathrm{DMA}^{\bullet+}\right]$ radical pair, it was possible to extract detailed information on the radical pair diffusion processes. Monte Carlo simulations allowed the formulation of a number of guiding principles for the qualitative shape and features of MARY spectra. Measurements of the effect of static magnetic fields are clearly a rich source of information about radical pair reactions.

According to the RPM, magnetic fields alter the yield of RP reactions through their influence on the dynamics of singlet–triplet interconversion in the RP. By analogy with other magnetic resonance techniques, it seems likely that oscillating magnetic fields should also influence this coherent spin evolution. Indeed, since a typical RP lifetime is of the order of 10 ns–1 µs, we anticipate that fields with frequency $\nu_{\mathrm{rf}} \gtrsim 1\,\mathrm{MHz}$ could show resonant effects. Further consideration of the RP energy level spacings makes it clear that radio (MHz) or microwave (GHz) frequency magnetic fields are most appropriate.

For strong static magnetic fields ($\sim 1\,\mathrm{T}$) one would consider applying microwave frequencies — in other words, one would naturally consider a form of EPR. Although such time-resolved EPR techniques are versatile and powerful [171], it is often less than straightforward to study radical pairs directly, principally because of their transient nature. Furthermore, despite the enormous non-equilibrium electron spin po-

larisation with which the radical pairs are created, such experiments suffer from the limited sensitivity associated with detecting low energy microwave photons. Many of these limitations may be avoided by monitoring reaction yields optically rather than observing microwave absorption or free induction decays. This technique is known as reaction yield detected magnetic resonance (RYDMR). RYDMR experiments detect, indirectly via changes in reaction yield, the (usually microwave) EPR transitions between states split by the Zeeman interaction with a strong static magnetic field. The RYDMR technique is quite established and has been applied in many systems [33, 36, 37, 64, 172–174].

It is reasonable to consider also the other extreme, making measurements of the reaction yield in the presence of an oscillating magnetic field, but with no static field present. The appropriate frequencies are now $\sim 10\,\mathrm{MHz}$, since these drive coherent spin evolution between energy levels split by the electron–nuclear hyperfine interaction. Detection is once again through spectroscopic monitoring of the reaction yield, for example through measurements of exciplex fluorescence intensity. Such oscillating magnetic field effect (OMFE) experiments have been performed in Oxford on several systems during the last decade [175–178]. An attractive feature of OMFE spectra is that, rather than depending on properties of the whole RP, they probe the hyperfine couplings within each radical. Such information might be used in identifying the radical species involved as intermediates in a complex system. It should be noted, however, that the OMFE experiment is quite demanding to perform. First, the sample must be shielded from the Earth's field using μ-metal sheeting. Second, the experiment requires RF circuitry and field coils that are capable of being smoothly adjusted over the range ~ 1–$100\,\mathrm{MHz}$ without introducing power variations, pick-up or other artefacts. Finally, the observed changes in reaction yield are found to be relatively small, which diminishes the possible signal-to-noise ratio.

The techniques described above provide insight into the effects of oscillating fields in the presence of strong, or zero static magnetic field. In this chapter, we investigate the effects of oscillating fields in the presence of low static magnetic fields [43, 179, 180]. In this context, "low" refers to fields that are comparable in energy to RP hyperfine interactions, *i.e.* to fields in the range ~ 0–$20\,\mathrm{mT}$. The low field regime is worthy of study for several reasons. First, as will become apparent shortly, many of the selection rules and assumptions which simplify the analysis of zero field and high field experiments cease to apply in the low field regime. On the one hand, this makes theoretical analysis and modelling more challenging at low fields. Yet, it also provides an opportunity to develop new theoretical methods and to gain additional insight into radical chemistry and physics. Second, the Earth's magnetic field has a typical strength of $50\,\mu\mathrm{T}$ and therefore magnetic field effects in nature will operate in this low field regime. This work is therefore relevant to the debate on the putative adverse health effects of environmental magnetic fields, and also to the fascinating debate on the origins of the magnetic compass sense of migratory birds. We propose that experiments similar to those described here might form the basis of a powerful test for the involvement of the RPM in — often complex — biological systems [179].

We consider selected measurements of reaction yield as a function of static field strength in the presence of an RF field: an experiment termed "MARY-ν". Experiments were conducted for radical ion pairs in viscous solvents by Henbest, Kukura, Norman and Wedge [139, 179–182]. The primary aim of this work is to analyse and

interpret these experimental data. We focus particularly on the new information which emerges at low fields. For example, we investigate effects of the relative orientation of the static and RF fields. Secondly, in order to model these effects efficiently in the low field regime, it was necessary to develop a new algorithm for the calculation of RP reaction yields. This algorithm, which exploits the periodicity of the Hamiltonian in the presence of an RF field, is described below.

4.2 Product yield in the presence of an RF field

4.2.1 Framework

We consider a spin-correlated radical pair evolving under the influence of isotropic electron-nuclear hyperfine interactions and isotropic Zeeman interactions of the electron spins with (a) a static magnetic field of strength $B_0 = -\omega_0/\gamma_e$ and (b) a linearly polarised radio frequency field of peak strength $B_1 = -\omega_1/\gamma_e$ and frequency $\nu_{rf} = \omega_{rf}/2\pi$ (where γ_e is the magnetogyric ratio of the electron). The coherent evolution of the radical pair, described by a spin density operator $\hat{\rho}(t)$, is governed by the spin Hamiltonian (in angular frequency units):

$$\hat{H}(t;\gamma) = \sum_{\mathrm{N=A}}^{\mathrm{B}} \sum_i a_{i\mathrm{N}} \hat{\boldsymbol{I}}_{i\mathrm{N}} \cdot \hat{\boldsymbol{S}}_{\mathrm{N}} + \omega_0 \left[\hat{S}_{\mathrm{Nx}} \cos\theta + \hat{S}_{\mathrm{Nz}} \sin\theta\right] + \omega_1 \hat{S}_{\mathrm{Nx}} \sin\left(\omega_{rf} t + \gamma\right) \quad (4.1)$$

in which N labels the radical and iN labels the i^{th} nuclear spin within radical N, $\hat{\boldsymbol{S}}$ and $\hat{\boldsymbol{I}}$ are electron and nuclear spin angular momentum operators, $a_{i\mathrm{N}}$ are the hyperfine coupling constants, t is the time after the formation of the radical pair, θ is the angle between the two magnetic fields, and γ is the phase of the RF field at $t = 0$. If the nuclear spin space is of dimension M (= 2^n for n spin-½ nuclei), $\hat{H}(t;\gamma)$ is represented by a $4M \times 4M$ Hermitian matrix. Anisotropic magnetic interactions are assumed to be averaged by molecular motion. Spin evolution arising from the difference in the two electronic g-values and from the nuclear Zeeman interactions is negligible at the magnetic field strengths considered here ($\leq 4\,\mathrm{mT}$). We assume that the exchange and dipolar interactions between the radicals and all spin relaxation processes may be neglected.

Concurrent with their spin evolution, the two radicals undergo rapid translational motions and are assumed to recombine in a diffusion-controlled manner whenever they encounter in a singlet state but to be mutually unreactive in the triplet state. We treat this reaction-diffusion process using the exponential model in which the two radicals of a spin-correlated pair undergo a single encounter, with a distribution of encounter times given by $f(t) = k\mathrm{e}^{-kt}$ where k is a first-order rate constant (see Chapter 2 and [10, 13, 108] for further details). The total probability that the radical pair recombines (the "singlet yield") is the integral over t of the probability that the encounter occurs at time t multiplied by the probability $\left\langle \hat{P}^{\mathrm{S}} \right\rangle (t)$ that the radical pair is in a singlet state at the moment of encounter

$$\Phi_{\mathrm{S}} = \int_0^\infty \left\langle \hat{P}^{\mathrm{S}} \right\rangle (t) f(t)\, \mathrm{d}t. \quad (4.2)$$

The expectation value of the singlet projection operator $\hat{P}^{\mathrm{S}}$ is given by

$$\left\langle \hat{P}^{\mathrm{S}} \right\rangle = \mathrm{Tr}\left[\hat{\rho}(t)\hat{P}^{\mathrm{S}}\right] = \frac{1}{M}\,\mathrm{Tr}\left[U(0,t;\gamma)\hat{P}^{\mathrm{S}}U(0,t;\gamma)^{\dagger}\hat{P}^{\mathrm{S}}\right], \tag{4.3}$$

in which the radical pair is assumed to be formed in a singlet state

$$\hat{\rho}(0) = \frac{\hat{P}^{\mathrm{S}}}{M} \tag{4.4}$$

and the spin evolution propagator for the interval $0 \rightarrow t$ and initial RF field phase γ is given in formal notation by

$$U(0,t;\gamma) = \hat{T}\exp\left(-\mathrm{i}\int_0^t \hat{H}(t';\gamma)\,\mathrm{d}t'\right). \tag{4.5}$$

The Dyson time ordering operator $\hat{T}$ reminds us that the exponential/integral expression which it precedes is a notational convenience and cannot be evaluated literally (see [84, 183, 184] for details).

4.2.2 Symmetries

In the experiments described below, radical pairs are formed by continuous illumination in the presence of a continuous RF field. A given pair may therefore be created, with equal likelihood, at any point during a cycle of the RF field. In other words, $\left\langle \hat{P}^{\mathrm{S}} \right\rangle$ must be averaged over a uniform distribution of γ in the interval $0 \rightarrow 2\pi$. Approaches to this calculation are complicated further by the time-dependence of the spin Hamiltonian: as the RF field is linearly polarised, comparable in strength to both the static field and the hyperfine couplings, and not necessarily perpendicular to the static field, the familiar rotating frame transformation [86, 185, 186] is not applicable. Instead, we exploit the properties of $\hat{H}(t;\gamma)$ to perform the full time-dependent calculation by treating only a single cycle of the RF field.

The important symmetries here are the periodicity of the RF field

$$\hat{H}(t;\gamma) = \hat{H}(t + 2m\pi/\omega_{\mathrm{rf}};\gamma) \quad \forall m \in \mathbb{Z} \tag{4.6}$$

and the fact that the initial phase can be treated as a time-shift

$$\hat{H}(t;\gamma) = \hat{H}(t + \gamma/\omega_{\mathrm{rf}};0). \tag{4.7}$$

These symmetries mean that the spin evolution may be divided into contributions from each whole RF period $T = 2\pi/\omega_{\mathrm{rf}}$ plus a residual contribution from times after the last complete RF period. In terms of the propagator, defined in equation (4.5), we see that the unit propagator $U(0,T;\gamma)$ is of central importance. Furthermore, the singlet probability that we desire therefore also contains contributions from each whole RF period with additional contributions arising because of spin evolution during the final partially completed RF period. These considerations allow an efficient approach to calculation employing the fast Fourier transform (FFT). Finally, equation (4.7) allows the averaging of different phases γ to be incorporated analytically into the calculation.

4.2.3 γ–COMPUTE

Mathematically similar properties are encountered in magic angle spinning (MAS) NMR, in which a rapidly rotating polycrystalline sample with anisotropic magnetic interactions is subject to a sequence of RF pulses such that the spin system evolves under a time-dependent Hamiltonian [187–193]. Furthermore, the random orientation of the crystallites means that the calculated response must be averaged over an ensemble of orientations ("carousel averaging" [194]). Unless done carefully, this averaging may seriously diminish the performance and hence the feasibility of the calculations. The magnetic resonance literature contains several articles devoted to efficient methods for carrying out such calculations [192, 193, 195, 196]. Here we adapt the γ–COMPUTE (Calculation over One Modulation Period Using Time Evolution with γ-averaging) algorithm as formulated by Hohwy *et al.* [192], where γ is one of the three Euler angles that relate the crystallite orientation to the MAS rotor axis system.

Discretisation

Following Hohwy *et al.* [192], we begin by approximating the continuously varying Hamiltonian defined in equation (4.1) with one that is piecewise constant. Dividing one period $T = 2\pi/\omega_{\mathrm{rf}}$ of the RF field into n time steps, each of length $\tau = T/n$, we define an integer index

$$j = \frac{t}{\tau}. \tag{4.8}$$

Similarly, in preparation for averaging over the RF phase γ, we divide γ into n steps with an integer index

$$p = \frac{\gamma}{2\pi/n}. \tag{4.9}$$

For brevity, we write the propagator for time $0 \rightarrow j\tau$ and RF phase $\gamma = p(2\pi/n)$ as

$$A(j,p) = U(0, j\tau; p2\pi/n). \tag{4.10}$$

For sufficiently large n, $\hat{H}(t;\gamma)$ varies negligibly within each time step τ and hence the integral in equation (4.5) is closely approximated by

$$A(j,p) \approx \exp\left\{-\mathrm{i}\tau\hat{H}([j-1/2]\tau; p2\pi/n)\right\} \cdots \exp\left\{-\mathrm{i}\tau\hat{H}(\tau/2; p2\pi/n)\right\}, \tag{4.11}$$

except for $A(0,p) = I$. Note that we take the value of $\hat{H}$ from the mid-point of each time step in order to reduce the discretisation error.

Now, by the symmetry relations given in equations (4.6) and (4.7), we may write $A(j,p)$ in terms of quantities $A(j) = A(j,0)$ with zero RF phase:

$$A(j,p) = A(j+p)A(p)^{\dagger} = A(j+p \bmod n)A(n)^m A(p \bmod n)^{\dagger} \tag{4.12}$$

$$\text{where } m = \mathrm{int}\left(\frac{j+p}{n}\right) - \mathrm{int}\left(\frac{p}{n}\right) \tag{4.13}$$

in which $\mathrm{int}(x)$ is the largest integer less than or equal to x. It is clear that any $A(j,p)$ may be expressed in terms of the n propagators $A(1 \ldots n)$. In practice, we calculate the n propagators sequentially at the start of the γ–COMPUTE algorithm, evaluating each matrix exponential in equation (4.11) only once.

Average Hamiltonian

As explained above, the spin evolution during one period $T = 2\pi/\omega_{\mathrm{rf}}$ of the RF field is of central importance. This spin evolution is usefully described in terms of the zero RF phase average Hamiltonian $\bar{H}$, defined such that

$$\exp\left(-\mathrm{i}\bar{H}T\right) = A(n). \tag{4.14}$$

Average Hamiltonian theory summarises the effects of the full time-dependent Hamiltonian over one period of the RF field with a notional system evolving under the time-independent average Hamiltonian $\bar{H}$ [84, 197, 198].

It would be useful to diagonalise the average Hamiltonian

$$\bar{H} = X\bar{\Omega}X^{\dagger} \tag{4.15}$$

where X is a unitary matrix of eigenvectors of $\bar{H}$ and $\bar{\Omega}$ is a diagonal matrix of eigenvalues of $\bar{H}$. In practice, we calculate $A(n)$ and not $\bar{H}$. Substituting into equation (4.14), we find

$$X^{\dagger}A(n)X = X^{\dagger}\exp\left(-\mathrm{i}\bar{H}T\right)X = \exp\left(-\mathrm{i}\bar{\Omega}T\right) = \Lambda. \tag{4.16}$$

In other words, the eigenvectors of $\bar{H}$ are the same as those of $A(n)$ and may therefore be calculated from $A(n)$. Meanwhile, the eigenvalues $\lambda_i = \Lambda_{ii}$ of $A(n)$, which we calculate, are related to those $\bar{\omega}_i = \bar{\Omega}_{ii}$ of $\bar{H}$, which we seek, by

$$\exp\left(-\mathrm{i}\bar{\omega}_i T\right) = \lambda_i. \tag{4.17}$$

We may almost find the eigenvalues of the average Hamiltonian by taking the complex logarithm to give

$$\bar{\omega}_i = \frac{\mathrm{i}\omega_{\mathrm{rf}}}{2\pi}\ln\lambda_i - \omega_{\mathrm{rf}}c_i. \tag{4.18}$$

Notice however that, since $\exp(x) = \exp(x + 2\pi\mathrm{i})$, we must introduce a (currently unknown) integer correction factor c_i in order to account for the possibility that this eigenvalue of the average Hamiltonian $\bar{H}$ contains some multiple of $2\pi/T = \omega_{\mathrm{rf}}$ which would be lost on taking exponentials. It is shown in §4.2.4 that the presence of these correction factors does not normally cause difficulties.

Transition frequencies

The singlet probability will be shown to depend on differences in the average Hamiltonian energy eigenstates. We write the difference between eigenstates r and s as

$$\bar{\omega}_{rs} = \bar{\omega}_r - \bar{\omega}_s = \frac{\mathrm{i}\omega_{\mathrm{rf}}}{2\pi}\left(\ln\lambda_r - \ln\lambda_s\right) - \omega_{\mathrm{rf}}c_{rs} \tag{4.19}$$

where $c_{rs} = c_r - c_s$. For brevity, we also define the uncorrected splittings

$$\bar{\omega}'_{rs} = \frac{\mathrm{i}\omega_{\mathrm{rf}}}{2\pi}\left(\ln\lambda_r - \ln\lambda_s\right) = \bar{\omega}_{rs} + c_{rs}\omega_{\mathrm{rf}}. \tag{4.20}$$

A particularly useful feature of the unit propagator's eigenvalues is that they are independent of γ. Consider the propagator for one RF period when $\gamma = p(2\pi/n)$:

$$\begin{aligned} A(n,p) &= A(n+p)A(p)^\dagger = A(p)A(n)A(p)^\dagger \\ &= A(p)X\Lambda X^\dagger A(p)^\dagger = X_p \Lambda X_p^\dagger. \end{aligned} \tag{4.21}$$

Since $A(p)$ and X are unitary, then so is $X_p \equiv A(p)X$. The eigenvalues of $A(n,p)$ are therefore clearly identical to those for $A(n)$. Thus, the transition frequencies $\bar{\omega}_{rs}$ calculated for zero RF phase are also appropriate at every other RF phase, although the amplitudes of each transition may well change. It is therefore possible to average over the phase γ by averaging the amplitudes of each frequency component separately. This makes the calculation significantly less demanding.

Singlet probability

Having made these definitions, we consider the probability that a radical pair created in a pure singlet state (at RF field phase $\gamma = p(2\pi/n)$) may be found in a singlet state at time $j\tau$. This singlet probability, given in equation (4.3) may be expanded using equations (4.12) and (4.16) as follows

$$\begin{aligned} \left\langle \hat{P}^{\mathrm{S}} \right\rangle (j\tau; p2\pi/n) &= \frac{1}{M} \mathrm{Tr}\left[A(j,p)\hat{P}^{\mathrm{S}} A(j,p)^\dagger \hat{P}^{\mathrm{S}} \right] \\ &= \frac{1}{M} \mathrm{Tr}\left[\begin{array}{c} A(j+p \bmod n)A(n)^m A(p \bmod n)^\dagger \hat{P}^{\mathrm{S}} \ldots \\ \ldots A(p \bmod n) \left\{A(n)^m\right\}^\dagger A(j+p \bmod n)^\dagger \hat{P}^{\mathrm{S}} \end{array} \right] \\ &= \frac{1}{M} \mathrm{Tr}\left[\begin{array}{c} A(j+p \bmod n)X\Lambda^m X^\dagger A(p \bmod n)^\dagger \hat{P}^{\mathrm{S}} \ldots \\ \ldots A(p \bmod n)X \left(\Lambda^m\right)^\dagger X^\dagger A(j+p \bmod n)^\dagger \hat{P}^{\mathrm{S}} \end{array} \right]. \end{aligned} \tag{4.22}$$

Cyclic permutation of the trace gives terms depending on p and on $j+p$

$$\left\langle \hat{P}^{\mathrm{S}} \right\rangle (j\tau; p2\pi/n) = \frac{1}{M} \mathrm{Tr}\left[\Lambda^m \hat{P}^{\mathrm{ST}}(p) \left(\Lambda^m\right)^\dagger \hat{P}^{\mathrm{ST}}(j+p) \right] \tag{4.23}$$

$$\text{where } \hat{P}^{\mathrm{ST}}(x) = X^\dagger A(x \bmod n)^\dagger \hat{P}^{\mathrm{S}} A(x \bmod n) X. \tag{4.24}$$

We have factored out $\hat{P}^{\mathrm{ST}}$ because it is a function with period n that is determined by the precalculated propagators. The periodicity will allow use of the discrete Fourier transform in a later step.

Physically, the change from $\hat{P}^{\mathrm{S}} \rightarrow \hat{P}^{\mathrm{ST}}$ transforms the problem into the eigenbasis of the zero initial RF phase average Hamiltonian $\bar{H}$. The similarity transform $A(x \bmod n)^\dagger \cdots A(x \bmod n)$ makes a shift from time $x\tau$ to the start of the preceding complete RF cycle. With this time shift, and because of the symmetry of the Hamiltonian described in equation (4.7), the *effective* initial RF phase γ is always zero. We then try to encapsulate as much of the RP spin evolution as possible into the zero initial RF phase average Hamiltonian $\bar{H}$. Therefore, we make the similarity transform $X^\dagger \cdots X$ into the average Hamiltonian eigenbasis. This transformation leaves terms Λ^m which represent the spin evolution in every complete RF cycle from time zero to present. These terms are simple to evaluate because Λ is diagonal in this basis.

We proceed by expanding the trace and using equation (4.20) to show that

$$\left\langle \hat{P}^{\mathrm{S}} \right\rangle (j\tau; p2\pi/n) = \frac{1}{M} \sum_{r,s=1}^{4M} \mathrm{e}^{\mathrm{i}m\bar{\omega}'_{rs}T} \hat{P}^{\mathrm{ST}}_{sr}(p) \hat{P}^{\mathrm{ST}}_{rs}(j+p). \tag{4.25}$$

Note that m depends on j and p by equation (4.13).

Average over RF phase γ

As explained earlier, under the continuous UV irradiation employed experimentally, radical pairs are created continuously with a random distribution of RF phases γ. Hence, the observed singlet yield will be an average over all possible values of γ. As an approximation, we average over the n values of γ given by $p = 0, \ldots, n-1$. The γ-averaged singlet probability at time $j\tau$ may therefore be written

$$\left\langle \hat{P}^{\mathrm{S}} \right\rangle (j\tau) = \frac{1}{Mn} \sum_{p=0}^{n-1} \left[\sum_{r,s=1}^{4M} \mathrm{e}^{\mathrm{i}m\bar{\omega}'_{rs}n\tau} \hat{P}^{\mathrm{ST}}_{sr}(p) \hat{P}^{\mathrm{ST}}_{rs}(j+p) \right]. \tag{4.26}$$

Together with a suitable re-encounter distribution $f(t)$, the γ-averaged singlet probability determines the observed singlet yield.

Discrete correlation

The right hand side of equation (4.26) is almost the cross-correlation of two functions with period n — except that m is also a function of p. Such a cross-correlation could be performed efficiently using the FFT (see §B.9). Therefore, we expand m using equation (4.13) and multiply through by a carefully chosen form of "1", *i.e.* $\exp(-\mathrm{i}\bar{\omega}'_{rs}(j+p)\tau)\exp(\mathrm{i}\bar{\omega}'_{rs}p\tau)\exp(\mathrm{i}\bar{\omega}'_{rs}j\tau)$. Collecting terms we find that

$$\left\langle \hat{P}^{\mathrm{S}} \right\rangle (j\tau) = \frac{1}{Mn} \sum_{r,s=1}^{4M} \left\{ \sum_{p=0}^{n-1} \left[\begin{array}{c} \mathrm{e}^{\mathrm{i}\bar{\omega}'_{rs}\left(p-\mathrm{int}\left(\frac{p}{n}\right)n\right)\tau} \hat{P}^{\mathrm{ST}}_{sr}(p) \\ \times \mathrm{e}^{-\mathrm{i}\bar{\omega}'_{rs}\left(j+p-\mathrm{int}\left(\frac{j+p}{n}\right)n\right)\tau} \hat{P}^{\mathrm{ST}}_{rs}(j+p) \\ \times \mathrm{e}^{\mathrm{i}\bar{\omega}'_{rs}j\tau} \end{array} \right] \right\} \tag{4.27}$$

$$= \frac{1}{Mn} \sum_{r,s=1}^{4M} \left\{ \left[\sum_{p=0}^{n-1} g^*_{rs}(p) g_{rs}(j+p) \right] \times \mathrm{e}^{\mathrm{i}\bar{\omega}'_{rs}j\tau} \right\}. \tag{4.28}$$

The function

$$g_{rs}(x) = \mathrm{e}^{-\mathrm{i}\bar{\omega}'_{rs}(x \bmod n)\tau} \hat{P}^{\mathrm{ST}}_{rs}(x) \tag{4.29}$$

clearly has period n. Therefore, we take the DFT of the square-bracketed term in equation (4.28) using equation (B.27):

$$\mathrm{DFT}_k \left(\sum_{p=0}^{n-1} g^*_{rs}(p) g_{rs}(j+p) \right) = G^*_{rs}(k) G_{rs}(k) = |G_{rs}(k)|^2 . \tag{4.30}$$

Inverting the DFT by equation (B.23), we substitute back into equation (4.28) to give

$$\left\langle \hat{P}^{\mathrm{S}} \right\rangle (j\tau) = \frac{1}{Mn} \sum_{r,s=1}^{4M} \left\{ \left[\frac{1}{n} \sum_{k=0}^{n-1} |G_{rs}(k)|^2 \, \mathrm{e}^{2\pi\mathrm{i}jk/n} \right] \times \mathrm{e}^{\mathrm{i}\bar{\omega}'_{rs}j\tau} \right\}. \tag{4.31}$$

Trigonometric interpolant

As it stands, this expression gives values for the singlet yield at instantaneous sampling times — with one sample per time step τ. In order to calculate the singlet yield by

equation (4.2), we require knowledge of $\langle \hat{P}^{\mathrm{S}} \rangle (t)$ for all time. Our final approximation is to replace the square-bracketed inverse DFT with a trigonometric interpolant. This procedure introduces no further error providing that $\langle \hat{P}^{\mathrm{S}} \rangle (t)$ is band-limited and that n is large enough to satisfy the Nyquist condition. Subject to these caveats, the full time-dependent singlet probability is given by

$$\begin{aligned}\langle \hat{P}^{\mathrm{S}} \rangle (t) &= \frac{1}{Mn^2} \sum_{r,s=1}^{4M} \left\{ \left[\sum_{k=-n/2}^{n/2-1} |G_{rs}(k)|^2 \, \mathrm{e}^{2\pi \mathrm{i} k t / n\tau} \right] \times \mathrm{e}^{\mathrm{i}\bar{\omega}'_{rs} t} \right\} \\ &= \frac{1}{Mn^2} \sum_{r,s=1}^{4M} \sum_{k=-n/2}^{n/2-1} |G_{rs}(k)|^2 \, \mathrm{e}^{\mathrm{i}(\bar{\omega}'_{rs} + k\omega_{\mathrm{rf}})t}. \end{aligned} \tag{4.32}$$

It is clear that the singlet probability contains $16M^2 n$ oscillating terms. These are gathered together in $16M^2$ groups with a common central frequency split apart by multiples of ω_{rf} into n terms. In the original MAS NMR context, these groups of terms are the spinning sidebands seen at low rotational speeds.

Frequency domain

Equations (4.2) and (4.32) allow calculation of the singlet yield for systems subject to RF fields. In practice, however, it is more convenient to perform the final integral in the frequency domain. The Fourier transform of equation (4.32) given by equation (B.20) is

$$\langle \hat{P}^{\mathrm{S}} \rangle (\omega) = \frac{\sqrt{2\pi}}{Mn^2} \sum_{r,s=1}^{4M} \sum_{k=-n/2}^{n/2-1} |G_{rs}(k)|^2 \, \delta(\omega + \bar{\omega}'_{rs} + k\omega_{\mathrm{rf}}). \tag{4.33}$$

Substituting into equation (B.21), the singlet yield

$$\begin{aligned}\Phi_{\mathrm{S}} &= \int_0^\infty \left[\frac{\sqrt{2\pi}}{Mn^2} \sum_{r,s=1}^{4M} \sum_{k=-n/2}^{n/2-1} |G_{rs}(k)|^2 \, \delta(\omega + \bar{\omega}'_{rs} + k\omega_{\mathrm{rf}}) \right] F(\omega)^* \, \mathrm{d}\omega \\ &= \frac{\sqrt{2\pi}}{Mn^2} \sum_{r,s=1}^{4M} \sum_{k=-n/2}^{n/2-1} |G_{rs}(k)|^2 \, F(\bar{\omega}'_{rs} + k\omega_{\mathrm{rf}}). \end{aligned} \tag{4.34}$$

where $F(\omega)$ is the Fourier transform of the re-encounter probability distribution $f(t)$.

Summary

To recap, in order to calculate the singlet probability in the frequency domain using the γ–`COMPUTE` algorithm, one must:

1. Form the RP spin Hamiltonian $\hat{H}(t;0)$ at times $\frac{1}{2}\tau$, $\frac{3}{2}\tau$, …, $\frac{2n-1}{2}\tau$.
2. Form and store the n propagators $A(1 \ldots n)$.
3. Diagonalise the unit propagator $A(n)$, obtaining X and Λ.
4. Take the complex logarithm of Λ to find the $\bar{\omega}'_{rs}$.

5. Use X, $A(1\ldots n)$ and the $\bar{\omega}'_{rs}$ to form the $g_{rs}(x)$.

6. Fast Fourier transform these to give the $G_{rs}(k)$.

7. Calculate the singlet probability using (4.34).

This algorithm was implemented in `Matlab`. It is used below to analyse several sets of experimental data.

Relationship to MAS NMR calculations

In summary, the following modifications to the γ–`COMPUTE` algorithm [192] were made:

1. the calculation is set up in the laboratory frame of reference rather than in an axis system rotating in step with the RF field;

2. the periodicity of the spin Hamiltonian arises from the interaction of the electron spins with the RF field rather than the modulation of anisotropic NMR interactions by sample spinning;

3. the integral over the powder angle becomes an average over the phase of the RF field at the moment of creation of the radical pair; and

4. instead of the NMR spectrum, we compute the singlet product yield using a re-encounter distribution function $f(t)$. In the calculations presented below, we used the exponential model $f(t) = k\mathrm{e}^{-kt}$ for re-encounters [10].

We believe this type of approach, which seems not to have been used before in the context of spin chemistry, is an attractive alternative to "brute-force" methods in situations where the rotating frame transformation is invalid.

4.2.4 Practical details

Before applying the γ–`COMPUTE` algorithm in an experimental context, there are a few matters that remain to be discussed.

Correction terms c_{rs}

The transformation $\hat{P}^{\mathrm{S}} \rightarrow \hat{P}^{\mathrm{ST}}$ to the zero initial RF phase average Hamiltonian eigenbasis defined by equation (4.24) is intended to shift as much of the time dependence as possible into the Λ terms. The average Hamiltonian encapsulates the cumulative effects of each full RF cycle, which will clearly dominate the spin evolution at long times. The $\hat{P}^{\mathrm{ST}}$ should therefore contain only contributions for the oscillatory spin evolution during one RF cycle which vanish by the start of the next cycle.

However, as was explained above, we do not know the average Hamiltonian. Instead, we calculate the unit propagator $A(n)$ and hence, by equation (4.18), determine the average Hamiltonian eigenvalues $\bar{\omega}_i$ up to an unknown integer multiple of the radio frequency $\omega_{\mathrm{rf}} c_i$. When $c_i \neq 0$, the transformation $\hat{P}^{\mathrm{S}} \rightarrow \hat{P}^{\mathrm{ST}}$ does not remove as much of the time dependence from the $\hat{P}^{\mathrm{ST}}$ as it ought.

The correction terms c_{rs} appear twice in the formula for the singlet yield, equation (4.34). The first appearance is in the definition of the $G_{rs}(k)$:

$$G_{rs}(k) = \sum_{j=0}^{n-1} g_{rs}(j) \mathrm{e}^{-2\pi \mathrm{i} jk/n} \tag{4.35}$$

$$= \sum_{j=0}^{n-1} \left[\hat{P}_{rs}^{\mathrm{ST}}(j) \mathrm{e}^{-\mathrm{i}\bar{\omega}_{rs} j\tau} \right] \mathrm{e}^{-\mathrm{i}c_{rs}\omega_{\mathrm{rf}} j\tau} \mathrm{e}^{-2\pi \mathrm{i} jk/n} \tag{4.36}$$

$$= \sum_{j=0}^{n-1} \left[\hat{P}_{rs}^{\mathrm{ST}}(j) \mathrm{e}^{-\mathrm{i}\bar{\omega}_{rs} j\tau} \right] \mathrm{e}^{-2\pi \mathrm{i} j(c_{rs}+k)/n}. \tag{4.37}$$

The correction factors acts to shift the elements of $G_{rs}(k)$ by c_{rs} places. The second appearance is in the term

$$F(\bar{\omega}'_{rs} + k\omega_{\mathrm{rf}}) = F(\bar{\omega}_{rs} + (c_{rs}+k)\omega_{\mathrm{rf}}). \tag{4.38}$$

Providing that n is large enough to satisfy the Nyquist condition, these two frequency shifts cancel one another. Therefore, working with quantities derived from the unit propagator rather than the true average Hamiltonian will cause no error in the singlet yield when $n \gtrsim 2\max(\bar{\omega}_i)/\omega_{\mathrm{rf}}$, where $\max(\bar{\omega}_i)$ is the largest eigenvalue of the average Hamiltonian.

Choice of n

The γ–COMPUTE algorithm makes the following four approximations:

1. That the Hamiltonian varies negligibly during each time interval $j\tau \to (j+1)\tau$.
2. That a weighted sum over n initial RF phases is equivalent to the true integral $\int_0^{2\pi} \left\langle \hat{P}^{\mathrm{S}} \right\rangle (t;\gamma)\, \mathrm{d}\gamma$.
3. That the singlet probability at arbitrary times is given accurately by trigonometric interpolation.
4. That the functions $g_{rs}(x)$ vary sufficiently slowly so as not to suffer aliasing during the FFT. (In other words, that $n \gtrsim 2\max(\bar{\omega}_i)/\omega_{\mathrm{rf}}$, as was seen above.)

The errors introduced by the first two approximations diminish as n is increased. In general, these sources of error will be larger at high RF field strengths. The last two approximations will introduce no error, providing that n is sufficient to satisfy the Nyquist condition [199]. Both types of error should be easy to detect numerically by gradually increasing n and monitoring Φ_{S} for convergence.

It is worth noting that the γ–COMPUTE algorithm gives the same results as would be obtained using Floquet theory [200–202]. Note, however, that "while the Floquet approach is an elegant way of handling the time dependence from an analytical viewpoint, its usual formulation has major drawbacks as a numerical technique" [187]. The γ–COMPUTE algorithm is numerically efficient and has a sound theoretical grounding.

A final consideration is the performance of the fast Fourier transform step [199, 203, 204]. The FFT is more efficient when n has small prime factors. The best case is when n is a power of 2.

Equivalent nuclei

The first step in the γ–COMPUTE algorithm is to form the Hamiltonian matrices at times $\frac{1}{2}\tau$, $\frac{3}{2}\tau$, ..., $\frac{2n-1}{2}\tau$. In RPs that have a number of equivalent nuclei, a considerable saving in computational effort may be made by writing the Hamiltonian in the fully coupled basis described in §2.2.3. In this basis, the Hamiltonians are block diagonal. For any states r and s which are in different blocks, $H_{rs} = 0$ and there is no contribution to the singlet yield. We may therefore run the γ–COMPUTE algorithm several times, once for each block. The singlet yield is an appropriately weighted sum of these results.

MySQL database

The γ–COMPUTE algorithm was implemented in `Matlab`. In our analysis of chemical magnetic field effects, such as those discussed below, we often need to calculate singlet yields at many different values in order to produce a spectrum. Furthermore, it is quite natural to measure the response of a chemical system to several different parameters, e.g. making measurements of the effect of a static field strength in the presence of a RF field and then measuring the effect of RF frequency in the presence of a static magnetic field.

These considerations mean that field effect calculations are *embarrassingly parallel*. They also imply that singlet yield data points calculated for the analysis of one experiment are likely to be of needed again during the analysis of a related experiment.

The `Matlab` code was adjusted to cache calculated singlet yield values and associated model parameters in a relational database table. At the start of any singlet yield calculation, the database is consulted to see whether a previously computed value may be returned immediately. The database is also consulted to see whether another computer is currently calculating the data point in question. This allows calculations to be run across a cluster of computers by starting identical jobs on each processor. The database automatically distributes the workload amongst the available machines. The database also automates the pooling of results between members of the Oxford group who use the author's `Matlab` codes. To date, more than 6 500 000 singlet yield values are stored in a MySQL database [205]. These data represent several years of CPU time and are invaluable for planning future experiments.

4.3 Experimental methods

Magnetic field effects on the recombination of photo-induced radical ion pairs were measured by Henbest and Kukura [179–181]. These effects were detected as described previously [175, 176, 206, 207] via exciplex fluorescence. Radical pairs were produced by photochemical electron transfer driven by continuous UV illumination from a Xe arc lamp. In the chemical systems studied, singlet pairs can recombine to produce a fluorescent exciplex state while triplet pairs diffuse apart to form free radicals. Applied static and oscillating magnetic fields affect the extent and frequency of singlet–triplet interconversion and so alter the fraction of radical pairs that form exciplexes, which in turn results in a change in the fluorescence intensity. The continuous RF field (generated by a PTS-500 frequency-synthesiser) was 100% amplitude-modulated (at 381 Hz)

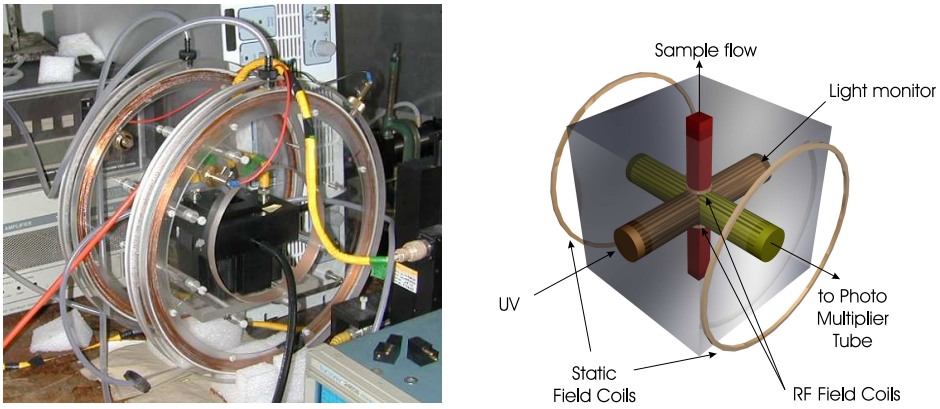

Figure 4.1: Experimental apparatus. (a) Photograph (b) Schematic

and the exciplex fluorescence was demodulated and recorded using phase-sensitive detection. The static magnetic field was supplied by water-cooled Helmholtz coils placed around both the sample cell and the RF coils which could, together, be rotated with respect to the static field to allow the orientation dependence of the RP spectra to be measured. A flow system was used to avoid sample photo-degradation. Samples were not shielded from the geomagnetic field because this additional, very small ($\sim 50\,\mu$T), static field is expected to have a negligible effect on the radical pair recombination, a conclusion that is supported by the insensitivity of the observed fluorescence intensity to small ($\sim 100\,\mu$T) changes in the applied static field (see e.g. Figure 4.5). The apparatus was controlled using `LabVIEW` [208] and is pictured in Figure 4.1.

The apparatus allows simultaneous application of a static magnetic field (of strength B_0) and an oscillating (radio frequency) magnetic field (of peak strength B_1 and frequency $\omega_{\mathrm{rf}}/2\pi$). The relative orientation of the two fields θ may also be controlled. The exciplex fluorescence is measured as a function of these parameters. A few modes of operation are particularly useful and have been given names. These are:

MARY: Only a static field is applied. Fluorescence is measured as a function of field strength. Typically the static field has a small audio frequency modulation superimposed. (See Chapters 2 and 3 for a more detailed discussion. Some important characteristic features of MARY spectra are discussed in §3.7.)

OMFE: Only a radio frequency field is applied. Fluorescence is measured as a function of radio frequency. Typically, the RF field strength is modulated to improve the signal-to-noise ratio.

MARY-ν: Both static and RF fields are applied. Fluorescence is measured as a function of static field strength. The RF field strength is modulated.

OMFE-B_0: Both static and RF fields are applied. Fluorescence is measured as a function of radio frequency. The RF field strength is modulated.

4.4 Chrysene / DCB system

Using the apparatus described above, magnetic field effects on the photochemical reaction of chrysene (Chr) with isomers of dicyanobenzene (DCB), whose structures are given in Figure 4.3, were detected via exciplex fluorescence. The fluorescent exciplex is formed exclusively from the singlet state of the radical ion pair $\left[\mathrm{Chr}^{\bullet+}\ \mathrm{DCB}^{\bullet-}\right]$ created by photo-induced intermolecular electron transfer. A summary of the reaction scheme for this system is shown in Figure 4.2. Experiments were performed by Henbest and Kukura on a solution of 5×10^{-4} M Chr and 10^{-2} M DCB in a viscous solvent mixture of 9:1 cyclohexanol:acetonitrile (by volume) at room temperature.

4.4.1 Effects of radio frequency and orientation

Figure 4.4 shows measurements of the demodulated fluorescence intensity for the $\left[\text{Chr-d}_{12}^{\bullet+}\text{1,4-DCB}^{\bullet-}\right]$ radical pair. Data are presented for both parallel and perpendicular orientations of the RF and static fields. The overall effective hyperfine coupling constant, given in Table 4.1, is 15.7 MHz in this radical pair. Measurements are made at radio frequencies that are smaller than (5 MHz), comparable to (10–20 MHz) and greater than (50 MHz) the overall effective HFC. Corresponding simulations, made using the γ−`COMPUTE` algorithm outlined above, are shown alongside the experimental data. Whilst the simulations are not perfect, there is good qualitative agreement between experiment and theory.

It is immediately apparent that both radio frequency and field orientation have a significant effect on MARY-ν spectra. When the radio frequency is larger than the overall effective HFC, *i.e.* for the 50 MHz spectra, we see that a perpendicular arrangement of fields gives the strongest response. This response is centred around the static field that would, through the electron Zeeman interaction, produce an energy level splitting resonant with the RF. This field is shown by a grey vertical line. The 50 MHz spectra appear very much as would be expected in high field RYDMR [207] or EPR [212], where we see strong transitions at the Zeeman frequency. However, in RYDMR and EPR, transitions are forbidden when the fields are parallel, yet in Figure 4.4 parallel fields produce a significant peak. Therefore, the high field regime is breaking down even in the $\nu_{\mathrm{rf}} = 50$ MHz spectra.

At lower frequencies, the breakdown of the traditional RYDMR or EPR selection rules is much greater. At smaller frequencies, a parallel arrangement of fields is often seen to produce the strongest response. Similarly, the spectra cease to be dominated by a "Zeeman resonance". At low frequencies, it is the interplay of the hyperfine interaction and the RF field that is responsible for the shape of the spectra [213–215].

We observe that all the spectra show rather small signals at static fields $B_0 \geq 3$ mT. These small signals confirm that the spectra are indeed caused by resonant interactions with the Zeeman and hyperfine interactions together.

Finally, it is clear that the orientation dependence vanishes when $B_0 \leq 500\,\mu$T. At these low field strengths, the RF field becomes rather strong relative to the static field. When the RF field dominates, the relative orientation of the static field becomes less important. Strong RF fields produce other interesting effects which we discuss in more detail later (see §5.5).

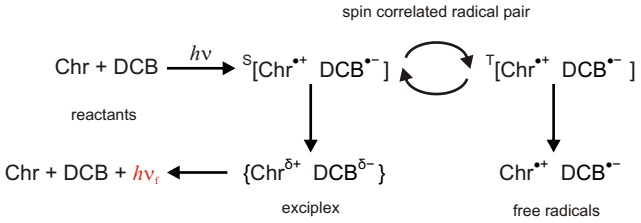

Figure 4.2: Simplified photochemical reaction scheme for chrysene (Chr) and isotopomers of dicyanobenzene (DCB). This scheme is drawn by analogy with the reactions between Py and DMA [136, 137] and between Py and DCB [109, 209]. The agreement between experiment and simulation seen in Figures 4.4 and 4.5 may be taken as indirect evidence for such a scheme.

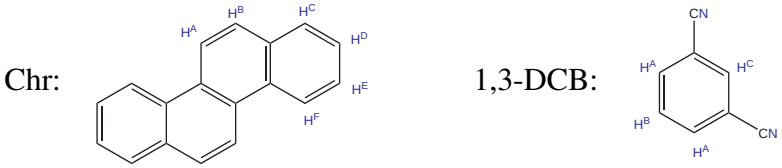

Figure 4.3: Structure of chrysene (Chr) and 1,3-dicyanobenzene (DCB).

In $\left[\text{Chr-d}_{12}^{\bullet+}\ \text{1,4-DCB}^{\bullet-}\right]$

Radical N	a_{1N}/mT	a_{2N}/mT	$\tilde{a}_N$/mT[a]	$\tilde{a}_{RP}$/mT[b]	$\tilde{a}_{RP}$/MHz
Chr-d$_{12}^{\bullet+}$ [c]	0.085 (2D)		0.196		
1,4-DCB$^{\bullet-}$	0.181 (2N)	0.159 (4H)	0.525	0.561	15.7

In $\left[\text{Chr-h}_{12}^{\bullet+}\ \text{1,x-DCB}^{\bullet-}\right]$

Radical N	a_{1N}/mT	a_{2N}/mT	$\tilde{a}_N$/mT	$\tilde{a}_{RP}$/mT	$\tilde{a}_{RP}$/MHz
Chr-h$_{12}^{\bullet+}$	0.556 (2H)	0.265 (2H)	0.871		
1,2-DCB$^{\bullet-}$	0.413 (2H)		0.584	1.049	29.4
1,3-DCB$^{\bullet-}$	0.829 (2H)		1.172	1.461	40.9
1,4-DCB$^{\bullet-}$	0.181 (2N)		0.418	0.966	27.1

[a] Effective hyperfine coupling constants are calculated using equation (3.32).

[b] Overall effective hyperfine coupling constants are calculated using equation (3.47) and the HFC values for each constituent radical.

[c] The D (*i.e.* ^{2}H) couplings were obtained using $a_{\text{deuterated}}/a_{\text{protonated}} = \gamma_D/\gamma_H = 0.1535$.

Table 4.1: Hyperfine coupling constants in $\left[\text{Chr}^{\bullet+}\ \text{DCB}^{\bullet-}\right]$ radical pairs. Hyperfine coupling constants are listed for the three groups of equivalent nuclei in each radical that have the largest couplings. H, D and N indicate ^{1}H, ^{2}H and ^{14}N. The number of equivalent nuclei in each group is given in parentheses. Effective HFC constants are given for each radical and for the four radical pairs discussed in the text. Data for Chr were obtained from [210] and those for DCB were obtained from [211].

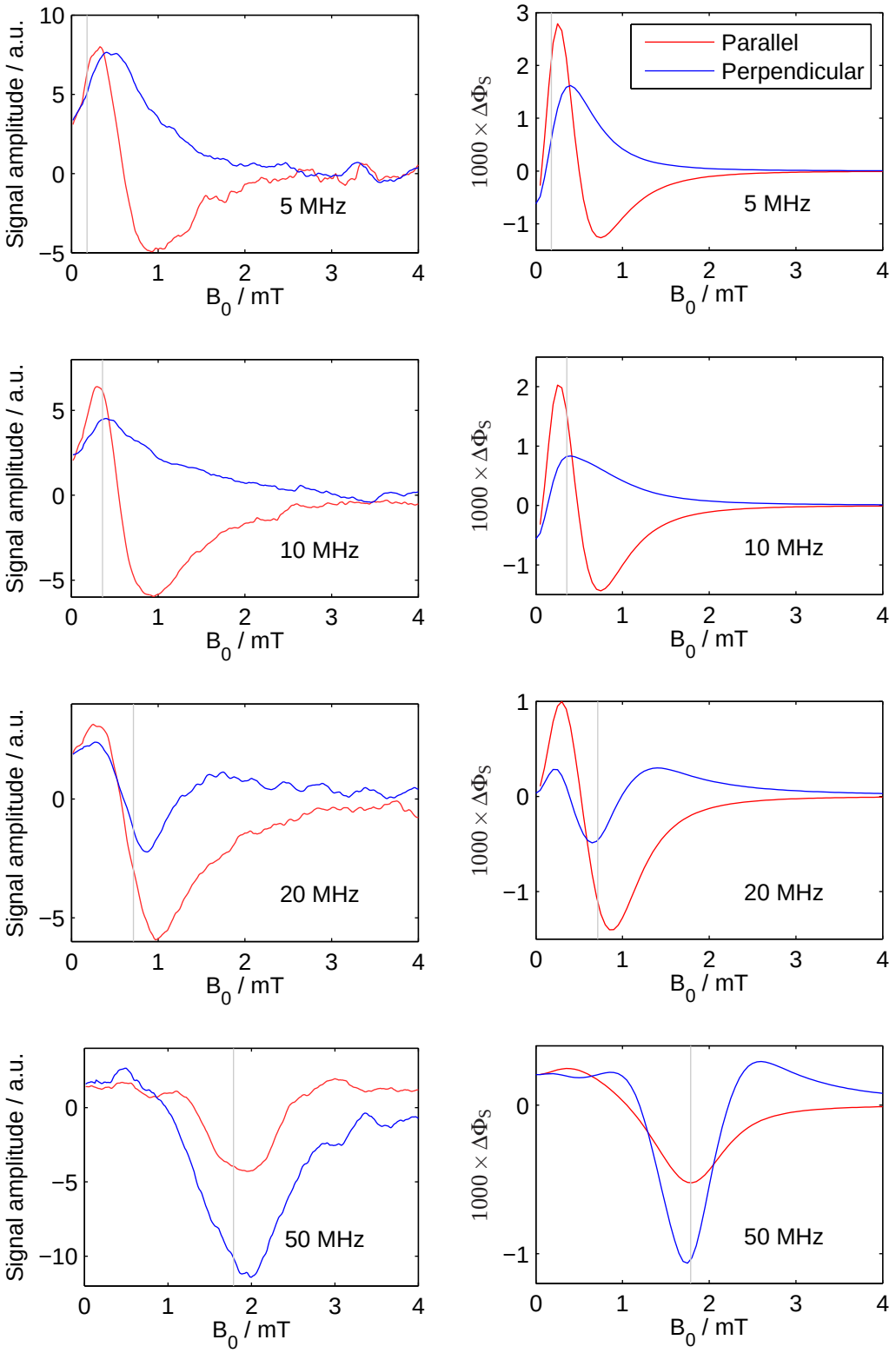

Figure 4.4: Left: Experimental MARY-v spectra measured in the $\left[\text{Chr-d}_{12}^{\bullet+}\ \text{1,4-DCB}^{\bullet-}\right]$ radical pair. The frequency ν_{rf} of the RF field is indicated for each spectrum. Right: Corresponding simulations made with γ–COMPUTE using $B_1 = -\omega_1/\gamma_e = 100\,\mu\text{T}$, exponential model rate constant $k = 5.6 \times 10^7\,\text{s}^{-1}$ and $n = 64$. Hyperfine coupling constants are given in Table 4.1. Grey vertical lines show the static field at which a Zeeman resonance might be anticipated ($B_0 = -2\pi\nu_{\text{rf}}/\gamma_e$).

4.4.2 Effect of hyperfine couplings in the low frequency limit

In light of these results, measurements were made in three other radical pair systems comprising Chr and an isomer of DCB. These systems cover a range of effective hyperfine couplings but they react in a similar manner. A radio frequency of 5 MHz was used in order to probe more carefully the novel responses seen at low frequencies in Figure 4.4. The resulting MARY-ν spectra for parallel and perpendicular field orientations are presented in Figure 4.5 alongside simulations made using the γ−COMPUTE algorithm described above. All spectra and simulations in this figure have been normalised to have the same maximum value because the exciplex intensities are known to differ amongst the isomers of DCB.

It is apparent that parallel and perpendicular fields produce different responses in all four systems. Furthermore, the position of the maximum signal follows the overall effective HFC for perpendicular fields; in parallel fields, the position of the minimum signal follows suit. The width of the peak also increases as the overall effective HFC increases. Notice however, that the qualitative shape of the field effect curve does not differ substantially between these four radical pair systems.

Two slight defects in the calculations are also apparent in Figure 4.5: the simulated lineshapes are always narrower than their experimental counterparts and the simulated lineshapes show large minima for $B_0 \leq 0.3\,\mathrm{mT}$ which are not present in the experimental data. Both of these effects may be attributed, at least in part, to the neglect of small hyperfine couplings in the calculations. As additional groups of HFCs are added, these two defects are ameliorated. Unfortunately, the time for calculation increases dramatically as more HFCs are included and a compromise must be struck.

4.4.3 Effect of RF field strength

Figure 4.6 shows two sets of simulated MARY-ν spectra in the $\left[\text{Chr-d}_{12}^{\bullet+}\ \text{1,4-DCB}^{\bullet-}\right]$ radical pair. The left column shows spectra calculated with an RF field strength of 100 µT and the right column with 300 µT. All spectra show an increase in amplitude as the RF field strength is increased. Nevertheless, it is clear that the detailed effects of increasing RF field strength differ with radio frequency.

At low frequencies, we see that the region in which parallel and perpendicular orientations give the same signal is extended. As explained above, this region covers "small" static fields, where the RF field dominates the static field. Therefore, it is perfectly reasonable that a stronger RF field should remain dominant over a larger range of static field strengths.

At high frequencies, we see that the orientation effect is amplified. Indeed, in the 50 MHz, 300 µT spectra, the perpendicular signal has opposite phase to that with parallel fields. This inversion of signals has been observed experimentally [36, 216–220]. It is the hallmark of "spin-locking", that is of strong RF field effects. We return to this point in more detail in §5.5.

Finally, as the RF field strength increases, the spectral features become broader. This power broadening effect may be seen clearly in the 20 MHz and 50 MHz portions of Figure 4.6. At lower frequencies, the most noticeable result of broadening is a suppression of the unphysical sharp drop in signal approaching zero static field.

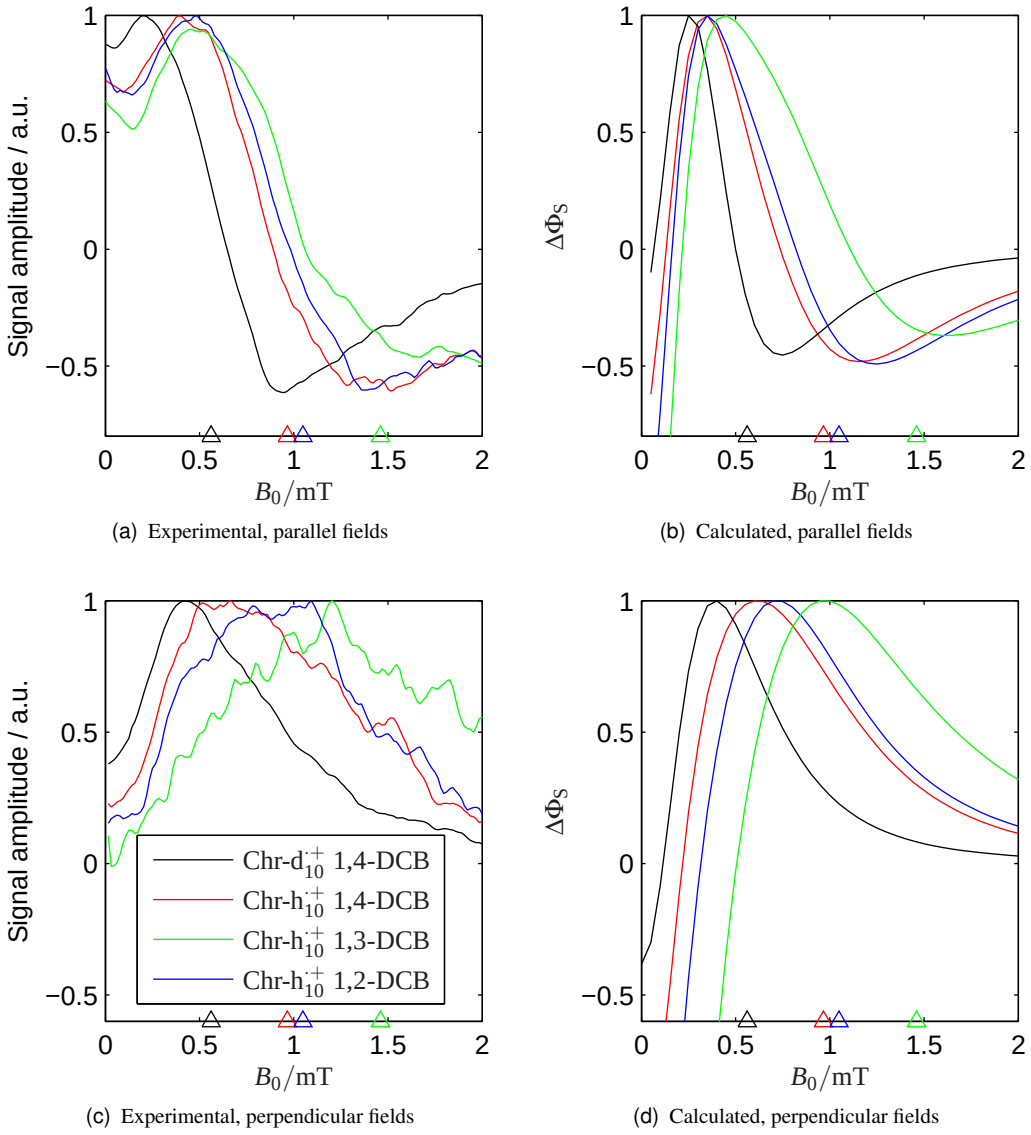

(a) Experimental, parallel fields

(b) Calculated, parallel fields

(c) Experimental, perpendicular fields

(d) Calculated, perpendicular fields

Figure 4.5: Left: Experimental MARY-ν spectra measured in four isomer/isotopomer variants of the $\left[\mathrm{Chr}^{\bullet+}\ \mathrm{DCB}^{\bullet-}\right]$ radical pair at $\nu_{\mathrm{rf}} = 5\,\mathrm{MHz}$. Right: Corresponding simulations made with γ–COMPUTE using $B_1 = -\omega_1/\gamma_e = 100\,\mu\mathrm{T}$, $\nu_{\mathrm{rf}} = 5\,\mathrm{MHz}$, exponential model rate constant $k = 5.6 \times 10^7\,\mathrm{s}^{-1}$ and $n = 64$. Hyperfine coupling constants are given in Table 4.1. All plots have been scaled to the same maximum intensity because the different exciplexes have different intensities. Overall effective HFCs from Table 4.1 are marked with small triangles for each system.

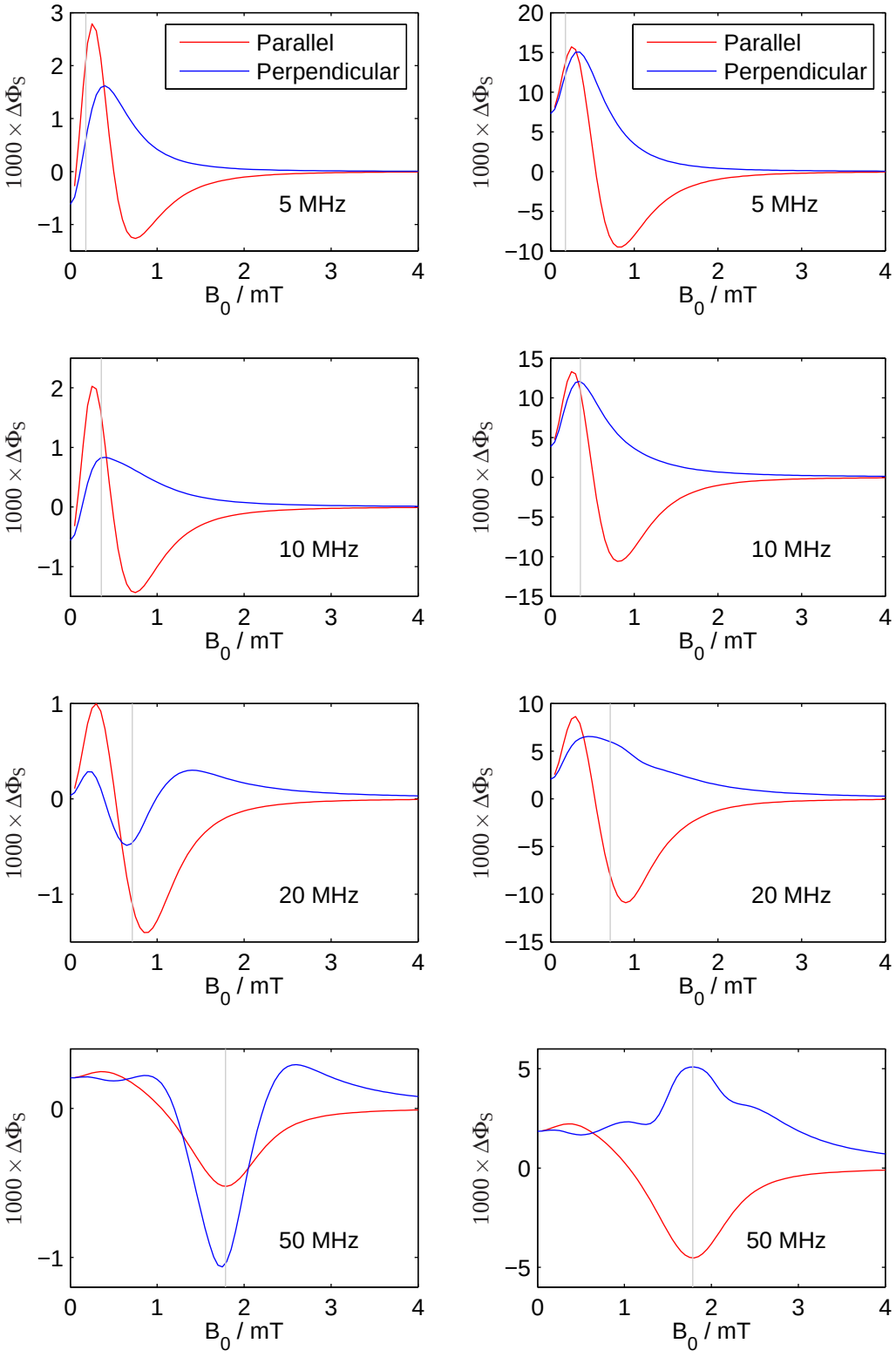

Figure 4.6: Comparison of $\left[\text{Chr-d}_{12}^{\bullet+}\ \text{1,4-DCB}^{\bullet-}\right]$ MARY-ν spectra simulated with RF field strength $B_1 = -\omega_1/\gamma_e = 100\,\mu\text{T}$ (left) and $B_1 = 300\,\mu\text{T}$ (right). The frequency ν_{rf} of the RF field is indicated for each spectrum. All simulations were made using γ–COMPUTE, an exponential model rate constant $k = 5.6 \times 10^7\,\text{s}^{-1}$ and $n = 64$. Hyperfine coupling constants are given in Table 4.1. Grey vertical lines show the static field at which a Zeeman resonance might be anticipated ($B_0 = -2\pi\nu_{rf}/\gamma_e$).

4.4.4 Effect of re-encounter rate

Figure 4.7 shows a series of MARY-ν spectra in the $\left[\text{Chr-d}_{12}^{\bullet+}\ \text{1,4-DCB}^{\bullet-}\right]$ radical pair, simulated at different radio frequencies and relative field orientations. Each plot shows spectra calculated for several choices of the exponential model rate constant k.

For each choice of radio frequency and orientation, we observe that the rate constant k has little influence over the location of extrema in the calculated signals. However, a small value of k tends to produce stronger, sharper features at these locations for all frequencies and orientations. In contrast a large value of k tends to broaden, and reduce the amplitude of the spectral features. This effect arises because a small k corresponds to a long RP lifetime. Long-lived radical pairs have more chance to expose the resonant structure in their oscillating singlet probabilities. In principle, this means that longer lived radical pairs may be expected to give more informative experimental spectra.

4.4.5 Calibration

It is a difficult task to measure experimentally the peak RF field strength experienced by the sample in a MARY-ν experiment. Physically, access is restricted since the gap left for the sample cuvette is only 5×5 mm square. It is also difficult to calculate accurately the propagation of RF signals from the power amplifiers through the circuitry to the RF field coils. The most promising means of measuring the RF field strength is by using a small search coil connected to an oscilloscope. This coil must be calibrated and then may be used to make accurate RF field strength measurements at a certain frequency. Unfortunately, this calibration process, discussed in detail by Norman [139], is also challenging.

The net result is that there is some uncertainty in the RF field strength applied during the experiments discussed in this chapter. When analysing the data in Figures 4.4 and 4.5 we made simulations at RF field strengths $B_1 = 100$, 150, 200, 300, 400 and 500 μT. These were chosen to cover the range of plausible RF field strengths. The onset of spin-locking in the 50 MHz spectrum is a particularly sensitive indicator of the RF field strength. We therefore chose a value of $B_1 = 100\,\mu\text{T}$ in order to reproduce the extent of spin locking in the $\nu_{\text{rf}} = 50$ MHz spectra most accurately. This point is taken up again in Chapter 5.

In preliminary work on this system [180], we estimated that the RF field strength was 300 μT. At that time, we had not incorporated an efficient treatment of magnetically equivalent nuclei into the γ−`COMPUTE` code. This made it infeasible to calculate with as many HFC as have been included in the present calculations. Furthermore, we were interested primarily in the low frequency regime. As is clear from Figures 4.4 and 4.6, the low static field parts of the 5 MHz MARY-ν spectra are most closely reproduced when the RF field strength is taken to be $B_1 = 300\,\mu\text{T}$. It is probable that this close agreement for $B_0 \leq 500\,\mu\text{T}$ occurs by chance as the power broadening caused by stronger RF compensates for the neglect of small hyperfine coupling constants. Spin-locking effects are a sensitive means of calibrating RF field strength in low field OD EPR experiments. This point is taken up in §5.5.

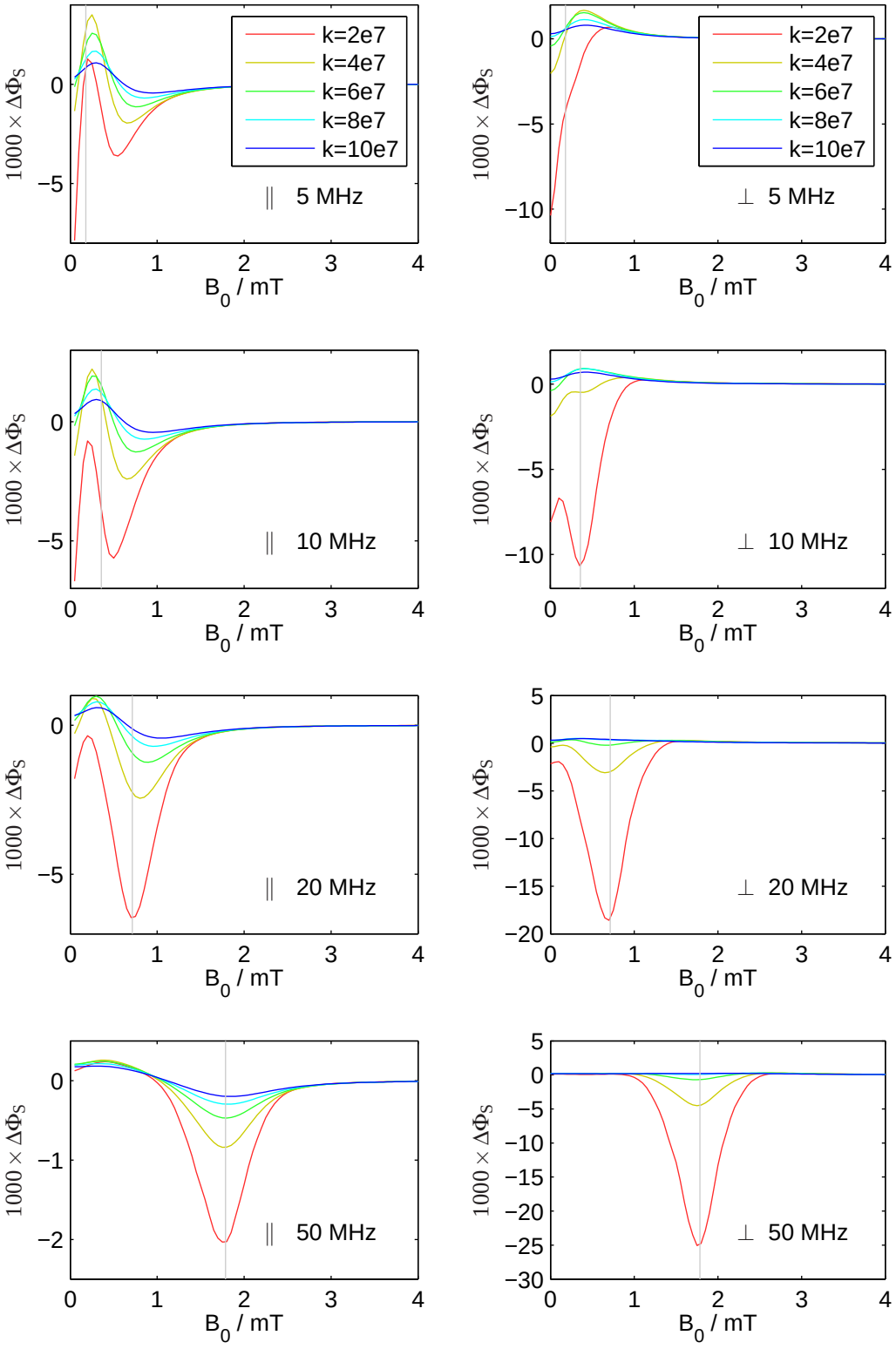

Figure 4.7: Comparison of $\left[\text{Chr-d}_{12}^{\bullet+}\ \text{1,4-DCB}^{\bullet-}\right]$ MARY-v spectra simulated with different exponential model rate constants. The frequency ν_{rf} of the RF field and the relative orientation of the RF and static fields are indicated for each subfigure. All simulations were made using γ–COMPUTE, RF field strength $B_1 = -\omega_1/\gamma_e = 100\,\mu\text{T}$ and $n = 64$. Hyperfine coupling constants are given in Table 4.1. Grey vertical lines show the static field at which a Zeeman resonance might be anticipated ($B_0 = -2\pi\nu_{\text{rf}}/\gamma_e$).

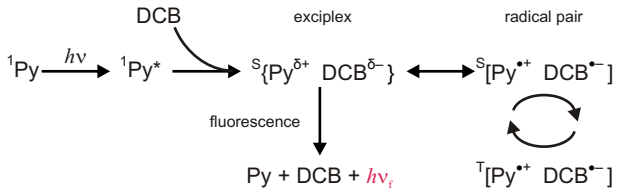

Figure 4.8: Simplified photochemical reaction scheme for pyrene (Py) and 1,3-dicyanobenzene (1,3-DCB). This scheme is taken from [109, 209] and was proposed by those workers as analogous to the well-known kinetic scheme for Py and DMA [136]. The important feature for our purposes is that the fluorescence intensity is proportional to the fraction of singlet radical pairs due to a rapid equilibrium between the singlet exciplex and the singlet radical pair.

In $\left[\text{Py-d}_{10}^{\bullet+}\ \text{1,3-DCB}^{\bullet-}\right]$

Radical N	$a_{1\text{N}}/\text{mT}$	$a_{2\text{N}}/\text{mT}$	$\tilde{a}_{\text{N}}/\text{mT}^{a}$	$\tilde{a}_{\text{RP}}/\text{mT}^{b}$	$\tilde{a}_{\text{RP}}/\text{MHz}$
$\text{Py-d}_{10}^{\bullet+}$ [c]	0.083 (4D)		0.271		
$\text{1,3-DCB}^{\bullet-}$ [d]	0.829 (2H)	0.144 (1H)	1.181	1.212	33.9

[a] Effective hyperfine coupling constants are calculated using equation (3.32).

[b] Overall effective hyperfine coupling constants are calculated using equation (3.47) and the HFC values for each constituent radical.

[c] The D (*i.e.* ^{2}H) couplings were obtained using data from [221] and the relationship $a_{\text{deuterated}}/a_{\text{protonated}} = \gamma_{\text{D}}/\gamma_{\text{H}} = 0.1535$.

[d] Data were obtained from [211].

Table 4.2: Hyperfine coupling constants in $\left[\text{Py-d}_{10}^{\bullet+}\ \text{1,3-DCB}^{\bullet-}\right]$ radical pairs. Hyperfine coupling constants are listed for the three groups of equivalent nuclei in each radical that have the largest couplings. H, D and N indicate ^{1}H, ^{2}H and ^{14}N. The number of equivalent nuclei in each group is given in parentheses. Effective HFC constants are given for each radical and for the four radical pairs discussed in the text.

4.5 Pyrene / DCB system

Further experiments were performed to measure the magnetic field response in a solution comprising 5×10^{-4} M perdeuterated pyrene (Py-d_{10}) and 10^{-2} M 1,3-dicyanobenzene (1,3-DCB) in a viscous solvent mixture of 9:1 cyclohexanol:acetonitrile (by volume) at room temperature. The apparatus used was as described in §4.3. An outline reaction scheme is given in Figure 4.8 and the structures of Py and 1,3-DCB are given in Figures 2.6 and 4.3. Reaction is initiated by photochemical electron transfer which generates a singlet exciplex that is in rapid equilibrium with a singlet radical pair state. The observed exciplex fluorescence is proportional to the concentration of this singlet radical pair $^{\text{S}}\left[\text{Py-d}_{10}^{\bullet+}\ \text{1,3-DCB}^{\bullet-}\right]$. This system shows strong exciplex fluorescence; field effects may therefore be measured with a large signal-to-noise ratio. This system is also expected to show a strong low field effect since the ratio of effective hyperfine couplings $\tilde{a}_{\text{1,3-DCB}^{\bullet-}}/\tilde{a}_{\text{Py-d}_{10}^{\bullet+}}$ is large (see Table 4.2).

4.5.1 Influence of audio frequency modulation

The weak radio frequency fields used here $B_1 \sim 100$–$300\,\mu\mathrm{T}$ produce correspondingly small changes in the singlet yield and hence in the exciplex fluorescence of the systems studied. In order to measure these effects accurately, without their being swamped by experimental noise, we employ a modulation technique. The RF signal is multiplied by a sinusoid with frequency 381 Hz. This modulated signal is then amplified and fed to the experiment. Any sources of fluorescence which depend on the RF field will therefore change their intensity in concert with the field modulation, whilst other sources of fluorescence will not. Using a lock in amplifier, we detect only the component of the fluorescence that oscillates at 381 Hz. This is the experimental signal.

To assess the impact of this modulation procedure on the observed MARY-ν spectra, we employ the following model of modulation and phase-sensitive detection. We define the varying amplitude of the quantity being modulated as

$$A(t) = \left[1 - M\sin^2(\pi t/2)\right] A_{\max} \tag{4.39}$$

where M is the fractional modulation depth, $A_{\max}$ is the peak value of the modulated quantity and time t is measured in modulation cycles. Taking the experimental signal to be given by $\Phi_S(A(t),\ldots)$ when the modulation has instantaneous amplitude $A(t)$ we may model the phase sensitive detection or demodulation process as giving a signal

$$s = \frac{4}{A_{\max} M} \int_0^1 \Phi_S(A(t),\ldots)\cos(\pi t)\,\mathrm{d}t. \tag{4.40}$$

In the special case where the singlet yield depends linearly on RF field strength, *i.e.* $\Phi_S(A) = k_1 A + k_0$ then

$$s = k_1. \tag{4.41}$$

In this situation, the signal may be calculated by simple subtraction of the singlet yield without RF from that with RF: $s = \Phi_S(B_1) - \Phi_S(0)$.

When this linearity breaks down, things are not so simple. For example, when $\Phi_S(A) = k_3A^3 + k_2A^2 + k_1A + k_0$

$$s = k_1 + k_2(2-M)A_{\max} + k_3\left(\frac{5}{16}M^2 - 3M + 3\right)A_{\max}^2. \tag{4.42}$$

Figure 4.9(a) shows singlet yield as a function of static field strength at several different RF field strengths. Each curve corresponds to a different value of $A(t)$ in $\Phi_S(A(t),\ldots)$. Figure 4.9(b) compares the signal calculated using equation (4.40) with that obtained by a simple subtraction of the singlet yield with RF from that without RF. It is clear that, at the low RF field strengths used in this work, audio frequency modulation may be treated quite adequately by simply subtracting the singlet yield with RF from that without RF. Practically, this makes calculations significantly faster than would be the case if explicit evaluation of equation (4.40) were required. The subtraction approach is used throughout the current chapter.

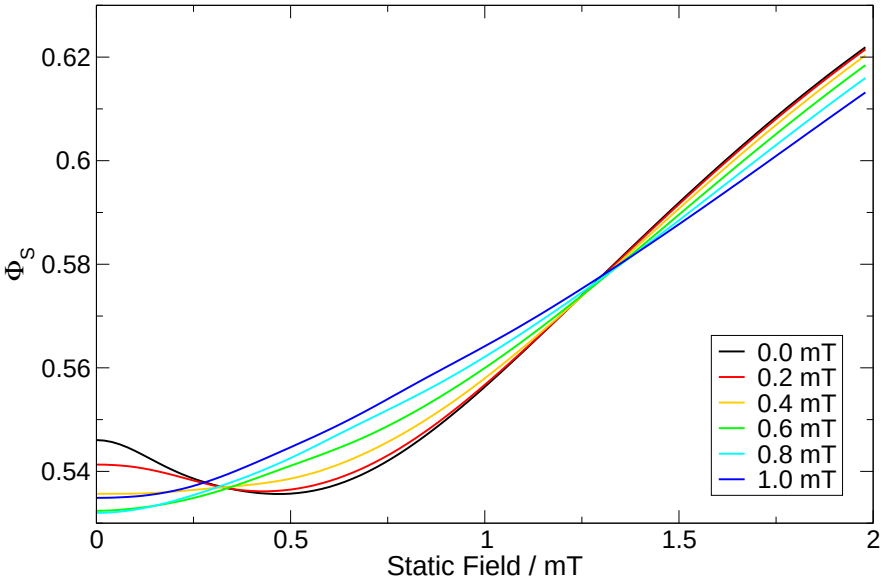

(a) Simulated effects of simultaneously applied parallel static and RF magnetic fields on the $\left[\text{Py-d}_{10}^{\bullet+}\ \text{1,3-DCB}^{\bullet-}\right]$ radical pair, $k = 4.0 \times 10^7\,\text{s}^{-1}$, $\omega_{\text{rf}}/2\pi = 5\,\text{MHz}$ and $\theta = 0$. The singlet yield is plotted as a function of B_0 for values of B_1 between 0.0 and 1.0 mT.

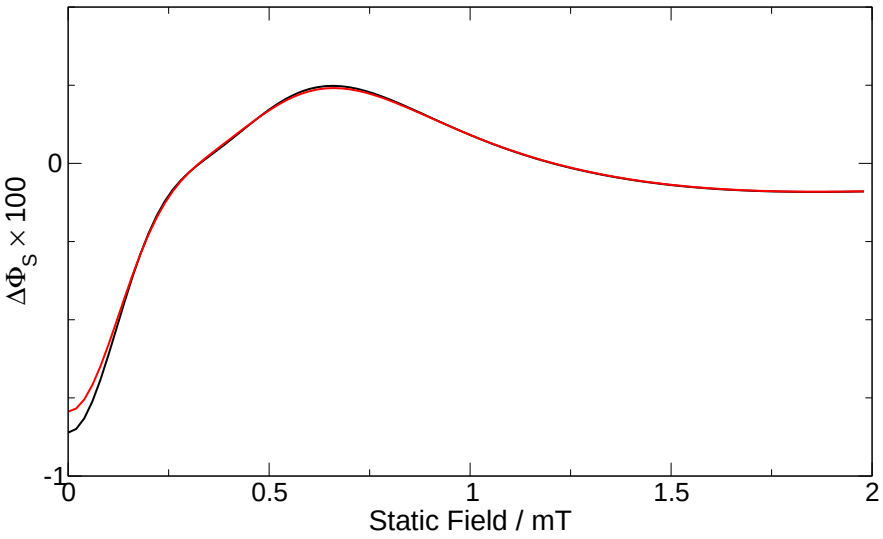

(b) Change in the singlet yield produced by a 0.3 mT RF field calculated under the same conditions as in part A. The result of exact numerical integration over one cycle of the RF field (black) is compared with simple subtraction, $\Phi_S(B_1) - \Phi_S(0)$ (red).

Figure 4.9: The impact of audio frequency modulation.

4.5.2 Effect of RF field

Figure 4.9(a) also serves to illustrate the effects of a RF field on singlet yield in the $\left[\text{Py-d}_{10}^{\bullet+}\ \text{1,3-DCB}^{\bullet-}\right]$ radical pair. It is apparent that the low field effect, visible as a minimum in Φ_S at $B_0 \approx 0.5\,\text{mT}$ is abolished by the RF field when B_1 is stronger than $\sim 0.3\,\text{mT}$. The magnitudes of the changes in Φ_S produced by the two fields acting alone are roughly similar; for example relative to $B_0 = B_1 = 0$, the reduction in Φ_S caused by $B_0 = 0.2\,\text{mT}$ (with $B_1 = 0\,\text{mT}$) is very similar to that arising from $B_1 = 0.2\,\text{mT}$ (with $B_0 = 0\,\text{mT}$). There is no obvious resonance at or near the field where the RF would be in resonance with the electron Zeeman splitting ($B_0 = 0.18\,\text{mT}$) [33, 172]. As discussed below, such a resonance appears only at higher radio frequencies.

4.5.3 Effect of radio frequency and orientation

Figure 4.10 shows experimental (left hand side) and calculated (right hand side) spectra for the Py-d_{10} / 1,3-DCB reaction at three radio frequencies: 5 MHz (top), 20 MHz (middle) and 65 MHz (bottom), chosen to be respectively smaller than, comparable to, and larger than 33.9 MHz, the average hyperfine interaction in the radical pair (see Table 4.2). Each panel shows spectra for several relative orientations θ of the RF and static fields. The principal features of the experimental data are discussed in the following paragraphs.

The effect of the RF field depends strongly on its frequency. At 65 MHz, a dominant peak appears close to the usual high-field EPR resonance condition arising from the electron Zeeman interaction ($\sim 0.036\,\text{mT}/\text{MHz}^{-1}$, *i.e.* $\sim 2.3\,\text{mT}$). The shoulders and satellite peaks, approximately 0.8 mT either side of the central resonance, arise from the largest hyperfine coupling in the radical pair (two equivalent protons with $a = 0.829\,\text{mT}$ in 1,3-DCB$^{\bullet-}$). The signal is strongest when the RF and static fields are perpendicular, but there is still a weak signal for parallel fields. At 65 MHz the high field EPR selection rule requiring perpendicular fields for the Zeeman resonance [213–215, 222] is only slightly broken. Essentially similar spectra can be expected for radio frequencies higher than 65 MHz. These spectra will be centred around correspondingly stronger static fields, the signal strength will depend more strongly on the relative orientation of the two magnetic fields and the asymmetry in the hyperfine structure should disappear. This high frequency limit is discussed further in §4.5.5 below.

At lower radio frequencies of 20 MHz and 5 MHz, the responses for parallel and perpendicular fields have comparable amplitudes. The shape of the signal as a function of B_0 is most sensitive to the relative orientation of the two fields at 20 MHz, reflecting the comparable size of the hyperfine interactions ($\sim 1.0\,\text{mT}$), the B_0 field required for the Zeeman resonance (0.71 mT), and the B_1 field strength ($\sim 0.3\,\text{mT}$). The θ-dependence is less complex at 5 MHz, at which frequency the Zeeman resonance ($B_0 = 0.18\,\text{mT}$) is obscured by resonances with hyperfine splittings. At these low frequencies, the high field EPR selection rule requiring perpendicular fields is quite clearly broken. The 5 MHz spectra in particular are typical of those in the low field regime: where the hyperfine interaction dominates the RP spin evolution.

At all three frequencies the signals are weak for $B_0 > 4\,\text{mT}$, when the RF field is off-resonance with respect to both Zeeman and hyperfine interactions. This supports our supposition that these two interactions are most important to the form of MARY-ν

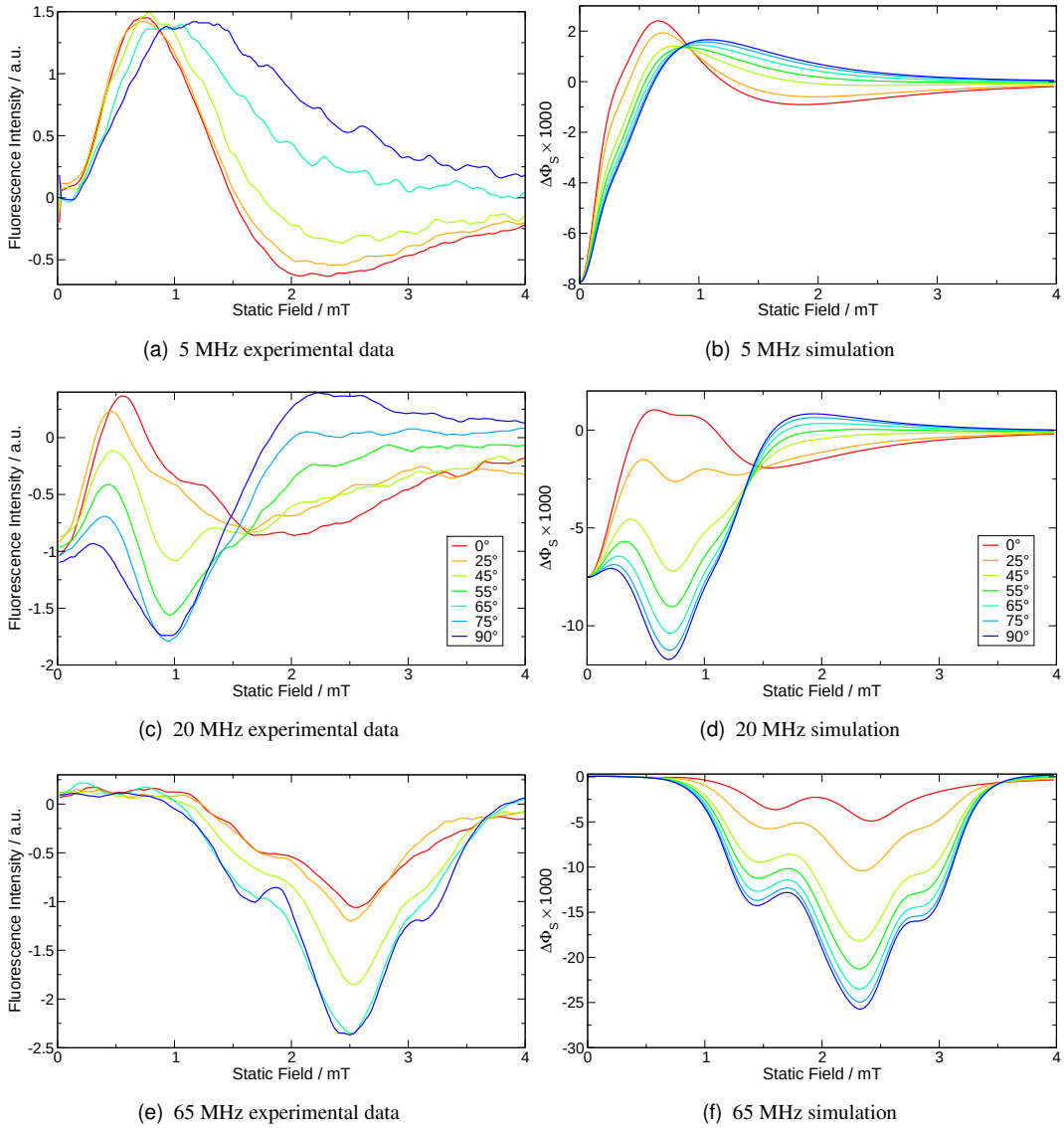

(a) 5 MHz experimental data

(b) 5 MHz simulation

(c) 20 MHz experimental data

(d) 20 MHz simulation

(e) 65 MHz experimental data

(f) 65 MHz simulation

Figure 4.10: Experimental (left) and simulated (right) low-field optically detected EPR spectra of $\left[\text{Py-d}_{10}^{\bullet+}\ \text{1,3-DCB}^{\bullet-}\right]$ at radio frequencies of $\nu_{\text{rf}} = 5\,\text{MHz}$ (top), $20\,\text{MHz}$ (centre) and $65\,\text{MHz}$ (bottom). Values of θ are as indicated in the legend. The same colours are used for all plots, even though experimental data were not collected for some combinations of ν_{rf} and θ. The simulations were performed using $B_1 = 0.3\,\text{mT}$ and $k = 4 \times 10^7\,\text{s}^{-1}$. The experimental spectra represent the changes in the exciplex fluorescence produced by the radio frequency field.

spectra, as reflected in our choice of spin Hamiltonian: equation (4.1).

Furthermore, the MARY-ν spectra are seen to change smoothly between limiting shapes at $\theta = 0^\circ$ and 90°; there are no new peaks at intermediate orientations. This is as we would expect for a single photon process using the spin Hamiltonian above. The observed MARY-ν spectra therefore illustrate a change in selection rules between the high- and low-field (or frequency) limits.

With the exception of the 65 MHz data, it is difficult to rationalise the form of the observed spectra using physical arguments familiar from conventional EPR and RYDMR spectroscopies. Outside of the high-field limit, the distribution of spin energy levels and the probabilities of RF-induced transitions between them become highly complex. Numerical simulations are therefore indispensable in this low-field regime if sense is to be made of the observed spectra.

The simulations shown on the right hand side of Figure 4.10 were performed using the adapted γ–`COMPUTE` algorithm described in §4.2.3. Values of hyperfine coupling constants are given in Table 4.2. Calculations were made using the exponential model with a recombination rate constant $k = 4 \times 10^7\,\mathrm{s}^{-1}$ and a RF field strength $B_1 = 0.3\,\mathrm{mT}$. Beyond choosing physically plausible values of the last two parameters, no attempt has been made to optimise the resemblance to the experimental data. The agreement at each of the three frequencies, while clearly not perfect, is nonetheless striking. All the major features of the experimental spectra are reproduced in the simulations at approximately correct B_0 field positions. This correspondence is particularly satisfying given the complexity of the spin systems, the approximate treatment of the radical diffusion and the very limited number of variable parameters. Perhaps the most dramatic discrepancy between theory and experiment is seen at 5 MHz for $B_0 < 0.5\,\mathrm{mT}$ where the simulated signals are quite strongly negative in contrast to the experimental intensities which are close to zero. This difference probably stems from excluding the smaller hyperfine interactions in the two radicals.

Finally, it is apparent that at certain B_0 fields ($\sim 0.9\,\mathrm{mT}$ at 5 MHz and $\sim 1.5\,\mathrm{mT}$ at 20 MHz), the exciplex fluorescence is independent of θ. Although the origin of this effect is unclear, it is reassuring to see similar features in the simulations.

4.5.4 Low radio frequency limit

It is instructive to consider separately the limiting cases of low and high frequency oscillating fields. Consider first the case of low frequencies, for example the 5 MHz measurements in Figure 4.10. Radical pair lifetimes are typically $\sim$ 10–100 ns. Therefore, for sufficiently low frequency oscillating fields, any particular radical pair will not persist for long enough to notice the oscillation in field strength. As far as each radical pair is concerned the oscillating field is merely an additional *static* contribution to the field strength. The only remaining effect of the field oscillations is that, since radical pairs are created with equal probability at any initial RF phase γ, different radical pairs will experience a different effective static field. This effective static field varies between the extreme values of $B_{\mathrm{eff}} = |B_0 - B_1|$ and $B_{\mathrm{eff}} = B_0 + B_1$ when $\theta = 0^\circ$ and between $B_{\mathrm{eff}} = B_0$ and $B_{\mathrm{eff}} = \sqrt{B_0^2 + B_1^2}$ when $\theta = 90^\circ$. Figure 4.11 shows the MARY-ν spectra calculated using a suitable ensemble of radical pairs subject to appropriate effective static fields. It is clear that this approach provides a reasonable approximation to the exact time-dependent calculations shown in Figure 4.10(b). Differences between

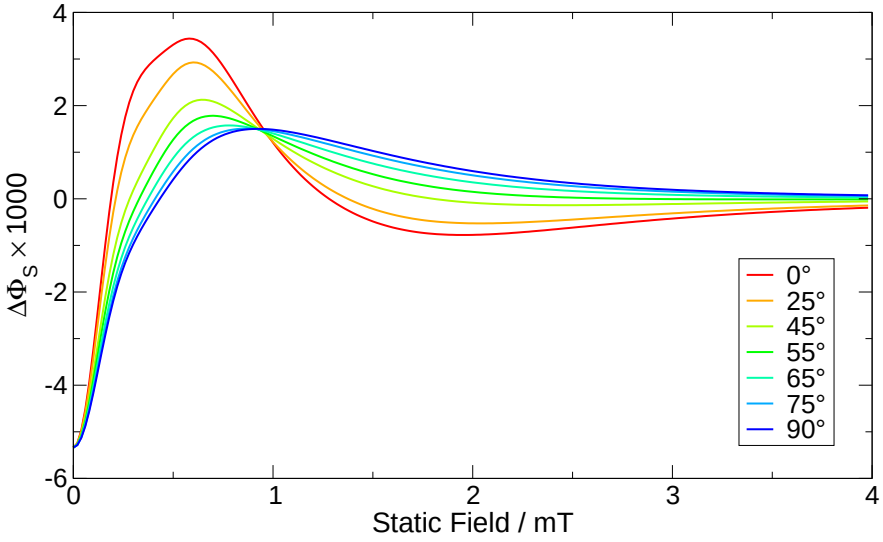

Figure 4.11: Approximate, simulated low-field optically detected EPR spectra of $\left[\text{Py-d}_{10}^{\bullet+}\ \text{1,3-DCB}^{\bullet-}\right]$ a radio frequency of 5 MHz. The simulations were performed by treating the RF field as invariant during a radical pair lifetime. Values of θ are as indicated. $B_1 = 0.3\,\text{mT}$ and $k = 4 \times 10^7\,\text{s}^{-1}$. The full time-dependent calculation for these parameters is shown in Figure 4.10(b).

the two sets of simulations are noticeable, but not pronounced. Further calculations (not shown) suggest that the low-frequency limit is essentially exact for this particular choice of k, B_1 and hyperfine couplings, providing the radio frequency is less than about 1 MHz; *i.e.* providing the radical pair lifetime is less than $\sim 3\%$ of one period of the RF field.

4.5.5 High radio frequency limit

Having considered the case of low frequencies, we ought also to comment on the limiting behaviour at high radio frequencies. Figure 4.12(c) shows a series of MARY-ν spectra calculated in a one-proton radical pair at different radio frequencies ν_{rf}. As the radio frequency increases we see that the Zeeman resonance becomes the only significant spectral feature, that it becomes more symmetric in shape and that the depth of the Zeeman resonance approaches a saturation value. The MARY-ν spectra for parallel fields (not shown) show signals that decay to zero as the radio frequency is increased. By $\nu_{\text{rf}} = 200\,\text{MHz}$, when B_0 (at the Zeeman resonance) is stronger than all hyperfine interactions, the MARY-ν spectra for parallel and perpendicular orientations appear as would be expected in a traditional high field RYDMR experiment [213–215, 222].

Figures 4.12(a) and (b) give some insight into the saturation of the MARY-ν Zeeman resonance at high frequencies (or fields). In the high field limit, the radical pair Hamiltonian eigenstates may be labelled S, T_0 and $\text{T}_\pm$. Treating the energy level diagram as a correlation diagram, we may continue to use the high field labels for the eigenstates in weaker static fields. The Zeeman resonance is accurately described by first order perturbation theory: the RF field drives coherent oscillations between $\text{T}_0 \leftrightarrow \text{T}_\pm$ and between $\text{S} \leftrightarrow \text{T}_\pm$ providing that its frequency matches the energy level splitting between these states [92, Fermi's golden rule]. In the high field limit, the

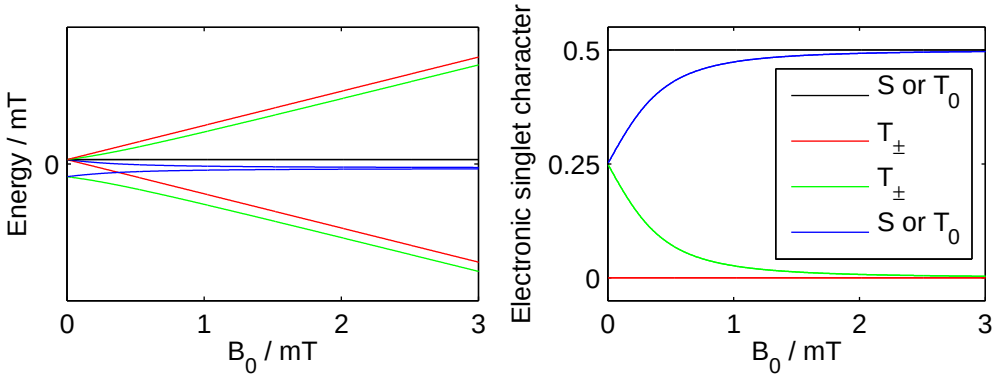

(a) Energy levels

(b) Singlet character of the levels in (a)

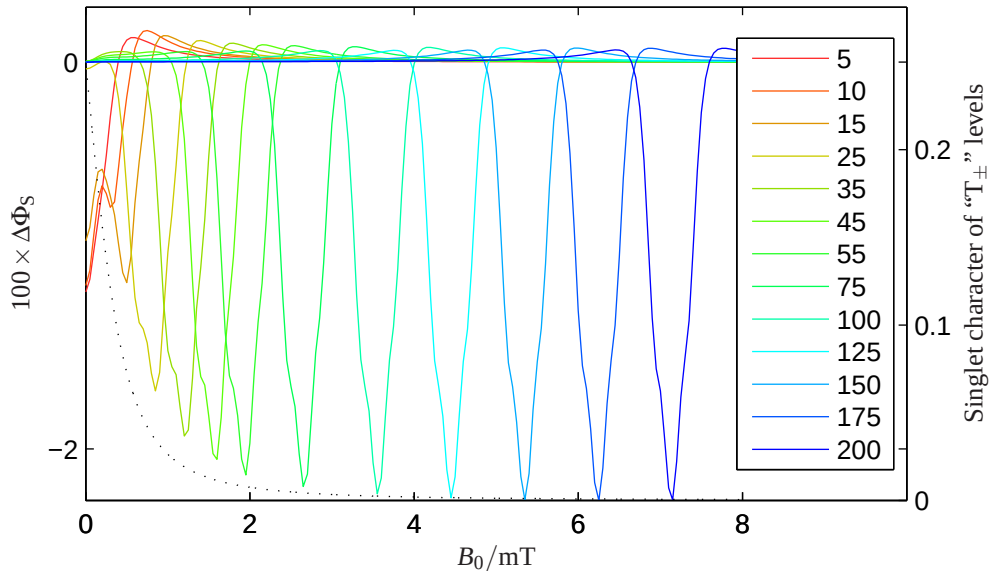

(c) Selection of MARY-ν spectra at different radio frequencies (coloured lines). The green curve from (b) is plotted as a dotted black line to aid comparison with the peak depths.

Figure 4.12: Calculations in a one-proton radical pair using γ−COMPUTE with the following parameters: $a = 0.5\,\mathrm{mT}$, $I = {}^1/_2$, $k = 2.8 \times 10^7\,\mathrm{s}^{-1}$, $n = 64$, $B_1 = 100\,\mu\mathrm{T}$, $\theta = 90°$. High radio frequencies cause a change from the low field regime towards the behaviour seen in high field RYDMR. The depth of the Zeeman peak saturates as the $T_\pm$ levels — shown as green lines in (a) and (b) — become pure triplets.

triplet–triplet transition has no effect on the singlet probability and hence does not affect the singlet product yield. On the other hand, the singlet–triplet transition acts to "dilute" the initial pure singlet state over time, causing a reduction in the singlet yield. At weaker static fields, in contrast, Figure 4.12(b) shows that two of the "$T_{\pm}$" states begin to acquire singlet character at the expense of the two of the "S or T_0" states. This has two effects: (i) it means that in the RP's initial pure singlet state, the population difference between the "S or T_0" and the "$T_{\pm}$" states decreases and (ii) it means that the difference in singlet character between the "S or T_0" and the "$T_{\pm}$" states also decreases. Both of these effects make the resonant transitions that are driven by the RF field less effective at reducing the singlet probability of the radical pair. Hence, the Zeeman resonance becomes less pronounced at lower fields / frequencies. This description has been given in the case of a one-proton radical pair. Nevertheless, realistic radical pairs with many hyperfine coupling constants show similar behaviour, a point which is taken up further on in §5.4.3.

4.5.6 Effect of rate constant k and RF field strength B_1

Although the values of k and B_1 used for the simulations presented in Figure 4.10 are physically plausible, their values are not known precisely. The value of the rate constant k, in particular, is to some extent ill-defined because it parameterises an approximate model of the radical encounters (*viz.* the exponential model). It is therefore important to investigate the sensitivity of the simulated spectra to the values of these two quantities.

Figure 4.13 shows calculations for $k = 2\times10^7\,\mathrm{s}^{-1}$, $4\times10^7\,\mathrm{s}^{-1}$ and $6\times10^7\,\mathrm{s}^{-1}$ and for $B_1 = 0.3\,\mathrm{mT}$ and $0.5\,\mathrm{mT}$ with a radio frequency $\nu_{\mathrm{rf}} = 20\,\mathrm{MHz}$ — the frequency for which the spectra are expected to be most sensitive to k and B_1. Overall, comparison of Figure 4.13 with the experimental spectra in Figure 4.10 suggests that the values of k and B_1 used for the simulations in Figure 4.10 are probably close to optimal. Similar calculations for $\nu_{\mathrm{rf}} = 5\,\mathrm{MHz}$ and $65\,\mathrm{MHz}$ (not shown) bear substantially less resemblance to the experimental data when $k = 2\times10^7\,\mathrm{s}^{-1}$ and are not much different from Figure 4.10 for $k = 6\times10^7\,\mathrm{s}^{-1}$ or for $B_1 = 0.5\,\mathrm{mT}$.

The spectra in Figure 4.13 show broadening of spectral features at high k or B_1. They also show the onset of "spin-locking" inversions at low k and high B_1. These trends are similar to those noted in relation to Figures 4.6 and 4.7 for the $\left[\mathrm{Chr}^{\bullet+}\ \mathrm{DCB}^{\bullet-}\right]$ radical pair. However, there are clearly additional complexities here that reflect, in a highly complex manner, the resonances between the RF field and the energy levels arising from the hyperfine and electron Zeeman interactions. The spectra are particularly complicated because the B_1 field is not weak enough to be considered as merely probing without perturbing the energy level splittings produced by the intrinsic magnetic interactions.

4.6 RF insensitive point

When calculating MARY-ν spectra, we begin by calculating the singlet yield with the RF field present and then subtracting that without RF. In many instances, there is a static field value at which the singlet yield changes negligibly on application of RF fields of a variety of strengths. For example, such a "nodal point" may be seen in

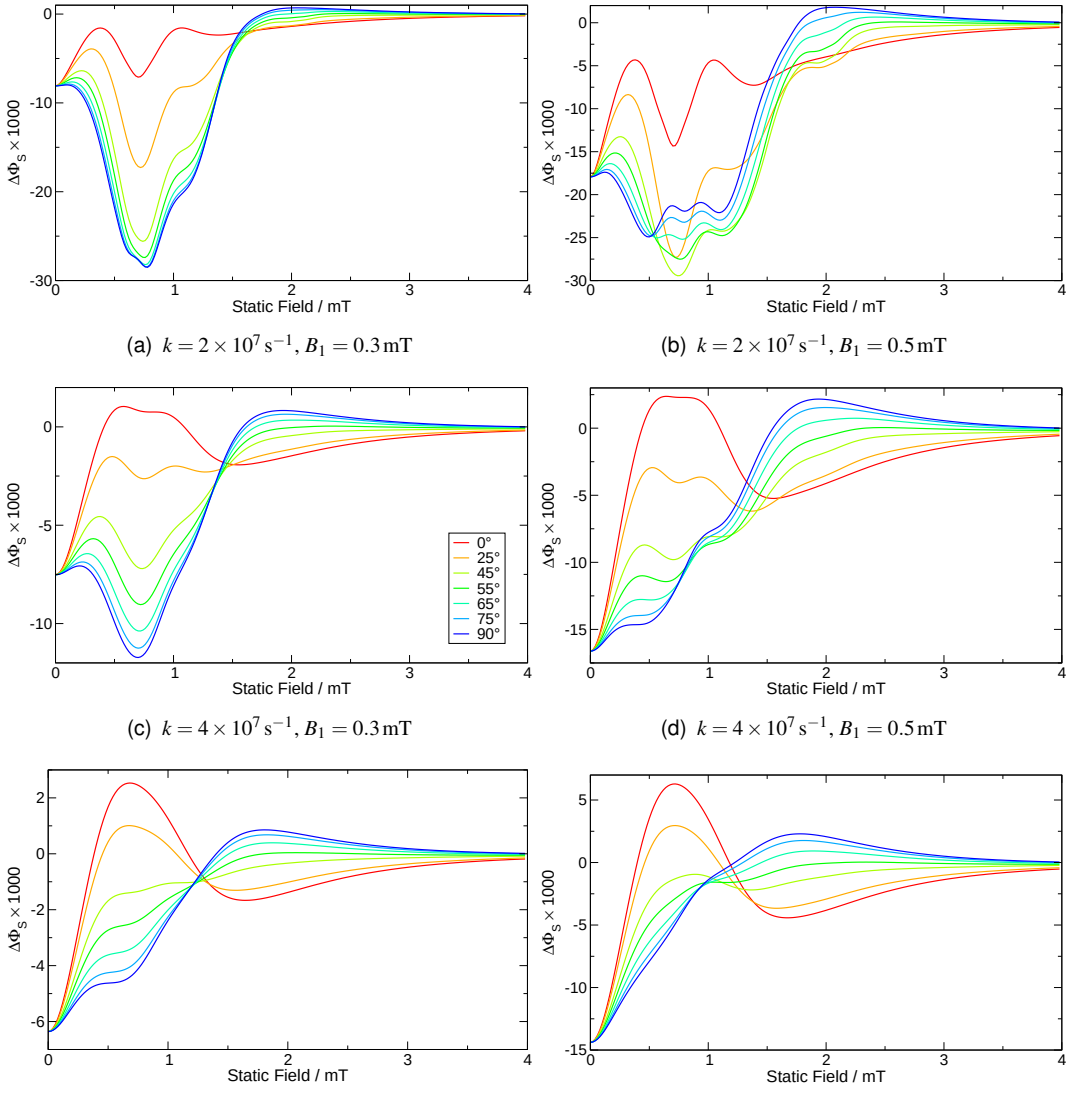

(a) $k = 2 \times 10^7\,\mathrm{s}^{-1}$, $B_1 = 0.3\,\mathrm{mT}$ (b) $k = 2 \times 10^7\,\mathrm{s}^{-1}$, $B_1 = 0.5\,\mathrm{mT}$

(c) $k = 4 \times 10^7\,\mathrm{s}^{-1}$, $B_1 = 0.3\,\mathrm{mT}$ (d) $k = 4 \times 10^7\,\mathrm{s}^{-1}$, $B_1 = 0.5\,\mathrm{mT}$

(e) $k = 6 \times 10^7\,\mathrm{s}^{-1}$, $B_1 = 0.3\,\mathrm{mT}$ (f) $k = 6 \times 10^7\,\mathrm{s}^{-1}$, $B_1 = 0.5\,\mathrm{mT}$

Figure 4.13: Simulated low-field optically detected EPR spectra of $\left[\text{Py-d}_{10}^{\bullet+}\ \text{1,3-DCB}^{\bullet-}\right]$ at a radio frequency of 20 MHz. $B_1 = 0.3\,\mathrm{mT}$ (left) and $0.5\,\mathrm{mT}$ (right). $k = 2 \times 10^7\,\mathrm{s}^{-1}$ (top), $4 \times 10^7\,\mathrm{s}^{-1}$ (middle) and $6 \times 10^7\,\mathrm{s}^{-1}$ (bottom). Values of θ are as indicated.

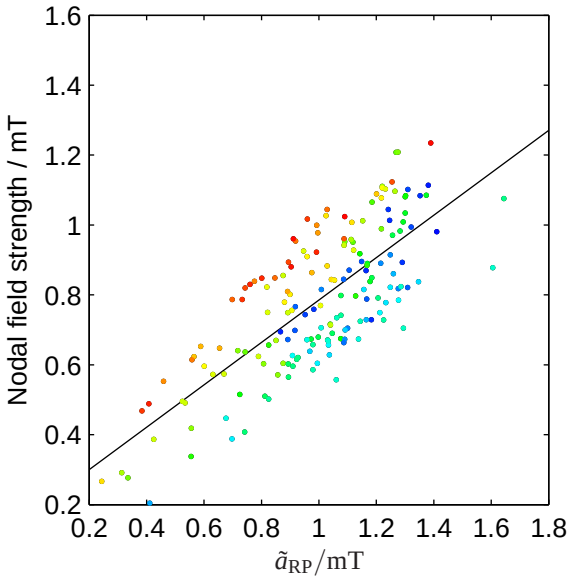

Figure 4.14: "Nodal field strengths" (the static field at which MARY spectra do not change significantly with RF field strength) as a function of overall effective hyperfine coupling in an ensemble of radical pairs. Each member of the ensemble has two HFCs on radical A and one HFC on radical B. The hyperfine constants were all chosen from a uniform distribution between 0–1 mT. All nuclei were spin-½. Calculations were made using γ–COMPUTE and an exponential model rate constant of $2.8 \times 10^7\,\mathrm{s}^{-1}$, linear RF field polarisation, $\theta = 0°$, $\nu_{\mathrm{rf}} = 5\,\mathrm{MHz}$, $B_1 = 0.3\,\mathrm{mT}$ and $n = 64$. The data points are coloured according to $\tilde{a}_{\mathrm{A}}/\tilde{a}_{\mathrm{B}}$. Red points have very dissimilar effective HFCs on the two radicals, blue points have identical effective HFCs. The solid black line is the best fit to the points.

Figure 4.9(a) at $B_0 \approx 1.3\,\mathrm{mT}$. In order to investigate this behaviour further, calculations were made in an ensemble of radical pairs with random hyperfine coupling constants. For each member of the ensemble, the nodal point was found. These are shown in Figure 4.14 plotted as a function of the overall effective hyperfine coupling constant. It is clear that the position of the nodal point depends on the overall effective hyperfine coupling constant $\tilde{a}_{\mathrm{RP}}$ and on the ratio of effective hyperfine coupling constants in radicals A and B ($\tilde{a}_{\mathrm{A}}/\tilde{a}_{\mathrm{B}}$). This behaviour is similar to the "rules of thumb" that we developed in Chapter 3 for the prediction of MARY spectra. Unfortunately, it has not proved possible to provide a theoretical explanation for the insensitivity to RF fields at such nodal points.

4.7 Conclusions

It is clear from data presented in Figures 4.4, 4.5 and 4.10 that the low-field optically detected EPR spectra of transient ($\lesssim 100\,\mathrm{ns}$) radical pairs can be strikingly sensitive to the weak applied magnetic fields needed to record them. The response of the reaction product yield to the linearly polarised RF field depends in a complex manner not only on its frequency and on the strength of the applied static magnetic field, but also on the relative orientation of the two fields. The spectra are thus a rich source of information on the kinetics, motions and relaxation of the radicals, reflecting the comparable magnitude of the relevant applied static, applied RF and intrinsic hyperfine magnetic fields. Simpler, less potentially informative spectra would no doubt be observed in various limiting cases, none of which is generally applicable here: the static field is not strong enough for the high field approximation to be valid; neither field is weak enough to be treated or thought of as a perturbation; and the radio frequency is for the most part too high for the RF field to be effectively static on the timescale of radical recombination.

The customary approaches to simulating such spectra, based on the rotating frame transformation, are not applicable. Instead, we have adapted from solid state NMR a numerical approach (γ–COMPUTE) valid for a periodic but otherwise arbitrary spin Hamiltonian. In this way, we have shown that the essential features of the spectra are consistent with the radical pair mechanism (RPM) and can be satisfactorily simulated using parameters whose values are either known independently or for which reasonable estimates are readily available. The calculations are efficient enough that it should be possible to extract quantitative information from the spectra by fitting suitable models of the radical motion. It may even be possible to invert the data to obtain an empirical re-encounter probability distribution $f(t)$, as was done for static magnetic fields in Chapter 2. Unlike the approach of Canfield *et al.* [223–225], in which the interaction with the oscillating magnetic field is treated as a perturbation on the hyperfine and static field Zeeman interactions, γ–COMPUTE allows exact calculations whatever the magnitude of B_1. It is therefore to be preferred in the present case where B_0, B_1 and the hyperfine couplings are of comparable size.

The agreement between the simulated and experimental spectra although clearly not perfect is most encouraging. Despite its simplicity, the exponential model — combined with the assumptions of diffusion control, singlet-only reactivity and a single encounter for all radical pairs — appears to be an excellent basis for understanding the complex field and orientation dependence of the spectra. As noted above, the corre-

spondence between theory and experiment could be improved by the inclusion in the calculations of a few more of the smaller hyperfine couplings at a cost of additional processor time.

This work provides a potent combination of experimental measurements in a simple chemical system, a relatively simple quantum mechanical model to explain these results and an efficient algorithm for making the necessary calculations. Taken together these contributions lay a solid foundation for the discussion of low-field, steady-state radio frequency magnetic field effects in other contexts. Later chapters will present several further experiments that have been inspired or interpreted using the model developed here. For example, theory predicts that in the low-field regime, there will be a sizeable difference in the OD EPR spectra measured with linearly and circularly polarised RF fields. Theory also predicts that under certain conditions MARY-ν spectra adopt an inverted line shape, as so-called "spin locking" effects develop. These predictions inspired a series of experiments and further calculations presented in Chapter 5.

Calculations show that low-field, steady-state radio frequency magnetic field effects are to be expected quite generally. These RF effects are expected in radicals over a wide range of hyperfine coupling constants and for reasonable radical pair lifetimes, although the details of the spectrum depend critically upon the radical pair in question. This broad sensitivity of the chemical response to simultaneously applied static and RF magnetic fields could form the basis of a diagnostic test for the operation of the RPM. This might be valuable in the context of magnetic field effects in complex (e.g. biological) systems in which the identities and properties of any radicals involved might be completely unknown. The unique features of radical pair reactions are that, as well as responding to an applied static field, they should (a) also be sensitive to the frequency and direction of an additional RF field of comparable intensity and (b) exhibit a Zeeman resonance at a frequency that is not strongly dependent on the hyperfine interactions provided that these are weaker than the static field required for resonance ($\sim 0.036\,\mathrm{mT\,MHz^{-1}}$).

A fascinating biological response to magnetic fields is found in many migratory birds. Such birds have been shown to detect the Earth's magnetic field and to use that information to assist them whilst navigating their migratory route [74, 226, 227]. The physical mechanism by which this magnetic "compass sense" operates remains the subject of lively debate [105, 228, 229]. One hypothesis that has, so far, stood the test of time is that a bird detects the Earth's magnetic field through its influence on a chemical, radical pair reaction in the eye [29, 106, 107]. Inspired by calculations in a simple model system, Ritz proposed that exposure to RF fields in addition to the Earth's magnetic field might temporarily disrupt the bird's compass sense. Subsequent behavioural experiments confirmed this prediction, showing that for certain frequencies, strikingly weak RF fields disrupt the bird's magnetic sense [230–232].

Using the model developed and tested here, we consider the interpretation of these behavioural studies and their implications for the radicals involved in avian magnetoreception in Chapter 9. For example, during discussion of Figure 4.9(a) in §4.5.2, we observed that static and RF fields of comparable strength produce comparable changes in product yield except when the RF field is at a resonant frequency. This prediction is borne out experimentally; neither $\left[\mathrm{Chr}^{\bullet+}\ \mathrm{DCB}^{\bullet-}\right]$ (in Figure 4.5) nor $\left[\mathrm{Py\text{-}d}_{10}^{\bullet+}\ \mathrm{1,3\text{-}DCB}^{\bullet-}\right]$ (in Figure 4.10) show an obvious Zeeman resonance at or near the B_0 field at which the radio frequency matches the electron Zeeman splitting in the spec-

tra with $\nu_{\mathrm{rf}} = 5\,\mathrm{MHz}$. This is seemingly at odds with Canfield *et al*, who predicted a sharp Zeeman resonance for a one-proton radical pair with a long lifetime subject to a very weak radio frequency field [223, Figure 5]. Moreover, the fact that 1.315 MHz RF fields of strength $\sim 15\,\mathrm{nT}$ can disrupt robins' magnetic sense [230] implies the operation of a resonant effect at the Zeeman resonant frequency for the Earth's magnetic field in Frankfurt ($46\,\mu\mathrm{T}$). Whether such a resonance may be expected in general has important implications in the design of experiments to test the origins of the magnetic "compass" sense in birds. We discuss this question — and the related issue of what properties such a resonance might have in systems with immobile radicals and anisotropic hyperfine interactions — in greater detail in Chapter 9.

Finally, new experimental measurements of the influence of RF fields on the yield of radical pair reactions have recently been made in the Oxford group [233]. These experiments generate radicals not by continuous illumination but by flash photolysis with the laser pulses locked to the RF phase. Hence, the MFE at different initial RF phases γ may be measured directly. It seems likely that these experiments may be simulated efficiently using the `COMPUTE` algorithm [234]. `COMPUTE` was the forerunner of γ–`COMPUTE`; it differs from γ–`COMPUTE` in that it omits the γ-averaging step. In the solid state NMR context, this is undesirable, but in the context of chemical magnetic field effects, the algorithm might be ideally suited for simulation of the new phase locked experiment.

Chapter 5

RF polarisation effects in OD EPR

5.1 Introduction

Radio waves are central to a host of magnetic resonance techniques. In pulse NMR and EPR, application of carefully controlled RF fields gives exquisite control over the relevant spin systems allowing a wealth of useful information to be extracted [84, 86, 186, 212, 235–237]. Given the strong connections between magnetic field effects on the rates and/or yields of radical pair reactions and traditional forms of magnetic resonance, it seemed interesting to explore the combined effects of weak static and RF magnetic fields on radical pair reactions. Such an experiment, dubbed "MARY-ν", and associated theory is presented in Chapter 4.

In high-field magnetic resonance, it is common to make the so-called "rotating frame approximation" [185, 238–242]. This amounts to assuming that the RF fields that are applied to the sample are circularly polarised in the plane perpendicular to the static field. In large static magnetic fields, this approximation is very accurate and substantially eases the theoretical treatment.

Turning to magnetic field effects in chemical systems, the situation is rather more complex. We are especially interested in the applications of radical pair theory to the areas of animal navigation [105, 106] or to the putative health hazards posed by environmental magnetic fields [68, 79]. The magnetic fields relevant to these areas are most often linearly polarised and are certainly most unlikely to be circularly polarised. Furthermore, since environmental magnetic fields are much weaker than those inside an NMR spectrometer, the usual approximations made for high magnetic fields may not apply. In this chapter, we investigate in some detail the effect of RF polarisation on chemical magnetic field effects at low fields.

In 2002, Kukura [181] made a series of measurements of the influence of RF magnetic fields on reaction yield. He found that OMFE spectra (*i.e.* measurements of product yield *vs.* radio frequency with no static field present) could not be adequately simulated using the rotating frame approximation; there were significant discrepancies at low radio frequencies. Using a time-dependent Hamiltonian with linearly polarised RF and a brute-force time domain evaluation of the density matrix, Kukura obtained considerably improved simulations, such as [181, Fig 6.3].

In Chapter 4, we saw that an adapted version of the γ–COMPUTE algorithm allows efficient calculation of the effects of a linearly polarised RF field by exploiting two remaining symmetries in the Hamiltonian, discussed in §4.2.2. Using γ–COMPUTE,

we were able to incorporate several hyperfine couplings on each radical in order to give reasonably accurate simulations. These γ–COMPUTE simulations were shown to agree qualitatively with experimental measurements in two chemical systems. However, even though γ–COMPUTE calculations are much faster than Kukura's brute-force approach, they are still much more demanding than calculations made using the rotating frame approximation. It would be useful, therefore, to understand under what conditions the rotating frame approximation may be used and when a full time-dependent calculation must be made using γ–COMPUTE. We discuss the validity of the rotating frame approximation for different model parameters (field strengths, radio frequencies, *etc.*) below.

The γ–COMPUTE algorithm is equally well suited to calculating the effects of linearly or circularly polarised RF fields within the RPM model outlined in Chapter 4. Yet, very few experimental measurements have been made of the effects of circularly polarised RF fields. Those measurements that are extant were made in the early days of NQR [243, 244] and EPR [245, 246]. No such measurements have been made in relation to chemical magnetic field effects, nor in the low-field regime considered here.

In this chapter, we present results from a series of experiments, performed by Norman and Wedge [139, 182, 247], that are designed to test the predictions made using the RPM model described previously. We focus particular attention on three types of experiment: OMFE spectra, MARY-ν spectra and measurements taken using strong RF fields generated with a tuned field coil. The results presented here provide a powerful validation of the RPM model. Furthermore, the experiments involving strong RF fields often show inverted lineshapes that are sensitive to the RF field strength. Such "spin locking" phenomena provide a means of calibrating the RF field strength in MFE apparatus. Such RF field strengths are difficult to calculate or to measure by other methods. Overall, this chapter may be described as "theory first" and therefore complements the "experiment first" approach of Chapter 4.

5.2 Theory

5.2.1 Radio frequency polarisation

Radio waves propagate according to the Maxwell equations [248]. In free space, the relevant solutions to the Maxwell equations are simultaneous transverse travelling waves of electric and magnetic fields. The electric and magnetic fields at each point in space are necessarily perpendicular to one another and also to the direction of propagation of the wave. This means that, in contrast to [2-D] transverse waves, a full description of a radio wave specifies both the direction of propagation and the relative orientation of the magnetic field, *i.e.* the *polarisation*. Two limiting cases of this polarisation are often used. A *linearly polarised* wave is one where the magnetic field is always parallel to a particular fixed direction, but changes in amplitude as it propagates. Linearly polarised waves are described by specifying this fixed direction. For example, one might talk of horizontally or vertically polarised fields. A *circularly polarised* wave is one where the magnetic field has fixed magnitude, but changes its orientation continuously during propagation. Circularly polarised waves are described by specifying whether the field vectors rotate in a left- or right-hand screw sense about the direction of propagation. For waves having the same direction of propagation,

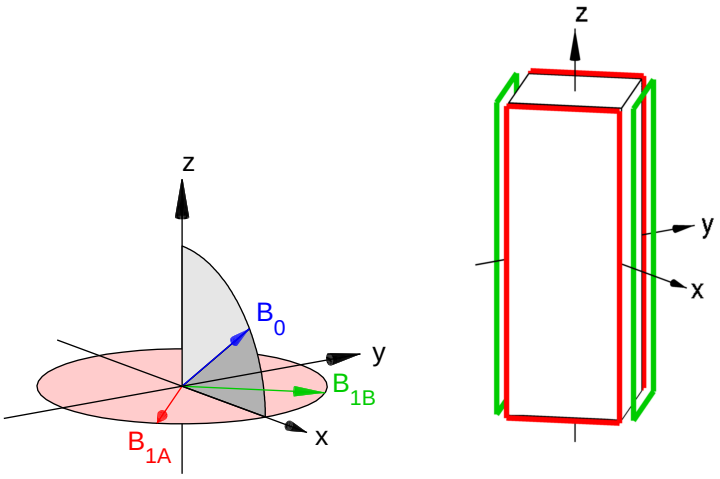

(a) Field geometry (b) Sample cuvette and field coils

Figure 5.1: Figures illustrating the field geometry. The static field $\boldsymbol{B}_0$ is applied in the xz-plane at an angle θ to the x-axis. For linearly polarised RF ($\phi_{\mathrm{rf}} = 0$) this means that $\theta = 0$ gives parallel RF and static fields, whilst $\theta = \pi/2$ gives perpendicular RF and static fields; this convention matches that used in Chapter 4. The RF field is applied through two pairs of field coils, marked in red and green. By adjusting the phase difference ϕ_{rf} between the two coils, linearly or circularly polarised fields may be generated in the xy-plane. In the experimental measurements, these coils are 12 mm $\times$ 5 mm rectangular loops, separated by 5 mm.

any linearly polarised wave may be considered as the superposition of two opposite circularly polarised waves with an appropriate phase shift. Similarly, any circularly polarised wave may be considered as the superposition of two non-parallel linearly polarised waves with an appropriate phase shift.

In the present work, we are concerned with the magnetic field experienced by a radical pair as it undergoes spin-selective reaction in solution. During a typical radical pair lifetime of $\sim$ 10–100 ns, the radicals will diffuse a few nm. For radio frequencies between 5–80 MHz, corresponding to wavelengths of $\sim$ 60–4 m, it is clear that the radicals hardly move with respect to the radio wavelength. Hence, we focus attention on the time evolution of the magnetic field around the radical pair.

We proceed to write this magnetic field experienced by the radical pair as

$$\boldsymbol{B} = \boldsymbol{B}_0 + \boldsymbol{B}_1(t) \tag{5.1}$$

where $\boldsymbol{B}_0$ is a static contribution and $\boldsymbol{B}_1(t)$ is a time-dependent, radio frequency contribution. As illustrated in Figure 5.1, we describe the static field orientation in terms of its strength B_0 and an angle θ such that

$$\boldsymbol{B}_0 = B_0 \left[\boldsymbol{i}\cos\theta + \boldsymbol{k}\sin\theta\right] \tag{5.2}$$

where $\boldsymbol{i}$, $\boldsymbol{j}$, $\boldsymbol{k}$ are unit vectors along the laboratory x-, y- and z-axes respectively. The radio frequency field is described in terms of its RMS strength B_1, frequency $\nu_{\mathrm{rf}} =$

$\omega_{\mathrm{rf}}/2\pi$, initial phase γ and a polarisation parameter ϕ_{rf}. Written explicitly,

$$\boldsymbol{B}_1(t) = \underbrace{B_1\sqrt{\frac{1}{2}}\,(\boldsymbol{i}-\boldsymbol{j})\cos(\omega_{\mathrm{rf}}t+\gamma)}_{-\omega_{1A}(t)/\gamma_{\mathrm{e}}} + \underbrace{B_1\sqrt{\frac{1}{2}}\,(\boldsymbol{i}+\boldsymbol{j})\cos(\omega_{\mathrm{rf}}t+\gamma-\phi_{\mathrm{rf}})}_{-\omega_{1B}(t)/\gamma_{\mathrm{e}}}, \tag{5.3}$$

where we have marked the contributions from the two perpendicular sets of field coils shown in Figure 5.1.

The important limiting cases of the RF polarisation ϕ_{rf} are:

$\phi_{\mathrm{rf}} = 0$**:** The $\boldsymbol{j}$ components cancel entirely, leaving a linearly polarised field along the x-axis. This is referred to as "LIN" polarisation below. Notice that the peak RF field strength is $\sqrt{2}B_1$ and that the RMS RF field strength is B_1.

$\phi_{\mathrm{rf}} = \pm\pi/2$**:** Generates a circularly polarised field in the xy-plane. This is referred to as "CPL±" polarisation below. Notice that the RF field strength is always B_1 and that the RMS RF field strength is therefore also B_1.

Figure 5.2 shows how the RF field depends on time for these limiting cases of the RF polarisation ϕ_{rf}. This choice for $\boldsymbol{B}_1(t)$ keeps the RMS RF field strength constant irrespective of the polarisation.

5.2.2 Hamiltonian

In order to calculate magnetic field effects in the presence of such linearly or circularly polarised RF fields, we consider a radical pair evolving under a Hamiltonian containing contributions for isotropic electron–nuclear hyperfine interactions and for Zeeman interactions of the unpaired electron in each radical with the applied magnetic field:

$$\hat{H}(t;\gamma) = \sum_{\mathrm{N=A}}^{\mathrm{B}} \left(\sum_i a_{i\mathrm{N}}\,\hat{\boldsymbol{I}}_{i\mathrm{N}}\cdot\hat{\boldsymbol{S}}_{\mathrm{N}} - \gamma_{\mathrm{e}}\boldsymbol{B}(t)\cdot\hat{\boldsymbol{S}}_{\mathrm{N}} \right) \tag{5.4}$$

where N labels the radical and iN labels the i^{th} nuclear spins within radical N. The hyperfine coupling between nuclear spin $\hat{\boldsymbol{I}}_{i\mathrm{N}}$ and electron spin $\hat{\boldsymbol{S}}_{\mathrm{N}}$ is governed by a constant $a_{i\mathrm{N}}$, which depends on the electronic and vibrational properties of the radical concerned.

For convenience, we substitute the field geometry described in Figure 5.1 into equation (5.4), giving the following more explicit form of the Hamiltonian:

$$\hat{H}(t;\gamma) = \sum_{\mathrm{N=A}}^{\mathrm{B}} \left\{ \begin{array}{l} \displaystyle\sum_i a_{i\mathrm{N}}\,\hat{\boldsymbol{I}}_{i\mathrm{N}}\cdot\hat{\boldsymbol{S}}_{\mathrm{N}} + \omega_0\left[\hat{S}_{\mathrm{Nx}}\cos\theta + \hat{S}_{\mathrm{Nz}}\sin\theta\right] \\ \quad + \omega_1\sqrt{\frac{1}{2}}\left(\hat{S}_{\mathrm{Nx}} - \hat{S}_{\mathrm{Ny}}\right)\cos(\omega_{\mathrm{rf}}t+\gamma) \\ \quad + \omega_1\sqrt{\frac{1}{2}}\left(\hat{S}_{\mathrm{Nx}} + \hat{S}_{\mathrm{Ny}}\right)\cos(\omega_{\mathrm{rf}}t+\gamma-\phi_{\mathrm{rf}}) \end{array} \right\}, \tag{5.5}$$

where the static field is of strength $B_0 = -\omega_0/\gamma_{\mathrm{e}}$ and the RF field has RMS strength $B_1 = -\omega_1/\gamma_{\mathrm{e}}$. When $\phi_{\mathrm{rf}} = 0$, this Hamiltonian is identical to that defined in the previous chapter by equation (4.1).

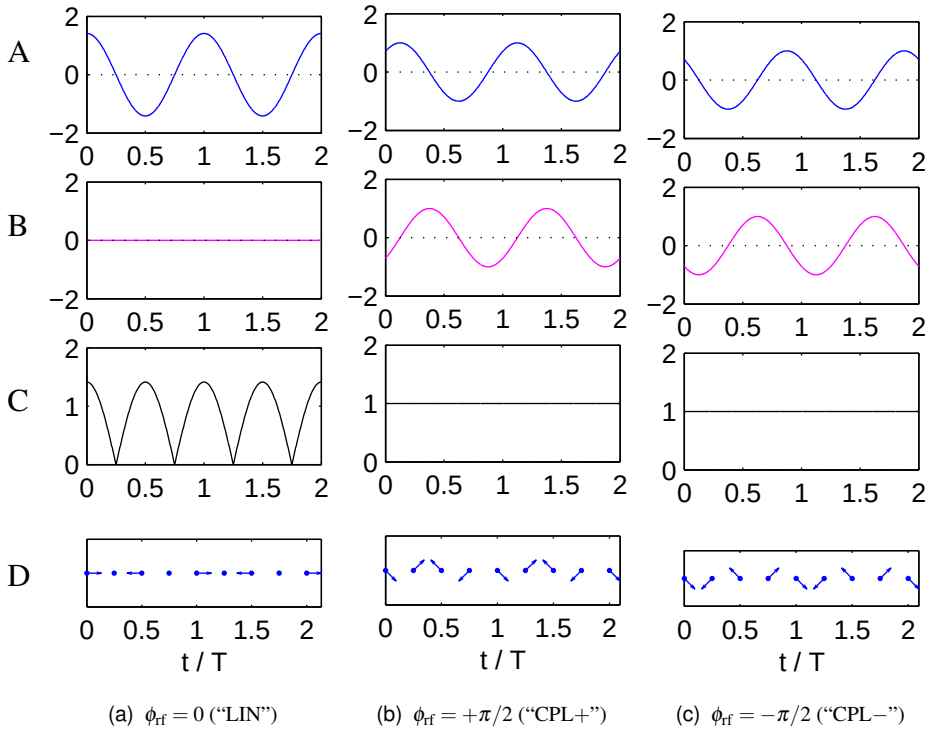

(a) $\phi_{\mathrm{rf}} = 0$ ("LIN") (b) $\phi_{\mathrm{rf}} = +\pi/2$ ("CPL+") (c) $\phi_{\mathrm{rf}} = -\pi/2$ ("CPL−")

Figure 5.2: Effects of the RF polarisation parameter ϕ_{rf}. These figures show four measures of the RF field described by equation (5.3) during two complete cycles, of period T, in a system with initial RF phase $\gamma = 0$ and RMS RF field strength $B_1 = 1$. Notice that the linearly polarised field changes in strength over time, whereas the circularly polarised fields change in direction. The plots in each column are: (A) field component along the x-axis $B_{1x}(t)$; (B) field component along the y-axis $B_{1y}(t)$; (C) instantaneous field strength $|\boldsymbol{B}_1(t)|$; (D) series of arrows denoting the magnetic field at various points during the RF cycle.

5.2.3 Rotating frame transformation

Since the earliest days of the theory of NMR, the rotating frame transformation (RFT) has been used in suitable systems to convert a time-dependent Hamiltonian $\hat{H}(t)$ written in the laboratory co-ordinate system into a time-independent Hamiltonian $\hat{H}'$. This is advantageous because it is much simpler to calculate the spin dynamics in a system with a time-independent Hamiltonian.

The transformation is often explained pictorially in terms of classical mechanics. For example, in high field NMR, the RFT switches to a co-ordinate system that rotates about the static magnetic field B_0 at the Larmor frequency (see [86] for further details). In these rotating co-ordinates, the Hamiltonian for a single nuclear spin with a resonant RF field becomes time-independent, allowing the description of RF pulses in terms of nutation angles: e.g. a π_x pulse.

However, it is also possible to present the RFT in the quantum mechanical formalism that we use to calculate magnetic field effects. The RFT amounts to a change of basis states from a normal time-independent basis such as the product basis to a cleverly chosen set of time-dependent basis states. In favourable cases, the transformation succeeds in shifting all of the time-dependence from the Hamiltonian into the definition of the basis states.

Following [85, 223], we consider a radical pair subject to orthogonal static and circularly polarised RF fields; in other words, where $\theta = \pi/2$ and $\phi_{rf} = \pi/2$. Substituting into equation (5.5), we write the time-dependent Hamiltonian as

$$\hat{H}(t;\gamma) = \sum_{N=A}^{B} \sum_{i} a_{iN} \hat{\boldsymbol{I}}_{iN} \cdot \hat{\boldsymbol{S}}_N + \omega_0 \hat{S}_{Nz} + \omega_1 \sqrt{\frac{1}{2}} \begin{bmatrix} \left(\hat{S}_{Nx} - \hat{S}_{Ny}\right) \cos\left(\omega_{rf} t + \gamma\right) \\ + \left(\hat{S}_{Nx} + \hat{S}_{Ny}\right) \sin\left(\omega_{rf} t + \gamma\right) \end{bmatrix}. \tag{5.6}$$

The wave function $|\psi\rangle(t)$ for a pure state in the laboratory co-ordinate system evolves according to the Schrödinger equation:

$$\frac{\partial |\psi\rangle(t)}{\partial t} = -\mathrm{i}\hat{H}(t;\gamma)|\psi\rangle(t). \tag{5.7}$$

The RFT produces a new set of wave functions $|\phi\rangle(t) = T(t)|\psi\rangle(t)$, where $T(t)$ is a time-dependent unitary transformation matrix. Differentiating this expression, we write

$$\frac{\partial |\phi\rangle(t)}{\partial t} = \frac{\partial T(t)}{\partial t}|\psi\rangle(t) + T(t)\frac{\partial |\psi\rangle(t)}{\partial t}. \tag{5.8}$$

Using equation (5.7) and the fact that $|\psi\rangle(t) = T^\dagger(t)|\phi\rangle(t)$, we write

$$\begin{aligned} \frac{\partial |\phi\rangle(t)}{\partial t} &= \left[\frac{\partial T(t)}{\partial t} - \mathrm{i}T(t)\hat{H}(t;\gamma)\right]|\psi\rangle(t) \\ &= -\mathrm{i}\underbrace{\left[\mathrm{i}\frac{\partial T(t)}{\partial t}T^\dagger(t) + T(t)\hat{H}(t;\gamma)T^\dagger(t)\right]}_{\hat{H}'}|\phi\rangle(t). \end{aligned} \tag{5.9}$$

This equation for the evolution of the rotating frame wave functions $|\phi\rangle(t)$ is identical in form to the Schrödinger equation if we identify the bracketed quantity as an effective

rotating frame Hamiltonian $\hat{H}'$. For this system, the rotating frame Hamiltonian does not depend on time if we choose the transformation operator

$$T(t) = \exp\left(\mathrm{i}\omega_{\mathrm{rf}} t \sum_{\mathrm{N=A}}^{\mathrm{B}} \left[\hat{S}_{\mathrm{Nz}} + \sum_i \hat{I}_{i\mathrm{z}}\right]\right). \tag{5.10}$$

Since spin operators for different spins commute, we may write this as

$$T(t) = \prod_i \exp\left(\mathrm{i}\hat{L}_{i\mathrm{z}}\omega_{\mathrm{rf}} t\right), \tag{5.11}$$

where the product is taken over all electron and nuclear spins $\hat{\boldsymbol{L}}_i$ in the radical pair.

Product operator rules

In order to find the rotating frame Hamiltonian, we evaluate equation (5.9), taking each term in the full Hamiltonian separately. First, however, we note a few useful identities for a general spin $\hat{\boldsymbol{L}}$ under a unitary transformation $U = \exp\left(\mathrm{i}\theta\hat{L}_{\mathrm{z}}\right)$:

$$\begin{aligned} U\hat{L}_{\mathrm{x}}U^{\dagger} &= \hat{L}_{\mathrm{x}}\cos\theta - \hat{L}_{\mathrm{y}}\sin\theta \\ U\hat{L}_{\mathrm{y}}U^{\dagger} &= \hat{L}_{\mathrm{x}}\sin\theta + \hat{L}_{\mathrm{y}}\cos\theta \\ U\hat{L}_{\mathrm{z}}U^{\dagger} &= \hat{L}_{\mathrm{z}}. \end{aligned} \tag{5.12}$$

Hyperfine term

Applying these rules to the hyperfine term, $\hat{\boldsymbol{I}}_{i\mathrm{N}} \cdot \hat{\boldsymbol{S}}_{\mathrm{N}}$, gives a contribution

$$\begin{aligned} &T(t)\left(\hat{\boldsymbol{I}}_{i\mathrm{N}} \cdot \hat{\boldsymbol{S}}_{\mathrm{N}}\right) T^{\dagger}(t) \\ &\quad= \left[\exp\left(\mathrm{i}\hat{I}_{i\mathrm{z}}\omega_{\mathrm{rf}} t\right)\hat{\boldsymbol{I}}_{i\mathrm{N}}\exp\left(-\mathrm{i}\hat{I}_{i\mathrm{z}}\omega_{\mathrm{rf}} t\right)\right] \cdot \left[\exp\left(\mathrm{i}\hat{S}_{\mathrm{Nz}}\omega_{\mathrm{rf}} t\right)\hat{\boldsymbol{S}}_{\mathrm{N}}\exp\left(-\mathrm{i}\hat{S}_{\mathrm{Nz}}\omega_{\mathrm{rf}} t\right)\right] \\ &\quad= \left[\hat{I}_{i\mathrm{x}}\cos\omega_{\mathrm{rf}} t - \hat{I}_{i\mathrm{y}}\sin\omega_{\mathrm{rf}} t\right]\left[\hat{S}_{\mathrm{Nx}}\cos\omega_{\mathrm{rf}} t - \hat{S}_{\mathrm{Ny}}\sin\omega_{\mathrm{rf}} t\right] \\ &\qquad+ \left[\hat{I}_{i\mathrm{x}}\sin\omega_{\mathrm{rf}} t + \hat{I}_{i\mathrm{y}}\cos\omega_{\mathrm{rf}} t\right]\left[\hat{S}_{\mathrm{Nx}}\sin\omega_{\mathrm{rf}} t - \hat{S}_{\mathrm{Ny}}\cos\omega_{\mathrm{rf}} t\right] + \hat{I}_{i\mathrm{z}}\hat{S}_{\mathrm{Nz}} \\ &\quad= \hat{\boldsymbol{I}}_{i\mathrm{N}} \cdot \hat{\boldsymbol{S}}_{\mathrm{N}}. \end{aligned} \tag{5.13}$$

In other words, the hyperfine term is unaffected by the RFT. Note that this is only the case when the hyperfine tensor is isotropic, or when it has axiality directed along the axis of rotation of the RF field.

Static field term

When the static field is oriented along the axis of rotation of the RF field, *i.e.* when $\theta = \pi/2$, it makes a contribution of $\omega_0\hat{S}_{\mathrm{Nz}}$ to both the full and rotating frame Hamiltonians. If $\theta \neq \pi/2$ then the rotating frame Hamiltonian would become time-dependent, and therefore cease to be useful.

RF field term

The RF field term makes a contribution proportional to

$$T(t)\left[\left(\hat{S}_{\mathrm{Nx}}-\hat{S}_{\mathrm{Ny}}\right)\cos\left(\omega_{\mathrm{rf}}t+\gamma\right)+\left(\hat{S}_{\mathrm{Nx}}+\hat{S}_{\mathrm{Ny}}\right)\sin\left(\omega_{\mathrm{rf}}t+\gamma\right)\right]T^{\dagger}(t)$$
$$=\hat{S}_{\mathrm{Nx}}\left(\cos\gamma+\sin\gamma\right)+\hat{S}_{\mathrm{Ny}}\left(\sin\gamma-\cos\gamma\right). \tag{5.14}$$

In other words, the RF field makes a contribution to the rotating frame Hamiltonian as if it were a static field with the same strength, oriented along the direction that the RF field has instantaneously at $t=0$ in the laboratory frame. Since there is axial symmetry about the z-axis for the RP systems that we consider, γ is irrelevant and we may choose our coordinate system such that $\gamma=\pi/4$ for convenience. There is therefore no need to average over γ when the RFT is applicable.

"Coriolis" term

The term $\mathrm{i}\frac{\partial T(t)}{\partial t}T^{\dagger}(t)$ is an additional contribution that arises in the rotating frame Hamiltonian as a side-effect of the time dependence of the transformed basis states. It is analogous to the Coriolis "force" that must be included when working in a non-inertial reference frame in classical mechanics [249]. Using the definition of $T(t)$ in equation (5.11), we write

$$\mathrm{i}\frac{\partial T(t)}{\partial t}T^{\dagger}(t)=\mathrm{i}\sum_{i}\mathrm{i}\hat{L}_{iz}\omega_{\mathrm{rf}}T(t)T^{\dagger}(t)=-\omega_{\mathrm{rf}}\sum_{i}\hat{L}_{iz}. \tag{5.15}$$

This term is almost equivalent to the Zeeman interaction with a fictitious magnetic field along the $-z$-axis. The only quirk with this interpretation is that the field appears to have strength $B_1^{\mathrm{eff}}=\omega_{\mathrm{rf}}/\gamma_{\mathrm{e}}$ to the electrons but it must appear much stronger ($B_1^{\mathrm{eff}}=\omega_{\mathrm{rf}}/\gamma_{\mathrm{n}}$) to the nuclei in order that both electron and nuclear spins precess at the same frequency.

Liouville–von Neumann equation

Thus far, we have shown how a clever choice of basis states transforms the Hamiltonian of a RP in the presence of a circularly polarised RF field into a time-independent rotating frame Hamiltonian $\hat{H}'$. In terms of these new basis states, the wave function of the RP evolves according to the normal time-dependent Schrödinger equation with the $\hat{H}'$ replacing the Hamiltonian.

Now, in order to calculate magnetic field effects, we frequently need to treat systems that are not found in a pure state. For example, we normally consider that there is negligible nuclear spin polarisation at the instant of RP creation and therefore consider an ensemble of RPs with all possible nuclear spin states. This is most easily done by using the density matrix formalism. A system is described by its density matrix

$$\hat{\rho}(t)=|\psi\rangle\langle\psi|(t) \tag{5.16}$$

which evolves under the action of the Liouville–von Neumann equation

$$\frac{\partial\hat{\rho}(t)}{\partial t}=-\mathrm{i}\left[\hat{H}(t),\hat{\rho}(t)\right]. \tag{5.17}$$

The expectation value of an operator $\hat{\Omega}$ is given by

$$\left\langle \hat{\Omega} \right\rangle (t) = \mathrm{Tr}\left[\hat{\Omega}\hat{\rho}(t)\right]. \tag{5.18}$$

Making the transformation to the rotating frame, we find that the system may also be described by its rotating frame density matrix

$$\hat{\rho}'(t) = |\phi\rangle\langle\phi|(t) = T(t)\hat{\rho}(t)T^{\dagger}(t) \tag{5.19}$$

which evolves under the action of the Liouville–von Neumann equation

$$\frac{\partial \hat{\rho}'(t)}{\partial t} = -\mathrm{i}\left[\hat{H}'(t), \hat{\rho}'(t)\right]. \tag{5.20}$$

The expectation value of an operator $\hat{\Omega}$ is given by

$$\left\langle \hat{\Omega} \right\rangle (t) = \mathrm{Tr}\left[\hat{\Omega}\hat{\rho}(t)\right] = \mathrm{Tr}\left[\hat{\Omega}T^{\dagger}(t)T(t)\hat{\rho}(t)T^{\dagger}(t)T(t)\right] \tag{5.21}$$

which by cyclic permutation of the trace gives

$$\left\langle \hat{\Omega} \right\rangle (t) = \mathrm{Tr}\left[T(t)\hat{\Omega}T^{\dagger}(t)T(t)\hat{\rho}(t)T^{\dagger}(t)\right] = \mathrm{Tr}\left[\hat{\Omega}'\hat{\rho}'(t)\right]. \tag{5.22}$$

Singlet projection operator

In order to calculate RP singlet probabilities in the rotating frame it remains only to consider the form of the singlet projection operator, $\hat{P}^{\mathrm{S}} = \frac{1}{4} - \hat{\boldsymbol{S}}_{\mathrm{A}} \cdot \hat{\boldsymbol{S}}_{\mathrm{B}}$, as we transform to the rotating frame. Applying equation (5.12) gives

$$\begin{aligned}
&T(t)\left(\frac{1}{4} - \hat{\boldsymbol{S}}_{\mathrm{A}} \cdot \hat{\boldsymbol{S}}_{\mathrm{B}}\right) T^{\dagger}(t) \\
&\quad = \frac{1}{4} - \left[\exp\left(\mathrm{i}\hat{S}_{\mathrm{Az}}\omega_{\mathrm{rf}}t\right)\hat{\boldsymbol{S}}_{\mathrm{A}}\exp\left(-\mathrm{i}\hat{S}_{\mathrm{Az}}\omega_{\mathrm{rf}}t\right)\right] \cdot \left[\exp\left(\mathrm{i}\hat{S}_{\mathrm{Bz}}\omega_{\mathrm{rf}}t\right)\hat{\boldsymbol{S}}_{\mathrm{B}}\exp\left(-\mathrm{i}\hat{S}_{\mathrm{Bz}}\omega_{\mathrm{rf}}t\right)\right] \\
&\quad = \frac{1}{4} - \left[\hat{S}_{\mathrm{Ax}}\cos\omega_{\mathrm{rf}}t - \hat{S}_{\mathrm{Ay}}\sin\omega_{\mathrm{rf}}t\right]\left[\hat{S}_{\mathrm{Bx}}\cos\omega_{\mathrm{rf}}t - \hat{S}_{\mathrm{By}}\sin\omega_{\mathrm{rf}}t\right] \\
&\qquad - \left[\hat{S}_{\mathrm{Ax}}\sin\omega_{\mathrm{rf}}t + \hat{S}_{\mathrm{Ay}}\cos\omega_{\mathrm{rf}}t\right]\left[\hat{S}_{\mathrm{Bx}}\sin\omega_{\mathrm{rf}}t - \hat{S}_{\mathrm{By}}\cos\omega_{\mathrm{rf}}t\right] - \hat{S}_{\mathrm{Az}}\hat{S}_{\mathrm{Bz}} \\
&\quad = \frac{1}{4} - \hat{\boldsymbol{S}}_{\mathrm{A}} \cdot \hat{\boldsymbol{S}}_{\mathrm{B}}.
\end{aligned} \tag{5.23}$$

In other words, the singlet projection operator is unaffected by the RFT. The same result also holds for the triplet projection operator.

Summary

The derivation above is for CPL+ RF fields ($\phi_{\mathrm{rf}} = +\pi/2$) which rotate in the same sense as the Larmor precession. CPL− RF fields may be treated in the same manner. The CPL− Hamiltonian may also be obtained by symmetry, replacing $\omega_0 \rightarrow -\omega_0$ in the Hamiltonian.

Combining these results, the rotating frame Hamiltonian for a system with $\theta = \pi/2$ and $\phi_{\mathrm{rf}} = \pm\pi/2$ (*i.e.* CPL±) is

$$\hat{H}' = \sum_{\mathrm{N=A}}^{\mathrm{B}} \left(\pm\omega_0 - \omega_{\mathrm{rf}}\right)\hat{S}_{\mathrm{Nz}} + \omega_1\hat{S}_{\mathrm{Nx}} + \sum_i \left\{a_{i\mathrm{N}}\hat{\boldsymbol{I}}_{i\mathrm{N}} \cdot \hat{\boldsymbol{S}}_{\mathrm{N}} - \omega_{\mathrm{rf}}\hat{I}_{iz}\right\}. \tag{5.24}$$

In such systems, the rotating frame Hamiltonian given here is exact. This Hamiltonian is time-independent and contains no interactions between the two radicals; it is of the form $\hat{H} = \hat{H}^{\mathrm{A}} + \hat{H}^{\mathrm{B}}$. Since the singlet and triplet projection operators are unaffected by the RFT, we may henceforth calculate singlet yields in appropriate cases using the efficient approaches derived in §2.2.

In radical pairs with non-axial hyperfine interactions, or where the hyperfine axiality is not along the RF axis, or when the RF field is not circularly polarised, or when there is a static field that is not along the RF axis, the rotating frame Hamiltonian is time-dependent. In such situations, the RFT provides no benefit for an exact calculation.

On a practical note, it is possible to determine quite simply whether a given radical pair and set of magnetic field parameters are suitable for exact calculation using the RFT. Hence, the core `Matlab` code developed in Chapters 2 and 4 and the MySQL database [205] of singlet yields discussed in §4.2.4 were extended such that whenever a singlet yield calculation is requested, the results are either looked up in the database very rapidly, or, failing that, calculated using an exact RFT, or, failing that calculated using the full γ–`COMPUTE` algorithm. This simple enhancement improves the performance of many calculations without any burden of deciding manually which method to employ for each data point in a calculated spectrum.

5.2.4 Rotating frame approximation

In high field NMR, the RF fields applied by the spectrometer probe are typically linearly polarised. Similarly, in high field EPR, the microwaves applied to the sample are linearly polarised. Nevertheless, as explained in §5.2.1, such linearly polarised fields may be considered to be the superposition of two *notional* circularly polarised fields. For example, we may write a linearly polarised field of RMS RF field strength $B_1 = -\omega_1/\gamma_{\mathrm{e}}$ as

$$\boldsymbol{B}_{\mathrm{LIN}}(t) = \boldsymbol{i}\sqrt{2}\omega_1 \cos\omega_{\mathrm{rf}} t = \tilde{\boldsymbol{B}}_{\mathrm{CPL}+}(t) + \tilde{\boldsymbol{B}}_{\mathrm{CPL}-}(t), \tag{5.25}$$

where the notional circularly polarised fields are

$$\tilde{\boldsymbol{B}}_{\mathrm{CPL}\pm}(t) = \boldsymbol{i}\sqrt{\frac{1}{2}}\omega_1 \cos\omega_{\mathrm{rf}} t \pm \boldsymbol{j}\sqrt{\frac{1}{2}}\omega_1 \sin\omega_{\mathrm{rf}} t. \tag{5.26}$$

Notice that each notional circularly polarised RF field has RMS strength $B_1^{\diamond} = B_1/\sqrt{2}$.

The RFT outlined above is not capable of eliminating the time-dependence of the Hamiltonian exactly for a system under the influence of $\boldsymbol{B}_{\mathrm{LIN}}(t)$. However, when the radio frequency ν_{rf} is close to resonance, the $\tilde{\boldsymbol{B}}_{\mathrm{CPL}+}(t)$ component satisfies the Zeeman resonance condition, whilst the $\tilde{\boldsymbol{B}}_{\mathrm{CPL}-}(t)$ component is $\sim 2\nu_{\mathrm{rf}}$ away from resonance. This is significantly more than the linewidth. Therefore, in high field NMR and EPR, it is an excellent approximation to neglect the effects of the $\tilde{\boldsymbol{B}}_{\mathrm{CPL}-}(t)$ component of the RF field. It is then quite possible to calculate the effects of the $\tilde{\boldsymbol{B}}_{\mathrm{CPL}+}(t)$ component alone using the RFT outlined above. Neglecting the effects of the $\tilde{\boldsymbol{B}}_{\mathrm{CPL}-}(t)$ component of a linearly polarised RF field is known as the "rotating frame approximation" [185, 238–242].

The rotating frame approximation is well-attested experimentally at high fields. It gives excellent agreement with measured signals. Furthermore, in pulse NMR, quadrature detection of the RF fields emitted by the sample shows that they are circularly polarised. Similarly, in recent work on THz frequency EPR techniques, a Fabry-Perot interferometer is often employed to detect the EPR signal. Such detectors function because the sample preferentially absorbs the on-resonance $\tilde{\boldsymbol{B}}_{\mathrm{CPL}+}(t)$ component of the microwave field converting the linear polarisation of the incident microwaves into elliptical polarisation [250, 251].

The situation is expected to be more complex in the low magnetic fields employed here for measurements of chemical magnetic field effects. As the static field strength decreases, the EPR resonant frequency will become comparable to the width of the optically-detected EPR (OD EPR) line. In this low field regime, we may expect that the $\tilde{\boldsymbol{B}}_{\mathrm{CPL}-}(t)$ component is no longer truly off resonance, and hence the rotating frame approximation will break down. We consider this change from high field to low field behaviour in more detail below.

Finally, the experiments discussed below are amongst the first direct tests of the effect of polarisation in the *incident* RF field. The only other area of magnetic resonance where circularly polarised fields are sometime employed is in magnetic resonance imaging [252, 253] and [86, p218]. These experiments therefore form a useful contribution to the broader field of magnetic resonance.

5.3 OMFE polarisation effects

5.3.1 Introduction

An oscillating magnetic field effect (OMFE) experiment comprises a series of measurements of reaction product yield in the presence of an RF magnetic field but without any static field. Measurements of the yield are taken for many different radio frequencies $\nu_{\mathrm{rf}} = \omega_{\mathrm{rf}}/2\pi$. In the present work, these cover the range 5–80 MHz. The OMFE spectrum is a plot of product yield against radio frequency. OMFE experiments have been performed in Oxford on several systems during the last decade [175–178].

OMFE spectra taken using circularly polarised RF fields may be calculated most efficiently using the rotating frame transformation outlined in §5.2.3. For other RF polarisations, the γ–`COMPUTE` algorithm outlined in §4.2.3 is most suitable. In both cases, the appropriate Hamiltonian is given by equation (5.5), with $\omega_0 = 0$ since no static field is present. This Hamiltonian defines the RF field in terms of its RMS strength $B_1 = -\omega_1/\gamma_{\mathrm{e}}$.

5.3.2 Preliminary calculations

Figures 5.3–5.6 show preliminary calculations of the OMFE spectra in a radical pair containing a single spin-½ magnetic nucleus. These results demonstrate that, in the absence of a static field, CPL+ and CPL− fields have identical effects on singlet yield. Furthermore, we recall from §5.2.1 that a LIN field may be considered as a superposition of CPL± fields. Since the latter have identical effects on singlet yield, it is striking that the effects of a LIN field should differ so markedly. Remarkably, these calculations predict significant differences in the OMFE spectra for LIN and CPL fields over a

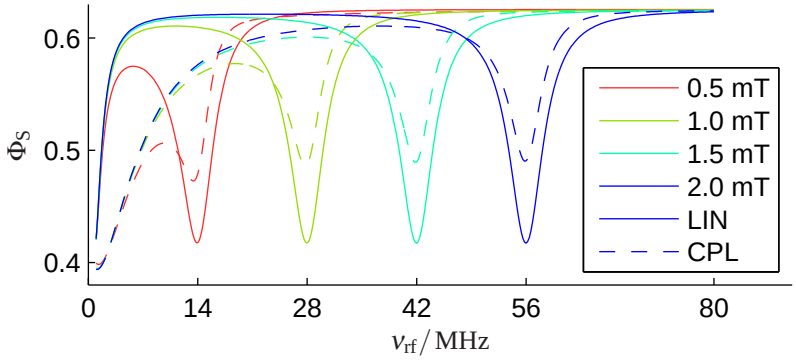

Figure 5.3: Influence of hyperfine coupling constant and RF polarisation on calculated OMFE spectra. As indicated in the legend, each spectrum is for a radical pair with a single spin-½ nucleus, whose HFC is shown, with an RF field that is either linearly or circularly polarised. Calculations were performed using γ–COMPUTE or the RFT as appropriate. Other parameters: $k = 2.8 \times 10^6\,\mathrm{s}^{-1}$, $n = 64$, $\theta = \pi/2$, $B_1 = 0.1\,\mathrm{mT}$ and $B_0 = 0\,\mathrm{mT}$. CPL+ and CPL− fields have identical effects and are labelled CPL in the figure.

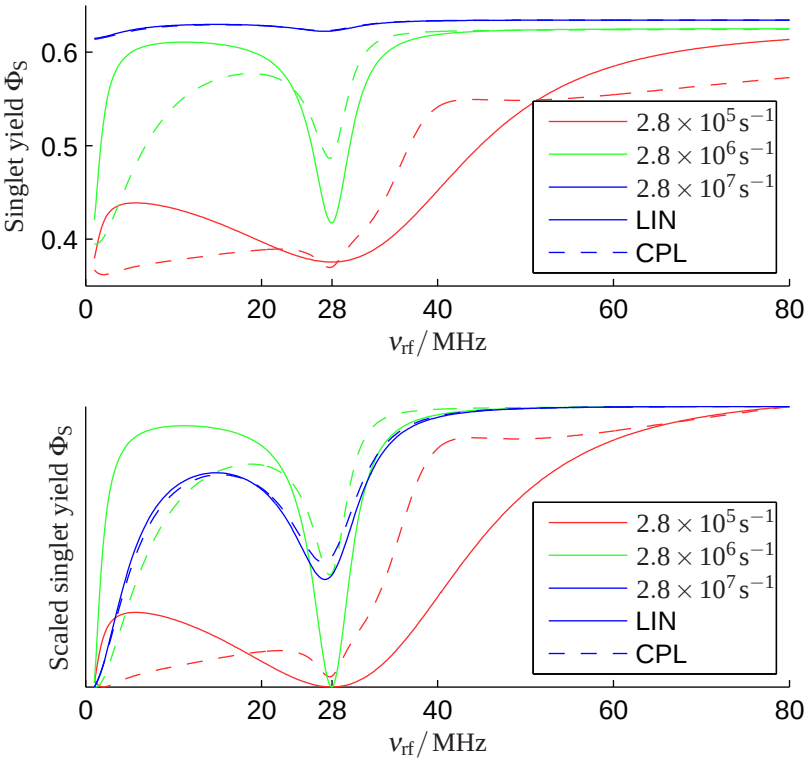

Figure 5.4: Influence of exponential model rate constant k and RF polarisation, both shown in the legend, on calculated OMFE spectra. Calculations were performed using γ–COMPUTE or the RFT. Each spectrum is for a radical pair with a single spin-½ nucleus, with a $1.0\,\mathrm{mT}$ HFC, $n = 64$, $\theta = \pi/2$, $B_1 = 0.1\,\mathrm{mT}$ and $B_0 = 0\,\mathrm{mT}$. The lower figure shows the singlet yields after normalisation in order to emphasise changes in the spectral shape. CPL+ and CPL− fields have identical effects and are labelled CPL in the figure.

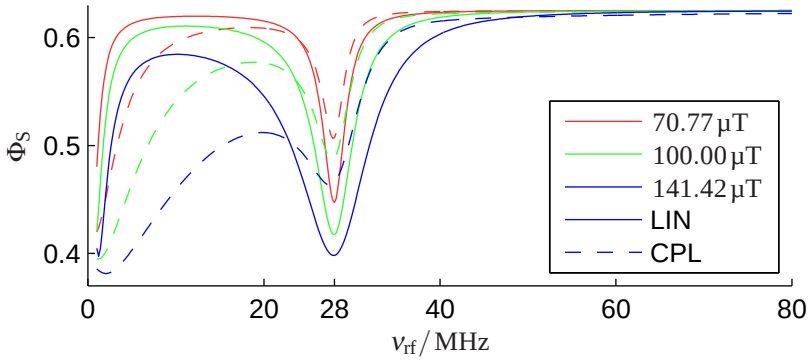

Figure 5.5: Influence of RF field strength $B_1 = -\omega_1/\gamma_e$ and polarisation, both shown in the legend, on calculated OMFE spectra. Calculations were performed using γ–COMPUTE or the RFT. Each spectrum is for a radical pair with a single spin-½ nucleus, with a 1.0 mT HFC, $n = 64$, $\theta = \pi/2$, $k = 2.8 \times 10^6\,\mathrm{s}^{-1}$ and $B_0 = 0$ mT. CPL+ and CPL− fields have identical effects and are labelled CPL in the figure.

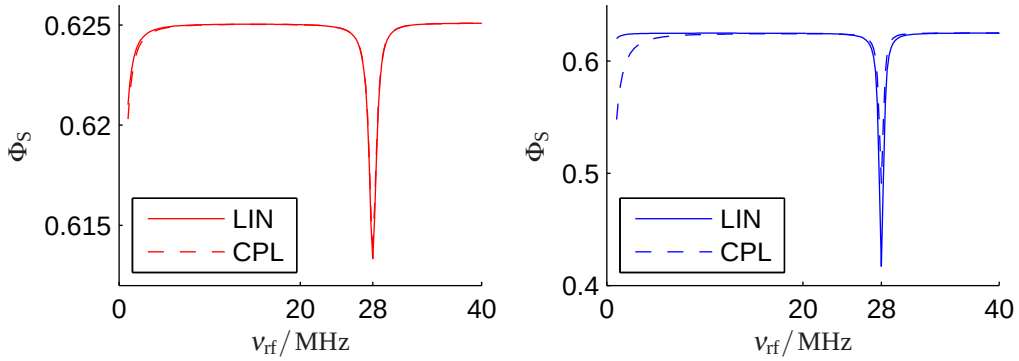

(a) $k = 2.8 \times 10^6\,\mathrm{s}^{-1}$ (b) $k = 2.8 \times 10^5\,\mathrm{s}^{-1}$

Figure 5.6: Influence of RF polarisation on calculated OMFE spectra in systems with $B_1 = -\omega_1/\gamma_e = 10\,\mu$T at two different rate constants k. Calculations were performed using γ–COMPUTE or the RFT. Each spectrum is for a radical pair with a single spin-½ nucleus, with a 1.0 mT HFC, $n = 128$, $\theta = \pi/2$ and $B_0 = 0$ mT. There is essentially no change in singlet yield as the radio frequency is increased above 40 MHz. CPL+ and CPL− fields have identical effects and are labelled CPL in the figure.

range of physically sensible choices of hyperfine coupling constant, exponential model rate constant and RF field strength.

Figure 5.3 shows OMFE spectra in radical pairs with a single spin-½ nucleus. Spectra are calculated with four choices of isotropic hyperfine constant a. Each spectrum shows resonant features around $\nu_{\mathrm{rf}} = 0\,\mathrm{MHz}$ and around the hyperfine resonance frequency $\nu_{\mathrm{rf}} = -\gamma_{\mathrm{e}} a/2\pi \approx a \times 28\,\mathrm{MHz}$, where the hyperfine constant a is measured in mT. RF polarisation affects the depth and width of these two features, but not their position. Around the hyperfine resonance, the CPL resonance is less pronounced than that for LIN. Whilst around the zero-frequency resonance, the CPL resonance is marginally deeper and significantly wider than the LIN. As the frequency increases above the hyperfine resonance, RF polarisation ceases to have any discernible effect.

Figure 5.4 shows OMFE spectra calculated with three different choices of exponential model rate constant k. The top subfigure shows that for reasonably long-lived radicals, with $k = 2.8 \times 10^6\,\mathrm{s}^{-1}$, there are pronounced polarisation effects on the zero-frequency and hyperfine resonance intensity and linewidth. As the radical pair lifetime is increased, e.g. with $k = 2.8 \times 10^5\,\mathrm{s}^{-1}$, these resonances merge to give a broad spectral feature whose shape depends on the RF polarisation. The third spectrum, with $k = 2.8 \times 10^7\,\mathrm{s}^{-1}$ demonstrates that whatever its polarisation, the effects of an RF field diminish as the radical pair lifetime is shortened. The lower subfigure plots the same OMFE spectra, normalising the singlet yield in order to emphasise lineshape effects. It is clear that the influence of RF polarisation on lineshape decreases as the radical pair lifetime falls.

Figure 5.5 shows OMFE spectra calculated for LIN and CPL fields with three different RF field strengths $B_1 = -\omega_1/\gamma_{\mathrm{e}}$. As the field strength is increased, the resonances in all six OMFE spectra increase in depth and width; the difference between LIN and CPL spectra also increases. Between the three spectra, the RMS RF field strength is increased each time by a factor of $\sqrt{2}$. Since all six spectra are visibly different, we can be confident that these polarisation effects are not merely an artefact of choosing to keep the RMS RF field strength B_1 constant as we change polarisation. For example, the red LIN and green CPL spectra both have a peak RF field strength of $100\,\mu\mathrm{T}$, yet they differ markedly at frequencies below the hyperfine resonance.

Finally, Figure 5.6 shows magnified OMFE spectra calculated at a rather weak RF field strength: $10\,\mu\mathrm{T}$. Figure 5.6a demonstrates that hyperfine and zero-frequency resonances become rather sharp and small at low RF field strengths. Furthermore, LIN and CPL fields produce almost indistinguishable changes in singlet yield at such small RF field strengths. However, Figure 5.6b demonstrates that as the radical pair lifetime increases, RF polarisation effects persist for progressively weaker RF fields. Taken together these figures suggest that LIN and CPL fields are never truly equivalent, but that as the field strength is decreased, it takes a longer time for the polarisation effects to manifest themselves as differences in the RP singlet probability. The figures also confirm that we are sensible in comparing LIN and CPL fields of the same RMS field strength B_1. Any other scaling of the LIN and CPL field strengths would produce markedly different OMFE spectra (calculated, but not shown) even with such weak fields.

To summarise, in radical pairs with a single spin-½ nucleus, theory predicts significant differences between the OMFE spectra measured with LIN and CPL RF fields. These RF polarisation effects occur for a plausible range of hyperfine coupling con-

stants, exponential model rate constants and RF field strengths. The effects are most pronounced in long-lived radical pairs subjected to strong RF fields. It is sensible to compare RF fields that have the same RMS field strength, since these give the same OMFE spectra in systems with very weak RF fields or with short-lived radical pairs. Furthermore, the effects of polarisation are not simply a scaling of RF field strength by a factor of 2 or $\sqrt{2}$.

5.3.3 Interpretation

At first glance, one might argue that CPL and LIN polarised RF fields should produce identical OMFE spectra. The argument would proceed along the following lines: CPL$\pm$ fields produce identical OMFE spectra; a LIN field is the superposition of two notional CPL$\pm$ fields; therefore, a LIN field should produce the same OMFE spectra as a CPL$\pm$ field of equivalent power. However, we have demonstrated above that OMFE spectra of several radical pair systems are sensitive in a non-trivial manner to RF polarisation. We now show from a theoretical viewpoint that OMFE spectra may normally be expected to be sensitive to RF polarisation.

Eigenvalues of the Hamiltonian

For the first approach, we consider a one-proton radical pair with Hamiltonian

$$\hat{H}_{\mathrm{LIN}}(t) = a\hat{\boldsymbol{I}}\cdot\hat{\boldsymbol{S}}_{\mathrm{A}} + \omega_1\sqrt{2}\cos\left(\omega_{\mathrm{rf}}t+\gamma\right)\left(\hat{S}_{\mathrm{Az}}+\hat{S}_{\mathrm{Bz}}\right) \tag{5.27}$$

$$\hat{H}_{\mathrm{CPL}}(t) = a\hat{\boldsymbol{I}}\cdot\hat{\boldsymbol{S}}_{\mathrm{A}} + \omega_1\cos\left(\omega_{\mathrm{rf}}t+\gamma\right)\left(\hat{S}_{\mathrm{Az}}+\hat{S}_{\mathrm{Bz}}\right) \pm \omega_1\sin\left(\omega_{\mathrm{rf}}t+\gamma\right)\left(\hat{S}_{\mathrm{Ax}}+\hat{S}_{\mathrm{Bx}}\right) \tag{5.28}$$

in the presence of LIN and CPL[1] RF respectively. Notice that we have chosen to compare systems with the same RMS RF field strength $B_1 = -\omega_1/\gamma_{\mathrm{e}}$. Writing spin operators explicitly in the product basis gives an 8×8 real, symmetric Hamiltonian with eigenvalues

LIN	**CPL**
$\frac{a}{4}$ (twice)	$\frac{a}{4}$ (twice)
$\frac{a}{4}\pm\sqrt{2}\omega_1 c$	$\frac{a}{4}\pm\omega_1$
$\frac{1}{4}\left(-a\pm 2\sqrt{2}\omega_1 c\pm 2\sqrt{a^2+2\omega_1^2c^2}\right)$	$\frac{1}{4}\left(-a\pm 2\sqrt{a^2+2\omega_1^2\pm 2\omega_1\sqrt{a^2+\omega_1^2}}\right)$

where $c=\cos\left(\omega_{\mathrm{rf}}t+\gamma\right)$ and where all combinations of the $\pm$ in the final row should be taken to give four eigenvalues.

Although these eigenvalues appear similar to one-another, there is a critical difference: the eigenvalues in the CPL case do not depend on time, whereas those in the LIN case are time-dependent. Physically, this corresponds to the fact that the strength of a CPL field does not depend on time, whereas the strength of a LIN field is time-dependent. Since this radical pair system contains only isotropic interactions, the

[1] Since CPL$\pm$ have identical effects at zero static field, we refer to CPL+ as "CPL" in this section for brevity.

Zeeman interaction energy is the same whatever the orientation of the applied field. Combining these arguments, the CPL field must have a time-independent set of energy levels (*i.e.* eigenvalues of the Hamiltonian). In contrast, the LIN field does change field strength over time, and hence its energy levels must do likewise.

The significance of this time-dependence may be exposed by expanding the Hamiltonian using the spectral theorem.

$$\hat{H}_{\mathrm{LIN}}(t) = X_{\mathrm{LIN}}(t)\Lambda_{\mathrm{LIN}}(t)X_{\mathrm{LIN}}^{\dagger}(t) \tag{5.29}$$

$$\hat{H}_{\mathrm{CPL}}(t) = X_{\mathrm{CPL}}(t)\Lambda_{\mathrm{CPL}}X_{\mathrm{CPL}}^{\dagger}(t) \tag{5.30}$$

where X is the unitary matrix of eigenvectors and Λ is the diagonal matrix of eigenvalues of $\hat{H}$.

Suppose in the CPL case that there exists a time-dependent unitary matrix $T(t)$ such that

$$T(t)X_{\mathrm{CPL}}(t) = Y_{\mathrm{CPL}}, \tag{5.31}$$

where Y_{CPL} does not depend on time. Then, the quantity

$$T(t)\hat{H}_{\mathrm{CPL}}(t)T^{\dagger}(t) = Y_{\mathrm{CPL}}\Lambda_{\mathrm{CPL}}Y_{\mathrm{CPL}}^{\dagger} \tag{5.32}$$

will not depend on time. Providing that the "Coriolis" term $\frac{\partial T(t)}{\partial t}T^{\dagger}(t)$ also does not depend on time, we can make a change of basis to produce a time-independent effective Hamiltonian. The rotating frame transformation, outlined in §5.2.3, arises from one such choice of time-dependent unitary transform $T(t)$.

Unfortunately, in the linear case, even if there exists an equivalent unitary matrix $T(t)$ then the quantity

$$T(t)\hat{H}_{\mathrm{LIN}}T^{\dagger}(t) = Y_{\mathrm{LIN}}\Lambda_{\mathrm{LIN}}(t)Y_{\mathrm{LIN}}^{\dagger} \tag{5.33}$$

is still time-dependent. Except in very special cases where the "Coriolis" term exactly counteracts this time dependence, equation (5.33) means that the Hamiltonian for a LIN field is inherently time-dependent and that this time dependence cannot be removed by a unitary transform (*i.e.* by a change of basis). Therefore, not only does the rotating frame transformation not hold for LIN fields, but there is no possibility to find an analogous transformation either.

Baker-Campbell-Hausdorff and Zassenhaus formulae

In the second approach, we consider a one-proton radical pair with Hamiltonians

$$\hat{H}_{\mathrm{LIN}}(t) = a\hat{\boldsymbol{I}}\cdot\hat{\boldsymbol{S}}_{\mathrm{A}} + \omega_1\cos\omega_{\mathrm{rf}}t\left(\hat{S}_{\mathrm{Az}} + \hat{S}_{\mathrm{Bz}}\right) \tag{5.34}$$

$$\hat{H}_{\mathrm{CPL}\pm}(t) = a\hat{\boldsymbol{I}}\cdot\hat{\boldsymbol{S}}_{\mathrm{A}} + \omega_1\cos\omega_{\mathrm{rf}}t\left(\hat{S}_{\mathrm{Az}} + \hat{S}_{\mathrm{Bz}}\right) \pm \omega_1\sin\omega_{\mathrm{rf}}t\left(\hat{S}_{\mathrm{Ax}} + \hat{S}_{\mathrm{Bx}}\right) \tag{5.35}$$

in the LIN and CPL cases respectively. Notice that this time the RF fields are defined in terms of their peak strength $B_1 = -\omega_1/\gamma_{\mathrm{e}}$. Systems with initial RF phase $\gamma \neq 0$ may be treated using equivalent working.

The spin evolution during the interval $0 \rightarrow t$ may be written in terms of a propagator

$$U(0,t) = \hat{T}\exp\left(-\mathrm{i}\int_0^t \hat{H}(t')\,\mathrm{d}t'\right). \tag{5.36}$$

Assuming that the Hamiltonian is constant within n short time intervals τ_k at times t_k, we expand the propagator to give

$$U(0,t) \approx \exp\left(-\mathrm{i}\hat{H}(t_1)\tau_1\right)\exp\left(-\mathrm{i}\hat{H}(t_2)\tau_2\right)\cdots\exp\left(-\mathrm{i}\hat{H}(t_n)\tau_n\right). \tag{5.37}$$

As the number of intervals n increases, this product converges exactly to the desired propagator $U(0,t)$.

Now, let us focus on a single time interval τ_k and the associated propagator

$$U_k = \exp\left(-\mathrm{i}\hat{H}(t_k)\tau_k\right). \tag{5.38}$$

During this interval spin evolution under the LIN field is

$$U_{\mathrm{LIN}} = \exp\left(-\mathrm{i}\hat{H}_{\mathrm{LIN}}(t_k)\tau_k\right) = \exp\left(-\frac{\mathrm{i}}{2}\left[\hat{H}_{\mathrm{CPL}+}(t_k)+\hat{H}_{\mathrm{CPL}-}(t_k)\right]\tau_k\right). \tag{5.39}$$

The second of these exponentials may be expanded using the Zassenhaus formula [254, 255], which is the dual of the celebrated Baker-Campbell-Hausdorff (BCH) formula [256–259]. (To give an idea of interest in these formulae, no fewer than seven proofs of the BCH formula are given in [260] and references therein.) The Zassenhaus formula states that

$$\mathrm{e}^{t(A+B)} = \mathrm{e}^{tA}\mathrm{e}^{tB}\mathrm{e}^{-\frac{t^2}{2}[A,B]}\mathrm{e}^{\frac{t^3}{6}(2[B,[A,B]]+[A,[A,B]])}\mathrm{e}^{t^4\ldots}\ldots \tag{5.40}$$

where t is a complex number and A and B multiply non-commutatively. Applying the Zassenhaus formula to the single time step propagator U_{LIN}, we find that

$$U_{\mathrm{LIN}} = \mathrm{e}^{-\frac{\mathrm{i}\tau_k}{2}\hat{H}_{\mathrm{CPL}+}(t_k)}\mathrm{e}^{-\frac{\mathrm{i}\tau_k}{2}\hat{H}_{\mathrm{CPL}-}(t_k)}\mathrm{e}^{\frac{\tau_k^2}{8}\left[\hat{H}_{\mathrm{CPL}+}(t_k),\hat{H}_{\mathrm{CPL}-}(t_k)\right]}\ldots. \tag{5.41}$$

In other words, the spin evolution during one step of the LIN field is equivalent to evolution during half a step of CPL+, then half a step of CPL− and then some correction factors. The first of these correction factors depends on the commutator

$$\left[\hat{H}_{\mathrm{CPL}+}(t_k),\hat{H}_{\mathrm{CPL}-}(t_k)\right]$$

which vanishes only when $\omega_1 = 0$. Hence, even though CPL± produce the same changes in singlet yield, we should not expect a LIN field to be the same.

5.3.4 Equivalence of weak LIN and CPL fields

The preceding arguments show conclusively that LIN and CPL fields may not in general be expected to produce identical OMFE spectra. However, it is clear from Figure 5.6a that very weak LIN and CPL fields with the same RMS field strength often *do* have equivalent effects. Indeed in the limit as $\omega_1 \to 0$, $\hat{H}_{\mathrm{LIN}} = \hat{H}_{\mathrm{CPL}}$; there can be no "polarisation" effect without an RF field. Since the RP Hamiltonian is differentiable with respect to RF field strength, one could envisage expanding all the resulting properties as a Taylor series in B_1. It therefore seems quite plausible that the polarisation effect of a weak RF field should be small.

Timescale of RF polarisation effects

Figures 5.7 and 5.8 present several calculations of the time-dependent singlet probability in the one-proton radical pair that was used for Figures 5.5 and 5.6. A radio frequency of 28 MHz is chosen, corresponding to the centre of the hyperfine resonance seen in the OMFE spectra. In the RP used, singlet yield is most sensitive to RF polarisation around this frequency.

In Figure 5.7, the RF field strength $B_1 = 100\,\mu\text{T}$, which is sufficient to produce a significant polarisation effect with an exponential model rate constant $k = 2.8 \times 10^6\,\text{s}^{-1}$. Figure 5.7a shows strong hyperfine-driven singlet–triplet probability oscillation in the absence of an RF field. Both LIN and CPL fields act to modulate these hyperfine-driven oscillations. Notice in particular that the differences between the no RF, LIN and CPL singlet probability set in gradually during the first few 100 ns. The polarisation effect (LIN *vs*. CPL) takes longer to develop than the OMFE (no RF *vs*. with RF). This explains why the exponential model rate constant k is critical to the observation of a polarisation effect. If the rate constant is too large, then no appreciable difference in singlet probability will have accumulated during the RP lifetime and there will be no polarisation effect.

Figure 5.7b shows the change in singlet probability caused by an RF field in the same system. Notice that, once three or four RF cycles (36 ns each) have elapsed, the spin evolution depends markedly on the initial RF phase. After about 450 ns, the singlet probabilities with different γ become very similar. For longer times, there is a beating effect where the singlet probabilities for different γ alternate between being disparate and similar. Experimentally, RPs are generated by continuous UV photolysis and therefore we must average over the initial RF phase. The results of this γ-averaging are shown in Figure 5.7c. The averaging process delays the onset of a significant effect of RF polarisation on singlet probability.

Finally, Figure 5.8 repeats these calculations in the presence of a weaker RF field ($B_1 = 10\,\mu\text{T}$). With an exponential model rate constant $k = 2.8 \times 10^6\,\text{s}^{-1}$, this RF field produces a barely perceptible polarisation effect as shown in Figure 5.6. Nevertheless, it is clear that there are significant differences between the singlet probability for LIN and CPL fields for many values of the RF phase γ. Yet, the γ-averaging step eliminates these polarisation effects (to plotting accuracy).

Time-dependent perturbation theory

In light of the slow, RF-field-strength-dependent onset of polarisation effects, it seems natural to make a perturbation theory analysis. We present here the most fruitful of several such approaches that we attempted.

First, we separate the Hamiltonian for a one-proton radical pair into terms

$$\hat{H} = \hat{H}_0 + \hat{V}(t), \tag{5.42}$$

where $\hat{H}_0 = a\hat{\boldsymbol{I}} \cdot \hat{\boldsymbol{S}}_\text{A}$ does not depend on time and where

$$\hat{V}(t) = \begin{cases} \omega_1 \sqrt{2} \cos\left(\omega_\text{rf} t + \gamma\right) \left(\hat{S}_\text{Az} + \hat{S}_\text{Bz}\right) \\ \omega_1 \cos\left(\omega_\text{rf} t + \gamma\right) \left(\hat{S}_\text{Az} + \hat{S}_\text{Bz}\right) \pm \omega_1 \sin\left(\omega_\text{rf} t + \gamma\right) \left(\hat{S}_\text{Ax} + \hat{S}_\text{Bx}\right) \end{cases} \tag{5.43}$$

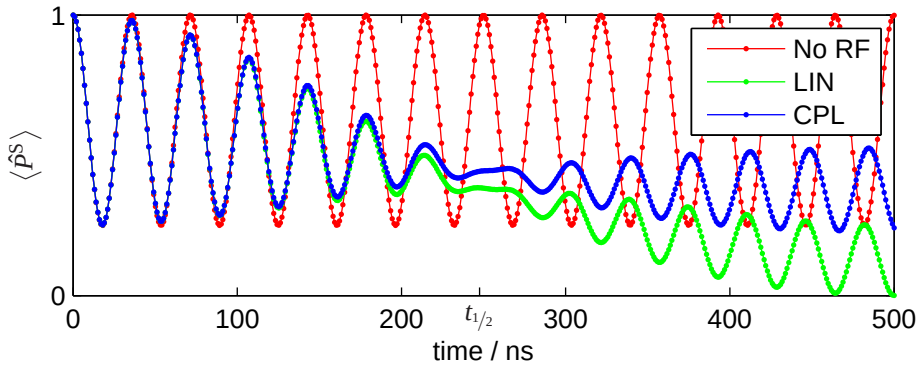

(a) Singlet probability with CPL or LIN RF fields and RF phase $\gamma = 0$ or with $B_1 = 0\,\mathrm{mT}$.

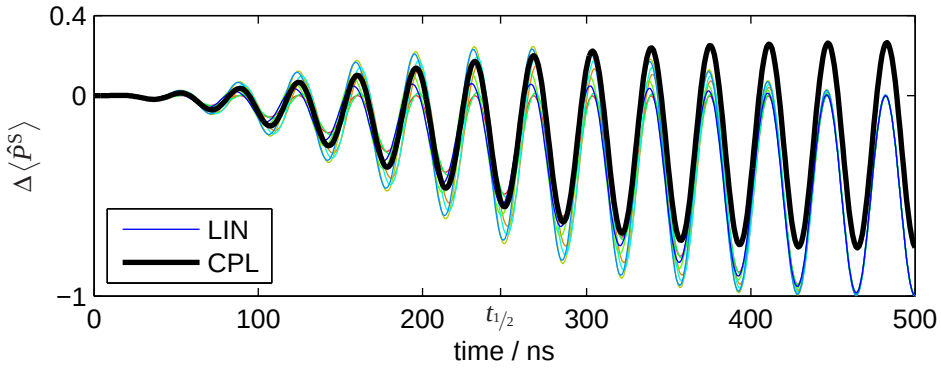

(b) Differences between the singlet probability with and without RF. The LIN calculations are repeated for 16 values of the RF phase γ. The CPL singlet probability does not depend on γ.

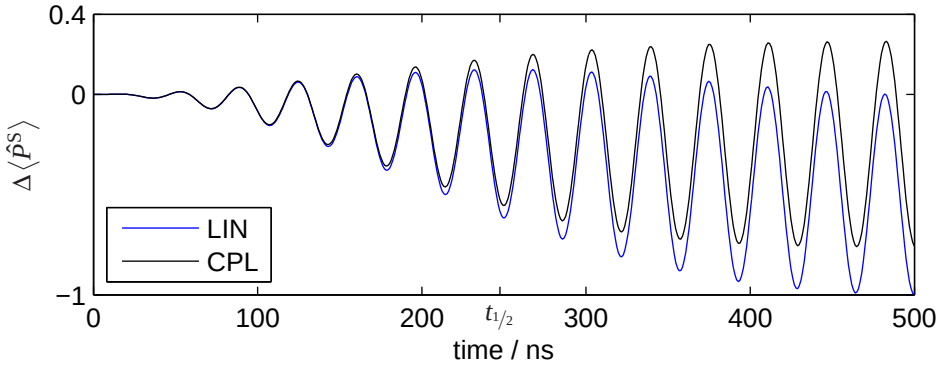

(c) As above, except that we plot the γ-averaged LIN singlet probability.

Figure 5.7: Time dependence of the singlet probability $\langle \hat{P}^S \rangle$ for different RF fields. Calculations were performed by applying a Runge-Kutta (4,5) solver to the Liouville–von Neumann equation in a one-proton radical pair. The following parameters were used: $B_1 = 100\,\mu\mathrm{T}$ RMS, $\nu_{\mathrm{rf}} = 28\,\mathrm{MHz}$, $a = 1.0\,\mathrm{mT}$, $B_0 = 0\,\mathrm{mT}$. CPL+ and CPL− fields have identical effects and are labelled CPL in the figure. The half-life $t_{1/2}$ for exponential model kinetics with $k = 2.8 \times 10^6\,\mathrm{s}^{-1}$ is marked on the x-axis for reference.

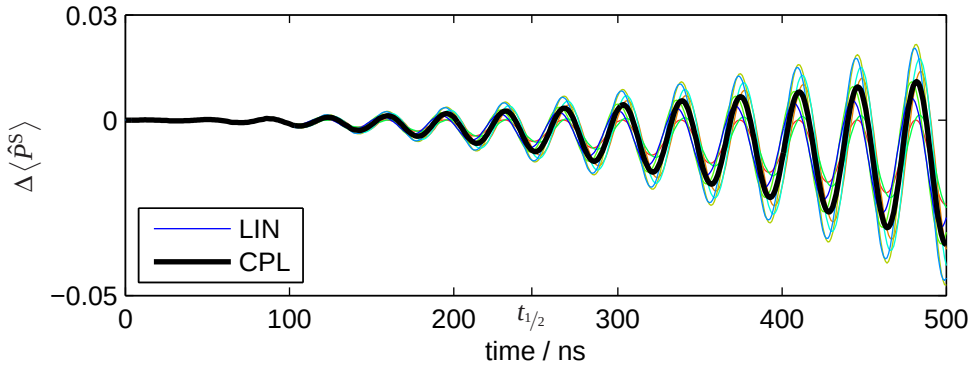

(a) Differences between the singlet probability with and without RF. The LIN calculations are repeated for 16 values of the RF phase γ. The CPL singlet probability does not depend on γ.

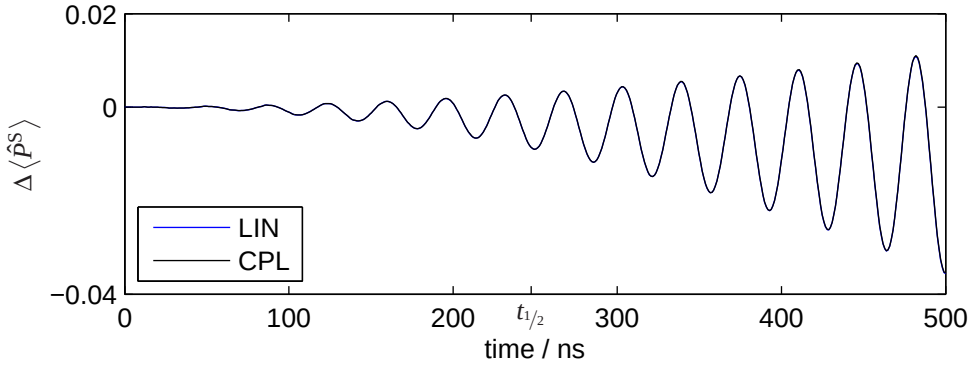

(b) As above, except that we plot the γ-averaged LIN singlet probability.

Figure 5.8: Time dependence of the singlet probability $\langle\hat{P}^S\rangle$ for different RF fields with $B_1 = 10\,\mu$T RMS. All other parameters are as described in Figure 5.7.

for linearly and circularly polarised RF respectively. We proceed by transforming into the "interaction representation" [119, 261], defining an interaction representation Hamiltonian $\hat{H}_{\mathrm{I}}(t)$ as

$$\hat{H}(t) \rightarrow \hat{H}_{\mathrm{I}}(t) = \hat{V}_{\mathrm{I}}(t) = \mathrm{e}^{\mathrm{i}\hat{H}_0 t}\hat{V}(t)\mathrm{e}^{-\mathrm{i}\hat{H}_0 t}. \tag{5.44}$$

In order to remain consistent with the normal Schrödinger representation, all other operators transform as

$$\hat{\Omega}(t) \rightarrow \hat{\Omega}_{\mathrm{I}}(t) = \mathrm{e}^{\mathrm{i}\hat{H}_0 t}\hat{\Omega}(t)\mathrm{e}^{-\mathrm{i}\hat{H}_0 t} \tag{5.45}$$

and the new basis states $|\psi_{\mathrm{I}}(t)\rangle = \mathrm{e}^{\mathrm{i}\hat{H}_0 t}|\psi\rangle$ evolve according to

$$\mathrm{i}\frac{\partial |\psi_{\mathrm{I}}(t)\rangle}{\partial t} = \hat{V}_{\mathrm{I}}(t)|\psi_{\mathrm{I}}(t)\rangle \tag{5.46}$$

where $\hat{V}_{\mathrm{I}}(t)$ is measured in angular frequency units.

Now, since $\left|\hat{V}_{\mathrm{I}}(t)\right| = \left|\hat{V}(t)\right| \propto \omega_1$, the interaction representation Hamiltonian is "small" when the RF field is weak. We may therefore solve equation (5.46) by iterative expansion into the following Neumann series:

$$|\psi_{\mathrm{I}}(t)\rangle = \left\{1 - \mathrm{i}\int_0^t \mathrm{d}t_1 \hat{V}_{\mathrm{I}}(t_1) - \int_0^t \mathrm{d}t_1 \int_0^{t_1} \mathrm{d}t_2 \hat{V}_{\mathrm{I}}(t_1)\hat{V}_{\mathrm{I}}(t_2) + \ldots\right\}|\psi_{\mathrm{I}}(0)\rangle. \tag{5.47}$$

For our purposes, it is most convenient to make calculations using the interaction representation density matrix

$$\hat{\rho}_{\mathrm{I}}(t) \equiv |\psi_{\mathrm{I}}(t)\rangle\langle\psi_{\mathrm{I}}(t)|. \tag{5.48}$$

Substituting the Neumann series from equation (5.47) and collecting terms of the same order [85], we write

$$\hat{\rho}_{\mathrm{I}}(t) = \left\{1 - \mathrm{i}\int_0^t \mathrm{d}t_1 \hat{V}_{\mathrm{I}}(t_1) + \ldots\right\}|\psi_{\mathrm{I}}(0)\rangle\langle\psi_{\mathrm{I}}(0)|\left\{1 + \mathrm{i}\int_0^t \mathrm{d}t_1 \hat{V}_{\mathrm{I}}(t_1) + \ldots\right\} \tag{5.49}$$

$$= \hat{\rho}(0) - \mathrm{i}\int_0^t \mathrm{d}t_1 \left[\hat{V}_{\mathrm{I}}(t_1), \hat{\rho}(0)\right] - \int_0^t \mathrm{d}t_1 \int_0^{t_1} \mathrm{d}t_2 \left[\hat{V}_{\mathrm{I}}(t_1), \left[\hat{V}_{\mathrm{I}}(t_2), \hat{\rho}(0)\right]\right] + \ldots \tag{5.50}$$

This expression may be used to calculate contributions to the singlet probability

$$\left\langle \hat{P}^{\mathrm{S}} \right\rangle(t) = \mathrm{Tr}\left[\hat{P}^{\mathrm{S}}\hat{\rho}(t)\right] = \mathrm{Tr}\left[\hat{P}^{\mathrm{S}}_{\mathrm{I}}(t)\hat{\rho}_{\mathrm{I}}(t)\right]. \tag{5.51}$$

We evaluated this expression with the aid of the symbolic manipulation program `Mathematica`. To first order, the singlet probability

$$\left\langle \hat{P}^{\mathrm{S}} \right\rangle(t) = \frac{5}{8} + \frac{3}{8}\cos at \tag{5.52}$$

for both linearly and circularly polarised RF fields. In other words, the RF field does not have any first order effect on singlet probability in the one-proton radical pair. Continuing to second order, the singlet probability is given by an expression containing

sines, cosines and powers of ω_{rf}, ω_1, a, t and γ. This expression is too bulky to give here, but the difference between RF polarisations is reasonably compact:

$$\left\langle \hat{P}^{\mathrm{S}} \right\rangle_{\mathrm{LIN}} - \left\langle \hat{P}^{\mathrm{S}} \right\rangle_{\mathrm{CPL}} = \frac{a\omega_1^2 \cos(\omega_{\mathrm{rf}} t + 2\gamma)}{8\left(\omega_{\mathrm{rf}}^3 - a^2\omega_{\mathrm{rf}}\right)^2} \times \begin{bmatrix} 3\omega_{\mathrm{rf}}^2 a - a^3 + \left(a^2 - \omega_{\mathrm{rf}}^2\right)\cos(\omega_{\mathrm{rf}} t)a \\ +\cos(at)\left(\omega_{\mathrm{rf}}^2 - a^2 + \left(a^2 - 3\omega_{\mathrm{rf}}^2\right)\cos(\omega_{\mathrm{rf}} t)\right)a \\ -2\omega_{\mathrm{rf}}^3 \sin(at)\sin(\omega_{\mathrm{rf}} t) \end{bmatrix}. \quad (5.53)$$

It is clear that the second order contributions to the singlet probability produce a polarisation effect that is proportional to ω_1^2 as we would expect.

However, if, as is necessary to model the experiments accurately, we average over the initial RF phase γ we find that

$$\frac{1}{2\pi}\int_0^{2\pi} \left\{ \left\langle \hat{P}^{\mathrm{S}} \right\rangle_{\mathrm{LIN}} - \left\langle \hat{P}^{\mathrm{S}} \right\rangle_{\mathrm{CPL}} \right\} \mathrm{d}\gamma = 0. \quad (5.54)$$

In other words, after averaging over the RF phase, linearly and circularly polarised fields are equivalent even to second order. It is for this reason that linearly and circularly polarised RF fields produce identical OMFE spectra in the limit of weak RF field strength and of rapid exponential model decay. The fact that OMFE polarisation effects arise from third and higher orders of perturbation theory also explains why it is so challenging to provide a simple physical picture of their origin.

5.3.5 Propagators

It is possible to gain some insight into the significant coherent spin evolution by plotting propagators explicitly. Figure 5.9 shows the propagators in a one-proton radical pair for time intervals $t = 0 \rightarrow 3T/4$ and $t = 0 \rightarrow 30T$. The plots are formed by first computing the requisite propagator, then subtracting a unit matrix in order to emphasise the coherent spin evolution and finally plotting the propagator as a group of squares whose side lengths are proportional to the absolute values of the corresponding elements. Propagators are plotted for spin evolution in CPL$\pm$ and LIN polarised fields.

After three quarters of an RF cycle, the figures in the left hand column show small, but significant differences in spin evolution under different RF polarisations. After 30 RF cycles, the figures on the right show marked differences. This is the same situation as we discussed in connection with Figures 5.7 and 5.8, where the singlet probabilities under different RF polarisations were initially similar but were then gradually seen to diverge. It should be noted that not all of these coherences are of direct relevance to the singlet probability. Only those coherences, highlighted with a grey box, that cause singlet–triplet interconversion directly affect the singlet probability.

Finally, it is apparent that despite giving identical singlet probabilities, CPL+ and CPL$-$ fields cause visibly different spin evolution. For example, one may compare Figures 5.9b and f. For a system whose Hamiltonian is given by equation (5.5) with $\omega_0 = 0$, we notice that the difference between CPL$\pm$ polarisations could be expressed by spin operator transformations: $\hat{S}_{\mathrm{y}} \leftrightarrow -\hat{S}_{\mathrm{y}}$ and $\hat{I}_{\mathrm{y}} \leftrightarrow -\hat{I}_{\mathrm{y}}$. In the absence of a static

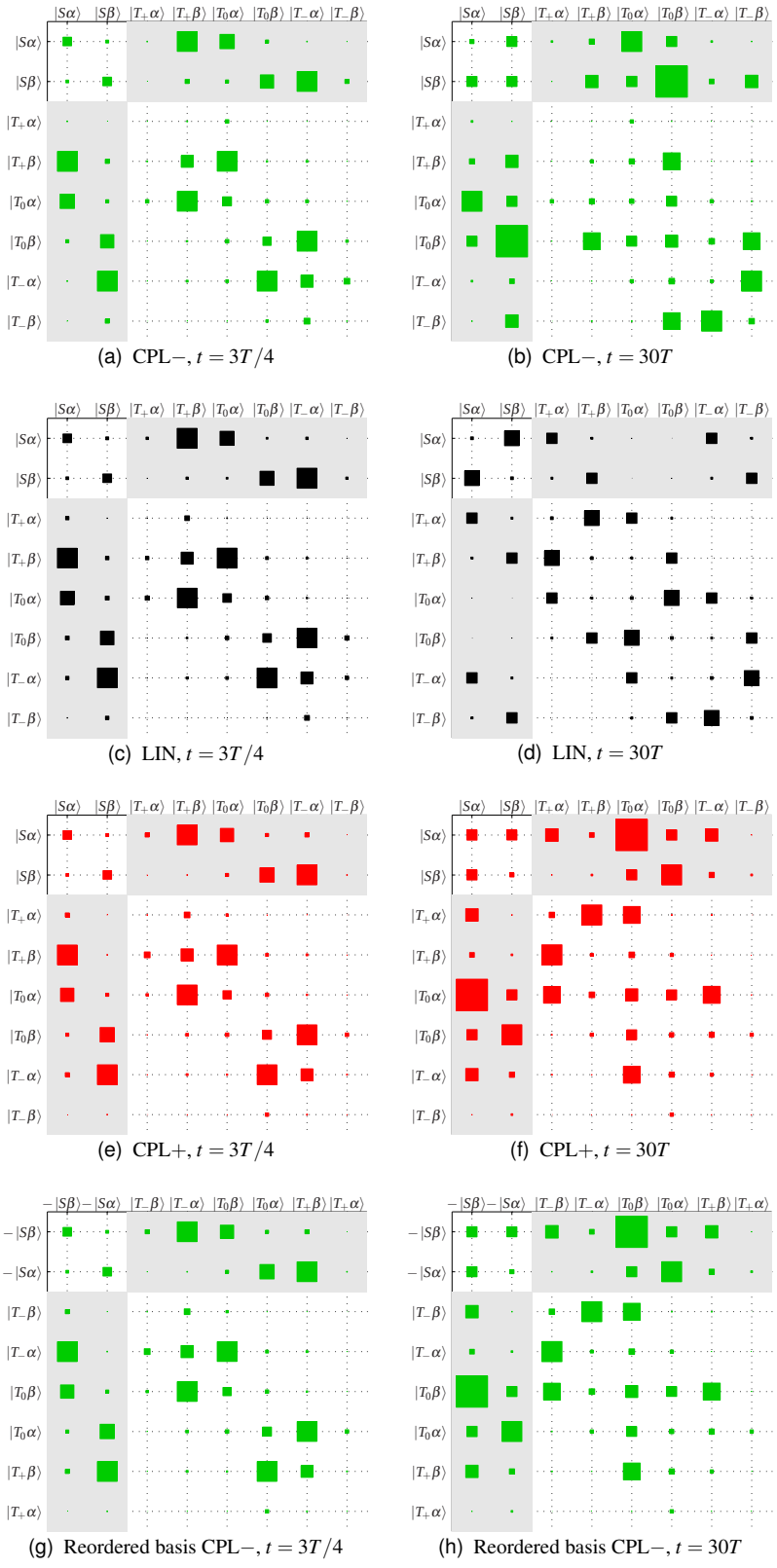

(a) CPL−, $t = 3T/4$ (b) CPL−, $t = 30T$

(c) LIN, $t = 3T/4$ (d) LIN, $t = 30T$

(e) CPL+, $t = 3T/4$ (f) CPL+, $t = 30T$

(g) Reordered basis CPL−, $t = 3T/4$ (h) Reordered basis CPL−, $t = 30T$

Figure 5.9: Propagators in a one-proton radical pair with $\nu_{\mathrm{rf}} = 28\,\mathrm{MHz}$, $B_1 = 100\,\mu\mathrm{T}$, $a = 1.0\,\mathrm{mT}$ and $B_0 = 0\,\mathrm{mT}$. The propagators are plotted using the electron S–T basis. Each square represents an element whose absolute value is proportional to the side length. In order to emphasise coherent evolution of states, we subtract an identity matrix from each propagator before plotting.

field, we could make the further transformation: $\hat{S}_z \leftrightarrow -\hat{S}_z$ and $\hat{I}_z \leftrightarrow -\hat{I}_z$ without any change to the Hamiltonian. Together, these transformations correspond to a "π_x pulse" — that is, to a certain relabelling of the basis states. Figures 5.9g and h plot the propagators for CPL− fields using a different order of basis states. These reordered plots are clearly identical to the CPL+ ones above. This demonstrates graphically that CPL± fields produce different, but equivalent, spin evolution in the absence of a static field. Hence, they give rise to the same time-dependent singlet probability.

5.3.6 Other approaches

There are several other avenues for interpreting the different responses of a radical pair to LIN and CPL fields which we mention here for the sake of future workers.

Average Hamiltonian theory

Using the Magnus expansion [84, 254, 262–264, 264–266], we calculated the average Hamiltonian [197, 266–268] to zeroth and first order. The zeroth order average Hamiltonian is equal to the full Hamiltonian with $\omega_1 = 0$ for both LIN and CPL fields. The first order average Hamiltonians differ markedly — for example, in the electron singlet–triplet basis, the first order LIN average Hamiltonian contains 16 non-zero elements, whilst the CPL average Hamiltonian contains 40 non-zero elements. In both cases, the first order average Hamiltonian depends on the initial RF phase γ.

Importance of initial RP state

The initial RF phase γ has pronounced effects on the singlet probability, as seen in Figure 5.7. This suggests that a significant contribution to the difference between LIN and CPL fields may be the initial eigenstate occupancy. For a radical pair created in a pure singlet state, the eigenstates of the Hamiltonian at the instant of RP creation will depend strongly on γ. If we assume that since the RF field varies "slowly", subsequent spin evolution will be largely adiabatic, then the eigenstate occupancy at later times will still bear a strong "imprint" of the initial occupancy. Hence, the initial RF phase may have a relatively strong effect on the singlet probability even after several RF cycles.

Analogy to the Bloch-Siegert shift

There are clearly some parallels between the OMFE polarisation effects discussed above and the Bloch-Siegert shift that arises in NMR [186, 241, 269, 270]. The Bloch-Siegert shift is the first adjustment to an NMR resonance when the applied RF field is linearly rather than circularly polarised. A related series of expressions have been derived [271] for a two-level system in the context of atomic beam electric resonance experiments.

5.3.7 Multinuclear radical pairs

Hitherto, we have worked only with one-proton RPs in our discussion of RF polarisation effects on OMFE spectra. Actual chemical radical pairs usually contain many

magnetic nuclei on each radical. In an attempt to explore the range of RF polarisation responses that might be expected experimentally, we performed a large number of simulations in multinuclear radical pairs, using γ–COMPUTE or the rotating frame transformation as appropriate. Although it is not possible to present more than a tiny fraction of these calculated spectra here, we proceed to discuss some of the general principles and interesting special cases that emerged.

"1–1" radical pairs

The one-proton RPs discussed above sometimes demonstrate rather atypical magnetic field effects because of the "bare" counter radical that has no magnetic nuclei. Figure 5.10 shows various OMFE spectra calculated for "1–1" RPs, in other words RPs with one magnetic nucleus on each radical. Such RPs no longer have a "bare" counter radical and may be expected to show behaviour that is more typical of realistic chemical RPs. Indeed, as shown for the effects of static fields in Chapter 3, for qualitative analysis it is often possible to replace the hyperfine couplings on each radical with a single effective hyperfine coupling $\tilde{a}_{\mathrm{N}}$. At this level of approximation, any RP may be identified with a corresponding "1–1" RP.

When the hyperfine couplings on radicals A and B differ significantly, we see two well resolved peaks at frequencies of 28 MHz/mT, as in Figure 5.10a. A "1–0" OMFE spectrum is shown in red for comparison. There, we also see two peaks: one at the hyperfine resonance position of 28 MHz/mT and one around 0 MHz. When the hyperfine couplings on radicals A and B are equal, we often see shouldering — or even full inversion — of the LIN peak at the hyperfine resonance.

In general, just as was the case in one-proton RPs, we find that the RF field acts to reduce the singlet yield. In other words, the RF field enhances the efficiency of S–T interconversion. Comparing the depth of the red spectra to the others in Figures 5.10a and c, it is apparent that under equivalent conditions, an RF field produces about half the change in singlet yield in a "1–1" RP that it does in a "1–0" RP.

Figure 5.10b plots the RF polarisation effect: the singlet yield for CPL RF minus that for LIN RF. It is clear that except for "1–0" RPs, or RPs with equal HFCs, the singlet yield in a LIN field is usually lower than that in a CPL field. In other words, at the modest RF field strength of 0.1 mT used here, LIN RF is usually more efficient at increasing S–T interconversion than CPL RF. It is also evident that the RF polarisation effect $\Delta\Phi_{\mathrm{S}}$ in a "1–1" RP is about half that in a "1–0" RP.

Figure 5.10c shows OMFE spectra calculated in the same system as in Figure 5.10a, but with faster re-encounter kinetics. As was seen in one-proton RPs, increasing the rate constant k causes the OMFE spectra to become broader, less well resolved and less intense.

"2–1" radical pairs

Having considered the most important ("1–1") multinuclear RPs, we examine briefly the situation when a further magnetic nucleus is incorporated. Figure 5.11 shows OMFE spectra in a series of "2–1" RPs. These spectra are rather similar to those in Figure 5.10. In particular, the RF-induced changes in singlet yield are comparable for "1–1" and "2–1" RPs. So too are the magnitudes of the RF polarisation effects. The "2–1" RPs show peaks of a similar width at the hyperfine resonant frequency of

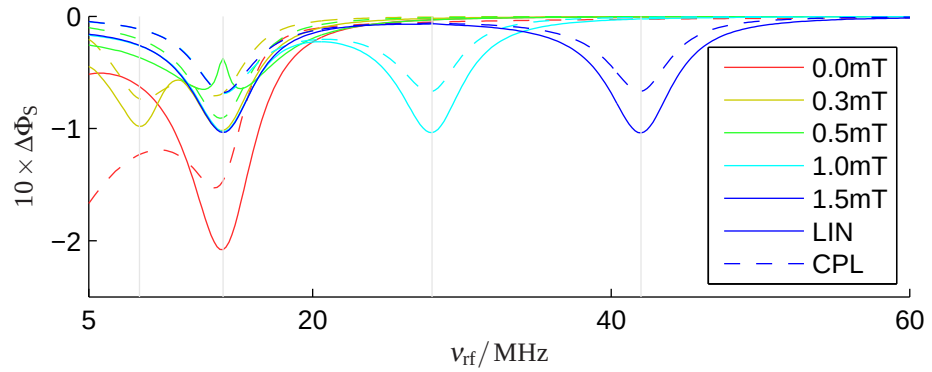

(a) Difference between singlet yield with RF and that without RF, exponential model $k = 2.8 \times 10^6\,\mathrm{s}^{-1}$.

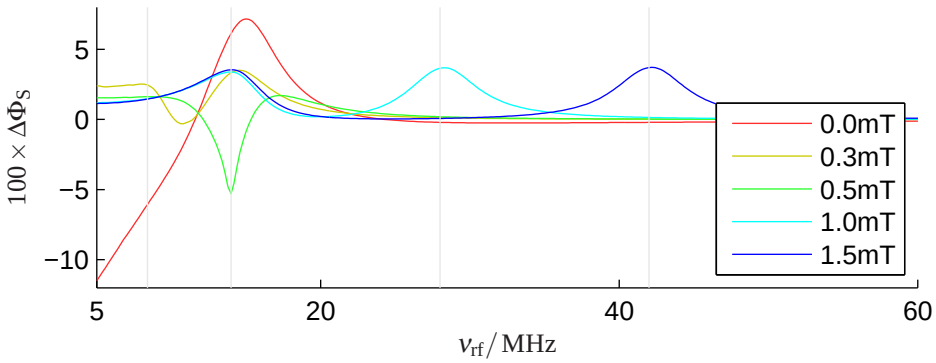

(b) Difference between LIN and CPL singlet yields, exponential model $k = 2.8 \times 10^6\,\mathrm{s}^{-1}$.

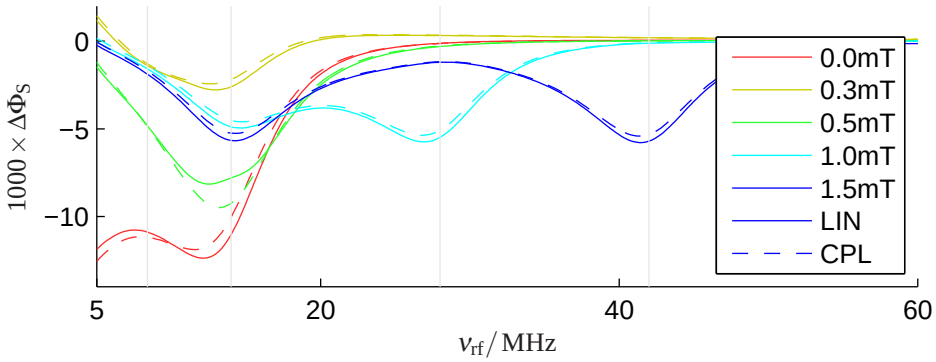

(c) Difference between singlet yield with RF and that without RF, exponential model $k = 2.8 \times 10^7\,\mathrm{s}^{-1}$.

Figure 5.10: Influence of hyperfine coupling constant and exponential model rate constant in "1–1" radical pairs. Singlet yields are calculated for radical pairs with one spin-½ nucleus on each radical. The HFC to radical A is fixed at $a_A = 0.5\,\mathrm{mT}$, whilst that to radical B is indicated in the legend. Other parameters: $B_0 = 0\,\mathrm{mT}$, $B_1 = 0.1\,\mathrm{mT}$, $\theta = \pi/2$ and $n = 64$. Vertical grey lines are drawn where a hyperfine resonance would be expected for HFCs of: $0.3\,\mathrm{mT}$, $0.5\,\mathrm{mT}$, $1.0\,\mathrm{mT}$ and $1.5\,\mathrm{mT}$ (*i.e.* at $0.3 \times 28 = 8.4\,\mathrm{MHz}$, etc.). In (a) and (c), we emphasise the RF-induced effects by subtracting the singlet yield in the absence of RF (a vertical shift of each curve). In (b), we emphasise the effect of RF polarisation by showing the difference between singlet yields for LIN and CPL fields.

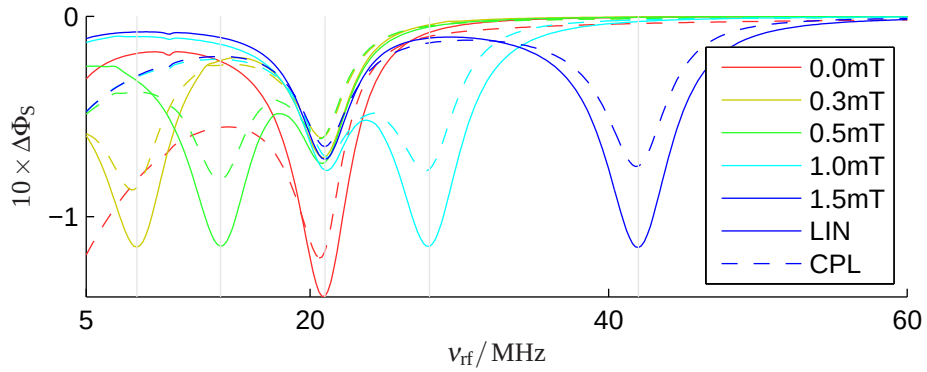

(a) Difference between singlet yield with RF and that without RF.

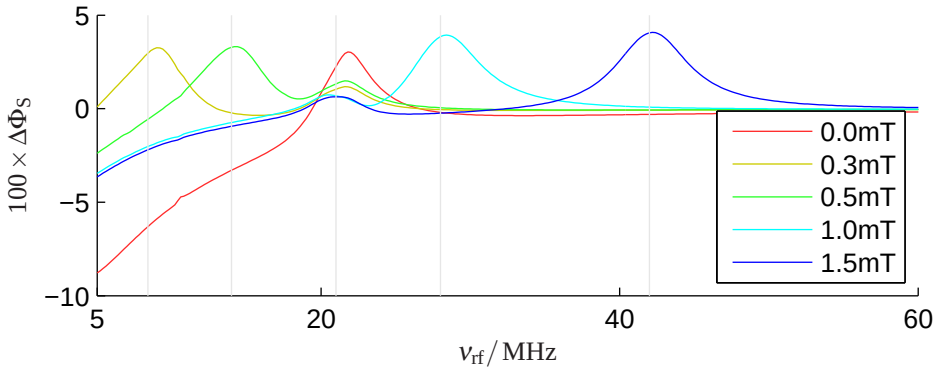

(b) Difference between LIN and CPL singlet yields.

Figure 5.11: Influence of hyperfine coupling constant and exponential model rate constant in "2–1" radical pairs. Singlet yields are calculated for radical pairs with two spins-½ in radical A, both with HFC $a_A = 0.5\,\text{mT}$, and one spin-½ in radical B, whose HFC is indicated in the legend. Other parameters: $k = 2.8 \times 10^6\,\text{s}^{-1}$, $B_0 = 0\,\text{mT}$, $B_1 = 0.1\,\text{mT}$, $\theta = \pi/2$ and $n = 64$. Vertical grey lines are drawn where a hyperfine resonance would be expected for HFCs of: $0.3\,\text{mT}$, $0.5\,\text{mT}$, $\frac{3}{2} \times 0.5\,\text{mT} = 0.75\,\text{mT}$, $1.0\,\text{mT}$ and $1.5\,\text{mT}$ (*i.e.* at $0.3 \times 28 = 8.4\,\text{MHz}$, etc.). In (a), we emphasise the RF-induced effects by subtracting the singlet yield in the absence of RF (a vertical shift of each curve). In (b), we emphasise the effect of RF polarisation by showing the difference between singlet yields for LIN and CPL fields.

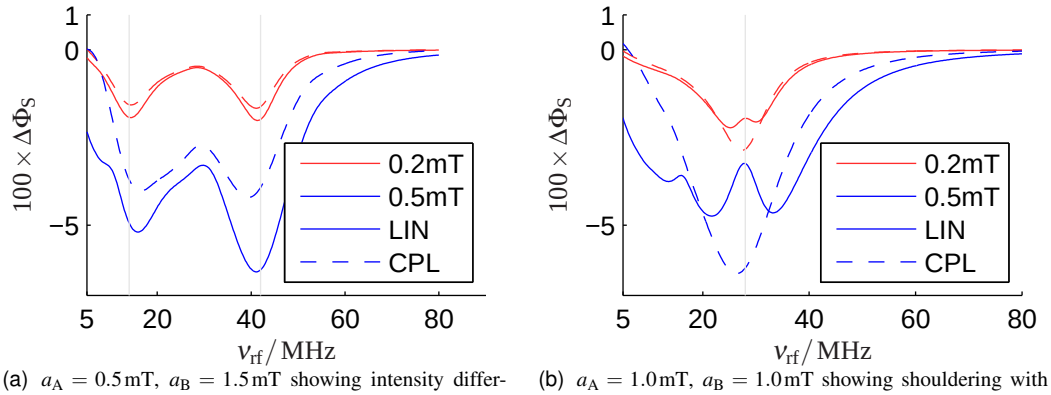

(a) $a_A = 0.5\,\mathrm{mT}$, $a_B = 1.5\,\mathrm{mT}$ showing intensity differences between two peaks.

(b) $a_A = 1.0\,\mathrm{mT}$, $a_B = 1.0\,\mathrm{mT}$ showing shouldering with LIN but not CPL fields.

Figure 5.12: Multinuclear radical pairs with interesting spectral shapes that would be especially suitable for experimental measurement. Calculations were performed on "1–1" RPs (containing one spin-½ per radical). The RF field strength B_1 and polarisation are indicated in the legend. Parameters: $k = 2.8 \times 10^7\,\mathrm{s}^{-1}$, $n = 128$, $\theta = \pi/2$, $B_0 = 0\,\mathrm{mT}$. Vertical grey lines are drawn where a hyperfine resonance would be expected for the HFCs used (*i.e.* at $a \times 28\,\mathrm{MHz}$).

28 MHz/mT. The only significant difference is that the peak corresponding to radical A has shifted from 14 MHz to 21 MHz. This shift is straightforward to understand when we recall (see §2.2.3) that two equivalent spins-½ may be treated as if they were effectively spin-1 and spin-0 nuclei. The spin-0 effective nucleus has no OMFE spectrum, whilst, since the position of the resonance is proportional to $I(I+1)$, the effective spin-1 gives a peak at a radio frequency

$$\nu_{rf} = \frac{1 \times (1+1)}{\frac{1}{2} \times (\frac{1}{2}+1)} \times a \times 28\,\mathrm{MHz} = 21\,\mathrm{MHz}. \tag{5.55}$$

The similarity of "1–1" and "2–1" OMFE spectra suggests that addition of further magnetic nuclei will tend merely to refine spectral details such as lineshape and peak depth. Indeed, larger multinuclear RPs are found to show behaviour analogous to that discussed here. However, since the parameter space expands markedly with each additional magnetic nucleus, it is difficult to make further systematic calculations.

Lineshape

Many of the calculated RF polarisation effects shown in this chapter are for the most part a scaling of the magnitude of the RF-induced change in singlet yield upon changing polarisation. Experimentally, it is challenging to ensure that LIN and CPL fields are generated with exactly the same RMS field strength B_1. It would, therefore, be advantageous to work in a system where the RF polarisation effect could not be confused with power-matching artefacts. Figure 5.12 shows two classes of system that might be useful experimentally. In Figure 5.12a, we see that RPs with HFCs that differ substantially between the two radicals may show changes in the relative intensity of the two peaks with RF polarisation. Alternatively, RPs with very similar HFCs on the two radicals may show shouldering or partial inversion of the LIN polarised lineshape, as in Figure 5.12b.

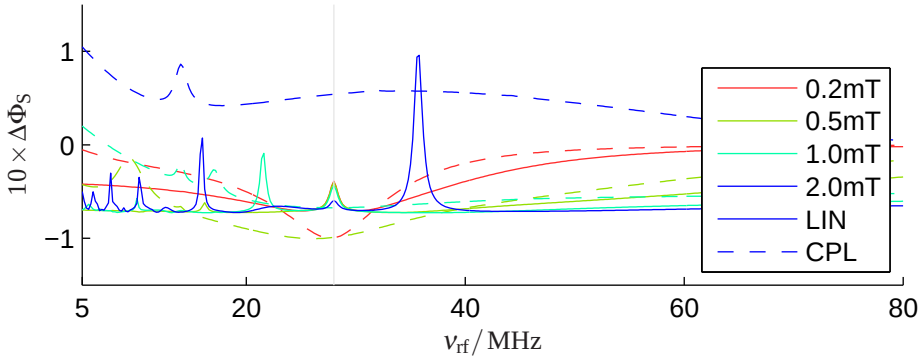

Figure 5.13: Influence of strong RF fields on a "1–1" radical pair containing one spin-½ per radical. Parameters: $a_A = a_B = 1.0\,\text{mT}$, $k = 2.8 \times 10^6\,\text{s}^{-1}$, $n = 128$, $\theta = \pi/2$, $B_0 = 0\,\text{mT}$. A vertical grey line is drawn at 28 MHz where a hyperfine resonance would be expected for the 1.0 mT HFCs used. This figure is converged to plotting accuracy, as was demonstrated by recalculating points at 1 MHz intervals using $n = 256$.

Such shouldering or inversion effects occur in many systems and may be very pronounced. Figure 5.13 shows calculated OMFE spectra in a "1–1" RP with slow reencounter kinetics ($k = 2.8 \times 10^6\,\text{s}^{-1}$) and in the presence of strong RF fields. As the RF field strength is increased, both LIN and CPL lines become very broad. Furthermore, the LIN spectra develop a series of rather sharp inverted peaks whose frequencies depend on the RF field strength. For example, notice that the $B_1 = 2.0\,\text{mT}$ LIN spectrum has a single broad peak that is more than 80 MHz wide, but that within this broad envelope there are superimposed several sharp, inverted peaks.

Further calculations (not shown), reveal that these inverted peaks are most pronounced when $a_A = a_B$ or when k is small. As the RF field strength is increased, the inverted peaks become more numerous and intense. Eventually, at sufficiently high RF field strengths a second pattern of inverted peaks develops in the CPL spectra. We return to discuss the effects of strong RF fields in more detail later (see §5.5).

Optimal RPs for RF polarisation studies

To summarise: in order to observe a strong OMFE spectrum RF polarisation effect, we should use a strong RF field (large B_1) applied to a long-lived radical pair (small k) that has similar hyperfine couplings in both radicals ($a_A \approx a_B$). Alternatively, choosing radicals that have rather different HFCs in each radical may provide a good test of the theory — allowing comparison of the relative intensity of the two OMFE spectral peaks.

5.3.8 Experimental methods

Experimental measurements of OMFE spectra in the presence of LIN and CPL fields were made by Norman [139] and Wedge [182]. We summarise here briefly the apparatus and protocol that they used.

Samples containing 1 mM Py-d_{10} and 20 mM 1,3-DCB dissolved in a 1:9 v:v mixture of acetonitrile and cyclohexanol were illuminated continuously in the ultra violet by a 1 kW Oriel Xe arc lamp. The solutions were flowed continuously through a

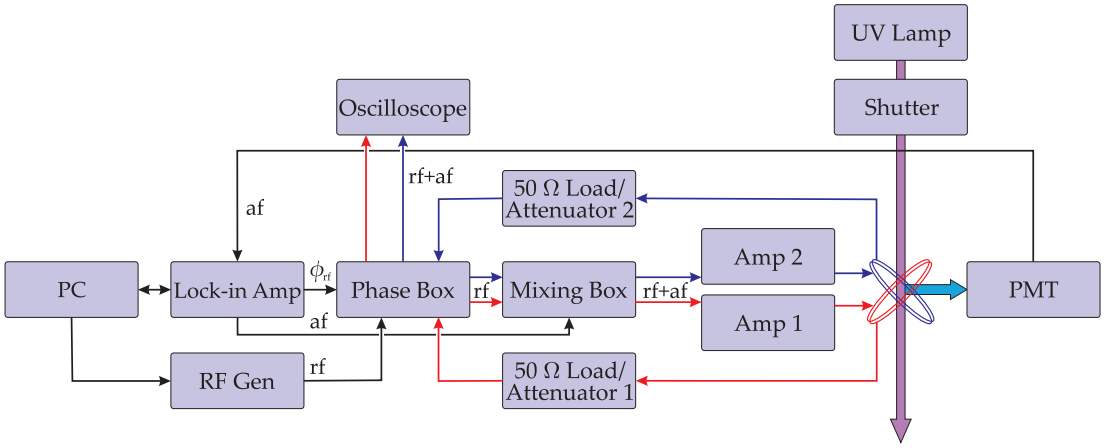

Figure 5.14: Block diagram of the OMFE experiment taken from [139]. This apparatus was designed and constructed by Neville Baker from the PTCL Electronics Workshop. Radio-frequency and audio-frequency signals are denoted 'rf' and 'af' respectively. The two radio frequency channels and coils are shown coloured red and blue, and the phase-angle between them is ϕ_{rf}. Detected magnetic-field-dependent exciplex emission, collected at 90° to the incident UV light is shown by the light blue arrow.

3×3 mm sample cell by a motorised syringe driver in order to avoid photo-degradation. As shown in Figure 4.8, the UV illumination drives photochemical electron transfer to create a spin-correlated radical pair $\left[\text{Py-d}_{10}^{\bullet+}\ \text{1,3-DCB}^{\bullet-}\right]$. This RP is generated exclusively in the singlet spin state. Subsequently, the RP undergoes coherent singlet–triplet interconversion under the influence of internal hyperfine and external magnetic fields. The singlet RP is in rapid equilibrium with a fluorescent exciplex. The exciplex fluorescence is filtered to remove scattered light from the Xe arc lamp and detected by a Hamamatsu R928 photomultiplier tube mounted on Hamamatsu C6271 high-voltage power supply unit. The observed fluorescence intensity is directly proportional to the concentration of singlet RP.

In order to measure an OMFE spectrum, an RF field is applied to the sample using a pair of coils whose geometry is shown in Figure 5.1. In order to improve the signal-to-noise ratio, phase-sensitive detection is employed: the RF field is 100% amplitude modulated (at 381 Hz) and the PMT output is fed to a lock-in amplifier (Stanford Research SR830). By this procedure, they detect only the magnetic-field-sensitive contribution to the fluorescence that arises from the exciplex. The experimentally measured signal is proportional to the difference in singlet yield with and without RF.

It is technically demanding to ensure that the signals fed to the two RF coils maintain the desired amplitude and relative phase as the radio frequency is swept from 5–80 MHz for an OMFE spectrum. Nevertheless, such control is essential if one is to generate the linearly and circularly polarised RF fields that are desired. To accomplish this feat, an RF signal is generated by a Programmed Test Sources PTS500 frequency generator under computer control and passed to a home-made "phase control box". In conjunction with control software written in `LabVIEW`, the phase control box splits the RF signal into two channels and introduces a controlled phase-shift between them in the range ±0–120°. These signals are then amplified (using Kalmus 116FC-CE and Wessex Electronics RC114-100 amplifiers) and fed to the coils. Beyond each coil, the majority of the RF power is dissipated into a 50 Ω 20 dB attenuator. Finally, the attenu-

ator output is passed back to the phase control box where the relative phase and power of the channels is monitored. Using this information in a feedback loop, the phase control box is able to maintain a constant relative phase and field strength throughout the 5–80 MHz OMFE spectrum. All experiments are run at the same root mean square power: the amplifiers always produce the same RF field strength, but the relative phase of the two coils is adjusted to give LIN and CPL± fields.

5.3.9 Results and discussion

Figure 5.15a shows OMFE spectra measured for $\left[\text{Py-d}_{10}^{\bullet+}\ \text{1,3-DCB}^{\bullet-}\right]$ with LIN and CPL± RF fields. Each spectrum is the average of results from six experimental runs, each comprising three scans. For each set of three runs (LIN and CPL±), the order of RF polarisation was chosen at random in order to minimise the chances of systematic error.

The $\left[\text{Py-d}_{10}^{\bullet+}\ \text{1,3-DCB}^{\bullet-}\right]$ system was chosen for these measurements because it has a strong OMFE spectrum that is composed of two well-resolved peaks. As discussed in connection with Figure 5.12, these features arise because $\tilde{a}_{\text{Py-d}_{10}^{\bullet+}} \ll \tilde{a}_{\text{1,3-DCB}^{\bullet-}}$. The difference between effective HFCs is less pronounced for $\left[\text{Py-h}_{10}^{\bullet+}\ \text{1,3-DCB}^{\bullet-}\right]$, making Py-$h_{10}$ less suitable for RF polarisation effect measurements and justifying the expense of deuteration.

Several aspects of the data in Figure 5.15a deserve attention. The OMFE spectra comprise two peaks, which are close to the frequencies expected for resonance with the effective HFCs: $0.25\,\text{mT} \times 28\,\text{MHz/mT} = 7\,\text{MHz}$ for $\text{Py-d}_{10}^{\bullet+}$ and $1.04\,\text{mT} \times 28\,\text{MHz/mT} = 29\,\text{MHz}$ for $\text{1,3-DCB}^{\bullet-}$. At frequencies less than 10 MHz, the singlet yield in the presence of LIN polarised RF is greater than for CPL, whilst at frequencies greater than 10 MHz the CPL RF has the greater singlet yield. At frequencies greater than either of the effective HFCs, the OMFE gradually disappears — causing the RF polarisation effect to vanish also. The spectra for CPL± are very similar to one-another, except for a small region around 15 MHz. This confirms that the experimental RF phase control is functioning as it ought. Furthermore, the difference between CPL± spectra gives an impression of the remaining uncertainty in these measurements. Judging by eye, the differences between LIN and CPL RF polarisations seem to be significant. The statistical significance of these differences has been confirmed after an analysis by Norman [139].

Figure 5.15b shows calculated OMFE spectra for the same system. The calculations incorporate one group of equivalent nuclei on $\text{Py-d}_{10}^{\bullet+}$ and two groups of nuclei on $\text{1,3-DCB}^{\bullet-}$. In reality, there are several further magnetic nuclei in each of these radicals. Unfortunately, since the number of spin states grows exponentially with each additional nucleus, we must neglect the smaller HFCs in order to allow calculation in a reasonable amount of time and memory.

Figures 5.16 and 5.17 assess the validity of this approximation. Figure 5.16, shows OMFE spectra calculated with either one group or two groups of equivalent nuclei on $\text{1,3-DCB}^{\bullet-}$. There is a relatively small difference — mainly in the depth and width of the 7 MHz peak — between these two cases. Notice particularly, that the point where LIN and CPL spectra cross is almost unchanged. Furthermore, the RF polarisation effects shown in Figure 5.16b are remarkably similar.

It is computationally infeasible to calculate for larger spin systems using the γ–

COMPUTE algorithm, but we can perform such calculations for CPL fields using the rotating frame transformation and the frequency-domain binning algorithm described in §2.2.2. Such calculations are presented in Figure 5.17. It is reassuring to see that there are only minor changes upon addition of nuclei to the "1–2" spin system used in Figure 5.15. In particular, the shapes of the OMFE spectra are almost unchanged. We may therefore be confident that the simulated spectra in Figure 5.15 include sufficient magnetic nuclei.

Figure 5.15c shows a direct comparison between the experimental and calculated RF polarisation effect. There is clearly close agreement. This is quite probably the first experimental demonstration of the different MFEs produced by linearly and circularly polarised RF; it is certainly so for the low-field regime.

5.3.10 Limitations

The OMFE RF polarisation effects for $\left[\text{Py-d}_{10}^{\bullet+}\ \text{1,3-DCB}^{\bullet-}\right]$ presented in Figure 5.15 are a powerful validation of our model for RP reactions. Nevertheless, this OMFE RF polarisation experiment is not ideal for wider application. The experiment suffers from several limitations.

First, OMFE spectra present as rather small changes in exciplex fluorescence. This makes them difficult to measure experimentally. Indeed, only a small number of RP systems produce OMFE spectra that are clearly observable above the noise background.

Second, OMFE RF polarisation effects are difficult to calculate. The RF polarisation effect often manifests as a small change in peak intensity or width. Peak intensities and widths are sensitive even to small HFCs in the RP. Yet, because computational resources are finite, it is not normally feasible to include these small HFCs when calculating spectra.

Finally, it is technically demanding to sweep the radio frequency whilst maintaining a constant RF field strength and polarisation. For example: small differences between the CPL$\pm$ spectra around 15 MHz in Figure 5.15a remain despite a great deal of effort to develop robust RF electronics. The requirement to sweep the radio frequency field imposes severe limitations on the maximum attainable RF field strength.

These limitations suggest that OMFE experiments may not be the best means of observing experimentally the effects of RF field polarisation. As discussed in Chapter 4, it is expedient to make measurements of the effects of an RF field in the presence of an additional static field. As indicated in §4.3, we could apply a static field and continue to sweep the radio frequency. This experiment, known as OMFE-B_0, gives stronger signals than those seen in OMFE experiments, but still suffers from the limitations associated with sweeping the radio frequency. Alternatively, we can fix the radio frequency and sweep the static field strength in an experiment known as MARY-ν.

5.4 MARY-ν

MARY-ν spectroscopy is familiar from Chapter 4. Previously, we focused on the role of the relative angle θ between static and RF fields. We observed and simulated marked changes in the MARY-ν spectral shape on going from parallel to perpendicular relative orientations. At high radio frequencies, these effects were in accordance with

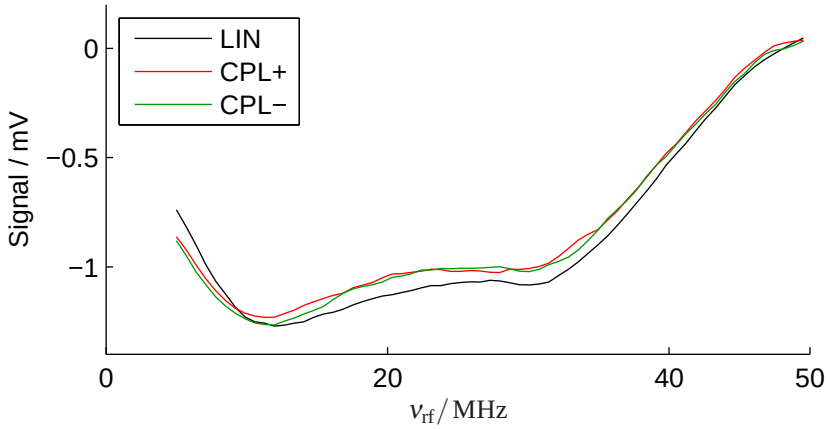

(a) Experimental OMFE spectra from [139, 182]. Both CPL± results, which should be identical, are included to give an impression of experimental error.

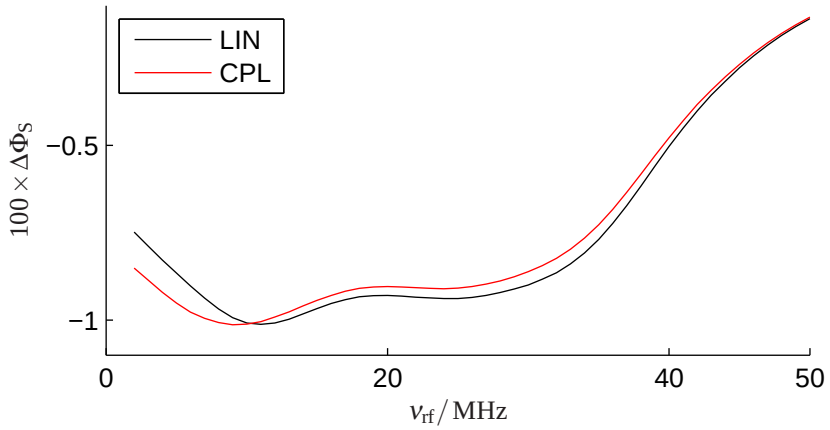

(b) Simulated OMFE spectra, showing the difference in singlet yield with RF and without RF.

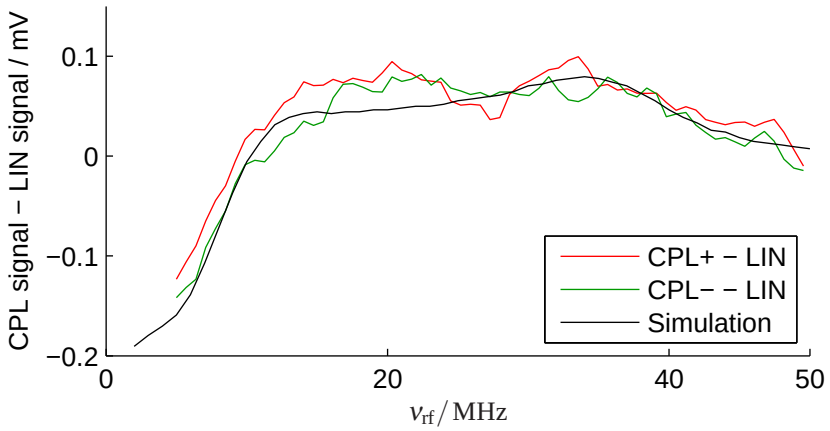

(c) Comparison of the experimental and simulated differences between LIN and CPL± spectra. Since the conversion factor between the PMT signal (in mV) and singlet yield is not known, the simulated curve is scaled by an arbitrary amount. This scaling constant was chosen as 1.85 mV by least squares fitting.

Figure 5.15: Comparison of experimental and simulated OMFE spectra for the reaction of Py-d_{10} and 1,3-DCB. Calculations were performed using γ–COMPUTE or the RFT. Parameters: $k = 5 \times 10^7\,\mathrm{s}^{-1}$, $n = 64$, $\theta = \pi/2$, $B_1 = 0.25\,\mathrm{mT}$ and $B_0 = 0\,\mathrm{mT}$. Hyperfine coupling constants were: $4 \times 0.083\,\mathrm{mT}$ (^{2}D) on Py-$d_{10}^{\bullet+}$; and $2 \times 0.829\,\mathrm{mT}$ (^{1}H), $1 \times 0.144\,\mathrm{mT}$ (^{1}H) on 1,3-DCB$^{\bullet-}$. These values are summarised in Table 4.2.

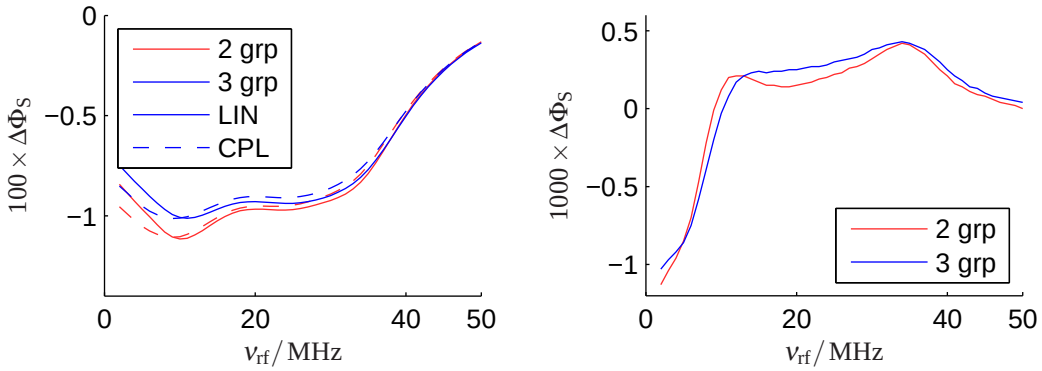

(a) Simulated OMFE spectra, showing the difference in singlet yield with RF and without RF.

(b) Simulated OMFE polarisation effects, showing the difference in singlet yield in the presence of LIN and CPL RF.

Figure 5.16: Effect of adding a third group of equivalent nuclei to the simulated signals. Calculations were made using either γ–COMPUTE or the RFT. Parameters: $k = 5 \times 10^7\,\mathrm{s}^{-1}$, $n = 64$, $\theta = \pi/2$, $B_1 = 0.25\,\mathrm{mT}$ and $B_0 = 0\,\mathrm{mT}$. Hyperfine coupling constants were: $4 \times 0.083\,\mathrm{mT}$ (^{2}D) on Py-d$_{10}^{\bullet+}$; and either $2 \times 0.829\,\mathrm{mT}$ (^{1}H) on 1,3-DCB$^{\bullet-}$ ("2 gps") or $2 \times 0.829\,\mathrm{mT}$ (^{1}H), $1 \times 0.144\,\mathrm{mT}$ (^{1}H) on 1,3-DCB$^{\bullet-}$ ("3 gps"). These values are summarised in Table 4.2.

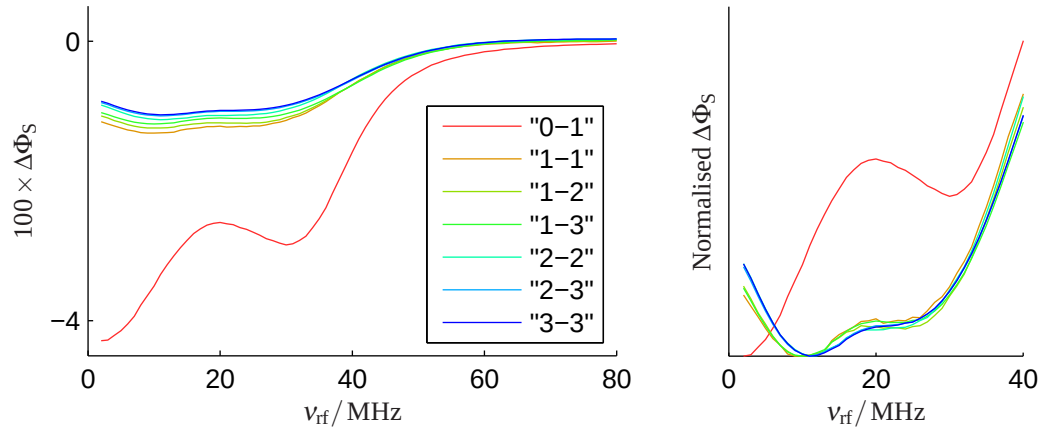

(a) Simulated OMFE spectra showing the difference in singlet yield with RF and without RF.

(b) Spectra from (a) scaled to give the same peak depth.

Figure 5.17: Effect of including more groups of equivalent nuclei on $\left[\text{Py-d}_{10}^{\bullet+}\ \text{1,3-DCB}^{\bullet-}\right]$ OMFE spectra for CPL RF fields. Calculations were made using the RFT. In the larger spin systems, frequency-domain binning was employed to give acceptable performance. Parameters: $k = 5.6 \times 10^7\,\mathrm{s}^{-1}$, $\theta = \pi/2$, $B_1 = 0.3\,\mathrm{mT}$ and $B_0 = 0\,\mathrm{mT}$. A legend entry "m–n" signifies that the m groups of equivalent nuclei with the largest HFCs have been included in Py-d$_{10}^{\bullet+}$ and likewise for n groups in 1,3-DCB$^{\bullet-}$. The HFC values that were used are listed in Appendix A.

the selection rules known in high-field EPR. However, as the radio frequency was reduced to a point where it became comparable with the hyperfine interactions, these high-field EPR selection rules broke down. For example, with 5 MHz RF, we observed comparable signal strengths for parallel and perpendicular RF fields.

Our attention here is directed towards the effect of RF polarisation on MARY-ν spectra. As will become clear, MARY-ν spectra depend markedly on RF polarisation. In some circumstances, these effects are equivalent to those in traditional high-field magnetic resonance. Once again, however, we find that the high-field picture breaks down at low field strengths or at low radio frequencies to give complex spectra.

5.4.1 Preliminary calculations

In order to gain some understanding of the features that may be expected in the MARY-ν spectra of real chemical systems, we begin with a series of calculations in simple model radical pairs. Figures 5.18–5.25 show a representative selection of MARY-ν spectra calculated for a one-proton radical pair.

5.4.2 Effect of ν_{rf} and k

Figure 5.18 shows MARY-ν spectra in a one-proton RP calculated for four different choices of radio frequency ν_{rf} and exponential model rate constant k. Several features are apparent. First, the MARY-ν spectra shown are almost zero for most static fields. In other words, weak RF fields produce negligible changes in singlet yield except in special cases. Second, for the most part, the peaks are negative. That is, weak RF fields — when they do have a significant effect — tend to decrease the singlet yield or equivalently to increase the efficiency of singlet–triplet interconversion in the RP.

In terms of radio frequency, there is a marked difference between MARY-ν spectra at radio frequencies that substantially exceed the HFC (*i.e.* $\omega_{\mathrm{rf}} \gg a$) and those at lower frequencies $\omega_{\mathrm{rf}} \lesssim a$. The high frequency MARY-ν spectra for CPL+ and LIN polarisations are dominated by a set of peaks centred around a static field strength that satisfies the high-field EPR Zeeman resonance condition: $B_0 = \nu_{\mathrm{rf}} \times 35.7\,\mu\mathrm{T}\,/\,\mathrm{MHz}$. This Zeeman resonance takes on fine structure due to the hyperfine interactions in the RP. In contrast, the CPL− polarisation shows negligible changes in singlet yield at this field strength. On the other hand, low frequency MARY-ν spectra show complex lineshapes that depend on the precise combination of HFCs in the RP. An expanded view of these lineshapes is given in Figure 5.19a.

The radical re-encounter kinetics, treated here using the exponential model [13, 15, 79], also play a critical role in determining MARY-ν spectra. As the rate constant k decreases, MARY-ν spectral lines generally become narrower and stronger. This behaviour is seen particularly in Figures 5.18a–c, 5.19a and the central portion of Figure 5.19b. For sufficiently long-lived RPs, the Zeeman peak reaches saturation at a depth $\Delta\Phi_{\mathrm{S}} \sim -0.25$ and a two-photon-excitation peak, shown in the right hand portion of Figure 5.19b, develops at twice the Zeeman resonance static field. For short-lived RPs with high k values, the RF field does not have time to produce a significant change in singlet yield. Such RPs give rise to small MARY-ν signals, which are of comparable magnitude but quite distinct in shape for LIN and CPL± polarised fields. These are illustrated in Figure 5.18d. Finally, experimental values of the rate constant often

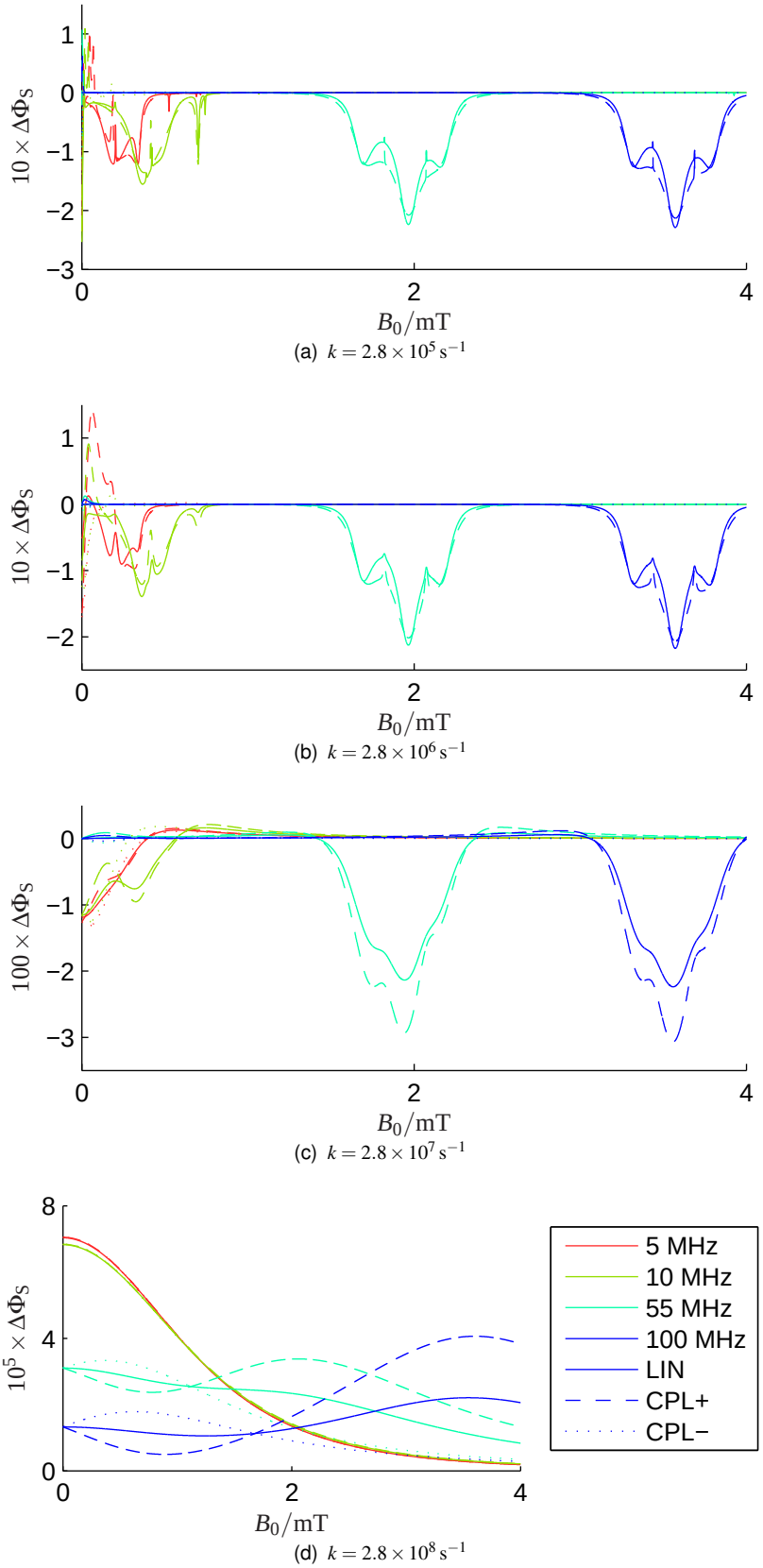

Figure 5.18: Influence of exponential model rate constant k and radio frequency ν_{rf} on MARY-ν polarisation effects in a RP that contains a single spin-½ nucleus. Spectra are shown for four radio frequencies, chosen to range around the HFC of $0.5\,\mathrm{mT} = 14\,\mathrm{MHz}$. Parameters: $n = 64$, $\theta = \pi/2$ and $B_1 = 0.1\,\mathrm{mT}$.

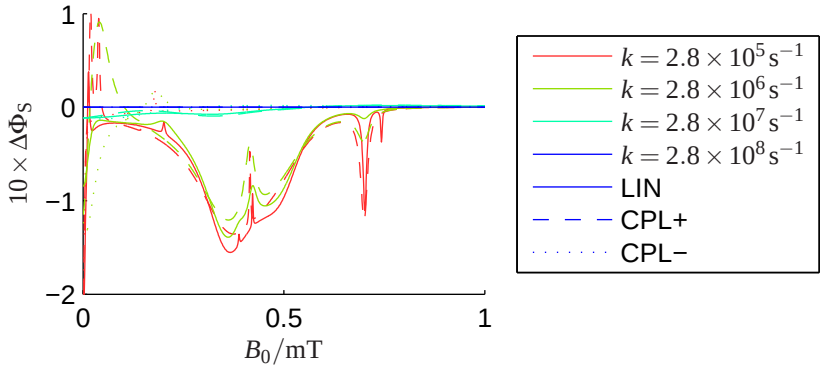

(a) $\nu_{\mathrm{rf}} = 10\,\mathrm{MHz}$. There are no substantial signals in the region $B_0 = 1$–$4\,\mathrm{mT}$ (not shown).

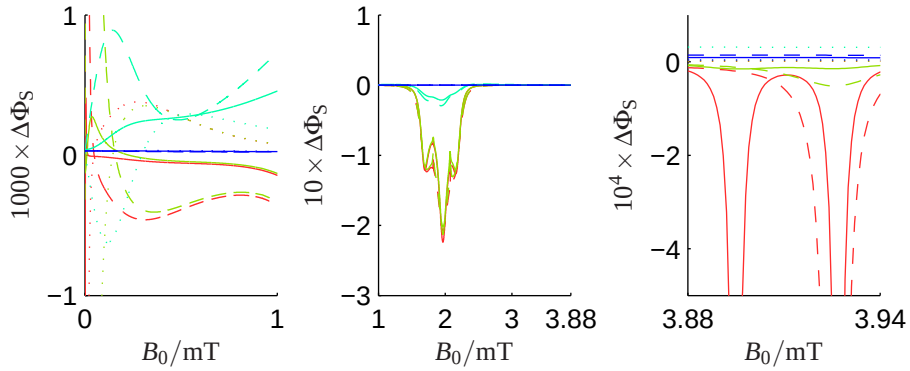

(b) $\nu_{\mathrm{rf}} = 55\,\mathrm{MHz}$. The B_0 axis is broken into sections with different vertical scales.

Figure 5.19: Details of the effect of exponential model rate constant k on MARY-ν polarisation effects in a RP that contains a single spin-½ nucleus with HFC $a = 0.5\,\mathrm{mT} = 14\,\mathrm{MHz}$. Figures are plotted with (a) $\omega_{\mathrm{rf}} < a$ and (b) $\omega_{\mathrm{rf}} \gg a$. Parameters: $n = 64$, $\theta = \pi/2$ and $B_1 = 0.1\,\mathrm{mT}$.

lie between these extremes. Figure 5.18c shows typical behaviour: MARY-ν spectral peaks are somewhat broadened and are not yet saturated.

5.4.3 Zeeman resonance

We may obtain some insight into the origin of these effects when $\omega_{\rm rf} \gg a$ by considering the energy level diagram for a one-proton RP shown in Figure 5.20. Providing that the RF field is weak, it will act to mix states that are separated in energy by $\omega_{\rm rf}$. When $\omega_{\rm rf} \gg a$, this will occur around a field strength of $B_0 = \nu_{\rm rf} \times 35.7\,\mu{\rm T}$ / MHz. Around this energy, the RF field will introduce additional interconversion between (S & T_0) $\leftrightarrow$ (T_+ & T_-) states. As a result, the singlet probability will tend to be decreased and so also will the singlet yield. An expanded view of the Zeeman resonance is given in Figure 5.21. In weak RF fields, the MARY-ν spectrum the sum of the conventional EPR spectra, albeit slightly distorted because of the small B_0, for each radical in the RP.

For sufficiently long-lived radical pairs, this interconversion will be essentially complete. In the absence of an RF field, such RPs would have 50% probability of being in S or T_0 states and hence $\Phi_{\rm S} \rightarrow \frac{1}{2}$. After introduction of the RF field, the RP now has access to all four (S, T_0, $T_\pm$) states with equal probability. The singlet yield is therefore reduced to $\frac{1}{4}$. Thus, for sufficiently long-lived RPs, the MARY-ν spectrum will show a Zeeman peak of depth $\frac{1}{4} - \frac{1}{2} = -\frac{1}{4}$. Such behaviour can be seen in Figure 5.18a. These arguments may be formalised by treating the energy levels involved as an effective two-level system and applying Rabi's formula [119, Ch IV-C].

The two-photon-excitation processes seen on the right of Figure 5.19 arise when $2 \times \omega_{\rm rf}$ matches an energy level splitting. This is illustrated for $B_0 = 8.0\,{\rm mT}$ in Figure 5.20. Such transitions are normally rather weak because (a) they are necessarily second-order processes and (b) they are only weakly allowed by virtue of the hyperfine interaction.

Of course, when the radio frequency is smaller than or comparable to the hyperfine interaction, these arguments do not apply. Then, the MARY-ν spectrum becomes rather complicated — reflecting the hyperfine structure of the RP in a non-trivial manner.

5.4.4 Polarisation effects

The foregoing discussion makes it clear that a MARY-ν signal should be observed at a field strength corresponding to the Zeeman resonance when $\omega_{\rm rf} \gg a$. However, it does not explain the different effects of LIN, CPL+ and CPL− polarised RF fields. The simplest means of considering these polarisation effects is by means of the appropriate rotating frame transformations.

Figure 5.22 shows several rotating frame energy level diagrams for the one-proton radical pair considered in Figure 5.20. Figures 5.22a,c,e show energy levels in the absence of an RF field (*i.e.* when $B_1 = 0\,{\rm mT}$) in frames rotating at $+112\,{\rm MHz}$ (a, c) and $-112\,{\rm MHz}$ (e). Despite the striking differences between these figures, we must remember that physically these must give rise to *identical* singlet yields since the RF field strength $B_1 = 0\,{\rm mT}$.

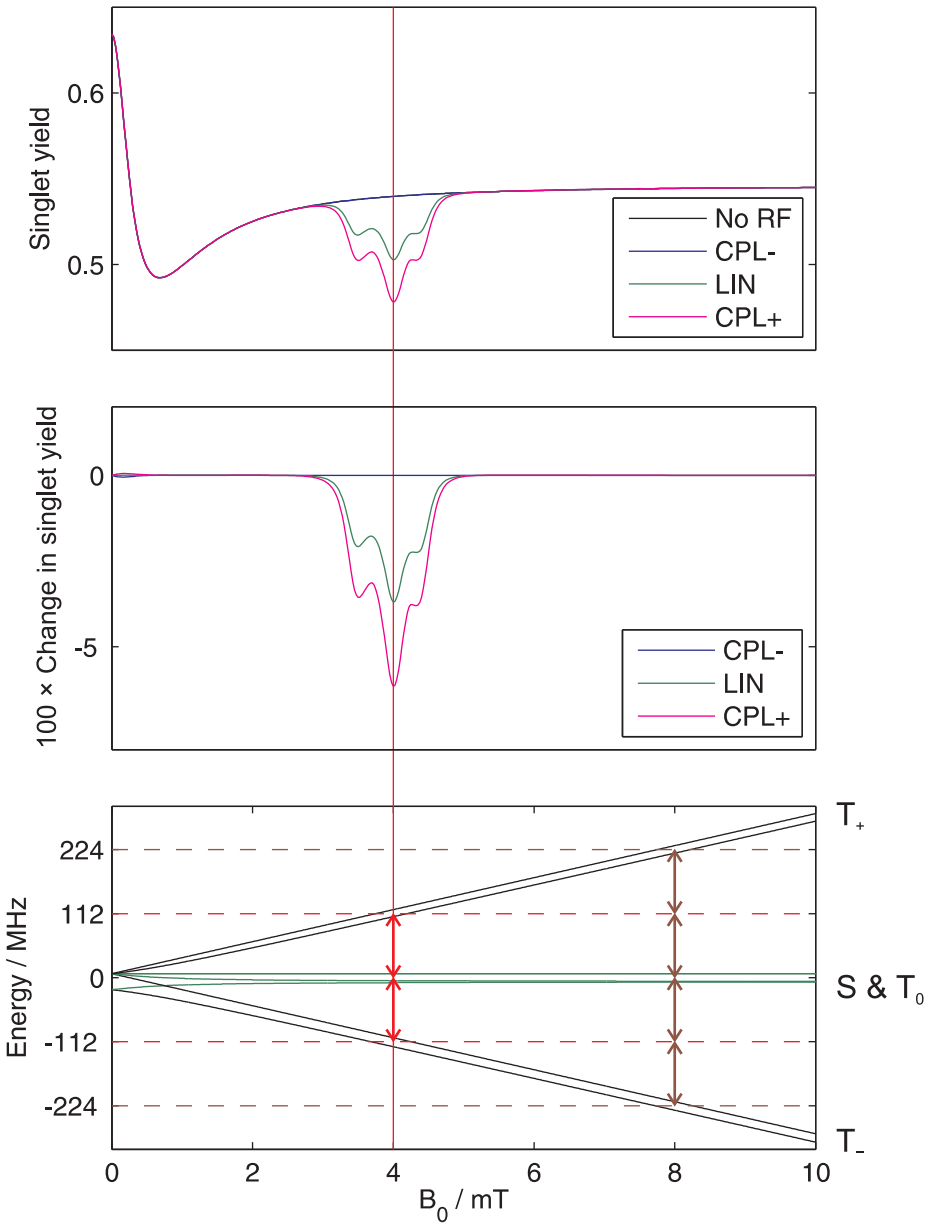

Figure 5.20: MARY spectra (top), MARY-ν spectra (middle) and the corresponding energy level diagram (bottom) for a RP that contains a single spin-½ nucleus. Parameters: $\nu_{\mathrm{rf}} = 112\,\mathrm{MHz}$, $B_1 = 0.1\,\mathrm{mT}$, $a = 1.0\,\mathrm{mT}$, $n = 64$, $\theta = \pi/2$ and $k = 2.8 \times 10^7\,\mathrm{s}^{-1}$. Energies corresponding to absorption or emission of a one or two RF photons are shown by dashed horizontal lines. The Zeeman resonance, where these dashed lines cross the RP energy levels, is indicated by a vertical red line. Possible two-photon processes would occur at $8\,\mathrm{mT}$.

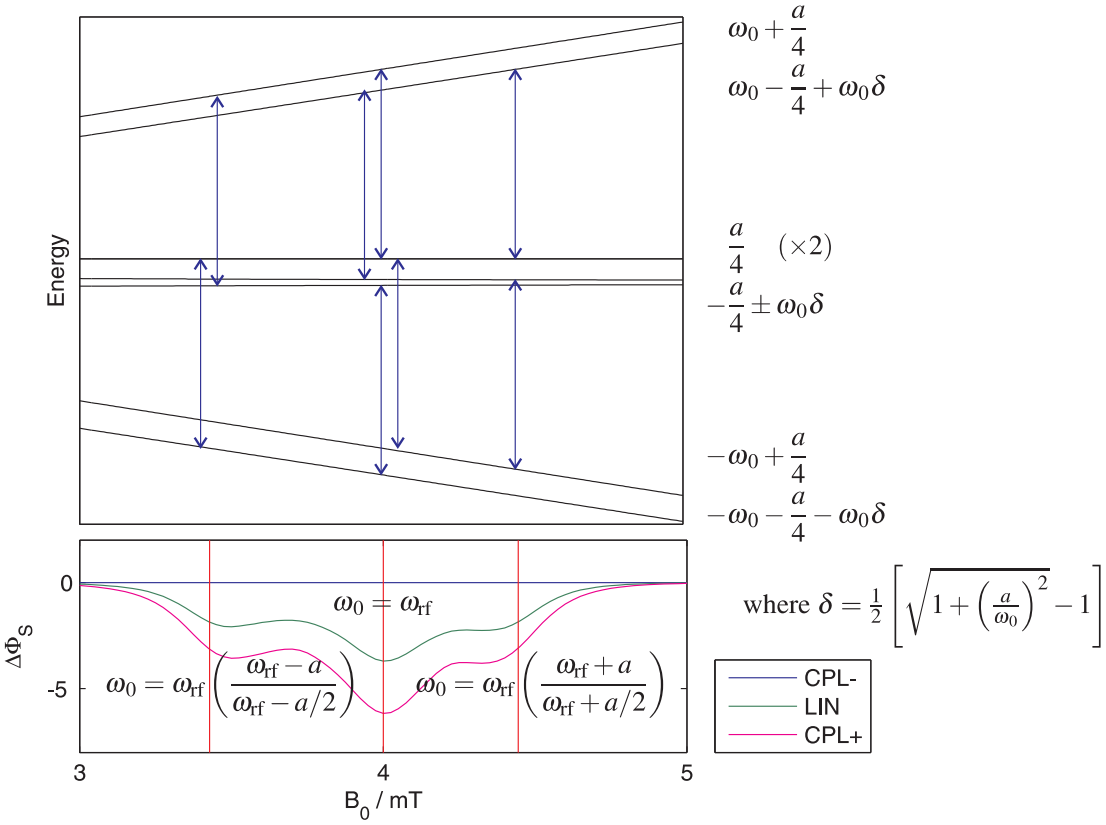

Figure 5.21: Expanded view of the energy levels (top) and MARY-ν spectra (bottom) for a RP that contains a single spin-½ nucleus. The same RP was used in Figure 5.20. Parameters: $\nu_{rf} = 112\,\text{MHz}$, $B_1 = 0.1\,\text{mT}$, $a = 1.0\,\text{mT}$, $n = 64$, $\theta = \pi/2$ and $k = 2.8 \times 10^7\,\text{s}^{-1}$. Energies corresponding to absorption or emission of an RF photon are shown by vertical lines. The three peaks in the MARY-ν spectrum are marked with their positions calculated using first order perturbation theory for a weak RF field. It is clear that they form a singlet and a distorted doublet.

Now, Figures 5.22b,d,f show the changes introduced as we "switch on" a weak RF field of strength $B_1 = 0.1\,\mathrm{mT}$. In the top two figures, corresponding to CPL+ RF polarisation, the RF field causes avoided crossings to be generated around the Zeeman resonance field. These avoided crossings are indicative of a resonant effect [119, Ch IV-C] in an effective two-level system: the CPL+ component of RF causes strong, resonant changes in the RP energy levels and associated eigenstates. We should not be surprised that it causes a significant change in singlet–triplet mixing and hence a strong MARY-ν signal. Yet, in the bottom figure, we see that a CPL− field causes almost no perceptible effect. Since there were no level crossings in (e), the CPL− RF field is not in a position to produce avoided crossings in (f). It is therefore unable to produce strong, resonant changes in the RP energy levels and associated eigenstates. A CPL− RF field does not produce any significant changes in singlet yield.

Having contrasted the effects of CPL± fields, we ought also to consider the effects of LIN polarised RF fields. We recall that a LIN field may be treated as the superposition of CPL+ and CPL− fields. Treating the CPL+ component first, we transform into the appropriate rotating frame. In an OMFE experiment, the CPL+ rotating frame Hamiltonian, given by equation (5.24), is

$$\hat{H}'_{\mathrm{OMFE}} = \sum_{\mathrm{N=A}}^{\mathrm{B}} -\omega_{\mathrm{rf}}\hat{S}_{\mathrm{Nz}} + \omega_1\hat{S}_{\mathrm{Nx}} + \sum_i \left\{ a_{i\mathrm{N}}\hat{\boldsymbol{I}}_{i\mathrm{N}}\cdot\hat{\boldsymbol{S}}_{\mathrm{N}} - \omega_{\mathrm{rf}}\hat{I}_{iz} \right\} \tag{5.56}$$

whereas for a MARY-ν experiment, it is

$$\hat{H}'_{\text{MARY-}\nu} = \sum_{\mathrm{N=A}}^{\mathrm{B}} (\omega_0 - \omega_{\mathrm{rf}})\hat{S}_{\mathrm{Nz}} + \omega_1\hat{S}_{\mathrm{Nx}} + \sum_i \left\{ a_{i\mathrm{N}}\hat{\boldsymbol{I}}_{i\mathrm{N}}\cdot\hat{\boldsymbol{S}}_{\mathrm{N}} - \omega_{\mathrm{rf}}\hat{I}_{iz} \right\}. \tag{5.57}$$

In order to change from a CPL+ with RMS field strength B_1 to a LIN field with RMS field strength $\sqrt{2}B_1$, we must add a counter-rotating contribution

$$\hat{H}_\diamond(t) = \sum_{\mathrm{N=A}}^{\mathrm{B}} \omega_1\hat{S}_{\mathrm{Nx}}\cos 2\omega_{\mathrm{rf}}t - \omega_1\hat{S}_{\mathrm{Ny}}\sin 2\omega_{\mathrm{rf}}t. \tag{5.58}$$

In the OMFE experiment, the $-\omega_{\mathrm{rf}}\hat{S}_{\mathrm{Nz}}$ term creates energy level splittings of $2\omega_{\mathrm{rf}}$ which are at just the right energy to show resonant effects from the counter-rotating contribution $\hat{H}_\diamond(t)$. Hence, we expect to see significant differences between OMFE spectra generated by a CPL+ field of strength B_1 and by a LIN field of strength $\sqrt{2}B_1$. However, in MARY-ν, the relevant term becomes $(\omega_0 - \omega_{\mathrm{rf}})\hat{S}_{\mathrm{Nz}}$. Except by chance, there will no longer be any energy level splittings of $2\omega_{\mathrm{rf}}$. Therefore, in high radio frequency MARY-ν spectra, the additional CPL− field is unlikely to have any significant effect. We expect that high frequency MARY-ν spectra generated by a CPL+ field of strength B_1 and by a LIN field of strength $\sqrt{2}B_1$ will be very similar.

We note that for small static fields $\omega_0 \lesssim a$, the hyperfine interaction comes to dominate the spin evolution. We observe small peaks at these weak static fields whose precise form depends critically on the hyperfine interactions in the RP. This is illustrated by the left hand portion of Figure 5.19b. Finally, for reasons discussed above in connection with the OMFE, as $B_0 \to 0\,\mathrm{mT}$ the effects of CPL± fields become identical.

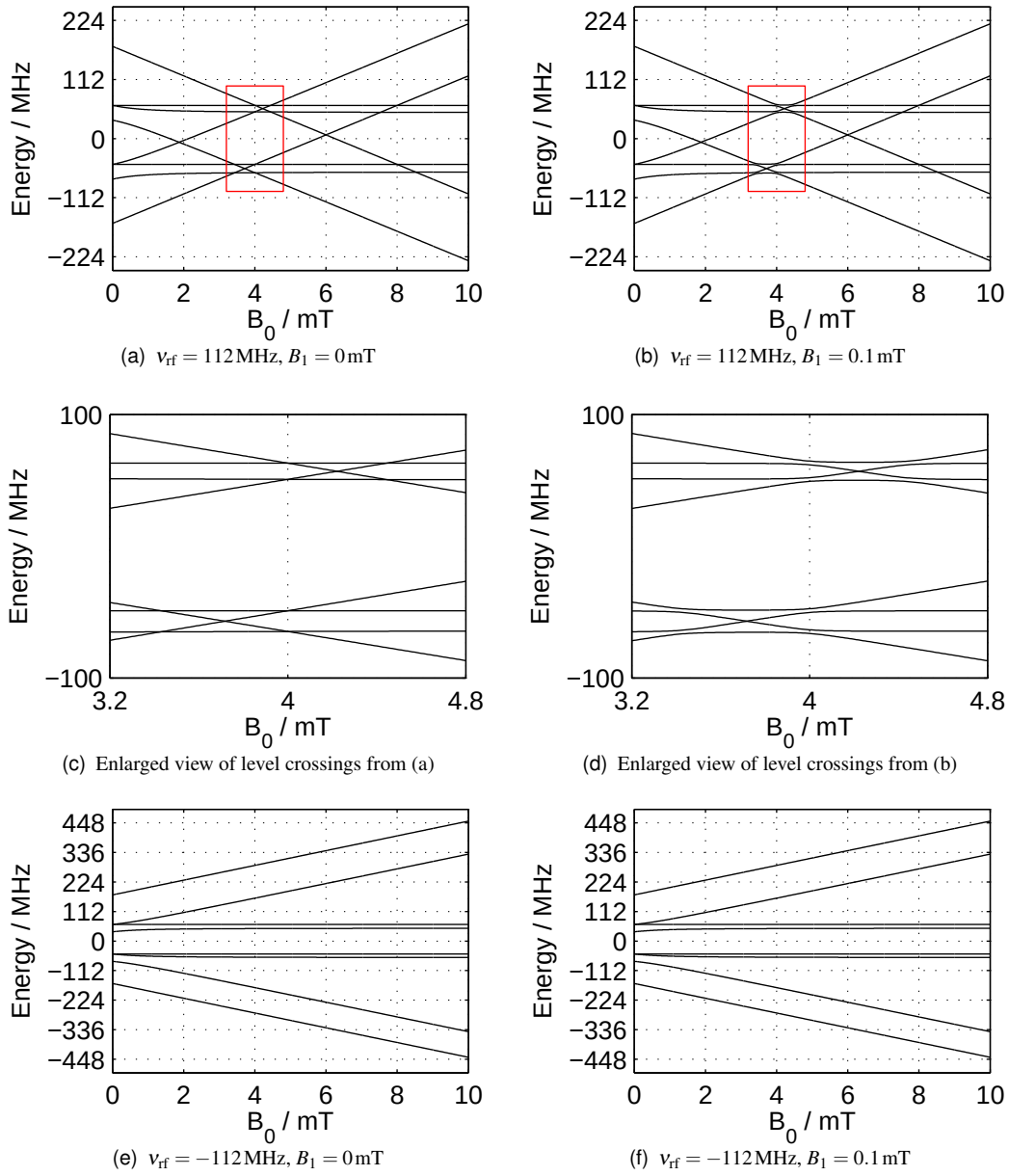

(a) $\nu_{\mathrm{rf}} = 112\,\mathrm{MHz}$, $B_1 = 0\,\mathrm{mT}$

(b) $\nu_{\mathrm{rf}} = 112\,\mathrm{MHz}$, $B_1 = 0.1\,\mathrm{mT}$

(c) Enlarged view of level crossings from (a)

(d) Enlarged view of level crossings from (b)

(e) $\nu_{\mathrm{rf}} = -112\,\mathrm{MHz}$, $B_1 = 0\,\mathrm{mT}$

(f) $\nu_{\mathrm{rf}} = -112\,\mathrm{MHz}$, $B_1 = 0.1\,\mathrm{mT}$

Figure 5.22: Rotating frame energy level diagrams for a RP that contains a single spin-½ nucleus. Parameters: $\nu_{\mathrm{rf}} = \pm 112\,\mathrm{MHz}$, $B_1 = 0$ or $0.1\,\mathrm{mT}$, $a = 1.0\,\mathrm{mT}$ and $\theta = \pi/2$. Notice that the RF field generates avoided crossings, which are indicative of a resonance effect in the CPL+ case (a–d). However, in the CPL− case (e–f), there are no avoided crossings.

5.4.5 Relative amplitude of CPL± MARY-ν spectra

As the radio frequency increases, we expect MARY-ν spectra to move out of the low-field regime and to become more like the spectra seen in microwave high-field RYDMR. One important feature of high-field RYDMR spectra is that they are caused only by the $\perp$ CPL+ component of the incident RF or microwave field. Put another way, the rotating frame approximation holds for high-field RYDMR.

Figures 4.12 and 5.23 show MARY-ν spectra for a one-proton model RP at radio frequencies between 5 and 200 MHz. Spectra are plotted for LIN, CPL+ and CPL− polarisation. In both LIN and CPL+ cases, the spectra saturate following the green curve from Figure 4.12b as explained above in the associated discussion. The MARY-ν spectra for the LIN polarisation are $\sqrt{2}$ less intense than those for CPL+. This is because for fields with the same RMS strength B_1, the LIN field only has a CPL+ component with strength $B_1/\sqrt{2}$. Finally, Figures 5.23b and c demonstrate that the MARY-ν spectra for CPL− RF are dominated by an inverted resonance between the static field B_0 and the hyperfine interaction. As the radio frequency increases, this inverted peak becomes gradually smaller. Whilst at high frequencies the LIN and CPL+ spectra are dominated by a Zeeman resonance peak whose central B_0 value is proportional to ν_{rf}, the CPL− spectra are always dominated by this fixed hyperfine resonance. Therefore, the CPL− MARY-ν signal around the Zeeman resonance field strength diminishes as ν_{rf} increases primarily because the CPL− peak is a fixed-field hyperfine resonance and not because of a complex change in selection rules. The low-field limit is rather complex because the hyperfine and Zeeman resonances would occur at similar frequencies, which causes them to mix in a non-trivial manner.

5.4.6 Effect of RF field strength

Figure 5.24 shows MARY-ν spectra for a one-proton radical pair model system at several different RF RMS field strengths B_1. Calculations are repeated for radio frequencies of 5 MHz, which is smaller than the HFC, and 55 MHz which is greater than the HFC. Several features are apparent, which we discuss below.

As the RF field strength is increased from 0.1–10 mT, the MARY-ν spectra become steadily stronger regardless of the radio frequency. It is physically quite reasonable that strong RF fields produce large changes in singlet yield.

For $\nu_{\mathrm{rf}} = 5$ MHz (*i.e.* the left hand column), we see that increasing RF field strength causes a change in the ordering of MARY-ν spectra for the different polarisations. At low RF field strengths, the LIN polarisation lies between the CPL+ and CPL− polarisations. Yet at high RF field strength, CPL+ and CPL− fields show rather similar MARY-ν spectra that are quite different from the smaller signals produced by LIN fields. Figures 5.24c and e show that for a radio frequency of 5 MHz, a LIN field of RMS field strength $\sqrt{2}B_1$ produces effects that are quite different from those of a CPL+ field of RMS field strength B_1.

At $\nu_{\mathrm{rf}} = 55$ MHz, we see a clear Zeeman resonance in Figures 5.24b and d. In particular, Figure 5.24d shows that a LIN field of strength $B_1 = \sqrt{2}$ mT produces changes in singlet yield that are almost identical to those from a CPL+ field of strength $B_1 = 1.0$ mT. This supports the above arguments made in connection with equation (5.58). Finally, in Figure 5.24f, we see that an RF field which is stronger than the RP HFCs causes the MARY-ν Zeeman resonance to show a dramatic inverted line-

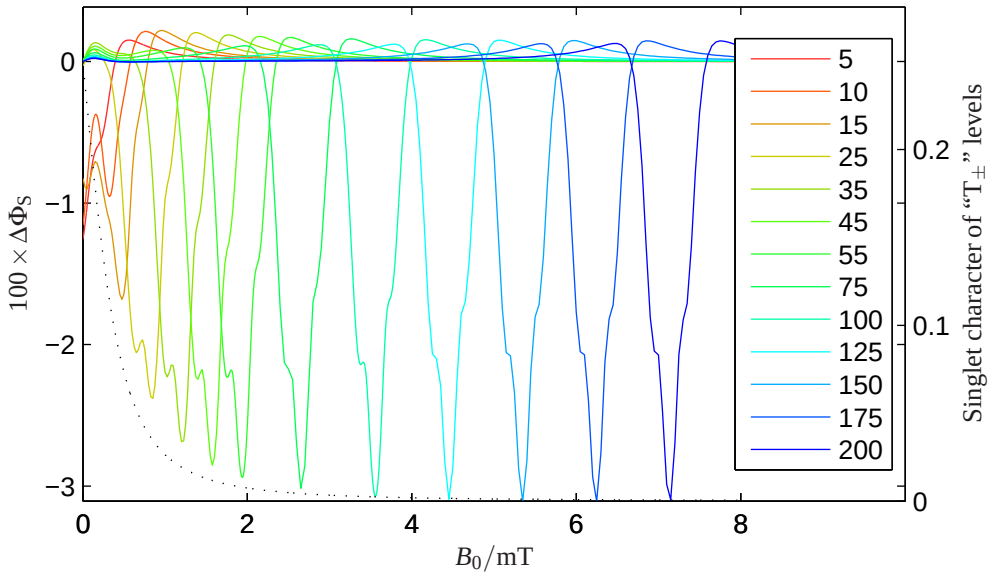

(a) Selection of MARY-ν spectra for CPL+ polarisation with ν_{rf}/MHz as shown. These curves are plotted using the left-hand vertical axis. The green curve from Figure 4.12b is plotted using the right-hand vertical axis as a dotted black line to aid comparison with the peak depths.

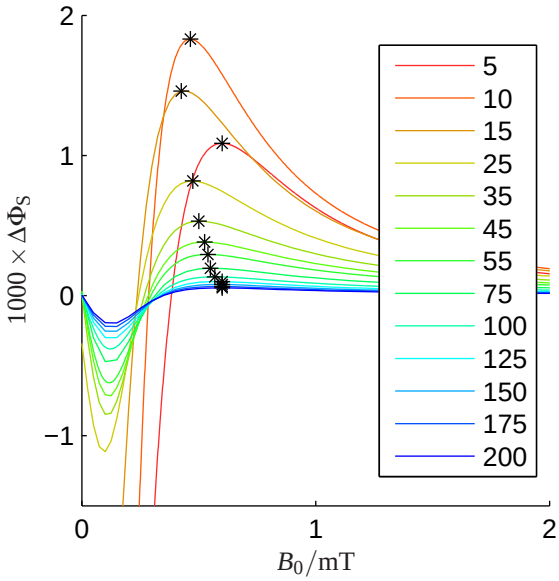

(b) Selection of MARY-ν spectra for CPL− polarisation with ν_{rf}/MHz as shown.

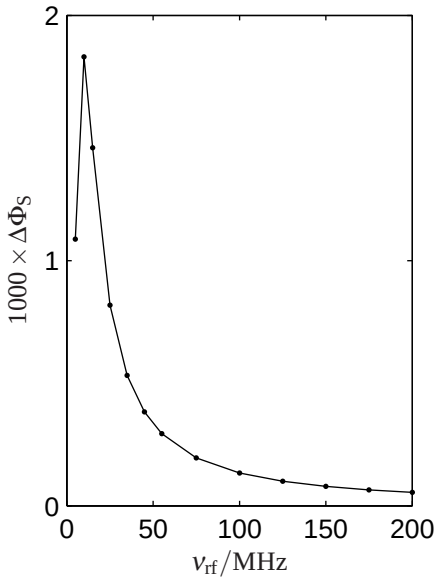

(c) Maximum singlet yields for each MARY-ν spectrum in (b).

Figure 5.23: Calculations in a one-proton radical pair using the RFT with the following parameters: $a = 0.5\,\mathrm{mT}$, $k = 2.8 \times 10^7\,\mathrm{s}^{-1}$, $n = 64$, $B_1 = 100\,\mu\mathrm{T}$, $\theta = \pi/2$. Equivalent calculations for LIN polarisation are shown in Figure 4.12.

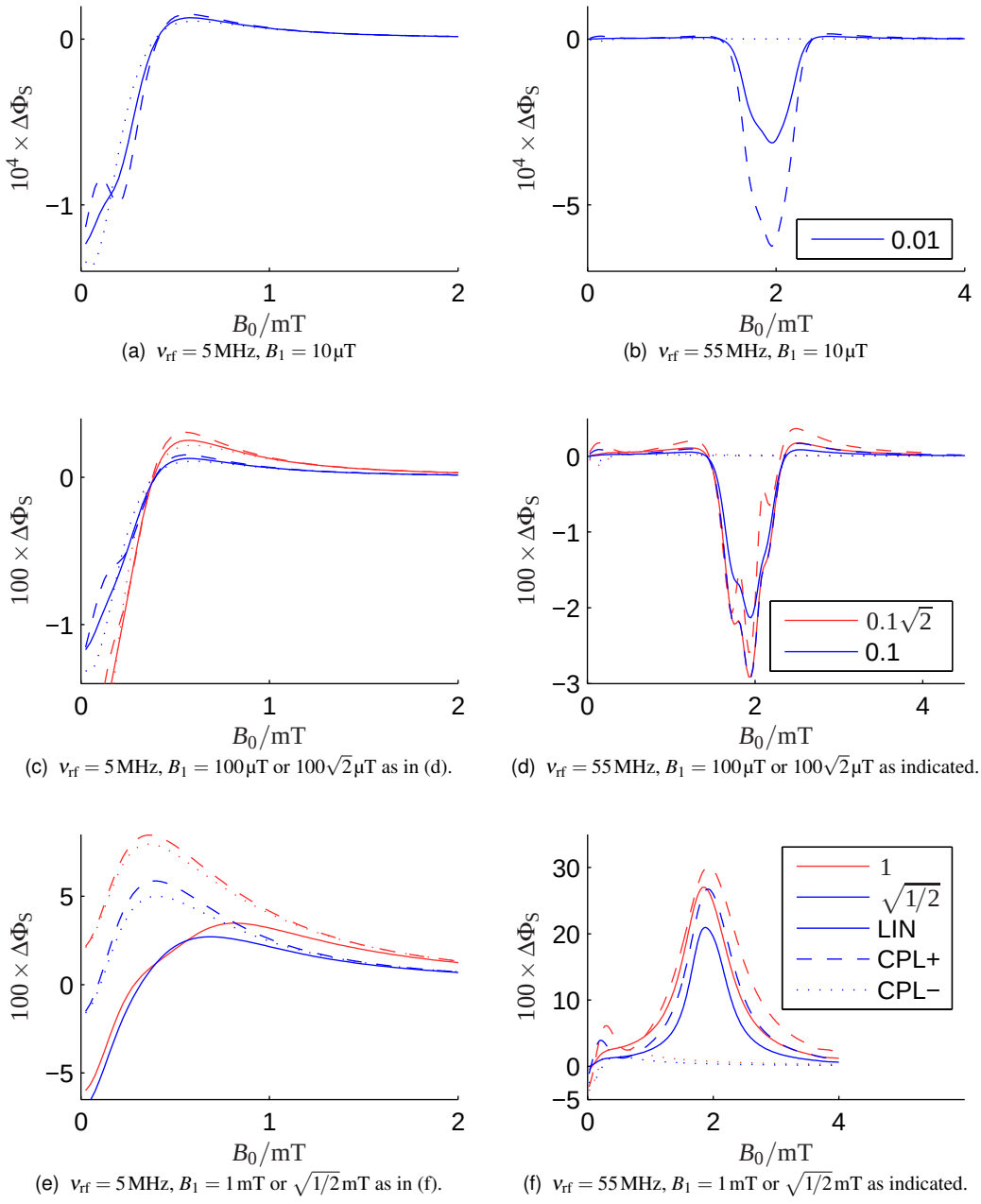

(a) $\nu_{\mathrm{rf}} = 5\,\mathrm{MHz}$, $B_1 = 10\,\mu\mathrm{T}$

(b) $\nu_{\mathrm{rf}} = 55\,\mathrm{MHz}$, $B_1 = 10\,\mu\mathrm{T}$

(c) $\nu_{\mathrm{rf}} = 5\,\mathrm{MHz}$, $B_1 = 100\,\mu\mathrm{T}$ or $100\sqrt{2}\,\mu\mathrm{T}$ as in (d).

(d) $\nu_{\mathrm{rf}} = 55\,\mathrm{MHz}$, $B_1 = 100\,\mu\mathrm{T}$ or $100\sqrt{2}\,\mu\mathrm{T}$ as indicated.

(e) $\nu_{\mathrm{rf}} = 5\,\mathrm{MHz}$, $B_1 = 1\,\mathrm{mT}$ or $\sqrt{1/2}\,\mathrm{mT}$ as in (f).

(f) $\nu_{\mathrm{rf}} = 55\,\mathrm{MHz}$, $B_1 = 1\,\mathrm{mT}$ or $\sqrt{1/2}\,\mathrm{mT}$ as indicated.

Figure 5.24: Effect of RF field strength $B_1 = -\omega_1/\gamma_e$ on MARY-ν polarisation effects in a RP that contains a single spin-½ nucleus with HFC $a = 0.5\,\mathrm{mT} = 14\,\mathrm{MHz}$. Figures are plotted with (left column) $\omega_{\mathrm{rf}} < a$ and (right column) $\omega_{\mathrm{rf}} \gg a$. Parameters: $n = 64$, $\theta = \pi/2$ and $k = 2.8 \times 10^7\,\mathrm{s}^{-1}$. On the left, all MARY-$\nu$ spectra tend smoothly to zero in the region $B_0 = 2$–$4\,\mathrm{mT}$.

shape. At the Zeeman resonance, the singlet yield without RF is 0.637 whereas in the presence of a CPL+ field of $B_1 = 10\,\mathrm{mT}$, the singlet yield becomes 0.938. The RF field has almost completely suspended singlet–triplet mixing. We discuss this "spin locking" effect in more detail in §5.5.

5.4.7 Effect of hyperfine constant

Figure 5.25 shows how MARY-ν spectra depend on the hyperfine coupling constant in a one-proton radical pair. At high radio frequencies, the main effect of the hyperfine coupling is to produce shoulders around the Zeeman resonance peak. These shoulders correspond to transitions between the different energy levels split by the hyperfine coupling within the Zeeman manifold as shown in Figure 5.20. However, at low radio frequencies, the hyperfine couplings produce more subtle changes in the shape and intensity of the MARY-ν spectra.

Figure 5.26 shows that similar effects are found when we add a second magnetic nucleus to form a "1–1" RP. At 55 MHz, this causes a change in the hyperfine fine structure around the Zeeman resonance, whilst at 5 MHz, the effects are rather complex and difficult to rationalise on the basis of simple physical arguments.

5.4.8 Experimental results and discussion

Experimental measurements of MARY-ν spectra were made in a variety of chemical systems by Norman and Wedge using the apparatus described in §5.3.8. Since MARY-ν spectra are taken at a fixed radio frequency, many of the difficulties that were experienced with the OMFE experiment in maintaining accurate RF phase and power matching were alleviated. Furthermore, since the field effects responsible for MARY-ν spectra produce larger changes in singlet yield than are seen in OMFE spectra, it was possible to observe signals in a far wider range of radical pair systems. We present here only a few examples of the MARY-ν spectra measured by Norman and Wedge. The interested reader should consult [139] for many further details.

Figures 5.27 and 5.28 show experimental MARY-ν spectra and corresponding simulations in $\left[\text{Py-h}_{10}^{\bullet+}\ \text{1,3-DCB}^{\bullet-}\right]$ and $\left[\text{Py-d}_{10}^{\bullet+}\ \text{1,4-DCB}^{\bullet-}\right]$ respectively. These systems were chosen since $\left[\text{Py-h}_{10}^{\bullet+}\ \text{1,3-DCB}^{\bullet-}\right]$ has

$$\begin{aligned}\tilde{a}_{\text{Py-h}_{10}^{\bullet+}} &= 1.2\,\mathrm{mT}\\ \tilde{a}_{\text{1,3-DCB}^{\bullet-}} &= 1.2\,\mathrm{mT}\\ \tilde{a}_{\mathrm{RP}} &= 1.7\,\mathrm{mT} = 47\,\mathrm{MHz}\end{aligned}$$

which is the largest effective HFC amongst all the systems that were studied whereas $\left[\text{Py-d}_{10}^{\bullet+}\ \text{1,4-DCB}^{\bullet-}\right]$ has

$$\begin{aligned}\tilde{a}_{\text{Py-d}_{10}^{\bullet+}} &= 0.3\,\mathrm{mT}\\ \tilde{a}_{\text{1,4-DCB}^{\bullet-}} &= 0.5\,\mathrm{mT}\\ \tilde{a}_{\mathrm{RP}} &= 0.6\,\mathrm{mT} = 17\,\mathrm{MHz}\end{aligned}$$

which is the smallest effective HFC. Taken together these two sets of results are representative of the whole range of MARY-ν spectra that were measured. Furthermore, the $\left[\text{Py-h}_{10}^{\bullet+}\ \text{1,3-DCB}^{\bullet-}\right]$ spectra have an unusually large signal-to-noise ratio.

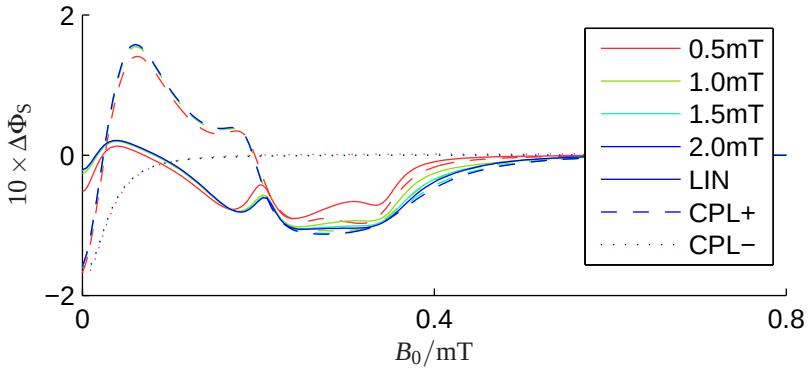

(a) Radio frequency $\nu_{\mathrm{rf}} = 5\,\mathrm{MHz}$. This is equivalent to an HFC or static field of 0.18 mT. All MARY-ν spectra tend smoothly to zero in the region $B_0 = 0.8$–$4\,\mathrm{mT}$.

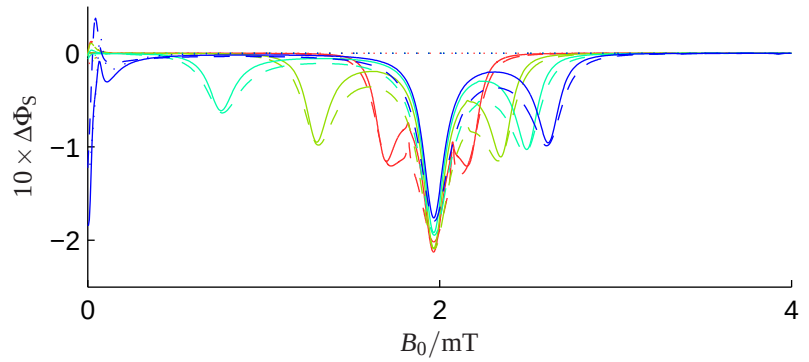

(b) Radio frequency $\nu_{\mathrm{rf}} = 55\,\mathrm{MHz}$. This is equivalent to an HFC or static field of 1.96 mT.

Figure 5.25: Effect of hyperfine coupling constant on MARY-ν polarisation effects in a RP that contains a single spin-½ nucleus. HFC values are shown in the legend. Parameters: $n = 64$, $\theta = \pi/2$ and $k = 2.8 \times 10^6\,\mathrm{s}^{-1}$. The central feature around $B_0 = 2\,\mathrm{mT}$ is due to the radical with no magnetic nuclei. This point is discussed in detail in Chapter 9.

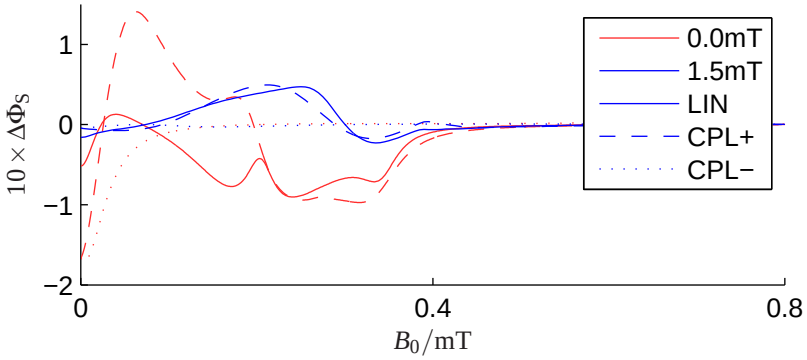

(a) Radio frequency $\nu_{rf} = 5\,\mathrm{MHz}$. This is equivalent to an HFC or static field of 0.18 mT. All MARY-ν spectra tend smoothly to zero in the region $B_0 = 0.8$–$4\,\mathrm{mT}$.

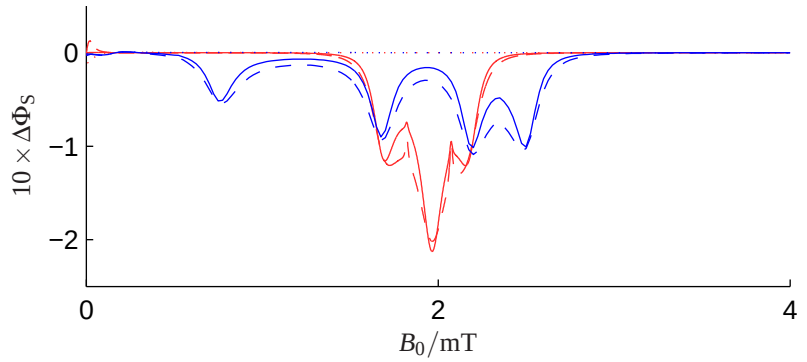

(b) Radio frequency $\nu_{rf} = 55\,\mathrm{MHz}$. This is equivalent to an HFC or static field of 1.96 mT. The shape of the blue curve may be interpreted as a doublet of doublets distorted by low-field effects.

Figure 5.26: Change in MARY-ν polarisation effects on adding a second spin-½ nucleus to give a "1–1" RP. Hyperfine couplings are $a_A = 0.5\,\mathrm{mT}$ and $a_B = 0\,\mathrm{mT}$ or $a_B = 1.5\,\mathrm{mT}$ as indicated in the legend. Parameters: $n = 64$, $\theta = \pi/2$, $B_1 = 0.1\,\mathrm{mT}$ and $k = 2.8 \times 10^6\,\mathrm{s}^{-1}$.

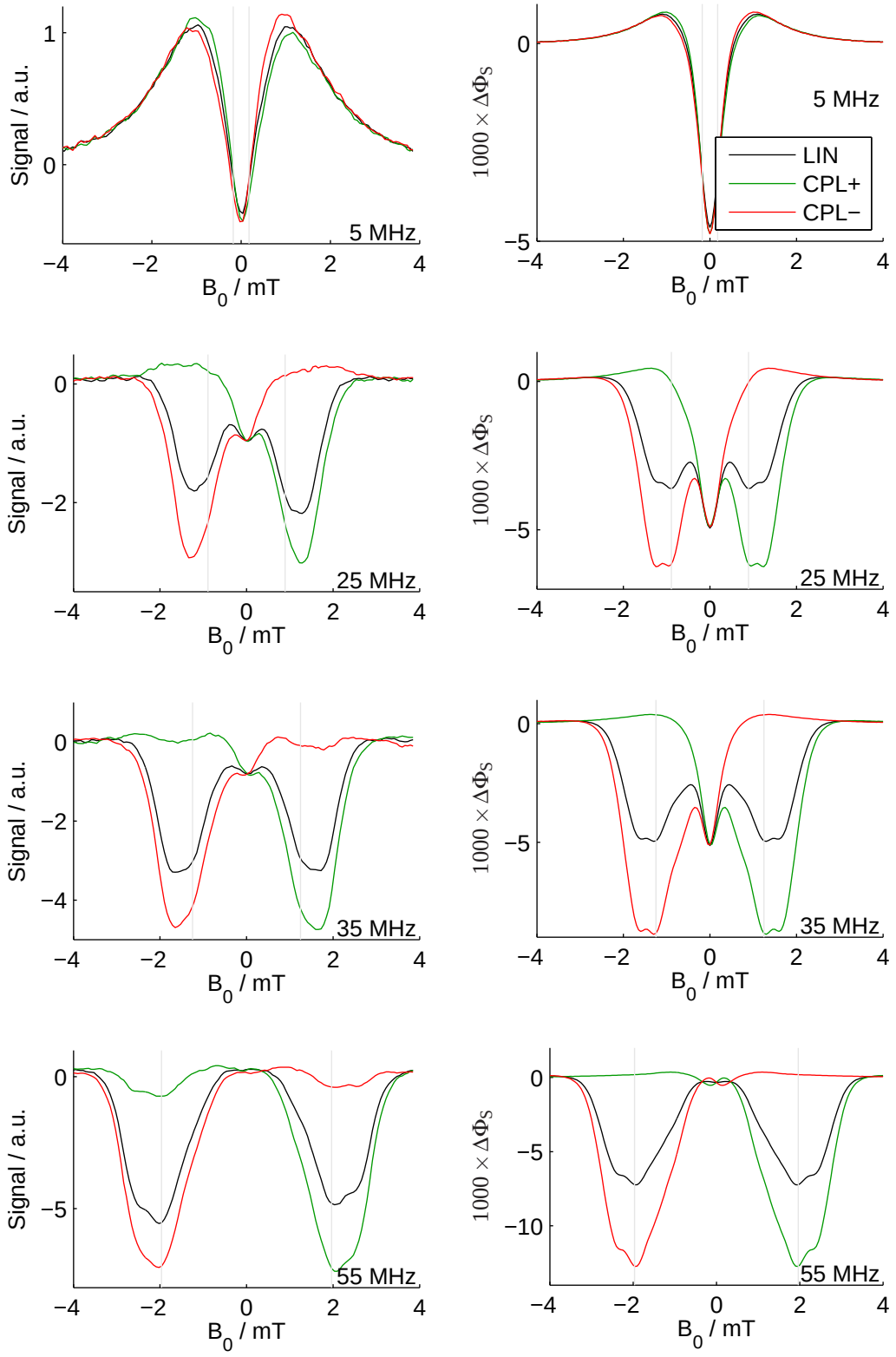

Figure 5.27: Left: Experimental MARY-v spectra measured in the $[\text{Py-h}_{10}^{\bullet+}\ \text{1,3-DCB}^{\bullet-}]$ radical pair. The frequency of the RF field is indicated for each spectrum. Grey vertical lines show the static field at which a Zeeman resonance might be anticipated. Right: Corresponding simulations made with γ–COMPUTE or the RFT. Parameters: HFCs of $4 \times 0.538\,\text{mT}$ (^{1}H) on Py-h$_{10}^{\bullet+}$; and $2 \times 0.829\,\text{mT}$ (^{1}H), $1 \times 0.144\,\text{mT}$ (^{1}H) on 1,3-DCB$^{\bullet-}$, $k = 5.5 \times 10^7\,\text{s}^{-1}$, $n = 64$, $\theta = \pi/2$ and $B_1 = 0.15\,\text{mT}$.

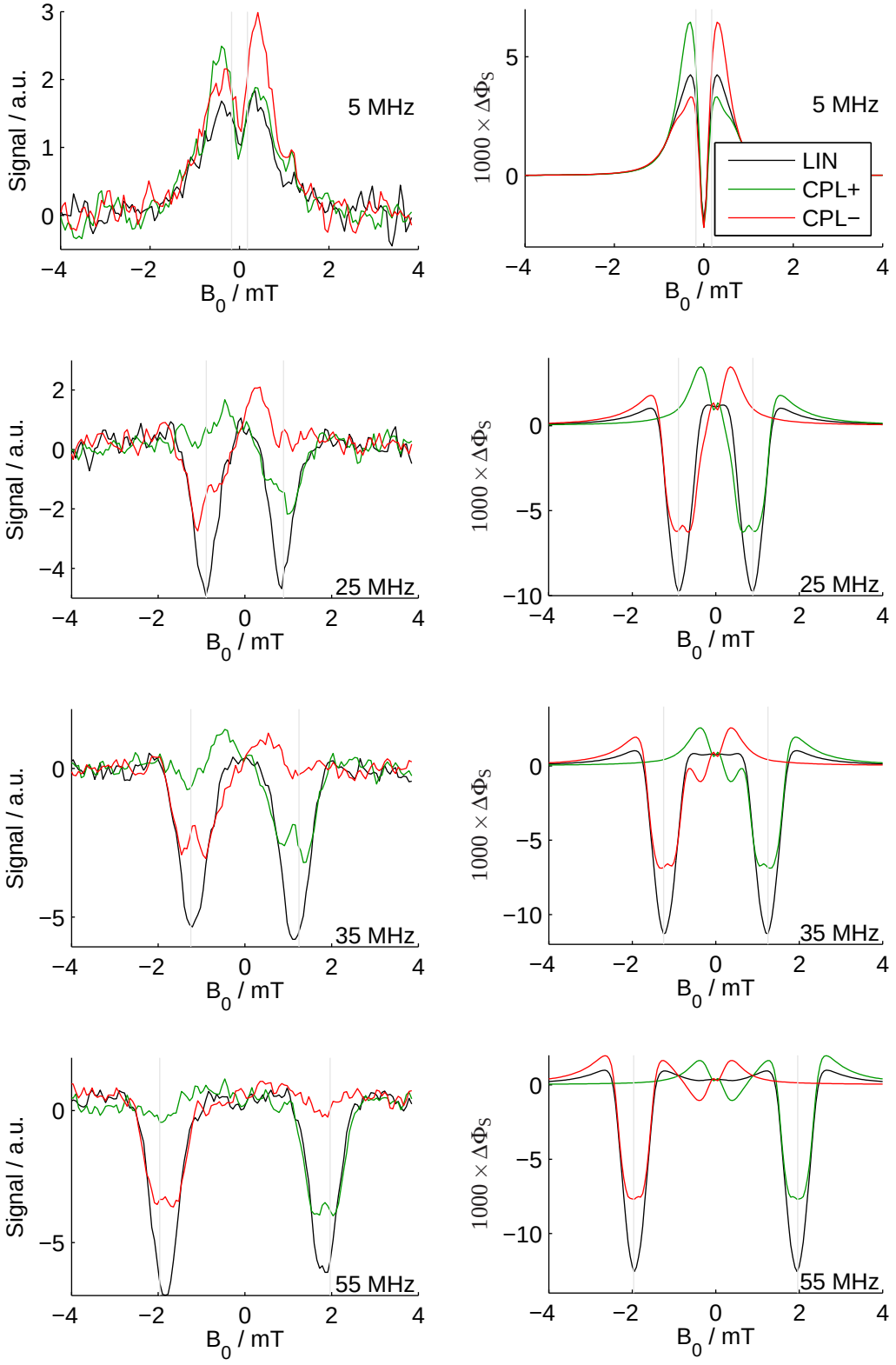

Figure 5.28: Left: Experimental MARY-v spectra measured in the $\left[\text{Py-d}_{10}^{\bullet+}\ \text{1,4-DCB}^{\bullet-}\right]$ radical pair. The frequency of the RF field is indicated for each spectrum. Grey vertical lines show the static field at which a Zeman resonance might be anticipated. Right: Corresponding simulations made with γ–COMPUTE or the RFT. Parameters: HFCs of $4 \times 0.083\,\text{mT}$ (^{2}D) on Py-d$_{10}^{\bullet+}$; and $2 \times 0.181\,\text{mT}$ (^{14}N) on 1,4-DCB$^{\bullet-}$, $k = 3 \times 10^7\,\text{s}^{-1}$, $n = 64$, $\theta = \pi/2$ and $B_1 = 0.15\,\text{mT}$.

The experimental figures all show a high degree of symmetry about the vertical axis. If one reflects a given figure such that $B_0 \rightarrow -B_0$, the LIN curves are all almost unchanged whilst the circularly polarised curves are interchanged such that CPL+ $\leftrightarrow$ CPL−. This behaviour is required physically by symmetry and is seen in the calculated spectra. The fact that the experimental data behave in this manner increases our confidence that the RF phase-shift and power matching are functioning correctly.

The most noticeable differences between simulation and experiment occur around $B_0 = 0\,\mathrm{mT}$, where the hyperfine interaction dominates the radical pair spin Hamiltonian. The simulated strong negative-going peaks around zero static field are an artefact caused by the neglect of small hyperfine couplings. Unfortunately, given current computer hardware, it is not possible to calculate using all the known hyperfine couplings in these RPs because the spin Hamiltonian grows exponentially with each additional magnetic nucleus.

Nevertheless, apart from the negative-going artefacts in the 5 MHz simulations, there is excellent qualitative agreement between experimental and simulated spectra. This agreement is particularly striking when we consider that the simulations were made using literature values for all parameters except the RF field strength B_1 and exponential model rate constant k. As is discussed below, the RF field strength B_1 is closely determined by the onset of "spin locking" effects in Figure 5.28, which leaves only the exponential model rate constant k as a variable parameter. Indeed, all the simulations of experimental data in Chapters 4 and 5 require very similar, and physically reasonable, values of k and B_1. The close agreement between simulation and experiment provides a powerful validation of the model for magnetic field effects that we have developed here and in Chapter 4.

On further inspection, we see that the MARY-ν spectra presented in Figures 5.27 and 5.28 depend strongly on the radio frequency ν_{rf} in a manner that is strongly reminiscent of the preliminary calculations shown in Figures 5.18c, 5.25 and 5.26.

When $\nu_{\mathrm{rf}} = 5\,\mathrm{MHz}$, there is generally little RF polarisation effect; LIN and CPL$\pm$ spectra have similar amplitudes. Comparing spectra for the two systems, it is apparent that the CPL− curves have significant amplitude at frequencies of 35 MHz or above in $\left[\text{Py-h}_{10}^{\bullet+}\ \text{1,3-DCB}^{\bullet-}\right]$, whereas in $\left[\text{Py-d}_{10}^{\bullet+}\ \text{1,4-DCB}^{\bullet-}\right]$ the CPL− component is minimal even in the 25 MHz spectra. These differences reflect the larger effective HFC in the protonated RP, demonstrating the importance of the ratio $\omega_{\mathrm{rf}}/\tilde{a}_{\mathrm{RP}}$ in controlling MARY-ν polarisation effects. In other words, small polarisation effects are observed in the low-frequency limit when the hyperfine interaction is large compared to the Zeeman energy, *i.e.* in systems where $\tilde{a}_{\mathrm{RP}} \gtrsim \omega_{\mathrm{rf}}$.

When $\nu_{\mathrm{rf}} = 55\,\mathrm{MHz}$, both systems show RF polarisation effects that are dominated by a strong Zeeman resonance. In $\left[\text{Py-h}_{10}^{\bullet+}\ \text{1,3-DCB}^{\bullet-}\right]$, this Zeeman resonance is strongest for CPL+ fields and negligible for CPL− fields; LIN fields produce a peak that lies between these. Such behaviour is as would be expected in the high-frequency limit, where only the resonant CPL+ field (or the CPL+ component of the LIN field) has any effect. The $\left[\text{Py-d}_{10}^{\bullet+}\ \text{1,4-DCB}^{\bullet-}\right]$ system also shows a strong Zeeman resonance, but here the ordering has changed such that CPL+ signal is less intense than the LIN signal. This "spin locking" effect is discussed further below. Finally, we see that the width of the Zeeman resonance is substantially less in $\left[\text{Py-d}_{10}^{\bullet+}\ \text{1,4-DCB}^{\bullet-}\right]$ than in $\left[\text{Py-h}_{10}^{\bullet+}\ \text{1,3-DCB}^{\bullet-}\right]$. This is a result of the smaller effective HFCs in the former RP. Similar behaviour was observed for one-proton RPs in Figure 5.25. There,

the hyperfine interaction gave rise to distinct shoulders and satellite peaks, whereas in the experimental systems the rate constant k is larger, giving rise to a single broad line whose width reflects the unresolved hyperfine structure.

5.5 Spin locking

In the OMFE and MARY-ν magnetic field effects considered above, an RF field acts for the most part to decrease the singlet yield in a singlet-born RP. In other words, application of an RF field is found to increase the efficiency of singlet–triplet interconversion. For weak RF fields, such behaviour is quite natural: the RF field may be treated as a first order perturbation that opens new channels for coherent spin evolution between states that are separated by ω_{rf} in energy. Such arguments were presented in connection with Figure 5.20.

However, in the presence of strong RF fields, this perturbative approach breaks down. In Figures 5.13 and 5.24f, we see that a strong RF field occasionally causes an increase in singlet yield, giving rise to an inverted lineshape. In other words, the RF field now acts to *restrict* singlet–triplet interconversion. It is as though an appropriate strong RF field "locks" the electron spins into their singlet state. Similar effects have been observed in NMR [86, p552] and in high-field RYDMR studies on bacterial photosynthetic centres [217, 218]. In an NMR context, spin locking allows the rotating frame magnetisation of nuclei with different resonance frequencies to be "locked" along a particular direction in the rotating frame xy-plane. The normal dephasing that would occur because of the spins' resonance offsets is suppressed. In the context of RP reactions, spin locking has a similar interpretation. Here, a strong RF field dominates the evolution of each unpaired electron spin. Since the electron spin motion is now orchestrated by the *same* RF field, the electron spins remain in phase with the RF field and hence with one-another. Whereas in NMR, two nuclear spins with different resonant frequencies remain locked in phase, now it is the two electron spins in the RP that evolve in phase regardless of any differences in hyperfine interactions or nuclear spin states between the radicals. In the limit of infinitely strong RF fields, the electron spins evolve completely in phase with one-another, and there can be no singlet–triplet mixing.

It is clear from the above figures that the response to a strong RF field depends strongly, and in a complicated manner, on the frequency, polarisation and strength of that field as well as on the RP hyperfine structure and on the strength of any static field. One can envisage a wealth of new experiments to probe these parameters. Although a few investigations into the effect of microwave field strength on OD EPR have been made for strong microwave fields [36, 58, 64, 217, 219, 272, 273], we believe that the current work is the first to treat the effects of radio frequency fields, or the issue of RF polarisation, or to consider static fields lying within the low-field regime.

The closing sections of this chapter are devoted to the study of such spin locking effects. Once again, we see good qualitative agreement between experimental results and simulations made using the model that we have developed. This agreement further validates our model. In addition, the simulations below present a number of as-yet-unsolved theoretical challenges. There is much further work to be done here in order to give solid physical explanations for the unusual spectra that are predicted numerically. Finally, we show that spin locking effects provide a powerful tool for calibrating

experimental RF field strengths in the presence of weak ($\lesssim 10\,\mathrm{mT}$) static fields.

5.5.1 Calibration of RF field strengths

Figure 5.29 is a vivid illustration of the onset of spin locking in the MARY-ν spectrum of $\left[\text{Py-d}_{10}^{\bullet+}\ \text{1,4-DCB}^{\bullet-}\right]$. Notice that the experimental spectrum shows an unusual ordering of the different polarisations at the Zeeman resonance peak. Here, the CPL+ peak is less deep than the LIN peak, whereas typically the CPL+ peak is the deeper. Furthermore, the CPL+ peak shows a distinctive partially inverted feature at its centre.

Alongside the experimental data are presented seven simulations at RF field strengths from 0.05–0.3 mT. When the RF field strength is 0.05 mT, we see the normal ordering of polarisations at the Zeeman resonance: CPL− shows a negligible signal, CPL+ shows the deepest signal and LIN lies between the two. As the RF field strength is increased, we see the LIN and CPL+ spectra drawing together; then the CPL+ spectrum rises above the LIN spectrum and inverts; finally the LIN spectrum inverts too. The combined LIN and CPL+ lineshapes are quite different in each of the seven simulated MARY-ν spectra. Notice that around the onset of spin locking, adjusting the RF field strength by as little as 0.025 mT produces a marked change in lineshape.

As will be shown below, the onset of spin locking depends on the overall RP effective HFC. By measuring MARY-ν spectra of an appropriate RP with LIN and CPL$\pm$ polarised RF, one is likely to observe the onset of these characteristic spin locking effects. Comparison with simulated spectra, such as those in Figure 5.29, will provide a high quality estimate of the weak RF field that is generated experimentally. The strength of such an RF field is very difficult to measure directly in-situ or to calculate accurately from coil design parameters [139]. Yet, the RF field strength is an important model parameter. By fixing this parameter, our method of RF field strength estimation improves the quality of simulations for any other experiments performed using the same apparatus.

5.5.2 Spin locking in model radical pairs

As is evident in Figure 5.29, the singlet yield at the Zeeman resonance field ($B_0 = -\omega_{\mathrm{rf}}/\gamma_{\mathrm{e}}$) is most characteristic of spin locking in MARY-ν spectra. A graph showing the change in singlet yield caused by the introduction of an RF field with RMS strength B_1 when the radio frequency and static field strength satisfy the Zeeman resonance condition summarises these spin locking effects. In the context of experiments involving strong static fields and microwave frequency oscillating fields, such a plot is known as a "RYDMR B_1 plot" [36, 219, 273]; here we refer merely to "B_1 plots".

Effect of hyperfine couplings

Figure 5.30 shows a series of B_1 plots calculated in simple one- and two-proton radical pairs. Calculations were made for both linearly and circularly polarised RF fields, in contrast to previous high-field RYDMR studies [36, 219, 273] where calculations were made only with circularly polarised fields and experimental measurements with linearly polarised fields.

The B_1 plots in Figure 5.30 all share the same basic shape. Irrespective of the RP hyperfine structure, a weak resonant RF field produces a decrease in singlet yield

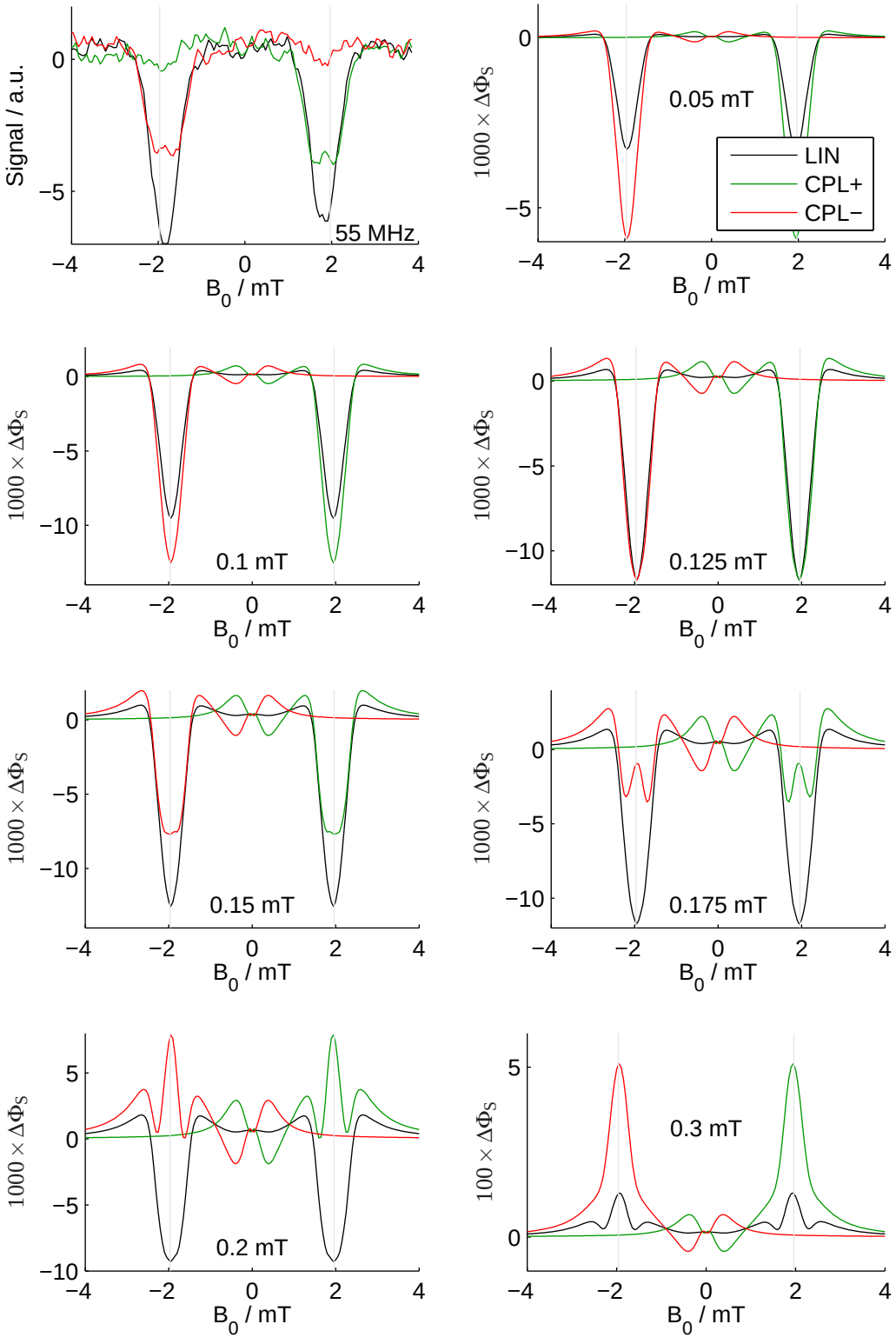

Figure 5.29: Spin locking effects provide a means of calibrating RF field strength. Top left: Experimental MARY-v spectra measured in the $\left[\text{Py-d}_{10}^{\bullet+}\ \text{1,4-DCB}^{\bullet-}\right]$ radical pair at $\nu_{\text{rf}} = 55\,\text{MHz}$. Other figures: Simulations made with γ–COMPUTE or the RFT. Parameters: RMS RF field strength B_1 is marked on each figure, HFCs of $4 \times 0.083\,\text{mT}$ (^{2}D) on Py-$\text{d}_{10}^{\bullet+}$; and $2 \times 0.181\,\text{mT}$ (^{14}N) on 1,4-$\text{DCB}^{\bullet-}$, $k = 3 \times 10^7\,\text{s}^{-1}$, $n = 64$, $\theta = \pi/2$ and $\nu_{\text{rf}} = 55\,\text{MHz}$. Grey vertical lines show the Zeeman resonance static field.

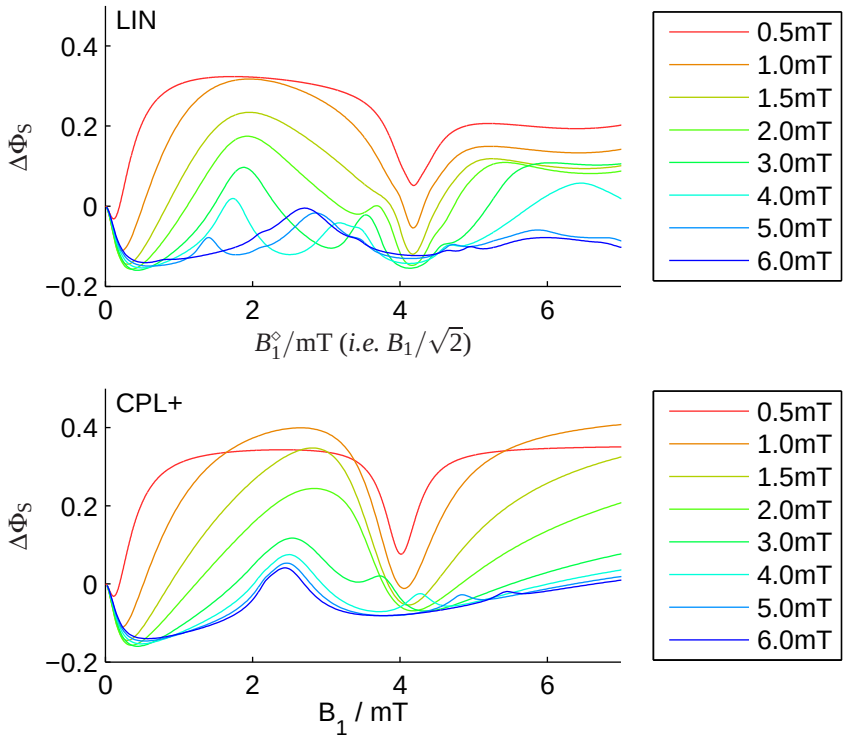

(a) B_1 plots for "1–0" RPs having a single spin-½ whose HFC is given in the legend.

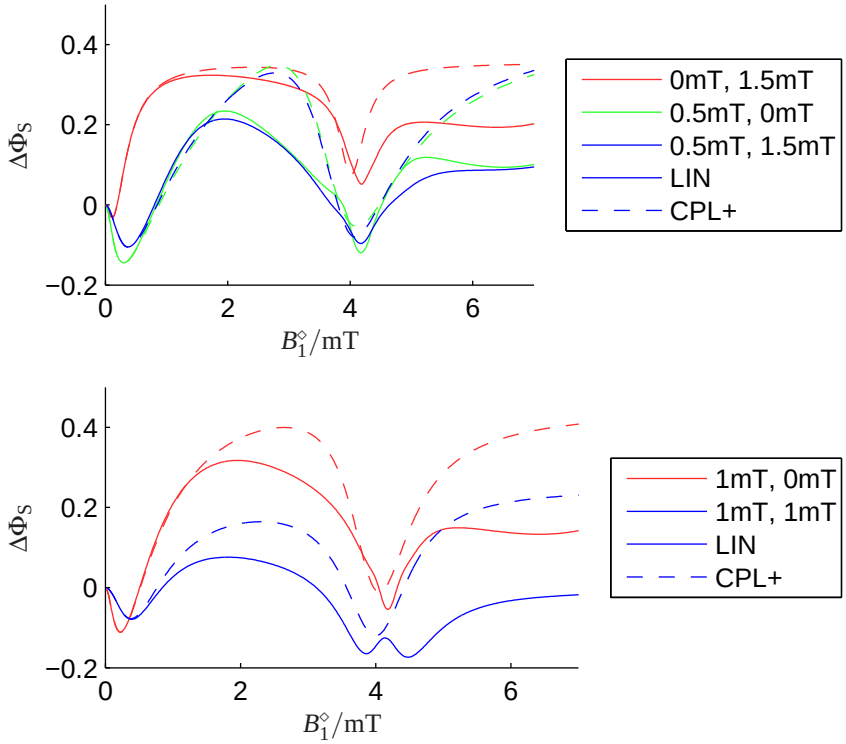

(b) Effect on B_1 plots of adding a second spin-½ nucleus to form a "1–1" RP. HFCs on each radical (a_A, a_B) are given in the legend.

Figure 5.30: Effect of hyperfine structure on spin locking in "1–0" and "1–1" model RPs. RF field strengths for LIN polarised fields are described in terms of the strength of their CPL+ component $B_1^{\diamond} = B_1/\sqrt{2}$ (see §5.2.4). Calculations were made using γ–COMPUTE or the RFT. Parameters: $\nu_{rf} = 112\,\text{MHz}$, $B_0 = 4\,\text{mT}$, $k = 2.8 \times 10^7\,\text{s}^{-1}$, $n = 256$ and $\theta = \pi/2$. CPL− fields produced only small featureless changes in singlet yield.

compared to that in the absence of an RF field, *i.e.* when $B_1 = 0\,\mathrm{mT}$. This is as expected for an RF field that acts merely as a weak perturbation connecting the $(\mathrm{S},\mathrm{T}_0) \leftrightarrow \mathrm{T}_\pm$ energy levels.

As B_1 is increased, the Zeeman peak becomes progressively deeper until an RF field strength of around 0.5 mT. The maximum depth of the Zeeman resonance peak depends on the HFCs; in general, RPs with larger HFCs show deeper Zeeman resonance peaks in the presence of weak RF fields.

As the RF field is increased still further, the singlet yield begins to rise. The Zeeman peak becomes less deep, and in many cases it inverts because the RF field now causes "spin locking" — *i.e.* the field now acts to *prevent* singlet–triplet interconversion. Systems with small HFCs tend to invert at smaller B_1 values and to produce larger positive Zeeman peaks. Systems that contain a large hyperfine coupling (*i.e.* where $a \gtrsim -\omega_{\mathrm{rf}}/\gamma_{\mathrm{e}}$) tend to show very little if any inversion. It appears that spin locking is only effective when both ν_{rf} and B_1 exceed the HFCs.

Finally, as the RF and static field strengths become equal, at $B_0 = B_1^\diamond = 4\,\mathrm{mT}$ in this system, there is a sharp fall in singlet yield. In some cases the Zeeman peak even returns to its normal polarity. We consider the origins of this feature in further detail below.

So far, we have not mentioned the effects of RF polarisation. At 112 MHz and for the RF field strengths considered here, CPL− fields give negligible changes in singlet yield. The corresponding B_1 spectra are flat and featureless and hence are not shown in Figure 5.30.

Linearly polarised fields are best considered as a superposition of CPL± fields as described in §5.2.4. A LIN field with RMS RF field strength B_1 has a CPL+ component with RMS field strength $B_1^\diamond = B_1/\sqrt{2}$. Meanwhile, for a CPL+ field with RMS field strength B_1, the strength of the CPL+ "component" is obviously $B_1^\diamond = B_1$. Adopting this convention, we see that LIN and CPL+ B_1 spectra are practically identical when $B_1^\diamond \lesssim 1\,\mathrm{mT}$ for all the RPs shown in Figure 5.30. In many cases, this close resemblance continues until $B_1^\diamond = 2$ or 3 mT. Such RF field strengths are greater than any that we have obtained experimentally.

Figure 5.30b shows B_1 spectra for multinuclear "1–1" RPs along with B_1 spectra in related RPs that include only one of these nuclei at a time. Keeping only the nucleus with the largest hyperfine coupling gives B_1 spectra that most closely resemble those from the full multinuclear RP. It would appear that the onset of the Zeeman resonance is mainly controlled by the largest HFC in a multinuclear RP. Furthermore, since both "1–1" and "1–0" RPs show similar spectral shapes and features, it seems reasonable to expect that our observations in model systems will be broadly applicable to realistic chemical RPs.

Effect of exponential model rate constant

Figure 5.31 shows the B_1 spectra for a one-proton RP with a 0.5 mT HFC for three values of the exponential model rate constant k. The blue curve has a rate constant $k = 2.8 \times 10^7\,\mathrm{s}^{-1}$ that is typical for aromatic radical ion pairs reacting in solution. As the rate constant is decreased, we see that the B_1 spectra develop sharper more clearly resolved features. This corresponds to a reduction in "lifetime broadening" as the RP lifetime increases. We also note that the changes in singlet yield in the presence of

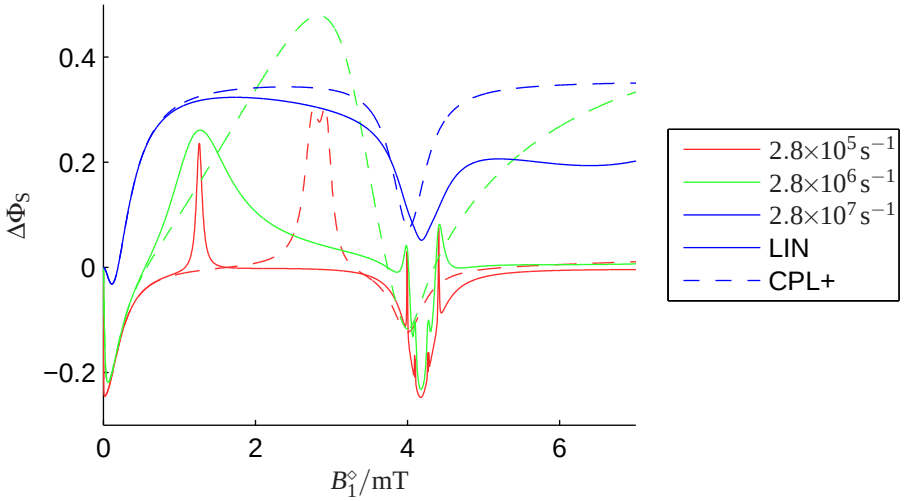

Figure 5.31: Influence of exponential model rate constant k (shown in the legend) on spin locking in a one-proton RP. RF field strengths for LIN polarised fields are described in terms of the strength of their CPL+ component $B_1^\diamond = B_1/\sqrt{2}$ (see §5.2.4). Calculations were made using γ–COMPUTE or the RFT. Parameters: $a = 0.5\,\mathrm{mT}$, $\nu_{\mathrm{rf}} = 112\,\mathrm{MHz}$, $B_0 = 4\,\mathrm{mT}$, $n = 256$ and $\theta = \pi/2$. CPL− fields produced only small featureless changes in singlet yield.

weak RF fields become much more pronounced as the RP lifetime increases between the blue and green curves. Longer lifetimes allow the RF field to more fully distribute the RP spin populations between the singlet and triplet levels that the field connects. This increase in singlet–triplet interconversion causes a fall in singlet yield. Increasing the lifetime still further in the red curve has little further effect because the RP spin populations are now evenly spread between the different eigenstates on the timescale of the RP lifetime. Finally, we notice that the extent of the RF polarisation effect depends strongly on the rate constant. Below $B_1^\diamond \sim 1\,\mathrm{mT}$, there is little difference between the signals for LIN and CPL+ fields. However, at higher field strengths, we sometimes see pronounced effects. These are strongest when $k = 2.8\times10^6\,\mathrm{s}^{-1}$ (the green curve).

Effect of relative orientation of RF and static fields

It is possible to gain some further insight into the physical origins of the inverted Zeeman peaks in MARY-ν spectra by considering the role of the relative orientation of RF and static fields. Figure 5.32 shows a series of calculated MARY-ν spectra for the $\left[\text{Py-d}_{10}^{\bullet+}\ \text{1,4-DCB}^{\bullet-}\right]$ radical pair. Spectra are shown for LIN and CPL± polarisations, at several different relative RF and static field orientations θ and at RMS RF field strengths which differ by a factor of $\sqrt{2}$.

Inspecting the figure, it is apparent that the MARY-ν spectra vary smoothly as θ is changed between the extremes of $\theta = 0$ ($\|$) and $\theta = \pi/2$ ($\perp$). Such a response is familiar from our work with linearly polarised RF fields in Chapter 4 and [179, 180].

For parallel fields, *i.e.* when $\theta = 0$, it is clear that CPL+ and CPL− RF fields produce identical spectra. This equivalence is required by the physical symmetry of the system; it is reassuring to see that the simulations deal with this case correctly. It is also apparent that the small HFC-driven feature at $B_0 \sim 0.5\,\mathrm{mT}$ tends to vanish as

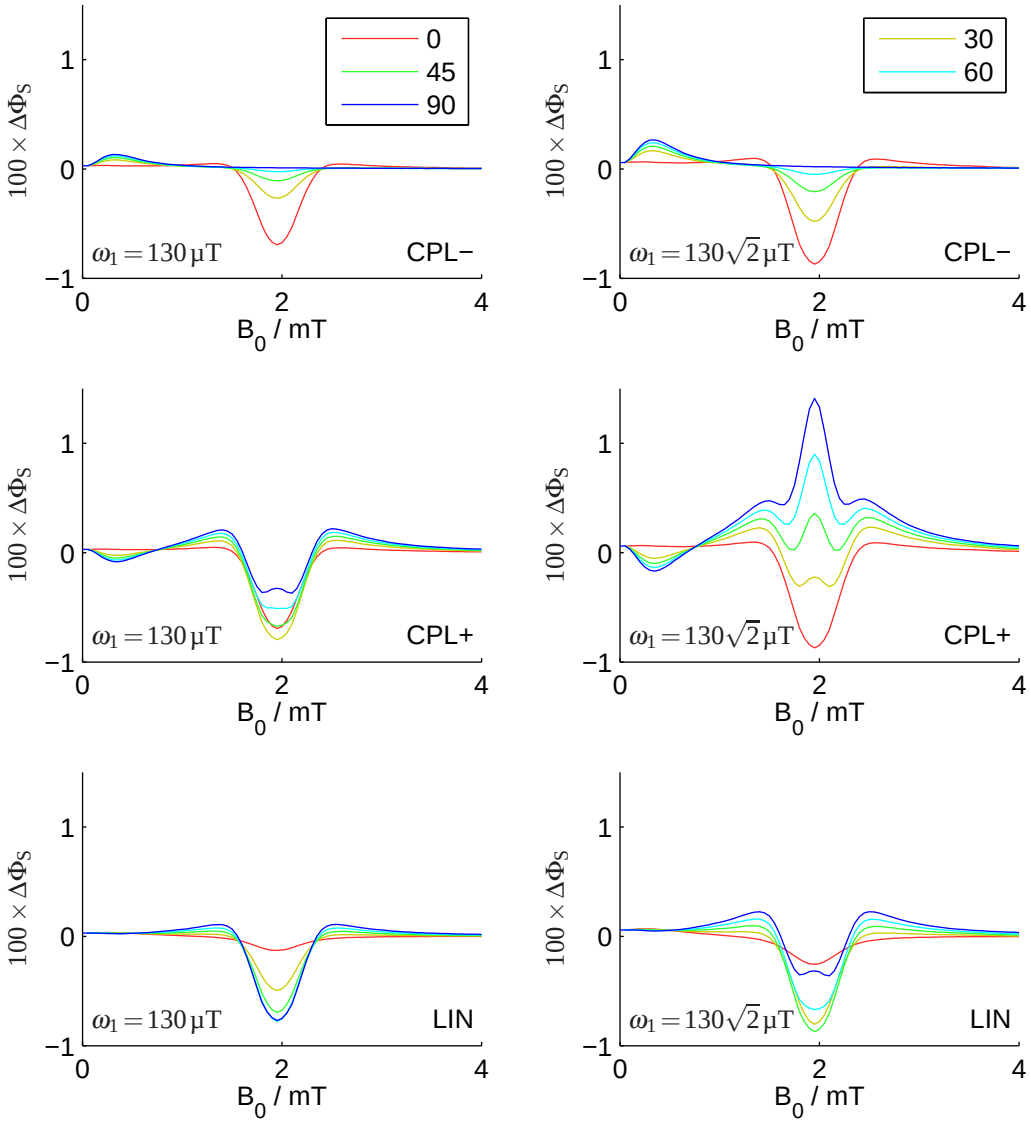

(a) Effect of relative orientation θ (indicated by line colour), RF polarisation and field strength on MARY-ν spin locking.

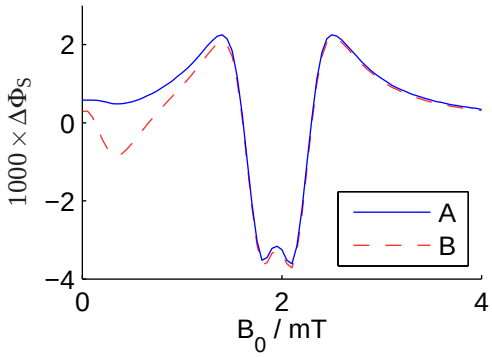

(b) Comparison of spectra for (A) LIN polarisation, $\theta = \pi/2$ and $B_1 = 130\sqrt{2}\,\mu T$; and (B) CPL+ polarisation, $\theta = \pi/2$ and $B_1 = 130\,\mu T$.

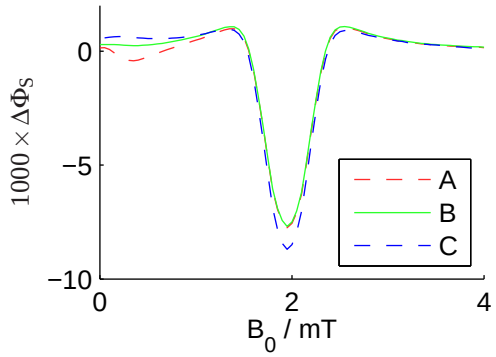

(c) Comparison of spectra for (A) CPL+ polarisation, $\theta = 0$ and $B_1 = 130\sqrt{2}\,\mu T$; (B) LIN polarisation, $\theta = \pi/2$ and $B_1 = 130\,\mu T$; and (C) CPL+ polarisation, $\theta = \pi/2$ and $B_1 = 130\sqrt{1/2}\,\mu T$.

Figure 5.32: Effect of relative RF and static field orientation θ (defined in Figure 5.1) on spin locking in $\left[\text{Py-d}_{10}^{\bullet+}\ \text{1,4-DCB}^{\bullet-}\right]$. Calculations were made with γ–COMPUTE and the RFT. Parameters: HFCs of $4 \times 0.083\,\text{mT}$ (^{2}D) on Py-d$_{10}^{\bullet+}$ and $4 \times 0.159\,\text{mT}$ (^{1}H) on 1,4-DCB$^{\bullet-}$, $k = 3 \times 10^7\,\text{s}^{-1}$, $\nu_{\text{rf}} = 55\,\text{MHz}$ and $n = 64$.

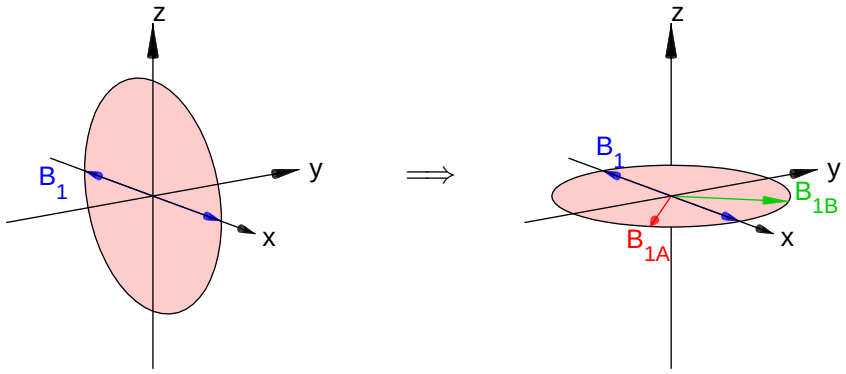

Figure 5.33: Geometrical relationship between (a) CPL±, RMS strength B_1, $\theta = 0$; (b) LIN, RMS strength $B_1/\sqrt{2}$, $\theta = \pi/2$; and (c) CPL+, RMS strength $B_1/2$, $\theta = \pi/2$. Left: (a) → (b). Right: (b) → (c). See text for details.

$\theta \to 0$ regardless of the RF polarisation or field strength.

Out of the six plots in Figure 5.32a, only that for CPL+ at $B_1 = 130\sqrt{2}\,\mu\text{T}$ shows an inverted Zeeman peak. For RF fields having a given RMS field strength, CPL+ polarisation is clearly most effective for causing spin locking effects.

Finally, we notice that some of the MARY-ν spectra in Figure 5.32a are rather similar. For example, the MARY-ν spectrum calculated under the influence of a $\perp$ LIN field with RMS RF field strength $B_1 = 130\sqrt{2}\,\mu\text{T}$ and the spectrum for a $\perp$ CPL+ field with $B_1 = 130\,\mu\text{T}$ show remarkably similar Zeeman resonances, although the HFC-dominated peaks at $B_0 \sim 0.5\,\text{mT}$ differ. These spectra are plotted again in Figure 5.32b for ease of comparison.

Another example is given in Figure 5.32c, where we see three MARY-ν spectra that are strikingly similar at the Zeeman resonance. The three RF fields used are illustrated graphically in Figure 5.33. We start with a $\parallel$ CPL+ field of RMS strength B_1, represented by the pink disc in the xz-plane on the left of Figure 5.33. Projecting out the perpendicular component gives a $\perp$ LIN field of RMS strength $B_1/\sqrt{2}$, represented by the blue arrows along the x-axis in Figure 5.33. Finally, we decompose this LIN field into $\perp$ CPL± fields of RMS strength $B_1/2$ as shown on the right of Figure 5.33. Further calculations (not shown) in a RP with HFCs of $3 \times 0.411\,\text{mT}$ (^{2}D) on one radical and $1 \times 0.785\,\text{mT}$ (^{1}H) on the other radical show the same similarity in MARY-ν spectra around the Zeeman resonance for three RF fields that have the same geometrical relationship.

5.5.3 Analysis in the rotating frame

The equivalence of the MARY-ν spectra in Figures 5.30b, 5.32b and 5.32c strongly suggests that it is only the $\perp$ CPL+ component of an RF field that is responsible for spin locking effects around the Zeeman resonance. At the RF field strengths of interest, neglecting all other components of the RF field does not seriously alter the calculated spectra. In other words, just as in the case of high-field EPR or NMR, the rotating frame approximation works well for the description of these low-field spin locking effects at the RF field strengths of interest.

The rotating frame Hamiltonian for MARY-ν in the presence of a $\perp$ CPL+ RF field

is given by equation (5.24). At the Zeeman resonance, where $\omega_{\mathrm{rf}} = \omega_0$, this simplifies to

$$\hat{H}' = \sum_{\mathrm{N=A}}^{\mathrm{B}} \omega_1 \hat{S}_{\mathrm{Nx}} + \sum_i \left\{ a_{i\mathrm{N}} \hat{\boldsymbol{I}}_{i\mathrm{N}} \cdot \hat{\boldsymbol{S}}_{\mathrm{N}} - \omega_{\mathrm{rf}} \hat{I}_{iz} \right\}, \tag{5.59}$$

in which $\hat{\boldsymbol{S}}_{\mathrm{N}}$ is the electron spin on radical N and $\hat{\boldsymbol{I}}_{i\mathrm{N}}$ is the i^{th} nuclear spin. RF fields of CPL− or LIN polarisation, or fields with a $\|$ component would give rise to other time-dependent contributions to $\hat{H}'$ which we neglect.

Figure 5.34 shows calculated MARY-ν spectra in a one-proton RP for fields with a CPL+ component of RMS strength $B_1^{\diamond} = 0$–$8\,\mathrm{mT}$. The eigenvalues of $\hat{H}'$ and the singlet character of the corresponding eigenstates of $\hat{H}'$ are plotted immediately below these spectra for comparison. It is evident that the regions of lower singlet yield around $B_1^{\diamond} = 0\,\mathrm{mT}$ and $4\,\mathrm{mT}$ coincide with avoided crossings between near-degenerate rotating frame eigenstates that have different amounts of singlet character.

For example, near $B_1^{\diamond} = 4\,\mathrm{mT}$, the blue, green and red eigenstates are very close in energy and are likely to show substantial coherent interconversion. At the instant of creation an ensemble of singlet-born RPs will have 50% population in the red eigenstates and 25% in the green and blue ones. Since these eigenstates are nearly degenerate their populations will rapidly interconvert and thus the additional population in the red eigenstates will be efficiently spread to the blue and green eigenstates. Since the latter have less singlet character, this causes efficient singlet–triplet interconversion; hence the singlet yield falls from unity.

Near $B_1^{\diamond} = 0\,\mathrm{mT}$, we again see avoided crossings between eigenstates with different amounts of singlet character that are close in energy. The same argument explains the drop in singlet yield around $B_1^{\diamond} = 0\,\mathrm{mT}$.

In the presence of very weak RF fields, we see a feature that resembles the low field effect in MARY spectroscopy. In the rotating frame, this is caused by the lifting of degeneracies in the presence of small radio frequency fields and the associated change in selection rules. Of course, in the laboratory frame, this initial fall in singlet yield may equally well be interpreted by treating the RF field as a first-order perturbation that "reconnects" the $(\mathrm{S},\mathrm{T}_0) \leftrightarrow \mathrm{T}_{\pm}$ energy levels causing an increase in singlet–triplet interconversion.

5.5.4 Relationship between B_1 and MARY spectra

The rotating frame Hamiltonian given in equation (5.59) for B_1 spectra is rather similar to the laboratory frame Hamiltonian for MARY spectra given in equation (2.5). Were it not for the $-\omega_{\mathrm{rf}}\hat{I}_{iz}$ term in equation (5.59), these Hamiltonians would be identical. We could then think of B_1 spectra as "rotating frame MARY spectra".

Previous workers have used this relationship to calibrate the field strength generated by the RF coils in their apparatus. On the basis of calculations in $\left[\text{Py-h}_{10}^{\bullet+}\right.$ $\left.\text{1,3-DCB}^{\bullet-}\right]$, it is reported in [36, Fig 15] that the zero-crossing point in MARY and B_1 spectra occurs at the same field strength, *i.e.* when $B_0 = B_1$.

However, similar calculations made for two "1–1" RPs in Figure 5.35 do not show such behaviour. Given the great differences between the MARY and B_1 spectra for these two RPs, it would appear that the $-\omega_{\mathrm{rf}}\hat{I}_{iz}$ term has a significant impact on RP spin evolution. Indeed, the $-\omega_{\mathrm{rf}}\hat{I}_{iz}$ term is responsible for splitting the $B_1 = 0\,\mathrm{mT}$

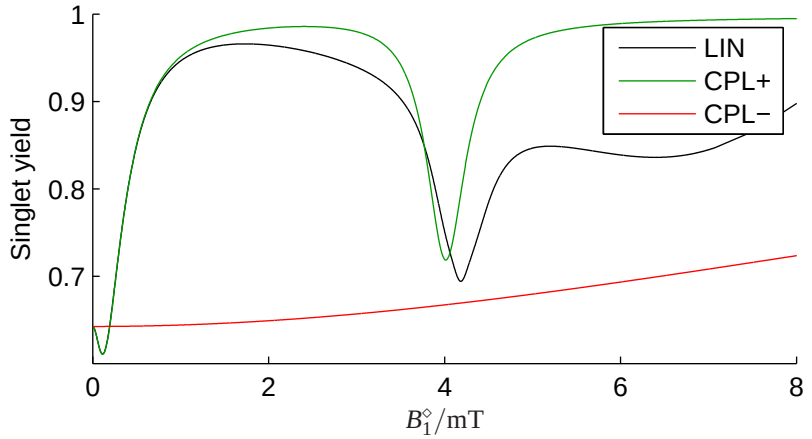

(a) B_1 spectrum showing strong changes in singlet yield for LIN and CPL+ fields when $B_1^\diamond \approx 0\,\mathrm{mT}$ or $B_1^\diamond \approx 4\,\mathrm{mT}$.

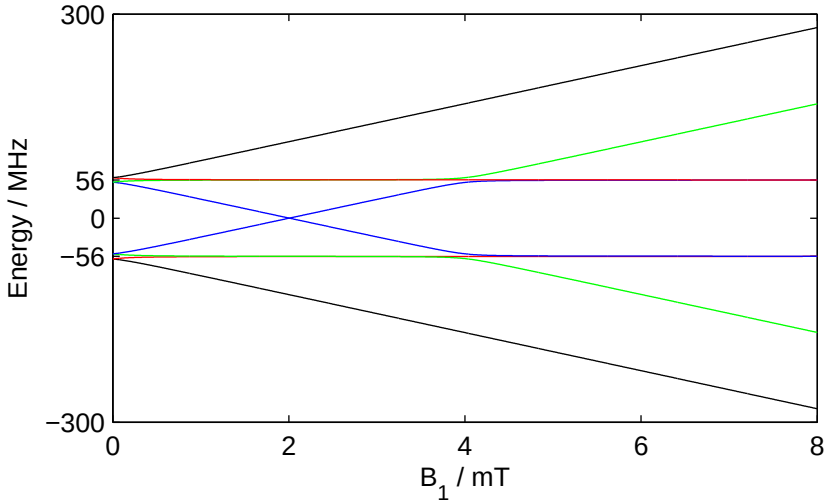

(b) Rotating frame energy level diagram for CPL+ fields showing avoided crossings at $B_1 = 0\,\mathrm{mT}$ and $B_1 = 4\,\mathrm{mT}$. Eigenstates $|\phi\rangle$ are coloured according to their singlet character as shown in (c).

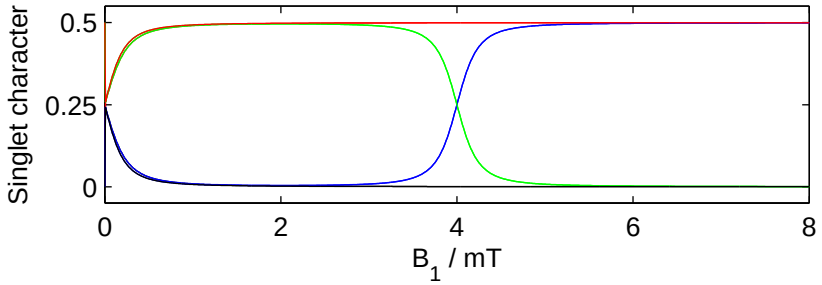

(c) Singlet character $\langle\phi|\hat{P}^S|\phi\rangle$ of the levels in (b).

Figure 5.34: Effect of RF polarisation on spin locking in a one-proton RP. RF field strengths for LIN polarised fields are described in terms of the strength of their CPL+ component $B_1^\diamond = B_1/\sqrt{2}$ (see §5.2.4). Calculations were made using γ-COMPUTE or the RFT. Parameters: $a = 0.5\,\mathrm{mT}$, $\nu_{\mathrm{rf}} = 112\,\mathrm{MHz}$, $B_0 = 4\,\mathrm{mT}$, $k = 2.8 \times 10^7\,\mathrm{s}^{-1}$, $n = 256$ and $\theta = \pi/2$.

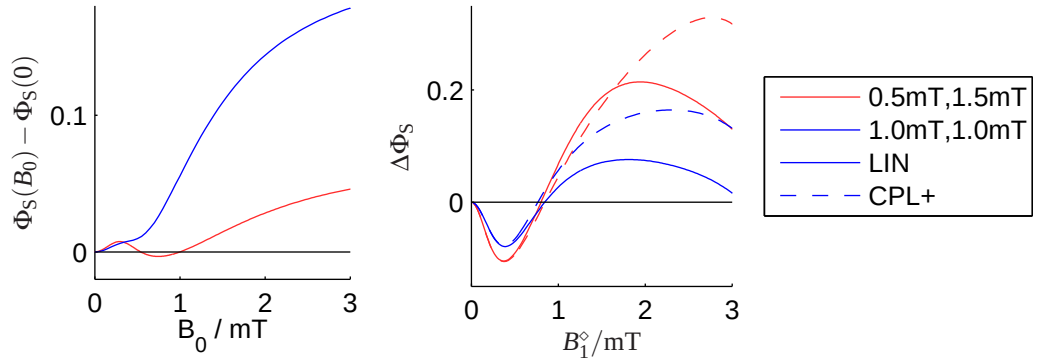

(a) MARY spectra: $B_1 = 0\,\mathrm{mT}$.

(b) B_1 spectra: $n = 256$, $\theta = \pi/2$, $\nu_{\mathrm{rf}} = 112\,\mathrm{MHz}$ and $B_0 = 4\,\mathrm{mT}$.

Figure 5.35: Comparison of B_1 and MARY (B_0) spectra in model RPs containing two spins-½. Hyperfine couplings (a_A, a_B) are indicated in the legend. An exponential model rate constant $k = 2.8 \times 10^7\,\mathrm{s}^{-1}$ was used. Calculations were done using γ–COMPUTE, the RFT and an exact frequency domain method. $B_1^\diamond$ is defined in §5.2.4.

eigenstates apart by $\pm 56\,\mathrm{MHz}$ in Figure 5.34. At small RF field strengths, this term dominates the Hamiltonian and ought not to be neglected. In light of these comments, we believe that our procedure for calibrating RF field strengths by comparing MARY-ν spectra at the onset of spin locking with γ–COMPUTE simulations is superior. Further details are given in §5.5.1.

5.5.5 High RF field strength limit

Figure 5.36 extends the B_1 spectra from Figure 5.34 to very high RF field strengths. Three features are apparent.

First, as $B_1 \to \infty$, the singlet yield in the presence of CPL+ and CPL− polarisations becomes equivalent. According to equation (5.24), the relevant rotating frame Hamiltonians are

$$\hat{H}' = \sum_i \left\{ a_{i\mathrm{N}}\hat{\boldsymbol{I}}_{i\mathrm{N}} \cdot \hat{\boldsymbol{S}}_{\mathrm{N}} - \omega_{\mathrm{rf}}\hat{I}_{i\mathrm{z}} \right\} + \sum_{\mathrm{N=A}}^{\mathrm{B}} \begin{cases} \omega_1 \hat{S}_{\mathrm{Nx}} & : \mathrm{CPL+} \\ \omega_1 \hat{S}_{\mathrm{Nx}} - 2\omega_{\mathrm{rf}}\hat{S}_{\mathrm{Nz}} & : \mathrm{CPL-}. \end{cases} \tag{5.60}$$

In either case, the electron spins see an effective static field. When the RF field strength is large, $\omega_1 \gg 2\omega_{\mathrm{rf}}$ and the two Hamiltonians are practically identical. Calculations in Mathematica for a one-proton radical pair, neglecting off-diagonal elements in the Hamiltonian that connect states with different ω_1 contributions, give an explicit formula for the singlet yield in this high RF field strength limit. The resulting expression is too bulky to give here, but we note that it predicts a limiting singlet yield of 0.99807 for the RP in Figure 5.36. This supports the validity of our numerical calculations.

Second, whereas the CPL+ spectrum shows a sharp resonance around $B_1 = 4\,\mathrm{mT}$, the CPL− spectrum rises monotonically with B_1. This is because the energy levels for the CPL− rotating frame Hamiltonian do not cross, in a similar manner to Figure 5.22 and the discussion in §5.4.4.

The third feature emerges in the presence of LIN polarised RF fields. There, we see a remarkable train of peaks extending out to $> 125\,\mathrm{mT}$. These calculations have

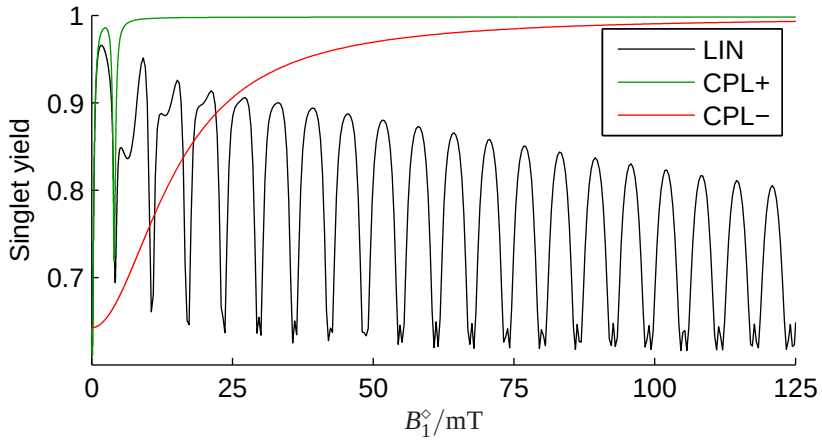

Figure 5.36: B_1 spectrum showing limiting behaviour in (unattainably) strong RF fields. RF field strengths for LIN polarised fields are described in terms of the strength of their CPL+ component $B_1^\diamond = B_1/\sqrt{2}$ (see §5.2.4). Calculations were made using γ–COMPUTE or the RFT. Parameters: $a = 0.5\,\mathrm{mT}$, $\nu_{\mathrm{rf}} = 112\,\mathrm{MHz}$, $B_0 = 4\,\mathrm{mT}$, $k = 2.8 \times 10^7\,\mathrm{s}^{-1}$, $n = 256$ and $\theta = \pi/2$. This figure has been checked for convergence by recalculating several points with $n = 512$.

been checked for convergence by increasing n to 512 and recalculating a selection of data points. It seems likely that these peaks represent "overtone" resonances. In the Floquet formalism [84], these would occur whenever there were level crossings in one of the higher order Floquet Hamiltonian contributions. Unfortunately, it is not as yet possible to produce sufficiently intense RF fields to test whether such effects may be observed experimentally.

5.5.6 Experiments using a tuned RF coil

The simulations presented above suggest that spin locking effects may produce strong signals and novel features in MARY-ν spectra. For example, we anticipate that a sufficiently strong RF field will cause complete inversion of a Zeeman resonance peak. Encouraged by these predictions and by observations of the onset of spin locking shown in Figure 5.29, Norman [139] and Wedge [247] measured a number of MARY-ν spectra in the presence of strong linearly polarised RF fields.

Measurements were performed using apparatus described in [139, Chapter 5]. This is similar to that described in §5.3.8 with the following modifications:

- The RF field was generated using a pair of air cooled coils in a tuned circuit. This allows the generation of strong, linearly polarised RF fields at a single frequency, namely 36 MHz.
- The experimental RF field strength was estimated using a calibrated search coil following the protocol in [139].
- A sample of 800 µM Chr-d_{12} and 20 mM 1,4-DCB dissolved in 9:1 cyclohexanol/acetonitrile was recirculated through the system to avoid photo-degradation.
- A water bath maintained the sample temperature at $\sim 20°$.

- Incident UV light was passed through a $200-400\,\mathrm{nm}$ bandpass filter.
- Fluorescence was filtered at $548\,\mathrm{nm}$ and detected using a PMT.

5.5.7 Results and discussion

The resulting high RF field strength MARY-ν spectra and corresponding simulations are shown in Figure 5.37. Once again, these show good qualitative agreement. In particular, we notice that when $B_0 = 0\,\mathrm{mT}$ or $B_0 > 3\,\mathrm{mT}$ both experiment and simulation show singlet yield rising monotonically with RF field strength. Yet, at the Zeeman resonance, when $B_0 = 36/28 = 1.3\,\mathrm{mT}$, the singlet yield at first rises with increasing RF field strength before it plateaus and begins to fall. This is expected in light of Figure 5.36 and the surrounding discussion. Presumably if one were able to attain still higher RF field strengths experimentally, the singlet yield at the Zeeman resonance would rise and fall following Figure 5.36.

Nevertheless, some issues remain. First, to produce similar MARY-ν spectra, the RF field strength used in simulations must exceed that estimated experimentally by a factor of $\sim 40\%$. It is not currently clear whether this represents a failure of the theory, or whether the experimental RF calibration is in error. Certainly, it is a non-trivial procedure to measure accurately the experimental RF field using a search coil. The most reliable procedure would involve using the search coil in question to perform pulse NMR or EPR in a superconducting magnet. Measurement of the $\pi/2$ pulse time would determine the RF field strength beyond doubt. Regrettably, this procedure carries a risk of damaging the valuable electronics of the NMR or EPR spectrometer that is used and has not, therefore, been possible to perform.

The second issue is that compared to the fully-inverted Zeeman peak, the negative-going Zeeman peak at small RF field strengths is somewhat deeper in experiment than in the simulations. Further work is required to explain this discrepancy.

Finally, additional experimental measurements (not shown) were made in a variety of other RPs. These support our conclusion, made above on the basis of calculations in simple model RPs, that the onset of spin locking is governed by the magnitude of the hyperfine couplings in a radical pair as expressed by the effective average HFC.

5.6 Conclusions

These studies are the first to investigate experimentally and by simulation the role of RF field polarisation on the production of chemical magnetic field effects. Indeed, there are very few investigations of polarisation effects across the field of magnetic resonance [243–246]. As such, this work represents a significant contribution to our understanding of the basic physics of magnetic resonance. It is also fascinating to watch as the tried-and-tested rotating frame approximation breaks down at the low field strengths and radio frequencies of interest here.

Throughout this chapter, we have seen good qualitative agreement between simulations and the corresponding experimental measurements. This close correspondence is a powerful validation of our model for magnetic field effects. For example, it is clearly not unreasonable to neglect exchange and dipolar interactions, or to assume that hyperfine anisotropies are averaged away by molecular tumbling, or to separate

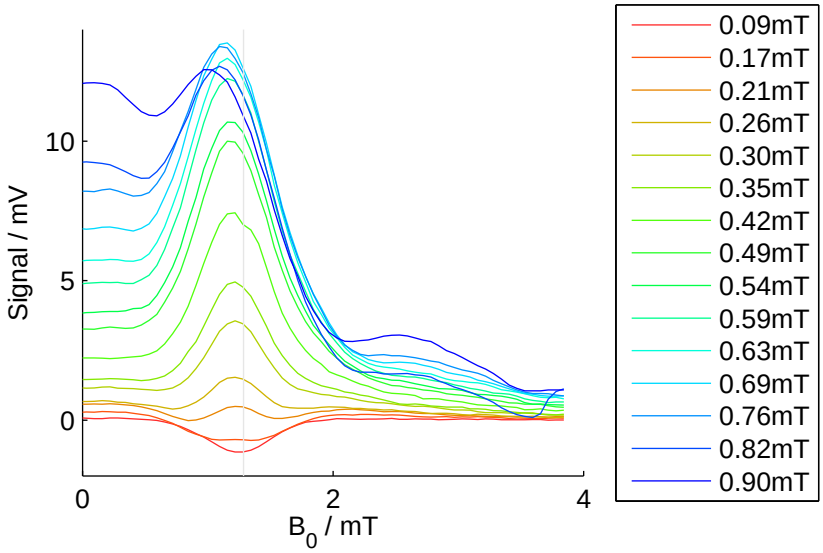

(a) Experimental MARY-ν spectra measured by Wedge [247]. Estimated B_1 values are shown in the legend. A tuned circuit was used to obtain these high RF field strengths.

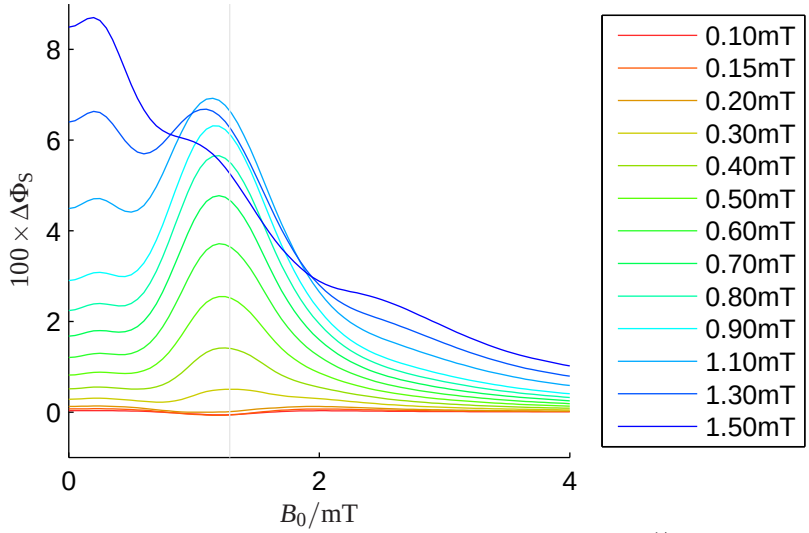

(b) Simulations made using γ–COMPUTE. Parameters: HFCs $2\times0.181\,\mathrm{mT}$ (^{14}N), $4\times0.159\,\mathrm{mT}$ (^{1}H) on 1,4-DCB$^{\bullet-}$ and $2\times0.085\,\mathrm{mT}$ (^{2}D) on Chr-d$^{\bullet+}_{12}$, $k=6\times10^{7}\,\mathrm{s}^{-1}$, $n=64$, $\theta=\pi/2$ and $\nu_{\mathrm{rf}}=36\,\mathrm{MHz}$. Linearly polarised RF was used.

Figure 5.37: Spin locking of MARY-ν spectra in $\left[\text{Chr-d}^{\bullet+}_{12}\ \text{1,4-DCB}^{\bullet-}\right]$. Linearly polarised RF with a frequency of $36\,\mathrm{MHz}$ was used.

the spin evolution from diffusional motion described in terms of a re-encounter probability $f(t) = k\mathrm{e}^{-kt}$. These assumptions allow an enormous reduction in the computational cost of simulating MFEs, which allows a much wider range of model parameters to be explored using the available CPU time. Although these approximations do not allow exact quantitative calculation of RF field effects, they have been shown to be quite sufficient to guide and interpret a wide range of MFE experiments.

Experimentally measured changes in product yield caused by RF fields that have different polarisations demonstrate unequivocally that the rotating frame approximation, which is so accurate in high field NMR and EPR, must be treated carefully when applied to low-field MFEs. Many applications of the low-field MFE theory, such as spectroscopy, the geomagnetic sense of animals and the putative health effects of mobile phones involve time-dependent fields that are very unlikely to be circularly polarised and have $\theta = \pi/2$. Therefore, it is important to treat the RF polarisation properly when modelling these systems. The adapted γ–`COMPUTE` algorithm outlined in Chapter 4 allows an efficient treatment of these fields. It is clearly an important contribution to this field. The computer programs developed in conjunction with the present work are already being used by other workers in Oxford.

Finally, the onset of spin locking in MARY-ν spectra allows the calibration of RF field strengths for MFE experiments, which is very challenging to perform in any other way. It would also allow the calibration of home-built search coils in order to determine the RF field strength in apparatus which is incapable of generating circularly polarised RF fields. Such RF field strength calibration is important, because in many cases it leaves only a single free model parameter: often the exponential model rate constant k. It is interesting that spin locking effects sufficient to cause an inverted lineshape develop in MARY-ν spectra at RF field strengths far smaller than would be expected on the basis of NMR spin locking. This perhaps reflects the rather different time evolution important in radical pairs.

5.7 Suggestions for further work

As discussed in the previous chapter, work is currently underway to measure RF-induced magnetic field effects using phase-locked pulsed laser irradiation to generate the RPs. Such an experiment would eliminate the requirement for γ-averaging associated with the generation of RPs by continuous UV photolysis. Following the discussion in §5.3.4, it seems likely that this phase-locked technique will show rather stronger polarisation effects than the present steady-state method. Measurement of RF polarisation effects in a phase-locked experiment should provide additional insight into radical pair processes and give another powerful test of the theory outlined in this thesis. The `COMPUTE` algorithm [234] is likely to provide an efficient means for making appropriate simulations.

Many birds and other animals have a magnetic "compass" sense. The biophysical mechanism underlying this sense remains unknown. Several studies have demonstrated that weak RF fields may temporarily disrupt the ability of European robins to orient themselves. These RF effects provide good evidence for the involvement of a spin chemical mechanism in the magnetic sense. Nevertheless, there have as yet been few simulations investigating the details of this model. Early simulations used the rotating frame approximation. It is important to treat RF polarisation properly in these

models if they are to be physically meaningful. We take up this task in later chapters.

Figure 5.32 showed the orientation dependence of MARY-ν spectra for different RF polarisations. These simulations are consistent with the hypothesis that only the $\perp$ CPL+ component of the RF field is responsible for inversion of the Zeeman resonance and that other components of the RF affect other regions of the MARY-ν spectrum. These orientation effects should be measured experimentally in a number of radical pairs in order to provide experimental verification for our hypothesis.

It is important to calibrate the RF field strengths produced by the coils that are used for MFE measurements. One method relies on introducing a small search coil in place of the sample cuvette. The search coil develops an oscillating voltage by induction. Providing that this search coil voltage can be calibrated, the RF field strength generated during an MFE measurement can be determined. It would be useful to calibrate a search coil using the onset of spin locking at different RF polarisations in the $\left[\text{Py-d}_{10}^{\bullet+}\right.$ $\left.\text{1,4-DCB}^{\bullet-}\right]$. The calibrated coil could then be used to determine RF field strengths in other MFE spectrometers.

Chapter 6

Introduction to avian navigation

6.1 Introduction

From elephants to *E. coli* and from eels to eagles, many organisms possess the ability to navigate around their environments. The cues that they use and the mechanisms by which these are detected are extraordinarily diverse [274, 275]. Migratory animals perform some truly awesome feats of navigation. For example, salmon spend much of their life at sea, yet they return for breeding every year to the area of river in which they were spawned [276, 277]. In North America, Monarch butterflies born in the late summer travel in excess of 3 500 km in order to overwinter in the forests of central Mexico [278, 279]. Juvenile marine turtles in the Atlantic Ocean swim along a 12 000 km migratory route by instinct [280, 281].

Historically, these movements have been studied in the wild by capturing, marking and releasing animals at their breeding site before returning later and looking for the marked individuals. Over land, animals may be tagged with a small radio transmitter and followed by scientists in a motor vehicle. This laborious procedure was used by Cochran and coworkers to study the migration of thrushes [282]. The advent of small solar or battery-powered GPS receivers has led to the development of GPS "tags". For example, studies such as that conducted by the Conservation Foundation and Ladbrokes (the "Big Bird Race") found that albatrosses in the Southern Ocean may fly thousands of miles on a single foraging expedition before returning to their nesting site. Other workers have followed individual albatrosses over the course of two years [283] using the Argos system of satellites [284] to receive the birds' positions. Our knowledge of animal migration patterns is likely to improve substantially in the next decade as satellite tracking systems become cheaper and more lightweight.

In addition to field studies, laboratory experiments allow the cues available to an animal to be carefully controlled. With sufficient ingenuity, it has been possible in some species to determine which cues are used for navigation. Animals are known that navigate using their sense of smell, the position of the sun in the sky, the polarisation of skylight or the positions of the stars. To give one example, it has been shown that Monarch butterflies use the position of the sun in the sky and not the polarisation of skylight for navigation [285]. Research into animal navigation is very active. In the UK, the Royal Institute of Navigation has a special interest group devoted to the subject. Their animal navigation bibliography contains 8363 papers [286].

Figure 6.1: The European robin (*Erithacus rubecula rubecula*) was shown to possess a magnetic compass sense in 1966 [73]. This work was later published in English [74].

6.2 A magnetic sense

The Earth's magnetic field is an important source of orientational and navigational cues for many species [287]. Behavioural studies have reported the existence of a magnetic sense in species ranging from magnetotactic bacteria [288], through sea molluscs [289], turtles [280, 281] and elasmobranch fish [290], to honeybees [291], butterflies [279] and at least twenty species of bird [227, 292]. Electro-physiological studies in the marine mollusc *Tritonia diomeda* [289, 293] and in the bobolink bird [294] show unequivocal effects of an Earth-strength magnetic field on the firing of certain neurons. Claims of a magnetic sense in humans were made by Baker [295], but these have a more chequered history. Unlike the robust results reported for animals, replication studies have failed to confirm the existence of a magnetic sense in humans [287, 296, 297].

The European "redbreast" robin (*Erithacus rubecula rubecula*) is resident in many parts of continental Europe. Figure 6.1 shows a photograph of a typical specimen. To avoid the harsh winter, Robins from Scandinavia and Russia migrate to western Europe and Britain annually [298]. In 1966, robins caught in Frankfurt, Germany were shown to use the Earth's magnetic field to orient themselves in the correct direction for migration [73, 74]. These experiments were the first to demonstrate the existence of an avian magnetic compass sense. Since those early days, many other species of bird have been shown to possess such a geomagnetic compass sense [299]. In the following chapters, we shall be concerned chiefly with the magnetic compass of two night-migrants: robins and garden warblers [105].

6.3 Key observations

Since those first observations of the compass sense in robins, an expansive body of literature has built up. In the following pages, we present a few of the most important observations necessary to critically appraise the model that we explore in Chapters 7–9.

Many further details are given in [227, 287, 292, 297, 299, 300].

6.3.1 Methodology

Most experimental measurements of orientation in migratory birds have been made using the following procedure, which was pioneered by the Wiltschkos in the 1960's [73, 74, 226].

- Wild birds are mist-netted as they migrate past Frankfurt am Main, Germany in the autumn. (See Figure 6.3(b).)
- These birds are kept over winter for testing that autumn and in the following spring. This does not harm the birds — indeed, since they are well fed and kept away from predators, participation in the experiments increases the birds' chances of breeding the following summer.
- The European robin and the garden warbler are night-migrants: they tend to make their migratory flights at dusk. In order to stimulate migratory behaviour, light levels in the bird house are artificially controlled. By adjusting the timing of the daily light–dark cycle, a desire to migrate may be induced.
- To test a bird's ability to orient magnetically, it is removed from the bird house and placed into a special cage shown in Figure 6.2. The cage is built from non-magnetic components and located in a wooden hut that is well-removed from anthropogenic magnetic fields.
- The bird stands in the bottom of a plastic "funnel", which is covered with typewriter correction paper. Diffuse light is provided from above. In this manner, the bird is deprived of other navigational cues.
- During the time following "dusk", the bird may exhibit "migratory restlessness". In this state, the bird faces in the direction that it intends to migrate, flaps its wings and scratches at the plastic funnel. These scratches are recorded on the typewriter correction paper lining the funnel.
- After 75 minutes, the bird is removed from the funnel and returned to the bird house.
- Dividing the paper into sectors and counting the scratches provides the raw data from these behavioural studies. These data are analysed to see whether there is a preferred heading using the circular Rayleigh test [301].
- Each bird may be tested once per day during the spring and autumn migratory seasons, but many tests are needed in order to obtain statistically significant results. These experiments are quite laborious.
- It is also possible to test under other magnetic conditions. Using sets of Helmholtz coils running around the testing cage, such as those shown in Figure 6.3(a), it is possible to subject the birds to many different combinations of static and RF fields.

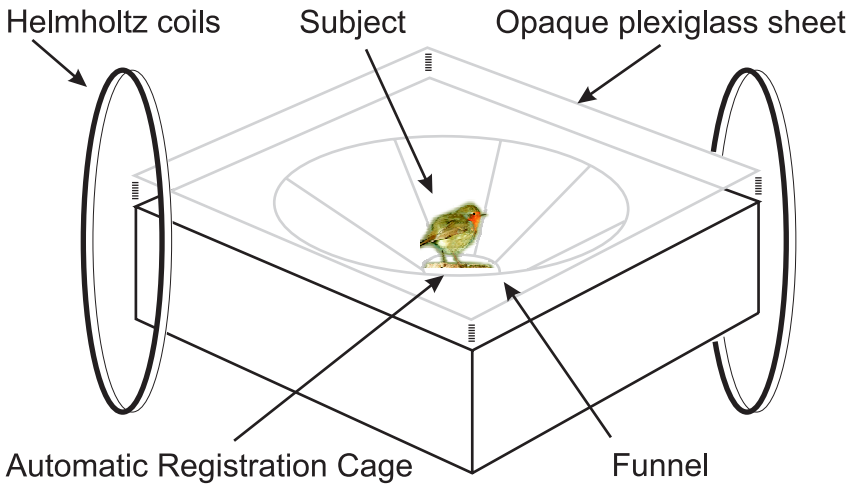

Figure 6.2: Typical apparatus for testing the orientation response in migratory birds.

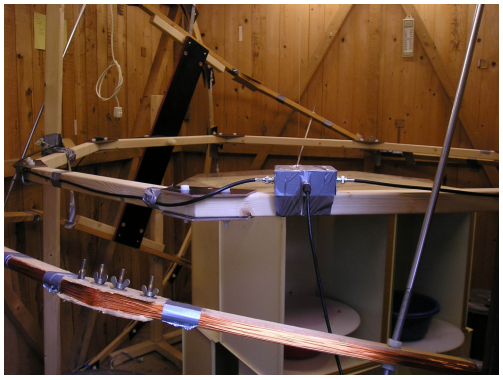

(a) Photograph of the apparatus used for measuring RF field effects in European robins. This image was kindly supplied by R. Wiltschko.

(b) Eurasian Blackbird being extracted from a mist net. Photo credit: Júlio Reis.

Figure 6.3: Photographs of bird experiments.

- With data obtained in the geomagnetic field alone as a control, the Mardia-Watson-Wheeler test [301] determines whether there is a statistically significant difference in the birds' ability to orient.

6.3.2 Statistics

The standard methods of linear statistics do not always apply directly to problems involving circular (or periodic) data. Consider, for example, a sample of three directions, given by the angles:

$$\phi_1 = 15^\circ \qquad \phi_2 = 355^\circ \qquad \phi_3 = 5^\circ. \tag{6.1}$$

The arithmetic mean of these angles is 125°, which gives far too much weight to the point $\phi_2 = 355^\circ$. To give another example, consider a sample of three times of day:

$$t_1 = 23.50 \qquad t_2 = 00.15 \qquad t_3 = 01.00. \tag{6.2}$$

Again, the arithmetic mean, 08.22, is clearly not representative of these nighttime data points.

In order to properly average these periodic data, we represent each datum by a unit vector. The appropriate average is the vector mean

$$\boldsymbol{m} = \frac{1}{3}\left(\boldsymbol{\phi}_1 + \boldsymbol{\phi}_2 + \boldsymbol{\phi}_3\right). \tag{6.3}$$

We write this vector in polar coordinates $\boldsymbol{m} = (r, \bar{\phi})$, where $\bar{\phi} = 5^\circ$ is the desired circular mean angle and $r = 0.9899$ is a measure of the variation about this mean.

Simple algebra reveals that the following are analogues of important linear statistical quantities:

Linear statistics	Circular statistics
$(x_i - \bar{x})$	$\sin\left(\phi_i - \bar{\phi}\right)$
$\sum (x_i - \bar{x}) = 0$	$\sum \sin\left(\phi_i - \bar{\phi}\right) = 0$
$(x_i - \bar{x})^2$	$2\left[1 - \cos\left(\phi_i - \bar{\phi}\right)\right]$
$\frac{1}{n}\sum (x_i - \bar{x})^2 = s^2$	$\frac{1}{n}\sum 2\left[1 - \cos\left(\phi_i - \bar{\phi}\right)\right] = 2(1-r) = s^2$

(6.4)

Batschelet [301] gives an accessible cookbook-style account of circular statistics. In particular, he lists a number of tests for determining whether circular data samples have a preferred direction and for deciding whether two sets of circular data are significantly different. We summarise here two important tests that have been applied frequently in studies of avian magnetic orientation.

Rayleigh test

The Rayleigh test uses the length of the mean vector, r, to test whether the population from which the data are drawn is directed (one-sided). Having calculated r, the test proceeds by consulting a table, such as [301, Table H], of critical levels P in relation to r and the sample size n. If the tabulated critical level P is less than a preassigned limit, *e.g.* 0.05 or 0.001, then the data are significantly ordered. In many animal studies, this analysis is reversed and the value of r corresponding to orientation at 0.05 and 0.001 confidence limits is plotted on the figure.

Mardia-Watson-Wheeler test

The Mardia-Watson-Wheeler test is a simple, non-parametric method to test whether two independent random samples from circular observations differ significantly in terms of their mean angle, angular variance or both. Consider an illustrative pair of samples with $n_1 = 4$ and $n_2 = 3$ data points:

$$\phi_1, \phi_2, \phi_3, \phi_4 \qquad \text{and} \qquad \psi_1, \psi_2, \psi_3. \tag{6.5}$$

To test these samples against one another, we first pool all the data points and sort them into ascending order. In the case where two data points have the same angle, we order these points at random. For example, the full data may now be:

$$\psi_3, \phi_1, \phi_4, \psi_1, \phi_2, \psi_2, \phi_3. \tag{6.6}$$

We then shift these data points so that they are evenly spaced around the unit circle. In other words, we discard the original data, retaining only the ordering of the data points. Using the shifted points from the first data set only, we form their average resultant vector

$$B = R_1^2/n_1. \tag{6.7}$$

Comparing B with tabulated values, such as [301, Table Q], we may determine whether the two data sets differ significantly in mean angle, angular variance or both. This test has good statistical power in small samples. However, in large samples there are frequent *ties* where two data points have the same angle, which are detrimental to the performance of the test.

These tests may both be performed efficiently using a computer. Free `Matlab` routines are available for this purpose. Alternatively, one can use more specialist statistical software such as `Oriana` or `SAS`.

One aspect of the statistical analysis presented in the literature remains unclear to the author: in many behavioural studies, scratch counts from each bird are combined to give a mean vector for that individual. These mean vectors are used as the basis for further analysis. It would seem intuitively more satisfactory to retain the raw scratch counts throughout the statistical analysis. Nevertheless, there may be sound statistical reasons for the established procedure.

6.3.3 Compass sense

Figure 6.4 summarises orientation tests conducted on European robins in 2003 [232] following the procedure detailed above. The triangles around the edge of the figure represent the mean heading for each test subject. These headings are averaged to give a grand mean heading vector which is plotted as an arrow. The inner solid and dashed circles mark the 1% and 5% significance limits of the Rayleigh test [301]. In other words, the chance that the apparent preferred orientation arises accidentally is $< 1\%$. European robins are clearly able to orient using the Earth's magnetic field. The direction that they choose reflects their annual migration: in spring, they head North towards their summer breeding grounds and in autumn, they head South to overwinter in western Europe.

Similar results have been obtained by a number of researchers during the last forty years. We may be confident in the existence of the avian geomagnetic sense. Of course, establishing the existence of the avian compass sense is only the first step. The central question to be addressed is *how* birds sense the Earth's magnetic field.

6.3.4 Inclination not polarity

The first important observation is that robins are not sensitive to the polarity of the geomagnetic field, but rather to its inclination. In other words, they cannot distinguish North from South per se, but are able instead to perceive the axis of the field lines.

Figure 6.5 illustrates the approximate dipole field of the Earth. For an observer in Frankfurt, the geomagnetic field lines make an inclination angle $\theta = 66^\circ$ with the horizontal. If one could see the field lines, they would fall into the ground in a northerly direction, making an angle of 66° with level ground.

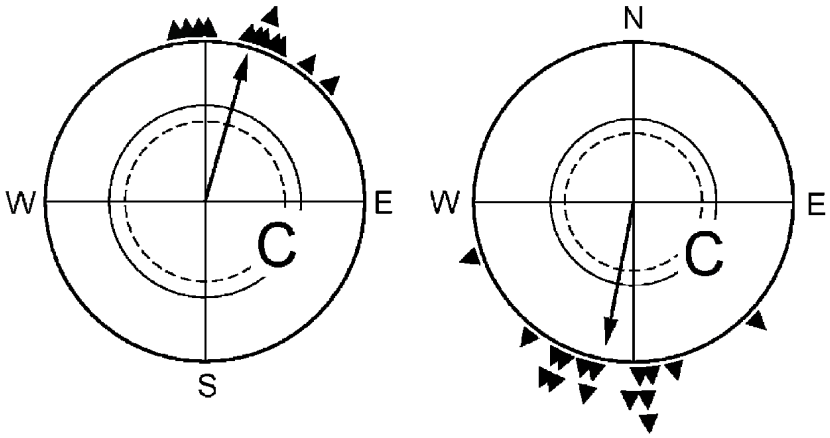

Figure 6.4: Experimental data from [232, Fig 1] showing statistically significant geomagnetic orientation of European robins in Frankfurt am Main, Germany. Left: Spring 2003, Right: Autumn 2003. The two letters "C" indicate that these were control experiments in the original paper.

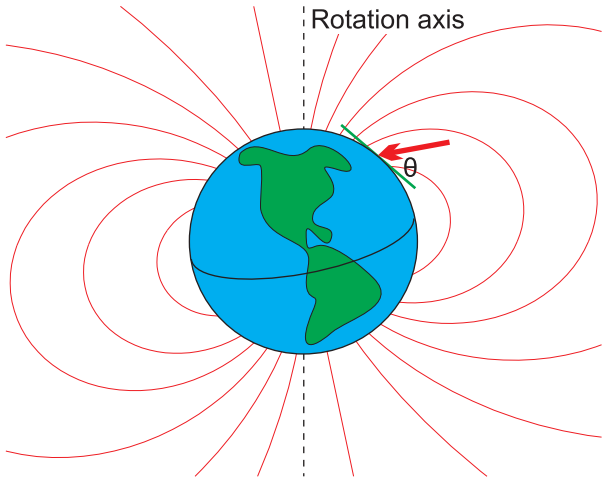

Figure 6.5: Approximate diagram of the Earth's magnetic field. Notice that the magnetic field in Frankfurt (shown as a red arrow) makes an *inclination* angle θ with the horizontal (shown as a green line).

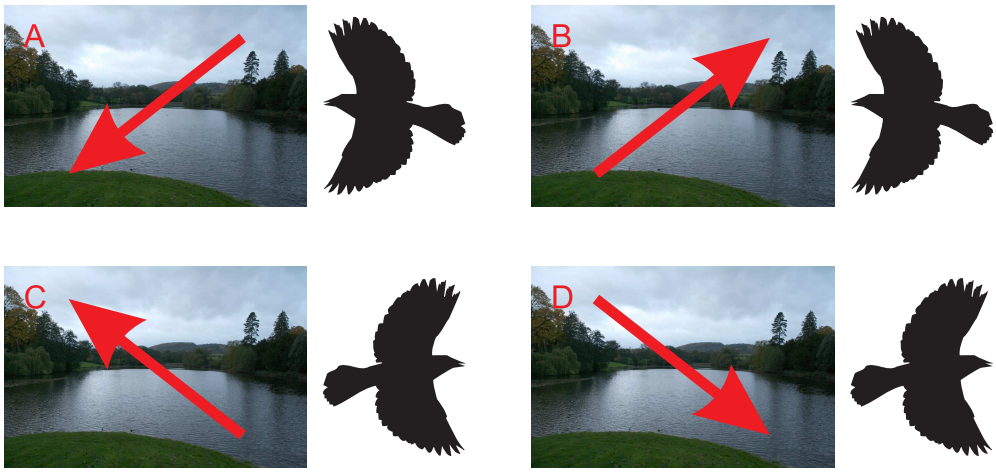

Figure 6.6: Summary of behaviour reported in [74]. See main text for details.

Figure 6.6 summarises the findings of the Wiltschkos' pioneering measurements in the spring of 1971 [74]. Four test conditions are important. (A) birds in the natural geomagnetic field preferred to orient in a northerly direction, as discussed in connection with 6.4. (B) Using a set of Helmholtz coils to apply the necessary static field, birds were tested in a magnetic field the same strength as the geomagnetic field (46 μT) but with opposite polarity. These birds continued to orient in a northerly direction. (C) The vertical component of the magnetic field was reversed, causing the birds to orient in an incorrect, southerly direction. (D) The horizontal component of the magnetic field was reversed, causing the birds to orient in an incorrect, southerly direction. Taking these four measurements together, it appears that at Frankfurt in the spring, robins head in the direction where the geomagnetic field lines dip down towards the ground.

6.3.5 Light intensity and colour

Figure 6.7 summarises the results of orientation experiments on four species of migratory bird made under different coloured low-level monochromatic illumination [292, 302]. In all four species, we see that light in the blue–green part of the spectrum is necessary for magnetoreception. Evidence for light-dependent magnetoreception in several other species is reviewed by Deutschlander [303].

This analysis may be extended to consider light intensity. Muheim and coworkers have collated results from a substantial number of orientation experiments [304, Fig 5]. Operation of the magnetic compass sense is seen to depend in a complex manner on the ambient light colour and intensity. A particular challenge here is to design experiments that eliminate the possibility that light colour and intensity affect motivation instead of magnetoreception [229, 300]. To give a simple example, it is possible that birds are distressed by red light and therefore do not orient. Further work is needed to properly elucidate these dependencies.

6.3.6 Eyes

Knowing that many migratory birds require appropriate ambient light in order to orient magnetically, it is natural to question where in the bird this light has its effect. Birds are

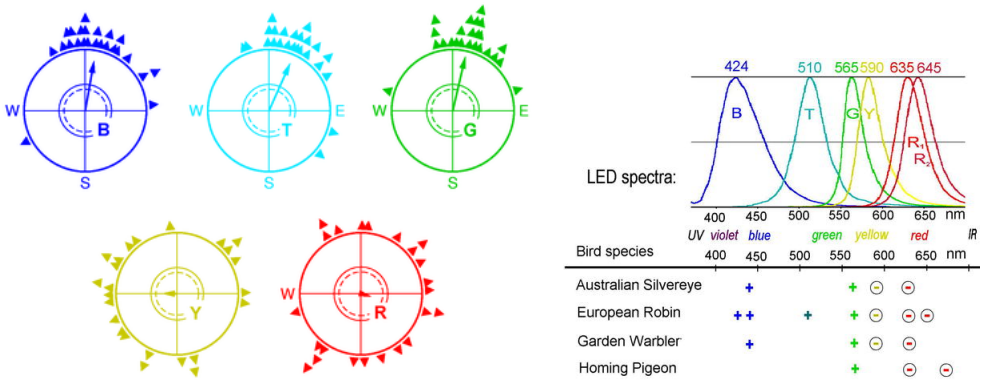

(a) Results of orientation experiments carried out on European robins in spring under low level monochromatic illumination. The light intensity is estimated to be $\sim 10^{16}$ photons per second. The letters B, T, G, Y and R indicate illumination colour, as shown in (b). This figure is adapted from [302, Fig 3].

(b) Summary of orientation experiments in four species of bird with monochromatic illumination. "+" indicates successful orientation, "⊖" indicates disorientation. This figure is adapted from [292].

Figure 6.7: Influence of light colour on orientation ability at low light levels.

Figure 6.8: European robins prepared for monocular testing [305].

known to show light sensitivity in the eyes and in the pineal gland. An important study measured the orientation response of European robins wearing an eye cap as shown in Figure 6.8. Robins whose left eye was covered were able to orient just as well as control birds with unimpeded vision, whereas robins whose right eye was covered were not able to orient [305]. This study demonstrates clearly that the light receptors involved in the geomagnetic sense are located in the eyes of robins.

Further studies by Mouritsen and coworkers found that garden warblers perform head scanning movements during a magnetic orientation task [306]. The details of this motion were seen to change when the birds were shielded from the geomagnetic field. This provides additional evidence that the magnetoreceptor is located in the head of birds.

Finally, measurements of the expression of ZENK and c-fos immediate early genes in the brains of garden warblers and European robins found significant neural activity during night-time orientation tasks in a region of the brain dubbed "cluster N" [307]. No such activity was observed in the brains of two distantly related species of non-migratory songbirds. It seems quite plausible that "cluster N" is involved in neural processing for the avian compass sense, although it has been difficult to show this conclusively [308].

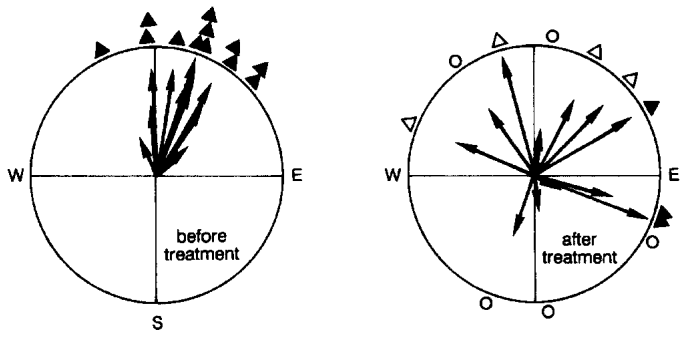

Figure 6.9: Orientation of European robins during spring migration before (left) and after (right) treatment with a ~ 4 ms, 500 mT magnetic pulse under "white" incandescent and green LED illumination. Right: the response to the field pulse for each bird is denoted by the symbols around the outside of the circle. Solid triangles: significant deviation from the control; open triangles: significant samples that do not differ from the control; open circles: significant increase in scatter. Figure from [309].

6.3.7 Pulsed magnetic fields

Magnetic orientation responses before and after exposure to a short, strong magnetic field pulse have been measured in a few species of bird. It is thought that a magnetite-based compass might be realigned following a magnetic field pulse, whereas there should be no lasting effect on a RPM reaction. However, depending on the size and shape of any magnetite particles in an organism, it may only be possible for them to remagnetise in the same direction in which they were originally magnetised. This would be the case for long, thin particles of magnetite.

Figure 6.9 shows a set of data for European robins [309]. It is apparent that a short, strong magnetic pulse does have an effect on magnetic orientation in robins. However, details of the response are not clear. In some test subjects, the pulse appears to have no affect, in others it produces reorientation in an incorrect direction whilst in still others it merely increases the scatter in the orientation response.

6.3.8 Changing B_0

As long ago as 1978, it was found that European robins are disoriented by quite small changes in field strength. Figure 6.10 illustrates some of these measurements. European robins that orient successfully in the geomagnetic field (of strength 46 µT in Frankfurt) are unable to orient in fields of 34 µT or 60 µT. However, as shown in Figure 6.11, robins are able to orient at other field strengths if they are acclimatised to the new field strength for one hour before being tested [310]. It is interesting to note that the geomagnetic field varies in intensity on a daily cycle and also in response to the solar cycle. The daily variations in field strength on a "magnetically quiet day in Frankfurt" are $\Delta B_0 \sim 100$ nT [287, Fig 1.5]. During magnetic storms (triggered by the ejection of massive quantities of charged particles from the sun) these variations may be much larger. It is known that pigeons can stray off course during magnetic storms [311].

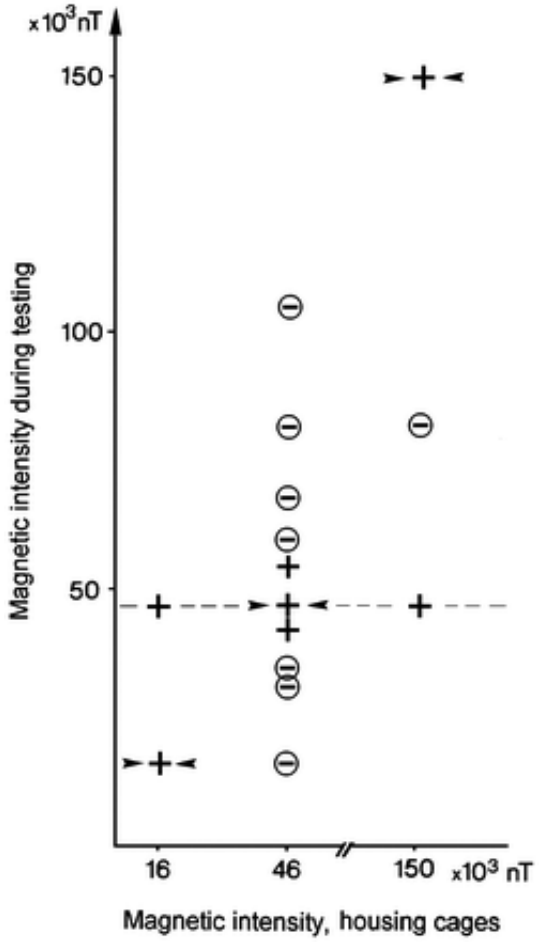

Figure 6.10: European robins housed in a 46 µT field (*i.e.* the geomagnetic field at Frankfurt) become disoriented if tested in fields greater than 60 µT or smaller than 34 µT. Acclimatisation allows the magnetic compass sense to operate over a wider range of field strengths. "+" denotes successful orientation and ⊖ disorientation. Figure from [302].

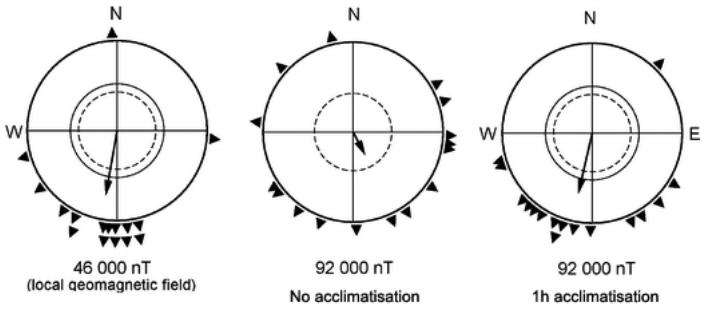

Figure 6.11: European robins acclimatise to a 92 µT field within one hour. Figure adapted from [310].

6.3.9 RF fields

The most recent class of behavioural experiments involve the use of radio frequency magnetic fields. In spring 2003, Ritz and coworkers [231] found that an RF field one thousand times weaker than the geomagnetic field, that is with $B_1 = 470\,\mathrm{nT}$ and $\omega_{\mathrm{rf}} = 7\,\mathrm{MHz}$, could disorient European robins. The apparatus used is shown in Figure 6.3(a) and the results of this study are summarised in Figure 6.12. Interestingly, the relative orientation of the RF field relative to the geomagnetic field was critical. With parallel fields, the robins continued to orient successfully, whereas fields making an angle of 24° or 48° caused disorientation.

Similar studies, at a frequency $\omega_{\mathrm{rf}} = 1.315\,\mathrm{MHz}$ and with RF field strength $B_1 = 485\,\mathrm{nT}$ were conducted by Thalau and coworkers in the spring and autumn of 2003 [232]. Once again, the robins remained oriented when the RF and geomagnetic fields were parallel, but were disoriented when the RF and geomagnetic fields made an angle of 24°. The frequency $1.315\,\mathrm{MHz}$ was chosen because it matches the Zeeman resonance splitting for a free electron in the geomagnetic field at Frankfurt: $B_0 = 46\,\mu\mathrm{T}$.

Practical considerations impose a limit of about eight test conditions per season for these orientation studies. Painstaking work in the springs of 2004–06 has allowed tests at a range of different frequencies and RF field strengths. These results are summarised in the upper part of Figure 6.13. The results appear to show a resonant response at $1.315\,\mathrm{MHz}$ which does not occur at double or half this frequency. Further measurements in a static field $B_0 = 2 \times 46 = 92\,\mu\mathrm{T}$ show a shift in the resonance position.

It is worth noting that although an RF field strength of $15\,\mathrm{nT}$ may seem very small, it is likely to be significantly higher than the natural background field. Styles estimates that the MHz background field strength is $\sim 10\,\mathrm{pT}$ [312], which is comparable to the $30\,\mathrm{pT}$ mentioned by Canfield [313]. This value is expected to increase substantially during magnetic storms. We note in passing that it is quite conceivable that magnetic storms disorient animals through increased RF noise and not changes in the geomagnetic B_0 field. This hypothesis would need to be tested statistically in animal studies analogous to those made for the geomagnetic B_0 field [311].

The results of these RF field effect studies make an important contribution to the debate on the mechanistic basis of avian magnetoreception. In Chapter 9, we present a number of calculations of RF field effects in model RP systems. These calculations helped guide the design of the behavioural experiments. As we will see later, they also demonstrate that the behavioural data are consistent with a magnetoreceptor based on the radical pair mechanism. Taken together, the response to RF fields in Figures 6.12 and 6.13 gives rise to some important restrictions on the RPs involved in magnetoreception.

6.4 Proposed mechanisms

Compared to the "five senses", the organ responsible for magnetoreception and its mechanistic basis remains enigmatic. Primary receptors responsible for magnetic field detection have not been identified with certainty in any animal [300]. Nevertheless, a number of mechanisms have been proposed by which magnetoreception might operate. Three of these proposals are physically plausible, well established in the literature and consistent with behavioural experiments in certain species. It is likely that magnetore-

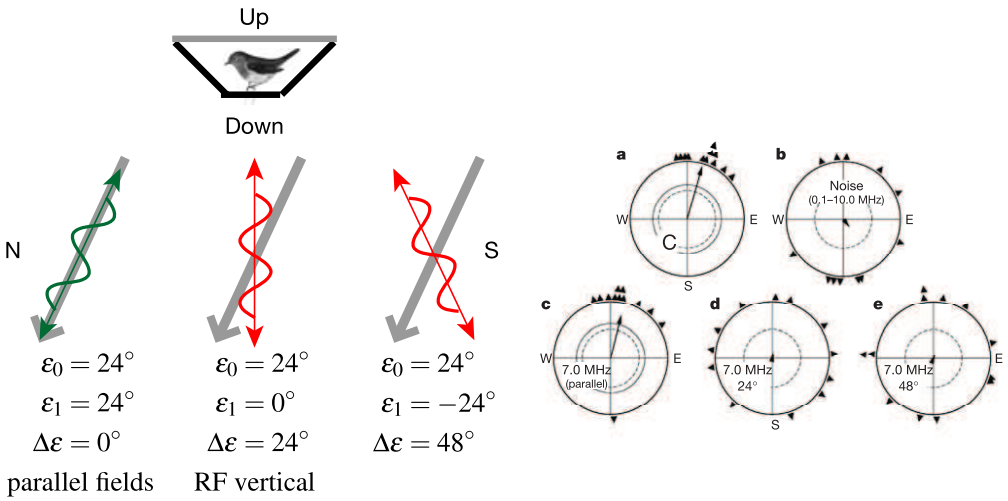

(a) The magnetic compass sense of European robins was disrupted (red) by 7 MHz RF when it was at an angle $\Delta\varepsilon = 24°$ or $\Delta\varepsilon = 48°$ to the geomagnetic field. The robins' compass sense was unimpeded (green) when the RF field was parallel to the geomagnetic field.

(b) Summary of orientation effect measurements. The fields used in each case were: (a) control with the geomagnetic field alone $\varepsilon_0 = 24°$ in Frankfurt; (b) $\Delta\varepsilon = 24°$ with (vertical) broadband RF $\omega_{rf} = 0.1$–10 MHz, $B_1 = 85$ nT; (c–e) $\omega_{rf} = 7.0$ MHz, $B_1 = 470$ nT with (c) $\Delta\varepsilon = 0°$; (d) $\Delta\varepsilon = 24°$ (vertical RF); and (e) $\Delta\varepsilon = 48°$.

Figure 6.12: Very weak radio frequency fields may disrupt orientation in European robins. The effect depends on the relative orientation $\Delta\varepsilon$ of RF and static fields. The field geometry is specified by ε_0, ε_1 and $\Delta\varepsilon$ which are defined in §9.5. These figures are adapted from [231].

ceptors operating by means of each of the three mechanisms will eventually be found. A few other suggestions are extant in the literature, but have not found experimental support [315–317].

The first proposal is magnetoreception by electromagnetic induction. Elasmobranch fishes such as sharks and rays are known to swim following magnetic field anomalies on the ocean floor. It is suggested that they detect the EMF induced as they swim through the geomagnetic field [290]. Certainly, these fishes can detect and act upon the remarkably weak electric fields emanating from their prey. However, since sea water currents would also generate induced EMFs, there remains some uncertainty as to the precise means by which induced EMFs arising from motion through the geomagnetic field could be disentangled from other electric fields in the ocean [318, 319]. Electromagnetic induction is unlikely to form the basis of viable magnetoreceptors in land or airborne animals.

The second proposal is that magnetoreception rests on the response of small crystals of magnetite (Fe_3O_4). To quote Kirschvink, the leading proponent of magnetite-based magnetoreception, "it is the opinion of the authors that all magnetic field sensitivity in living organisms ... is the result of a highly evolved, finely-tuned sensory system based on single domain, ferromagnetic crystals" [229]. Magnetite magnetoreception is certainly responsible for the orientation of magnetotactic bacteria [288]. Magnetite deposits have been found in many animals, but it has been challenging to demonstrate a connection to the nervous system. Furthermore, since magnetite deposits are used by many species as an iron reserve, the mere presence of biogenic magnetite is not evidence for magnetite-based magnetoreception. The two species

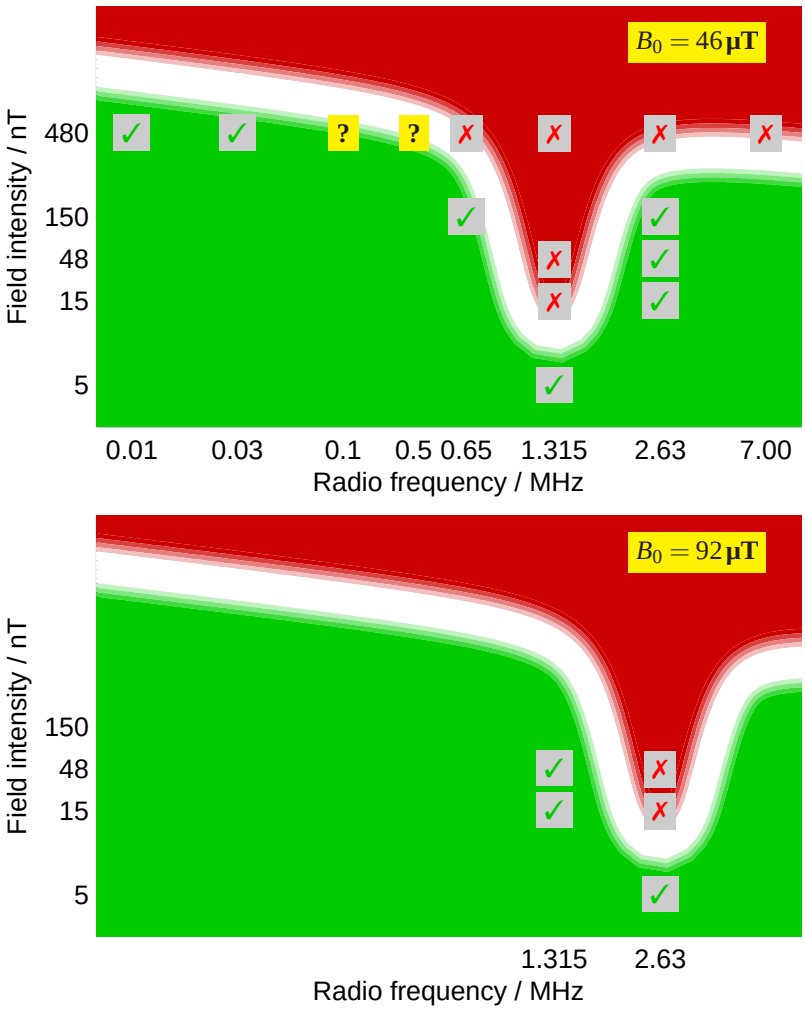

Figure 6.13: Summary of recent RF field effect studies on European robins [230, 314]. Measurements were made in Frankfurt ($B_0 = 46\,\mu T$) with a vertical RF field (*i.e.* at an angle of 24° relative to the geomagnetic field). Green ticks denote successful seasonally-appropriate orientation; red crosses denote disorientation; question marks denote biaxial distributions where some subjects headed in the seasonally-appropriate direction whilst others headed in the opposite direction.

which show the best behavioural evidence for magnetite-based magnetoreception are trout and pigeons [300]. Kirschvink has proposed a number of hypothetical sensory structures based on the magnetite mechanism [228, 229, 297]

6.5 Radical pair mechanism hypothesis

The third proposal is that magnetoreception operates by means of anisotropic chemical magnetic field effects on the rate or product yield of a biochemical radical pair reaction [29, 106, 107, 320–322]. According to its original proponents,

> "our conjecture is that the biomagnetic sensory mechanism entails either a dark or a light-driven biochemical electron transfer reaction generating radical pairs (in either the singlet or triplet state) in which consecutively an *anisotropic* hyperfine interaction and external magnetic fields induce a coherent electron spin motion. This motion, *i.e.* the relative orientation of the two unpaired electron spins, determines the spin multiplicity of the radical products appearing through electron back transfer. These products can be modulated by the strength as well as by the direction of an external magnetic field establishing, thus, a chemical compass." [107]

A contemporary variant of this hypothesis is illustrated in Figure 6.14. We discuss the salient points below.

6.5.1 Solid state radical pair mechanism

The radical pair mechanism (RPM) is long established as the basis of many magnetic field effects during chemical reactions, such as those considered in Chapters 2–5. RPM field effects have been observed in biologically-relevant systems [39, 41, 79]. Examples include effects in coenzyme B_{12} [39, 313] and in modified photosynthetic reaction centres [323–325] where fields as small as $B_0 = 1\,\mathrm{mT}$ produce changes in the yield of singlet O_2 [81]. Measurable effects from an Earth-strength field, $B_0 = 50\,\mu\mathrm{T}$, have been found recently in Oxford [326].

In the solid state, the RPM proceeds as shown schematically in Figure 6.14(a).

- In the course of some reaction pathway, a diamagnetic precursor (Pre) reacts to form a *pair* of radicals ($A^\bullet$ and $B^\bullet$). This step often involves photochemically-driven electron transfer.
- Since the two radicals are created in a single event, their electron spins are correlated. We assume for simplicity of exposition that the RP is created in a singlet (S) state, but extending the theory to triplet-born (T) RPs is trivial.
- After creation, the spin state of the RP evolves under the influence of the RP Hamiltonian. The ensuing interconversion between singlet and triplet states depends upon the applied magnetic field and is depicted by a double-headed arrow in the figure.
- Singlet and triplet RPs react to form different products (or the same product at different rates). For example, back electron transfer is often possible only

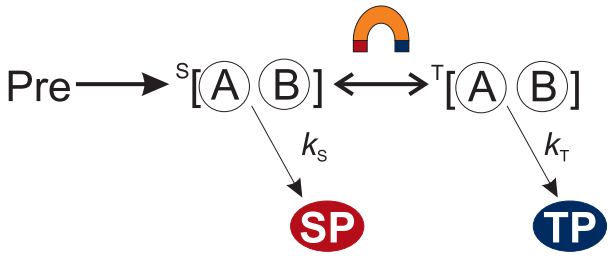

(a) Schematic of the RPM in a solid state system. A diamagnetic precursor molecule (Pre) reacts to form a spin correlated radical pair $[A^\bullet\ B^\bullet]$ in an initial singlet (S) state. Singlet–triplet interconversion is driven by magnetic interactions. The RPs react to form distinct singlet (SP) and triplet (TP) products at rates k_S and k_T respectively.

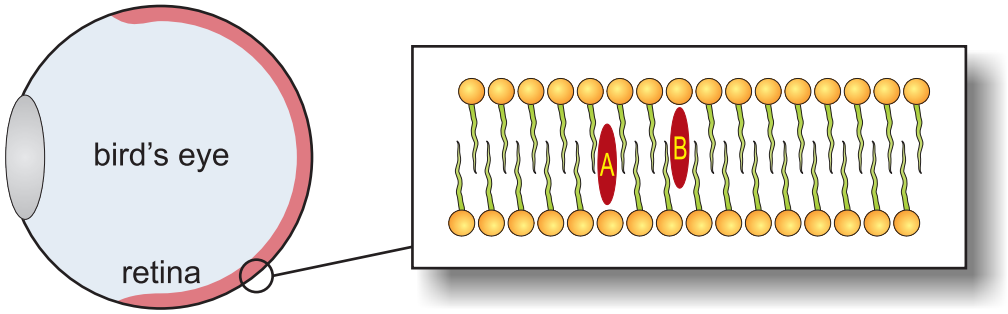

(b) Oriented radical pairs $[A^\bullet\ B^\bullet]$ could be created photochemically in the retina. The "tadpoles" represent an oriented lipid bilayer, such as that found in a membrane.

Figure 6.14: Schulten proposed that avian magnetoreception functions by virtue of a photochemical reaction between oriented radical pairs in the retina [107].

for singlet RPs because of the Pauli principle. These reactions are assumed for simplicity to have first order kinetics with rate constants k_S and k_T respectively.

- Therefore, the yields of singlet product Φ_S and triplet product Φ_T vary according to the applied magnetic field.

The assumption of first-order kinetics for the formation of SP and TP makes the population of RPs decay exponentially after the instant of creation. If we assume further that $k = k_S = k_T$, the resulting product yield expressions are the same as those for liquid phase RPM reactions. However, it is important to remember that whereas in the liquid phase, k governs the probability distribution of re-encounters between a diffusing RP within the exponential model: $f(t) = ke^{-kt}$, in the solid state k is a true first order rate constant.

6.5.2 An RPM compass

Another important difference is that in the solid state the radicals may be assumed to be *immobile*. They undergo no significant diffusive translational motion, nor are they able to rotate. Whereas in the liquid phase, diffusive motion of the radicals causes anisotropic hyperfine and dipolar interactions to be averaged away, in the solid state it is quite possible for RPM reaction yields in an oriented sample to depend on the relative alignment of the magnetic field with respect to the sample [324, 325]. This opens the possibility of forming a RPM-based compass.

In §6.3.5, we saw that avian magnetoreception requires ambient light in the higher energy blue-green region of the spectrum. It is reasonable to presume that blue-green light is required in order to form radical pairs by photochemically-driven electron transfer. We also saw in §6.3.6 that magnetoreception is disrupted by covering the eyes, showing that the source of radical pairs is located therein. Furthermore, we know that oriented radicals are necessary in order not to average away any anisotropic magnetic field effects. The retina contains an exquisite array of ordered cells, including the "rods" and "cones" responsible for vision. The anatomy of the eye is designed to bathe these cells in light. It is, therefore, natural to surmise that magnetoreception might be founded on a photochemical reaction occurring between oriented molecules fixed within the retina. The retina is well innervated. Hence, it is easy to imagine transduction of the magnetic sense to the nervous system if either the singlet or triplet products were a neurotransmitter, or if the RP were connected with the visual pathway. Modelling studies confirm that an RPM-based magnetoreceptor could feasibly detect the geomagnetic field even in the presence of stochastic noise and changes due to physiological temperature variations [327].

The identity of the radical pair involved in magnetoreception remains unknown, but a few candidates have been proposed. Leask suggested that the pigment rhodopsin might be responsible for magnetoreception [315]; Schulten and Windemuth proposed that one reaction in the retinal cGMP reaction cycle might be responsible, favouring one of the reaction steps connected with bleached rhodopsin or iodopsin at the meta$_{II}$ stage [320]. More recently, Ritz *et al.* named the retinal cryptochrome proteins [106, 328, 329] as promising candidates for magnetoreception. By analogy with the closely related DNA photolyase proteins, Ritz suggested the involvement of a radical pair

comprising the cryptochrome flavin (FADH) cofactor and an as-yet-unknown counter-radical [106].

6.6 Overview

Animals from all five classes of vertebrate are known to possess a magnetic compass sense. Behavioural studies conducted in many laboratories over several decades confirm the existence of this sense beyond doubt. However, the physiological basis of magnetoreception remain an enigma. Amidst a large amount of commentary and debate, several key studies, whose results were outlined above, provide firm experimental clues to the operation of the avian compass sense.

It seems possible that the compass sense of migratory birds, such as the European robin, is based on a radical pair reaction. This RPM compass model has, thus far, stood the test of time and is consistent with available behavioural evidence. In particular, effects of light colour and the action of RF fields fit well with a photochemically-induced RP reaction. Only results from pulse magnetisation studies remain difficult to reconcile with an RPM-based compass.

However, although the RPM hypothesis is plausible and fits the available data, many questions remain unanswered. Most important amongst these is the identity and location of the RP responsible for magnetoreception. The work to be presented in the following chapters makes an important contribution to the debate on the origins of the avian magnetic compass sense.

To date, rather few calculations have been performed on multinuclear RPs. In Chapter 7, we perform several such calculations in model systems inspired by the cryptochrome and photolyase proteins. We are able to make a number of comments on the "design features" necessary to make a RP suitable for magnetoreception.

In Chapter 8, we introduce a new quantitative method for analysing the enormous quantities of data that are generated by anisotropic modelling calculations. Decomposing the singlet yield in terms of spherical harmonics enables trends to be elucidated and presented clearly. We present several methods of calculating such spherical harmonic decompositions and assess their merits. The work in this chapter paves the way for Monte Carlo calculations in a large ensemble of radical pairs. Such calculations will provide important "rules of thumb" for anisotropic magnetic field effects just as were found for isotropic magnetic field effects in Chapter 3.

Finally, in Chapter 9, we apply the γ–COMPUTE algorithm developed in Chapter 4 to the simulation of anisotropic magnetic field effects. For the first time, these calculations deal properly with the linearly polarised RF fields employed experimentally. We apply the γ–COMPUTE algorithm to interpret the RF behavioural effects described above. Surprisingly, it transpires that only radical pairs with a magnetically isolated electron spin on one radical are consistent with the experimental data.

Finally, during the course of this DPhil research, several important results have emerged from workers from the field of molecular biology. In particular, evidence for the involvement of cryptochrome proteins in magnetoreception is growing. We touch on a number of these observations and their implications for the RPM compass in the following chapters.

Chapter 7

Anisotropy in model radical pairs

7.1 Introduction

Numerous behavioural studies, reviewed in Chapter 6, have found species that detect the geomagnetic field, using its direction as a cue for navigation. In the present work, we concentrate particularly on the magnetic compass sense of migratory birds. Despite many years of research, the organ responsible for avian magnetoreception and the biophysical basis of this sense remain to be elucidated.

In 1978, Schulten proposed that the avian magnetic sense derives from anisotropic yields in a biochemical reaction that proceeds according to the radical pair mechanism [107]. To form an RPM-based compass, the RP involved must have some anisotropic interactions. There are several possibilities, such as the hyperfine, exchange, dipolar or electron-Zeeman interactions. Of these, Schulten put forward anisotropic hyperfine interactions as most likely to form the basis of a chemical compass at fields $B_0 \sim 50\,\mu\mathrm{T}$ comparable to the Earth's [107, 320]. More recently, Ritz has revived the idea that anisotropic hyperfine interactions in a biochemical RP reaction are responsible for the magnetic compass sense of birds [106]. The Wiltschkos, Ritz and coworkers have since conducted a number of behavioural experiments using radio frequency fields that support the role of such an RPM-based compass [231, 232, 314].

Nevertheless, to date, only two studies [321, 322] have tested this RPM hypothesis from a theoretical standpoint. If the RPM hypothesis is true, then the as-yet-unknown biochemical RP involved must show a significant and intelligible variation in product yield as it is rotated relative to the geomagnetic field. Otherwise, there would be no "compass" to speak of.

In this chapter, we make a series of calculations in model RPs. We aim to see whether anisotropic hyperfine interactions produce a corresponding product yield anisotropy that could *plausibly* form the basis of a compass sense. After initial calculations in simple model RPs, we proceed to larger multinuclear systems inspired by the cryptochrome family of photoreceptor proteins. We consider how the product yield in a RP builds up as further magnetic nuclei are added. Finally, we consider whether one could design a RP that would be well suited for use as a compass. These calculations, and those that follow in later chapters, provide a means of testing the RPM hypothesis which complements animal studies.

7.2 Anisotropic hyperfine interactions

The hyperfine interaction between an electron and a magnetic nucleus is described by a hyperfine tensor (HFT) A, which may be represented as a real, symmetric, 3×3 matrix:

$$\mathsf{A} = \begin{pmatrix} a_{xx} & a_{xy} & a_{xz} \\ a_{xy} & a_{yy} & a_{yz} \\ a_{xz} & a_{yz} & a_{zz} \end{pmatrix}. \tag{7.1}$$

In earlier chapters, we dealt with liquid phase radical reactions. In liquids, rapid tumbling of the radicals averages away any anisotropic parts of the hyperfine interaction, leaving only an isotropic hyperfine coupling. Such isotropic hyperfine couplings are characterised by a constant a, which is equivalent to the hyperfine tensor

$$\mathsf{A} = \begin{pmatrix} a & 0 & 0 \\ 0 & a & 0 \\ 0 & 0 & a \end{pmatrix}. \tag{7.2}$$

Physically, the hyperfine interaction arises from two sources. The anisotropic part is due to coupling between the electron and nuclear magnetic moments when both are treated as point dipoles. Within the Born-Oppenheimer approximation, the spatial distribution of the unpaired electron around the fixed nuclei depends on the molecular orbital that the electron occupies. It is quite easy to calculate molecular orbitals for reasonably sizeable molecules using quantum chemical packages such as `Gaussian03` [94]. Hence, it is also relatively simple to determine the anisotropic part of the hyperfine tensor.

The isotropic contribution to the hyperfine interaction is due to the breakdown of the aforementioned point dipole approximation. This breakdown is known as the Fermi contact interaction [92]. The strength of the isotropic hyperfine interaction is determined by the value of the electron wavefunction very close to the nucleus. The Coulomb interaction between the nuclear and electron charges is very strong in this region and electron correlation effects are marked. Furthermore, since most molecular properties are governed by the electron wavefunction outside the core nuclear region, typical quantum chemistry basis sets are chosen to concentrate computational resources on the outer valence (frontier) orbitals.

Isotropic contributions to the hyperfine interaction are, therefore, rather challenging to compute accurately. Successful calculations rely on specially-designed basis sets, such as Barone's EPR-III, which focus computational resources on the region around the nucleus. Density functional theory calculations using the UB3LYP functional and Barone's EPR-III basis set give reasonably accurate values of the isotropic hyperfine interaction [330–333]. Figures 7.16–7.19 show the results of such a calculation in four radicals relevant to the current work. Unfortunately, to obtain accurate values, it is necessary to average the molecular geometry over vibrational motions, which can be a very time consuming procedure for large molecules [331, 334].

Hyperfine tensors can be determined experimentally using modern pulse EPR techniques such as hyperfine sublevel correlation spectroscopy (HYSCORE) and electron–nuclear double resonance (ENDOR) [335].

7.2.1 Axiality and rhombicity

In some cases, we wish to quantify the extent of anisotropy, but need not specify its orientation. This is most easily done in terms of the eigenvalues of A: a_1, a_2 and a_3. From these, we extract the isotropic part of the hyperfine interaction

$$a = \frac{1}{3}(a_1 + a_2 + a_3). \tag{7.3}$$

Without loss of generality, we order the eigenvalues such that

$$|a_1 - a| \leq |a_2 - a| \leq |a_3 - a|. \tag{7.4}$$

The anisotropic part of the hyperfine tensor may then be defined by two numbers: the axiality parameter

$$\alpha = \frac{1}{2}(a_3 - a) = \frac{1}{6}(2a_3 - a_1 - a_2) \tag{7.5}$$

and the rhombicity parameter

$$\beta = \frac{1}{2}(a_1 - a_2). \tag{7.6}$$

Notice that these definitions mean that a, α and β have the same units as the hyperfine tensor A. Several other definitions are used in the literature, including some which make α and β dimensionless. Care must be taken when comparing results from different sources.

7.3 Hamiltonian

We wish to test Schulten's hypothesis that anisotropic hyperfine interactions give rise to a viable RPM-based compass. If a RP reaction is to be sensitive to a magnetic field at all, there must also be a Zeeman interaction between the unpaired electron spins and the magnetic field. Hence, we consider the simplest Hamiltonian containing contributions from these interactions:

$$\hat{H}(\boldsymbol{B}) = \hat{H}_{\mathrm{HFI}} + \hat{H}_{\mathrm{Z}}(\boldsymbol{B}), \tag{7.7}$$

where $\boldsymbol{B}$ is the magnetic field vector, $\hat{H}_{\mathrm{HFI}}$ is the hyperfine contribution and $\hat{H}_{\mathrm{Z}}$ the Zeeman contribution to the Hamiltonian.

The hyperfine interaction between a magnetic nucleus with spin $\hat{\boldsymbol{I}}$ and the unpaired electron spin $\hat{\boldsymbol{S}}$ on one radical may be written

$$\hat{H}_{\mathrm{HFI}} = \hat{\boldsymbol{I}} \cdot \mathsf{A} \cdot \hat{\boldsymbol{S}}. \tag{7.8}$$

The dot products "$\cdot$" are taken for x-, y- and z-components in the laboratory coordinate system. They may be expanded to give

$$\hat{H}_{\mathrm{HFI}} = a_{xx}\hat{I}_{\mathrm{x}}\hat{S}_{\mathrm{x}} + a_{xy}\hat{I}_{\mathrm{x}}\hat{S}_{\mathrm{y}} + a_{xz}\hat{I}_{\mathrm{x}}\hat{S}_{\mathrm{z}} + a_{yx}\hat{I}_{\mathrm{y}}\hat{S}_{\mathrm{x}} + \ldots \tag{7.9}$$

Meanwhile, the Zeeman interaction between the magnetic field and the unpaired electron spin $\hat{\boldsymbol{S}}$ on one radical is introduced as follows:

$$\hat{H}_{\mathrm{Z}} = -\gamma_{\mathrm{e}} \boldsymbol{B} \cdot \hat{\boldsymbol{S}}, \tag{7.10}$$

where γ_{e} is the electron magnetogyric ratio. For simplicity, we have assumed that the electron g-tensor is isotropic and close to that of a free electron. This is a good approximation for the organic radicals considered in this work.

Neglecting all other interactions, such as the exchange and dipolar interactions, we write the full RP spin Hamiltonian as a sum of terms for radicals A and B

$$\hat{H} = \hat{H}^{\mathrm{A}} + \hat{H}^{\mathrm{B}}, \tag{7.11}$$

where the contribution from radical N is

$$\hat{H}^{\mathrm{N}} = \sum_i \hat{\boldsymbol{I}}_{i\mathrm{N}} \cdot \mathsf{A}_{i\mathrm{N}} \cdot \hat{\boldsymbol{S}}_{\mathrm{N}} - \gamma_{\mathrm{e}} \boldsymbol{B} \cdot \hat{\boldsymbol{S}}_{\mathrm{N}} \tag{7.12}$$

in which i labels the i^{th} nucleus in radical N.

Notice that there are strong similarities with our treatment of magnetic field effects in isotropic systems in Chapter 2. In particular, equation (7.11) makes it possible to use the efficient approach to calculation outlined in §2.2. However, the Hamiltonian now depends not only on the magnitude of the magnetic field but also on its direction, which may be specified using spherical polar coordinates (θ, ϕ). We anticipate that the singlet product yield $\Phi_{\mathrm{S}}(\theta, \phi)$ will also depend on the orientation of the applied field.

7.4 Perception

Having a Hamiltonian that depends on the orientation of an applied magnetic field is not, in itself, sufficient to form a RPM compass. For example, RPs in the liquid phase tumble continually (they undergo rotational diffusion). Although the radicals involved have anisotropic hyperfine tensors, their tumbling motion averages away any effects of hyperfine anisotropy. Indeed, as we saw in Chapters 2–5, it is a good approximation to neglect hyperfine anisotropy entirely for unconstrained RP reactions in the liquid phase. Furthermore, even RPs that are constrained from tumbling, such as RPs that are trapped in a glass by rapid sample cooling, do not necessarily show an anisotropic field response. If the RPs in a sample are not mutually aligned, then although the yield of each individual RP will depend on the applied field orientation, these effects will average away when we measure the product yield for a bulk sample. In order to form an RPM compass, we require RPs in which at least one of the radicals has anisotropic magnetic interactions. Furthermore, we require a macroscopic assemblage of RPs such that this radical is (or both radicals are) prevented from tumbling and is (are) aligned relative to the whole. In other words, there are restrictions on the dynamic *and* static disorder of RPs suitable to form the basis of a magnetoreceptor.

Behavioural experiments show that the avian compass sense operates only when blue–green light is allowed to enter the eye (see §6.3.5 and 6.3.6). As discussed in §6.5, the retina contains an exquisitely ordered array of cells in several layers. Many of these cells are exposed to ambient light, are thoroughly connected to the central nervous

system and are known to be involved in photoreception. It seems plausible that some of these cells may contain the RPs responsible for magnetoreception [106, 107, 315]. One could imagine a RP magnetic field effect in the retina giving rise to a neural impulse if one of the RP reaction products were a neurotransmitter or if one of the RP products caused its host protein to change conformation, as is common in biochemical signalling pathways.

Ritz developed a simple model [106] to show how a field-sensitive reaction in the visual pathway might allow a bird to perceive the geomagnetic field. Despite the naïveté of this model, it serves to show how the RPM could in principle produce an intelligible compass sense. Furthermore, this model gives some sense of the quality of compass information that might arise from a particular choice of RP and other model parameters.

Nonetheless, before proceeding, we must attach something of a health warning to this visual modulation model for several reasons. First, there is *far* less evidence available to settle questions of the mode of perception of a magnetic field than there are behavioural studies which confirm the *existence* of a magnetic sense. The neural activation recordings of Semm [294] and the brain activity measurements of Mouritsen [306–308, 336] probably come closest to tackling these questions. Indeed, sensory perception is not fully understood even for human subjects who are conscious and able to assist actively in experiments.

Second, the Ritz model treats the retina as a pinhole camera, but in reality it is far more complex than that. In humans, the retina has ten layers. Data from an estimated 160 million light sensitive rod and cone cells in the upper layers of the retina is compressed into signals along "only" 1.6 million fibres in the optic nerve. The lower layers of the retina perform a remarkable amount of signal processing such as detecting edges and motion in the retinal image.

Third, even if the magnetic field did act to modulate vision, it is entirely possible that this effect is separated out in the higher regions of the brain. Higher level neural responses are often far removed from the biophysical process in which they originate.

In reality, we may very well have a RPM compass located in the eye that is not directly connected to the visual system. Precedent for this is found in circadian rhythms, which are controlled by light incident upon the eyes but not through the visual system [337, 338].

7.4.1 Visual modulation

Despite these caveats, the Ritz model is interesting as a simple demonstration that an RPM-based compass is feasible. The model is developed as follows. Figure 7.1 shows a schematic cross-section of the eyeball, which we model as a unit sphere centred at the point O which has Cartesian coordinates $(0,0,0)$. Light travels from the scene under observation (at the top of the page), through the pupil (modelled as a pinhole at point N) and strikes the retina. One particular ray of light is drawn for illustration, which strikes the retina at point R. Mentally, the light is perceived as forming an image in the *xy*-plane at point I. Hence, a rectangular object creates a rectangular perceived image in the plane containing I. In summary, the eye is assumed to function as a pinhole camera.

We suppose that light incident on the retina creates RPs in an initial singlet state

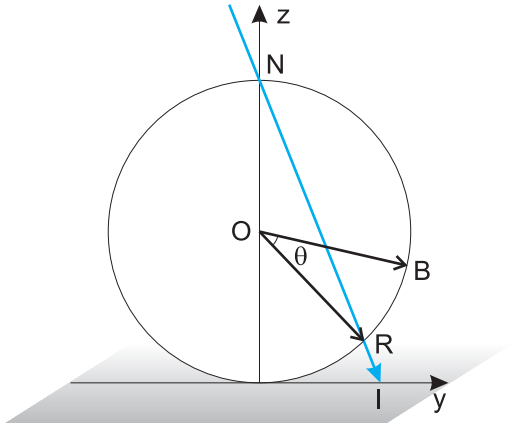

Figure 7.1: Cross section through the eyeball, modelled as a unit sphere. The points N, O, R and I all lie in the plane of the paper. B may be at any point on the surface of the eyeball, *i.e.* B is not constrained to lie in the plane NOR.

which react according to the RPM. Only the singlet product goes on ultimately to trigger an impulse in the optic nerve. In other words, for any point R on the retina or, equivalently, for any point I in the perceived image

$$\text{Perceived light intensity} = \text{Singlet yield at the retina} \times \text{True light intensity}. \quad (7.13)$$

The singlet yield depends on the relative orientation of the photoinduced RP and the geomagnetic field, which varies across the curved surface of the retina. Hence, the geomagnetic field modulates the contrast of the perceived image by different amounts at different points in the field of vision. We wish to calculate a picture showing that modulation throughout the field of vision.

To continue, we make a further assumption concerning the arrangement of RPs with respect to the retina. We assume that every RP has a well-defined orientation with respect to the retinal surface normal vector $\overrightarrow{\mathrm{OR}}$ but that they are otherwise randomly oriented. This seems reasonable given that histological images of the retina show long, thin light-receptor cells whose axis points towards the centre of the eyeball but which are not otherwise oriented. Presumably similar arguments explain the insensitivity of bird vision to polarised light.

The geomagnetic field is directed along the vector $\overrightarrow{\mathrm{OB}}$. The singlet yield for a RP at the point R is a function of the polar angle θ between $\overrightarrow{\mathrm{OR}}$ and $\overrightarrow{\mathrm{OB}}$ which is well defined, and the azimuthal angle ϕ (defined as a rotation about the vector $\overrightarrow{\mathrm{OR}}$) which is randomly distributed between 0 and 2π. To take account of this uniaxial alignment, we calculate an average axial singlet yield

$$\widetilde{\Phi}_{\mathrm{S}}(\theta) = \int_0^{2\pi} \Phi_{\mathrm{S}}(\theta,\phi)\,\mathrm{d}\phi. \quad (7.14)$$

Now, to determine the visual modulation pattern for each point I with Cartesian coordinates (x,y) in the field of vision, it remains only to relate those coordinates to the polar angle θ. To do this, we must first determine the position of the point R using the fact that the line NRI intersects the shaded plane at point I.

The position vector $\boldsymbol{r}_I$ satisfies the equation of a plane

$$\boldsymbol{r}_I \cdot \boldsymbol{k} = -1 \quad (7.15)$$

where $\boldsymbol{i}$, $\boldsymbol{j}$ and $\boldsymbol{k}$ are unit vectors along the x-, y- and z-axes. Meanwhile the position vector $\boldsymbol{r}_{NI}$ of any point on the line NRI satisfies the equation of a line

$$\boldsymbol{r}_{NI} = \alpha(\boldsymbol{r}_R - \boldsymbol{k}) + \boldsymbol{k} \tag{7.16}$$

in which α is an arbitrary real number.

Since the point I lies both on the line NRI and in the shaded plane, $\boldsymbol{r}_I$ satisfies both equations and hence

$$\begin{aligned} (\alpha(\boldsymbol{r}_R - \boldsymbol{k}) + \boldsymbol{k}) \cdot \boldsymbol{k} &= -1 \\ \alpha(\boldsymbol{r}_R \cdot \boldsymbol{k} - 1) &= -2 \\ \implies \alpha &= \frac{2}{1 - \boldsymbol{r}_R \cdot \boldsymbol{k}} \end{aligned} \tag{7.17}$$

and thus

$$\boldsymbol{r}_I = \frac{2(\boldsymbol{r}_R - \boldsymbol{k})}{1 - \boldsymbol{r}_R \cdot \boldsymbol{k}} + \boldsymbol{k}. \tag{7.18}$$

If we write $\boldsymbol{r}_R$ in spherical polar co-ordinates $\boldsymbol{r}_R = \sin\theta_R \cos\phi_R \boldsymbol{i} + \sin\theta_R \sin\phi_R \boldsymbol{j} + cos\theta_R \boldsymbol{k}$ then

$$x_I = \frac{2\sin\theta_R \cos\phi_R}{1 - \cos\theta_R} \quad \text{and} \quad y_I = \frac{2\sin\theta_R \sin\phi_R}{1 - \cos\theta_R} \tag{7.19}$$

which rearrange to give

$$\tan\phi_R = \frac{y_I}{x_I} \implies \cos\phi_R = \frac{x_I}{r_I} \quad \text{and} \quad \sin\phi_R = \frac{y_I}{r_I} \tag{7.20}$$

and

$$\cos\theta_R = \frac{r_I^2 - 4}{r_I^2 + 4} \quad \text{and} \quad \sin\theta_R = \frac{4r_I}{r_I^2 + 4} \tag{7.21}$$

where $r_I^2 \equiv x_I^2 + y_I^2$.

Having found the position vector $\boldsymbol{r}_R$ of the point R, the angle θ is given by the dot product

$$\begin{aligned} \cos\theta &= \boldsymbol{r}_R \cdot \boldsymbol{r}_B \\ &= \left(\frac{4r_I}{r_I^2 + 4}\right)\left(\frac{x_I}{r_I}x_B + \frac{y_I}{r_I}y_B\right) + \left(\frac{r_I^2 - 4}{r_I^2 + 4}\right) z_B \\ &= \frac{x_I x_B + y_I y_B + \left(\left(\frac{r_I}{2}\right)^2 - 1\right) z_B}{\left(\frac{r_I}{2}\right)^2 + 1} \end{aligned} \tag{7.22}$$

for a magnetic field $\boldsymbol{r}_B = x_B \boldsymbol{i} + y_B \boldsymbol{j} + z_B \boldsymbol{k}$.

Equation (7.22) allows us to calculate the intensity modulation at any point in an image from the magnetic field vector $\boldsymbol{r}_B$ and the average axial singlet yield $\widetilde{\Phi}_S(\theta)$. Examples of these intensity modulation plots are given later for a one-proton RP model system. Figure 7.9 shows the modulation patterns for the one-proton RP whose singlet yield anisotropy is given in Figure 7.8.

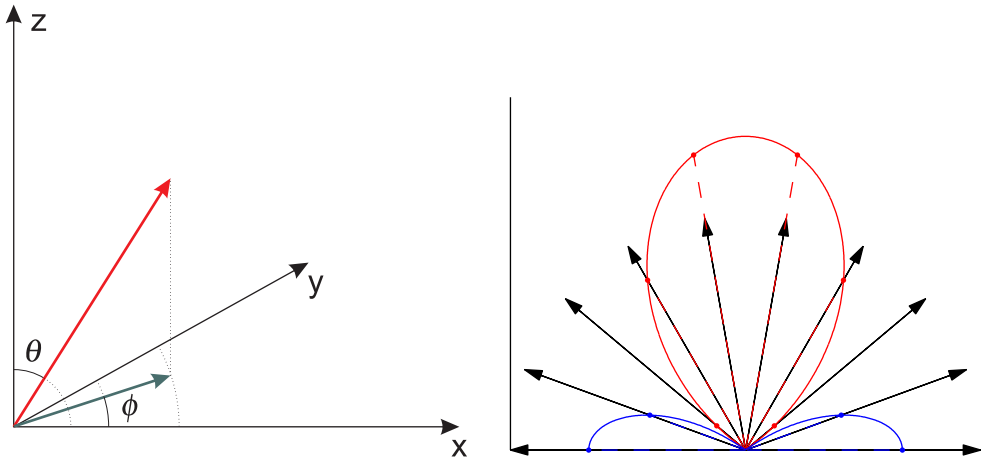

(a) Definition of the spherical polar coordinates (θ, ϕ) for the red vector. The polar angle from the z-axis is $0 \leq \theta \leq \pi$. Projecting the red vector into the xy-plane gives the green vector. The azimuthal angle from the x-axis is $0 \leq \phi < 2\pi$.

(b) Illustration of the polar plotting procedure.

Figure 7.2: Polar plots (see text for details).

7.5 Polar plots

It is helpful to display anisotropic singlet yields and other orientation-dependent data in the form of polar plots. Consider a quantity f that depends on orientation expressed in spherical polar coordinates, as defined in Figure 7.2(a), according to the function $f(\theta, \phi)$. For example, $f(\theta, \phi)$ might be the singlet yield $\Phi_S(\theta, \phi)$ for a radical pair with particular hyperfine tensors, exponential model rate constant, etc. when the applied magnetic field makes an angle (θ, ϕ) with the RP molecular axis system. As illustrated in Figure 7.2(b), a polar plot is constructed in the following manner:

- We choose a set of orientations, *i.e.* a list of particular (θ_k, ϕ_k) values. This choice of *mesh* is discussed further in §7.5.2. In the figure, these orientations are marked as black arrows radiating from the origin.

- We calculate values for the quantity to be plotted at each orientation $f_k = f(\theta_k, \phi_k)$. For example, we might calculate the singlet yield in a RP at each orientation of an applied magnetic field.

- Starting at the origin, for each orientation we move outwards along the direction (θ_k, ϕ_k) a distance $|f_k|$ and draw a point.

- We colour this point according to (the real part of) the value f_k. The most positive value is red, and the most negative value is blue. The colour scale that we use throughout this thesis is shown in Figure 7.3.

- We finish by connecting these points together to form a surface, interpolating the colours as necessary.

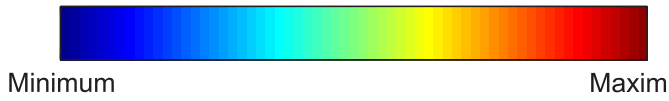

Figure 7.3: Colour scale used for three dimensional plots in this thesis. The brightness of the colours in a given figure depends on the choice of rendering parameters such as lighting.

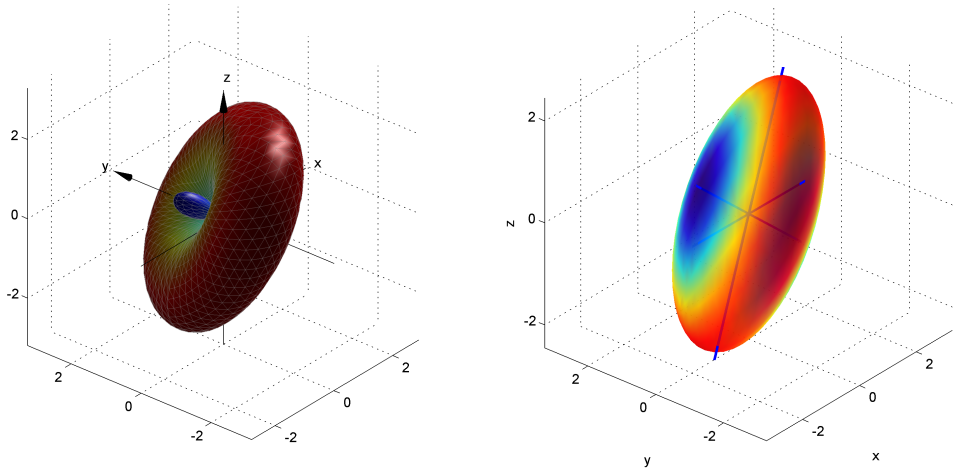

(a) Polar plot (b) Ellipsoid plot

Figure 7.4: Comparison of two different plots for a hyperfine tensor whose principal values are $-1.25\,\mathrm{mT}$, $2.64\,\mathrm{mT}$ and $2.81\,\mathrm{mT}$.

7.5.1 Visualising hyperfine tensors

Hyperfine tensors may be represented as a polar plot. For a hyperfine tensor A, the relevant function is

$$f(\theta,\phi) = \hat{\boldsymbol{r}}(\theta,\phi)\cdot \mathsf{A}\cdot\hat{\boldsymbol{r}}(\theta,\phi) \tag{7.23}$$

where

$$\hat{\boldsymbol{r}}(\theta,\phi) = \cos\phi\sin\theta\boldsymbol{i} + \sin\phi\sin\theta\boldsymbol{j} + \cos\theta\boldsymbol{k} \tag{7.24}$$

is the unit vector along the direction specified by the spherical polar coordinates (θ,ϕ). Physically, this function $f(\theta,\phi)$ is the hyperfine interaction energy for an electron and nuclear spin both oriented along $\hat{\boldsymbol{r}}$. An example polar plot is given in Figure 7.4(a).

Alternatively, the hyperfine tensor may be represented as an ellipsoid. The axes of the ellipsoid are drawn along the eigenvectors of A with lengths equal to the absolute values of the corresponding eigenvalues. The same hyperfine tensor A is plotted as an ellipsoid in Figure 7.4(b) for comparison.

7.5.2 Choice of mesh

Famously, there is no general constructive algorithm for partitioning the unit sphere into polygons that subtend an equal solid angle. Hence, a wealth of *ad hoc* spherical meshing methods have grown up to suit different applications [339, 340]. Figure 7.5 shows the two types of mesh used for making polar plots in this thesis.

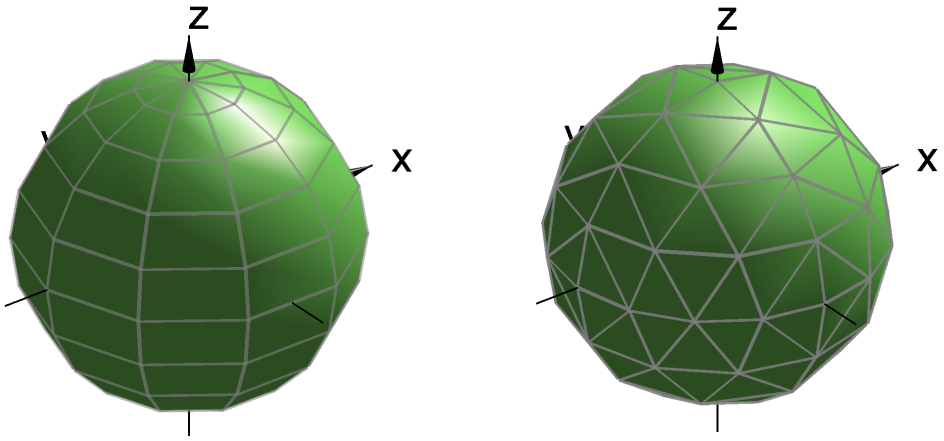

(a) Equiangular mesh ($m = n = 11$). (b) SOPHE mesh (N=5).

Figure 7.5: The unit sphere, $f(\theta,\phi) = 1$, plotted using two different types of mesh. The mesh spacing is deliberately coarse in order to make the different distributions of vertices and faces clearer.

The simplest mesh has vertices at combinations of m regularly spaced θ values and n regularly spaced ϕ values which cover the unit sphere:

$$\begin{aligned} \theta &= 0,\ \delta\theta,\ 2\delta\theta,\ 3\delta\theta,\ \ldots,\ \pi & \delta\theta &= \frac{\pi}{m-1} \\ \phi &= 0,\ \delta\phi,\ 2\delta\phi,\ 3\delta\phi,\ \ldots,\ 2\pi & \delta\phi &= \frac{2\pi}{n-1}. \end{aligned} \tag{7.25}$$

The unit sphere is plotted using this mesh in Figure 7.5(a). Although this "equiangular mesh" is easy to generate and conceptually simple, the distribution of vertices over the unit sphere is rather uneven. In particular, too many vertices are placed near the poles at the expense of the equatorial regions. Indeed, the north and south pole are both sampled n times. If the function to be plotted $f(\theta,\phi)$ is time consuming to evaluate, then this unevenness wastes computational resources. The same is true if we wish to integrate over the mesh — in order to find the average singlet yield, for example.

To mitigate the deficiencies in the equiangular mesh, we frequently employ a SOPHE (**S**ydney **Op**era **H**ous**e**) mesh [341]. A SOPHE mesh has vertices that are spread nearly uniformly over the unit sphere in a manner reminiscent of the roof of that famous building. The vertices lie on a series of well defined curves [341, eq.1]

$$\theta = C_1 \qquad \text{and} \qquad \theta\phi = C_2 \qquad \text{and} \qquad \theta\phi = \frac{\pi\theta}{2} - C_2 \tag{7.26}$$

where

$$C_1 = i\Delta\theta \qquad \text{and} \qquad C_2 = (i-1)\frac{\pi}{2}\Delta\theta \qquad \text{and} \qquad \Delta\theta = \frac{\pi}{2(N-1)} \tag{7.27}$$

in which the parameter N controls the mesh spacing. These vertices are joined to form almost equilateral triangular faces. SOPHE is designed to allow efficient mesh refinement by splitting selected faces into smaller subunits. SOPHE allows interpolation of

the value of $f(\theta,\phi)$ within each triangular face in order to improve the accuracy of numerical integration.

These meshes were implemented as `Matlab` codes `MakeRegularThPhGrid` and `MakeSopheGrid`. From the mesh spacing parameters m,n or N, these functions return a list of θ_k and ϕ_k values for the vertices along with an associated list of weights w_k. The weights are proportional to the solid angle subtended around each vertex such that $\sum_k w_k = 1$. Therefore, the spherical average of a function $f(\theta,\phi)$ is approximated by

$$\bar{f} = \frac{1}{4\pi}\int_0^{2\pi}\int_0^{\pi} f(\theta,\phi)\sin\theta\,\mathrm{d}\theta\,\mathrm{d}\phi \approx \sum_k w_k f(\theta_k,\phi_k). \tag{7.28}$$

7.6 One-proton radical pairs

Having described the RP Hamiltonian and other machinery necessary for calculating anisotropic magnetic field effects, we turn our attention briefly to the simplest possible RPs: those containing only a single spin-½ magnetic nucleus. One-proton RPs are simple enough that we may make some general observations before tackling more complex multinuclear RPs in due course.

7.6.1 Energy levels

Figure 7.6(a) shows the energy levels in a one-proton RP with an axial hyperfine tensor (HFT). To make this figure applicable to a wide range of RPs, we plot the field strength B_0 and the energies E in multiples of the isotropic part of the hyperfine interaction a.

At high fields, the axiality of the hyperfine interaction makes little difference to the RP energy levels, since these are dominated by the Zeeman interaction. Indeed, when $B_0 \gg a$ so that the secular approximation holds, the only effect of hyperfine axiality is an orientation-dependent scaling of the hyperfine coupling constant. For a particular orientation of the static field, the system evolves as though it had an isotropic hyperfine coupling constant

$$a_{\mathrm{eff}} = \frac{\boldsymbol{B}_0\cdot\mathsf{A}\cdot\boldsymbol{B}_0}{\boldsymbol{B}_0\cdot\boldsymbol{B}_0}. \tag{7.29}$$

In the absence of a magnetic field, when $B_0 = 0$, there is a significant change in the RP energy levels. Figure 7.7 shows the changes in zero-field energy levels in greater detail. When the hyperfine coupling is isotropic, there are two sets of energy levels with 6-fold and 2-fold degeneracy. As the axiality becomes non-zero, the 6-fold degenerate level is split into 4-fold and 2-fold degenerate levels. When the HFT is fully rhombic, these are split further into four 2-fold degenerate levels. In the presence of a rhombic HFT, the only degeneracy at zero field arises from the unpaired electron spin of the counter-radical which contains no magnetic nuclei.

During our earlier work on RP reactions in the liquid phase, we saw that the response of a RP reaction to weak static fields $B_0 < 1\,\mathrm{mT}$ was dominated by the low field effect (LFE) [10, 108–113]. The Earth's field is around 50 μT and we might therefore expect that any RP response to the geomagnetic field would necessarily occur as a result of the LFE.

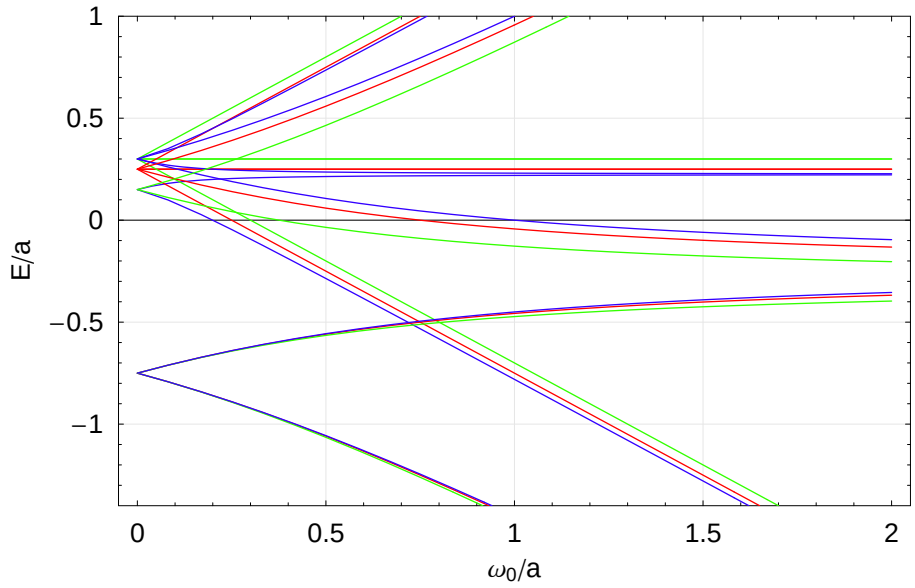

(a) Energy levels in a one-proton radical pair with isotropic HFC a and $\beta = 0$ subject to a static field $B_0 = -\omega_0/\gamma_e$. The axiality α is given by the colour code: (—) $\alpha = 0$; (—) $\alpha = a/10$ and $\theta = 0$; and (—) $\alpha = a/10$ and $\theta = \pi/2$.

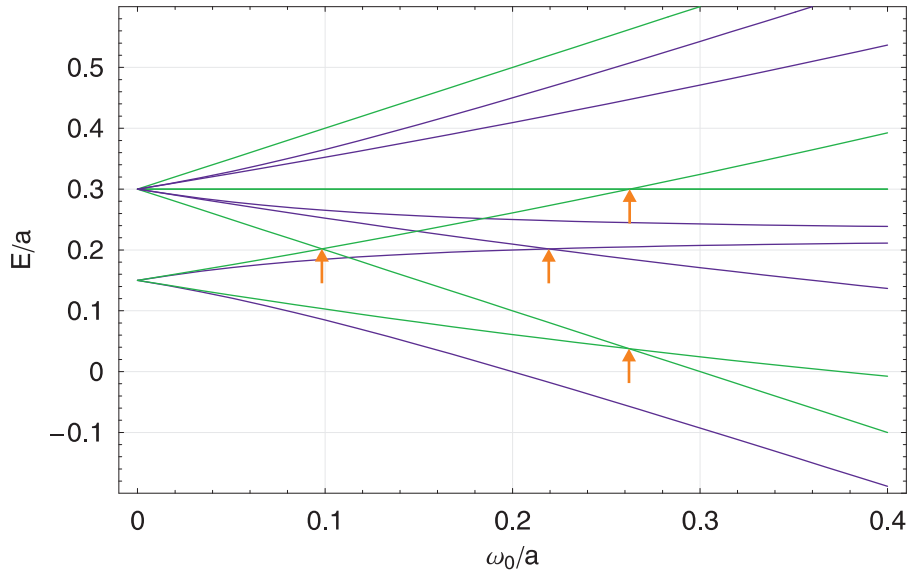

(b) Magnified view of the low-field energy level crossings when $\alpha = a/10$. Colour code: (—) $\theta = 0$; and (—) $\theta = \pi/2$. Energy level crossings are marked with red arrows.

Figure 7.6: Effect of hyperfine anisotropy on RP energy levels.

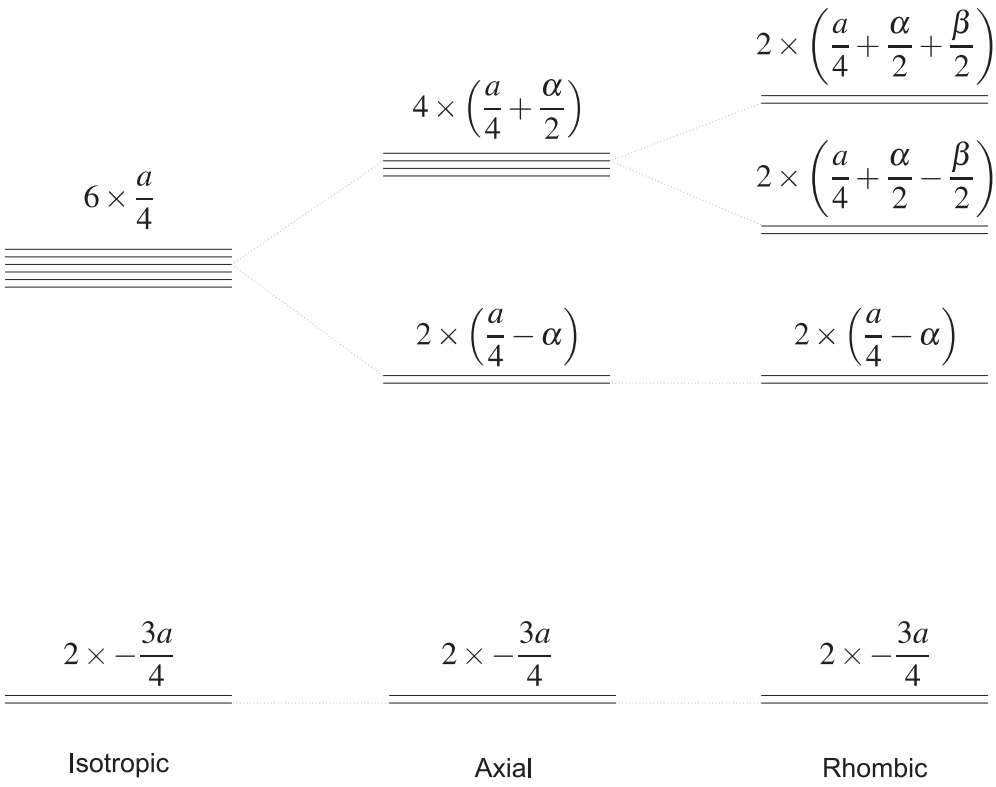

Figure 7.7: Zero-field energy levels in a one-proton radical pair. Hyperfine anisotropy introduces energy level splittings not present in the isotropic case.

However, the LFE arises because of the high degeneracy of the energy levels in a RP with isotropic HFCs at zero field [108]. A weak magnetic field removes this zero-field degeneracy, changing the RP eigenstates significantly. Hence, a weak magnetic field can have a pronounced effect on the singlet yield. RPs with axial, or worse still, rhombic HFTs do not have zero-field energy levels that are highly degenerate. It is clearly impossible for this high degeneracy to be lifted by a weak static field. Furthermore, lifting of the 2-fold degeneracies present on the right (rhombic case) of Figure 7.7 does not produce a LFE. It seems reasonable, therefore, to suppose that the LFE will be abolished by the presence of axial or rhombic hyperfine interactions. On the face of it, this argument seems to rule out significant effects of an Earth-strength magnetic field in a RP with anisotropic hyperfine interactions.

However, all is not lost. Although the zero-field degeneracy familiar from systems with isotropic HFTs has been lost, RPs with anisotropic hyperfine interactions gain several energy level crossings at weak fields $a \gg B_0 \neq 0$. Figure 7.6(b) shows an enlarged plot of the low-field energy levels in a RP that has an axial HFT. The energy level crossings caused by the anisotropic HFT are marked with red arrows.

These energy level crossings are associated with rapid changes in the RP eigenstates, and hence in the singlet yield. They are significant in two respects. First, they occur at fields $B_0 \ll a$, such as the Earth's magnetic field. Second, the B_0 fields at which these energy level crossings occur depend strongly on the orientation of the magnetic field. For a static field of fixed strength, there will be strong resonant effects on singlet yield at some orientation, but not at others.

7.6.2 Singlet yield anisotropy

Figure 7.8 shows the dependence of singlet yield on hyperfine axiality and on the strength B_0 and orientation θ of the magnetic field. Figures 7.8(b–e) show clearly how the non-zero axiality alters the LFE. When $\alpha = 0$, the blue curves show a sharp drop in singlet yield in the presence of small magnetic fields. As expected, this LFE does not depend on the orientation of the applied magnetic field. This sharp spike in singlet yield at $B_0 = 0$ does not appear once there is a significant axiality. However, rather than being abolished, it appears that the LFE is "shifted". The sharp spike in singlet yield moves, following the energy level crossings marked in Figure 7.6(b).

Contrasting Figures 7.8(b–e), we see clearly that in systems with an axial HFT, the static field corresponding to the spike in singlet yield depends on the orientation of the magnetic field. This is a manifestation of the sensitivity of the energy levels crossings to the orientation of the magnetic field. Figure 7.8(a) plots the singlet yield when $B_0/a = 0.2$ as a function of the field orientation θ. Although at first sight, it seemed that anisotropic HFTs would abolish the LFE and prevent a viable magnetic compass response, in fact we see that anisotropic HFTs "shift" the LFE to different field strengths in a manner that depends strongly on the orientation of the field. Hence, at fixed field strengths, anisotropic HFTs can produce strongly anisotropic singlet yields. We conclude this section by calculating the Ritz visual modulation pattern for this RP. This pattern, shown in Figure 7.9, clearly contains intelligible compass information.

7.7 Two-proton radical pairs

Real radical pairs, such as the as-yet-unknown RP involved in avian magnetoreception, contain more than one magnetic nucleus. In the following parts of this chapter, we investigate whether the strong, intelligible singlet yield anisotropy patterns that emerge from a one-proton RP are lost as we move to more realistic multinuclear RPs. We are particularly interested to see how the total anisotropy pattern develops. Is it dominated by the HFTs of a few special nuclei? Do the two radicals contribute separately to the overall singlet yield anisotropy? In other words, are the anisotropy patterns of "m–n" RPs (*i.e.* those having m magnetic nuclei on radical A and n on radical B) given as a sum of the singlet yield anisotropy of the corresponding "m–0" and "0–n" RPs? Is the singlet yield anisotropy stable in the face of addition of small random hyperfine couplings such as might arise from parts of a protein backbone or from the solvent?

As a first step in addressing these questions, Figures 7.10 and 7.11 show a series of singlet yield anisotropy calculations in "1–1" RPs. The RPs in these calculations have axial HFTs whose principal axes make an angle ξ with one-another.

In Figure 7.10, both radicals have identical HFTs except that the tensor in radical B has been rotated by an angle ξ. Figures 7.10(a) and (c) show the singlet yield when the radicals are taken separately. Comparing Figures 7.10(a) and (h), we see that the singlet yield anisotropy in the "1–1" RP is about six times larger than in the one-proton RPs. When radical B is rotated, the singlet yield anisotropy rises until Figure 7.10(k), where $\xi = 90^\circ$ and the singlet yield anisotropy is about fifty times larger than in the one-proton RPs. Meanwhile, the spherical average singlet yield, shown in Figure 7.10(b) falls by more than 10% as radical B is rotated. Presumably, this arises because as ξ increases, the spin evolution on the two radicals becomes more different for any

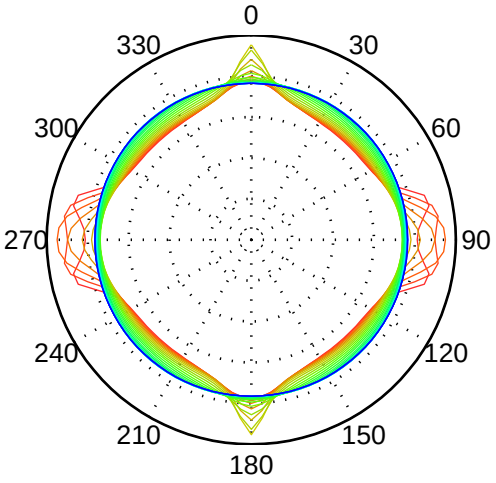

(a) Polar plot of singlet yield when $B_0/a = 0.2$, corresponding to the grey points below. Colours denote the axiality, using the same scale as in Figures (b–e).

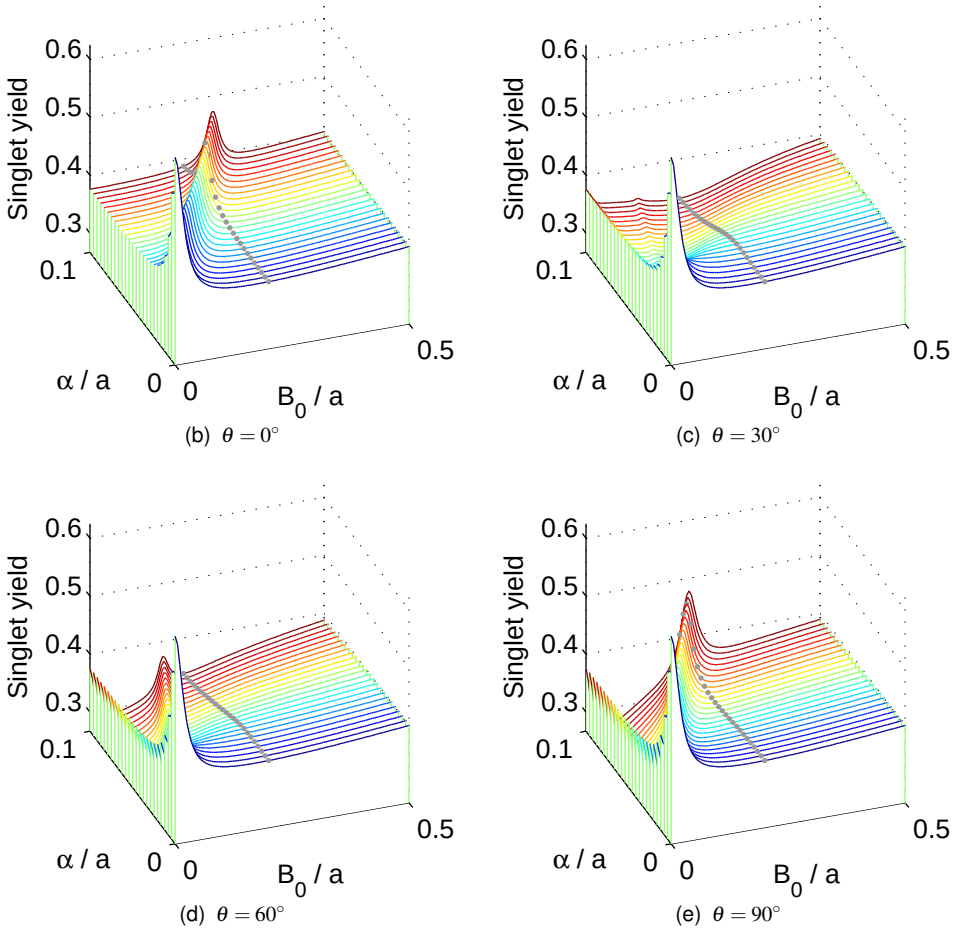

(b) $\theta = 0°$ (c) $\theta = 30°$

(d) $\theta = 60°$ (e) $\theta = 90°$

Figure 7.8: Singlet yield in a one-proton RP model system. The static field B_0 and axiality α are divided by the isotropic HFC a to make unitless quantities before plotting. Calculations in Figures (b–e) were made at four different orientations θ of the static field relative to the principal (z-) axis of the hyperfine tensor. An exponential model rate constant $k = a/100$ was used. Figure (a) shows singlet yield as a function of field orientation θ when $B_0/a = 0.2$.

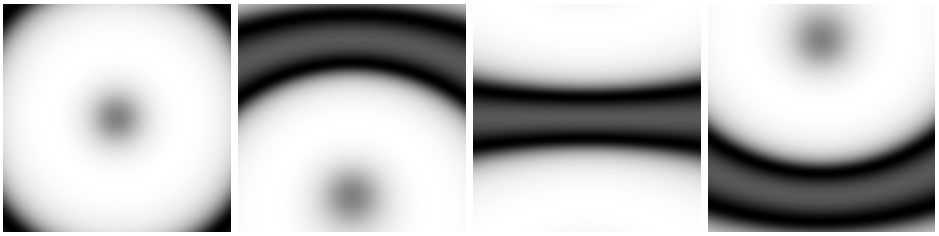

(a) $\zeta = 0°$ (b) $\zeta = 45°$ (c) $\zeta = 90°$ (d) $\zeta = 135°$

Figure 7.9: Visual modulation figures for a one-proton RP model system. The parameters were $B_0/a = 0.2$, $\alpha/a = 0.1$, $\beta/a = 0$ and $k/a = 0.01$. Each figure represents a $31° \times 31°$ field of view. The angle between the centre of view and the magnetic field is denoted ζ. The black regions have the highest singlet yield and white regions the lowest.

particular field orientation, meaning that the electron spins move out of phase more quickly — which is equivalent to saying that the singlet–triplet interconversion rate is increased.

It is harder to interpret the changes in the shape of the singlet yield anisotropy pattern. The yield pattern in Figure 7.10(h) is axially symmetric, and those in Figures 7.10(i–k) retain a symmetry under reflection in the *yz*-plane. Otherwise, the "1–1" RP singlet yield patterns are rather complicated. Regrettably, they are not even approximately a superposition of the separate one-proton RP singlet yield anisotropies.

Turning to Figure 7.11, where radicals A and B have different hyperfine tensors, a similar picture emerges. In Figure 7.11(h), the singlet yield anisotropy remains axially symmetric and is about ten times larger than in the corresponding one-proton RPs. When $\xi = 90°$ in 7.11(k), the singlet yield anisotropy is about twenty times larger than in the one-proton RPs, but its shape is remarkably complex.

In terms of their suitability for a RPM-based compass, these results are mixed. On the one hand, it is very encouraging to see that the singlet yield anisotropy can increase when we add magnetic nuclei to a radical pair regardless of the relative orientation of their hyperfine tensors. Yet, it seems unfortunate that the singlet yield anisotropy patterns in the "1–1" RPs are so complicated. Adding a second magnetic nucleus has made it harder to imagine these "1–1" RPs forming an *intelligible* compass.

However, this is not the end of the story. It is known that both "1–0" and "1–1" RPs sometimes give rather atypical magnetic field effects. In the following sections, we extend these model calculations to more realistic multinuclear RPs. We explore whether multinuclear RPs settle into more predictable patterns than their one- and two-proton RP counterparts.

7.8 Cryptochromes

The cryptochromes (CRY) are a family of photoreceptor proteins that absorb blue and UV-A light and which are found in many fungi, plants and animals [342]. In mammals, they are involved in regulating the circadian clock [337, 338], whilst in plants they regulate processes such as growth of the hypocotyl in seedlings [343]. After a great deal of effort, X-ray structures of two cryptochromes CRY-1 and CRY-3 from

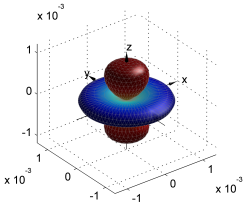

(a) Φ_S^{an} for radical A alone

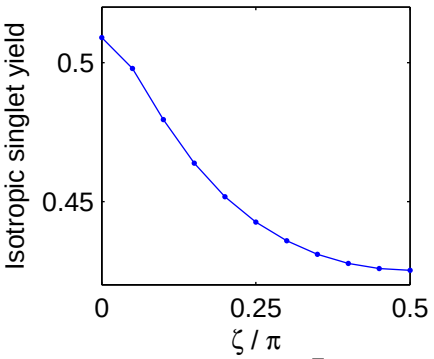

(b) Spherical average singlet yield $\bar{\Phi}_S$ at different orientations

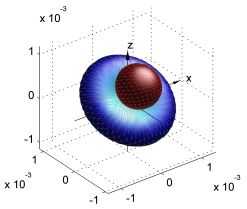

(c) Φ_S^{an} for radical B alone when $\xi = 45°$

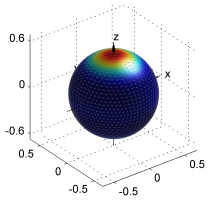

(d) Φ_S when $\xi = 0°$

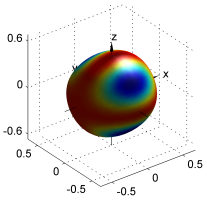

(e) Φ_S when $\xi = 9°$

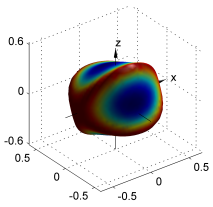

(f) Φ_S when $\xi = 45°$

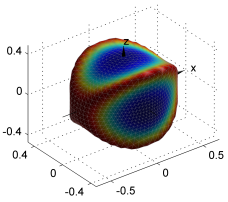

(g) Φ_S when $\xi = 90°$

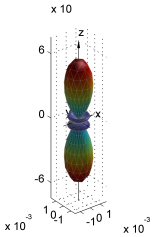

(h) Φ_S^{an} when $\xi = 0°$

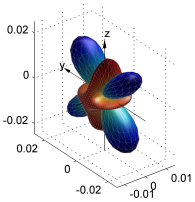

(i) Φ_S^{an} when $\xi = 9°$

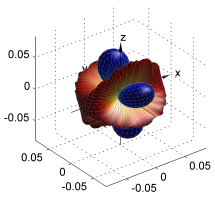

(j) Φ_S^{an} when $\xi = 45°$

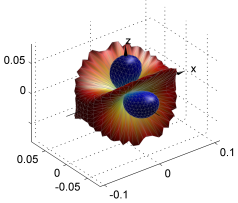

(k) Φ_S^{an} when $\xi = 90°$

Figure 7.10: Variation in singlet yield Φ_S and singlet yield anisotropy ($\Phi_S^{an} = \Phi_S(\theta,\phi) - \bar{\Phi}_S$) in a "1–1" RP as radical B is rotated. The radicals both have HFC $a = 100\,\mu T$, $\alpha = 2.5\,\mu T$ and $\beta = 0\,\mu T$. The principal hyperfine axis in radical A is aligned along the z-axis, whilst that in radical B is aligned at an angle ξ from the z-axis in the yz-plane. Other parameters: $B_0 = 50\,\mu T$, $k = 2 \times 10^5\,s^{-1}$ and $N = 20$. Calculations were made as described in §2.2.2.

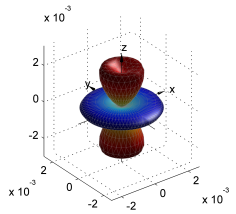

(a) Φ_S^{an} for radical A alone

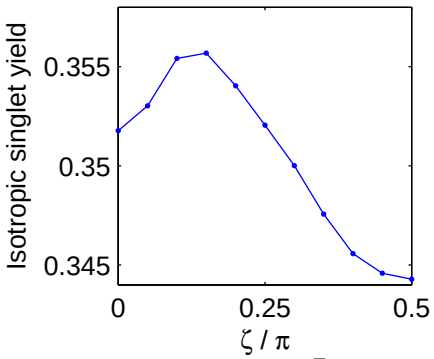

(b) Spherical average singlet yield $\bar{\Phi}_S$ at different orientations

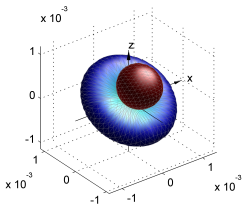

(c) Φ_S^{an} for radical B alone when $\xi = 45°$

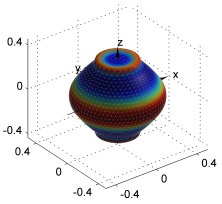

(d) Φ_S when $\xi = 0°$

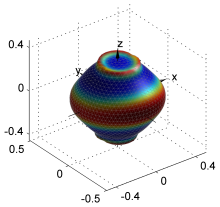

(e) Φ_S when $\xi = 9°$

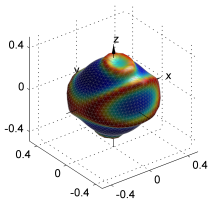

(f) Φ_S when $\xi = 45°$

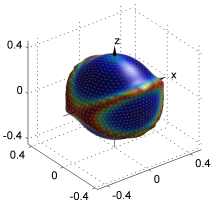

(g) Φ_S when $\xi = 90°$

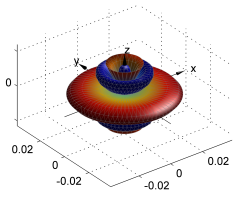

(h) Φ_S^{an} when $\xi = 0°$

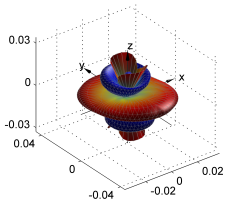

(i) Φ_S^{an} when $\xi = 9°$

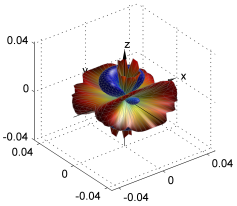

(j) Φ_S^{an} when $\xi = 45°$

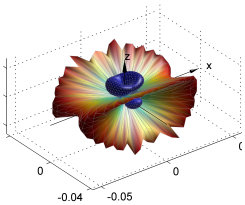

(k) Φ_S^{an} when $\xi = 90°$

Figure 7.11: Variation in singlet yield and singlet yield anisotropy in a "1–1" RP as radical B is rotated. Radical A has HFC $a = 100\,\mu\text{T}$, $\alpha = 2.5\,\mu\text{T}$ and $\beta = 0\,\mu\text{T}$. Radical B has HFC $a = 232\,\mu\text{T}$, $\alpha = 5.8\,\mu\text{T}$ and $\beta = 0\,\mu\text{T}$. The principal hyperfine axis in radical A is aligned along the z-axis, whilst that in radical B is aligned at an angle ξ from the z-axis in the yz-plane. Other parameters: $B_0 = 50\,\mu\text{T}$, $k = 2 \times 10^5\,\text{s}^{-1}$ and $N = 20$. Calculations were made as described in §2.2.2.

the mustard *Arabidopsis thaliana* have recently become available [344, 345]. These structures are shown in Figures 7.12 and 7.13. Cryptochromes show a high degree of sequence homology to DNA photolyases [328, 345] and to phototropins [346].

Our interest in cryptochromes stems from two sources. In the first instance, cryptochromes are flavoproteins — they bind FAD as a catalytic cofactor. Flavins have a rich photochemistry [347, 348] and are often involved in radical reactions [349]. Indeed, DNA photolyase, which has a very similar FAD binding fold to that in the cryptochromes has been shown by tr-EPR, see Figure 7.14, to form spin-correlated radical pairs with a remarkably long lifetime of 20 µs [321, 349–353]. Although the cryptochrome photocycle has not yet been elucidated [328, 329, 354], it seems quite likely that cryptochromes will also produce long-lived spin correlated radical pair intermediates, which are a necessary prerequisite for magnetic field effects and for any RPM-based compass. Figure 7.15 shows a proposed reaction scheme for CRY-1 in *A. thaliana*.

There is also evidence for the role of cryptochromes in magnetoreception from molecular biology studies in birds. Cryptochromes have been isolated in the retinae of the European robin *Erithacus rubecula* [355] and in migratory garden warblers *Sylvia borin* during times of migratory restlessness at night [336]. Far lower levels of retinal cryptochrome were expressed in a related non-migratory species, the zebra finch *Taeniopygia guttata*. In garden warblers, the expression of retinal cryptochromes increases when birds are orienting [105, 336]. Furthermore, this expression is connected with brain activity in "cluster N", a brain area that is responsible for navigation [307]. Finally, Ahmad and coworkers have recently reported effects of a 500 µT magnetic field on the cryptochrome-regulated hypocotyl growth in *A. thaliana* [343]. Taken together, these results suggest strongly that cryptochromes have magnetic field sensitive photochemistry and that they play a role in avian magnetoreception. Laser flash photolysis MFE experiments on samples of cryptochrome from *A. thaliana* have been performed by Robinson [356]. These experiments show some evidence of a chemical magnetic field effect, although further work will be necessary to prove this unequivocally.

Having explored the singlet yield anisotropy of simple one- and two-proton RP model systems, we wish to extend our analysis to multinuclear RPs. In Chapter 3, we found several "rules of thumb" for the behaviour of isotropic multinuclear RPs using a Monte Carlo approach. Here, that is not possible; it would take an unfeasibly large amount of processing power to calculate singlet yield anisotropy patterns for an ensemble of multinuclear RPs sufficiently large to be representative. Instead, we focus our attention on a few model RPs inspired by the cryptochrome proteins.

In order to calculate MFEs according to the RPM, we must know the hyperfine tensors of those species comprising the radical pair intermediate. At this moment in time

> "it is fair to state that … the substrate of the cryptochrome has not been identified, and until this is accomplished, it will not be possible to find out whether cryptochrome functions by photoinduced electron transfer in a manner analogous to photolyase or utilizes the same molecular framework and the same two chromophores to perform an entirely different photochemical reaction." [328]

Nevertheless, we assume that the cryptochromes do react via RP intermediates. We choose two particular RP species here for calculation. This is reasonable because our

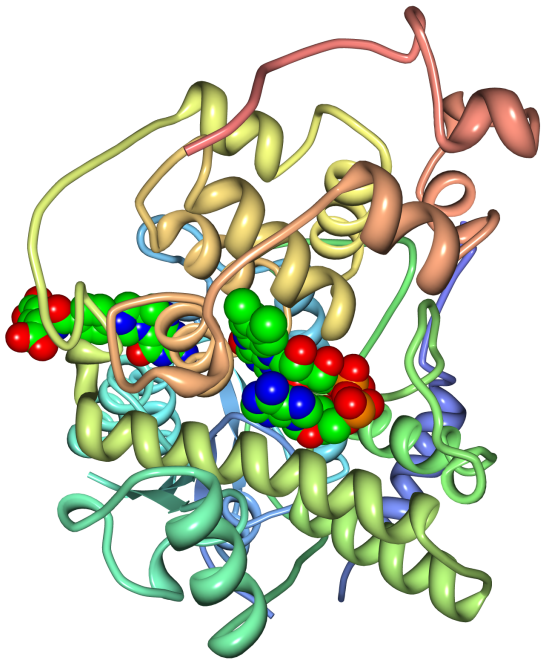

Figure 7.12: X-ray structure of cryptochrome 3 from *A. thaliana* showing the FADH cofactor (centre) and the light-harvesting cofactor 5,10-methenyl-tetrahydrofolyl-polyglutamate (MTHF, left) [344]. This figure was prepared using MBT ProteinWorkshop from PDB file 2IJG.

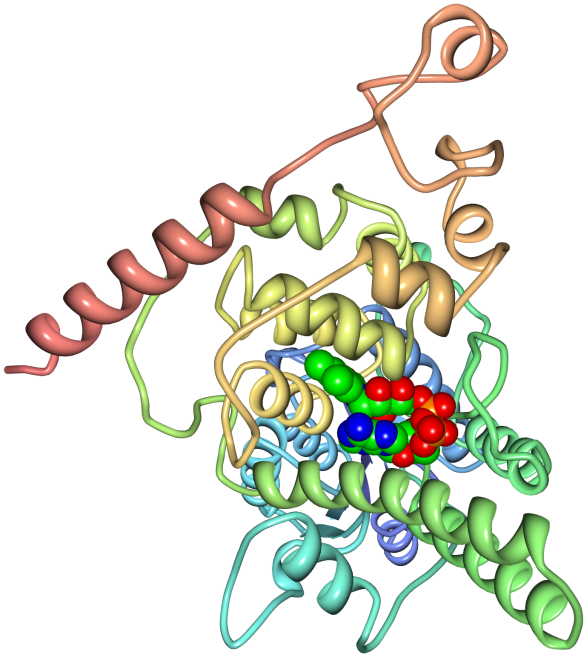

Figure 7.13: X-ray structure of the N-terminal photolyase homology (PHR) domain in cryptochrome 1 from *A. thaliana* [345]. This figure was prepared using MBT ProteinWorkshop from PDB file 1U3D.

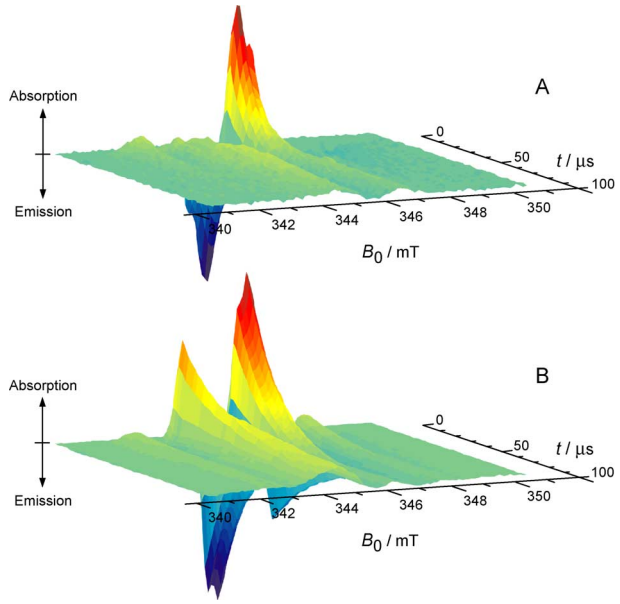

Figure 7.14: Time resolved EPR measurements in DNA photolyase show that it reacts via a radical pair intermediate, whose lifetime is $\sim 20\,\mu s$. Data are shown for (A) *X. laevis* (6–4) photolyase, and (B) *E. coli* CPD photolyase, recorded at $T = 278\,K$ following pulsed laser excitation at 440 nm [352].

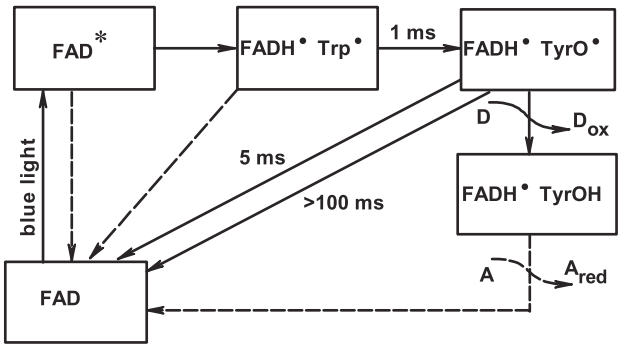

Figure 7.15: Proposed reaction scheme for CRY-1 from *A. thaliana*. FAD* is a singlet excited state of FAD, D and A are an external electron donor and acceptor respectively. Figure from [354].

conclusions do not depend critically on the still-debated oxidation state of the flavin moiety in the cryptochrome photocycle; neither do they depend on the identity of the amino acid counter-radical.

The RPs that we choose are inspired by research on DNA photolyase. Spin polarisation effects observed during EPR studies of *E. coli* DNA photolyase show that the photocycle proceeds via a long-lived ($\sim 20\,\mu s$) spin-correlated RP intermediate [349, 352]. The RP involved is assigned to comprise a flavin radical anion $FAD^{\bullet -}$ and a $WH^{\bullet +}$ radical cation (from Trp-306) on the basis of the CIDEP spectra [350, 357]. Other steps in the photocycle of *E. coli* DNA photolyase have been studied in some detail by Kay, Weber and coworkers [358, 359]. Meanwhile, DNA photolyase from the African clawed frog *Xenopus laevis* was found to undergo a similar photocycle, but this time involving a long-lived RP intermediate composed of $FADH^{\bullet}$ and $Y^{\bullet}$ neutral radicals [351]. In light of these observations, we choose to make calculations in $\left[FAD^{\bullet -}\ Y^{\bullet}\right]$ and $\left[FAD^{\bullet -}\ WH^{\bullet +}\right]$ radical pairs. Hyperfine tensors for these species, and for the $FADH^{\bullet}$ radical which will be used in Chapter 9, are given in Figures 7.16–7.19.

7.9 Adding magnetic nuclei in a single radical

We now turn our attention to the case of "n–0" RPs, where all the magnetic nuclei are concentrated on one radical, the other having no electron–nuclear hyperfine interactions. We consider the effect on singlet yield anisotropy of adding progressively more magnetic nuclei. Figures 7.20–7.22 show calculations of singlet yield anisotropy in "n–0" RPs composed of either $FAD^{\bullet -}$, $Y^{\bullet}$ or $WH^{\bullet +}$ with a bare electron as counter-radical.

7.9.1 Flavin radical anion

Figure 7.20 shows plots of the singlet yield anisotropy in several RPs, each containing a selection of nuclei from $FAD^{\bullet -}$. Figures 7.20(a) and (b) show the singlet yield in a "1–0" containing either N5 or N10. Both of these systems give rise a strong, simple anisotropy pattern, which would seem to be eminently suitable for use as a compass. Inspecting Figure 7.17, it is apparent that both N5 and N10 have strongly axial hyperfine tensors with $\alpha \approx 600$ and $200\,\mu T$ respectively.

Figures 7.20(d–f) show singlet yield anisotropies for the isoalloxazine ring protons H9, H6 and H3. These nuclei were selected because we may be reasonably confident in the computed values for the hyperfine tensors since their positions are rigidly constrained by conjugation in the isoalloxazine ring. In contrast to N5 and N10, these protons have rather rhombic HFTs and give rise to weaker and less straightforward singlet yield anisotropy patterns.

Figure 7.20(c) shows the singlet yield anisotropy in a "2–0" containing both N5 and N10. It is encouraging to see that the anisotropy pattern remains strong and simple. Indeed, the maximum absolute singlet yield anisotropy with both N5 and N10 is 23% larger than that for N10 alone. Just as we saw in §7.7, when the HFTs are strongly axial, multinuclear RPs can have stronger singlet yield anisotropy than for the individual nuclei taken separately. This bodes well for the possibility of a RPM-based compass.

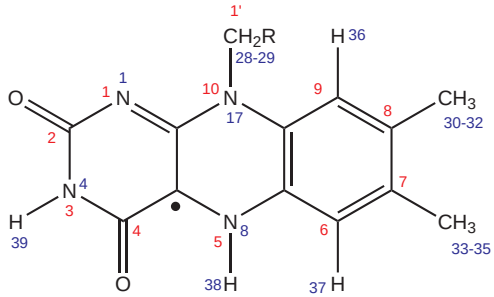

(a) Structure of the FADH• analogue showing the atom numbering used by `Gaussian` in blue. The traditional numbering is shown in red [347, 348].

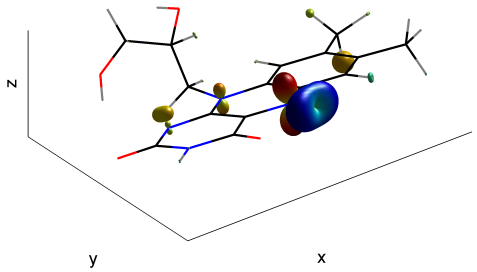

(b) Polar plots of the FADH• analogue hyperfine tensors on N and H atoms in the `Gaussian` principal axis system.

Nucleus	a/μT	α/μT	β/μT	A_{ii}/μT	Principal hyperfine axes		
N1 (*i.e.* N1)	123.8	88.3	2.3	33.2	0.738700	0.658600	−0.143700
				37.8	−0.669900	0.693700	−0.264500
				300.4	−0.074500	0.291600	0.953600
N4 (*i.e.* N3)	−59.1	7.2	6.2	−72.5	−0.243600	0.903600	−0.352300
				−60.1	0.939800	0.309700	0.144500
				−44.8	−0.239700	0.295900	0.924600
N8 (*i.e.* N5)	392.7	494.9	2.7	−104.9	0.438000	0.865500	−0.243200
				−99.6	0.898100	−0.409700	0.159500
				1382.6	−0.038400	0.288300	0.956800
N17 (*i.e.* N10)	211.5	237.8	4.1	−30.5	0.970300	−0.220700	0.099200
				−22.2	0.238300	0.942600	−0.234000
				687.2	−0.041900	0.250600	0.967200
H28 (*i.e.* H1'r)	389.9	47.5	14.2	328.2	−0.190200	0.396500	0.898100
				356.6	0.915600	0.401700	0.016500
				484.9	−0.354200	0.825500	−0.439500
H29 (*i.e.* H1')	31.9	43.5	2.4	−14.0	0.253900	0.182600	0.949800
				−9.3	0.902800	−0.397100	−0.165000
				119.0	0.347000	0.899400	−0.265700
H30 (*i.e.* H8)	192.0	18.3	4.2	169.4	−0.073400	0.083000	0.993800
				177.9	0.830200	−0.547100	0.107000
				228.7	0.552600	0.833000	−0.028800
H31 (*i.e.* H8)	481.7	20.4	3.9	457.4	−0.592800	0.804700	−0.031400
				465.2	0.340100	0.285600	0.896000
				522.5	0.730000	0.520500	−0.443000
H32 (*i.e.* H8)	74.9	21.1	1.0	52.8	0.060000	−0.322400	0.944700
				54.8	−0.350400	0.879400	0.322400
				117.1	0.934700	0.350400	0.060200
H33 (*i.e.* H7)	−9.1	16.1	3.4	−28.6	−0.136400	0.401100	0.905800
				−21.8	0.314800	0.884500	−0.344200
				23.1	0.939300	−0.238200	0.246900
H34 (*i.e.* H7)	−49.5	14.6	4.6	−68.7	0.170300	0.148900	0.974100
				−59.6	0.271600	0.943100	−0.191600
				−20.2	0.947200	−0.297200	−0.120100
H35 (*i.e.* H7)	−20.9	16.5	2.4	−39.9	−0.129700	0.352200	0.926900
				−35.0	0.205700	0.924000	−0.322300
				12.1	0.970000	−0.148800	0.192300
H36 (*i.e.* H9)	48.7	36.4	13.2	−0.9	−0.054500	0.263100	0.963200
				25.6	−0.501200	0.827100	−0.254300
				121.4	0.863600	0.496700	−0.086800
H37 (*i.e.* H6)	−158.0	51.8	8.2	−218.0	−0.036200	0.293700	0.955200
				−201.6	0.794800	0.587900	−0.150700
				−54.4	−0.605900	0.753700	−0.254600
H38 (*i.e.* H5)	−769.3	391.8	223.9	−1385.0	0.981900	0.188300	−0.020300
				−937.2	−0.034800	0.285000	0.957900
				14.3	−0.186100	0.939800	−0.286400
H39 (*i.e.* H3)	−24.7	35.4	15.4	−75.5	−0.068000	0.270800	0.960200
				−44.7	−0.208800	0.937300	−0.279100
				46.0	0.975600	0.219400	0.007200

Figure 7.16: Vacuum optimised geometry and hyperfine tensors of an FADH• analogue calculated by Kay [358, 359] using density functional theory in `Gaussian98`. The geometry run used the PM3 semi-empirical method and the hyperfine calculation used UB3LYP/EPR-II.

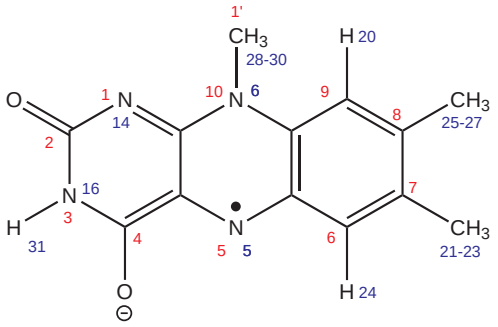

(a) Structure of the FAD$^{\bullet-}$ analogue showing the atom numbering used by `Gaussian` in blue. The traditional numbering is shown in red [347, 348].

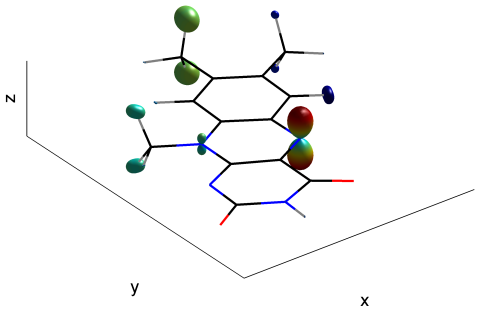

(b) Polar plots of the hyperfine tensors on N and H atoms in the FAD$^{\bullet-}$ analogue.

Nucleus	a/μT	α/μT	β/μT	A_{ii}/μT	Principal hyperfine axes		
N5 (*i.e.* N5)	523.3	616.8	6.6	−100.1	0.951800	−0.306800	0.000000
				−86.8	0.306800	0.951800	0.000000
				1756.9	0.000000	0.000000	1.000000
N6 (*i.e.* N10)	188.7	207.9	4.8	−24.1	0.684500	0.729100	0.000000
				−14.4	0.729100	−0.684500	0.000000
				604.6	0.000000	0.000000	1.000000
N14 (*i.e.* N1)	−3.5	20.8	3.0	−27.3	−0.467000	0.884300	0.000000
				−21.2	0.884300	0.467000	0.000000
				38.0	0.000000	0.000000	1.000000
N16 (*i.e.* N3)	−38.3	2.6	2.1	−43.1	0.852600	−0.522600	0.000000
				−38.8	0.000000	0.000000	1.000000
				−33.0	0.522600	0.852600	0.000000
H20 (*i.e.* H9)	56.5	31.6	29.9	−5.0	0.000000	0.000000	1.000000
				54.9	0.996100	−0.088200	0.000000
				119.6	0.088200	0.996100	0.000000
H21 (*i.e.* H7)	−201.1	19.0	7.6	−227.7	−0.231700	−0.015700	0.972700
				−212.5	−0.463500	0.880900	−0.096200
				−163.1	0.855300	0.473100	0.211300
H22 (*i.e.* H7)	−201.1	19.0	7.6	−227.7	0.231700	0.015700	0.972700
				−212.5	−0.463500	0.880900	0.096200
				−163.1	0.855300	0.473100	−0.211300
H23 (*i.e.* H7)	−22.5	23.9	3.7	−50.1	0.000000	0.000000	1.000000
				−42.7	−0.544600	0.838700	0.000000
				25.3	0.838700	0.544600	0.000000
H24 (*i.e.* H6)	−387.2	94.8	48.4	−530.4	0.422000	0.906600	0.000000
				−433.6	0.000000	0.000000	1.000000
				−197.6	0.906600	−0.422000	0.000000
H25 (*i.e.* H8)	649.3	37.8	1.0	610.6	0.688200	0.051700	0.723700
				612.5	0.696800	−0.325400	−0.639300
				724.8	0.202400	0.944200	−0.260000
H26 (*i.e.* H8)	649.3	37.8	1.0	610.6	−0.688200	−0.051700	0.723700
				612.5	0.696800	−0.325400	0.639300
				724.8	0.202400	0.944200	0.260000
H27 (*i.e.* H8)	21.2	31.7	2.2	−12.6	0.927300	0.374200	0.000000
				−8.3	0.000000	0.000000	1.000000
				84.5	−0.374200	0.927300	0.000000
H28 (*i.e.* H1')	9.9	44.6	5.7	−40.4	0.000000	0.000000	1.000000
				−28.9	0.228500	0.973500	0.000000
				99.0	0.973500	−0.228500	0.000000
H29 (*i.e.* H1')	407.0	42.5	11.1	353.4	0.301600	−0.039200	0.952600
				375.6	0.587100	0.794900	−0.153200
				492.0	0.751200	−0.605500	−0.262700
H30 (*i.e.* H1')	407.0	42.5	11.1	353.4	−0.301600	0.039200	0.952600
				375.6	0.587100	0.794900	0.153200
				492.0	0.751200	−0.605500	0.262700
H31 (*i.e.* H3)	−18.9	28.5	17.2	−64.6	0.000000	0.000000	1.000000
				−30.2	0.879000	−0.476900	0.000000
				38.1	0.476900	0.879000	0.000000

Figure 7.17: Vacuum optimised geometry and hyperfine tensors of riboflavin radical anion (used as an FAD$^{\bullet-}$ analogue) calculated by Kuprov using density functional theory in `Gaussian03`. The geometry run used the ROB33LYP/6-311++g(2d,2p) level of theory and the hyperfine calculation used UB3LYP/EPR-III.

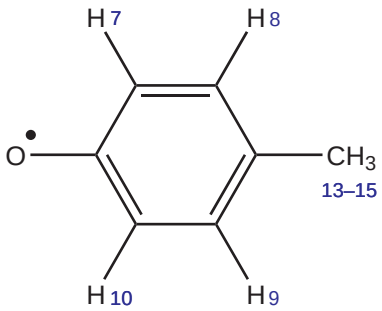

(a) Structure of the Y• analogue showing the atom numbering used by `Gaussian`.

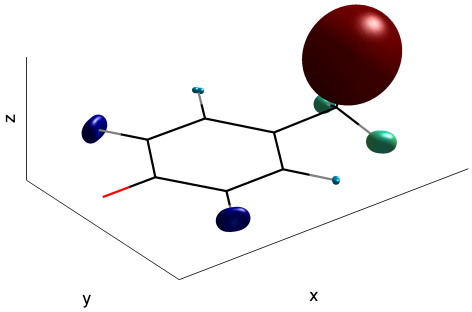

(b) Polar plots of the Y• analogue hyperfine tensors on N and H atoms in the `Gaussian` principal axis system.

Nucleus	a/μT	α/μT	β/μT	A_{ii}/μT	Principal hyperfine axes		
H7	−620.6	188.8	116.1	−925.6	0.928200	−0.372000	−0.007500
				−693.3	0.008300	0.000700	1.000000
				−242.9	0.372000	0.928200	−0.003700
H8	205.6	59.0	49.1	97.5	−0.011900	0.013300	0.999800
				195.7	0.813300	−0.581500	0.017400
				323.6	0.581700	0.813400	−0.003900
H9	206.2	58.9	49.3	98.0	−0.011900	−0.013300	0.999800
				196.5	0.811700	0.583800	0.017400
				324.1	−0.583900	0.811800	0.003900
H10	−625.0	190.0	117.3	−932.4	0.927700	0.373300	−0.007400
				−697.7	0.008200	−0.000700	1.000000
				−245.0	−0.373300	0.927700	0.003700
H13	2580.8	77.5	26.6	2476.7	−0.003200	0.999400	0.035500
				2530.0	−0.546900	−0.031500	0.836600
				2735.7	0.837200	−0.016700	0.546700
H14	676.8	67.9	11.6	597.3	0.247700	0.122100	0.961100
				620.5	0.439400	0.870000	−0.223800
				812.6	0.863400	−0.477800	−0.161900
H15	581.3	67.2	10.9	503.3	0.267000	−0.200200	0.942700
				525.0	−0.424400	0.853800	0.301500
				715.6	0.865200	0.480600	−0.143000

Figure 7.18: Optimised geometry and hyperfine tensors of a Y• analogue calculated by the author using density functional theory in `Gaussian03`. The geometry run used the ROB3LYP/6-31+g(3d,3p) level of theory with PCM solvation in water and the hyperfine calculation used UB3LYP/EPR-III with PCM solvation in water. Other calculations (not shown) were performed to investigate the effect on HFCs of rotating the methyl group H13–15. Experimental data are given in [360–362].

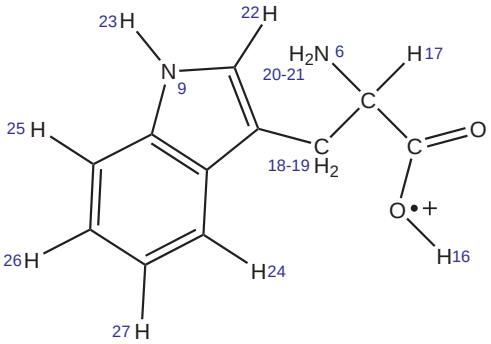

(a) Structure of $WH^{\bullet+}$ showing the atom numbering used by `Gaussian`. The positive charge is delocalised between the oxygen and nitrogen centres.

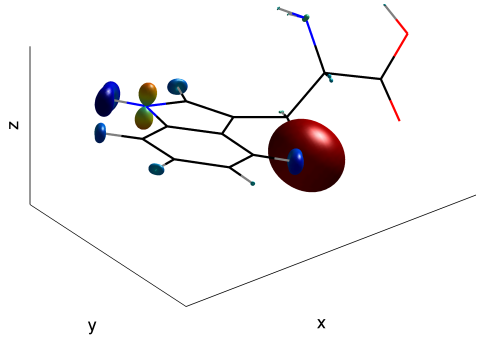

(b) Polar plots of the $WH^{\bullet+}$ hyperfine tensors on N and H atoms in the `Gaussian` principal axis system.

Nucleus	a/μT	α/μT	β/μT	A_{ii}/μT	Principal hyperfine axes		
N6	146.5	21.6	0.9	124.1	−0.407400	0.683700	0.605500
				125.8	0.601500	0.699700	−0.385400
				189.6	0.687200	−0.207200	0.696300
N9	321.5	379.8	5.3	−63.7	0.322300	0.935300	−0.146300
				−53.0	0.917200	−0.346800	−0.196300
				1081.2	0.234300	0.071000	0.969600
H16	−39.6	−30.2	−7.0	−100.1	0.244000	0.859900	−0.448300
				−16.4	0.110500	0.434600	0.893800
				−2.3	0.963500	−0.267600	0.011000
H17	−93.1	−54.6	−15.2	−202.3	−0.093400	0.511900	0.854000
				−53.7	0.936800	0.335700	−0.098800
				−23.3	−0.337200	0.790800	−0.510800
H18	1604.6	76.0	30.5	1498.1	0.296800	−0.393500	0.870100
				1559.0	0.818000	0.574900	−0.019000
				1756.7	−0.492800	0.717400	0.492500
H19	45.7	60.6	15.2	−30.1	0.333300	0.078300	0.939600
				0.4	−0.243000	0.970000	0.005300
				166.8	0.911000	0.230100	−0.342300
H20	−10.4	51.9	26.6	−88.8	0.218800	0.970900	−0.097100
				−35.7	−0.670100	0.221900	0.708300
				93.3	0.709300	−0.089900	0.699200
H21	23.3	37.9	23.9	−38.5	−0.443200	0.141700	0.885200
				9.3	−0.226700	0.937600	−0.263600
				99.1	0.867300	0.317500	0.383400
H22	−278.0	142.8	50.8	−471.6	0.919000	−0.302800	−0.252500
				−369.9	0.278200	0.044200	0.959500
				7.5	0.279300	0.952000	−0.124900
H23	−598.3	295.7	188.6	−1082.6	0.754000	0.613900	−0.233600
				−705.4	0.234400	0.080800	0.968800
				−6.9	−0.613600	0.785200	0.083000
H24	−488.0	150.0	102.0	−740.0	0.535900	0.827900	−0.165300
				−536.0	0.265700	0.020500	0.963800
				−187.9	0.801400	−0.560400	−0.208900
H25	−363.7	127.0	67.5	−558.2	0.577900	0.795900	−0.180300
				−423.1	0.249800	0.037800	0.967600
				−109.7	0.776900	−0.604200	−0.176900
H26	−208.3	99.0	49.6	−356.8	−0.629000	0.765900	0.133500
				−257.7	0.246300	0.033500	0.968600
				−10.4	0.737400	0.642100	−0.209700
H27	−40.0	62.4	0.8	−103.2	−0.552100	0.413000	0.724300
				−101.6	0.696400	−0.249300	0.673000
				84.8	0.458500	0.876000	−0.149900

Figure 7.19: Vacuum optimised geometry and hyperfine tensors of $WH^{\bullet+}$ calculated by Kuprov using density functional theory in `Gaussian03`. The hyperfine calculation used the UB3LYP/EPR-III level of theory. Similar calculations were performed in an EPR context by Lendzian [363].

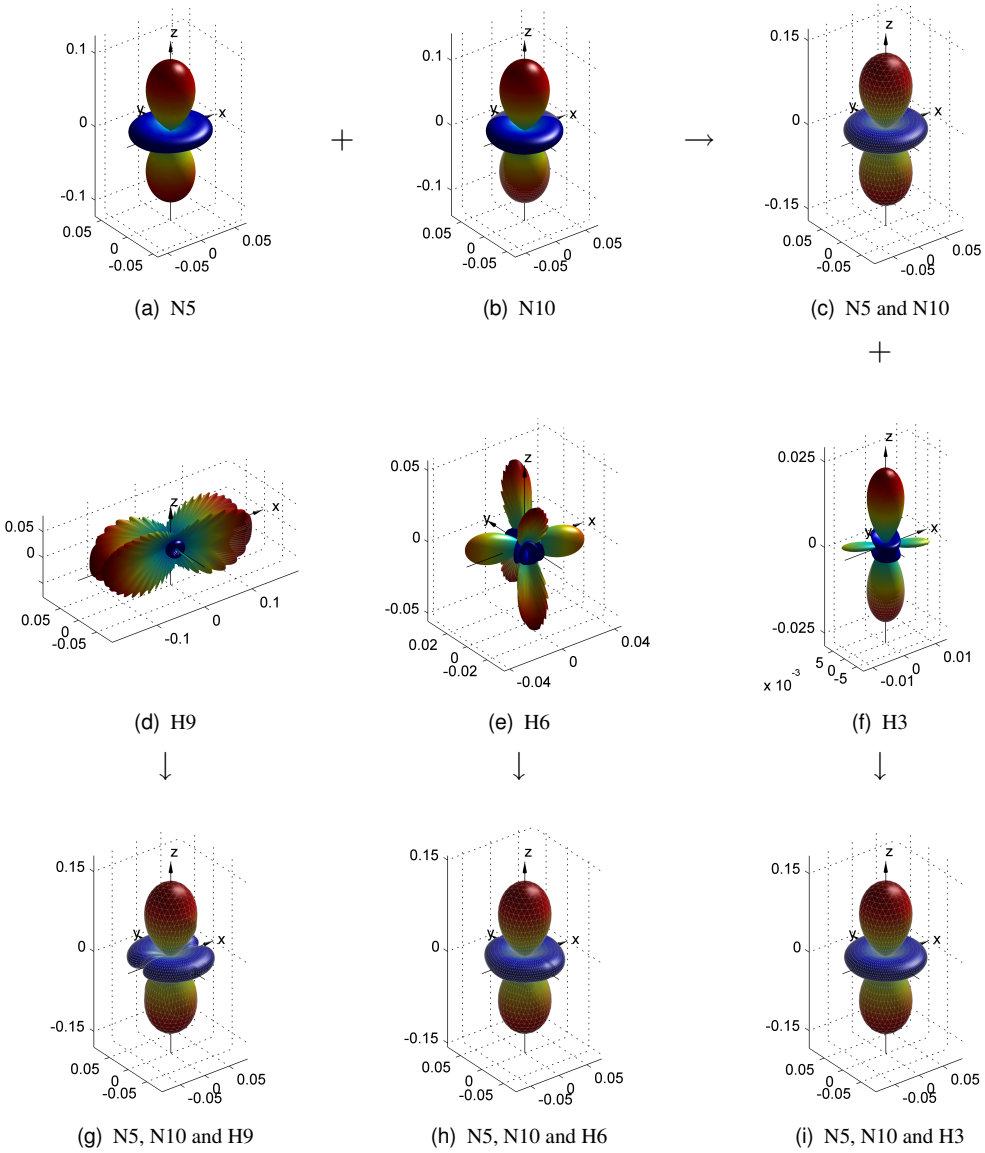

(a) N5 (b) N10 (c) N5 and N10

(d) H9 (e) H6 (f) H3

(g) N5, N10 and H9 (h) N5, N10 and H6 (i) N5, N10 and H3

Figure 7.20: Building up magnetic nuclei in an "n–0" RPs based on $FAD^{\bullet-}$. Selected nuclei from the isoalloxazine ring of $FAD^{\bullet-}$ were incorporated in each calculation as indicated above. Calculations were performed using an exponential model rate constant $k = 2 \times 10^5\,\mathrm{s}^{-1}$ and $B_0 = 50\,\mu\mathrm{T}$. The atomic numbering scheme and hyperfine tensors used here are described in Figure 7.17.

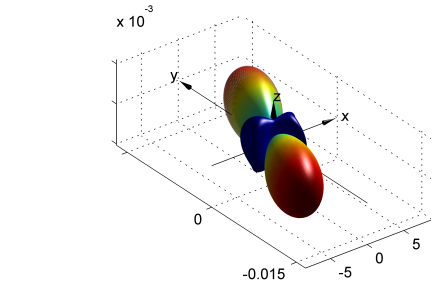

(a) Only ring proton H7

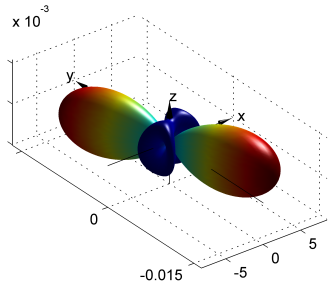

(b) Only ring proton H10

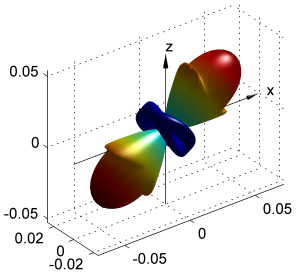

(c) Only side-chain proton H13

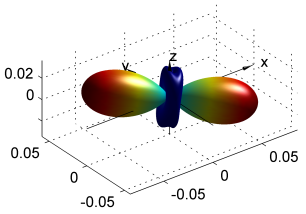

(d) Only side-chain proton H14

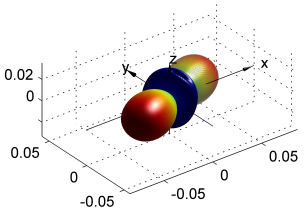

(e) Only side-chain proton H15

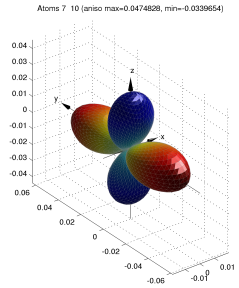

(f) Two ring protons H7 and H10

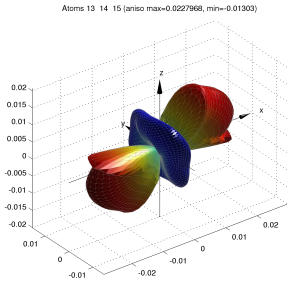

(g) Three side-chain protons H13–H15

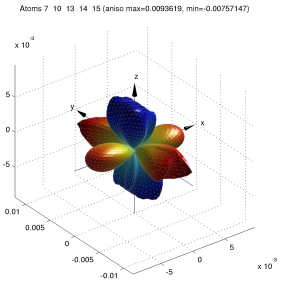

(h) All five protons H7, H10 and H13–H15

Figure 7.21: Polar plots of the singlet yield anisotropy in a series of "n–0" radical pairs containing a selection of magnetic nuclei from the Y$^\bullet$ radical. The atom numbering and HFTs are shown in Figure 7.18. Calculations were made with an applied field $B_0 = 50\,\mu\text{T}$ and $k = 2 \times 10^5\,\text{s}^{-1}$, giving a radical pair lifetime of $5\,\mu\text{s}$.

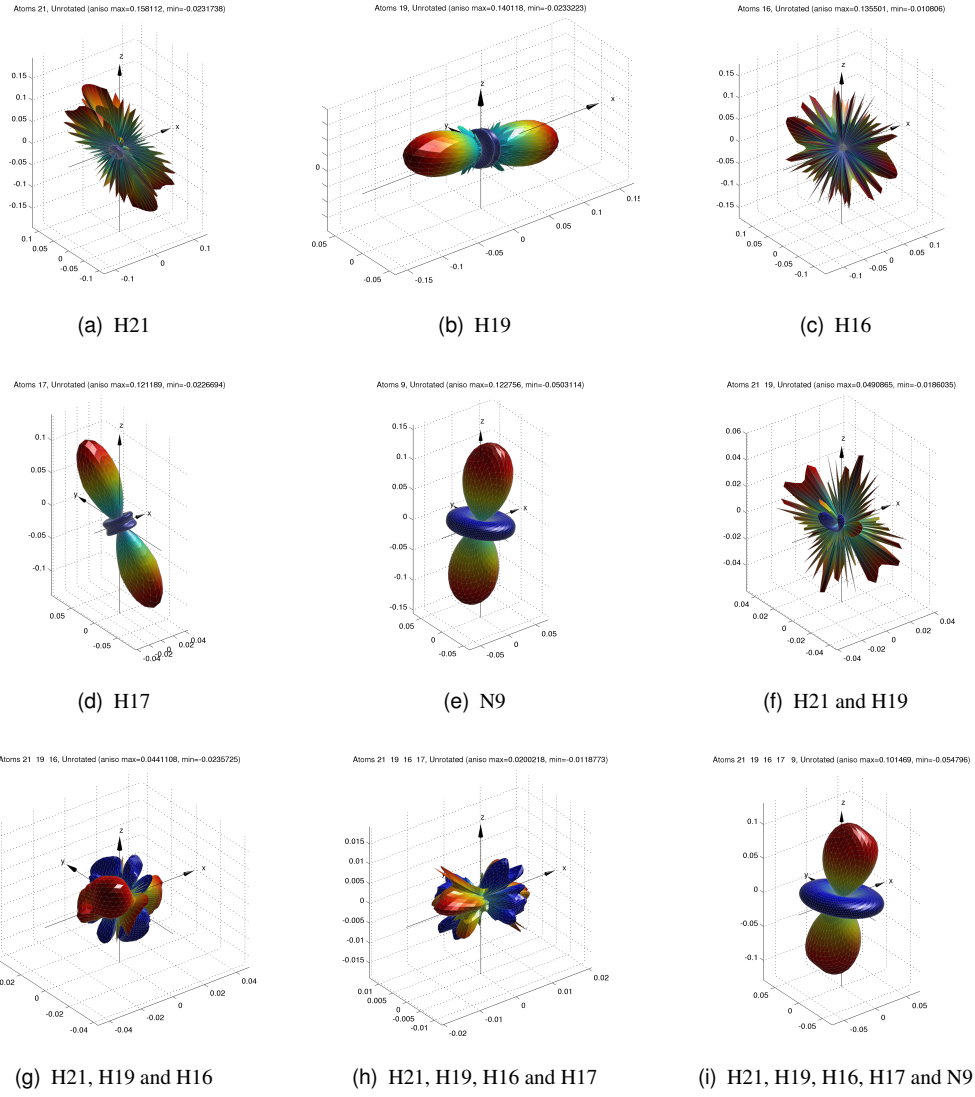

(a) H21 (b) H19 (c) H16

(d) H17 (e) N9 (f) H21 and H19

(g) H21, H19 and H16 (h) H21, H19, H16 and H17 (i) H21, H19, H16, H17 and N9

Figure 7.22: Build up of nuclei in the $WH^{\bullet+}$ radical. Figures (a–e) show the five largest singlet yield anisotropies in RPs that contain a single nucleus from $WH^{\bullet+}$. These nuclei are then added successively to make figures (f–i). The atom numbering scheme and hyperfine tensors used here are shown in Figure 7.19. Calculations were made for $B_0 = 50\,\mu\text{T}$ and $k = 2 \times 10^5\,\text{s}^{-1}$. The sharp spikes in Figures (a), (c) and (f) are a result of rapidly varying singlet yield anisotropy which is not sufficiently sampled even by the fine SOPHE mesh used here.

Figures 7.20(g–i) show the singlet yield anisotropy in a series of "3–0" RPs incorporating N5, N10 and one of the isoalloxazine ring protons. These three figures show a striking resemblance — in both magnitude and shape — to the singlet yield anisotropy with only N5 and N10. It would appear that the strong, axial nitrogen HFTs dominate the singlet yield anisotropy in these RPs.

7.9.2 Tyrosyl radical

Figure 7.21 shows a similar series of RP singlet yield anisotropies for selected nuclei from the $Y^{\bullet}$ radical. Unlike $FAD^{\bullet-}$, the $Y^{\bullet}$ does not contain any heteroatoms and there are no strongly axial HFTs. We wish to see whether the singlet yield anisotropy patterns build up in the same simple manner.

Figures 7.21(a–e) plot the singlet yield anisotropy for five protons taken one at a time. The anisotropy patterns are less straightforward than for N5 and N10 in $FAD^{\bullet-}$, but not as complicated as for the isoalloxazine ring protons. The anisotropy patterns do follow the symmetry properties of the tyrosyl ring. For example, the patterns in Figures 7.21(a) and (b) are both symmetric with respect to reflection in the *xy*-plane; and reflection of Figure 7.21(a) in the *xz*-plane gives Figure 7.21(b) and *vice versa*. These symmetries arise because the HFTs depend on the shape of the $Y^{\bullet}$ SOMO, which in turn reflects the symmetric nuclear charge distribution.

Similar arguments hold for the methyl protons H13–H15, except that the singlet yield anisotropy for H13 is twice as large as that for H14 and H15. This is because, in the geometry shown in Figure 7.18, the $C–H^{13}$ bond is hyperconjugated with the π-system of the benzene ring and hence the isotropic hyperfine coupling for H13 is much larger than for H14 or H15. Depending on the nature of the protein environment, such amino acid side chains may be held more or less rigidly. In radicals where the side-chains are free to move, we may expect such hyperconjugation effects to give a rapid modulation of the proton hyperfine tensor, which may well produce rapid relaxation and quench any observed magnetic field effect. In order to prevent rapid relaxation, the RPs in an RPM-based compass would need to be held firmly in place, presumably by a surrounding protein.

Figures 7.21(f–h) show multinuclear RPs containing several of the protons discussed above. Whilst the Figure 7.21(g) resembles a simple sum of the H13–15 singlet yield anisotropies, the same is not true for the ring protons H7 and H10 in Figure 7.21(f). When H7 and H10 are taken together, the resulting yield pattern seems to be constrained only by symmetry. For example, in the tyrosyl radical structure, the pair of protons H7 and H10 is left unaltered overall after a reflection in either the *xy*- or the *xz*-planes. Therefore, the resulting singlet yield anisotropy is also symmetric with respect to these reflections.

Finally, Figure 7.21(h) shows the singlet yield anisotropy with all five of these protons. This time, the singlet yield anisotropy seems to be dominated by that for H7 and H10, shown in Figure 7.21(f), with only a small contribution from H13–15. This may reflect the fact that H7 and H10 both have $\alpha \approx 190\,\mu\text{T}$, whereas H13–15 have $\alpha \approx 70\,\mu\text{T}$. Notice also that the singlet yield anisotropy in Figure 7.21(h) is significantly smaller than in any of the other figures, whereas $FAD^{\bullet-}$ retained a relatively strong singlet yield anisotropy as nuclei were added. It would appear that in the absence of nuclei with strong, axial hyperfine tensors, that the singlet yield anisotropy becomes

complicated and small in multinuclear RPs.

7.9.3 Tryptophan radical cation

The third radical that we consider is $WH^{\bullet+}$. We calculated the singlet yield anisotropy for each magnetic nucleus in $WH^{\bullet+}$ taken individually. The five nuclei with the greatest maximum absolute singlet yield anisotropy were H21, H19, H16, H17 and N9. Plots of the singlet yield anisotropy for these systems are given in Figures 7.22(a–e). Notice that H21 and H16 give rise to bizarre singlet yield anisotropy patterns, perhaps reflecting their highly rhombic hyperfine tensors. In a similar manner to N5 and N10 in $FAD^{\bullet-}$, the $WH^{\bullet+}$ N9 singlet yield anisotropy is strong and simple. This reflects the strong, axial hyperfine tensor in N9. It seems reasonably to suggest that the radicals involved in an RPM-based compass should contain conjugated nitrogen heterocycles, since these will give strong, axial hyperfine tensors because of the π-electron distribution above and below the plane of the ring.

Figures 7.22(f–h) show the singlet yield anisotropy patterns as the H21, H19, H16 and H17 protons are progressively incorporated. None of these yield anisotropy patterns are simple. Also, the yield anisotropy diminishes with each additional proton. As we commented in relation to the $Y^{\bullet}$ radical, this does not bode well for forming a RPM-based compass.

However, Figure 7.22(i) shows the singlet yield after N9 is included in the calculations. This "5–0" RP shows a strong, simple singlet yield anisotropy which is only 17% smaller than the anisotropy for N9 alone. It would appear that nuclei with strong, axial hyperfine tensors act powerfully to preserve a strong, intelligible singlet yield anisotropy pattern in the presence of other magnetic nuclei.

7.10 Building up radical pairs

We now turn our attention to full "m–n" radical pairs, with magnetic nuclei on both partners. We explore two ideas: that, to some approximation, the singlet yield anisotropies for a full radical pair are linear combinations of those obtained by taking the magnetic nuclei from only one of the radicals and that certain relative orientations of the radicals in a RP provide the most suitable anisotropy for use as a "compass".

Figures 7.23 and 7.24 show a set of singlet yield anisotropy patterns that illustrate the build-up of singlet yield anisotropy in the $\left[FAD^{\bullet-}\ Y^{\bullet}\right]$ RP. Figures 7.23(e–g), 7.24(d–f) and 7.24(j–l) show the singlet yield anisotropy for an "m–n" RP with magnetic nuclei on both radicals. Above these figures are shown the corresponding anisotropy patterns for "m–0" or "0–n" RPs containing nuclei only from $FAD^{\bullet-}$ in Figure 7.23(a), or only $Y^{\bullet}$ in Figures 7.23(b–d), 7.24(a–c) and 7.24(g–i). The columns show results for three orientations of the $Y^{\bullet}$ radical.

Inspecting these figures, we see that the singlet yield anisotropy in each "m–n" RP is close to a linear combination of the yield anisotropies for the corresponding "m–0" and "0–n" RPs. Indeed, most of the "m–n" yield anisotropies retain the broad shape of the $FAD^{\bullet-}$ yield anisotropy in Figure 7.23(a) with smaller contributions from the $Y^{\bullet}$ yield anisotropies. As to the magnitude of the singlet yield anisotropy, the $FAD^{\bullet-}$ pattern has maximum absolute singlet yield anisotropy of 0.130 and the $Y^{\bullet}$ radicals have 0.047, 0.023 and 0.009 depending on the nuclei that are included. The

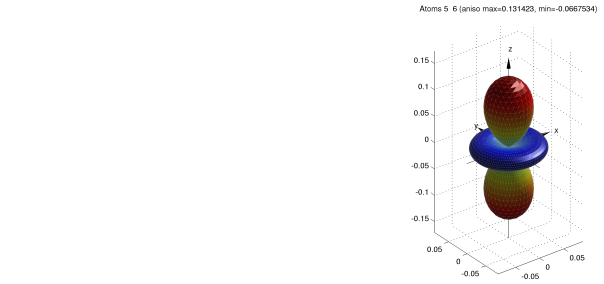

(a) N5 and N10 on radical A; no HFC in radical B

+

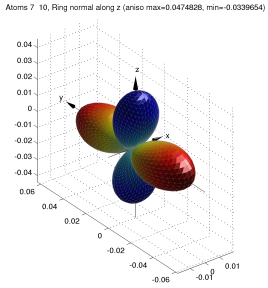

(b) No HFC in radical A; H7 and H10 on radical B

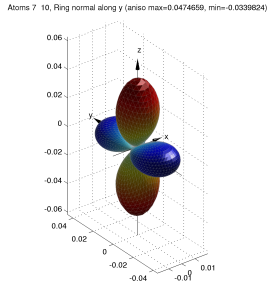

(c) As (b) but radical B is rotated 90° about the x-axis

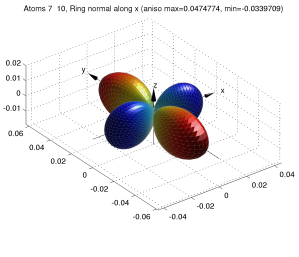

(d) As (b) but radical B is rotated 90° about the y-axis

↓ ↓ ↓

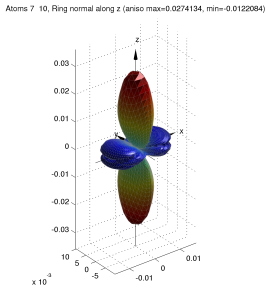

(e) Nuclei from (a) and (b)

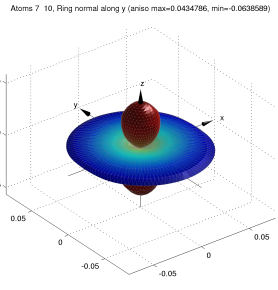

(f) Nuclei from (a) and (c)

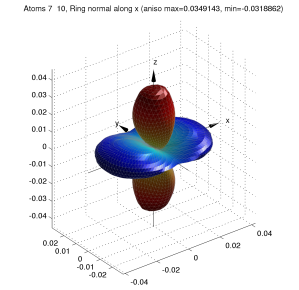

(g) Nuclei from (a) and (d)

Figure 7.23: Do hyperfine anisotropies in "m–0" and "0–n" RPs add when the radicals are combined to form an "m–n" RP? Calculations are performed for the $\left[\text{FAD}^{\bullet-}\ \text{Y}^{\bullet}\right]$ RP (*i.e.* A is $\text{FAD}^{\bullet-}$ and B is $\text{Y}^{\bullet}$) with $B_0 = 50\,\mu\text{T}$ and $k = 2 \times 10^5\,\text{s}^{-1}$ (equivalent to a RP lifetime of $5\,\mu\text{s}$). The atom numbering scheme and hyperfine tensors used are shown in Figures 7.17 and 7.18.

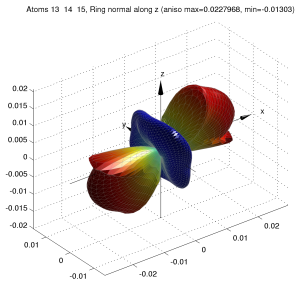

(a) No HFC in radical A; H13–15 on radical B

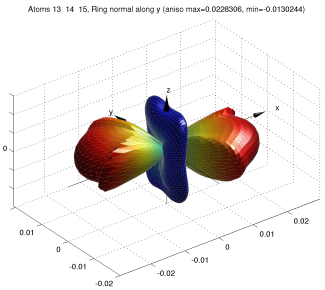

(b) As (a) but radical B is rotated 90° about the x-axis

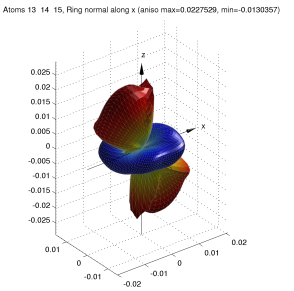

(c) As (a) but radical B is rotated 90° about the y-axis

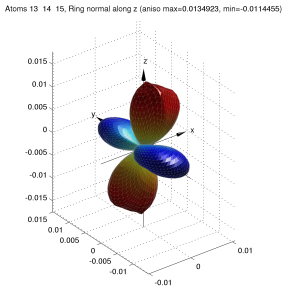

(d) Nuclei from Figure 7.23(a) and (a)

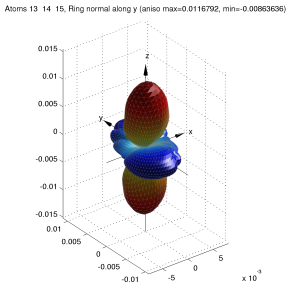

(e) Nuclei from Figure 7.23(a) and (b)

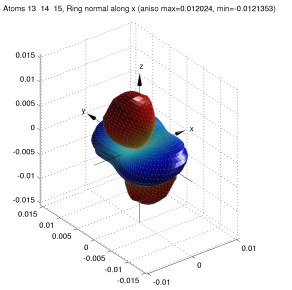

(f) Nuclei from Figure 7.23(a) and (c)

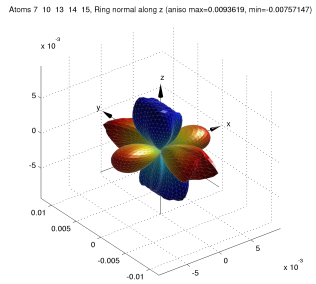

(g) No HFC in radical A; H7, H10 and H13–15 on radical B

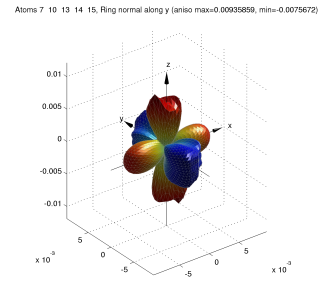

(h) As (g) but radical B is rotated 90° about the x-axis

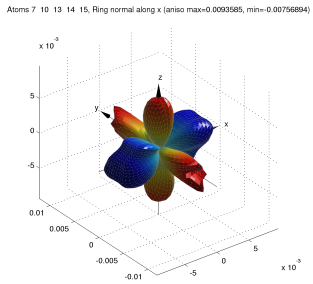

(i) As (g) but radical B is rotated 90° about the y-axis

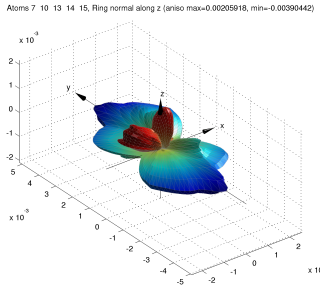

(j) Nuclei from Figure 7.23(a) and (g)

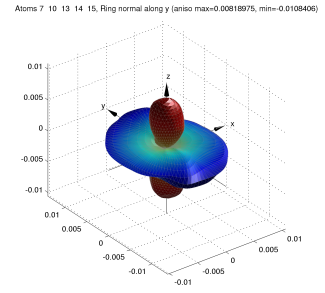

(k) Nuclei from Figure 7.23(a) and (h)

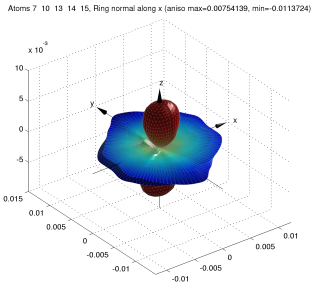

(l) Nuclei from Figure 7.23(a) and (i)

Figure 7.24: Do hyperfine anisotropies in "m–0" and "0–n" RPs add when the radicals are combined to form an "m–n" RP? Calculations are performed for the $\left[\text{FAD}^{\bullet-}\ \text{Y}^{\bullet}\right]$ RP (*i.e.* A is $\text{FAD}^{\bullet-}$ and B is $\text{Y}^{\bullet}$) with $B_0 = 50\,\mu\text{T}$ and $k = 2 \times 10^5\,\text{s}^{-1}$ (equivalent to a RP lifetime of $5\,\mu\text{s}$). The atom numbering scheme and hyperfine tensors used are shown in Figures 7.17 and 7.18.

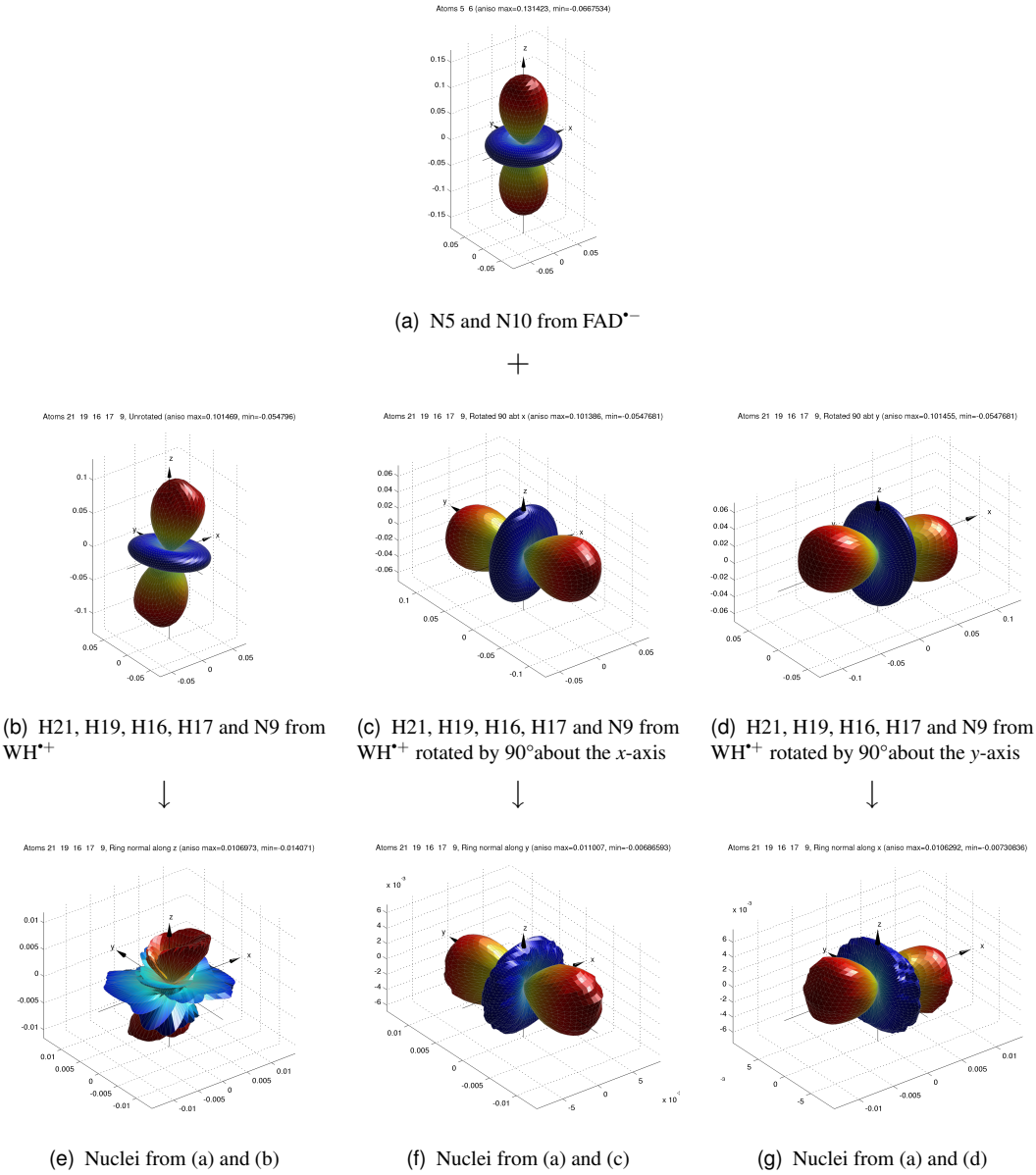

(a) N5 and N10 from $FAD^{\bullet-}$

$+$

(b) H21, H19, H16, H17 and N9 from $WH^{\bullet+}$

(c) H21, H19, H16, H17 and N9 from $WH^{\bullet+}$ rotated by 90°about the x-axis

(d) H21, H19, H16, H17 and N9 from $WH^{\bullet+}$ rotated by 90°about the y-axis

$\downarrow$ $\downarrow$ $\downarrow$

(e) Nuclei from (a) and (b)

(f) Nuclei from (a) and (c)

(g) Nuclei from (a) and (d)

Figure 7.25: Do hyperfine anisotropies in "m–0" and "0–n" RPs add when the radicals are combined to form an "m–n" RP? Calculations are performed for the $\left[FAD^{\bullet-}\ WH^{\bullet+}\right]$ RP (*i.e.* A is $FAD^{\bullet-}$ and B is $WH^{\bullet+}$) with $B_0 = 50\,\mu T$ and $k = 2 \times 10^5\,s^{-1}$ (equivalent to a RP lifetime of $5\,\mu s$). The atom numbering scheme and hyperfine tensors used are shown in Figures 7.17 and 7.19.

anisotropies for the full RPs are a little smaller at approximately 0.030, 0.012 and 0.007 respectively.

Figure 7.25 shows a similar analysis for the $\left[\mathrm{FAD}^{\bullet-}\ \mathrm{WH}^{\bullet+}\right]$ RP. There, we see that the "m–n" yield anisotropies are dominated by the $\mathrm{WH}^{\bullet+}$ radical, with small contributions from $\mathrm{FAD}^{\bullet-}$. The maximum absolute singlet yield anisotropies of the full RPs are about 0.010 which is significantly smaller than the 0.131 for $\mathrm{FAD}^{\bullet-}$ and the 0.101 for $\mathrm{WH}^{\bullet+}$.

Considering the results from both RPs, we observe that the singlet yield anisotropy patterns in Figures 7.23(e), 7.24(j) and 7.25(e) are more complicated than for other relative orientations of the radicals. These figures arise when the singlet yield anisotropies on radicals A and B are almost collinear. We observed similar behaviour for a simple model "1–1" RP in Figure 7.10. There, the yield anisotropy pattern contained high order, complicated, contributions when the radicals were aligned ($\xi = 0^\circ$).

In summary, when one radical has a simple, strong singlet yield anisotropy, multinuclear "m–n" RPs with as many as seven nuclei can also show simple, intelligible singlet yield anisotropy patterns. Often, these "m–n" RP anisotropy patterns resemble a linear combination of the anisotropy patterns from the corresponding "m–0" and "0–n" RPs. However, it is not obvious what factors govern the relative importance of the two radicals for determining the overall singlet yield anisotropy pattern. Although the magnitude of these anisotropies is somewhat smaller than in "m–0" RPs, they are still sufficiently strong that we could envisage a multinuclear "m–n" RP as the basis of a compass sense. Since the relative orientation of the radicals alters the overall "m–n" RP singlet yield anisotropy pattern, we could envisage "tuning" a magnetoreceptor by adjusting this relative orientation to the optimum value. In vivo, this might be accomplished by mutations in the protein that holds the radical partners.

7.11 Quantitative build-up of RPs

In the previous section, we saw that the singlet yield anisotropy pattern for an "m–n" RP often resembles those for the corresponding "m–0" and "0–n" RPs. Here, we assess quantitatively how closely the singlet yield anisotropy for an "m–n" RP may be given as a linear combination of singlet yield anisotropies for the corresponding "m–0" and "0–n" RPs. We also consider whether the isotropic part of the hyperfine tensor affects this additivity property.

Figure 7.26 illustrates the procedure that we follow.

- We begin by calculating the singlet yield anisotropy patterns $\Phi_{\mathrm{S}}^{\mathrm{an}}(A)$ with nuclei only on radical A, $\Phi_{\mathrm{S}}^{\mathrm{an}}(B)$ with nuclei only on radical B and $\Phi_{\mathrm{S}}^{\mathrm{an}}$ in the full RP. These are shown in Figures 7.26(a–c).

- From these we calculate an approximate overall singlet yield anisotropy

$$\Phi_{\mathrm{S}}^{\mathrm{an}}(x_{\mathrm{A}}, x_{\mathrm{B}}; \theta_k, \phi_k) = x_{\mathrm{A}}\Phi_{\mathrm{S}}^{\mathrm{an}}(A; \theta_k, \phi_k) + x_{\mathrm{B}}\Phi_{\mathrm{S}}^{\mathrm{an}}(B; \theta_k, \phi_k) \tag{7.30}$$

  for some value of the coefficients x_{A} and x_{B} at the vertices of an $N = 30$ SOPHE mesh (θ_k, ϕ_k).

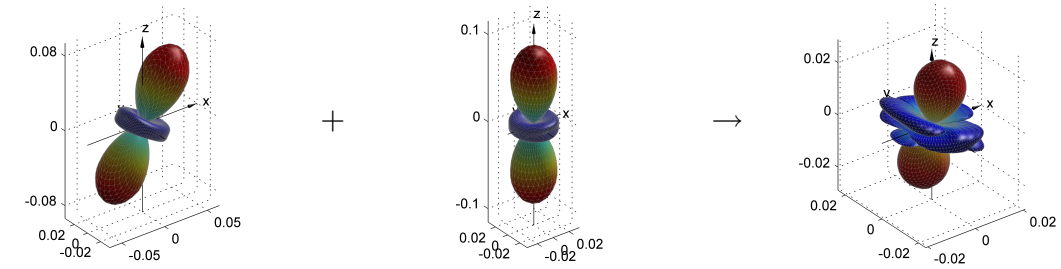

(a) $\Phi_S^{an}(A)$ with only radical A (b) $\Phi_S^{an}(B)$ with only radical B (c) Full Φ_S^{an}

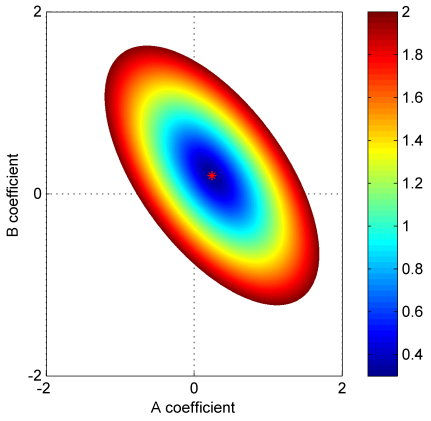

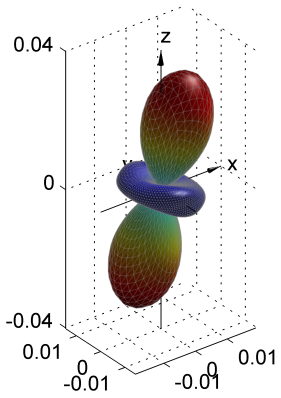

(d) Residual (error) norms (e) Approximate $\Phi_S^{an}(*) \approx 0.240 \times \Phi_S^{an}(A) + 0.200 \times \Phi_S^{an}(B)$

Figure 7.26: Illustration of the procedure used in Figure 7.27 for quantitative appraisal of whether the singlet yield anisotropy for a radical pair A/B is given by a weighted sum of contributions from "n–0" RPs containing either radical A or radical B.

- To evaluate the quality of a particular choice of x_A and x_B, we calculate the residual

$$r(\theta_k, \phi_k) = \Phi_S^{an}(x_A, x_B; \theta_k, \phi_k) - \Phi_S^{an}(\theta_k, \phi_k) \tag{7.31}$$

  at each mesh point. The residual norm ε is given by

$$\varepsilon = \sqrt{\sum_k r(\theta_k, \phi_k)^2}. \tag{7.32}$$

  Figure 7.26(d) shows a plot of ε as a function of x_A and x_B.

- The best linear combination, which minimises ε, is marked with a red point in the figure. The corresponding best-fit singlet yield anisotropy $\Phi_S(*)$ is shown in Figure 7.26(e).

- We measure the quality of the fit as a percentage error

$$\%\text{ error} = \frac{\varepsilon}{\sqrt{\sum_k \Phi_S^{an}(\theta_k, \phi_k)^2}} \times 100. \tag{7.33}$$

Figure 7.27 shows the quality of the best fits for a "1–1" RP as a function of the isotropic part of the hyperfine tensors a_A and a_B and of the relative orientation of the radicals ξ. The hyperfine tensors were chosen to be largely axial, but are otherwise arbitrary. Inspecting the figure, we see that in some circumstances, the true singlet yield anisotropy is given to within a few percent as the sum of the singlet yield anisotropies of the two radicals taken separately. Yet, on other occasions, the percentage error is enormous. The singlet yield anisotropies add most cleanly when $\xi = 0^\circ$ or $\xi = 90^\circ$ and when there are significant isotropic contributions to the two hyperfine tensors.

7.12 Stability

Organic chemical radicals usually contain many ^{1}H magnetic nuclei. Besides those radicals with large isotropic HFCs, or highly axial hyperfine tensors there is often a background of smaller hyperfine couplings. Indeed, in a protein environment, there may well be small hyperfine couplings to other amino acid residues that are physically close to the radical centre.

Figure 7.28 shows the effect on the singlet yield anisotropy in the $\left[\text{FAD}^{\bullet-}\ \text{Y}^{\bullet}\right]$ RP of adding a further magnetic nucleus with a random hyperfine tensor. Figure 7.28(a) shows the singlet yield anisotropy with N5 and N10 from $\text{FAD}^{\bullet-}$ and H7, H10 and H13–15 from $\text{Y}^{\bullet}$. Figures 7.28(b–l) show the same system with one additional proton on $\text{FAD}^{\bullet-}$. It is readily apparent that neither the shape nor the magnitude of the singlet yield anisotropy is significantly altered by the presence of this additional proton. These results suggest that it is reasonable approximation to include only the largest, axial hyperfine tensors when calculating the singlet yield anisotropy for a real RP. They also suggest that our discussions here in relation to relatively small model RPs are likely to generalise to real chemical systems.

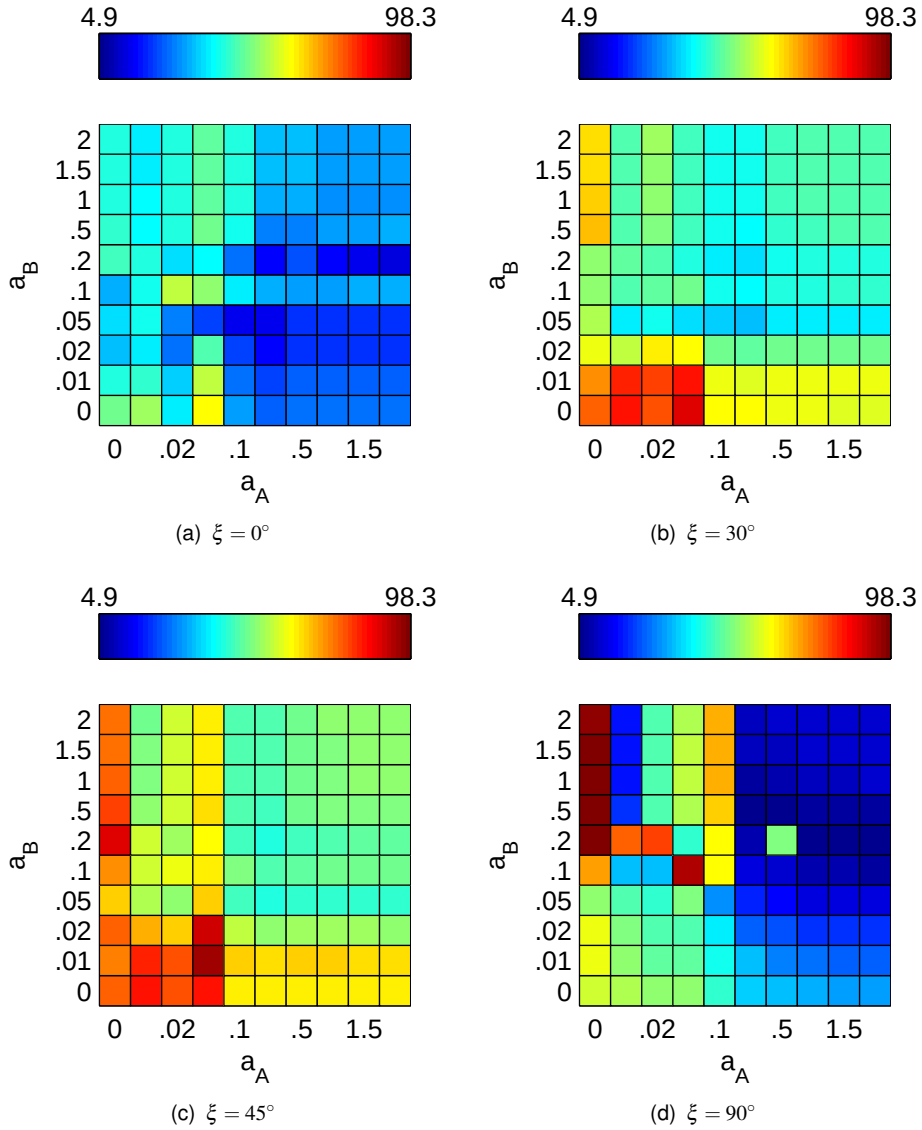

(a) $\xi = 0°$ (b) $\xi = 30°$

(c) $\xi = 45°$ (d) $\xi = 90°$

Figure 7.27: Percentage error, defined by equation (7.33), when the singlet yield anisotropy for a radical pair $\left[\mathrm{A}^{\bullet}\ \mathrm{B}^{\bullet}\right]$ is approximated by a weighted sum of contributions from "n–0" RPs containing either radical A or radical B. Calculations were performed following the procedure illustrated in Figure 7.26. Radical A has HFC a_{A} mT, $\alpha = 223\,\mu\mathrm{T}$ and $\beta = 18\,\mu\mathrm{T}$. Radical B has HFC a_{B} mT, $\alpha = 90\,\mu\mathrm{T}$ and $\beta = 17\,\mu\mathrm{T}$. The angle between the principal hyperfine axes of the radicals is ξ. The exponential model rate constant $k = 2 \times 10^5\,\mathrm{s}^{-1}$. The same selection of values were used for a_{A} and a_{B}.

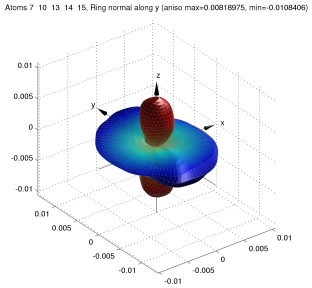

(a) Unperturbed

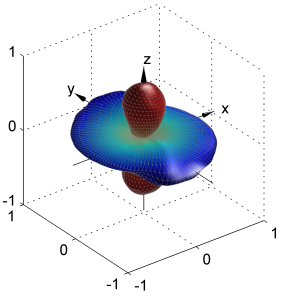

(b) $a = 35.5\,\mu\text{T}$, $\alpha = 17.2\,\mu\text{T}$ and $\beta = 4.7\,\mu\text{T}$

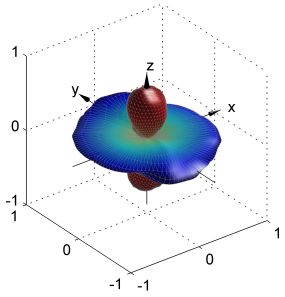

(c) $a = 56.0\,\mu\text{T}$, $\alpha = 51.6\,\mu\text{T}$ and $\beta = 21.0\,\mu\text{T}$

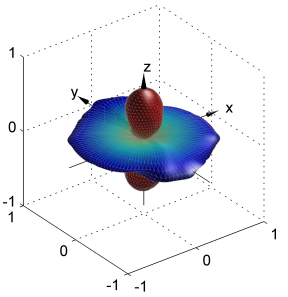

(d) $a = 56.9\,\mu\text{T}$, $\alpha = 48.7\,\mu\text{T}$ and $\beta = 13.5\,\mu\text{T}$

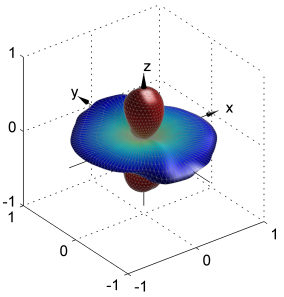

(e) $a = 94.4\,\mu\text{T}$, $\alpha = 62.3\,\mu\text{T}$ and $\beta = 55.5\,\mu\text{T}$

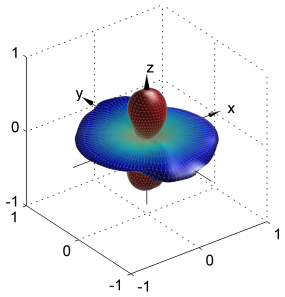

(f) $a = 167.7\,\mu\text{T}$, $\alpha = 84.9\,\mu\text{T}$ and $\beta = 46.1\,\mu\text{T}$

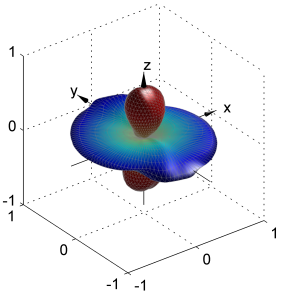

(g) $a = 98.7\,\mu\text{T}$, $\alpha = 110.3\,\mu\text{T}$ and $\beta = 41.8\,\mu\text{T}$

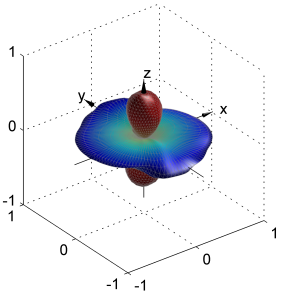

(h) $a = 170.4\,\mu\text{T}$, $\alpha = 194.0\,\mu\text{T}$ and $\beta = 75.6\,\mu\text{T}$

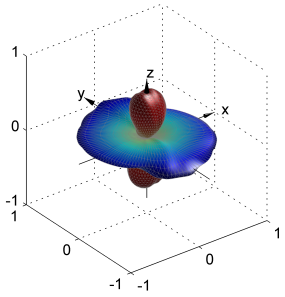

(i) $a = 132.7\,\mu\text{T}$, $\alpha = 186.0\,\mu\text{T}$ and $\beta = 21.8\,\mu\text{T}$

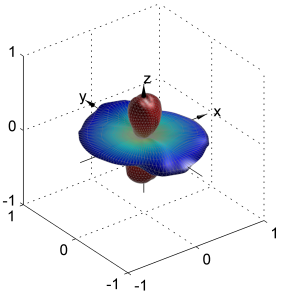

(j) $a = 261.6\,\mu\text{T}$, $\alpha = 205.5\,\mu\text{T}$ and $\beta = 48.9\,\mu\text{T}$

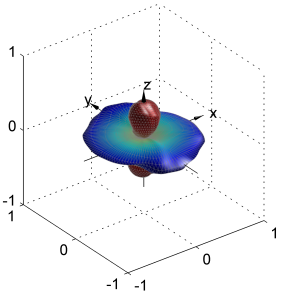

(k) $a = 356.5\,\mu\text{T}$, $\alpha = 198.4\,\mu\text{T}$ and $\beta = 90.0\,\mu\text{T}$

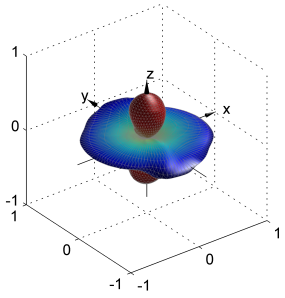

(l) $a = 73.3\,\mu\text{T}$, $\alpha = 188.4\,\mu\text{T}$ and $\beta = 165.7\,\mu\text{T}$

Figure 7.28: Stability of singlet yield anisotropy in a multinuclear "m–n" RP on addition of a random HFC. Each calculation includes N5 and N10 from $\text{FAD}^{\bullet-}$ and H7, H10 and H13–15 from $\text{Y}^{\bullet}$. An additional spin-½ hyperfine interaction is added at random to the $\text{FAD}^{\bullet-}$ radical as indicated. The applied field $B_0 = 50\,\mu\text{T}$ is comparable to the geomagnetic field and $k = 2 \times 10^5\,\text{s}^{-1}$, giving a radical pair lifetime of $5\,\mu\text{s}$. Figures (b–l) plot $100\times$ the singlet yield anisotropy.

7.13 Requirements for a RP compass

In order to form a viable RPM-based compass *in vivo* there are a number of requirements on the RPs involved.

- We saw in §6.3.5 that the magnetic compass sense of birds only operates in the presence of light from the blue–green part of the spectrum. The RPs involved are presumably, therefore, generated photochemically. Either the RP precursors themselves, or an antenna pigment, must absorb and be activated for electron transfer by blue–green light, but not by red–yellow light. Alternatively, the RP could be generated by another photochemical process, such as photo-induced H atom transfer. Nevertheless, electron transfer seems the most likely process because it is rapid and may occur over a long range.
- The RPs must have significant contributions to their spin Hamiltonian from anisotropic interactions. In particular, this implies that at least one of the radicals must be prevented from tumbling rapidly (and possibly from diffusing around the other radical) since these processes would average many anisotropic interactions to zero [100].
- The RPs must undergo spin-selective reaction. At least one of the reaction products must be involved in a further biochemical transduction pathway so that MFEs may result ultimately in a nerve impulse.
- Since magnetoreception in birds operates only when the eyes are not covered (see §6.3.6), the RP must be located either in the eye or at some point along the optic nerve or in the visual cortex.
- In order that the RP give compass information, it must be held in a well-defined orientation with respect to the organism as a whole.
- In order to produce a discernible magnetic field effect, RPs must be generated efficiently. This seems to imply that the precursor molecules must lie in close proximity so that ET is rapid.
- Yet, in order to produce a strong anisotropic magnetic field effect, the RPs must remain spin-correlated for several μs. Hence, the radicals must not undergo rapid back electron transfer, which suggests that they should be physically well-separated. To reconcile these seemingly contradictory requirements, it is likely that the RP is generated by sequential electron transfer, as is the case for the photosynthetic reaction centre. Indeed, the cryptochrome protein structures show a chain of aromatic amino acids that could support such a sequential electron transfer.
- Furthermore, in order to have a lifetime in the order of μs, the RP must have very slow relaxation. This suggests that any side-chains must be held immobile to prevent hyperfine tensor modulation and that the radicals must not contain paramagnetic centres such as oxygen-based radicals.
- Finally, the yield anisotropy pattern for a RP must be strong and simple if it is to give easily-intelligible compass information.

7.14 Conclusions

In this chapter, we have investigated the properties of RPs with anisotropic hyperfine interactions in order to assess whether they are a plausible source of magnetic compass information for an RPM-based magnetoreceptor.

One might have expected that RPs with anisotropic HFTs would not show a low field effect and therefore would not be sensitive to fields as weak as the Earth's $B_0 \approx 50\,\mu\text{T}$. However, although hyperfine anisotropy removes the zero-field degeneracies responsible for the LFE, it also introduces several orientation-dependent energy level crossings. Hence, such RPs may show strong singlet yield anisotropy even in weak magnetic fields $B_0 \ll a$ such as the Earth's.

In a number of multinuclear RP systems, we have found singlet yield anisotropies on the order of 20% for "n–0" RPs and of a few % in "2–5" RPs, *i.e.* in a system with seven magnetic nuclei. These changes are thought to be large enough to exceed the "noise" present within an organism and to produce a viable compass [327].

As well as having a significant amplitude, we believe that the singlet yield anisotropy pattern must be reasonably simple in order to give rise to intelligible compass information. In general, for arbitrary HFTs, the singlet yield anisotropy patterns may be very complex and therefore unsuitable to act as a compass. However, we have seen that in "m–0" and "m–n" RPs, the presence of nuclei with strong, axial HFTs produces strong and reasonably simple anisotropy patterns. Indeed, when nuclei with aligned axial HFTs are added to a RP, the singlet yield anisotropy can become progressively larger. In a series of DFT calculations, we found that nitrogen atoms in aromatic heterocyclic rings are a promising source of suitable axial HFTs.

Finally, in a series of calculations for $\left[\text{FAD}^{\bullet-}\ \text{Y}^{\bullet}\right]$ and $\left[\text{FAD}^{\bullet-}\ \text{WH}^{\bullet+}\right]$ RPs, we have seen that the singlet yield anisotropy in an "m–n" RP is often approximated reasonably as a weighted sum of the contributions from the corresponding "m–0" and "0–n" RPs. The relative orientation of the radicals provides scope for "tuning" of the singlet yield anisotropy for optimum magnetoreception. This orientation might, for example, be altered by mutations in the protein which surrounds the RP. When one radical contains strong axial HFTs, then the overall singlet yield anisotropy is often well suited as a source of compass information. Furthermore, the anisotropy pattern of such RPs is resilient to the addition of further nuclei with small random HFTs as would occur in nature.

In this work, we have considered RPs where the exchange and dipolar interactions between the radicals are negligible. If this is to be true, then the RP involved in magnetoreception must be quite special, being formed as a result of sequential electron transfer in a manner akin to the RPs in the photosynthetic reaction centre. However, Efimova has recently shown that RPs with non-zero exchange and dipolar interactions can show significant, intelligible singlet yield anisotropies when the exchange and dipolar interactions are of similar magnitude [364]. This encouraging result broadens considerably the range of RPs that might be responsible for an RPM-based compass.

Taken together, these calculations confirm that flavin-based RPs, such as those thought to exist in the cryptochrome family of proteins, are likely to show yield anisotropies suitable for an RPM-based compass.

Chapter 8

Spherical harmonic analysis

8.1 Introduction

Many migratory birds, such as the European robin *Erithacus rubecula*, are able to detect the Earth's magnetic field. During migration, birds use this magnetic compass sense as an aid to navigation — a fact established by the large body of behavioural studies reviewed in Chapter 6. Schulten and Ritz [106] hypothesise that this compass sense is based on a photochemical RPM reaction occurring in the retina as explained in §6.5.

Radical pairs created in a singlet state evolve under the influence of Zeeman and anisotropic hyperfine interactions. Hence, the yield of singlet product Φ_S depends on the orientation of an applied static field with respect to the radical pair. (It is trivial to adjust the theory for cases where either the initial or final states — or both — are triplets.) In the preceding chapter, we saw that it is straightforward to calculate the singlet yield as a function of the orientation of an applied field, described in a RP-fixed coordinate system by polar angles $\Phi_S(\theta,\phi)$. The singlet yield anisotropy Φ_S^{an} is obtained by subtracting the spherical average singlet yield

$$\bar{\Phi}_S = \int_0^{2\pi}\int_0^{\pi} \Phi_S(\theta,\phi)\sin(\theta)\,\mathrm{d}\theta\,\mathrm{d}\phi \tag{8.1}$$

and may be presented as a polar plot.

Such polar plots are visually striking, sometimes even beautiful. However, even in the case of a "1–1" RP, the polar plots show much structure and depend strongly on the model parameters used for simulation. Exploration of the model, for example by calculation of the singlet yield anisotropies at a variety of field strengths B_0, gives rise to a surfeit of data. Working by eye, it is difficult to spot any trends that might occur. Thus, analysis of singlet yield anisotropy by means of polar plots is a labour-intensive and somewhat bewildering process.

In order to understand anisotropic magnetic field effects more fully, we must introduce an automated method of extracting the essential details from this wealth of data. In this chapter, we show that singlet yields may sensibly be decomposed into a weighted sum of spherical harmonics. Such a decomposition reduces each polar plot to a list of numbers: the spherical harmonic expansion coefficients. These coefficients may be combined in various ways to give a statistic that quantifies the amplitude or shape of the singlet yield anisotropy. Such a statistic summarises the information in a

polar plot with a single number. These numbers may then be plotted as a function of one or more model parameters, such as the field strength B_0, in order to discover and explore which factors are significant in determining the singlet yield anisotropy.

In other areas of science, such as electrostatics or scattering theory, expansion in terms of spherical harmonics reveals the symmetry of a problem. Rotations in three dimensional space $\mathbb{R}^3$ form a group SO(3), of which spherical harmonics are the irreducible representations. Hence, this spherical harmonic decomposition provides a natural, robust and quantitative means of analysing singlet yield anisotropies. More importantly, by removing the need for human evaluation of each singlet yield anisotropy pattern, the spherical harmonic decomposition paves the way for establishing "rules of thumb" by Monte Carlo methods as was done for isotropic systems in Chapter 3.

In this chapter, we describe the spherical harmonics and show how to efficiently decompose a singlet yield anisotropy in terms of them. Furthermore, we show that in certain cases, it is possible to calculate the singlet yield spherical harmonic expansion coefficients directly, without first calculating singlet yields for specific field orientations. Such methods are a first step towards a more general, analytical theory of anisotropic magnetic field effects. Finally, we apply the methods that we have developed in order to discuss the factors that determine the singlet yield anisotropy of a model system.

8.2 Spherical harmonic decomposition

8.2.1 Spherical harmonics

The spherical harmonics $Y_l^m(\theta,\phi)$ are a well known family of special functions [120–122, 365]. They arise naturally in physics as the angular part of solutions to Laplace's equation ($\nabla^2\psi = 0$) in spherical polar coordinates. In quantum mechanics, they appear as eigenfunctions of the orbital angular momentum operator $\hat{L}^2$ with eigenvalue $l(l+1)$. The spherical harmonics are also irreducible representations of the rotation group SO(3). They may be defined for integer values of l and m as [122]

$$Y_l^m(\theta,\phi) = \mathrm{e}^{\mathrm{i}m\phi}\sqrt{\frac{2l+1}{4\pi}\frac{(l-m)!}{(l+m)!}}\,P_l^m(\cos\theta) \tag{8.2}$$

where $P_l^m(x)$ is an associated Legendre polynomial. The parameters are restricted to the range $l \geq 0$ and $l \geq |m|$. Care must be taken to use a consistent definition of Y_l^m and P_l^m. We adopt the Condon-Shortley phase convention [365, p788], which is also used by Varshalovich [122] and `Mathematica`. Polar plots of the first few spherical harmonics are given in Figure 8.1.

8.2.2 Decomposition

The spherical harmonics form a complete orthonormal set of functions over the spherical polar coordinates (θ,ϕ) [122]. The completeness relation is given by

$$\sum_{l=0}^{\infty}\sum_{m=-l}^{l}[Y_l^m(\theta,\phi)]^* Y_l^m(\theta',\phi') = \delta(\theta-\theta')\delta(\cos\phi-\cos\phi') \tag{8.3}$$

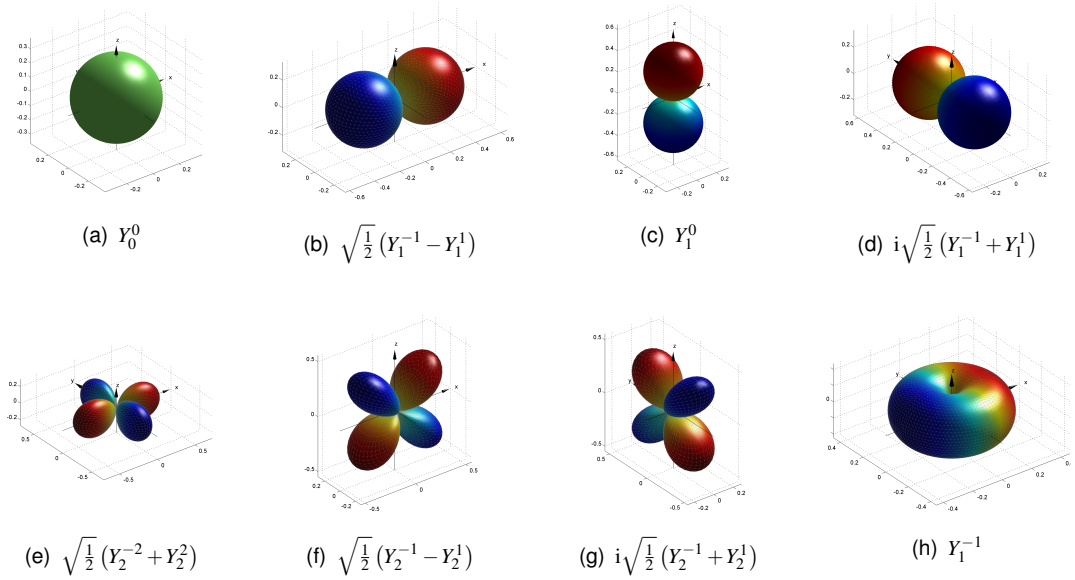

(a) Y_0^0 (b) $\sqrt{\frac{1}{2}}\left(Y_1^{-1}-Y_1^1\right)$ (c) Y_1^0 (d) $\mathrm{i}\sqrt{\frac{1}{2}}\left(Y_1^{-1}+Y_1^1\right)$

(e) $\sqrt{\frac{1}{2}}\left(Y_2^{-2}+Y_2^2\right)$ (f) $\sqrt{\frac{1}{2}}\left(Y_2^{-1}-Y_2^1\right)$ (g) $\mathrm{i}\sqrt{\frac{1}{2}}\left(Y_2^{-1}+Y_2^1\right)$ (h) Y_1^{-1}

Figure 8.1: Polar plots (see §7.5 for details) of a few spherical harmonics $Y_l^m(\theta,\phi)$ with $l=0$, 1 or 2. Notice that the familiar "orbital" shapes are often linear combinations of two $Y_l^m(\theta,\phi)$. Cases (a–g) are all real valued. Case (h) plots Y_1^{-1} which is complex valued. As explained in §7.5, the radius is determined by $\left|Y_1^{-1}\right|$ and the colouring by its real part.

and the spherical harmonics are orthonormal in the following sense

$$\int_0^{2\pi}\int_0^{\pi}\left[Y_l^m(\theta,\phi)\right]^* Y_{l'}^{m'}(\theta,\phi)\sin\theta\,\mathrm{d}\theta\,\mathrm{d}\phi=\delta_{ll'}\delta_{mm'}. \tag{8.4}$$

Together, these results mean that an arbitrary square-integrable function may be expanded as a weighted sum of spherical harmonics. In this chapter, we expand the singlet yield

$$\Phi_{\mathrm{S}}(\theta,\phi)=\sum_{l=0}^{\infty}\sum_{m=-l}^{l}a_l^m Y_l^m(\theta,\phi) \tag{8.5}$$

in terms of the coefficients a_l^m, which are complex numbers determined in principle by

$$a_l^m=\int_0^{2\pi}\int_0^{\pi}\left[Y_l^m(\theta,\phi)\right]^*\Phi_{\mathrm{S}}(\theta,\phi)\sin\theta\,\mathrm{d}\theta\,\mathrm{d}\phi. \tag{8.6}$$

In some branches of physics, this procedure is known as the "multipole expansion" and the coefficients a_l^m are called "multipole moments".

These results are very similar to the completeness and orthogonality relations for sine and cosine which lead to the method of Fourier series expansion. Indeed, as we shall see later, decomposition of a function $f(\theta,\phi)$ in terms of spherical harmonics is a type of Fourier transform, known as the spherical harmonic transform [366]. Many useful theorems carry over from Fourier series to spherical harmonic analysis.

Figure 8.2 illustrates the spherical harmonic decomposition in a one-proton RP. The singlet yield is fully described by the numerical coefficients a_l^m that weight contributions from different spherical harmonics. In many situations, only a few spherical

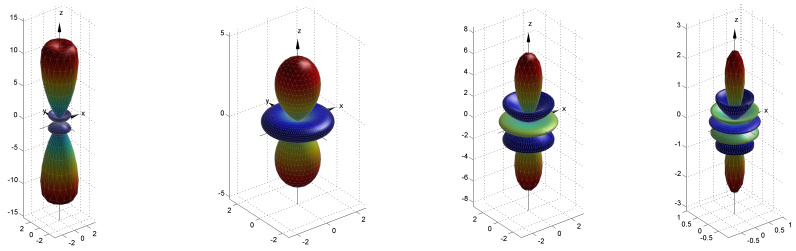

$$10^3 \times \Phi_S^{an}(\theta,\phi) \quad = \quad 6.282\,Y_2^0 \quad + \quad 7.644\,Y_4^0 \quad + \quad 2.362\,Y_6^0 \quad + \ldots$$

Figure 8.2: Graphical example of spherical harmonic decomposition of singlet yield anisotropy $\Phi_S^{an}(\theta,\phi) = \Phi_S(\theta,\phi) - \bar{\Phi}_S$. Left: Exact singlet yield anisotropy Φ_S^{an} calculated using the PyDMAFST algorithm in a one-proton RP with isotropic HFC $a = 2.5\,\text{mT}$, axiality $\alpha = 12.5\,\mu\text{T}$, rhombicity $\beta = 0\,\mu\text{T}$, exponential model rate constant $k = 2 \times 10^5\,\text{s}^{-1}$, static field strength $\omega_0 = 61.4\,\mu\text{T}$ and MaxL $= 35$. Right: First few spherical harmonics that contribute to the singlet yield anisotropy.

harmonics contribute significantly to the singlet yield — indeed, the $l = 2$ contributions often dominate.

8.2.3 Real combinations

Spherical harmonics with $m \neq 0$ are complex because of the $e^{im\phi}$ term in equation (8.2). A useful identity is

$$[Y_l^m(\theta,\phi)]^* = (-1)^m Y_l^{-m}(\theta,\phi) \tag{8.7}$$

where the $(-1)^m$ term is a consequence of the Condon-Shortley phase convention. Now, let us consider a real-valued function $f(\theta,\phi)$. Clearly

$$f(\theta,\phi) = [f(\theta,\phi)]^*. \tag{8.8}$$

Expanding both sides using equations (8.5) and (8.7) gives

$$\sum_{l,m} a_l^m Y_l^m(\theta,\phi) = \left[\sum_{l',m'} a_{l'}^{m'} Y_{l'}^{m'}(\theta,\phi)\right]^* = \sum_{l',m'} \left[a_{l'}^{m'}\right]^* (-1)^{m'} Y_{l'}^{-m'}(\theta,\phi). \tag{8.9}$$

Equation (8.4) allows us to equate terms in Y_l^m to give

$$a_l^m = (-1)^m \left[a_l^{-m}\right]^*. \tag{8.10}$$

This rule has been anticipated in cases (b), (d), (e) and (g) of Figure 8.1 to form real-valued combinations of spherical harmonics. Singlet yields are necessarily real; hence, any singlet yield spherical harmonic decomposition will obey this rule.

8.2.4 Rotations

When rotated, a spherical harmonic Y_l^m transforms into a weighted sum of spherical harmonics with the same l value. For a rotation $R(\alpha,\beta,\gamma)$ defined in terms of Euler

angles (α,β,γ) [122], the transformation is

$$R(\alpha,\beta,\gamma)Y_l^m(\theta,\phi) = Y_l^m(\theta',\phi') = \sum_{m'=-l}^{l} \mathfrak{D}_l^{mm'}(\alpha,\beta,\gamma)Y_l^{m'}(\theta,\phi) \tag{8.11}$$

where $\mathfrak{D}_l^{mm'}(\alpha,\beta,\gamma)$ is the Wigner $\mathfrak{D}$-function. An important corollary is that, for any l, the quantity

$$\sum_{m=-l}^{l} |a_l^m|^2 \tag{8.12}$$

remains unchanged under rotations. Such rotational invariants form the basis for a number of recent 3D shape recognition algorithms [367–369]. We will return to this point later when consider how to quantify the shape of a singlet yield anisotropy plot.

8.2.5 Product of spherical harmonics

Another important identity, which we will use extensively below, expresses the product of two spherical harmonics as a weighted sum of spherical harmonics: the Clebsch-Gordan series. We write this as

$$Y_{l_1}^{m_1}(\theta,\phi)Y_{l_2}^{m_2}(\theta,\phi) = \sum_{L,M} \sqrt{\frac{(2l_1+1)(2l_2+1)}{4\pi(2L+1)}} C_{l_1,0;l_2,0}^{L,0} C_{l_1,m_1;l_2,m_2}^{L,M} Y_L^M(\theta,\phi), \tag{8.13}$$

where l_1, m_1 and l_2, m_2 label the spherical harmonics to be multiplied and L, M label the result. The Clebsch-Gordan coefficients are zero unless $L = l_1 + l_2$, $l_1 + l_2 - 1$, ... or $|l_1 - l_2|$ and unless $M = m_1 + m_2$. Explicit expressions for the non-trivial Clebsch-Gordan coefficients $C_{l_1,m_1;l_2,m_2}^{L,M}$ are well known [122].

8.2.6 Vector representation

The $Y_l^m(\theta,\phi)$ may be considered as basis vectors in a Hilbert space that has an inner product defined by equation (8.4). In this Hilbert space, an arbitrary function $f(\theta,\phi)$ is a vector whose components are the expansion coefficients a_l^m. For numerical work, it is convenient to represent the function $f(\theta,\phi)$ by a column vector

$$f(\theta,\phi) = \boldsymbol{f} = \begin{pmatrix} a_0^0 \\ a_1^{-1} \\ a_1^0 \\ a_1^1 \\ a_2^{-2} \\ \vdots \end{pmatrix}. \tag{8.14}$$

For band-limited functions, the a_l^m vanish for sufficiently large l and we truncate the vector $\boldsymbol{f}$ appropriately.

We have developed code for manipulation and plotting of these "SphHReps" in `Matlab` and `Mathematica`. For example, the sum of two functions

$$f(\theta,\phi)+g(\theta,\phi)=\boldsymbol{f}+\boldsymbol{g} \tag{8.15}$$

is the sum of their SphHReps. The product of two functions

$$f(\theta,\phi)g(\theta,\phi)=\boldsymbol{h} \tag{8.16}$$

is a SphHRep whose elements are defined by equation (8.13). Rotating a function with SphHRep $\boldsymbol{f}$ through Euler angles (α,β,γ) gives another SphHRep whose elements are determined by equation (8.11). In `Matlab`, the utility functions `idx2jm` and `jm2idx` make it trivial to find the correct position for an element a_j^m in equation (8.14), whilst `PlotSphHRep` makes a polar plot from a SphHRep.

8.2.7 Inversion symmetry

The Hamiltonian for RPs evolving under the influence of only Zeeman and anisotropic hyperfine interactions is

$$\hat{H}(\boldsymbol{B})=\sum_{\mathrm{N=A,B}}\sum_{i}\hat{\boldsymbol{I}}_i\cdot\mathsf{A}_{i\mathrm{N}}\cdot\hat{\boldsymbol{S}}_{\mathrm{N}}-\gamma_{\mathrm{e}}\boldsymbol{B}\cdot\hat{\boldsymbol{S}}_{\mathrm{N}}.$$

The choice of axes here is completely arbitrary. Physically, the singlet probability is a scalar and must be unaffected by a change in axes. Let us relabel the nuclear spin coordinates such that $\hat{\boldsymbol{I}}\rightarrow-\hat{\boldsymbol{I}}$. The transformed Hamiltonian is

$$\hat{H}_{\mathrm{inv}}(\boldsymbol{B})=\sum_{\mathrm{N=A,B}}\sum_{i}-\hat{\boldsymbol{I}}_i\cdot\mathsf{A}_{i\mathrm{N}}\cdot\hat{\boldsymbol{S}}_{\mathrm{N}}-\gamma_{\mathrm{e}}\boldsymbol{B}\cdot\hat{\boldsymbol{S}}_{\mathrm{N}}.$$

Notice that $\hat{H}_{\mathrm{inv}}(-\boldsymbol{B})=-\hat{H}(\boldsymbol{B})$.

Now, the singlet probability in the normal axis system is given by

$$\left\langle\hat{P}^{\mathrm{S}}\right\rangle=\frac{1}{M}\mathrm{Tr}\left[\hat{P}^{\mathrm{S}}\mathrm{e}^{-\mathrm{i}\hat{H}(\boldsymbol{B})t}\hat{P}^{\mathrm{S}}\mathrm{e}^{\mathrm{i}\hat{H}(\boldsymbol{B})t}\right]. \tag{8.17}$$

Cyclically permuting the trace, we find that

$$\left\langle\hat{P}^{\mathrm{S}}\right\rangle=\frac{1}{M}\mathrm{Tr}\left[\hat{P}^{\mathrm{S}}\mathrm{e}^{\mathrm{i}\hat{H}(\boldsymbol{B})t}\hat{P}^{\mathrm{S}}\mathrm{e}^{-\mathrm{i}\hat{H}(\boldsymbol{B})t}\right] \tag{8.18}$$

$$=\frac{1}{M}\mathrm{Tr}\left[\hat{P}^{\mathrm{S}}\mathrm{e}^{-\mathrm{i}\hat{H}_{\mathrm{inv}}(-\boldsymbol{B})t}\hat{P}^{\mathrm{S}}\mathrm{e}^{\mathrm{i}\hat{H}_{\mathrm{inv}}(-\boldsymbol{B})t}\right], \tag{8.19}$$

which is the expression for spin evolution under a field $-\boldsymbol{B}$ in the alternative coordinate system. Therefore, the singlet probability is unaffected by reversing the magnetic field

$$\left\langle\hat{P}^{\mathrm{S}}\right\rangle(\boldsymbol{B},t)=\left\langle\hat{P}^{\mathrm{S}}\right\rangle(-\boldsymbol{B},t) \tag{8.20}$$

and hence the singlet yield is also unaffected

$$\Phi_{\mathrm{S}}(\boldsymbol{B})=\Phi_{\mathrm{S}}(-\boldsymbol{B}). \tag{8.21}$$

This has implications for the singlet yield spherical harmonic decomposition. According to Varshalovich [122, p141, §5.5, eq2], the spherical harmonics transform as

$$\hat{P}_r Y_l^m(\theta,\phi) = Y_l^m(\pi-\theta,\phi+\pi) = (-1)^l Y_l^m(\theta,\phi) \tag{8.22}$$

under an inversion $\hat{P}_r$. In other words, spherical harmonics with *odd* l change sign whilst those with *even* l are unaffected. In order to satisfy equation (8.21), the singlet yield spherical harmonic decomposition may only contain contributions with *even* values of l.

8.3 Point-by-point calculation

In the previous section, we introduced the spherical harmonics and discussed the properties that make them apt for studying anisotropic magnetic field effects. We turn now to consider how best to calculate particular radical pair singlet yield SphHReps. As we approach this task, we have twin aims: to find an efficient, stable numerical approach to calculating SphHReps and to reveal any underlying structure therein. We begin with the simplest approach to calculating RP singlet yield SphHReps, which starts out by calculating explicit singlet yield values $(\Phi_S)_k = \Phi_S(\theta_k,\phi_k)$ at the vertices (θ_k,ϕ_k) of a spherical mesh as if one were preparing a polar plot.

8.3.1 Integration

One way to extract the singlet yield SphHRep from a set of sampled singlet yield values is to use the spherical harmonic orthogonality integral. Writing the singlet yield in terms of spherical harmonics

$$\Phi_S(\theta,\phi) = \sum_{l=0}^{\infty}\sum_{m=-l}^{l} a_l^m Y_l^m(\theta,\phi) \tag{8.23}$$

and using the orthonormality property defined in equation (8.4) we write

$$\begin{aligned}
&\int_0^{2\pi}\int_0^{\pi} [Y_l^m(\theta,\phi)]^* \Phi_S(\theta,\phi)\sin\theta\,\mathrm{d}\theta\,\mathrm{d}\phi \\
&\qquad = \sum_{l'=0}^{\infty}\sum_{m'=-l'}^{l'} a_{l'}^{m'} \int_0^{2\pi}\int_0^{\pi} [Y_l^m(\theta,\phi)]^* Y_{l'}^{m'}(\theta,\phi)\sin\theta\,\mathrm{d}\theta\,\mathrm{d}\phi \\
&\qquad = \sum_{l'=0}^{\infty}\sum_{m'=-l'}^{l'} a_{l'}^{m'}\delta_{ll'}\delta_{mm'} = a_l^m.
\end{aligned} \tag{8.24}$$

Using equation (7.28) to approximate the integral on the left hand side, we find that

$$a_l^m \approx \sum_k w_k [Y_l^m(\theta_k,\phi_k)]^* \Phi_S(\theta_k,\phi_k). \tag{8.25}$$

This formula must be evaluated for each coefficient a_l^m until the coefficients become negligible or until a predefined cut-off at $l = \mathrm{MaxL}$.

8.3.2 Discretisation

Alternatively, we can solve for the a_l^m by discretising equation (8.23) over the spherical mesh. Flattening the indices $\{l,m\} \to L$ as described in §8.2.6 and evaluating at the mesh points (θ_k, ϕ_k), we find that

$$(\Phi_S)_k = \sum_L Y_{kL} a_L \tag{8.26}$$

or, in other words, that

$$\boldsymbol{s} = \mathsf{Y}\boldsymbol{a}, \tag{8.27}$$

where $\boldsymbol{s}$ is a vector of singlet yields evaluated over the mesh, Y is a matrix whose columns contain the spherical harmonics Y_L evaluated over the mesh and $\boldsymbol{a}$ is the unknown singlet yield SphHRep. The spherical harmonic matrix Y must contain enough columns to ensure that all significant coefficients a_l^m are found. Similarly, to ensure that the coefficients a_l^m are well determined, we must take enough singlet yield samples so that Y has full rank. Equation (8.27) may then be solved easily in a least squares sense using the standard "backslash" solver built into `Matlab`.

8.3.3 Spherical harmonic transform

Our final point-by-point method for computing singlet yield SphHReps is a Fourier transform technique. Driscoll and Healy [366, 370] show that finding the spherical harmonic coefficients a_l^m that represent a function $f(\theta,\phi)$ defined over the sphere, *i.e.* solving equation (8.23), is analogous to taking a Fourier transform. Indeed, this analogy may formalised; the "spherical harmonic transform" $f(\theta,\phi) \to a_l^m$ is a Fourier transform over the unit sphere S_2.

In our case, we start not with the function $f(\theta,\phi)$, but with a set of samples $f_k = f(\theta_k,\phi_k)$. Therefore, we must use the "discrete spherical harmonic transform" (DST), which is analogous to the well-known discrete Fourier transform discussed in Appendix B, §B.6ff. The theory of the DST has been developed by several authors. For our purposes, three results are especially pertinent.

The first of these is a sampling theorem [366, §4]. For clarity we present this theorem in the notation of the numerical library `S2kit` [371] which we discuss later. If $f(\theta,\phi)$ is a band limited function, *i.e.* if its spherical harmonic expansion coefficients $a_l^m = 0$ for $l \geq b$, then the full $f(\theta,\phi)$ may be reconstructed exactly from samples $f(\theta_i,\phi_j)$ taken over an equiangular mesh:

$$\begin{aligned} \theta_i &= i\pi/2b & i &= 0,\ \ldots,\ 2b-1 \\ \phi_j &= j\pi/b & j &= 0,\ \ldots,\ 2b-1. \end{aligned} \tag{8.28}$$

Furthermore, the non-vanishing coefficients a_l^m for $l < b$ may be determined from these samples. If b is accidentally taken to be smaller than the true band-limit then aliasing effects occur in much the same way as for normal discrete Fourier transforms.

The second important result is that this equiangular mesh contains an asymptotically optimal number of samples [366]. For multinuclear RPs, most of the computational effort will be spent evaluating the singlet yield samples $(\Phi_S)_k$. Therefore, since

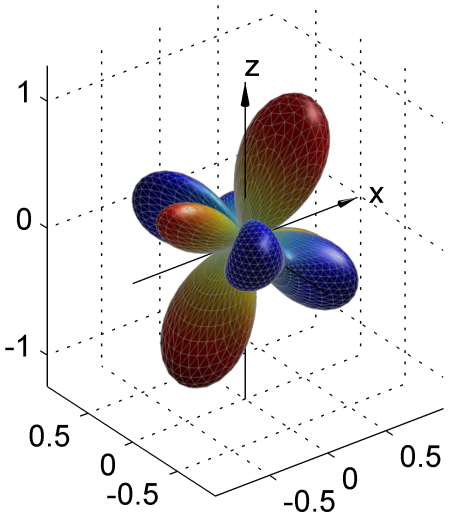

Figure 8.3: Function used for testing point-by-point spherical harmonic decompositions in Figure 8.4. This function contains only $l = 2$ and $l = 4$ spherical harmonics. It is formed from the function $f_0(\theta,\phi) = Y_2^{-2}(\theta,\phi) + Y_2^2(\theta,\phi) + Y_4^0(\theta,\phi)$ which is then rotated by $\pi/3$ about the y-axis using Wigner $\mathfrak{D}$-functions as described in §8.2.4.

it uses the minimum number of samples, the DST is the best means of calculating singlet yield SphHReps from explicit singlet yield values evaluated over a mesh.

The third important contribution is due to Kostelec and Rockmore. We recall that the DFT may be implemented efficiently using the FFT algorithm of Cooley and Tukey [203, 204]. Kostelec and Rockmore's `S2kit` library of `C` routines [371] applies similar algorithms to compute efficiently the discrete spherical harmonic transform and its inverse. We refer to their approach as the "fast spherical (harmonic) transform" (FST). The author of this thesis has published a `Matlab` interface to Kostelec and Rockmore's FST routines. This interface is used to make the calculations presented hereafter.

8.3.4 Comparison of point-by-point algorithms

Efficient methods for calculating singlet yields in systems with static or radio frequency fields were presented in Chapters 2 and 4 respectively. It is straightforward to apply these methods to determine singlet yield values $\Phi_S(\theta_k,\phi_k)$ at the vertices of a spherical mesh. Yet, the accuracy and performance of point-by-point approaches to finding RP singlet yield SphHReps depend critically on the method used for converting sampled singlet yield values into a SphHRep.

In order to evaluate the accuracy and performance of the three point-by-point algorithms presented above, we apply them to a problem with a known solution. We adopt the following procedure:

- We define a test function $f(\theta,\phi)$ that has a well-defined SphHRep $\boldsymbol{f}$. Figure 8.3 shows a polar plot of the function that we chose. We mimic the inversion symmetry of singlet yields by incorporating only spherical harmonics with *even* l values. The test function has been deliberately rotated off-axis since real RPs

are most unlikely to have their hyperfine tensors aligned along the laboratory z-axis.

- We choose an algorithm to test. For brevity, the algorithms are referred to using the abbreviations: "Int" for the numerical integration approach defined in §8.3.1; "LSq" for the least squares approach defined in §8.3.2; and "FST" for the approach defined in §8.3.3.

- We then calculate a set of data points $f_k = f(\theta_k, \phi_k)$ over the appropriate mesh. We denote the choice of mesh by: "Reg" for the equiangular mesh defined in equation (7.25); "Sophe" for the SOPHE mesh defined in equation (7.26); and "FST" for the equiangular mesh defined in equation (8.28).

- In some cases, we add noise to the data points f_k in order to test whether an algorithm is stable. A stable algorithm will produce changes in the SphHRep comparable to the noise level, whereas an unstable algorithm will amplify the noise, perhaps greatly. Normally distributed noise with standard deviation $\sigma = 10^{-6}$ was added for curves marked "Noisy".

- The data points f_k (with or without noise) are now provided as the sole input to the SphHRep algorithm under test, which returns an estimated SphHRep $\boldsymbol{g}$.

- After the algorithm has completed, we record the time taken and compare the recovered SphHRep $\boldsymbol{g}$ with the true SphHRep $\boldsymbol{f}$. A perfect algorithm would quickly give $\boldsymbol{g} = \boldsymbol{f}$. In practice, rounding errors mean that even the best algorithm may only be expected to return a SphHRep that is accurate to machine precision.

Figure 8.4 shows measurements of CPU time and accuracy for the SphHRep recovery methods detailed above. The accuracy for each l is quantified by calculating

$$\varepsilon(l) = \sqrt{\sum_m \left(g_l^m - f_l^m\right)^2} \tag{8.29}$$

where g_l^m are the recovered spherical harmonic coefficients and f_l^m are the true values. In the figure, we plot the logarithm of the largest error $\log_{10}[\max_l \varepsilon(l)]$ which gives a measure of the worst-case error in reproducing $\boldsymbol{f}$. Since calculating the individual singlet yield values is likely to be the slowest part of a point-by-point SphHRep calculation in a multinuclear RP and to assist in comparing the different approaches, we plot the timings and errors as a function of the number of mesh points used. Depending on the mesh, this number is controlled by the parameters: m and n; N; or b. Turning to inspect Figure 8.4, we make the following observations.

In Figures 8.4(b) and (d), we see clearly that the numerical integration approach ("Int") to finding SphHReps is rather inefficient. Even with 10^3 mesh points, the largest errors are $\sim 10^{-3}$. Indeed, the red and green curves are identical to plotting accuracy, implying that the errors from SphHRep recovery dwarf those from the small amount of noise added in the green curve to test numerical stability. Meanwhile, the least squares approach ("LSq") fares much better. With a sufficiently fine mesh, the noiseless blue curve is accurate to machine precision and the accuracy of the black curve is limited only by the added noise.

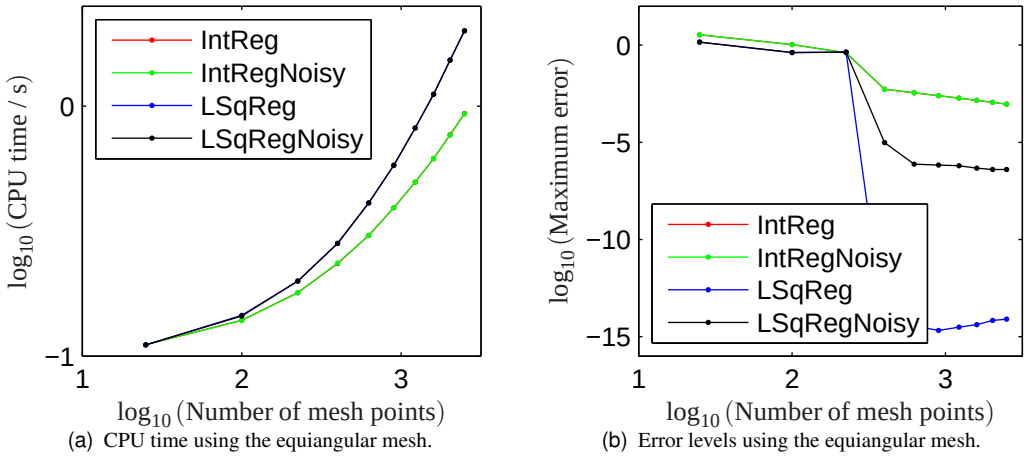

(a) CPU time using the equiangular mesh.

(b) Error levels using the equiangular mesh.

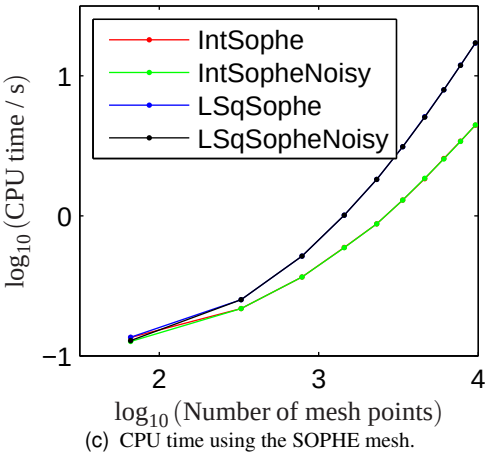

(c) CPU time using the SOPHE mesh.

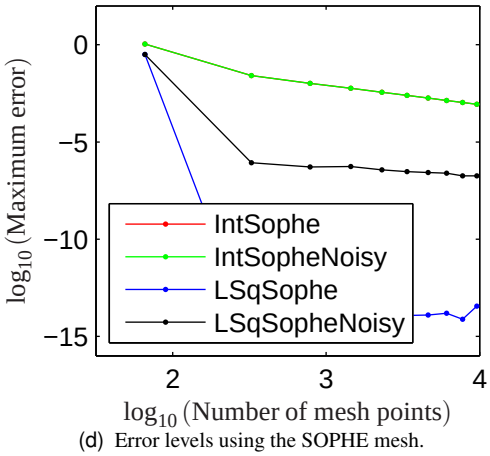

(d) Error levels using the SOPHE mesh.

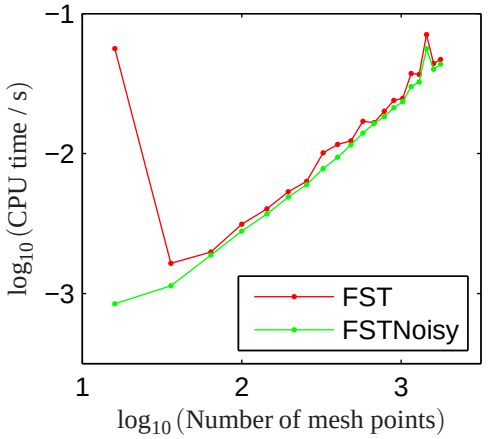

(e) CPU time using the fast spherical harmonic transform.

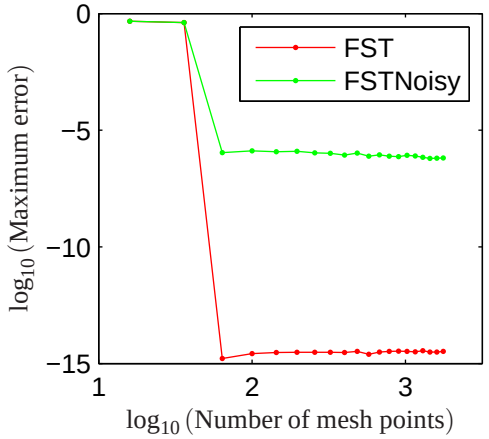

(f) Error levels using the fast spherical harmonic transform.

Figure 8.4: Convergence of spherical harmonic expansion coefficients determined by first evaluating explicit values over an appropriate mesh. See text for details. Note that in (a–d), the red and green curves are the same to plotting accuracy, as are the blue and black curves in (a) and (c). CPU times are measured for the inversion step itself and exclude mesh generation and evaluation of $f(\theta, \phi)$ over the mesh.

Inspecting Figures 8.4(a–d), we see that calculations using the equiangular and SOPHE meshes take a similar amount of time and give results of comparable accuracy. In both cases, a mesh with at least 300 points is satisfactory.

Finally, Figures 8.4(e) and (f) demonstrate the power of the FST algorithm. The FST algorithm requires fewer than 100 data points to give a fully converged SphHRep, which is limited only by machine precision (red curve) or by the added noise (green curve). Meanwhile, the CPU time required to make the transformation does not exceed 100 ms even with the finest mesh. Clearly, the FST algorithm is superior to the others; it provides a numerically stable and efficient point-by-point approach to finding SphHReps. Hence, we do not consider the other point-by-point methods any further.

8.3.5 Application to singlet yield calculations

The point-by-point algorithms for finding singlet yield SphHReps described in this section have been implemented by the author in a general purpose `Matlab` code `CalcSphHRep`. This code provides a common interface to all the algorithms described in this chapter. It takes as input a list of RP parameters, such as hyperfine tensors and field strengths, together with a short name specifying the algorithm to be used.

The methods with short names "PyDMAInt", "PyDMALSq" and "PyDMAFST" are applicable to RPs in the presence of static fields, or where the rotating frame transformation yields a time-independent RP Hamiltonian. These methods use the frequency domain approach to calculating singlet yields described in §2.2.2 to calculate samples over a SOPHE or FST mesh. These singlet yield samples are converted to a SphHRep as described above.

The method with short name "gCOMPFST" is suitable for RPs in the presence of radio frequency fields. It uses the γ–`COMPUTE` algorithm described in §4.2.3 to find singlet yield samples, which are then converted to a SphHRep using the FST.

8.3.6 Evaluation in a one-proton RP

Figure 8.5 presents a series of singlet yield SphHReps calculated using the PyDMAFST method in a one-proton RP. The hyperfine tensor and static field were chosen so that this RP is close to an energy level crossing. Since the eigenstates depend strongly on the orientation of $\boldsymbol{B}_0$ at field strengths near an energy level crossing, the singlet yield is strongly anisotropic. Therefore, the singlet yield anisotropy, shown in Figure 8.7(h), contains contributions from many spherical harmonics. Such a RP makes a good test for the accuracy of a spherical harmonic decomposition algorithm.

Inspecting Figure 8.5(a), it is clear that the contribution to the singlet yield SphHRep of spherical harmonics with odd l values is negligible, being on the order of machine precision. This is as expected physically because of the inversion symmetry $\Phi_{\mathrm{S}}(\boldsymbol{B}) = \Phi_{\mathrm{S}}(-\boldsymbol{B})$ discussed in §8.2.7.

Figures 8.5(a) and (b) show that the calculated SphHReps converge rapidly as MaxL is increased. Since the differences between the SphHReps for MaxL $= 20$ and 30 are $\sim 10^{-15}$ at worst, we assume in later tests that the MaxL $= 30$ SphHRep is fully converged, using it to determine the accuracy of the perturbation theory and algebraic approaches developed hereafter.

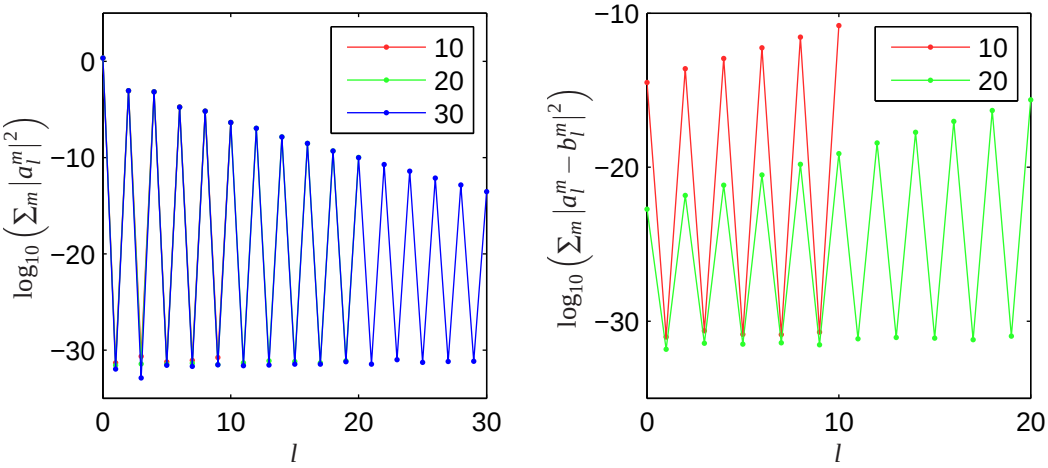

(a) Contributions to the singlet yield as a function of l. The contributions for odd l should be zero because of the inversion symmetry $\Phi_S(\boldsymbol{B}) = \Phi_S(-\boldsymbol{B})$.

(b) Comparison of SphHReps recovered at MaxL = 10 and 20 (a_l^m) with those for MaxL = 30 (b_l^m). Good convergence is seen.

Figure 8.5: Testing the convergence of PyDMAFST singlet yield SphHReps. Calculations were made in a one-proton RP using the `CalcSphHRep` code and the following parameters: $k = 2 \times 10^6\,\mathrm{s}^{-1}$, $a = 2.5\,\mathrm{mT}$, $\alpha = 12.5\,\mu\mathrm{T}$, $\beta = 0\,\mu\mathrm{T}$ and $B_0 = 50\,\mu\mathrm{T}$. The maximum l value, defined such that $a_l^m = 0\ \forall\ l >$ MaxL, is indicated in the legend.

8.4 Perturbation theory

Although, as explained above, it is possible to determine singlet yield SphHReps by first calculating the corresponding polar plots, that procedure provides little insight into the physical origins of the different spherical harmonic contributions. Following an initial suggestion by Kuprov [372], we show that in suitable systems, the singlet yield SphHRep may be calculated directly without any point-by-point calculation. It is hoped that this new method of calculation will provide greater physical insight into the effects contributing to singlet yield SphHReps.

8.4.1 Singlet yield in Liouville space

Working in Liouville space and using the exponential model, we wish to find an expression for the singlet yield. According to equation (2.1), the singlet yield is

$$\Phi_S = \int_0^\infty \left\langle \hat{P}^S \right\rangle (t) f(t)\,\mathrm{d}t \tag{8.30}$$

$$= k \int_0^\infty \left\langle \hat{P}^S \right\rangle (t) \mathrm{e}^{-kt}\,\mathrm{d}t. \tag{8.31}$$

In the Hilbert space version of the density matrix formalism, we know that

$$\left\langle \hat{P}^S \right\rangle (t) = \mathrm{Tr}\left[\hat{P}^S \hat{\rho}(t)\right] = \mathrm{Tr}\left[\left(\hat{P}^S\right)^\dagger \hat{\rho}(t)\right] \tag{8.32}$$

where we have made use of the Hermiticity of the singlet projection operator $\hat{P}^S$. According to equation (C.30), this means that in Liouville space

$$\left\langle \hat{P}^S \right\rangle (t) = \left(\hat{P}^S | \hat{\rho}(t)\right) \tag{8.33}$$

where $\left|\hat{P}^{\mathrm{S}}\right)$ and $|\hat{\rho}(t))$ are the Liouville kets corresponding to the singlet projection operator and the density matrix. According to equation (C.35), the density ket $|\hat{\rho}(t))$ evolves under the Liouvillian superoperator $\hat{\hat{L}}_{\diamond}$ (the "$\diamond$" distinguishes this Liouvillian from the more general case below) such that

$$|\hat{\rho}(t)) = \mathrm{e}^{-\mathrm{i}\hat{\hat{L}}_{\diamond}t}\,|\hat{\rho}(0))\,. \tag{8.34}$$

Hence, the singlet yield is given by

$$\Phi_{\mathrm{S}} = k\int_0^{\infty} \left(\hat{P}^{\mathrm{S}}\right| \mathrm{e}^{-\mathrm{i}\hat{\hat{L}}_{\diamond}t}\,|\hat{\rho}(0))\,\mathrm{e}^{-kt}\,\mathrm{d}t. \tag{8.35}$$

Thus far, we have considered RP spin evolution and reaction kinetics separately. As written, the Liouvillian superoperator $\hat{\hat{L}}_{\diamond}$ is Hermitian and hence the norm $(\hat{\rho}(t)|\hat{\rho}(t))$ does not decay with time. Physically, this Liouvillian describes only coherent processes. However, it is also possible to include a reaction term in the Liouvillian as follows

$$\hat{\hat{L}} = \hat{\hat{L}}_{\diamond} - \mathrm{i}k\hat{\hat{\mathbb{1}}} \tag{8.36}$$

in which case the singlet yield is given by

$$\Phi_{\mathrm{S}} = k\int_0^{\infty} \left(\hat{P}^{\mathrm{S}}\right| \mathrm{e}^{-\mathrm{i}\hat{\hat{L}}t}\,|\hat{\rho}(0))\,\mathrm{d}t. \tag{8.37}$$

The density ket now decays over time to represent the decreasing number of RPs that have not yet reacted.

This expression may be further simplified as follows

$$\begin{aligned}
\Phi_{\mathrm{S}} &= k\left(\hat{P}^{\mathrm{S}}\right|\left[\int_0^{\infty}\mathrm{e}^{-\mathrm{i}\hat{\hat{L}}t}\,\mathrm{d}t\right]|\hat{\rho}(0)) \\
&= k\left(\hat{P}^{\mathrm{S}}\right|\left[\left(-\mathrm{i}\hat{\hat{L}}\right)^{-1}\mathrm{e}^{-\mathrm{i}\hat{\hat{L}}t}\right]_0^{\infty}|\hat{\rho}(0)) \\
&= k\left(\hat{P}^{\mathrm{S}}\right|\left[\left(-\mathrm{i}\hat{\hat{L}}\right)^{-1}\mathrm{e}^{-\mathrm{i}\hat{\hat{L}}\infty} - \left(-\mathrm{i}\hat{\hat{L}}\right)^{-1}\mathrm{e}^{-\mathrm{i}\hat{\hat{L}}0}\right]|\hat{\rho}(0))\,.
\end{aligned} \tag{8.38}$$

Since $k > 0$, the $\mathrm{e}^{-\mathrm{i}\hat{\hat{L}}\infty}$ term vanishes and we find that

$$\begin{aligned}
\Phi_{\mathrm{S}} &= k\left(\hat{P}^{\mathrm{S}}\right|\left[-\left(-\mathrm{i}\hat{\hat{L}}\right)^{-1}\right]|\hat{\rho}(0)) \\
&= -\mathrm{i}k\left(\hat{P}^{\mathrm{S}}\right|\hat{\hat{L}}^{-1}\,|\hat{\rho}(0))\,.
\end{aligned} \tag{8.39}$$

As the singlet yield is real, an equivalent expression is

$$\Phi_{\mathrm{S}} = \mathrm{Im}\left\{k\left(\hat{P}^{\mathrm{S}}\right|\hat{\hat{L}}^{-1}\,|\hat{\rho}(0))\right\}. \tag{8.40}$$

8.4.2 Power series in the Zeeman interaction

In a RP with anisotropic interactions, the singlet yield $\Phi_S(\theta,\phi)$ depends on the orientation of the applied magnetic field, expressed here in spherical polar coordinates (θ,ϕ). In terms of the Liouville space expression given in equation (8.39), this angular dependence arises because the Liouvillian $\hat{\hat{L}}(\theta,\phi)$ also depends on the orientation of the applied field through the Zeeman interaction term. In some instances, it is possible to carry this angular dependence through the calculation analytically using spherical harmonics.

We begin by separating the Liouvillian into two contributions

$$\hat{\hat{L}} = \hat{\hat{L}}_0 + \hat{\hat{Z}}(\theta,\phi), \tag{8.41}$$

where only the Zeeman term

$$\hat{\hat{Z}}(\theta,\phi)\odot = \left[\boldsymbol{B}(\theta,\phi)\cdot \mathrm{g}\cdot\left(\hat{\boldsymbol{S}}_\mathrm{A}+\hat{\boldsymbol{S}}_\mathrm{B}\right),\odot\right] \tag{8.42}$$

depends on the orientation of the applied field (θ,ϕ). Assuming that the electron g-factor is isotropic and close to the free electron value, the Zeeman term simplifies to

$$\hat{\hat{Z}}(\theta,\phi)\odot = \left[\omega_0\left(\hat{\boldsymbol{S}}_\mathrm{A}+\hat{\boldsymbol{S}}_\mathrm{B}\right),\odot\right] \tag{8.43}$$

where $\omega_0 = -\gamma_\mathrm{e}B$. All other contributions to the spin evolution are collected into $\hat{\hat{L}}_0$. For the RPs considered here, $\hat{\hat{L}}_0$ contains terms for the anisotropic hyperfine interactions and for exponential model kinetics:

$$\hat{\hat{L}}_0\odot = \left[\sum_{\mathrm{N=A,B}}\sum_i \hat{\boldsymbol{I}}_{i\mathrm{N}}\cdot\mathsf{A}_{i\mathrm{N}}\cdot\hat{\boldsymbol{S}}_\mathrm{N},\odot\right] - \mathrm{i}k\hat{\hat{\mathbb{1}}}\odot\,. \tag{8.44}$$

Attaching the spherical coordinates (θ,ϕ) to the Zeeman interaction term means physically that we consider the RP fixed in space and the magnetic field free to move. This seems a natural description from the point of view of a bird flying along. Relative to the bird, its own body remains fixed whilst the Earth's magnetic field moves around it.

We expand the inverse Liouvillian $\hat{\hat{L}}^{-1}$ in powers of $\hat{\hat{Z}}$

$$\begin{aligned}\hat{\hat{L}}^{-1} = \left(\hat{\hat{L}}_0+\hat{\hat{Z}}(\theta,\phi)\right)^{-1} &= \left(\hat{\hat{L}}_0^{-1}\hat{\hat{L}}_0+\hat{\hat{L}}_0^{-1}\hat{\hat{Z}}(\theta,\phi)\right)^{-1}\hat{\hat{L}}_0^{-1}\\ &= \left(\hat{\mathbb{1}}+\hat{\hat{L}}_0^{-1}\hat{\hat{Z}}(\theta,\phi)\right)^{-1}\hat{\hat{L}}_0^{-1}.\end{aligned} \tag{8.45}$$

In making this expansion, we have remembered that $\hat{\hat{L}}_0^{-1}$ and $\hat{\hat{Z}}(\theta,\phi)$ are unlikely to commute.

8.4.3 Matrix binomial theorem

Normal matrices

Equation (8.45) contains a term $(\mathbb{1}-\mathsf{M})^{-1}$. Iff M is a normal matrix, then

$$\mathsf{M} = \mathsf{U}\Lambda\mathsf{U}^\dagger \tag{8.46}$$

where U is a unitary matrix whose columns are the eigenvectors of M and Λ is a diagonal matrix of eigenvalues of M. Therefore

$$(\mathbb{1}-\mathsf{M})^{-1}=\mathsf{U}\,(\mathbb{1}-\Lambda)^{-1}\,\mathsf{U}^{\dagger}. \tag{8.47}$$

Since the matrix $\mathbb{1}-\Lambda$ is diagonal, we may consider each eigenvalue $\lambda_i=\Lambda_{ii}$ separately. By the standard results of complex analysis, we know that

$$(1-\lambda_i)^{-1}=1+\lambda_i+\lambda_i^2+\lambda_i^3+\ldots \tag{8.48}$$

which converges whenever $|\lambda_i|<1$. Therefore

$$(\mathbb{1}-\mathsf{M})^{-1}=\mathbb{1}+\mathsf{M}+\mathsf{M}^2+\mathsf{M}^3+\ldots \tag{8.49}$$

which converges whenever all $|\mathrm{eig}\,\mathsf{M}|<1$.

All Hermitian matrices are normal matrices and so equation (8.49) holds for them. If M is a normal matrix then

$$\mathsf{M}-\mathrm{i}k\mathbb{1}=\mathsf{U}\Lambda\mathsf{U}^{\dagger}-\mathrm{i}k\mathsf{U}\mathsf{U}^{\dagger}=\mathsf{U}\,(\Lambda-\mathrm{i}k\mathbb{1})\,\mathsf{U}^{\dagger}. \tag{8.50}$$

Clearly, $\mathsf{M}-\mathrm{i}k\mathbb{1}$ is also a normal matrix with eigenvalues $\lambda_i-\mathrm{i}k$.

Nilpotent matrices

Some important matrices in spin dynamics are not Hermitian. For example, the raising and lowering operators $\hat{S}_{\pm}$ are not. However, the raising and lowering operators are nilpotent. All eigenvalues of a nilpotent matrix are zero. A rank-k nilpotent matrix M satisfies

$$\mathsf{M}^k=0. \tag{8.51}$$

Hence, for a rank-k nilpotent matrix, the series $\mathbb{1}+\mathsf{M}+\mathsf{M}^2+\mathsf{M}^3+\ldots$ terminates at M^{k-1}.

Consider the product

$$(\mathbb{1}-\mathsf{M})\left(\mathbb{1}+\mathsf{M}+\mathsf{M}^2+\ldots+\mathsf{M}^{k-1}\right)=\mathbb{1}+\mathsf{M}-\mathsf{M}+\mathsf{M}^2-\mathsf{M}^2-\mathsf{M}^k \tag{8.52}$$

$$=\mathbb{1}-\mathsf{M}^k=\mathbb{1}. \tag{8.53}$$

Therefore, the binomial series is a right inverse of $(\mathbb{1}-\mathsf{M})$. A similar proof shows that it is also a left inverse. Hence, the matrix binomial theorem holds for any nilpotent matrix M.

8.4.4 Series expansion

Since the hyperfine and Zeeman Hamiltonians are Hermitian, both $\hat{\hat{L}}_0$ and $\hat{\hat{Z}}$ are represented by normal matrices. Also, since the eigenvalues λ_i of a Hermitian matrix are real, then $|\lambda_i+\mathrm{i}k|>0$ for $k>0$. This guarantees the existence of the inverse $\hat{\hat{L}}_0^{-1}$.

Applying the matrix binomial theorem to equations (8.39) and (8.45), we see that

$$\Phi_{\mathrm{S}}=-\mathrm{i}k\left(\hat{P}^{\mathrm{S}}\right|\left(\hat{\mathbb{1}}-\hat{\hat{L}}_0^{-1}\hat{\hat{Z}}(\theta,\phi)+\hat{\hat{L}}_0^{-1}\hat{\hat{Z}}(\theta,\phi)\hat{\hat{L}}_0^{-1}\hat{\hat{Z}}(\theta,\phi)-\ldots\right)\hat{\hat{L}}_0^{-1}\left|\hat{\rho}(0)\right),\tag{8.54}$$

providing that all the eigenvalues of $\hat{\hat{L}}^{-1}\hat{\hat{Z}}$ satisfy

$$\left|\mathrm{eig}\left(\hat{\hat{L}}_0^{-1}\hat{\hat{Z}}(\theta,\phi)\right)\right|<1. \tag{8.55}$$

8.4.5 Decomposition of the Zeeman interaction

The magnetic field vector $\boldsymbol{B}$ can be written in spherical polar coordinates as

$$\boldsymbol{B} = B\left(\cos\phi\sin\theta\boldsymbol{i} + \sin\phi\sin\theta\boldsymbol{j} + \cos\theta\boldsymbol{k}\right) \tag{8.56}$$

where B is the field strength.

Written out in full, the rank-1 spherical harmonics are

$$\begin{aligned} Y_1^{-1}(\theta,\phi) &= \frac{1}{2}\mathrm{e}^{-\mathrm{i}\phi}\sqrt{\frac{3}{2\pi}}\sin\theta \\ Y_1^{0}(\theta,\phi) &= \sqrt{\frac{3}{4\pi}}\cos\theta \\ Y_1^{1}(\theta,\phi) &= \frac{-1}{2}\mathrm{e}^{\mathrm{i}\phi}\sqrt{\frac{3}{2\pi}}\sin\theta. \end{aligned} \tag{8.57}$$

The magnetic field may therefore be written

$$\boldsymbol{B} = B\sqrt{\frac{4\pi}{3}}\left\{\begin{array}{c} \sqrt{\frac{1}{2}}\left(Y_1^{-1}(\theta,\phi) - Y_1^{1}(\theta,\phi)\right)\boldsymbol{i} \\ +\mathrm{i}\sqrt{\frac{1}{2}}\left(Y_1^{-1}(\theta,\phi) + Y_1^{1}(\theta,\phi)\right)\boldsymbol{j} \\ +Y_1^{0}(\theta,\phi)\boldsymbol{k} \end{array}\right\}. \tag{8.58}$$

Substituting into the Zeeman term of the Liouvillian and collecting terms gives

$$\hat{\hat{Z}}(\theta,\phi) = \omega_0\left(\hat{\hat{T}}_1^{-1}Y_1^{-1}(\theta,\phi) + \hat{\hat{T}}_1^{1}Y_1^{1}(\theta,\phi) + \hat{\hat{T}}_1^{0}Y_1^{0}(\theta,\phi)\right) \tag{8.59}$$

where the $\hat{T}_l^m$ operators are defined to be

$$\begin{aligned} \hat{\hat{T}}_1^{-1}\odot &= \sum_{\mathrm{N=A,B}}\sqrt{\frac{2\pi}{3}}\left[\hat{S}_{\mathrm{Nx}} + \mathrm{i}\hat{S}_{\mathrm{Ny}},\odot\right] \\ \hat{\hat{T}}_1^{1}\odot &= \sum_{\mathrm{N=A,B}}\sqrt{\frac{2\pi}{3}}\left[-\hat{S}_{\mathrm{Nx}} + \mathrm{i}\hat{S}_{\mathrm{Ny}},\odot\right] \\ \hat{\hat{T}}_1^{0}\odot &= \sum_{\mathrm{N=A,B}}\sqrt{\frac{4\pi}{3}}\left[\hat{S}_{\mathrm{Nz}},\odot\right]. \end{aligned} \tag{8.60}$$

Note that these superoperators do not depend on the orientation of the magnetic field (θ,ϕ) and are *not* the familiar spherical tensor (super)operators. An alternative formulation of this problem would have fixed the magnetic field and rotated the radical pair. In that case, the orientation dependence of the Hamiltonian (and hence of the Liouvillian) would have been attached to the operators and not to the field vector $\boldsymbol{B}$. In that convention, we would have made an expansion in terms of the spherical tensor (super)operators.

8.4.6 Spherical harmonic decomposition

Substituting equation (8.59) into equation (8.54), we write

$$\Phi_{\mathrm{S}} = -\mathrm{i}k\left(\hat{P}^{\mathrm{S}}\right| \left\{ \begin{array}{l} \hat{\mathbb{1}} \\ -\omega_0 \sum\limits_{m=-1}^{1} \hat{\hat{L}}_0^{-1} \hat{\hat{T}}_1^m Y_1^m(\theta,\phi) \\ +\omega_0^2 \sum\limits_{m=-1}^{1} \sum\limits_{m'=-1}^{1} \hat{\hat{L}}_0^{-1} \hat{\hat{T}}_1^m \hat{\hat{L}}_0^{-1} \hat{\hat{T}}_l^{m'} Y_1^m(\theta,\phi) Y_l^{m'}(\theta,\phi) \\ -\ldots \end{array} \right\} \hat{\hat{L}}_0^{-1} \left|\hat{\rho}(0)\right). \tag{8.61}$$

Notice that each additional Zeeman interaction term that we include makes a contribution $-\omega_0 \sum_m \hat{\hat{L}}_0^{-1} \hat{\hat{T}}_1^m Y_1^m(\theta,\phi)$ to the bracketed superoperator product. Second order (and higher) terms contain products of spherical harmonics which we expand using the Clebsch-Gordan series, *i.e.* equation (8.13). Since the matrix binomial series converges, we expect to be able to truncate the singlet yield after the first few terms. Hence, ultimately

$$\Phi_{\mathrm{S}}(\theta,\phi) = \sum_{l,m} a_l^m Y_l^m(\theta,\phi). \tag{8.62}$$

By a careful numerical evaluation of the superoperator terms in equation (8.61), we may determine the desired SphHRep components a_l^m without ever calculating the singlet yield for a particular magnetic field orientation.

8.4.7 Algorithm

We implemented equation (8.61) under the short name "InvLSeries" in our general purpose `Matlab` code `CalcSphHRep`. That implementation uses the following iterative algorithm:

1. Since $1 = \sqrt{4\pi}\ Y_0^0(\theta,\phi)$ and using the Clebsch-Gordan series to expand any products of spherical harmonics, we write equation (8.61) in the following compact notation

$$\Phi_{\mathrm{S}} = \left(\hat{P}^{\mathrm{S}}\right| \left\{ \sum_{i=0}^{n} \left[\sum_{l,m} Y_l^m(\theta,\phi) \left| i;l,m \right) \right] \right\} \tag{8.63}$$

   where i, l and m label the different spherical harmonic Y_l^m contributions to the singlet yield from the i^{th} order term.

2. We begin by evaluating the following 0^{th}-order term, which is shown in square brackets in equation (8.63),

$$X_0 = \sum_{l,m} Y_l^m(\theta,\phi) \left|0;l,m\right) = Y_0^0(\theta,\phi) \left[-\mathrm{i}k\sqrt{4\pi}\ \hat{\hat{L}}_0^{-1} \left|\hat{\rho}(0)\right) \right]. \tag{8.64}$$

3. Using a vector representation for the Liouville ket, defined by equation (C.21), and a SphHRep vector representation for the spherical harmonic, defined by equation (8.14), we can write

$$X_0 = Y_l^m(\theta,\phi)\sum_{l,m}|0;l,m) = \left(\begin{array}{c|c|c|c|c} |0;0,0)\text{ for }Y_0^0(\theta,\phi) & |0;1,-1)\text{ for }Y_1^{-1}(\theta,\phi) & |0;1,0)\text{ for }Y_1^0(\theta,\phi) & |0;1,1)\text{ for }Y_1^1(\theta,\phi) & \cdots \end{array}\right). \tag{8.65}$$

4. Having stored X_0, we generate the next contribution X_1 using the Clebsch-Gordan series. The new terms in X_1 contain spherical harmonics Y_1^{-1}, Y_1^0 and Y_1^1. We expand products of these with the existing spherical harmonics in X_0 using the Clebsch-Gordan series to give X_1.

$$\begin{aligned} X_{i+1} &= -\omega_0\sum_{l,m}\sum_{m'=-1}^{1}\hat{\hat{L}}_0^{-1}\hat{\hat{T}}_1^{m'}|i;l,m)\,Y_l^m Y_1^{m'} \\ &= \sum_{L,M}\left\{-\omega_0\sum_{l,m}\sum_{m'=-1}^{1}\hat{\hat{L}}_0^{-1}\hat{\hat{T}}_1^{m'}|i;l,m)\sqrt{\frac{3(2l+1)}{4\pi(2L+1)}}C^{L,0}_{1,0;l,0}C^{L,M}_{1,m';l,m}\right\}Y_L^M \\ &= \sum_{L,M}|i+1;L,M)\,Y_L^M. \end{aligned} \tag{8.66}$$

The new term X_{i+1} will contain contributions with $L \leq i+1$ since the Zeeman interaction terms have $l = 1$ and introduce one unit of angular momentum at each order.

5. We repeat step 4 in a loop until the series converges and the X_i become negligible or until we reach a predefined limit. In the `Matlab` code, this predefined limit is set by the option "MaxL".

6. Finally, we substitute into equation (8.63) to give the singlet yield SphHRep components

$$\begin{aligned} \Phi_S &= \sum_{i=0}^{n}\left(\hat{P}^S\right|X_i \\ &= \sum_{i=0}^{n}\sum_{l,m}\left(\hat{P}^S|i;l,m\right)Y_l^m(\theta,\phi). \end{aligned} \tag{8.67}$$

This algorithm calculates the coefficients

$$a_l^m = \sum_{i=0}^{n}\left(\hat{P}^S|i;l,m\right) \tag{8.68}$$

in the singlet yield expansion

$$\Phi_S(\theta,\phi) = \sum_{l,m} a_l^m Y_l^m(\theta,\phi) \tag{8.69}$$

without ever calculating the singlet yield for a particular magnetic field orientation.

Physically, it shows that when the Zeeman interaction is significant to n^{th} order, the singlet yield contains spherical harmonic contributions with $l \leq n$. We saw in §8.2.7 that only spherical harmonics with even values of l contribute to the singlet yield. Hence, RPs subject to weak magnetic fields and whose energy levels are well separated have singlet yield anisotropies that strongly resemble the $Y_2^m(\theta,\phi)$ spherical harmonics.

8.4.8 Evaluation in a one-proton RP

Figures 8.6 and 8.7 show singlet yield SphHReps calculated using the InvLSeries perturbation theory expansion algorithm. In order to evaluate the accuracy of the InvLSeries algorithm, these calculations were made in the same RP system that was used above with the PyDMAFST algorithm. However, since the InvLSeries algorithm relies on a perturbative expansion in powers of the Zeeman interaction superoperator, it is reasonable to expect that it will perform best in the presence of weak fields. We therefore make tests first with a field $B_0 = 5\,\mu\text{T}$ and then with $B_0 = 50\,\mu\text{T}$.

Figures 8.6(a) and (b) show the behaviour in weak, $B_0 = 5\,\mu\text{T}$, fields. Notice that the singlet yield SphHRep converges rapidly as the number of iterations, *i.e.* the order of the perturbative expansion, is increased. Once again, the contributions from odd l values are negligible, as is expected on physical grounds. Furthermore, not only does the calculated SphHRep converge rapidly, but it clearly converges to the same value that the PyDMAFST algorithm finds. The discrepancies between the points and crosses in Figure 8.6(a) arise from rounding errors. They are of the order of machine epsilon, 10^{-16} and only appear large because of the logarithmic scale.

This good convergence is confirmed by the polar plots in Figures 8.7(a–d). After only two iterations, the singlet yield anisotropy in Figure 8.7(a) is hard to distinguish by eye from the fully converged PyDMAFST result in Figure 8.7(d).

However, when we increase the field to $B_0 = 50\,\mu\text{T}$, the results are less encouraging. Figures 8.6(c) and (d) show that the singlet yield SphHRep now diverges as the number of iterations is increased. After 20 iterations, errors in the InvLSeries SphHRep are in excess of 10^{20}, which is clearly pathological. This behaviour is confirmed by the polar plots in Figures 8.7(e–h). At no point does the InvLSeries SphHRep resemble the true singlet yield SphHRep in (h). Furthermore, after 10 iterations, the InvLSeries algorithm predicts singlet yields $> 10^5$, which is physically quite impossible.

Further calculations (not shown) suggest that the convergence of this Zeeman perturbation series is governed by the ratio B_0/k. Radical pairs that are likely to produce strong anisotropy, and which therefore seem likely candidates for involvement in the avian magnetic sense, tend to have long lifetimes and to have an energy level crossing at $B_0 \approx 50\,\mu\text{T}$. It is unfortunate that this perturbation theory approach breaks down for precisely those RPs that are of interest for modelling the avian compass sense.

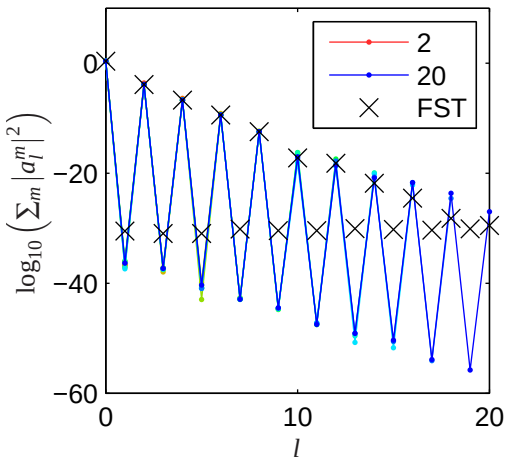

(a) Static field $B_0 = 5\,\mu\text{T}$. Comparison between InvLSeries SphHReps (lines) and converged PyDMAFST ones ($\times$).

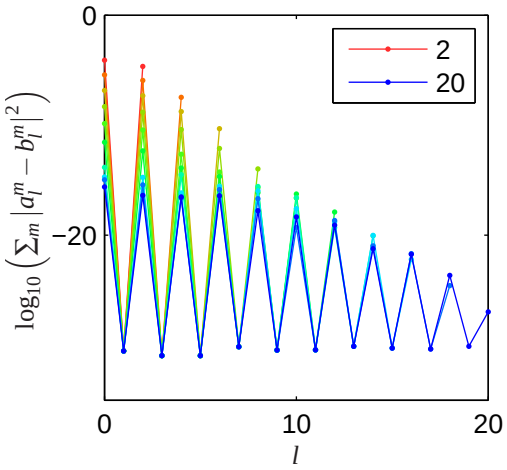

(b) Static field $B_0 = 5\,\mu\text{T}$. Differences between the InvLSeries SphHReps a_l^m and converged PyDMAFST b_l^m.

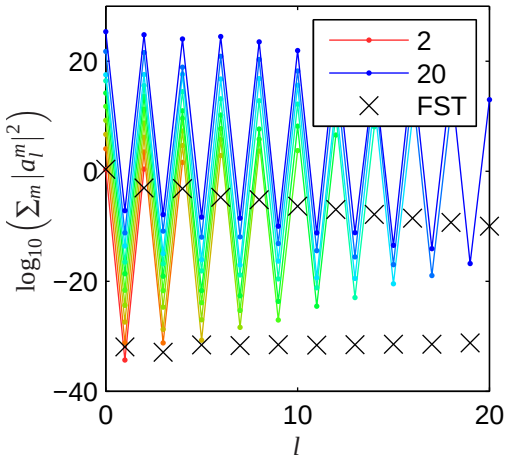

(c) Static field $B_0 = 50\,\mu\text{T}$. Comparison between InvLSeries SphHReps (lines) and converged PyDMAFST ones ($\times$).

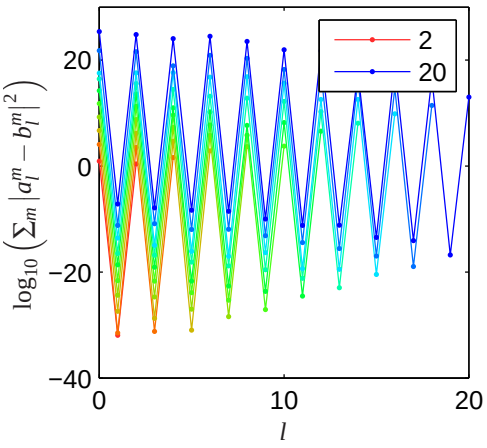

(d) Static field $B_0 = 50\,\mu\text{T}$. Differences between the InvLSeries SphHReps a_l^m and converged PyDMAFST b_l^m.

Figure 8.6: Comparison of InvLSeries perturbation theory SphHReps (a_l^m) and converged PyDMAFST SphHReps (b_l^m or $\times$). Calculations were made in a one-proton RP using the `CalcSphHRep` code and the following parameters: $k = 2 \times 10^6\,\text{s}^{-1}$, $a = 2.5\,\text{mT}$, $\alpha = 12.5\,\mu\text{T}$ and $\beta = 0\,\mu\text{T}$. The number of iterations is indicated in the legend. Calculations were run for 2, 4, ..., 18 and 20 iterations. A selection of corresponding polar plots are shown in Figure 8.7.

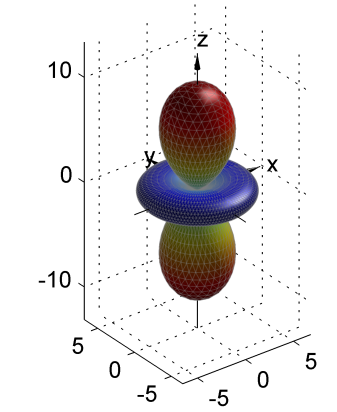

(a) InvLSeries for $B_0 = 5\,\mu\text{T}$ after 2 iterations.

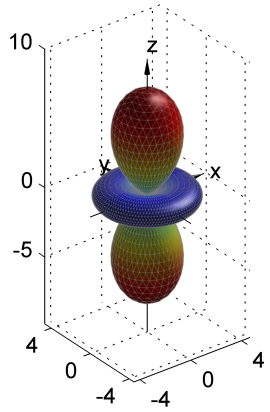

(b) InvLSeries for $B_0 = 5\,\mu\text{T}$ after 10 iterations.

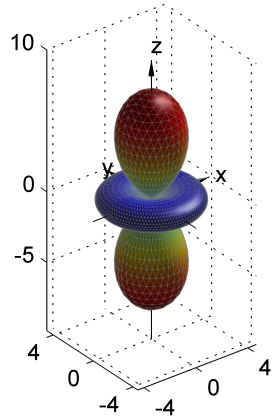

(c) InvLSeries for $B_0 = 5\,\mu\text{T}$ after 20 iterations.

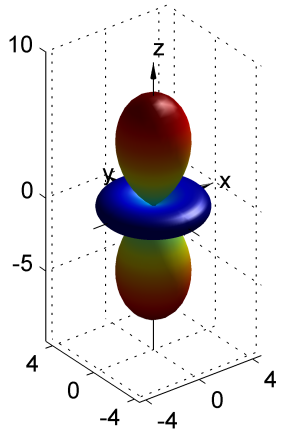

(d) Converged PyDMAFST result for $B_0 = 5\,\mu\text{T}$.

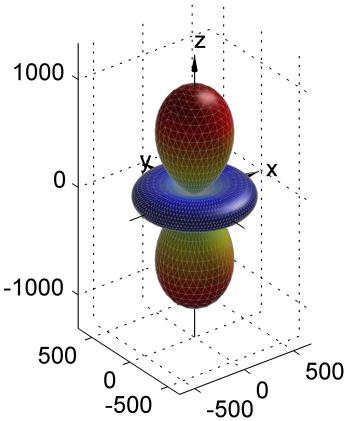

(e) InvLSeries for $B_0 = 50\,\mu\text{T}$ after 2 iterations.

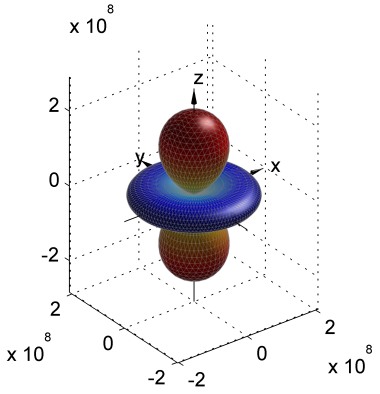

(f) InvLSeries for $B_0 = 50\,\mu\text{T}$ after 10 iterations.

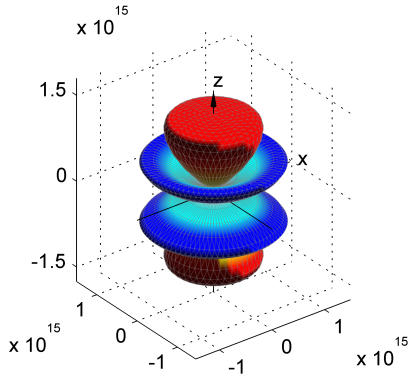

(g) InvLSeries for $B_0 = 50\,\mu\text{T}$ after 20 iterations.

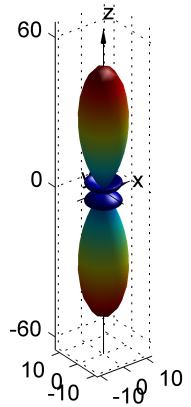

(h) Converged PyDMAFST result for $B_0 = 50\,\mu\text{T}$.

Figure 8.7: Polar plots of $1000\times$ singlet yield anisotropy to accompany Figure 8.6. Calculations were made in a one-proton RP using the `CalcSphHRep` code and the following parameters: $k = 2\times10^6\,\text{s}^{-1}$, $a = 2.5\,\text{mT}$, $\alpha = 12.5\,\mu\text{T}$ and $\beta = 0\,\mu\text{T}$.

8.5 Direct inversion

In §8.4.1, we saw that the dependence of singlet yield on the orientation of an applied magnetic field (θ,ϕ) arises from that of the inverse Liouvillian $\hat{\hat{L}}(\theta,\phi)^{-1}$ since

$$\Phi_{\mathrm{S}}(\theta,\phi) = -\mathrm{i}k\left(\hat{P}^{\mathrm{S}}\middle|\hat{\hat{L}}(\theta,\phi)^{-1}\middle|\hat{\rho}(0)\right).$$

In the previous section, we expanded $\hat{\hat{L}}(\theta,\phi)^{-1}$ as a power series in the electron Zeeman interaction. That approach holds quite generally when the static field is sufficiently weak, but breaks down for stronger fields. The perturbation theory method works well for "boring" RPs, but fails in the RPs that we would envisage forming the basis of an RPM compass. Therefore, in this section, we outline a different approach to finding singlet yield SphHReps. We show that $\hat{\hat{L}}(\theta,\phi)^{-1}|\hat{\rho}(0))$ may be expanded as a product of non-orientation-dependent Liouville kets multiplied by spherical harmonics. We demonstrate that finding this decomposition is equivalent to solving a system of algebraic simultaneous equations, which may be done using standard methods.

8.5.1 Axial, scalar analogue

The essence of this algorithm is most easily explained by considering a simpler analogous problem. In place of the Liouvillian superoperator, let us consider an axially symmetric function $f(\theta)$, written in terms of spherical harmonics as

$$f(\theta) = \sum_j b_j Y_j^0(\theta,\phi). \tag{8.70}$$

Starting from the coefficients b_j, we seek the spherical harmonic decomposition of $f(\theta)^{-1}$. Writing this explicitly,

$$f(\theta)^{-1} = \sum_l a_l Y_l^0(\theta,\phi) = \frac{1}{\sum_j b_j Y_j^0(\theta,\phi)} \tag{8.71}$$

and we wish to determine the a_l coefficients from the b_j ones.

To solve this equation, we multiply both sides by $f(\theta)$, which gives

$$\sum_{j,l} a_l b_j Y_l^0(\theta) Y_j^0(\theta) = 1 = \sqrt{4\pi}\, Y_0^0(\theta). \tag{8.72}$$

Expanding the product of spherical harmonics on the left using the Clebsch-Gordan series, *i.e.* equation (8.13) we see that

$$\sum_{L,l} a_l \left(\sum_j b_j \sqrt{\frac{(2l+1)(2j+1)}{4\pi(2L+1)}}\left[C^{L,0}_{l,0;j,0}\right]^2\right) Y_L^0(\theta,\phi) = \sqrt{4\pi}\, Y_0^0(\theta). \tag{8.73}$$

The expression in brackets, which we denote K_{Ll}, depends only on L and l. Hence, we can write this equation in the form of a matrix multiplication

$$\sum_{L,l} K_{Ll} a_l Y_L(\theta,\phi) = \sqrt{4\pi}\, Y_0(\theta). \tag{8.74}$$

Finally, using the orthogonality property of the spherical harmonics defined in equation (8.4), we arrive at the matrix equation $\mathsf{K}\boldsymbol{a} = \boldsymbol{c}$, which, in block form, is written

$$\begin{pmatrix} & & \\ & \mathsf{K} & \\ & & \end{pmatrix} \begin{pmatrix} a_0 \\ a_1 \\ a_2 \\ a_3 \\ \vdots \end{pmatrix} = \begin{pmatrix} c_0 \\ c_1 \\ c_2 \\ c_3 \\ \vdots \end{pmatrix} = \begin{pmatrix} \sqrt{4\pi} \\ 0 \\ 0 \\ 0 \\ \vdots \end{pmatrix}. \tag{8.75}$$

In principle, the vectors $\boldsymbol{a}$ and $\boldsymbol{c}$ continue indefinitely as $l \to \infty$, although they do have a definite first element when $l = 0$; they are said to be semi-infinite. Similarly, the matrix of Clebsch-Gordan coefficients K extends indefinitely downwards and to the right and is also said to be semi-infinite. The matrix K has non-zero elements that run in bands because of the rules for addition of angular momenta. Indeed, except for the first few elements in the top-left corner, K is almost a Toeplitz matrix. It seems probable that this structure arises from the asymptotic properties of the Clebsch-Gordan coefficients in the classical limit as discussed in [373] and summarised in [122, p264ff].

Specialist algorithms for inverting semi-infinite banded matrices such as K are known [374, 375]. However, in many cases the coefficients a_l fall away quickly as l increases. Visual inspection of polar plots shows that $f(\theta)^{-1}$ tends to adopt a simple shape with contributions only from a_l having small l values unless $f(\theta)$ is very small (or zero) at some angles.

We simplify equation (8.75) by truncation. If $a_l \approx 0$ for $l >$ MaxL and since the $c_l = 0$ for $l > 0$, there is no contribution from elements K_{Ll} having $L >$ MaxL or $l >$ MaxL. Hence, equation (8.75) simplifies to

$$\begin{pmatrix} & & \\ & \mathsf{K}' & \\ & & \end{pmatrix} \begin{pmatrix} a_0 \\ a_1 \\ a_2 \\ \vdots \\ a_{\mathrm{MaxL}} \end{pmatrix} \approx \begin{pmatrix} \sqrt{4\pi} \\ 0 \\ 0 \\ \vdots \\ 0 \end{pmatrix}. \tag{8.76}$$

where K' is the top-left corner of the full matrix K.

8.5.2 General scalar analogue

In general, the Liouvillian $\hat{\hat{L}}(\theta,\phi)$ does not have axial symmetry. Before tackling the full Liouville space inversion problem, it is instructive to try one further scalar analogue.

This time, we consider a function $g(\theta,\phi)$, defined in terms of its spherical harmonic expansion

$$g(\theta,\phi) = \sum_{j,m} b_j^m Y_j^m(\theta,\phi). \tag{8.77}$$

Once again, we wish to determine the spherical harmonic decomposition of $g(\theta,\phi)^{-1}$ starting from the b_j^m coefficients

$$g(\theta)^{-1} = \sum_{\ell,\mu} a_\ell^\mu Y_\ell^\mu(\theta,\phi) = \frac{1}{\sum_{j,m} b_j^m Y_j^m(\theta,\phi)}. \tag{8.78}$$

To solve this equation, we multiply both sides by $g(\theta,\phi)$, which gives

$$\sum_{j,m,\ell,\mu} a_\ell^\mu b_j^m Y_\ell^\mu(\theta) Y_j^m(\theta) = 1 = \sqrt{4\pi}\, Y_0^0(\theta). \tag{8.79}$$

This expression is very similar to that in equation (8.72), except that a and b now each have two indices instead of one. In order to avoid confusion, we combine the indices $\{j,m\} \rightarrow l$ and $\{\ell,\mu\} \rightarrow \lambda$ as explained in §8.2.6. Working with the new indices l and λ and expanding the product of spherical harmonics on the left using the Clebsch-Gordan series, *i.e.* equation (8.13) we see that

$$\sum_{L,\lambda} a_\lambda \left(\sum_l b_l \sqrt{\frac{(2\lambda+1)(2l+1)}{4\pi(2L+1)}} \tilde{C}^L_{\lambda;l} C^L_{\lambda;l} \right) Y_L(\theta,\phi) = \sqrt{4\pi}\, Y_0(\theta), \tag{8.80}$$

in which L is another combined index, the short index form $Y_0 = Y_0^0$ and $\tilde{C}^\bullet_{\bullet;\bullet}$ refers to the Clebsch-Gordan coefficient whose rank j is taken from the compact index L but where the order $m = 0$. The expression in brackets, which we denote $K_{L\lambda}$, depends only on L and λ. Hence, we can write this equation in the form of a matrix multiplication

$$\sum_{L,\lambda} K_{L\lambda} a_\lambda Y_L(\theta,\phi) = \sqrt{4\pi}\, Y_0(\theta). \tag{8.81}$$

Finally, using the orthogonality property of the spherical harmonics defined in equation (8.4), we arrive at the matrix equation $\mathsf{K}\boldsymbol{a} = \boldsymbol{c}$, which, in block form, is written

$$\begin{pmatrix} & & \\ & \mathsf{K} & \\ & & \end{pmatrix} \begin{pmatrix} a_0 \\ a_1 \\ a_2 \\ a_3 \\ \vdots \end{pmatrix} = \begin{pmatrix} c_0 \\ c_1 \\ c_2 \\ c_3 \\ \vdots \end{pmatrix} = \begin{pmatrix} \sqrt{4\pi} \\ 0 \\ 0 \\ 0 \\ \vdots \end{pmatrix}. \tag{8.82}$$

This equation is the same as in the axial case, except that each row and column now contains elements for all $\{j,m\}$ and not just for $m = 0$. As a consequence, the band structure of K is more complicated. Also, truncation of all elements in K with $j >$ MaxL leaves a much larger matrix K' than before.

Formation of K' is the slowest step and would be accelerated by using appropriate recurrence relations for the Clebsch-Gordan co-efficients. One possible implementation might be found in the C++ library `Matpack`.

8.5.3 Solving for singlet yield in Liouville space

Having illustrated the spherical harmonic inversion algorithm as applied to two scalar functions $f(\theta)$ and $g(\theta,\phi)$, we now direct our attention to the original Liouville space problem of finding the singlet yield spherical harmonic decomposition. The Liouville space derivation follows those above closely, except that now each element in K, $\boldsymbol{a}$, $\boldsymbol{b}$ and $\boldsymbol{c}$ must be expanded, using an appropriate Krønecker product, to accommodate a Liouville space ket or superoperator.

According to the definitions in §8.4.2 and 8.4.5, the Liouvillian

$$\begin{aligned}\hat{\hat{L}}(\theta,\phi) &= \hat{\hat{L}}_0 + \hat{\hat{Z}}(\theta,\phi) \\ &= \sqrt{4\pi}\,\hat{\hat{L}}_0 Y_0^0(\theta,\phi) + \omega_0 \hat{\hat{T}}_1^{-1} Y_1^{-1}(\theta,\phi) \\ &\quad + \omega_0 \hat{\hat{T}}_1^{-1} Y_1^0(\theta,\phi) + \omega_0 \hat{\hat{T}}_1^{-1} Y_1^1(\theta,\phi).\end{aligned} \tag{8.83}$$

The hyperfine interactions and exponential model kinetics determine $\hat{\hat{L}}_0$, which does not depend on the orientation of an applied field. Meanwhile, $\hat{\hat{Z}}(\theta,\phi)$ contains the electron Zeeman interaction which clearly does depend on the field orientation.

Combining these into a form similar to equation (8.77), we write the Liouvillian as

$$\hat{\hat{L}} = \sum_l \hat{\hat{B}}_l Y_l(\theta,\phi) \tag{8.84}$$

where the compact index l determines both the order j and rank m of the spherical harmonics. Notice that the scalar coefficients b_l from equation (8.77) have been replaced by superoperator coefficients $\hat{\hat{B}}_l$.

In order to compute the singlet yield spherical harmonic decomposition, we must first determine the spherical harmonic decomposition of the Liouville ket $\hat{\hat{L}}^{-1}|\hat{\rho}(0))$. We proceed by defining

$$\sum_\lambda |\lambda) Y_\lambda(\theta,\phi) = \hat{\hat{L}}^{-1}|\hat{\rho}(0))(\theta,\phi). \tag{8.85}$$

Premultiplying both sides by $\hat{\hat{L}}$ gives

$$\sum_\lambda \hat{\hat{L}}|\lambda) Y_\lambda(\theta,\phi) = |\hat{\rho}(0))\,. \tag{8.86}$$

Substituting (8.84) into (8.86) gives

$$\sum_{\lambda,l} \hat{\hat{B}}_l |\lambda) Y_l(\theta,\phi) Y_\lambda(\theta,\phi) = |\hat{\rho}(0))\,. \tag{8.87}$$

Recalling that $1 = \sqrt{4\pi}\,Y_0(\theta,\phi)$, we see that

$$\sum_{\lambda,l} \hat{\hat{B}}_l Y_l(\theta,\phi) Y_\lambda(\theta,\phi)\,|\lambda) = \sqrt{4\pi}\,|\hat{\rho}(0))\,Y_0(\theta,\phi). \tag{8.88}$$

Then, using the Clebsch-Gordan series, *i.e.* equation (8.13), to expand the pairs of spherical harmonics, we write

$$\sum_{L,\lambda}\left(\sum_l \hat{\hat{B}}_l \sqrt{\frac{(2\lambda+1)(2l+1)}{4\pi(2L+1)}}\tilde{C}^L_{\lambda;l} C^L_{\lambda;l}\right) Y_L(\theta,\phi)\,|\lambda) = \sqrt{4\pi}\,|\hat{\rho}(0))\,Y_0(\theta,\phi). \tag{8.89}$$

in which L is another combined index and $\tilde{C}^{\bullet}_{\bullet;\bullet}$ refers to the Clebsch-Gordan coefficient whose rank j is taken from the compact index L but where the order $m = 0$. Defining $K_{L\lambda} = (\ldots)$ as the bracketed part of this expression, we write

$$\sum_{L\lambda} K_{L\lambda}\,|\lambda)\,Y_L(\theta,\phi) = \sqrt{4\pi}\,|\hat{\rho}(0))\,Y_0(\theta,\phi). \tag{8.90}$$

We can collapse this into a standard, albeit large, matrix equation

$$\begin{pmatrix} \left(\sum_l \hat{\tilde{B}}_l \ldots \tilde{C}^0_{0;l} C^0_{0;l}\right) & \left(\sum_l \hat{\tilde{B}}_l \ldots \tilde{C}^0_{1;l} C^0_{1;l}\right) & \cdots \\ \left(\sum_l \hat{\tilde{B}}_l \ldots \tilde{C}^1_{0;l} C^1_{0;l}\right) & \left(\sum_l \hat{\tilde{B}}_l \ldots \tilde{C}^1_{1;l} C^1_{1;l}\right) & \cdots \\ \vdots & \vdots & \end{pmatrix} \begin{pmatrix} |\lambda = 0) \\ |\lambda = 1) \\ \vdots \end{pmatrix} = \begin{pmatrix} \sqrt{4\pi}\ |\hat{\rho}(0)) \\ |0) \\ \vdots \end{pmatrix}. \tag{8.91}$$

Finally, once the $|\lambda)$ are known, we substitute equation (8.85) into equation (8.39). The singlet yield is therefore

$$\Phi_{\mathrm{S}}(\theta,\phi) = \sum_{\lambda} -\mathrm{i}k \left(\hat{P}^{\mathrm{S}}|\lambda\right) Y_{\lambda}(\theta,\phi). \tag{8.92}$$

This formalism enables the singlet yield SphHRep to be determined for arbitrary magnetic field strengths without ever computing the singlet yield for a particular field orientation. We implemented this method using sparse matrix arithmetic in the general purpose `Matlab` code `CalcSphHRep` under the short name "SolveInvL".

8.5.4 Evaluation in a one-proton RP

Once again, we test the accuracy of the SolveInvL method by calculating the singlet yield SphHReps for the same one-proton RP as above. Figures 8.8 and 8.9 show the results obtained when $B_0 = 5\,\mu\mathrm{T}$ and when $B_0 = 50\,\mu\mathrm{T}$. The figures compare these results with converged calculations made using the PyDMAFST algorithm.

On inspection of Figures 8.8(a) and (b), the SolveInvL method clearly converges rapidly. It correctly determines that there are negligible contributions from spherical harmonics with odd l, as required on physical grounds. When MaxL = 10, the singlet yield SphHRep is accurate to within 10^{-16} and is clearly fully converged when MaxL = 20. The polar plots in Figures 8.9(a) and (b) confirm these findings.

In contrast to the InvLSeries perturbative approach, this algorithm is quite able to calculate the singlet yield anisotropy close to a level crossing. Figures 8.8(c) and (d) show that there is still good convergence when $B_0 = 50\,\mu\mathrm{T}$. The higher values of MaxL that are required here reflect the fact that high order spherical harmonics do actually make a significant contribution to the singlet yield anisotropy near a level crossing. Again, the polar plots in Figures 8.9(c) and (d) confirm these findings.

8.6 Scaling

At this point, we have introduced several methods for calculating the singlet yield SphHRep in a RP. Tests made in a carefully chosen one-proton RP show that in weak fields, the PyDMAFST, InvLSeries and SolveInvL methods all converge to the true singlet yield SphHRep. At higher fields, the PyDMAFST and SolveInvL methods remain accurate. We now turn our attention to the performance of these algorithms.

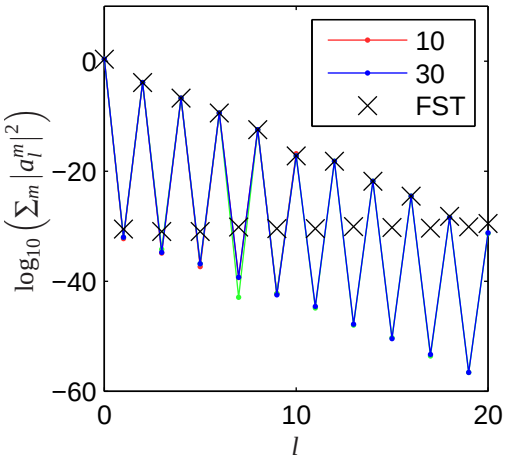

(a) Static field $B_0 = 5\,\mu\text{T}$. Comparison between SolveInvL SphHReps (lines) and converged PyDMAFST ones (×).

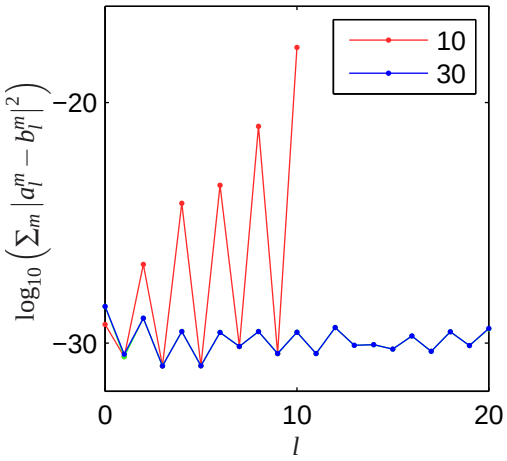

(b) Static field $B_0 = 5\,\mu\text{T}$. Differences between the SolveInvL SphHReps a_l^m and converged PyDMAFST b_l^m.

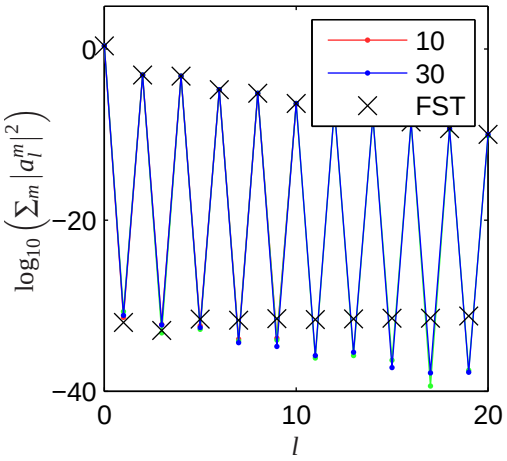

(c) Static field $B_0 = 50\,\mu\text{T}$. Comparison between SolveInvL SphHReps (lines) and converged PyDMAFST ones (×).

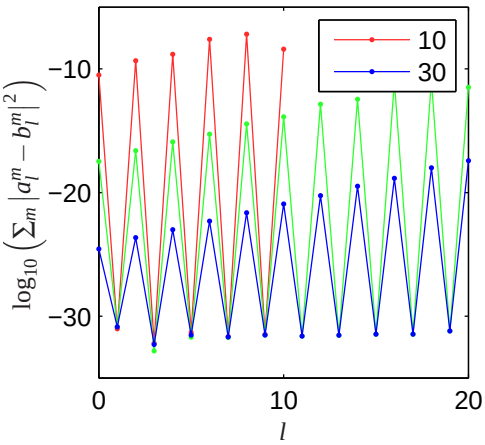

(d) Static field $B_0 = 50\,\mu\text{T}$. Differences between the SolveInvL SphHReps a_l^m and converged PyDMAFST b_l^m.

Figure 8.8: Comparison of SphHReps from the SolveInvL (a_l^m) and converged PyDMAFST (b_l^m or ×) methods. Calculations were made in a one-proton RP using the `CalcSphHRep` code and the following parameters: $k = 2 \times 10^6\,\text{s}^{-1}$, $a = 2.5\,\text{mT}$, $\alpha = 12.5\,\mu\text{T}$ and $\beta = 0\,\mu\text{T}$. The maximum l value before truncation of K (*i.e.* MaxL) is indicated in the legend. Results are given for MaxL values of 10, 20 and 30. A selection of the corresponding polar plots are shown in Figure 8.9.

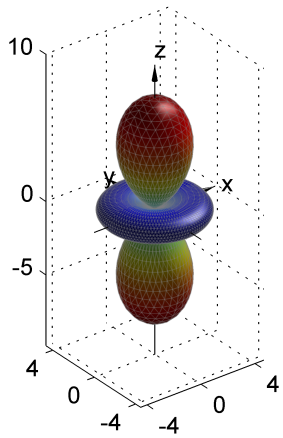

(a) SolveInvL for $B_0 = 5\,\mu\text{T}$ with MaxL = 10.

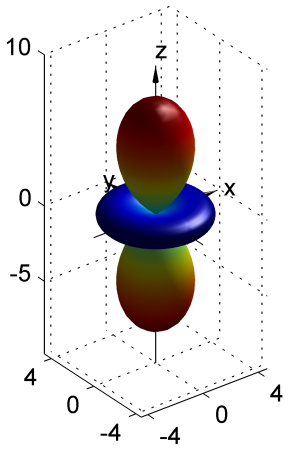

(b) Converged PyDMAFST result for $B_0 = 5\,\mu\text{T}$.

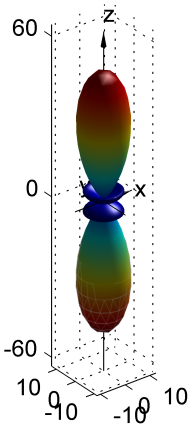

(c) SolveInvL for $B_0 = 50\,\mu\text{T}$ with MaxL = 10.

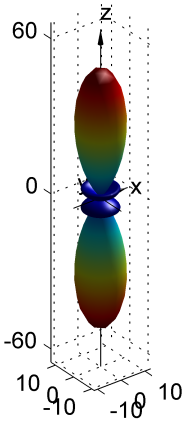

(d) Converged PyDMAFST result for $B_0 = 50\,\mu\text{T}$.

Figure 8.9: Polar plots of $1000\times$ singlet yield anisotropy to accompany Figure 8.8. Calculations were made in a one-proton RP using the `CalcSphHRep` code and the following parameters: $k = 2\times10^6\,\text{s}^{-1}$, $a = 2.5\,\text{mT}$, $\alpha = 12.5\,\mu\text{T}$ and $\beta = 0\,\mu\text{T}$.

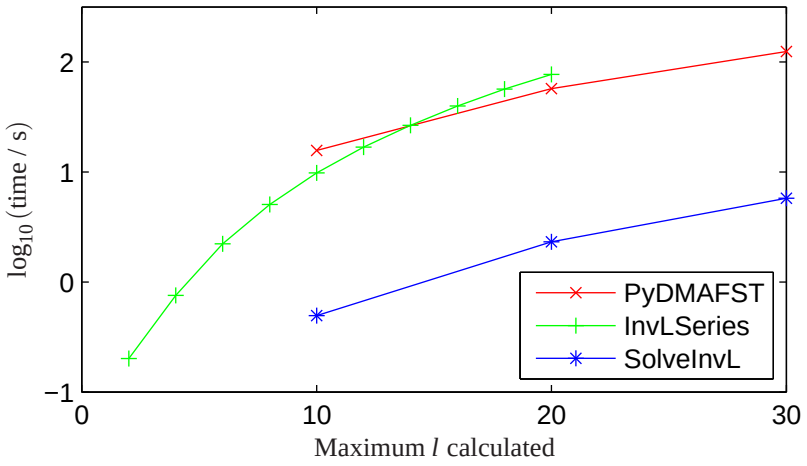

Figure 8.10: Comparison of times to compute the singlet yield SphHRep in a one-proton RP using the different methods developed above. Calculations were made using the `CalcSphHRep` code and the following parameters: $k = 2 \times 10^6\,\mathrm{s}^{-1}$, $a = 2.5\,\mathrm{mT}$, $\alpha = 12.5\,\mu\mathrm{T}$, $\beta = 0\,\mu\mathrm{T}$. The principal axis of the hyperfine tensor lies along the z-axis. These timings do not depend on the static field strength B_0. The corresponding SphHReps are shown in Figures 8.5, 8.6 and 8.8.

8.6.1 Maximum spherical harmonic order

Figure 8.10 compares the performance of these three algorithms by plotting the time taken to find the singlet yield SphHRep in a one proton RP. Timings were measured for a number of different choices of MaxL to assess the scaling of these algorithms when more detailed SphHReps are demanded. In this one-proton RP, the SolveInvL algorithm is clearly fastest; when MaxL $= 30$, it takes only 6 seconds to calculate the SphHRep whilst the PyDMAFST algorithm takes 124. The perturbation theory expansion InvLSeries takes a comparable amount of time to the point-by-point PyDMAFST method.

8.6.2 Multinuclear RPs

Since real RPs almost always contain several magnetic nuclei, we now move on from one-proton RP model systems to compare the accuracy and performance of these methods when applied to multinuclear RPs.

Figure 8.11 shows the time taken by each algorithm to calculate singlet yield SphHReps for a series of "n–0" RPs. All nuclei were spins-½ and the hyperfine tensor of each additional nucleus was chosen at random.

The SolveInvL method did not perform well in multinuclear RPs. Indeed, on a PC with 2GB of RAM, `Matlab`'s sparse matrix solver ran out of memory in a "2–0" RP. Repeating the tests in a series of RPs whose hyperfine tensors all had the same principal axes allowed calculation in a "2–0" RP, presumably because the matrices involved were more sparse. Nevertheless, calculation for three nuclei proved impossible. It is a pity that this algorithm scales so poorly. For one-proton RPs, it performed faster than the other approaches that we have considered. Conceptually, it was attractive to see that the problem of finding a singlet yield SphHRep was equivalent to solving a single

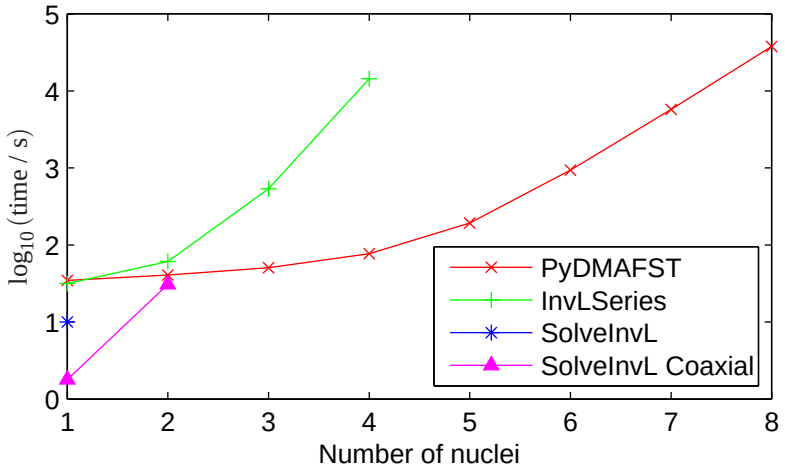

Figure 8.11: Scaling of the different SphHRep methods developed above in multinuclear "n–0" RPs. All nuclei were spins-½ with randomly chosen axial hyperfine tensors. The isotropic HFCs were uniformly distributed between 0 and 1.5 mT and the axiality was uniformly distributed between 0 and 30 µT in a random direction. The same hyperfine tensors were used for all methods before adding an additional nucleus. Calculations were made using the `CalcSphHRep` code and the following parameters: $k = 2 \times 10^6\,\mathrm{s}^{-1}$, $B_0 = 5\,\mu\mathrm{T}$ and MaxL or MaxIter $= 15$. The SphHReps calculated for 1, 2 and 3 nuclei are analysed in Figure 8.12.

matrix equation.

Comparing the InvLSeries and PyDMAFST algorithms, we see that for RPs with more than two magnetic nuclei, the PyDMAFST algorithm can compute with approximately twice as many nuclei as the InvLSeries algorithm in a given amount of time. This difference in scaling is almost certainly due to the fact that the InvLSeries algorithm works in Liouville space, where each superoperator has $(4M)^4$ elements (with M being the number of nuclear spin states), whilst the PyDMAFST algorithm works in Hilbert space, where each operator has only $(4M)^2$ elements. This switch to Liouville space is costly in terms of the memory and CPU time that are required for calculation. In our model, where we neglect relaxation and assume that $k_\mathrm{S} = k_\mathrm{T}$, it is not sensible to use the InvLSeries algorithm for multinuclear RPs. However, the InvLSeries algorithm would be a reasonable choice when working with a model that requires calculations to be made in Liouville space.

Speed is not the only consideration when choosing a computational algorithm. Figure 8.12 compares the SphHReps calculated by the different algorithms in RPs with up to three nuclei. Each figure shows results for PyDMAFST when MaxL $= 15$ and also a "high res" set of results when MaxL $= 30$. These agree very closely, which confirms that the PyDMAFST calculation is well converged.

In Figure 8.12(a), we see that all three methods give the singlet yield SphHRep very accurately. In Figures 8.12(b) and (c), we see that the InvLSeries method is accurate to about 10^{-12}. This level of convergence is reasonable, but the PyDMAFST algorithm does better.

We conclude this evaluation having seen that the PyDMAFST algorithm provides an accurate, efficient algorithm for calculating singlet yield SphHReps. It scales well for RPs containing many nuclei, or when SphHReps must be determined for a large

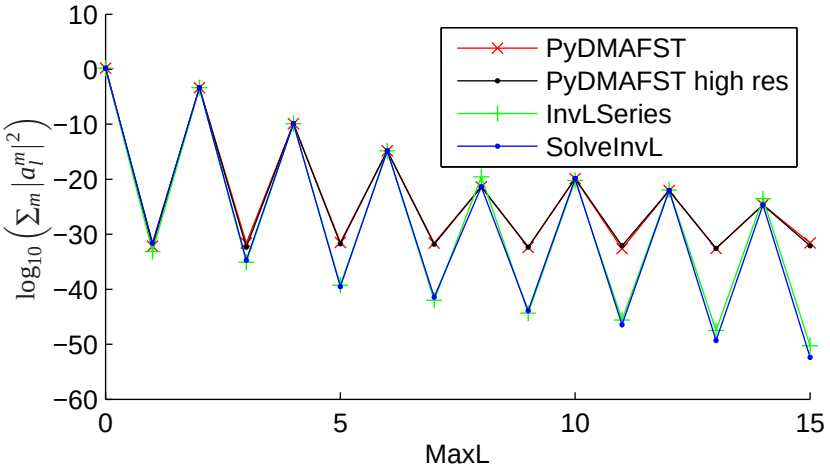

(a) RP with one spin-½ nucleus.

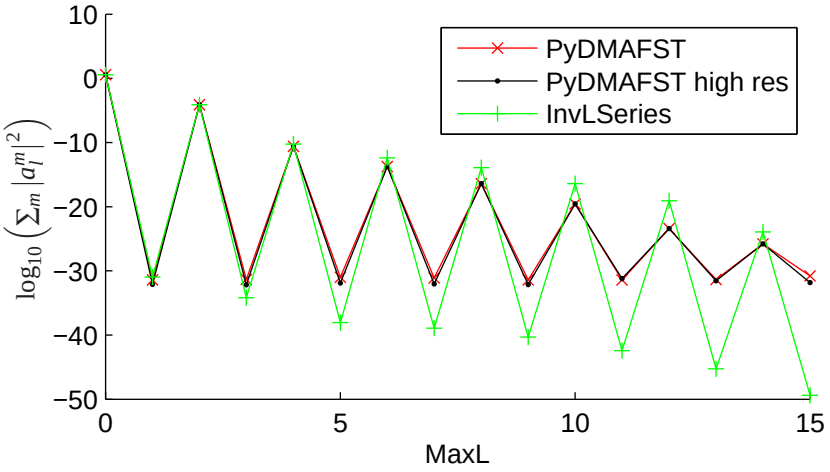

(b) RP with two spin-½ nuclei on the same radical.

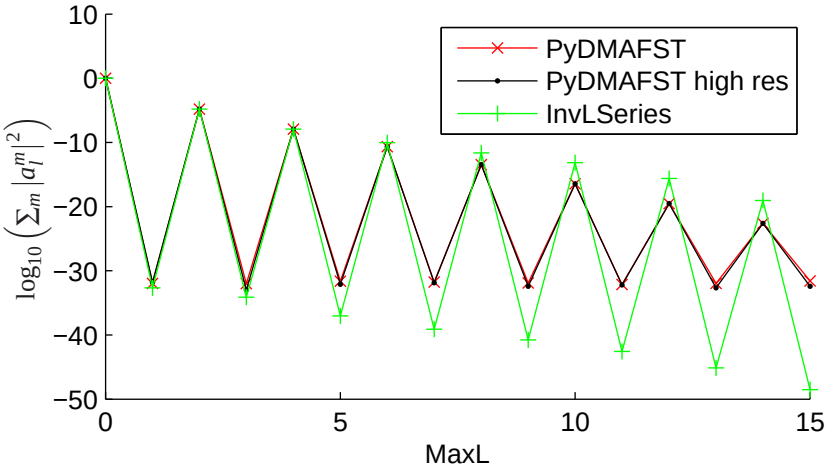

(c) RP with three spin-½ nuclei on the same radical.

Figure 8.12: Analysis of the SphHReps for multinuclear RPs calculated by the methods introduced in this chapter. MaxL $= 15$ for all calculations except for "PyDMAFST high res" which used MaxL $= 30$. Further details are given in the caption of Figure 8.11.

range of l values. Figure 8.11 shows that the PyDMAFST algorithm takes around 10 hours per SphHRep for a RP with 8 magnetic nuclei. Even using a large cluster of computers, such as that provided by the Oxford Supercomputing Centre, 8 magnetic nuclei represents the practical limit for calculation. The limit would be somewhat smaller if we wished to perform Monte Carlo calculations, or to investigate the response of a RP to changes in other model parameters.

8.7 An appropriate statistic

Now that we have a firm understanding of how to calculate singlet yield SphHReps in a wide variety of RP systems, we turn our attention to using the SphHReps to characterise the significant features of a singlet yield anisotropy pattern. In other words, we wish to find a suitable statistic that takes a singlet yield anisotropy pattern and gives a characteristic number that we can use for further analyses, such as plotting graphs.

In §6.3.8, we saw that European robins are only able to orient using static fields whose strength is similar to that of the geomagnetic field [302]. In experiments undertaken in Frankfurt, Germany, robins were able to orient in the Earth's field ($B_0 = 46\,\mu\text{T}$), but were disoriented when the field strength was artificially altered to $B_0 = 34\,\mu\text{T}$ or $B_0 = 60\,\mu\text{T}$. In light of this behaviour, we start our analysis by seeking to understand quantitatively how singlet yield anisotropy depends on B_0. In particular, we wish to see whether trends in the singlet yield anisotropy are consistent with the "B_0 functional window" observed in animal studies.

As test case, we begin with a simple one-proton RP, whose hyperfine tensor has been chosen so that there is an energy level crossing at a field strength comparable to the geomagnetic field. For this RP, we calculate 100 singlet yield anisotropy polar plots and SphHReps at fields distributed logarithmically in the range $B_0 = 1\,\mu\text{T}$–$1\,\text{mT}$. Four of these polar plots are shown in Figures 8.13(a–d). Figures 8.13(a) and (d) are representative of the response when $B_0 < 10\,\mu\text{T}$ and when $B_0 > 100\,\mu\text{T}$ respectively. Meanwhile, Figures 8.13(b) and (c) show the unusual shapes that arise for B_0 values close to the energy level crossing. Below these polar plots, Figures 8.13(e)–8.16 plot a variety of different statistics against the static field strength B_0. We now turn to discuss the merits of these different combinations of spherical harmonic coefficients.

8.7.1 Expectation value of "angular momentum"

The first statistic that we consider would be the expectation value of angular momentum for a quantum mechanical rigid rotor, whose eigenstates are the spherical harmonics. For a wavefunction $|l,m\rangle = Y_l^m(\theta,\phi)$, the angular momentum expectation value is

$$\left\langle \hat{L}^2 \right\rangle = \langle l,m|\,\hat{L}^2\,|l,m\rangle = l(l+1)\hbar^2. \tag{8.93}$$

Hence, by analogy, for a SphHRep with coefficients a_l^m, we consider the statistic

$$\left\langle l^2 \right\rangle = \sum_{l,m} |a_l^m|^2\, l(l+1). \tag{8.94}$$

This quantity is plotted against B_0 in Figure 8.13(e); the contributions from each value of l are shown in Figure 8.13(f).

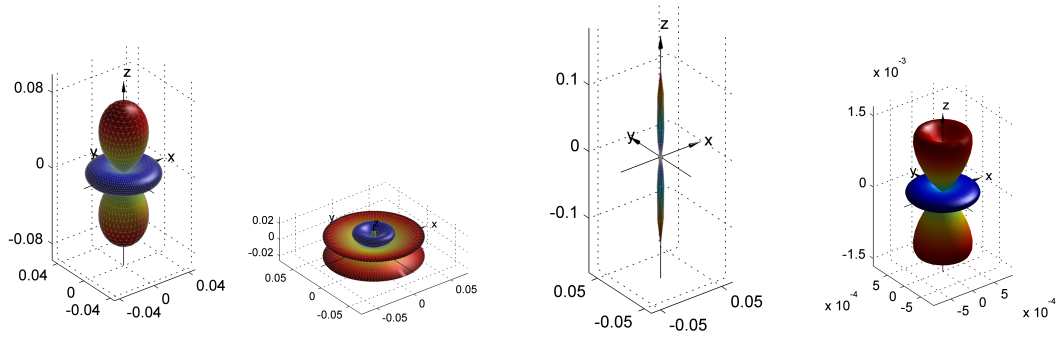

(a) Φ_S^{an} when $B_0 = 4.6\,\mu T$ (b) Φ_S^{an} when $B_0 = 23\,\mu T$ (c) Φ_S^{an} when $B_0 = 38\,\mu T$ (d) Φ_S^{an} when $B_0 = 160\,\mu T$

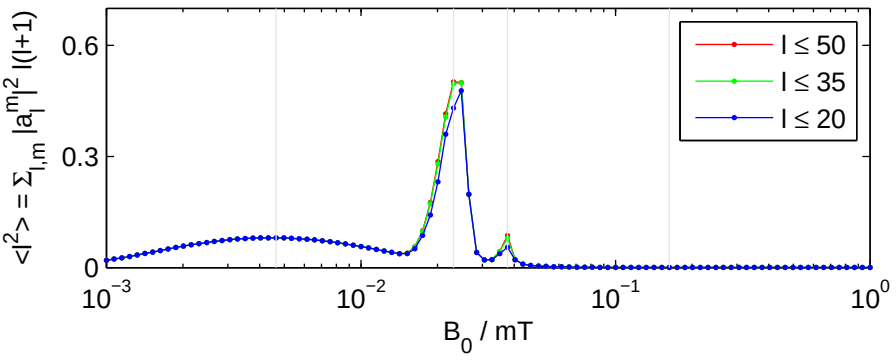

(e) Convergence of $\langle l^2 \rangle$ at MaxL = 20, 35 and 50

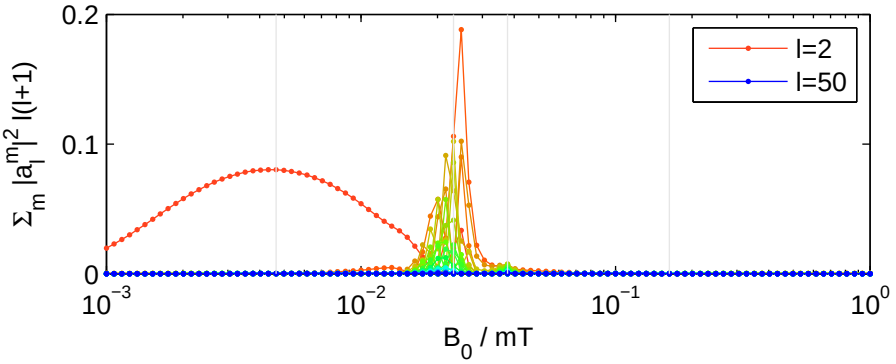

(f) Contributions to $\langle l^2 \rangle$ for each l value

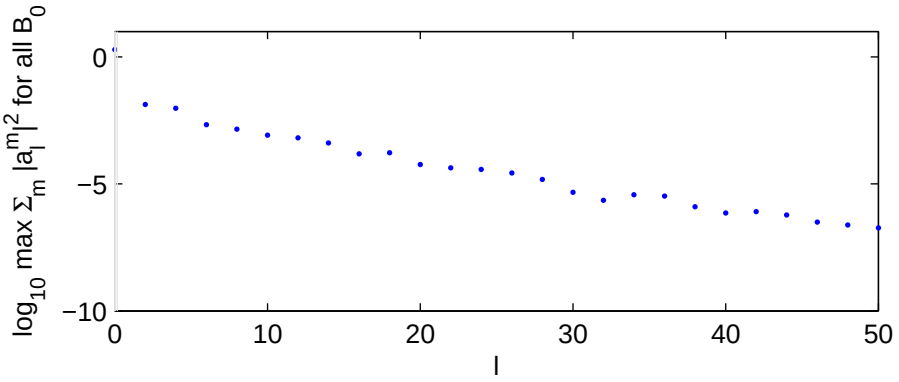

(g) Significance of contributions to the B_0 trend from each l value

Figure 8.13: Effect of B_0 on singlet yield $\Phi_S(\theta, \phi)$. Calculations were performed in a one-proton RP model system using the PyDMAFST algorithm with $k = 2 \times 10^5\,s^{-1}$, HFC $a = 2.5\,mT$, $\alpha = 12.5\,\mu T$, $\beta = 0$ and MaxL = 50. Figures (a–d) show singlet yield anisotropies at the B_0 values marked with grey vertical lines.

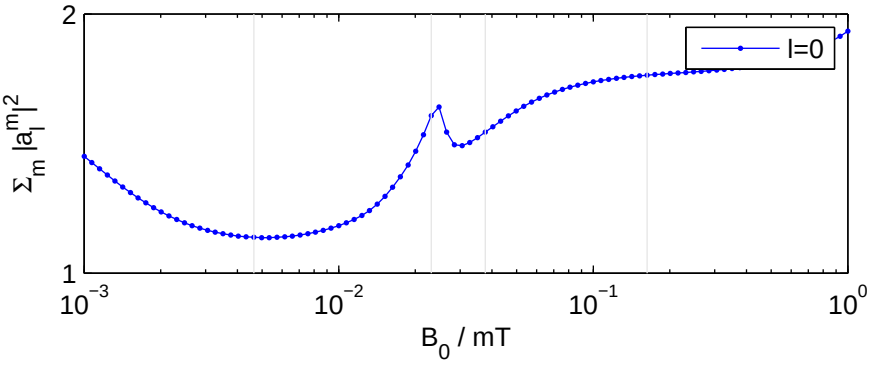

(a) Rotational invariant $\left|a_0^0\right|^2 = 4\pi \times \bar{\Phi}_S^2$

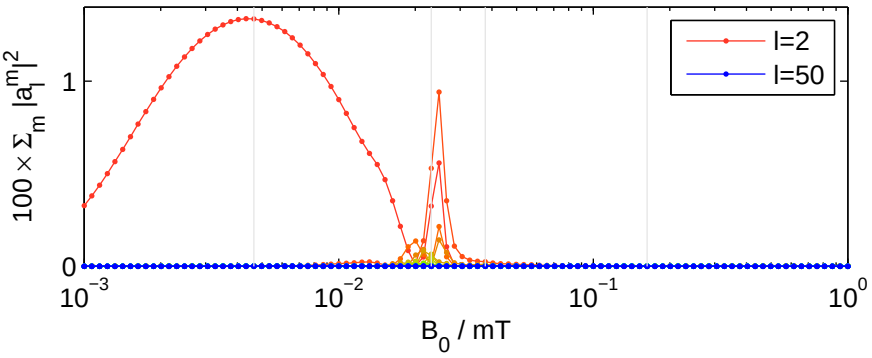

(b) Rotational invariants $\sum_m \left|a_l^m\right|^2$ for each l value

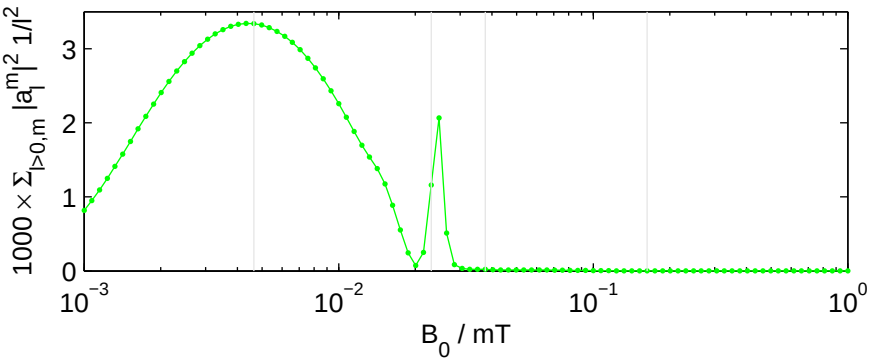

(c) Hybrid statistic which favours strong and simple (low l) singlet yield anisotropy

Figure 8.14: Further attempts to quantify the changes in singlet yield anisotropy caused by B_0. Parameters are given in Figure 8.13.

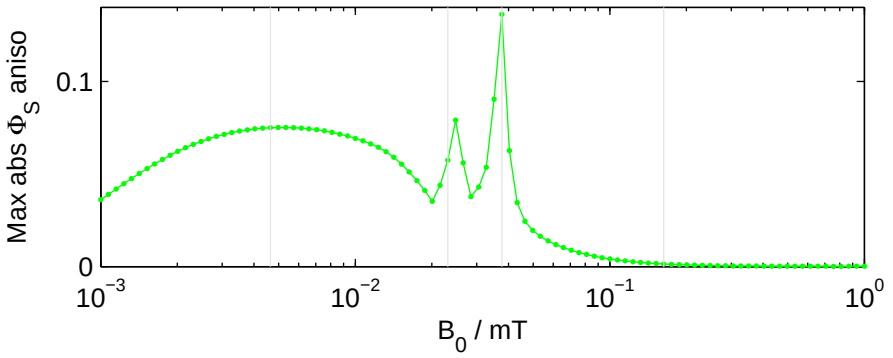

(a) Maximum $\left|\Phi_S^{\mathrm{an}}(\theta,\phi)\right|$

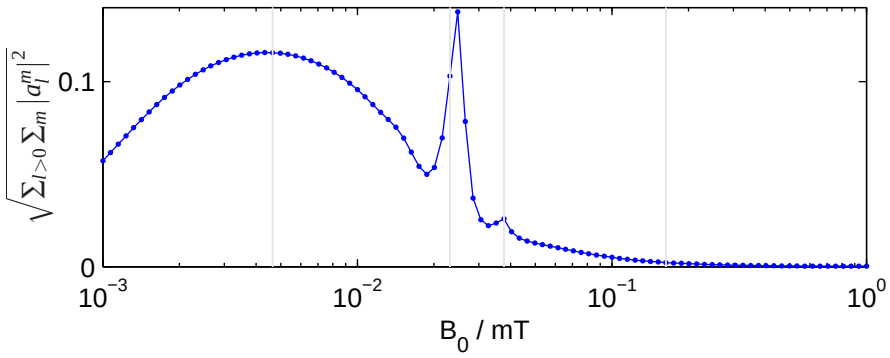

(b) RMS singlet yield anisotropy

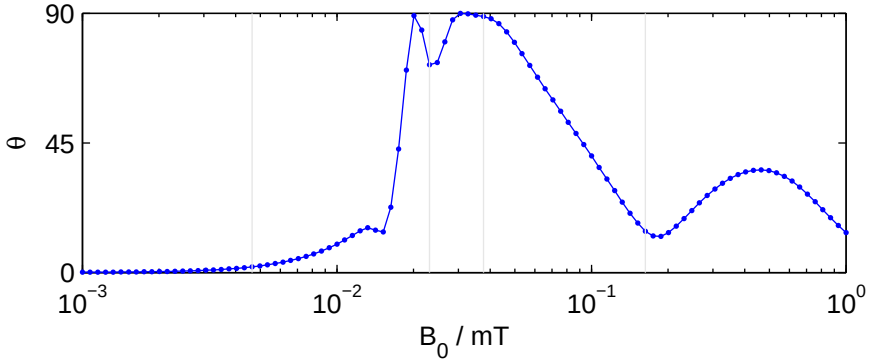

(c) "Angle" θ_1 between the yield patten and a pure $Y_2^m(\theta,\phi)$ defined by equation (8.100)

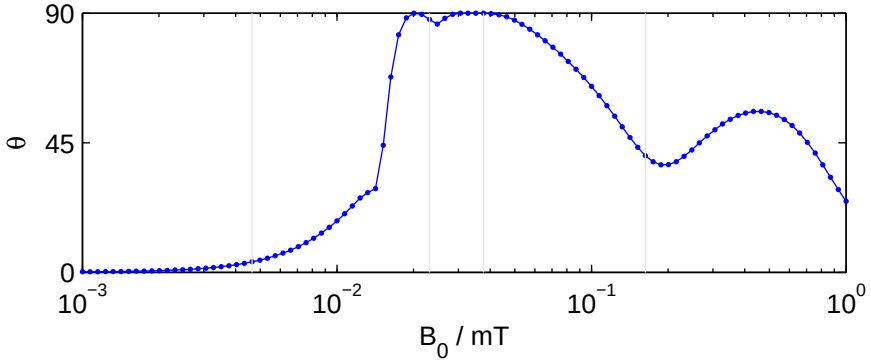

(d) Another "angle" θ_2 between the yield patten and a pure $Y_2^m(\theta,\phi)$ defined by equation (8.101)

Figure 8.15: Further attempts to quantify the changes in singlet yield anisotropy caused by B_0. Parameters are given in Figure 8.13.

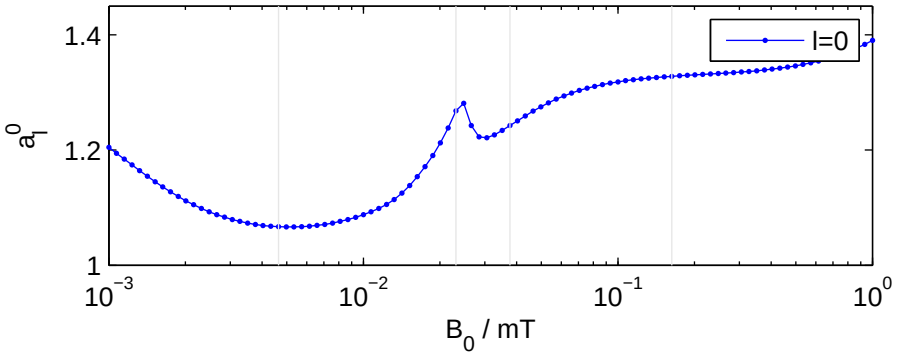

(a) Contributions with $m = 0$ that determine Ritz's visual modulation patterns

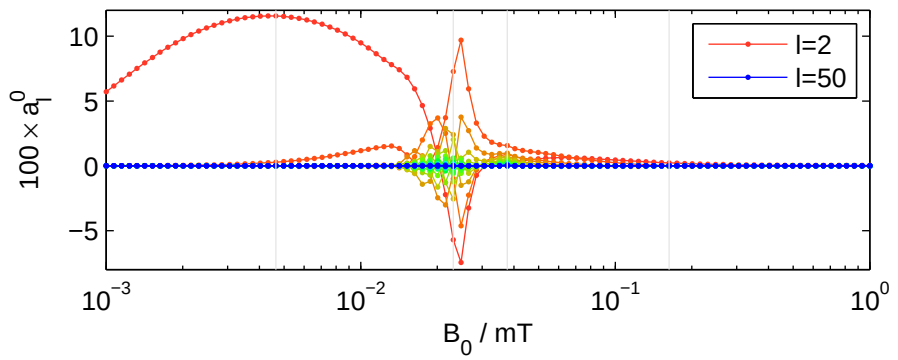

(b) Contributions with $m = 0$ that determine Ritz's visual modulation patterns

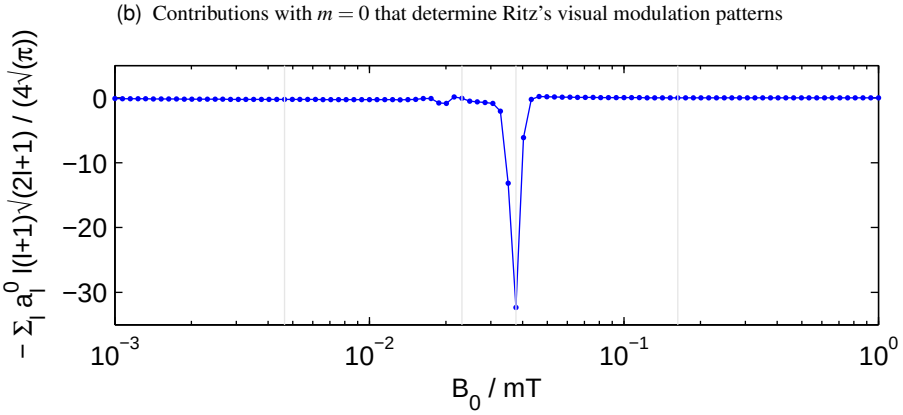

(c) Second derivative of the axial average singlet yield with respect to θ at the North pole

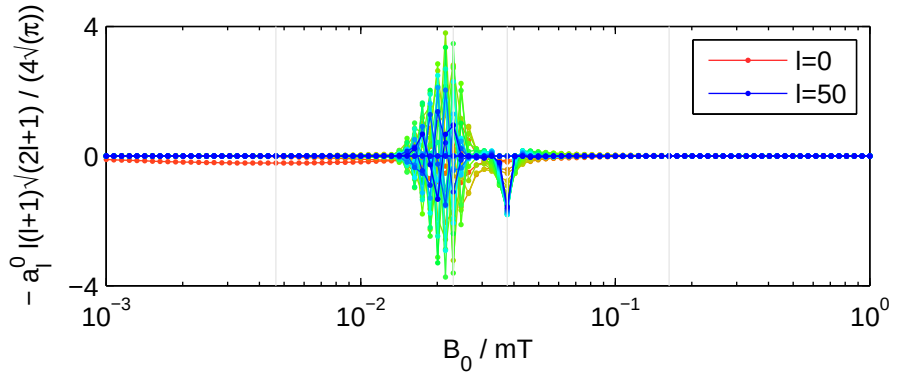

(d) Contributions to the second derivative of the axial average singlet yield with respect to θ at the North pole

Figure 8.16: Further attempts to quantify the changes in singlet yield anisotropy caused by B_0. Parameters are given in Figure 8.13.

Now, since the spherical harmonics are irreducible representations of the rotation group, we know that the quantities

$$\sum_m |a_l^m|^2 \tag{8.95}$$

are invariant under rotations. Hence, the statistic $\langle l^2 \rangle$ does not depend on the orientation of the RP with respect to the laboratory coordinate axes. This seems advantageous, since the amount of compass information available from a RP reaction ought not to depend on our choice of axis system.

The weighting factor $l(l+1)$ favours strongly anisotropic, high-order singlet yield patterns such as those found near energy level crossings. As a whole, the $\langle l^2 \rangle$ statistic favours singlet yield anisotropy patterns that are strong and which have distinctive, high-order shapes.

However, Figure 8.13(g) shows that the contributions to the B_0 trend decrease approximately exponentially with l. This decrease with eventually dominate the quadratically increasing weighting factor $l(l+1)$. Nevertheless, a disadvantage of this statistic is that it requires that the singlet yield SphHRep be determined for rather large values of MaxL in order to give good convergence, as is shown in Figure 8.13(e).

8.7.2 Rotational invariants

The rotational invariance arising from equation (8.95) is an attractive property when quantifying SphHReps. There is, however, no reason to be restricted to the $l(l+1)$ weighting factors that we used above. Figures 8.14(a) and (b) plot the rotationally invariant contributions $\sum_m \left|a_l^m\right|^2$ as a function of B_0. It is interesting to see the strong contributions from $l = 2$ spherical harmonics when $1\,\mu\text{T} < B_0 < 10\,\mu\text{T}$.

We may favour strong, but simple anisotropy patterns by weighting these rotational invariants. For example, the statistic in Figure 8.14(c) favours strong singlet yield anisotropy patterns that are dominated by the $l = 2$ spherical harmonics. One could imagine such "simple" anisotropy patterns forming the basis for a reliable compass. Notice also that only fields $1\,\mu\text{T} < B_0 < 10\,\mu\text{T}$ give a strong response to this statistic. This is reminiscent of the small range of field strengths for which European robins can orient successfully.

8.7.3 Magnitude of anisotropic response

The statistics that we have discussed so far measure both the magnitude and shape of a singlet yield anisotropy pattern. When further details of the biological processes involved in magnetoreception emerge, we may discover instead that either the magnitude or the shape of the anisotropy pattern is most important for the operation of magnetoreception. Figures 8.15(a) and (b) are two attempts to quantify the magnitude of the anisotropy pattern whilst ignoring its shape.

In Figure 8.15(a), we plot the maximum absolute singlet yield anisotropy. This statistic is very simple to determine directly from a singlet yield polar plot, without first performing a spherical harmonic decomposition analysis. We include it here for completeness. Despite its simplicity, this statistic has two important weaknesses. First, multinuclear RP singlet yield anisotropies often have very irregular shapes. In that

case, the maximum singlet yield anisotropy may depend critically on the relative orientation of the RP with respect to the mesh. For example, in Figures 7.25(b–d), which differ only in the orientation of the RP with respect to the laboratory axis system, the maximum absolute singlet yield anisotropy at the mesh resolution used would differ markedly. In order to prevent such problems, we would have to perform a time consuming calculation with a very fine mesh. Second, the maximum absolute singlet yield anisotropy gives undue significance to the sharp "spikes" and "wings" that appear in some singlet yield anisotropy polar plots. This does not seem physically reasonable.

Figure 8.15(b) attempts to give a more robust measure of the magnitude of the singlet yield anisotropy. For a function $f(\theta,\phi) = \sum_{l,m} a_l^m Y_l^m(\theta,\phi)$, it follows from equation (8.4) that

$$\int_0^{2\pi}\int_0^{\pi} |f(\theta,\phi)|^2 \sin\theta \,\mathrm{d}\theta \,\mathrm{d}\phi = \sum_l \sum_m |a_l^m|^2 . \tag{8.96}$$

Hence, the singlet yield anisotropy $\Phi_{\mathrm{S}}^{\mathrm{an}}(\theta,\phi)$ has root-mean-square value

$$\sqrt{\int_0^{2\pi}\int_0^{\pi} \left|\Phi_{\mathrm{S}}^{\mathrm{an}}(\theta,\phi)\right|^2 \sin\theta \,\mathrm{d}\theta \,\mathrm{d}\phi} = \sqrt{\sum_{l>0} \sum_m \left|a_l^m\right|^2}, \tag{8.97}$$

where $\Phi_{\mathrm{S}}(\theta,\phi) = \sum_{l,m} a_l^m Y_l^m(\theta,\phi)$. This statistic is rotationally invariant and captures the magnitude of the singlet yield anisotropy.

8.7.4 Shape of the anisotropic response

Alternatively, one may envisage the absolute magnitude of the singlet yield anisotropy being relatively unimportant. This might be the case if magnetoreception were to occur as an adjunct to vision, which was suggested in §6.5.2. Between conditions of bright sunlight and a dark overcast night, the eye undergoes dark adaptation, adjusting its sensitivity by many orders of magnitude. We might imagine that this process, or a similar one, could compensate for enormous changes in the overall magnitude of the singlet yield anisotropy. From this point of view, the existence of a narrow functional window of static field strengths in which robins can orient would arise from changes in the shape of the singlet yield anisotropy. A robin that had learned to recognise the pattern of singlet yield anisotropy at $B_0 = 46\,\mu\mathrm{T}$ might well become disoriented if a change in field strength caused the pattern to change substantially. However, the bird could learn to interpret the new anisotropy pattern if given time to acclimatise. This should be a rapid adjustment, because it involves no physiological changes. Behavioural experiments show that with one hour of acclimatisation, robins can orient in a much wider range of static field strengths [310].

Let us suppose that the "ideal" or "normal" singlet yield anisotropy pattern is a

pure $Y_2^0(\theta,\phi)$ spherical harmonic. This perfect pattern has the SphHRep

$$\boldsymbol{I} = \begin{pmatrix} 0 \\ 0 \\ 0 \\ 0 \\ 0 \\ 0 \\ 1 \\ 0 \\ 0 \\ \vdots \end{pmatrix}. \tag{8.98}$$

For a calculated singlet yield SphHRep $\boldsymbol{a}$, we wish in some sense to determine the angle θ defined by a "dot product" between the actual SphHRep $\boldsymbol{a}$ and the ideal SphHRep $\boldsymbol{I}$:

$$\cos\theta = \frac{\boldsymbol{a}\cdot\boldsymbol{I}}{|\boldsymbol{a}|\,|\boldsymbol{I}|}. \tag{8.99}$$

Once again, it would seem reasonable to choose a statistic that is rotationally invariant. Hence, we introduce the following measures of the shape of the anisotropy pattern:

$$\cos\theta_1 = \frac{\sum_m \left|a_2^m\right|^2}{\sum_{l>0}\sum_m \left|a_l^m\right|^2} \tag{8.100}$$

or

$$\cos\theta_2 = \frac{\sum_m 2(2+1)\left|a_2^m\right|^2}{\sum_l l(l+1)\sum_m \left|a_l^m\right|^2}. \tag{8.101}$$

When the singlet yield anisotropy is composed purely of $Y_2^m(\theta,\phi)$ spherical harmonics, then $\theta_1 = \theta_2 = 0^\circ$. On the other hand, when the singlet yield anisotropy has no $Y_2^m(\theta,\phi)$ contributions, then $\theta_1 = \theta_2 = 90^\circ$. These two statistics are plotted against B_0 in Figures 8.15(c) and (d). It is clear that the singlet yield anisotropy most closely resembles a pure $Y_2^m(\theta,\phi)$ shape when $B_0 < 10\,\mu\mathrm{T}$.

It is possible that one might envisage a particular yield pattern as "ideal" for a magnetic compass. Although we have not done so, it is possible to analyse the singlet yield SphHRep using FFT methods to determine what amount of this — possibly rotated — "ideal" shape is present in a particular yield pattern. Such spherical matched filtering techniques are mentioned by Healy [370, §7.2] and by Kostelec [376].

8.7.5 Visual modulation figures

The final set of statistics that we consider are inspired by the visual modulation patterns proposed by Ritz. As was explained in §7.4.1, if the avian magnetic compass is based on RPM reactions taking place in the retina, then it could be perceived as a modulation of the bird's vision. According to equations (7.14) and (7.22), the perceived pattern

depends on the average axial singlet yield $\widetilde{\Phi}_{\mathrm{S}}(\theta)$. Writing the singlet yield in terms of spherical harmonics, this is given by

$$\widetilde{\Phi}_{\mathrm{S}}(\theta) = \int_0^{2\pi} \Phi_{\mathrm{S}}(\theta,\phi)\,\mathrm{d}\phi \tag{8.102}$$

$$= \sum_{l,m} a_l^m \int_0^{2\pi} Y_l^m(\theta,\phi)\,\mathrm{d}\phi = \sum_l 2\pi a_l^0 Y_l^0(\theta). \tag{8.103}$$

In other words, only spherical harmonics with $m = 0$ contribute to the visual modulation patterns. Figure 8.17 shows visual modulation patterns for the first few spherical harmonics. It also shows how the modulation patterns vary when a bird looks in different directions ζ relative to the geomagnetic field. Notice that these modulation patterns have a characteristic pattern of rings around the North–South axis when $\zeta = 0^\circ$. There is also a characteristic symmetry axis when the bird heads due East or West with $\zeta = 90^\circ$.

Figures 8.16(a) and (b) show plots of the a_l^0 spherical harmonic coefficients that determine the visual modulation patterns. Whilst these quantities are not rotationally invariant, they do arise naturally in Ritz's model. Once again, we see many contribution from high-order harmonics around the level crossing when $B_0 \approx 20\,\mu\mathrm{T}$. At lower fields, the singlet yield anisotropy is dominated by $Y_2^0(\theta)$ contributions, whilst at higher fields, the singlet yield anisotropy diminishes rapidly.

The final statistic that we consider is also derived from the visual modulation figures. One might assume that a vivid central spot in the modulation pattern when looking along the geomagnetic field is important for orientation. This would be equivalent to favouring highly elongated, cigar shaped, singlet yield anisotropy patterns. We can quantify this by measuring the second derivative of the anisotropy pattern at the North pole. When the second derivative is large and negative, the singlet yield anisotropy will be highly curved at the North pole and the visual modulation pattern will show a bright central spot.

We calculate this derivative from the spherical harmonic decomposition using the fact that

$$\left.\frac{\mathrm{d}^2 Y_l^0(\theta)}{\mathrm{d}\theta^2}\right|_{\theta=0} = \frac{-l(l+1)\sqrt{2l+1}}{4\sqrt{\pi}}. \tag{8.104}$$

Hence, the statistic

$$-\sum_l \frac{-l(l+1)\sqrt{2l+1}}{4\sqrt{\pi}} a_l^0 \tag{8.105}$$

gives an indication of the presence of a bright central spot in the modulation pattern. This function is plotted in Figures 8.16(c) and (d).

8.8 Trends in singlet yield anisotropy

The foregoing discussion illustrates the versatility of spherical harmonic decomposition for the analysis of singlet yield anisotropy patterns. It is possible to combine the

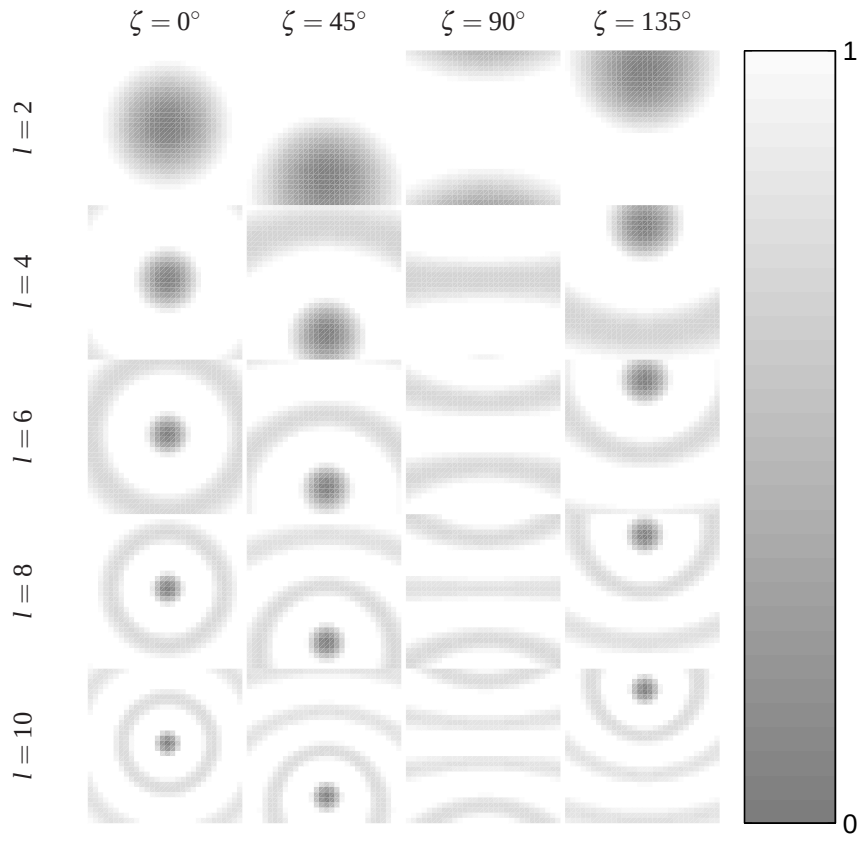

Figure 8.17: Visual modulation patterns for systems with average axial singlet yield $\widetilde{\Phi}_{\mathrm{S}} = Y_l^0(\theta)$. Patterns are calculated for the first few spherical harmonics according to the procedure in §7.4.1. The angle between the centre of view and the geomagnetic field is denoted ζ.

spherical harmonic coefficients to produce measures of the shape of a singlet yield anisotropy pattern, of its magnitude, or of a combination of the two. Since it is not yet known which of these properties is most important for the operation of an RPM-based compass in nature, we use three statistics to analyse the response of a one-proton RP model system. We quantify singlet yield anisotropies using equation (8.97) as a measure of their magnitude, equation (8.100) as a measure of shape and equation (8.94) as a hybrid measure of both.

8.8.1 Effect of RF field strength

Figure 8.18 shows the changes in singlet yield anisotropy brought about in our model RP by a radio frequency field. In these tests we apply no static field ($B_0 = 0\,\mathrm{mT}$) and the radio frequency is chosen to be in resonance with the isotropic part of the hyperfine interaction. Whereas previously the orientation of the static field $\boldsymbol{B}_0$ was described by spherical polar angles (θ, ϕ), we now move the RF field $\boldsymbol{B}_1$ instead.

Inspecting Figure 8.18(e), we see that when $B_1 = 16\,\mu\mathrm{T}$ the RMS singlet yield anisotropy is comparable to that produced by a static field of similar strength in Figure 8.15(b). This illustrates an important general principle: RF and static fields of similar magnitude $B_0 \approx B_1$ produce similar singlet yield anisotropies when both or neither is on resonance.

In Figures 8.18(b), (c), (e) and (f) we see that at higher RF field strengths, $100\,\mu\mathrm{T} < B_1 < 1\,\mathrm{mT}$, a resonant RF field can produce unusual non-Y_2^m-like singlet yield anisotropies. Notice also that the RMS anisotropy metric in Figure 8.18 correctly reports cases (b) and (c) as being less anisotropic than (a). Measurements of the maximum absolute singlet yield would not follow this trend.

Finally, we notice that at certain RF field strengths, the singlet yield anisotropy may be quite anomalous. For example, when $B_1 = 6.3\,\mathrm{mT}$, as shown in Figure 8.18(d). This anomaly is detected by all three statistics, although it is not clear where its physical origin lies.

8.8.2 Effect of radio frequency

We would expect that in addition to the RF field strength B_1, the radio frequency ν_{rf} should play an important role in determining the singlet yield response to an RF field. Figure 8.19 shows the effects of a $B_1 = 1\,\mu\mathrm{T}$ field at frequencies between 10 and 150 MHz. As we might expect, by far the strongest response is at 70 MHz: the frequency that is in resonance with the isotropic hyperfine interaction. However, the shape of the singlet yield anisotropy responds differently. In Figure 8.19(f), we see that the shape changes most at frequencies around 88 MHz.

Similar calculations are presented in Figure 8.20 for an RF field that is one hundred times stronger: $B_1 = 100\,\mu\mathrm{T}$. There, we see a rather broader resonance around the hyperfine resonance frequency of 70 MHz. Notice that the RMS singlet yield anisotropy is around 1000 times larger, even though B_1 only increased one-hundredfold; this is characteristic of a resonant response. Finally, we observe in Figure 8.20 that the RMS singlet yield anisotropy drops slightly around 70 MHz. As shown in the polar plot, Figure 8.20(b), this drop is due to developing contributions from high-order spherical

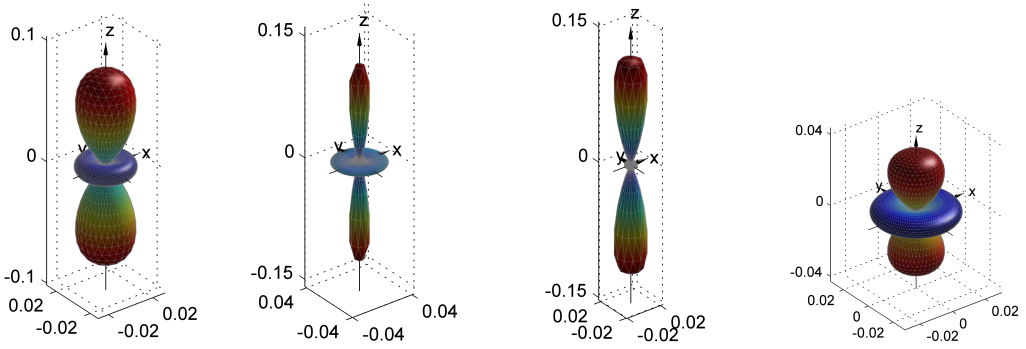

(a) Φ_S^{an} when $B_1 = 16\,\mu T$ (b) Φ_S^{an} when $B_1 = 60\,\mu T$ (c) Φ_S^{an} when $B_1 = 980\,\mu T$ (d) Φ_S^{an} when $B_1 = 6.3\,mT$

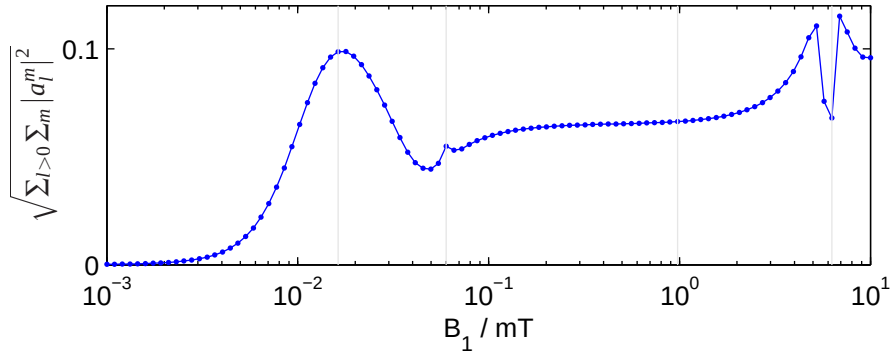

(e) Magnitude of singlet yield anisotropy

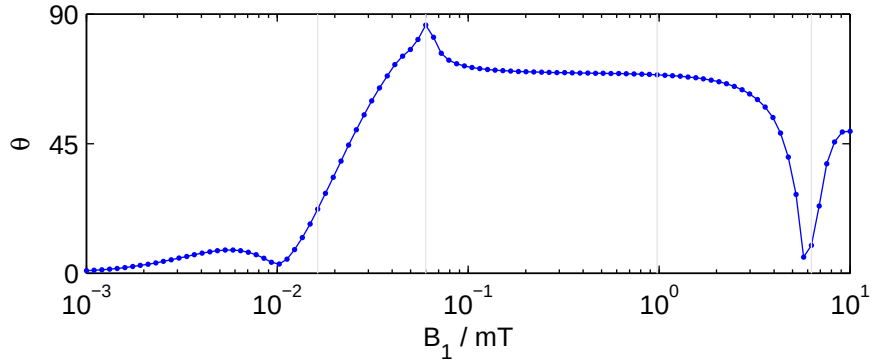

(f) Shape of singlet yield anisotropy where $\theta = \theta_1$ is defined by equation (8.100)

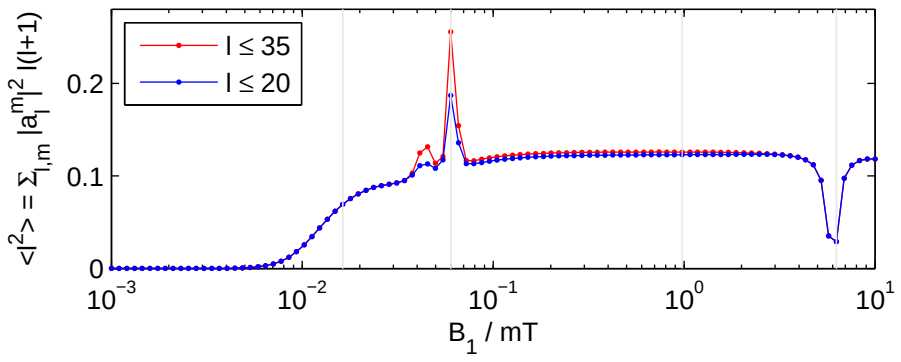

(g) Hybrid measure of magnitude and shape of singlet yield anisotropy

Figure 8.18: Effect of B_1 on singlet yield. Calculations were performed in a one-proton RP model system using the gCOMPFST algorithm with $k = 2 \times 10^5\,s^{-1}$, $B_0 = 0\,mT$, HFC $a = 2.5\,mT$, $\alpha = 12.5\,\mu T$, $\beta = 0$, $n = 128$, $\nu_{rf} = 2.5 \times 28 = 70\,MHz$, and MaxL $= 35$. Figures (a–d) show singlet yield anisotropies at the B_1 values marked with grey vertical lines.

harmonics that make the singlet yield anisotropy rather cigar shaped in the presence of these stronger resonant RF fields.

Figures 8.18–8.20 show that RF fields could form the basis of future animal behavioural studies. Since RF and static fields of similar strength produce similar RMS singlet yield anisotropy, we might envisage testing birds in the presence of an RF field alone. It seems reasonable to expect that, after acclimatisation, a bird with an RPM-based compass sense might be *reoriented* along the direction $\boldsymbol{B}_1$. It seems quite implausible that a magnetite-based compass would show the same reorientation behaviour. Such findings would provide positive evidence for the existence of an RPM-based compass that would compliment existing studies using combined RF and static fields to *disorient* birds (see Chapters 6, 9 and [231, 232, 314]).

8.8.3 Effect of exponential model rate constant

Figure 8.21 shows the effect of the exponential model rate constant k on singlet yield anisotropy. Increasing k, *i.e.* decreasing the lifetime of the RP, seems uniformly to decrease the RMS singlet yield anisotropy. The shape of the anisotropy that remains does not depend strongly on the rate constant k. For most values of k, the singlet yield anisotropy resembles the "ideal" Y_2^m shape as shown in Figure 8.21. These calculations confirm our belief that only a long-lived RP would be suitable as the basis of a magnetic compass sense.

8.8.4 Effect of axiality

The final parameter that we consider is the axiality of the hyperfine tensor. Figure 8.22 shows how the static field dependence of the singlet yield anisotropy depends on α/a. When $\alpha = 0$, the singlet yield is entirely isotropic. Hence, the deep blue curves in Figures 8.22(a) and (c) are zero for all B_0. The shape parameter in Figure 8.22(b) is large because the small numerical errors in calculating the singlet yield give rise to an "anisotropy" that differs markedly from the "ideal" Y_2^m shape.

In other cases, the energy level crossing moves in B_0 according to the extent of the axiality α. Hence, the sharp feature in Figures 8.22(a–c) appears at different B_0 values depending on the axiality α. This behaviour is as we would expect. Nonetheless, it demonstrates the power of these spherical harmonic analysis methods.

8.9 Conclusions

In the previous chapter, we investigated the singlet yield anisotropy patterns arising from several model RPs containing flavin. During that work, it became increasingly apparent that polar plots of singlet yield anisotropy are not ideal for analysing and interpreting trends in such model RP systems. Although such plots may be rather beautiful, they require detailed inspection before conclusions can be drawn. In this chapter, we introduced a set of tools designed to allow automated analysis of singlet yield anisotropy patterns.

We have shown that it is helpful to decompose the singlet yield into a sum of contributions from different spherical harmonics: into a SphHRep. We derived efficient algorithms for computing these SphHReps in RPs containing up to eight groups of

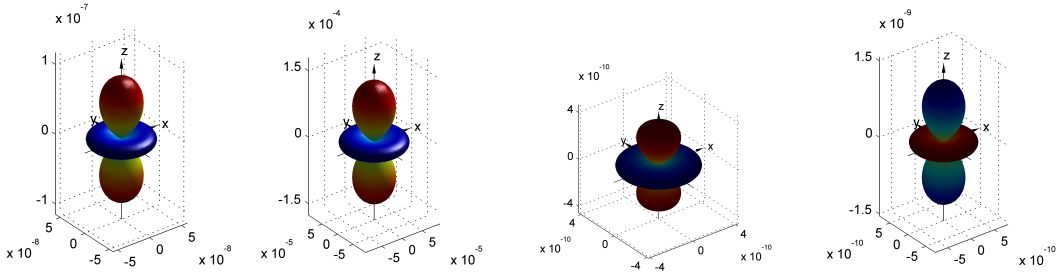

(a) Φ_S^{an} at $\nu_{rf} = 10\,\text{MHz}$ (b) Φ_S^{an} at $\nu_{rf} = 70\,\text{MHz}$ (c) Φ_S^{an} at $\nu_{rf} = 88\,\text{MHz}$ (d) Φ_S^{an} at $\nu_{rf} = 150\,\text{MHz}$

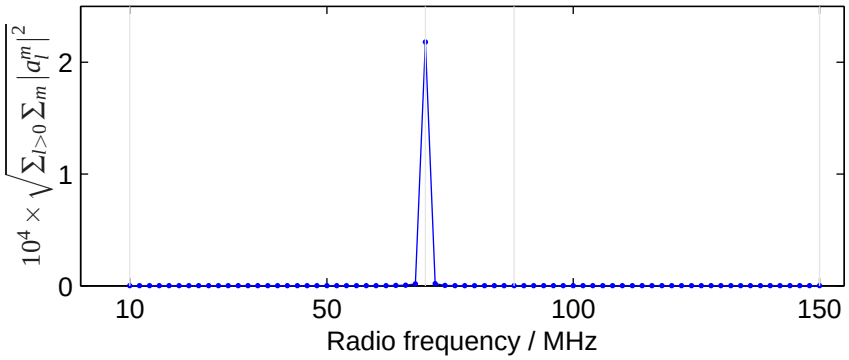

(e) Magnitude of singlet yield anisotropy

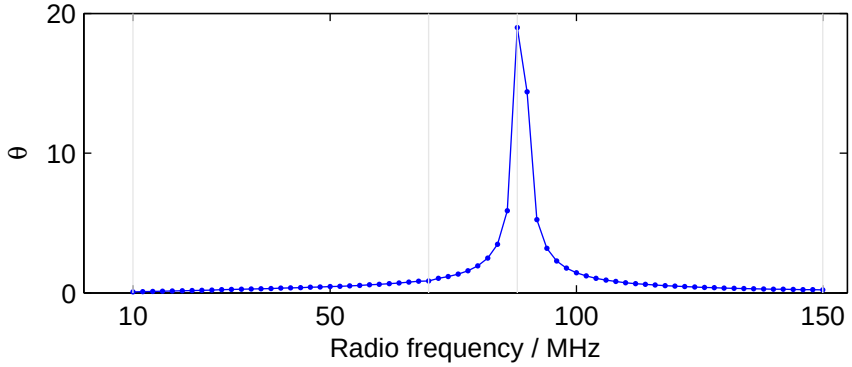

(f) Shape of singlet yield anisotropy where $\theta = \theta_1$ is defined by equation (8.100)

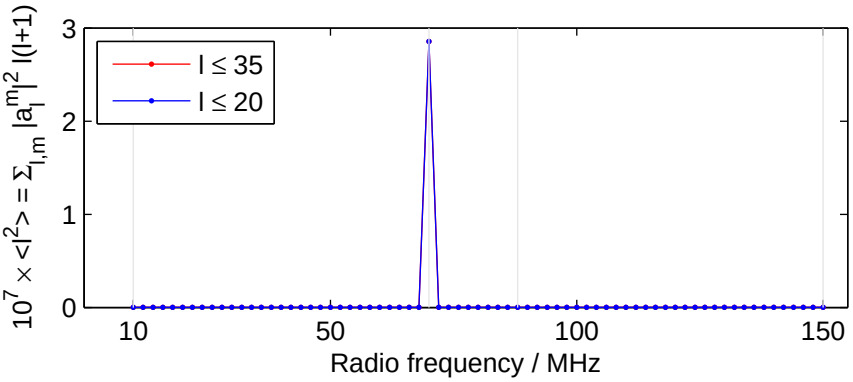

(g) Hybrid measure of magnitude and shape of singlet yield anisotropy

Figure 8.19: Effect of radio frequency ν_{rf} on singlet yield. Calculations were performed in a one-proton RP model system using the gCOMPFST algorithm with $B_1 = 1\,\mu\text{T}$, $k = 2 \times 10^5\,\text{s}^{-1}$, HFC $a = 2.5\,\text{mT}$, $\alpha = 12.5\,\mu\text{T}$, $\beta = 0$, $n = 128$, and MaxL $= 35$. Figures (a–d) show singlet yield anisotropies at the ν_{rf} values marked with grey vertical lines.

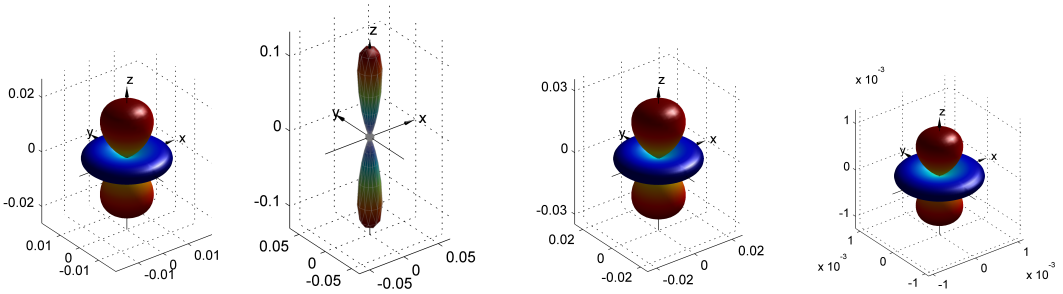

(a) Φ_S^{an} at $\nu_{rf} = 10\,\mathrm{MHz}$ (b) Φ_S^{an} at $\nu_{rf} = 70\,\mathrm{MHz}$ (c) Φ_S^{an} at $\nu_{rf} = 88\,\mathrm{MHz}$ (d) Φ_S^{an} at $\nu_{rf} = 150\,\mathrm{MHz}$

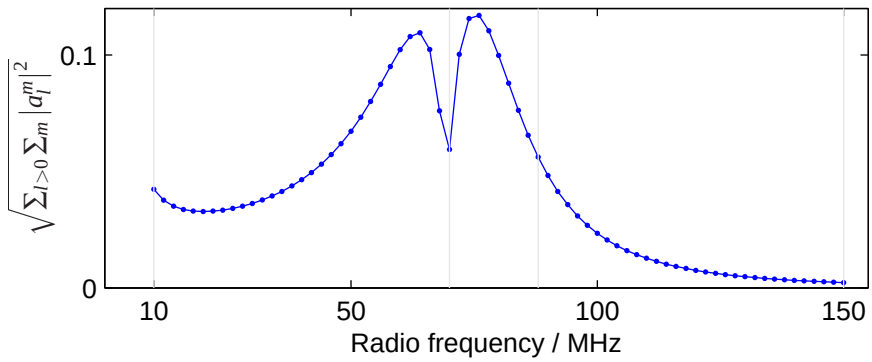

(e) Magnitude of singlet yield anisotropy

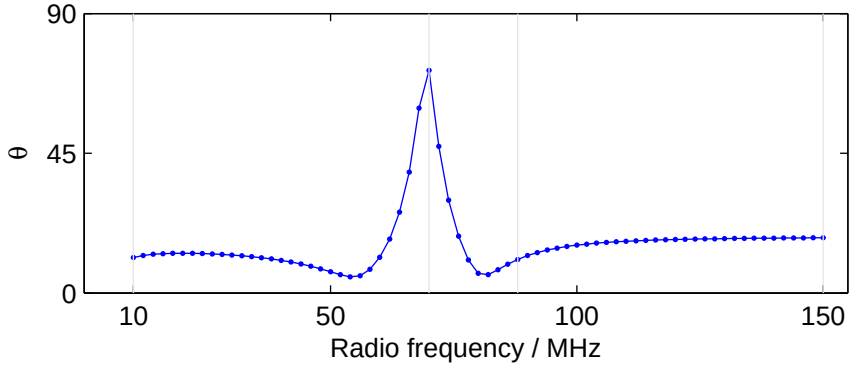

(f) Shape of singlet yield anisotropy where $\theta = \theta_1$ is defined by equation (8.100)

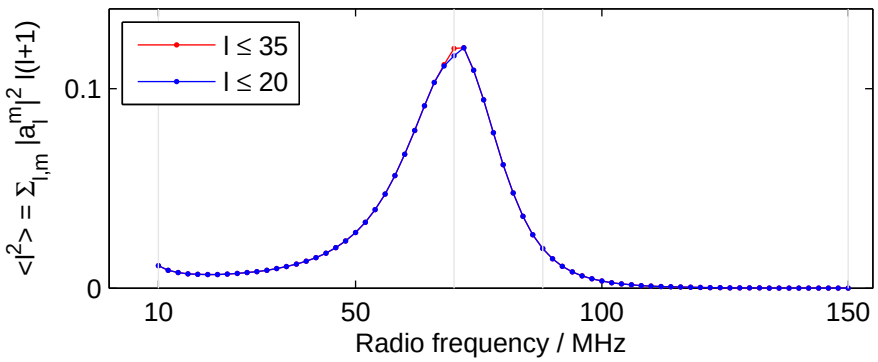

(g) Hybrid measure of magnitude and shape of singlet yield anisotropy

Figure 8.20: Effect of radio frequency ν_{rf} on singlet yield. Calculations were performed in a one-proton RP model system using the gCOMPFST algorithm with $B_1 = 100\,\mu\mathrm{T}$, $k = 2 \times 10^5\,\mathrm{s}^{-1}$, HFC $a = 2.5\,\mathrm{mT}$, $\alpha = 12.5\,\mu\mathrm{T}$, $\beta = 0$, $n = 128$, and MaxL $= 35$. Figures (a–d) show singlet yield anisotropies at the ν_{rf} values marked with grey vertical lines.

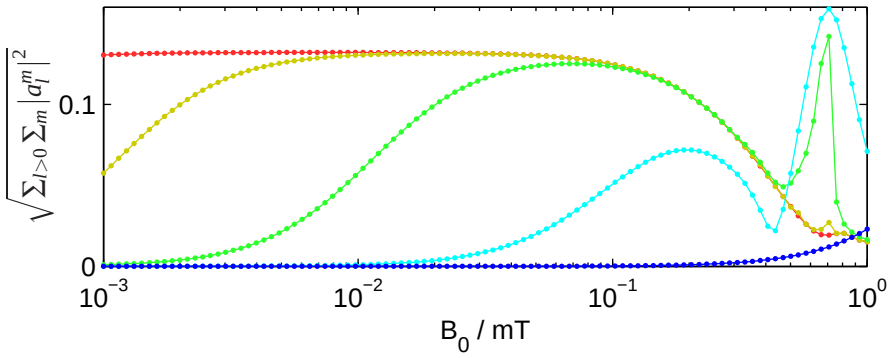

(a) Magnitude of singlet yield anisotropy

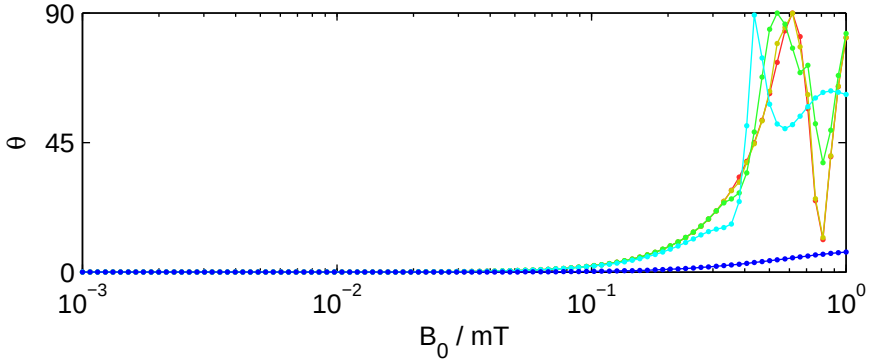

(b) Shape of singlet yield anisotropy where $\theta = \theta_1$ is defined by equation (8.100)

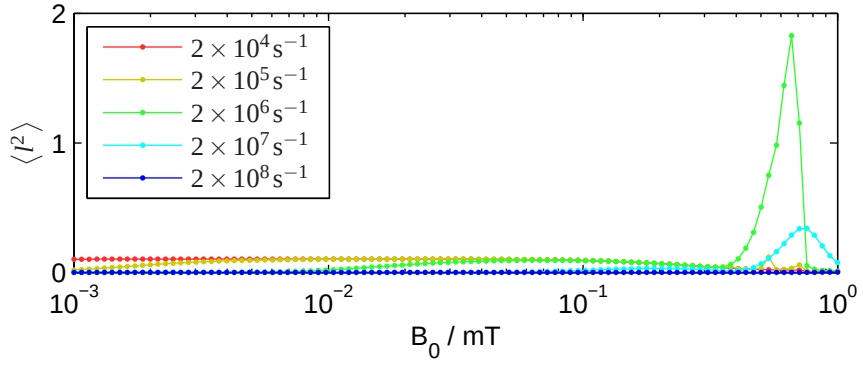

(c) Hybrid measure of magnitude and shape of singlet yield anisotropy

Figure 8.21: Effect of exponential model rate constant k, shown in the legend, on singlet yield in a one-proton RP model system. Calculations were performed using the PyDMAFST algorithm with HFC $a = 2.5\,\text{mT}$, $\alpha = 125\,\mu\text{T}$, $\beta = 0$ and MaxL $= 35$.

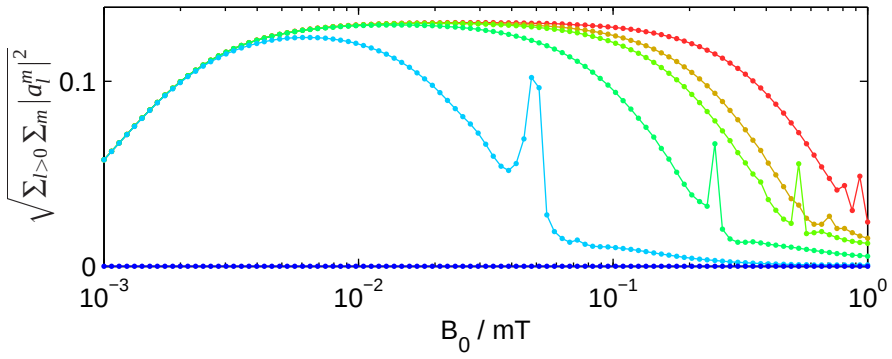

(a) Magnitude of singlet yield anisotropy

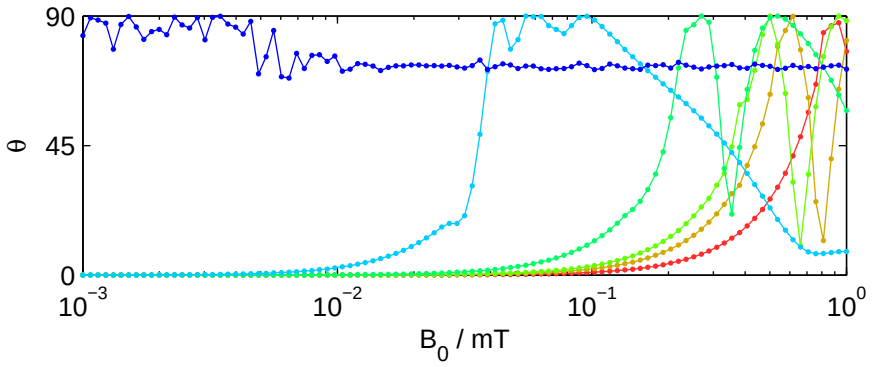

(b) Shape of singlet yield anisotropy where $\theta = \theta_1$ is defined by equation (8.100)

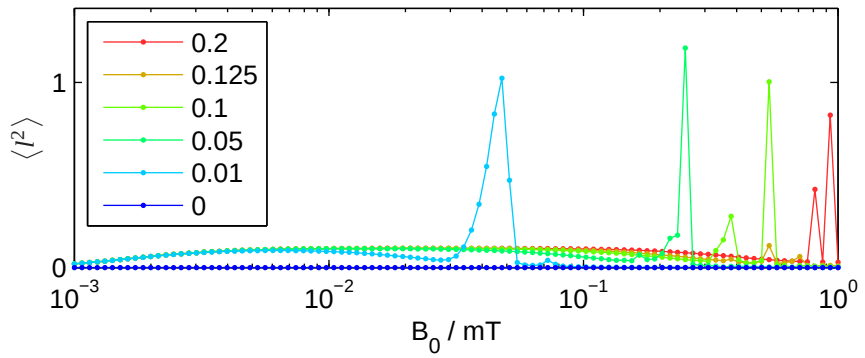

(c) Hybrid measure of magnitude and shape of singlet yield anisotropy

Figure 8.22: Effect of axiality on singlet yield in a one-proton RP model system. The legend shows α/a. Calculations were made using the PyDMAFST algorithm with $k = 2 \times 10^5\,\mathrm{s}^{-1}$, isotropic HFC $a = 2.5\,\mathrm{mT}$, $\beta = 0$ and MaxL $= 35$.

equivalent magnetic nuclei per radical in the presence of either static B_0 or radio frequency B_1 fields. We implemented these algorithms in a general purpose `Matlab` code `CalcSphHRep`.

Furthermore, using perturbation theory we have seen that singlet yield anisotropy patterns are often dominated by $l = 2$ spherical harmonics. Yet, in the presence of strong fields, or in the vicinity of energy level crossings where resonant effects are likely to occur, the singlet yield anisotropy patterns may contain many higher order harmonics.

Having developed these tools, we applied them to a one-proton RP model system. By introducing appropriate statistics, we saw that it is possible to extract details of the magnitude of a singlet yield anisotropy pattern, or its shape, or both without human intervention. We were able to show succinctly the trends in singlet yield anisotropy as a function of the model parameters B_0, B_1, ν_{rf}, k and α. Spherical harmonic decomposition is a powerful technique for the analysis and interpretation of singlet yield anisotropies.

8.10 Suggestions for further work

In §8.4, we introduced a perturbative approach to determining singlet yield spherical harmonic representations. In that formalism, it is clear that the singlet yield anisotropy often contains only contributions from the $Y_2^m(\theta,\phi)$ spherical harmonics. Contributions from harmonics with $l > 2$ appear near level crossings and in long-lived RPs when the Zeeman interaction makes significant higher order contributions. It would be interesting to see whether any further general insight into the origins of contributions to the singlet yield from different spherical harmonics can be gleaned by considering explicitly the form of the $\hat{\hat{L}}$ and $\hat{\hat{Z}}$ superoperators defined above.

Unfortunately, the matrix binomial power series used in equation (8.54) was found to diverge in precisely those RP systems that are most relevant to our discussion of the magnetic compass sense of birds. However, it is possible that this series could be preconditioned or replaced with another expansion that has better convergence properties. These ideas have been taken up in collaboration with Efimova.

Applying these methods to analyse the properties of a one-proton RP model system, we saw that static and RF fields of the same strength produce singlet yield anisotropies of similar magnitude and shape. It would be interesting to perform studies on animal subjects held in conditions where the geomagnetic field was nulled and a $50\,\mu\mathrm{T}$ RF field was applied instead. If these animals were able to orient using an RF field, that would give further evidence for the involvement of a RPM-based magnetoreceptor.

In this chapter, we have applied the spherical harmonic decomposition methods in a one-proton RP as a proof of concept and an illustration of the method. Given sufficient computational resources, it would be interesting to conduct a similar analysis on a large number of multinuclear RPs with randomly chosen hyperfine couplings in order to develop a set of "rules of thumb" for anisotropic magnetic field effects as was done in Chapter 3 for isotropic MFEs. In particular, it ought to be possible to extend the analysis conducted in Chapter 7 to large ensembles of RPs in order to explore the extent to which singlet yield anisotropy patterns are built up.

Finally, the `Matlab` toolkit developed in connection with this work should be use-

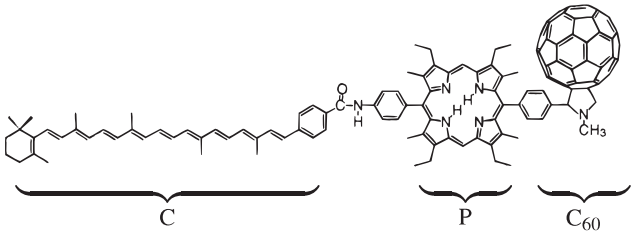

Figure 8.23: Carotenoid-porphyrin-fullerene model compound CPC_{60}.

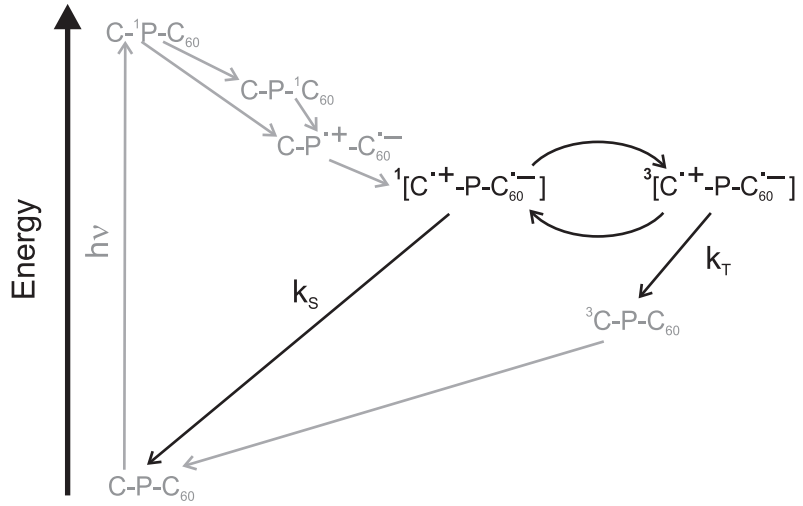

Figure 8.24: Simplified photochemical reaction scheme for CPC_{60}, after [377].

ful for interpreting a series of anisotropic MFE measurements made recently in Oxford on a chemical model system. The CPC_{60} triad, shown in Figure 8.23, undergoes efficient photochemically induced intramolecular electron transfer to form a long-lived spin correlated biradical [377]. This biradical decays by spin-selective reactions as summarised in Figure 8.24. The lifetime of the biradical shows strong magnetic field effects which may be detected by monitoring its absorption at 980 nm in a pump-probe laser flash photolysis experiment. If the 980 nm probe laser is polarised, the experiment is sensitive only to CPC_{60} molecules whose transition dipoles lie in a particular orientation. Using this photoselection approach, Maeda has measured the anisotropic response of the CPC_{60} triad lifetime to magnetic fields of a few mT. At the time of writing, Hall is applying the techniques developed in this chapter in order to interpret these experiments [378]. Some preliminary results, showing the distribution of a_2^0 spherical harmonic coefficients in model RPs formed by selecting six nuclei at random from the CPC_{60} triad, are shown in Figure 8.25.

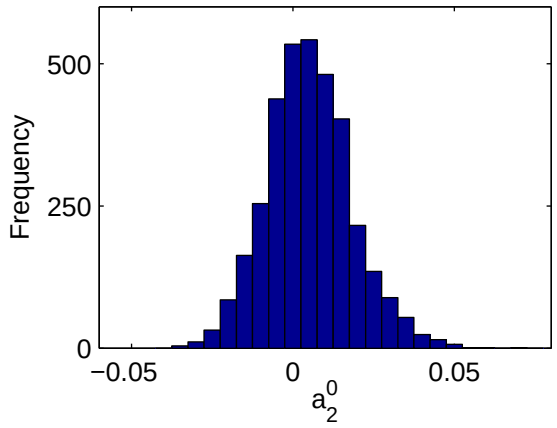

Figure 8.25: The anisotropic MFE for the CPC_{60} triad obtained using photoselection is expected to be proportional to the a_2^0 spherical harmonic expansion coefficient. Hall has performed calculations for a large ensemble of RPs, each of which contains a random selection of six nuclei from the CPC_{60} triad molecule [378]. The figure shows the distribution of a_2^0 values across this ensemble. The all-important sign of the photoselection experiment results is, unfortunately, highly dependent on the particular nuclei that are chosen.

Chapter 9

Anisotropic RF field effects

9.1 Introduction

The biophysical mechanism underlying the magnetic compass sense of birds has been vigorously debated for many years as outlined in Chapter 6. Almost thirty years ago, Schulten hypothesised that the avian magnetic compass is founded on a magnetic field sensitive biochemical reaction that proceeds via a radical pair intermediate [107]. Anisotropy in electron–nuclear hyperfine interactions would cause the yield of such a reaction to depend on the orientation of the RP relative to the geomagnetic field, forming an RPM-based compass. We have performed extensive modelling studies, which were presented in Chapters 7 and 8, in order to test the plausibility of this hypothesis.

In 2000, Ritz, Adem and Schulten rekindled interest in the RPM hypothesis, declaring that "a test of the radical-pair hypothesis might be possible by applying appropriate radio frequency (1–10 MHz) AC electromagnetic fields as suggested by Phillips" [106]. Weak RF fields are expected to impede the operation of an RPM-based compass but would leave a compass based on ferromagnetic particles such as magnetite quite unscathed. Painstaking work by the Wiltschkos, Ritz and coworkers in Frankfurt has subsequently revealed that weak RF fields are indeed able to disrupt the magnetic compass sense of European robins in certain circumstances [231, 232, 314]. These results are summarised in §6.3.9 and particularly in Figures 6.12 and 6.13. The focus of this chapter is to explain the origin of these RF field effects and to assess whether they are consistent with the hypothesis of an RPM-based compass. The calculations presented here were performed in tandem with the bird work in Frankfurt and have been the inspiration for many discussions with Ritz and others.

The literature contains very few calculations of the effects of weak RF fields on the product yield anisotropy of RPs. In the final paragraph of his paper reporting the first RF field effects in birds, Ritz alludes to a single calculation for a one-proton model RP subject to static and circularly polarised RF fields [231]. These fields were fixed in a single orientation with respect to the RP and no attempt to assess the product yield anisotropy is mentioned. The other calculations were made by Canfield in one-proton RPs as a demonstration of the perturbative algorithms for calculating product yields in the presence of weak RF fields that he developed [223–225, 313]. Finally, in response to our assertion (see below, particularly Figures 9.3 and 9.5) that RPs with magnetic nuclei in both radicals do not generally show a Zeeman resonance (defined in §1.5.4), Ritz has performed a number of calculations in model RPs with isotropic hyperfine

interactions subjected to circularly polarised RF fields [379]. There are no prior results for the effects of linearly polarised RF fields on the product yield of multinuclear RPs with anisotropic hyperfine interactions. Neither are there any studies of the effect of RF fields on the product yield anisotropy of RP reactions. Such calculations are vital if we are to interpret the results of animal behavioural experiments involving RF fields such as those described above.

In this chapter, we consider what changes in product yield may be required to disorient robins by comparison with behavioural experiments where the field strength B_0 is varied. We then proceed to calculate the effect of RF fields in a variety of model systems and in systems designed to replicate the conditions of recent animal experiments in Frankfurt. We consider whether there are particular radio frequencies that are most likely to give a strong response. Such information is useful for the design of animal experiments. We close by attempting to interpret the animal behavioural results given in Figure 6.13 within the RPM and with a discussion of their physical implications.

9.2 Choice of radio frequency for animal tests

Experimental measurements of the orientation of birds that are deprived of all other navigational cues except for a $B_0 \sim 50\,\mu\text{T}$ magnetic field affirm the existence of an avian magnetic compass sense. Further studies, reviewed in Chapter 6, have brought to light several operational features of this compass. However, it is only possible to perform orientation experiments on birds during the few weeks each year when they would normally migrate. Furthermore, even in those weeks, for night-migrants such as the European robin, experiments may only be performed once per day at dusk. At other times, birds have no strong desire to head in a particular direction and therefore would not orient themselves even if they were capable of doing so under the test conditions. This restriction to only a few weeks of testing per year, to testing only at dusk and the need to perform many repetitions of each experiment in order to obtain statistical significance means that tests may be made under only a few conditions each year. The substantial progress that has been made in characterising the avian magnetic compass sense experimentally is testimony to the care exercised in choosing test conditions.

The most likely explanations for the physical basis of the avian magnetic sense are that it arises from the magnetic field response of biogenic magnetite or from chemical magnetic field effects on a RP reaction. Both of these theories are largely consistent with the characteristic properties of the avian magnetic compass that have been elucidated by behavioural experiments. Radio frequency (1–10 MHz) fields are known to alter the yield of chemical reactions proceeding via the RPM. Indeed, we explored such RF field effects on small molecule chemical model systems in some detail in Chapters 4 and 5. Such RF fields might well affect the operation of an RPM-based compass, but would have no effect on a magnetite-based compass.

In an ideal world, one would perform a large number of animal experiments, measuring systematically the threshold RF field strength required to disorient a bird as a function of the radio frequency. Such a spectrum would resemble the OMFE-B_0 experiments undertaken by Norman and Wedge for chemical systems [139, 182]. The data from such an experiment would be amenable to the same sorts of analysis that we undertook in Chapters 4 and 5. We would expect to be able to identify the hyperfine coupling structure in the RP responsible for magnetoreception.

In practice, experimental constraints mean that we must select a very limited number of radio frequencies at which to test. These frequencies must be selected carefully, because only if there is a disruption of the robins' orientation will the experiments be conclusive. If the birds orient happily in the presence of the RF field that is used, this might mean that magnetoreception occurs via a magnetite-based receptor, but it could equally well be the case that the RF fields employed were too weak or that only the particular frequency chosen had no effect. The choice of frequency is further complicated since the identity of the RP involved in magnetoreception is not yet known. We consider, therefore, whether there are certain radio frequencies for which any RP will show strong changes in product yield. The best chance of finding such a frequency is that long-lived RPs, which would be suitable for magnetoreception, show a Zeeman resonance even in the geomagnetic field for which $B_0 \approx 50\,\mu\mathrm{T}$.

9.3 A one-proton RP model

In our studies of chemical magnetic field effects, we saw a consistent Zeeman resonance peak whenever the static field dominated the hyperfine couplings, *i.e.* when $B_0 \gg \tilde{a}_{\mathrm{RP}}$. This Zeeman resonance, defined in §1.5.4, occurs at a radio frequency

$$\nu_{\mathrm{rf}} = \frac{|\gamma_{\mathrm{e}}|}{2\pi} B_0 = \left(28.025\,\mathrm{MHz\,mT^{-1}}\right) \times B_0 \tag{9.1}$$

or equivalently at a field strength

$$B_0 = \frac{2\pi}{|\gamma_{\mathrm{e}}|} \nu_{\mathrm{rf}} = \left(35.682\,\mu\mathrm{T\,MHz^{-1}}\right) \times \nu_{\mathrm{rf}} \tag{9.2}$$

irrespective of the hyperfine structure, and hence of the identity, of the radical pair. In the weak field limit, when $B_0 \ll \tilde{a}_{\mathrm{RP}}$, we saw no hyperfine-independent RF response.

Figure 9.1(a) shows the singlet yield in a one-proton RP with an axial hyperfine coupling. The black curve shows the singlet yield in the presence of a static field B_0 along the z-axis. The red and green curves show the effect of introducing a weak $B_1 = 33\,\mathrm{nT}$ circularly polarised RF field in the xy-plane. These weak RF fields produce a sharp resonance at a field that depends on the radio frequency according to equation (9.2). We therefore identify this resonance as a Zeeman resonance.

To assess whether this small change in singlet yield might be sufficient to disorient a bird, we compare the depth of the Zeeman resonance $\Delta\Phi_{\mathrm{S}} = 1.7 \times 10^{-3}$ with the change in singlet yield $\Delta\Phi_{\mathrm{S}} = 1.4 \times 10^{-3}$, indicated by a horizontal grey line, caused by moving from $B_0 = 46\,\mu\mathrm{T}$ to $B_0 = 60\,\mu\mathrm{T}$ without any RF field. This change in static field is known to disorient European robins (see §6.3.8) and it therefore seems plausible that even such weak RF fields might also disorient a robin. A similar calculation is alluded to in the final paragraph of [231].

Of course, the operation of an RPM-based compass sense would depend on the yield anisotropy of a RP rather than merely on the changes in the response to fields of fixed orientation considered hitherto. Figure 9.2 shows a number of singlet yield anisotropy calculations in the same one-proton RP that was used in Figure 9.1. Figures 9.2(a) and (b) show polar plots of the singlet yield $\Phi_{\mathrm{S}}(\theta, \phi)$ in an Earth-strength static field and in a static field $B_0 = 34\,\mu\mathrm{T}$ in which robins are also known to be disoriented. The corresponding singlet yield anisotropies are shown in Figures 9.2(d) and

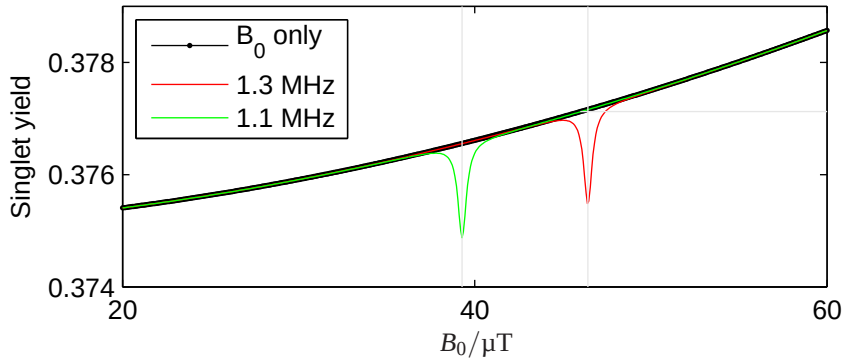

(a) Axiality $\alpha = 150\,\mu\text{T}$. A similar calculation is alluded to in the final paragraph of [231].

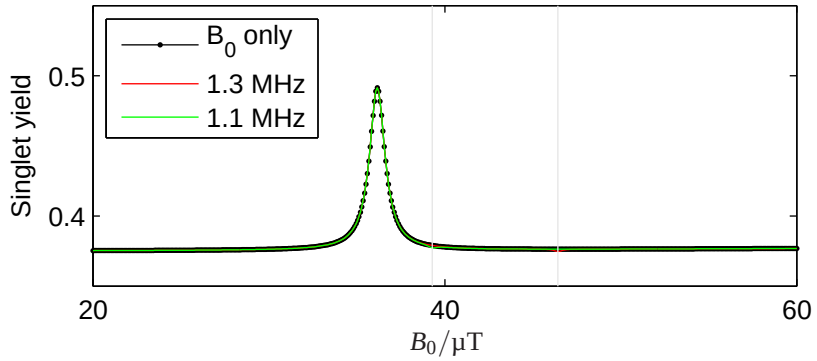

(b) Axiality $\alpha = 12.5\,\mu\text{T}$

Figure 9.1: Comparison of the changes in singlet yield produced by static B_0 and RF B_1 fields. Calculations were made in a one-proton RP using the RFT with $k = 5 \times 10^4\,\text{s}^{-1}$, isotropic HFC $a = 500\,\mu\text{T}$, axiality α as specified above and rhombicity $\beta = 0\,\mu\text{T}$. The axiality and static field B_0 were directed along the z-axis, whilst, when present, the RF field rotated in the xy-plane. In each figure, results are shown for $B_1 = 0\,\text{nT}$; $B_1 = 33\,\text{nT}$ with $\nu_{\text{rf}} = 1.3\,\text{MHz}$; and $B_1 = 33\,\text{nT}$ with $\nu_{\text{rf}} = 1.1\,\text{MHz}$. These radio frequencies would produce Zeeman resonances (indicated with grey lines) at $B_0 = 46\,\mu\text{T}$ and $B_0 = 39\,\mu\text{T}$.

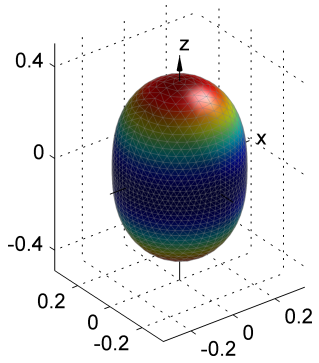

(a) Singlet yield $\Phi_S(\theta,\phi)$ when $B_0 = 1.3 \times 1000/28 \approx 46\,\mu\text{T}$ and $B_1 = 0\,\text{nT}$.

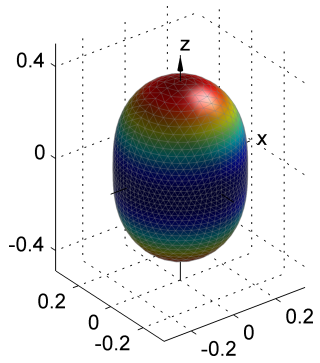

(b) Singlet yield $\Phi_S(\theta,\phi)$ when $B_0 = 1.3 \times 1000/28 - 12 \approx 34\,\mu\text{T}$ and $B_1 = 0\,\text{nT}$.

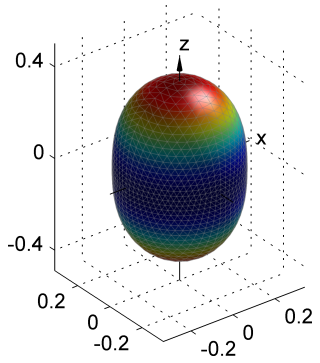

(c) Singlet yield $\Phi_S(\theta,\phi)$ when $B_0 \approx 46\,\mu\text{T}$ and $B_1 = 33\,\text{nT}$.

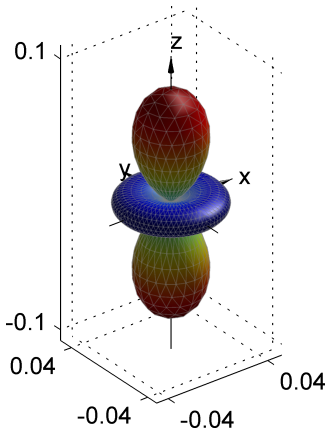

(d) Singlet yield anisotropy $\Phi_S^{an}(\theta,\phi)$ when $B_0 \approx 46\,\mu\text{T}$ and $B_1 = 0\,\text{nT}$.

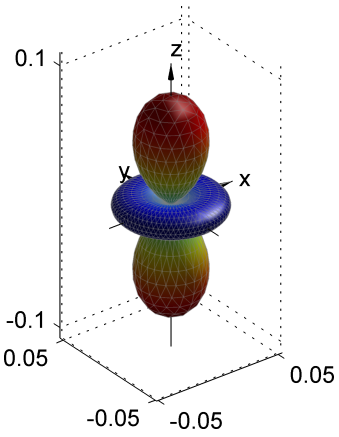

(e) Singlet yield anisotropy $\Phi_S^{an}(\theta,\phi)$ when $B_0 \approx 34\,\mu\text{T}$ and $B_1 = 0\,\text{nT}$.

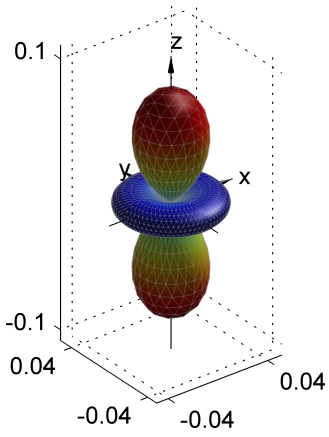

(f) Singlet yield anisotropy $\Phi_S^{an}(\theta,\phi)$ when $B_0 \approx 46\,\mu\text{T}$ and $B_1 = 33\,\text{nT}$.

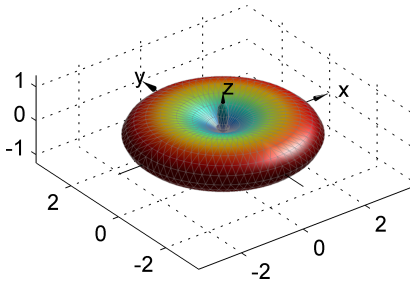

(g) 1000 × change in singlet yield $\Phi_S(B_0 \approx 46\,\mu\text{T}) - \Phi_S(B_0 \approx 34\,\mu\text{T})$ when $B_1 = 0\,\text{nT}$, *i.e.* between cases (a) and (b).

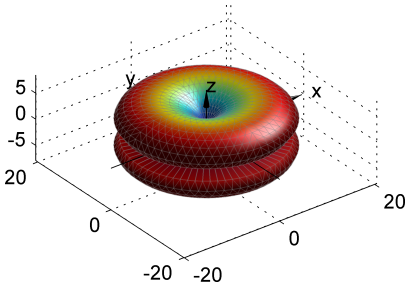

(h) 10^9 × change in singlet yield $\Phi_S(B_1 = 33\,\text{nT}) - \Phi_S(B_1 = 0\,\text{nT})$ when $B_0 \approx 46\,\mu\text{T}$, *i.e.* between cases (a) and (c).

Figure 9.2: Polar plots showing the effect on singlet yield of a $\Delta B_0 = 12\,\mu\text{T}$ change in static field and of a $B_1 = 33\,\text{nT}$, $\nu_{\text{rf}} = 1.3\,\text{MHz}$ RF field for the same system as in Figure 9.1. Calculations were made in a one-proton RP using γ–COMPUTE with $k = 5 \times 10^4\,\text{s}^{-1}$, isotropic HFC $a = 500\,\mu\text{T}$, axiality $\alpha = 150\,\mu\text{T}$ and rhombicity $\beta = 0\,\mu\text{T}$. The RF fields were linearly polarised and parallel to the static field.

(e). The difference in singlet yield between $B_0 = 46\,\mu\text{T}$ and $B_0 = 34\,\mu\text{T}$ is shown in Figure 9.2(g). Similarly, Figures 9.2(c), (f) and (h) show the effects of a $B_1 = 33\,\text{nT}$ resonant RF field. In order that the fields may be described by a single orientation (θ, ϕ), the RF field is taken to be linearly polarised and to always be parallel to the static field. Whereas the static field produces a maximum change in singlet yield anisotropy of about 5%, the RF field produces a minuscule 0.00005% change. Judging by eye, neither the B_0- or B_1-induced changes in singlet yield anisotropy appear significant.

Furthermore, Figure 9.1(b) shows the results of an equivalent singlet yield calculation for a different choice of hyperfine axiality α. This time, there is an energy level crossing when $B_0 \approx 36\,\mu\text{T}$, around which the static field produces strong, resonant changes in singlet yield $\Delta\Phi_S = 0.11$. The Zeeman resonance peaks are still present and are of a similar depth to those in Figure 9.1(a). In Chapter 8, we saw that energy level crossings produce strong singlet yield anisotropy, making RPs such as that in Figure 9.1(b) well suited for an RPM-based compass. Indeed, we interpreted the small range of B_0 values in which robins can orient as being indicative of the role of such an energy level crossing. All other factors being equal, we saw in Chapter 8, that B_0 and B_1 fields of a similar strength alter the singlet yield by a similar amount providing that they are either both non-resonant or that the RF field is resonant and the static field is of exactly the right strength to cause a level crossing in conjunction with the hyperfine coupling, for example. We refer to the latter case as a "resonant static field". The effects of weak RF fields at the Zeeman resonance frequency need to be investigated further before we will know whether they normally cause significant changes in singlet yield that might disrupt magnetoreception. In other words, further work is needed to judge whether Figure 9.1(a) or (b) or neither is typical of the response in realistic multinuclear RPs.

9.4 RPs with isotropic hyperfine tensors

To simplify our discussions, we assume for the moment that an RF field at the Zeeman frequency would disrupt magnetoreception providing that the RP involved has a Zeeman resonance. Moreover, to reduce the number of variables, let us focus our attention on the singlet yield of RPs with isotropic hyperfine tensors.

9.4.1 One-proton RPs

Figure 9.3 shows the change in singlet yield arising from the introduction of a weak $B_1 = 700\,\text{nT}$ circularly polarised RF field in one-proton RPs. Notice the strong central peak which occurs in every calculation. We identify this as a Zeeman resonance on three grounds. First, in Figure 9.3(a), the peak occurs at a radio frequency 1.4 MHz that satisfies equation (9.1). Second, when the static field strength is changed in Figure 9.3(b), the peak changes frequency in direct proportionality with B_0 in accordance with equation (9.1). Third, the peak occurs at the same frequency irrespective of the hyperfine structure of the radicals. The other peaks in Figures 9.3(a) and (b) are not Zeeman resonances because they do not have these three properties. Notice that we must calculate spectra for more than one value of B_0 or ν_{rf} in order to distinguish between a Zeeman resonance and a hyperfine-resonance that occurs accidentally at the Zeeman resonance frequency.

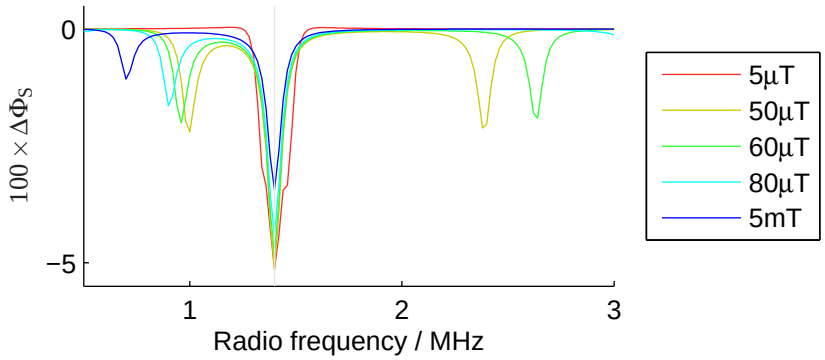

(a) $B_0 = 50\,\mu\mathrm{T}$

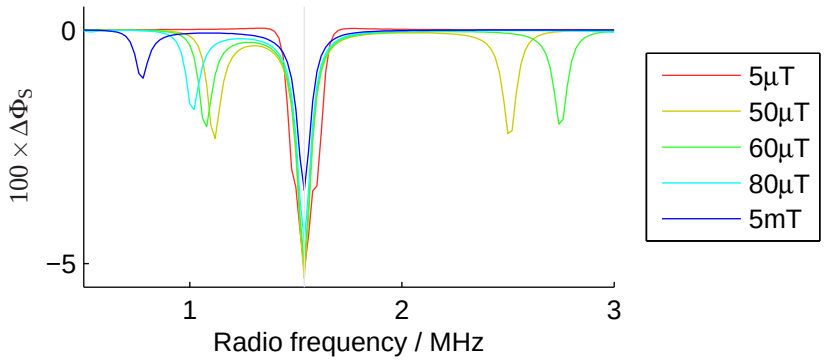

(b) $B_0 = 55\,\mu\mathrm{T}$

Figure 9.3: One-proton radical pairs show a prominent change in singlet yield at the Zeeman resonance with CPL RF, irrespective of the HFC a (shown in the legend). The Zeeman frequency $\nu_{\mathrm{rf}} = |\gamma_e| B_0/2\pi$ is indicated by a vertical grey line. Calculations were performed for CPL RF using the RFT with $k = 2 \times 10^5\,\mathrm{s}^{-1}$, $\theta = \pi/2$ and $B_1 = 700\,\mathrm{nT}$. The $a = 50\,\mu\mathrm{T}$ curve here is equivalent to [223, Fig 5a].

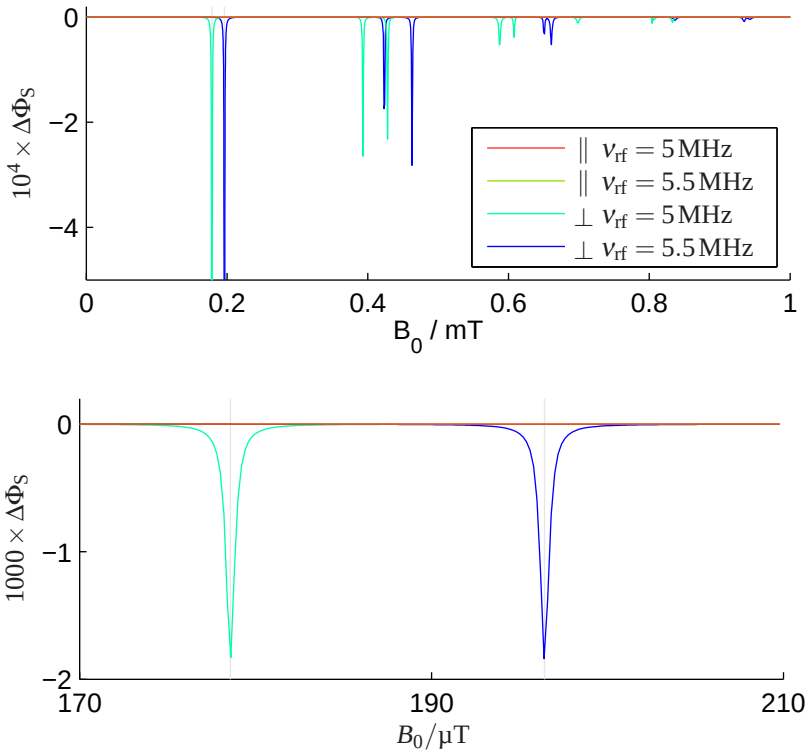

Figure 9.4: A multinuclear RP shows a prominent Zeeman resonance for perpendicular LIN RF, but not for parallel LIN RF. The Zeeman field $B_0 = 2\pi\nu_{rf}/|\gamma_e|$ is indicated by vertical grey lines. Calculations were performed for using γ–COMPUTE with HFCs of 2×0.829 mT ($I = 1/2$) on radical A and 4×0.538 mT ($I = 1/2$) on radical B, $k = 5 \times 10^4\,\mathrm{s}^{-1}$, $n = 64$ and $B_1 = 100$ nT. The lower figure gives an enlarged view of the Zeeman resonances.

9.4.2 A multinuclear RP

Figure 9.4 shows the results of a similar calculation for a "2–4" RP. To make this calculation more realistic, the hyperfine couplings used here are those for Py-$h_{10}^{\bullet+}$ and 1,3-$DCB^{\bullet-}$ but the RP lifetime, inspired by that for the RP in photolyase [352, 353], is taken to be 20 µs. In this figure, we use linearly polarised RF fields, since these are far easier to generate experimentally and are used in the bird behavioural studies.

Notice that once again, there are strong resonances at the Zeeman field when $\nu_{rf} = 5$ MHz. In order to test whether these are truly Zeeman resonances, or whether they merely happen to occur at the Zeeman field, the calculations are repeated for a slightly larger radio frequency $\nu_{rf} = 5.5$ MHz. The peaks in question change frequency in accordance with equation (9.2) and are thus confirmed as Zeeman resonances.

In high-field EPR, we would expect to see a Zeeman resonance when the RF and static fields are perpendicular, but not when they are parallel. Even at these remarkably weak fields $B_0 \approx 200\,\mu$T, the Zeeman resonance in Figure 9.4 does show this same dependence on the relative orientation of the RF and static fields. This is in sharp contrast with the behaviour seen in Chapter 4, where the changes in singlet yield brought about by parallel and perpendicular RF fields were of the same magnitude when $\nu_{rf} = 5$ MHz.

9.4.3 Elimination of the Zeeman resonance

The results of the preceding calculations are similar to the few published calculations that are relevant to this low-field regime [223–225, 231, 313]. Surprisingly, these results suggest — in the weak field $B_0 \ll a$, where hyperfine interactions may be expected to be dominant, and with the long-lifetimes relevant for modelling an RPM-based magnetoreceptor — that strong Zeeman resonances with all the properties familiar from high-field EPR may be expected. If this were the case, the animal behavioural results in Figures 6.12 and 6.13 would follow naturally. Yet such a conclusion would be at variance with the experimental and theoretical results presented in Chapter 4 where the Zeeman resonance disappeared when $B_0 \lesssim 1.5\,\mathrm{mT}$. Figure 9.5 allows us to reconcile these apparent differences.

Figure 9.5(a) shows the RF-induced changes in singlet yield for "2–0" RPs with various hyperfine coupling constants varying over three orders of magnitude. In all cases, such "2–0" RPs show a strong Zeeman resonance with all the properties familiar from high-field EPR.

In Figure 9.5(b), we see finally how one may abolish the Zeeman resonance. Figure 9.5(b) shows the changes in singlet yield for "1–1" RPs with a 500 µT hyperfine coupling on one radical and various hyperfine couplings on the counter-radical. Notice that, as we introduce a hyperfine coupling on the counter-radical, the Zeeman resonance is split into a doublet. A HFC of 10 µT is sufficient to ensure that there is no longer any strong change in singlet yield at the Zeeman resonance frequency.

9.4.4 Origin of the Zeeman resonance

We may explain the occurrence of a Zeeman resonance in Figures 9.1–9.4 and its absence in Figure 9.5 as follows. For non-interacting radicals, the RP Hamiltonian may be written

$$\hat{H} = \hat{H}_\mathrm{A} \otimes \hat{\mathbb{1}}_\mathrm{B} + \hat{\mathbb{1}}_\mathrm{A} \otimes \hat{H}_\mathrm{B} \tag{9.3}$$

where the "A" operators act on the electron and nuclear spins in radical A and the "B" operators act in radical B. As a result, the energy levels E_{mn} of the RP may be written

$$E_{mn} = E_m^\mathrm{A} + E_n^\mathrm{B} \tag{9.4}$$

where the indices m and n run over the eigenstates of $\hat{H}_\mathrm{A}$ and $\hat{H}_\mathrm{B}$ which have eigenvalues E_m^A and E_n^B respectively.

When there is no magnetic nucleus in radical B, say, then

$$\hat{H}_\mathrm{B} = -\gamma_\mathrm{e}\,(\boldsymbol{B}_0 + \boldsymbol{B}_1) \cdot \hat{\boldsymbol{S}}_\mathrm{B}. \tag{9.5}$$

Without loss of generality, we let the z-axis lie parallel to the static field $\boldsymbol{B}_0$ and hence

$$\hat{H}_\mathrm{B} = -\gamma_\mathrm{e} B_0 \hat{S}_{\mathrm{B}z} - \gamma_\mathrm{e} \boldsymbol{B}_1 \cdot \hat{\boldsymbol{S}}_\mathrm{B}. \tag{9.6}$$

For RF fields that are sufficiently weak so as to be considered as first order perturbations, such a Hamiltonian has energy levels corresponding exactly to the Zeeman resonance frequency. Indeed, providing that $B_1 \ll B_0$, it represents the limiting case of a "high-field" Hamiltonian however small the static field B_0. We may now see that a

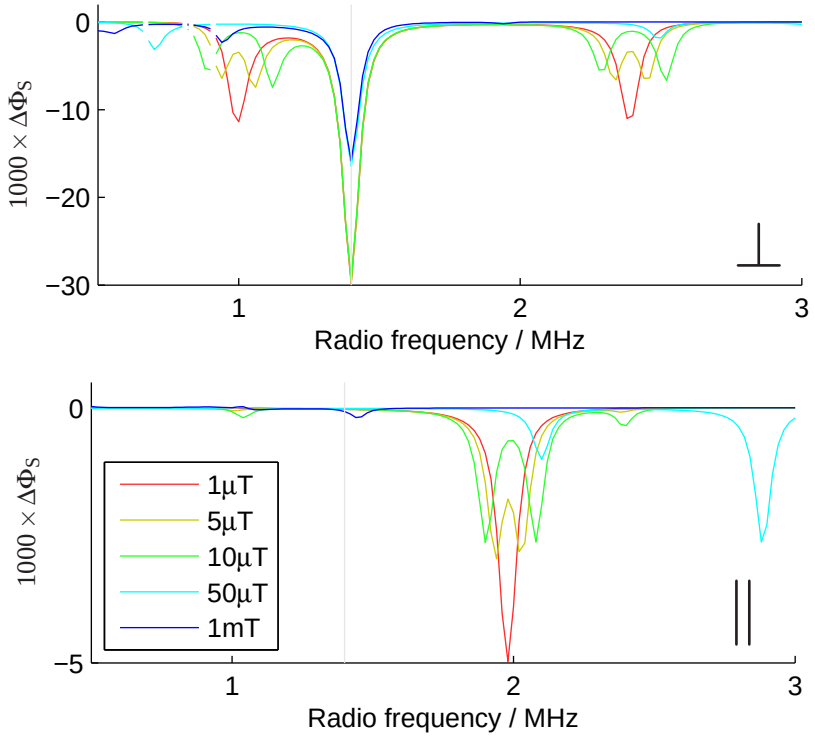

(a) "2–0" RPs with HFC $1 \times a$ mT (indicated in the legend) and 1×0.5 mT both on radical A show a Zeeman resonance for perpendicular RF, but not for parallel RF regardless of the HFCs.

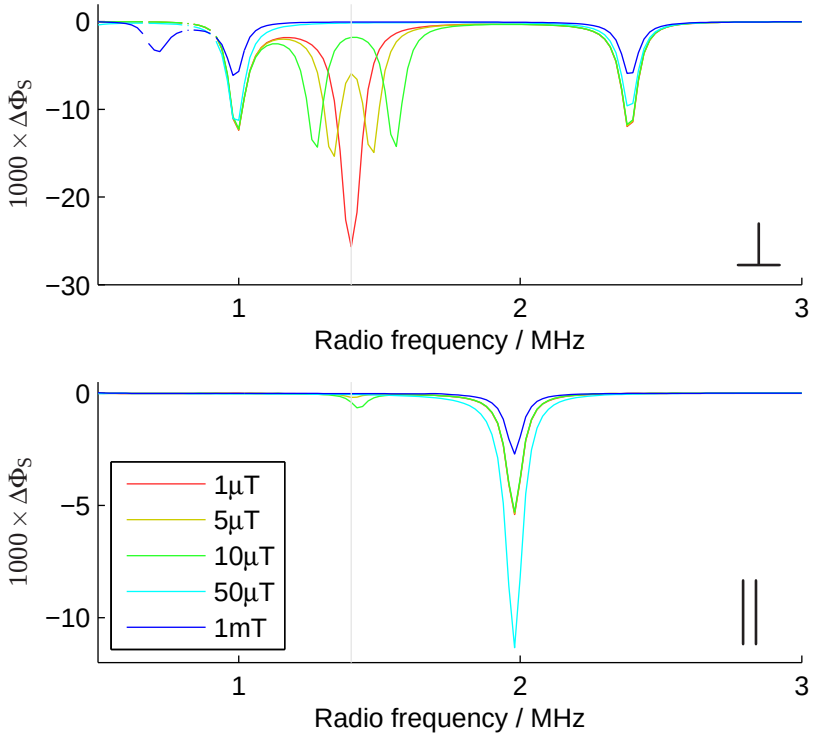

(b) "1–1" RPs with HFC $1 \times a$ mT (indicated in the legend) on radical A and 1×0.5 mT on radical B only show a Zeeman resonance for perpendicular RF and when a is very small.

Figure 9.5: Effect of adding a second magnetic nucleus. Simulations are made with LIN RF using γ−COMPUTE and the following parameters: $k = 2 \times 10^5\,\mathrm{s}^{-1}$, $n = 64$, $B_1 = 700\,\mathrm{nT}$ and $B_0 = 50\,\mu\mathrm{T}$. A grey line marks the Zeeman resonance frequency.

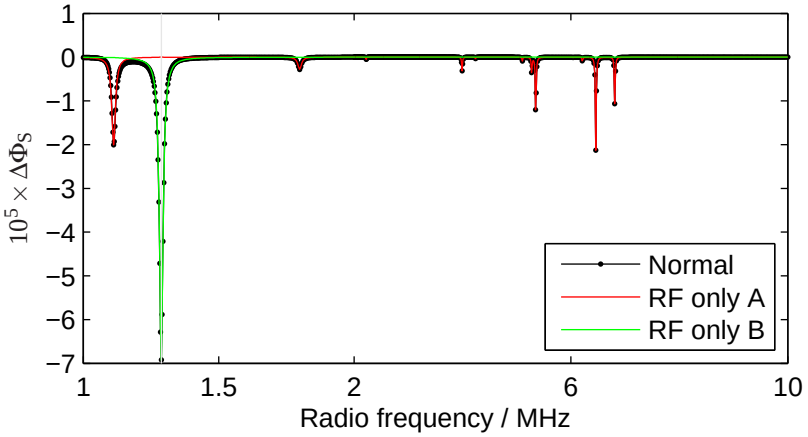

Figure 9.6: Demonstration that the Zeeman resonance in an "n–0" RP is caused by the radical that has no magnetic nuclei. The RF-induced change in singlet yield is shown for a RP with two spin-½ nuclei on radical A which have isotropic HFCs $a = 188.7\,\mu\text{T}$ and $a = 73.2\,\mu\text{T}$. There are no HFCs on radical B, $k = 5 \times 10^4\,\text{s}^{-1}$, $B_0 = 46\,\mu\text{T}$, $B_1 = 33\,\text{nT}$ and $n = 512$. The angle between the RF and static fields $\Delta\varepsilon = 24^\circ$. The black curve shows results when the normal RF Zeeman term is included in the Hamiltonian $\hat{H}_{\text{rf}} = -\gamma_{\text{e}}\boldsymbol{B}_1 \cdot (\hat{\boldsymbol{S}}_{\text{A}} + \hat{\boldsymbol{S}}_{\text{B}})$. The red curve shows the result when $\hat{H}_{\text{rf}} = -\gamma_{\text{e}}\boldsymbol{B}_1 \cdot \hat{\boldsymbol{S}}_{\text{A}}$ and the green curve is for $\hat{H}_{\text{rf}} = -\gamma_{\text{e}}\boldsymbol{B}_1 \cdot \hat{\boldsymbol{S}}_{\text{B}}$.

Zeeman resonance is to be expected in any "m–0" RP, which explains the resonances occurring in Figures 9.1–9.3 and 9.5(a).

This Zeeman response from radical B should be relatively strong (unless the RF and static fields are nearly parallel) because all B radicals exhibit the same resonant behaviour at the same frequency. In contrast, when $B_0 < \tilde{a}_{\text{RP}}$, the other resonant responses from radical A will be rather smaller. This is because, in the presence of HFCs, the resonances that do occur for radical A will, in general, be distributed over a range of frequencies between zero and the effective HFC $\tilde{a}_{\text{RP}}$. Each resonance is associated with a pair of energy levels that have the correct energy separation to give a resonant RF response. As the number of HFCs in radical A increases, the number of resonances will increase, but their individual intensities will become weaker because each pair of energy levels will have a smaller share of the total RP population.

To summarise, the response to an RF field of an immobilised radical pair with no HFCs in one of the radicals, subject to fields $B_0 \gg B_1$, with negligible J and D will be dominated by a prominent Zeeman resonance. The Zeeman resonance intensity is proportional to $(B_1/B_0)^2 \sin^2 \Delta\varepsilon$ for weak RF fields (where $\Delta\varepsilon$ is the angle between the RF and static fields, defined in §9.5). Other resonances will be much weaker.

Figure 9.6 demonstrates our argument in a "2–0" RP with two randomly chosen isotropic HFCs to spin-½ nuclei in radical A and none in radical B. Calculating with the normal RF Zeeman Hamiltonian, the RF-induced change in singlet yield is shown by the black curve. Notice that there is a dominating resonance at the Zeeman frequency 1.3 MHz along with other smaller hyperfine resonances elsewhere. If we adjust the RP spin Hamiltonian artificially so that the RF field only acts on the unpaired electron in either radical A or radical B, the RF-induced changes in singlet yield are as shown in the red and green curves. Notice that with the RF on radical A, all of the resonances are reproduced exactly, except for the Zeeman resonance which is entirely absent. On the

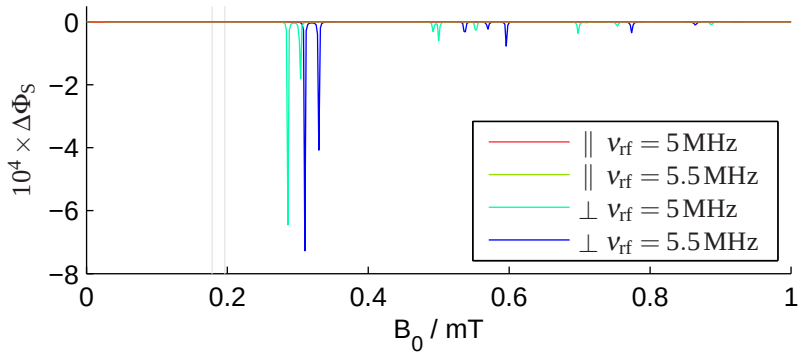

Figure 9.7: Most multinuclear RPs do not show a strong Zeeman resonance. This system is the same as that in Figure 9.4, except that HFCs of $3 \times 0.829\,\mathrm{mT}$ ($I = 1/2$) on radical A and $3 \times 0.538\,\mathrm{mT}$ ($I = 1/2$) on radical B were used.

other hand, when the RF field acts on radical B, only the Zeeman resonance emerges. Hence, the emergence of a strong Zeeman resonance in this low-field regime does, indeed, arise because of the radical with no magnetic nuclei.

Finally, RPs that contain groups of equivalent nuclei may also produce a Zeeman resonance. This occurs if, when the nuclear spins are coupled together as described in §2.2.3, there are blocks in the Hamiltonian where all the effective nuclear spins are $I = 0$. Such blocks will have equation (9.5) as their Hamiltonian and will show a Zeeman resonance by the same arguments as above. To demonstrate that this is the case, we may compare Figures 9.4 and 9.7. In Figure 9.4, there are an even number of nuclei in each group, which means that there are effective $I = 0$ blocks in the coupled basis Hamiltonian and a Zeeman resonance appears. For the same hyperfine coupling constants, but now with an odd number of nuclei in each group, Figure 9.7 has no effective $I = 0$ blocks in its coupled basis Hamiltonian and there is no Zeeman resonance.

9.5 RF field geometry

So far we have considered only very simple spin systems or multinuclear RPs with isotropic hyperfine coupling constants. In order to interpret the bird experiments, we must extend this work to consider multinuclear RPs with anisotropic HFTs and to consider systems with linearly polarised RF fields that are not collinear with the static field. In these more complicated systems, it is not apparent whether one should expect to see a strong Zeeman resonance. We address this question shortly, but first we consider how we should treat the field geometry when both static and RF fields are present.

Until now, we have only considered anisotropic MFEs when the applied magnetic field has a single characteristic direction, which may be expressed in spherical polar coordinates (θ, ϕ). For example, this is the case when either a static field, an RF field of a single frequency, or parallel static and RF fields are applied. In such systems, magnetic field effects are most easily analysed by treating the RP orientation as fixed and writing the singlet yield $\Phi_S(\theta, \phi)$ as a function of the magnetic field orientation. In Chapter 8, we saw that the spherical harmonics $Y_l^m(\theta, \phi)$ provide a complete orthonormal basis into which one may decompose such singlet yields in a first step towards

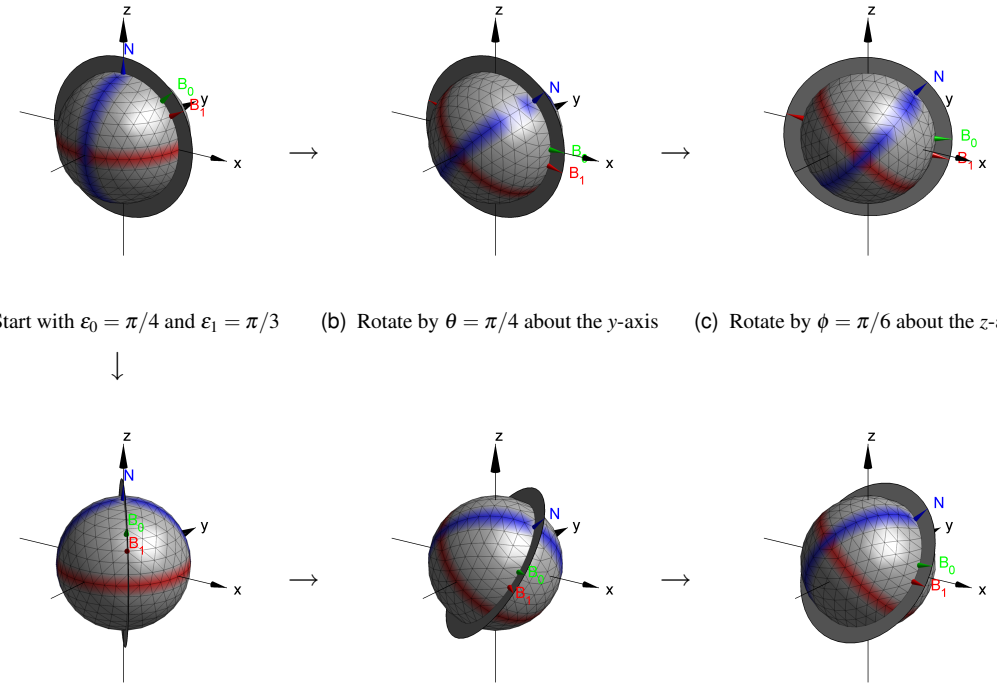

(a) Start with $\varepsilon_0 = \pi/4$ and $\varepsilon_1 = \pi/3$ (b) Rotate by $\theta = \pi/4$ about the y-axis (c) Rotate by $\phi = \pi/6$ about the z-axis

(d) OR: rotate first by $\alpha = 12\pi/7$ about the z-axis (e) Rotate by $\theta = \pi/4$ about the y-axis (f) Rotate by $\phi = \pi/6$ about the z-axis

Figure 9.8: Definitions of the field geometry (α, θ, ϕ) used in this chapter for simultaneous static B_0 and RF B_1 fields. Rotations are made according to the "zyz" convention for the Euler angles [122]. The north pole transforms to a point with spherical polar coordinates (θ, ϕ) in figures (c) and (f). This is illustrated for $(\alpha = 0, \theta = \pi/4, \phi = \pi/6)$ in figures (a–c). Figures (a, d–f) illustrate the general case when $(\alpha = 12\pi/7, \theta = \pi/4, \phi = \pi/6)$. The plane containing the north pole, B_0 and B_1 is shown as a darkened disc. This disc and a striped sphere are included to assist the reader in visualising the correct Euler angle rotations.

their interpretation.

We saw in Chapter 4 that there are significant changes in the MFE spectra for RPs with isotropic hyperfine couplings depending on the relative orientation of RF and static fields. Similar effects have been reported *in vivo*. In studies on the European robin (see §6.3.9 and [231, 232]), it was found that robins may be disoriented by weak RF fields at angles of 24° and 48° to the geomagnetic field. Yet the same RF fields had no effect when they were parallel to the geomagnetic field. To assess and interpret these results, we must model the MFEs arising from non-parallel RF and static fields in anisotropic RPs.

The field geometry in a system of parallel fields can be described by two angles: the spherical polar coordinates (θ, ϕ). This is no longer sufficient for systems with non-parallel fields. One approach would be to define the orientation of each field by its own spherical polar coordinates, e.g. we might have (θ_0, ϕ_0) for the static B_0 field and (θ_1, ϕ_1) for the RF B_1 field. The disadvantage of such an approach is that it provides no simple means to fix the relative orientation of RF and static fields that is vital to interpret the experiments.

Instead, we define the RF and static fields according to the following procedure, which is illustrated in Figure 9.8:

1. We begin by specifying the orientations of the static B_0 and RF B_1 fields with respect to the north pole "N" of an unrotated coordinate system. The angle between the north pole vector and the static field vector is ε_0, whilst that between the north pole vector and the RF field is ε_1. These two angles describe a definite field pattern in the unrotated xz-plane, which is represented by the darkened disc in Figure 9.8(a).

2. We rotate the fields by an angle θ about the y-axis to give Figure 9.8(b).

3. Next, we rotate the fields by an angle ϕ about the z-axis to give Figure 9.8(c).

These definitions arise quite naturally from the geometry of the bird experiments, shown in Figure 6.12(a). The Earth's field is at an angle $\varepsilon_0 = 24^\circ$ from vertical in Frankfurt. The RF field orientation ε_1 is chosen by rotating the Helmholtz coils that surround the bird in its testing cage as shown in Figures 6.2 and 6.3(a). During orientation, the bird is free to move within the cage. If we fix our axes relative to the bird, then this is equivalent to rotating the static and RF fields together as described above. An appealing consequence of this choice of coordinates, is that the spherical polar coordinates of the north pole in Figure 9.8(c) are simply (θ, ϕ). Thus, the preceding calculations for static or parallel fields are special cases of this new geometry where $\varepsilon_0 = \varepsilon_1 = 0^\circ$.

9.5.1 Third rotation angle

The astute will have noticed that the foregoing field geometry definitions involved only *two* rotations of the field (*i.e.* of the darkened disc). Yet, *three* angles are required to specify an arbitrary rotation in three dimensions. Figures 9.8(a,d–f) show the effect of making a rotation of α about the z-axis between steps 1 and 2 above. Notice that the north pole has spherical coordinates (θ, ϕ) in both Figures 9.8(c) and (f), but that other parts of the sphere are no longer in the same place. In other words, α affects the orientation of the static and RF fields unless $\varepsilon_0 = 0$ and $\varepsilon_1 = 0$ respectively.

It may be shown that these three Euler angles (α, θ, ϕ) describe every possible rotation of a three dimensional shape [122]. In other words, the Euler angles (α, θ, ϕ) parameterise the rotation group SO(3). To describe each possible rotation uniquely (except for singularities when rotating about the north pole), the Euler angles are taken to lie in the range

$$0 \leq \alpha < 2\pi \qquad 0 \leq \theta \leq \pi \qquad 0 \leq \phi < 2\pi. \tag{9.7}$$

This range is the "volume" V of the rotation group SO(3). The corresponding volume element is $\mathrm{d}V = \mathrm{d}\alpha \sin\theta \,\mathrm{d}\theta \,\mathrm{d}\phi$. Hence, we may easily average over all the possible rotations in three dimensions. For example, the isotropic part of the singlet yield is now given by the integral

$$\bar{\Phi}_\mathrm{S} = \iiint_V \Phi_\mathrm{S}(V)\,\mathrm{d}V = \int_0^{2\pi}\int_0^{\pi}\int_0^{2\pi} \Phi_\mathrm{S}(\alpha,\theta,\phi)\,\mathrm{d}\alpha \sin\theta \,\mathrm{d}\theta \,\mathrm{d}\phi \tag{9.8}$$

instead of by equation (8.1).

9.5.2 Wigner $\mathfrak{D}$-functions

In the previous chapter, we saw that the spherical harmonics $Y_l^m(\theta,\phi)$ provide a useful basis in which we can express functions of the spherical polar coordinates $f(\theta,\phi)$. We applied this decomposition fruitfully to describe the singlet yield $\Phi_S(\theta,\phi)$ in the presence of a static field B_0 along the direction (θ,ϕ).

When non-collinear static and RF fields are present, the singlet yield depends on the three Euler angles $\Phi_S(\alpha,\theta,\phi)$. In close analogy to the spherical harmonic expansion of functions $f(\theta,\phi)$, the Wigner $\mathfrak{D}$-functions form a complete orthonormal basis into which we may expand functions $g(\alpha,\theta,\phi)$, *i.e.* functions of the rotation group SO(3).

The Wigner $\mathfrak{D}$-functions are orthonormal in the sense that [122, p94ff]

$$\int_0^{2\pi}\int_0^{\pi}\int_0^{2\pi}\left[\mathfrak{D}_{j_2}^{m_2 m_2'}(\alpha,\theta,\phi)\right]^* \mathfrak{D}_{j_1}^{m_1 m_1'}(\alpha,\theta,\phi)\,\mathrm{d}\alpha\sin\theta\,\mathrm{d}\theta\,\mathrm{d}\phi = \frac{8\pi^2}{2j_1+1}\delta_{j_1 j_2}\delta_{m_1 m_2}\delta_{m_1' m_2'}. \quad (9.9)$$

Hence, from the standard methods of Lie algebra, any function of the rotation group $g(\alpha,\theta,\phi)$ that satisfies

$$\int_0^{2\pi}\int_0^{\pi}\int_0^{2\pi}|g(\alpha,\theta,\phi)|^2\,\mathrm{d}\alpha\sin\theta\,\mathrm{d}\theta\,\mathrm{d}\phi<\infty \quad (9.10)$$

may be expanded as a series of Wigner $\mathfrak{D}$-functions

$$g(\alpha,\theta,\phi)=\sum_{j=0,1,\ldots}^{\infty}\sum_{m=-j}^{j}\sum_{m'=-j}^{j}a_j^{mm'}\mathfrak{D}_j^{mm'}(\alpha,\theta,\phi), \quad (9.11)$$

where the coefficients $a_j^{mm'}$ represent $g(\alpha,\theta,\phi)$ in a manner analogous to the coefficients a_j^m in the spherical harmonic expansion of $f(\theta,\phi)$, defined in §8.2. Whereas the spherical harmonic expansion is a Fourier transform over the sphere S_2, decomposition in terms of Wigner $\mathfrak{D}$-functions is a Fourier transform over the rotation group SO(3).

Kostelec and Rockmore have implemented a discrete form of the Wigner $\mathfrak{D}$-function decomposition [376]. They prove that a band-limited function $g(\alpha,\theta,\phi)$ is fully characterised by the coefficients $a_j^{mm'}$ for j smaller than the band limit b. Furthermore, these coefficients $a_j^{mm'}$ may be determined in a stable and efficient manner from samples $g(\alpha_k,\theta_k,\phi_k)$ taken over an equiangular mesh with $2b\times 2b\times 2b$ points covering (α,θ,ϕ) using an FFT-based numerical algorithm, which is implemented in the `SOFT` ("SO(3) Fourier Transforms") package [376]. Similar methods have very recently been applied in the field of X-ray crystallography [380].

9.5.3 Compromise

A rigorous treatment of combined static and RF fields would involve calculating the full $\Phi_S(\alpha,\theta,\phi)$. This could then be decomposed in terms of the Wigner $\mathfrak{D}$-functions, analysing the coefficients $a_j^{mm'}$ in a manner analogous to our work in the previous chapter. However, there are two disadvantages to working with the full $\Phi_S(\alpha,\theta,\phi)$.

First, whereas a function of two angles $f(\theta,\phi)$ may be represented quite naturally by a polar plot, there is no straightforward means of plotting a function of all three

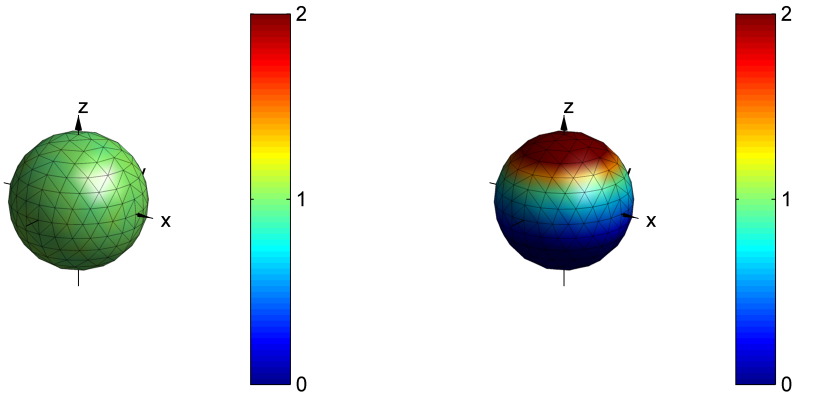

(a) Distribution of fields when $\varepsilon = 0^\circ$ and $\alpha = 0$

(b) Distribution of fields when $\varepsilon = 24^\circ$ and $\alpha = 0$

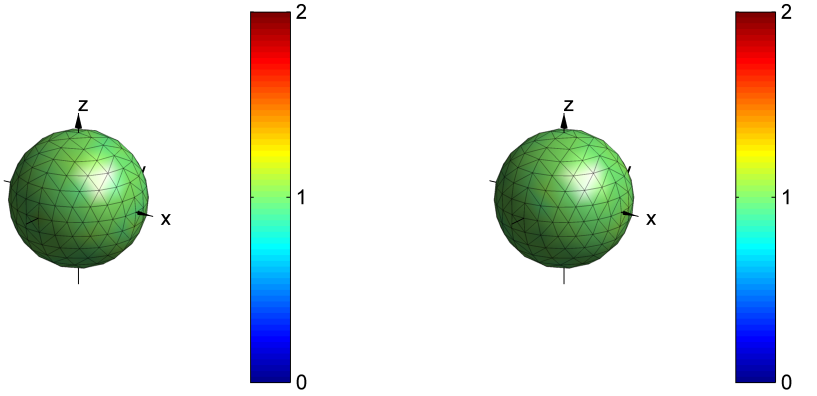

(c) Distribution of fields when $\varepsilon = 0^\circ$ and α is randomly distributed between 0 and 2π

(d) Distribution of fields when $\varepsilon = 24^\circ$ and α is randomly distributed between 0 and 2π

Figure 9.9: Failing to average over the Euler angle α results in an asymmetric distribution of fields when $\varepsilon \neq 0$. Each figure is the result of a Monte Carlo calculation. For each run, an initial unit vector at an angle ε to the z-axis in the xz-plane is rotated through a randomly chosen rotation $(0,\theta,\phi)$ or (α,θ,ϕ). The figures show the density of vectors around each vertex after many runs divided by the mean density of vectors. Figures (a) and (b) were made with 5×10^5 runs; (c) and (d) used 10^6 runs.

Euler angles $g(\alpha,\theta,\phi)$ in a single figure. The simplest approach is probably to make polar plots for several different values of α or to average over the α angle before plotting.

Second, calculating the Wigner $\mathfrak{D}$-function decomposition for a RP system is very demanding, even using efficient FFT-based methods. For a typical bandwidth $b = 15$, finding the singlet yield SphHRep requires $(2\times15)^2 = 900$ singlet yield evaluations, whereas finding the Wigner $\mathfrak{D}$-function representation requires $(2\times15)^3 = 27\,000$ singlet yield evaluations. It is only feasible to make such calculations in the simplest RPs.

In much of the following work, we compromise by fixing $\alpha = 0$. Instead of working with the full $\Phi_S(\alpha,\theta,\phi)$, we consider only $\Phi_S(0,\theta,\phi)$. These singlet yields may be analysed in the same manner as was used in Chapters 7 and 8. Notice in particular,

that we take the "isotropic singlet yield" to be defined as

$$\bar{\Phi}_{\mathrm{S}} = \int_0^{2\pi}\int_0^{\pi} \Phi_{\mathrm{S}}(0,\theta,\phi)\sin\theta\,\mathrm{d}\theta\,\mathrm{d}\phi. \tag{9.12}$$

The approximation here is illustrated in Figure 9.9. Similarly, the "maximum anisotropy" is taken to mean

$$\max_{\theta,\phi} \left|\Phi_{\mathrm{S}}(0,\theta,\phi) - \bar{\Phi}_{\mathrm{S}}\right|. \tag{9.13}$$

Although this procedure does not treat the full orientation dependence of the singlet yield, it makes the calculations computationally feasible and provides a means of visualising the results. Physically, we may imagine a robin under test turning its body in the horizontal plane (a rotation θ) and raising or lowering its head (a rotation ϕ). In fixing $\alpha = 0^\circ$, we neglect the possibility that the robin may twist its neck as it performs head-scanning movements to determine the field direction [306].

Finally, the close relationship between the full treatment of singlet yield anisotropy using Wigner $\mathfrak{D}$-functions and that using spherical harmonics for $\alpha = 0^\circ$ is demonstrated by

$$\mathfrak{D}_l^{0,m'}(0,\theta,\phi) = \sqrt{\frac{4\pi}{2l+1}}\,Y_l^{-m'}(\theta,\phi). \tag{9.14}$$

9.6 RF effects in one- and two-proton RPs

Anisotropic RF magnetic field effect calculations involve considerably more computational effort than is needed to compute the product yield anisotropy in the presence of a static field alone. Even when we compromise by fixing $\alpha = 0^\circ$, the need to use γ–`COMPUTE` increases the time taken to calculate the singlet yields at each particular orientation of fields. It is, therefore, not possible to conduct a full survey of the anisotropic RF field responses at this time. Instead, we show calculations for a number of model systems in the hope that these are representative.

Figures 9.10 and 9.11 show the singlet yield anisotropy for a set of "n–0" and "1–1" model RPs. In each case, the initial static field orientation $\varepsilon_0 = 0^\circ$. The static field strength $B_0 = 46\,\mu\mathrm{T}$ is chosen to match that in Frankfurt and the RF field strength $B_1 = 33\,\mathrm{nT}$ was chosen to be comparable to that used in the bird experiments. The radio frequency $\nu_{\mathrm{rf}} = 1.3\,\mathrm{MHz}$ matches the Zeeman resonance condition for this static field.

From the figures, we see that for static and RF fields taken separately, the static field has a substantially greater effect on the anisotropy. For example, in Figures 9.10(c) and (f), the singlet yield anisotropy in a static field is approximately $4\times10^6 \approx (B_0/B_1)^2$ times larger than that in an RF field. This quadratic dependence is to be expected since, as we saw in §8.4, the singlet yield anisotropy arises from second (and higher) orders of the Zeeman interaction. These results agree with the general principle that, all other things being equal, RF and static fields of similar strength produce similar changes in singlet yield.

The changes in singlet yield when an RF field is added to the static field are shown in the bottom two rows. Notice that when the RF and static fields are parallel, $\Delta\varepsilon =$

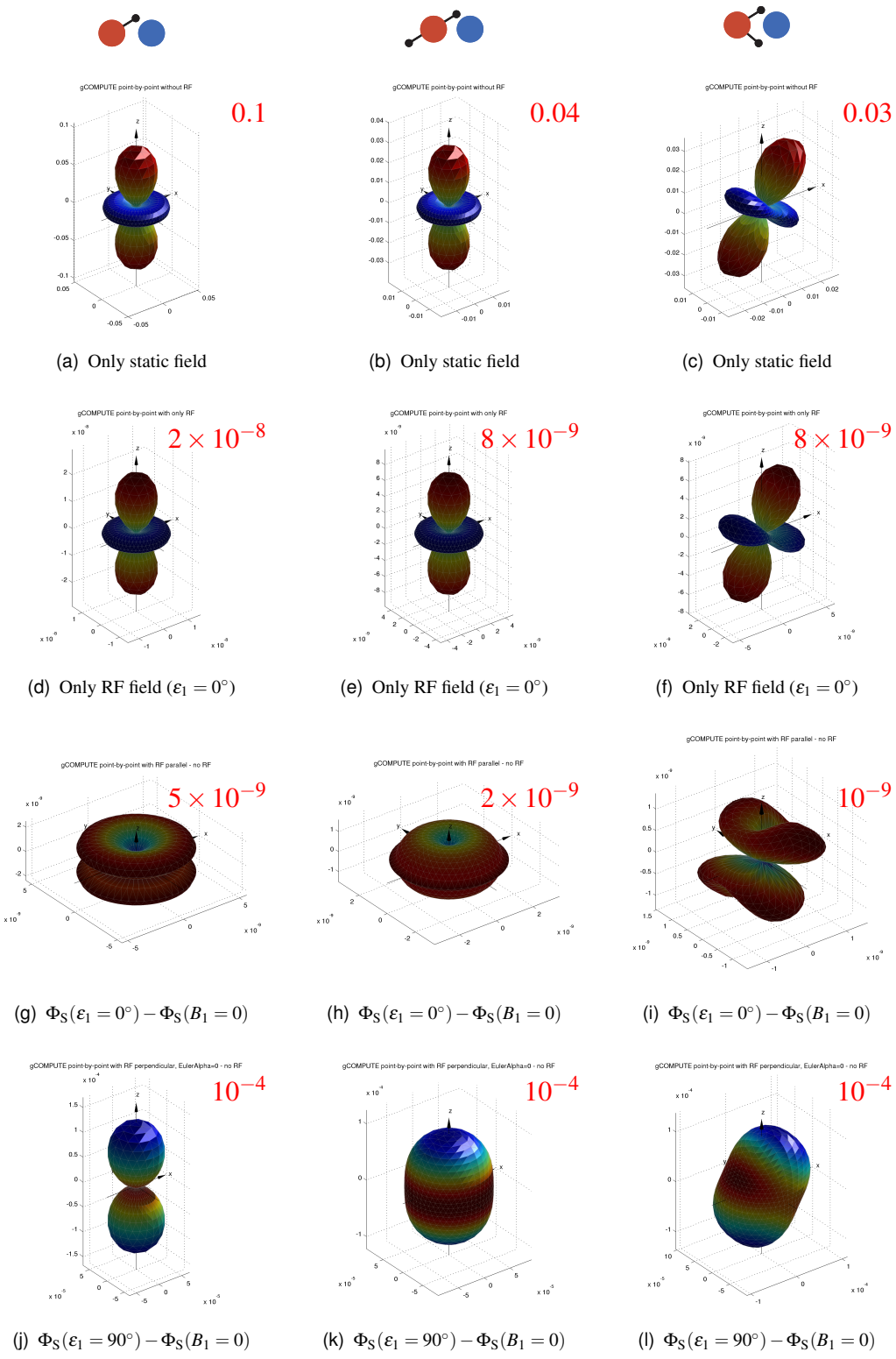

(a) Only static field (b) Only static field (c) Only static field

(d) Only RF field ($\varepsilon_1 = 0°$) (e) Only RF field ($\varepsilon_1 = 0°$) (f) Only RF field ($\varepsilon_1 = 0°$)

(g) $\Phi_S(\varepsilon_1 = 0°) - \Phi_S(B_1 = 0)$ (h) $\Phi_S(\varepsilon_1 = 0°) - \Phi_S(B_1 = 0)$ (i) $\Phi_S(\varepsilon_1 = 0°) - \Phi_S(B_1 = 0)$

(j) $\Phi_S(\varepsilon_1 = 90°) - \Phi_S(B_1 = 0)$ (k) $\Phi_S(\varepsilon_1 = 90°) - \Phi_S(B_1 = 0)$ (l) $\Phi_S(\varepsilon_1 = 90°) - \Phi_S(B_1 = 0)$

Figure 9.10: Effect of simultaneous static $B_0 = 46\,\mu\text{T}$ and RF $B_1 = 33\,\text{nT}$ fields on the singlet yield of simple "1–0" and "2–0" model RPs. The maximum absolute value in each figure is shown in red. In all cases, the initial static field orientation $\varepsilon_0 = 0°$, the rate constant $k = 5 \times 10^4\,\text{s}^{-1}$ and the radio frequency $\nu_{\text{rf}} = 1.3\,\text{MHz}$. Hyperfine tensors with $a = 500\,\mu\text{T}$, $\alpha = -150\,\mu\text{T}$ and $\beta = 0\,\mu\text{T}$; and $a = 730\,\mu\text{T}$, $\alpha = -153.3\,\mu\text{T}$ and $\beta = 0\,\mu\text{T}$ were used. The cartoons at the top indicate how many HFTs were used and their relative orientation. In the right-hand column, the second HFT was rotated so that it was not coaxial with the first.

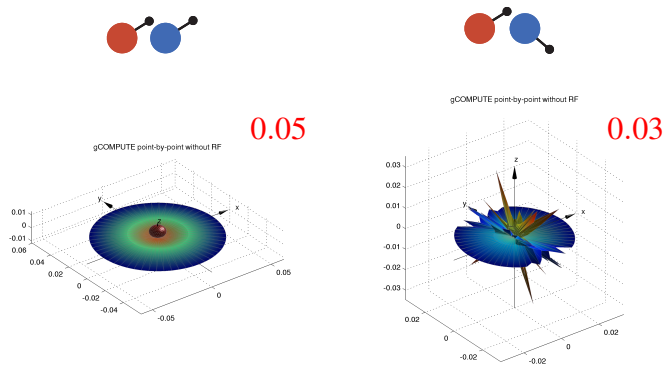

(a) Only static field (b) Only static field

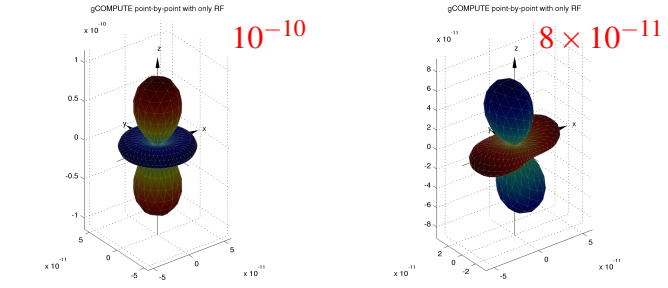

(c) Only RF field ($\varepsilon_1 = 0°$) (d) Only RF field ($\varepsilon_1 = 0°$)

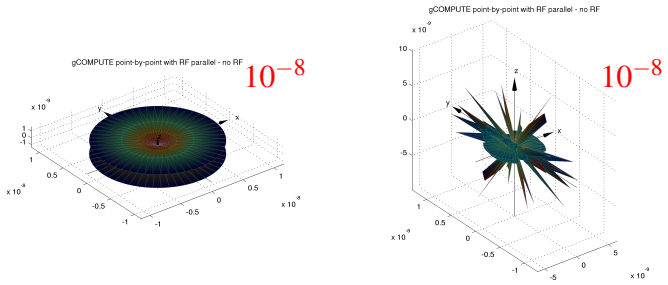

(e) $\Phi_S(\varepsilon_1 = 0°) - \Phi_S(B_1 = 0)$ (f) $\Phi_S(\varepsilon_1 = 0°) - \Phi_S(B_1 = 0)$

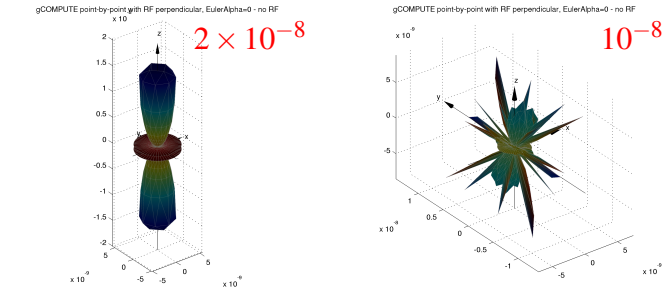

(g) $\Phi_S(\varepsilon_1 = 90°) - \Phi_S(B_1 = 0)$ (h) $\Phi_S(\varepsilon_1 = 90°) - \Phi_S(B_1 = 0)$

Figure 9.11: Effect of simultaneous static $B_0 = 46\,\mu\text{T}$ and RF $B_1 = 33\,\text{nT}$ fields on the singlet yield of simple "1–1" model RPs. The maximum absolute value in each figure is shown in red. In all cases, the initial static field orientation $\varepsilon_0 = 0°$, the rate constant $k = 5 \times 10^4\,\text{s}^{-1}$ and the radio frequency $\nu_{\text{rf}} = 1.3\,\text{MHz}$. Hyperfine tensors with $a = 500\,\mu\text{T}$, $\alpha = -150\,\mu\text{T}$ and $\beta = 0\,\mu\text{T}$; and $a = 730\,\mu\text{T}$, $\alpha = -153.3\,\mu\text{T}$ and $\beta = 0\,\mu\text{T}$ were used. The cartoons at the top indicate the relative orientation of the HFTs in each radical. In the right-hand column, the second HFT was rotated so that it was not coaxial with the first.

$\varepsilon_1 = 0°$, the change in singlet yield is comparable to that for the RF field alone. In other words, parallel RF fields do not produce resonance effects in these systems. On the other hand, when the RF and static fields are perpendicular, $\Delta\varepsilon = \varepsilon_1 = 90°$, the changes in singlet yield are sometimes rather larger. For the "n–0" RPs in Figure 9.10, the changes in singlet yield in the presence of perpendicular RF are $\Delta\Phi_S \sim 10^{-4}$. In contrast, the "1–1" RPs in Figure 9.11 show similarly small RF-induced singlet yield changes $\Delta\Phi_S \sim 10^{-8}$ for both parallel and perpendicular fields.

For these anisotropic systems, an RF field at the Zeeman resonance frequency produces significantly larger singlet yield anisotropy changes in "n–0" than in "1–1" RPs. In "n–0" RPs, perpendicular RF fields have a stronger effect than parallel fields, although in absolute terms neither changes the singlet yield anisotropy substantially. This behaviour suggests strongly that there are Zeeman resonances for "n–0" RPs with anisotropic HFTs, but not for "m–n" RPs, just as was the case for RPs with isotropic HFTs.

9.7 Calculations for the flavin radicals

We saw in Chapter 7 that the cryptochrome family of proteins are promising candidates for the RPM magnetoreceptor in birds. The cryptochromes are closely related to the DNA photolyases. Both are flavoproteins, containing an FAD cofactor. Although the cryptochrome photocycle is still not yet known, we assume here that it proceeds via a RP involving either the flavin radical anion $FAD^{\bullet-}$, whose structure and HFTs are given in Figure 7.17, or the flavin radical $FADH^{\bullet}$, whose structure and HFTs are given in Figure 7.16. We do not expect that our findings would change substantially if a different charge or oxidation state of $FAD(H_x)$ were used. In Chapter 7, we saw that the static field singlet yield anisotropy of RPs containing $FAD^{\bullet-}$ is often dominated by the strongly axial HFTs of the ring nitrogen atoms N5 and N10. A similar situation is found for $FADH^{\bullet}$ [321].

We are now in a position to model the results from the bird experiments with RF fields summarised in Figures 6.12 and 6.13. To this end, we model the response from a cryptochrome-based RPM magnetoreceptor by treating a series of RPs containing N5 and/or N10 from $FAD^{\bullet-}$ or $FADH^{\bullet}$ on one radical, with no magnetic nuclei on the counter-radical.

9.7.1 Significant changes in singlet yield

To aid our discussion of anisotropic RF field effects, we consider what magnitude of change in singlet yield might be sufficient to disrupt magnetoreception. It is known from behavioural studies (see §6.3.8) that robins are able to orient only in a rather small "window" of static field strengths. For robins accustomed to $B_0 = 46\,\mu T$, raising the field to $B_0 = 60\,\mu T$ or lowering the field to $B_0 = 34\,\mu T$ caused disorientation. Figure 9.12 shows the spherical average singlet yield and the maximum absolute singlet yield anisotropy for RPs containing N5 and/or N10 from $FAD^{\bullet-}$. The vertical lines show where $B_0 = 34$, 46 and $60\,\mu T$. We would expect RF fields to need to produce similar changes in the singlet yield (or its anisotropy) if they were also to disorient a robin. The figure shows that the isotropic singlet yield and the maximum anisotropy caused by a field $B_0 = 46\,\mu T$ (where orientation is possible) differs from the responses

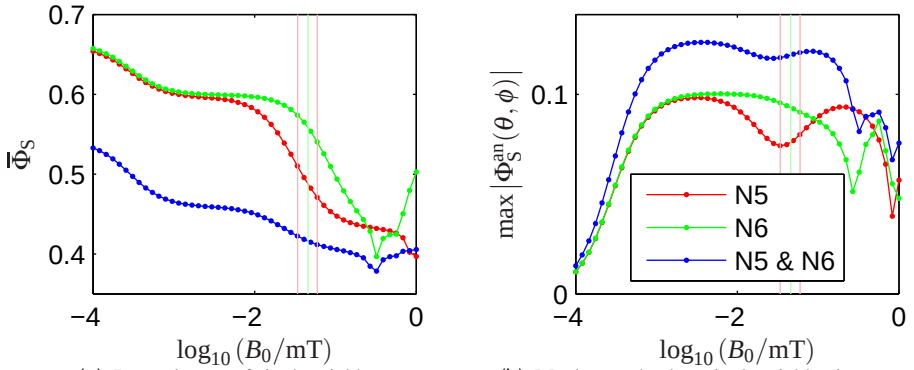

(a) Isotropic part of singlet yield (b) Maximum absolute singlet yield anisotropy

Figure 9.12: Effect of static field on isotropic singlet yield and maximum singlet yield anisotropy for three model radical pairs. The systems used here have hyperfine couplings from N5 and/or N10 (both I=1) in $FAD^{\bullet-}$ (see Figure 7.17) on radical A. Radical B has no magnetic nuclei. Other parameters: $k = 5\times10^4\,\mathrm{s}^{-1}$, $B_1 = 0\,\mathrm{mT}$. These calculations were made using the frequency domain method from §2.2.2.

at $B_0 = 34$ or $60\,\mu\mathrm{T}$ (where orientation is not possible) by $\sim 3\%$. Hence, it would appear that an RF field which causes a fractional change in isotropic singlet yield or in the maximum anisotropy of $\sim 3\%$ might have a significant disorienting effect.

9.7.2 Effect of radio frequency and orientation

In Figures 9.10 and 9.11, we treated RF fields in parallel and perpendicular orientations for only a single radio frequency. We now extend those calculations to cover radio frequencies in the range 1–10 MHz in order to assess whether there is a strong response at the Zeeman frequency as is seen in the bird experiments summarised in Figure 6.13.

Figure 9.13 shows the effects of RF fields between 1 and 10 MHz in RPs comprising N5 and/or N10 from $FAD^{\bullet-}$ with no magnetic nuclei in the counter-radical. The field geometry is chosen to match that used in the bird experiments. In all cases, $\varepsilon_0 = 24^\circ$, which is the angle that the geomagnetic field makes with vertical in Frankfurt. The RF field was either vertical $\varepsilon_1 = 0^\circ$ (green curves), parallel to the static field $\varepsilon_1 = 24^\circ$ (red curves) or perpendicular to the static field $\varepsilon_1 = 114^\circ$ (blue curves). To quantify the RF effects, we define

$$\Delta_{\mathrm{iso}} = \frac{\bar{\Phi}_S(B_1\ \&\ B_0) - \bar{\Phi}_S(B_0\ \text{alone})}{\bar{\Phi}_S(B_0\ \text{alone})} \tag{9.15}$$

as the RF-induced fractional change in spherical average singlet yield and

$$\Delta_{\mathrm{aniso}} = \frac{\max\left|\Phi_S^{\mathrm{an}}(B_1\ \&\ B_0)\right| - \max\left|\Phi_S^{\mathrm{an}}(B_0\ \text{alone})\right|}{\max\left|\Phi_S^{\mathrm{an}}(B_0\ \text{alone})\right|} \tag{9.16}$$

as the RF-induced fractional change in maximum absolute singlet yield anisotropy.

In every figure, there is a much stronger change in spherical average singlet yield and in maximum absolute singlet yield anisotropy at the Zeeman resonance frequency than at other frequencies. Indeed, the next strongest resonances, which lie between 7

and 10 MHz in Figures 9.13(c–f), are thirty times less intense and are hardly visible at this scale. Furthermore, the depth of the Zeeman resonance depends strongly on the relative orientation of the static and RF fields $\Delta\varepsilon$. The amplitude is approximately proportional to $\sin^2\Delta\varepsilon$, as would be expected in the high field limit, when the static field Zeeman interaction dominates the RP spin Hamiltonian.

Although the Zeeman resonance produces larger changes in singlet yield than at other frequencies, even the Zeeman resonance with perpendicular fields in Figure 9.13(b) only amounts to a 0.1% change in singlet yield anisotropy. This is much less than the 3% threshold for disorientation that we estimated above. It is possible that a different (more realistic) RP would produce stronger changes, or that an even longer-lived RP would show a stronger Zeeman resonance.

9.7.3 Effect of RF field strength

In Figure 9.14, we repeat these calculations in a RP containing N5 and N10 from $FAD^{\bullet-}$ for greater RF field strengths. In a field of 330 nT, the Zeeman resonance for perpendicular RF and static fields is already around 6%, which should be strong enough to disorient a bird. This rapid growth of the Zeeman resonance reflects its origins as a second order perturbation effect, and hence its dependence on B_1^2. In the lower figures, where $B_1 = 33\,\mu\text{T}$, the Zeeman resonance has saturated and there are large changes in singlet yield anisotropy in the presence of RF fields at many frequencies.

9.7.4 Effect of static field strength

In order to be confident that the peak occurring at $\nu_{\text{rf}} = 1.3\,\text{MHz}$ is truly a Zeeman resonance, we should alter the static field strength and verify that the resonance moves according to equation (9.1). Figure 9.15 shows the RF-induced changes in singlet yield when $B_0 = 46$ and $92\,\mu\text{T}$ with $\alpha = 0^\circ$ for two similar RPs containing three nuclei from $FADH^{\bullet}$ on one radical and no magnetic nuclei on the counter-radical. For both the RPs in Figures 9.15(a) and (b), we see a strong clear Zeeman resonant effect on the fractional RF-induced change in spherical average singlet yield Δ_{iso} and on the fractional change in maximum singlet yield anisotropy Δ_{aniso}. We may firmly identify this as a Zeeman resonance, because the resonant frequency shifts according to equation (9.1) when the static field strength is changed. The change in Δ_{aniso} at the Zeeman resonance frequency is at least 7.5 times larger than that at any other frequency.

Finally, we repeat this calculation for the full range of Euler angles (α, θ, ϕ). The results, taking 10 steps in α, are shown in Figure 9.16. In order to reduce the amount of processing time required, we calculated for 201 radio frequencies here, in contrast to the 501 that we used in Figure 9.15. Nonetheless, we are grateful to the Oxford Supercomputing Centre for the 1000 hours of CPU time that were used to calculate this figure. Once again, we see clear Zeeman resonance effects on Δ_{iso} and Δ_{aniso}. The Zeeman resonance when $B_0 = 46\,\mu\text{T}$ appears to be rather small. This is likely to be an artefact caused by the reduced number of RF field points used in this calculation.

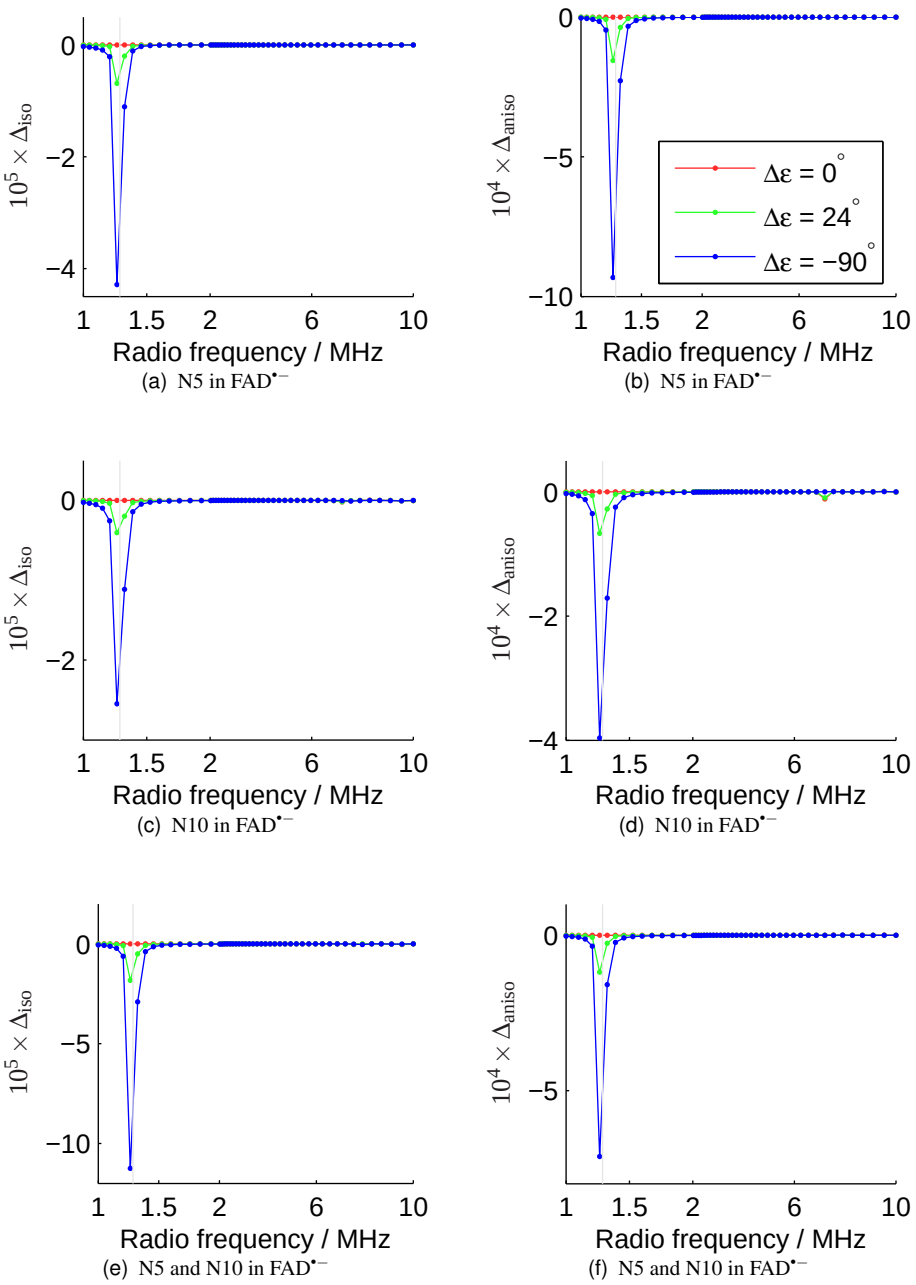

Figure 9.13: Influence of relative RF and static field orientation $\Delta\varepsilon$ in a selection of "n-0" radical pairs with anisotropic HFTs. Radical A has HFTs from FAD$^{\bullet-}$ (see Figure 7.17 for values and details of the atom numbering used). There are no magnetic nuclei in radical B. In all cases, the initial static field orientation $\varepsilon_0 = 24°$, which is the angle that the geomagnetic field makes with vertical in Frankfurt. The initial RF field orientation $\varepsilon_1 = 24°$, $0°$ (vertical) or $114°$ in the red, green and blue curves respectively. Other parameters: $k = 5 \times 10^4\,\mathrm{s}^{-1}$, $B_0 = 46\,\mu\mathrm{T}$, $B_1 = 33\,\mathrm{nT}$ and $n = 512$. The parameters Δ_{iso} and Δ_{aniso} are defined in the main text. The Zeeman resonance frequency is marked with a grey line. Note that the radio frequency axis scale changes at $2\,\mathrm{MHz}$.

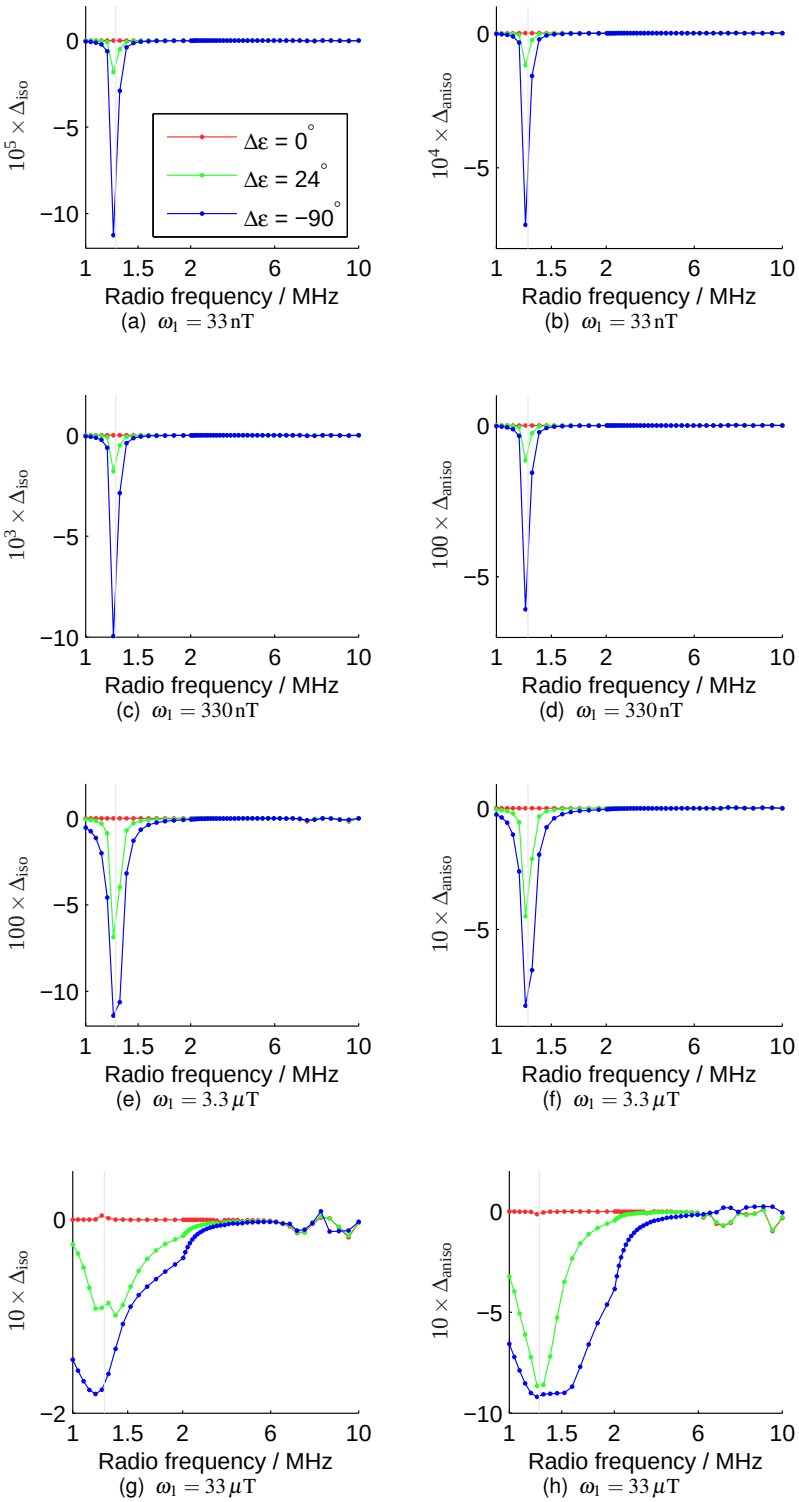

Figure 9.14: Effect of RF field strength in a "2-0" radical pair. Radical A comprises N5 and N10 (both I=1) from $FAD^{\bullet -}$ (see Figure 7.17); there are no magnetic nuclei in radical B. The initial RF field orientation $\varepsilon_1 = 24°$, $0°$ (vertical) or $114°$ in the red, green and blue curves respectively. Other parameters: $k = 5 \times 10^4\,\mathrm{s}^{-1}$, $B_0 = 46\,\mu\mathrm{T}$, $\varepsilon_0 = 24°$ and $n = 512$. The parameters Δ_{iso} and Δ_{aniso} are defined in the main text. The Zeeman resonance frequency is marked with a grey line. Note that the radio frequency axis scale changes at 2 MHz.

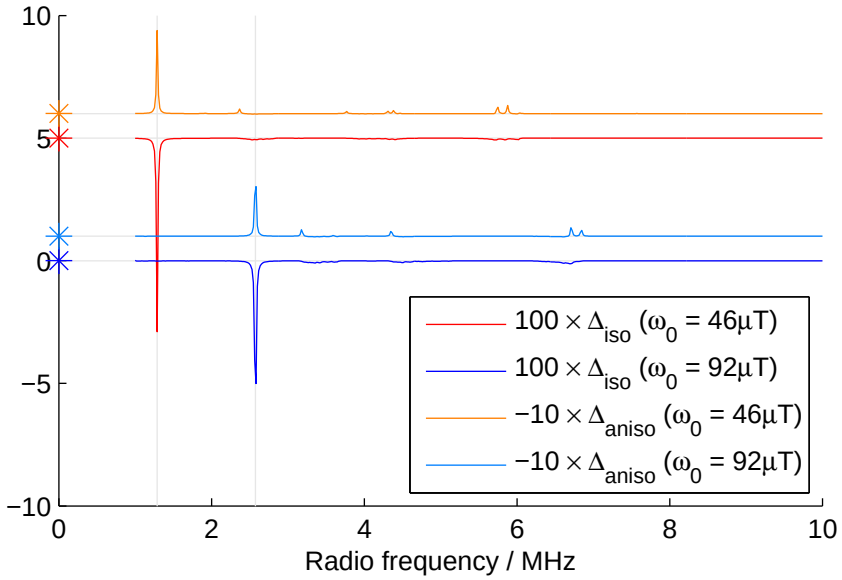

(a) Summary of calculations in a RP system containing N5, N10 and H6 from FADH•.

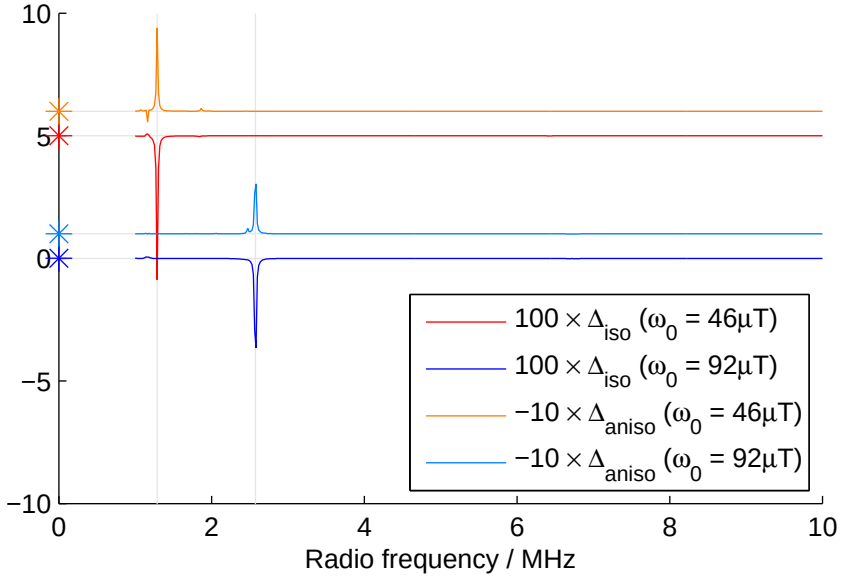

(b) Summary of calculations in a RP system containing N5, N10 and H5 from FADH•.

Figure 9.15: Summary of calculations with $\alpha = 0°$ for RPs containing three magnetic nuclei from FADH• in static fields $B_0 = 46$ and $92\,\mu$T. The corresponding Zeeman frequencies are marked with vertical grey lines. Hyperfine tensors and the atom numbering for FADH• are given in Figure 7.16. Other parameters: $\varepsilon_0 = 24°$, $\varepsilon_1 = 0°$, $k = 5 \times 10^4\,\text{s}^{-1}$, $B_1 = 1\,\mu$T and $n = 64$. As far as possible these values were chosen to match those in recent experiments on European robins [314]. Calculations were made using the gCOMPFST algorithm (see Chapter 8) with MaxL $= 11$. For clarity, the curves are offset vertically by 0, 1, 5 or 6 units. The point at zero frequency is calculated by treating the RF field as an additional static field contribution and averaging over the initial RF phase γ.

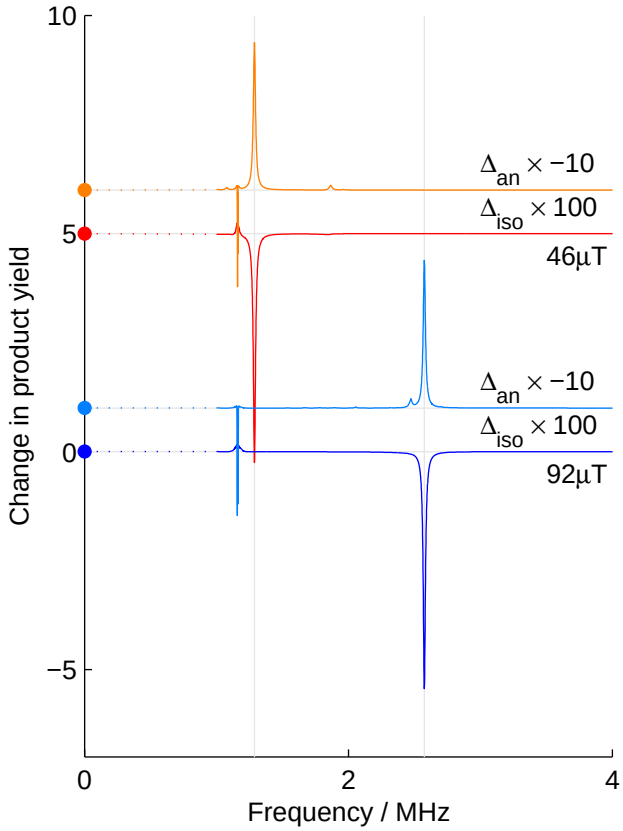

Figure 9.16: Summary of calculations over all three Euler angles (α, θ, ϕ) for RPs containing N5, N10 and H5 from FADH$^\bullet$ in static fields $B_0 = 46$ and $92\,\mu$T. The corresponding Zeeman frequencies are marked with vertical grey lines. Hyperfine tensors and the atom numbering for FADH$^\bullet$ are given in Figure 7.16. Other parameters: $\varepsilon_0 = 24°$, $\varepsilon_1 = 0°$, $k = 5 \times 10^4\,\mathrm{s}^{-1}$, $B_1 = 1\,\mu$T and $n = 64$. As far as possible these values were chosen to match those in recent experiments on European robins [314]. Calculations were made using the gCOMPFST algorithm (see Chapter 8) with MaxL $= 11$ at ten different values of α before being combined. The zero-frequency points were calculated by averaging singlet yield anisotropies calculated for an appropriate ensemble of static fields. For clarity, the curves are offset vertically by 0, 1, 5 or 6 units.

9.8 Comparison with bird results

Figures 9.15 and 9.16 come as close to modelling avian magnetoreception as is possible given our current level of understanding and with the available computing resources. Comparing these figures with Figure 6.13, we see that qualitatively they agree well with one another.

In particular, the sensitivity to different radio frequencies in both the animal experiments and our spin chemical calculations is characteristic of a Zeeman resonance. For the Earth-strength static fields relevant to magnetoreception, we have seen that only "n–0" RPs, which have no magnetic nuclei in one radical, produce such resonant features. This is a significant result, whose physical interpretation is discussed below.

Turning back to Figure 6.13, we see that as the RF field strength is increased, robins are disoriented over a wider range of frequencies. We observed similar behaviour for our model system in Figure 9.14. In the calculations, the width of the Zeeman resonance increases as the RF field strength is raised.

However, the agreement between these calculations and the animal studies is not perfect. First, the animal experiments assert that at the Zeeman resonance frequency, fields as weak as 15 nT cause disorientation. Yet, in Figure 9.13, we saw fractional RF-induced changes in the spherical average singlet yield or in its maximum anisotropy that were no larger than 0.1% for a stronger field $B_1 = 33\,\mathrm{nT}$. The RPM model is not currently able to explain how such weak magnetic fields are able to disrupt orientation. It does not seem plausible that such weak fields should give rise to substantially larger Δ_{iso} and Δ_{aniso} in a real biochemical system. Nor does it seem reasonable that an RPM-based compass should be so delicate as to be disrupted by fractional changes in the singlet yield on the order of 0.1%.

The second difference between these model calculations and experiment is in the response to stronger RF fields. Figure 6.13 shows that, as the RF field is increased in strength to $B_1 = 480\,\mathrm{nT}$, robins are disoriented at frequencies $100\,\mathrm{kHz} \leq \nu_{\mathrm{rf}} \leq 7\,\mathrm{MHz}$ but not when $\omega_{\mathrm{rf}} < 100\,\mathrm{kHz}$. Yet our calculations, such as Figures 9.12 and 9.14, suggest that stronger RF fields are most effective when $\nu_{\mathrm{rf}} < 2\,\mathrm{MHz}$. It is not readily apparent from where the sensitivity to 7 MHz RF arises. According to our model, the response to 7 MHz RF would come from a resonance with the hyperfine interaction. It is, therefore, possible that this sensitivity to weak 7 MHz RF fields provides a clue to the identity of the RP involved in magnetoreception.

9.9 Two site electron hopping in the solid state

Orientation experiments in European robins, summarised in Figure 6.13, show a clear Zeeman resonance in the birds' response to RF fields. We have shown that for a RP reaction with anisotropic HFTs, one may only expect a Zeeman resonance when $B_0 \gg \tilde{a}$ for either or both radicals. In order to fulfil this requirement in Earth-strength static fields, at least one of the radicals in the RP responsible for magnetoreception must have no hyperfine interactions larger than $\sim 1\,\mu\mathrm{T}$. It is not yet clear how one may satisfy this stringent requirement in a real, physical RP reaction.

One possibility is that, in the weak-field limit, rapid hopping of one of the unpaired electrons might suppress any hyperfine interactions that it would otherwise experience. This would give rise to an 'effective "n–0" radical pair'.

9.9.1 Kaplan-Alexander treatment

To test this hypothesis, we perform calculations in a solid-state radical pair. The unpaired electron on radical B is fixed, whilst that on radical A hops between two sites N1 and N2. Calculations are performed using the Kaplan-Alexander density matrix treatment of exchange [93, p303ff]. For simplicity, we consider a radical pair in which B has no magnetic nuclei, whilst sites N1 and N2 each have a single spin-½ nucleus. When the unpaired electron A is present on site N1 or N2 it experiences an isotropic hyperfine interaction a with the spin-½ nucleus there. The nucleus at the unoccupied site, N1 or N2, has no interactions whatsoever and remains frozen in its spin state until the electron hops onto that site. There may also be a static field of strength $B_0 = -\omega_0/\gamma_e$, giving rise to electron Zeeman interactions.

This system is described by the following Hamiltonian

$$\hat{H} = a\hat{\boldsymbol{S}}_{\mathrm{A}} \cdot \hat{\boldsymbol{I}}_{\mathrm{Nfull}} + \omega_0 \hat{S}_{\mathrm{Az}} + \omega_0 \hat{S}_{\mathrm{Bz}} \tag{9.17}$$

where $\hat{\boldsymbol{S}}$ is the electron spin vector operator, and $\hat{\boldsymbol{I}}_{\mathrm{Nfull}}$ is the nuclear spin operator for the occupied site Nfull (either N1 or N2), the other site being Nempty. The spin evolution is governed by a phenomenologically modified form of the Liouville-von Neumann equation:

$$\frac{\mathrm{d}\hat{\rho}}{\mathrm{d}t} = -\mathrm{i}\left[\hat{H}, \hat{\rho}\right] + k_{\mathrm{ex}}\left(\hat{P}\hat{\rho}\hat{P} - \hat{\rho}\right) \tag{9.18}$$

where k_{ex} is a first order rate constant for the electron hopping process. Working in the product basis $|\mathrm{A}\rangle \otimes |\mathrm{B}\rangle \otimes |\mathrm{Nfull}\rangle \otimes |\mathrm{Nempty}\rangle$, the operator $\hat{P}$ is block diagonal with the form

$$\hat{P} = \begin{pmatrix} \hat{q} & 0 & 0 & 0 \\ 0 & \hat{q} & 0 & 0 \\ 0 & 0 & \hat{q} & 0 \\ 0 & 0 & 0 & \hat{q} \end{pmatrix} \tag{9.19}$$

where

$$\hat{q} = \begin{pmatrix} 1 & 0 & 0 & 0 \\ 0 & 0 & 1 & 0 \\ 0 & 1 & 0 & 0 \\ 0 & 0 & 0 & 1 \end{pmatrix}. \tag{9.20}$$

In other words, electron hopping is treated by swapping the populations and coherences associated with Nfull and Nempty. Instead of the electron hopping, the mathematical treatment swaps and relabels the nuclear spins.

9.9.2 Runge-Kutta (4,5) solutions

Some numerical solutions to equation (9.18) are shown in Figure 9.17. These were computed for a range of hopping rates k_{ex} with $B_0 = 0$ or $200\,\mu\mathrm{T}$ using a Runge-Kutta (4,5) ODE solver in `Matlab`. The most important result of these calculations is that for no electron hopping rate k_{ex} does the singlet probability $\left\langle \hat{P}^{\mathrm{S}} \right\rangle(t)$ cease to oscillate.

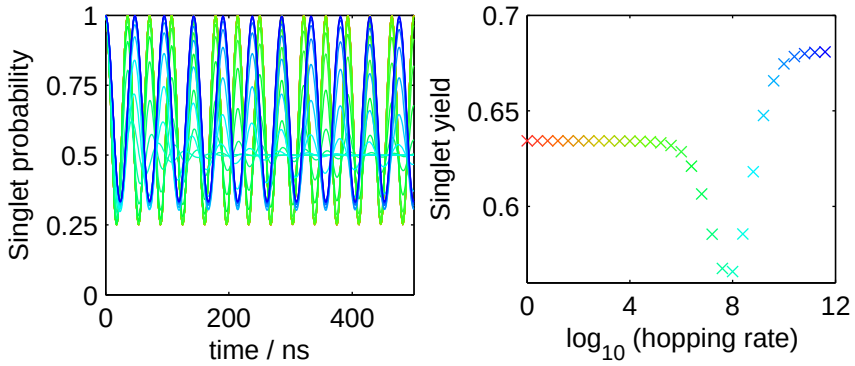

(a) Results when $B_0 = 0\,\mu\text{T}$

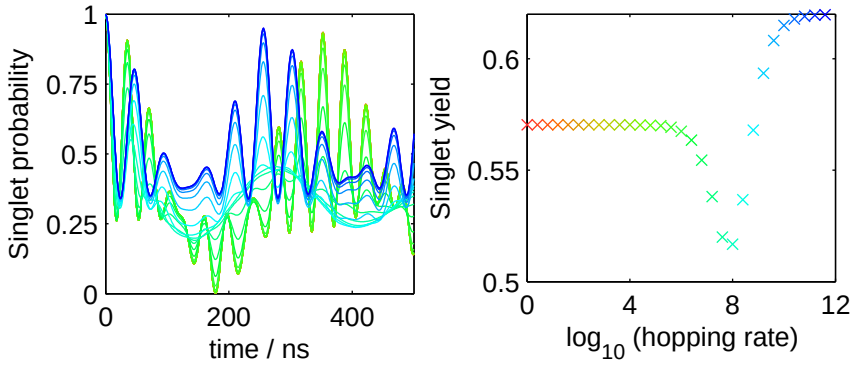

(b) Results when $B_0 = 200\,\mu\text{T}$

Figure 9.17: Runge-Kutta (4,5) solutions of equation (9.18) for $a = 1.0\,\text{mT}$ and $B_0 = 0$ or $200\,\mu\text{T}$. The singlet yields are calculated for an exponential model rate constant of $k = 2.8 \times 10^7\,\text{s}^{-1}$. Both figures are coloured according to the hopping rate k_{ex}.

If electron hopping in weak static fields did act to suppress the hyperfine interaction, we would have expected for certain hopping rates k_{ex} that the singlet probability $\langle \hat{P}^{\text{S}} \rangle (t) = 1$ at all times. Since this does not occur, electron hopping cannot be responsible for producing the 'effective "n–0" RP' involved in magnetoreception.

As an aside, we may interpret the results in Figure 9.17 using Brocklehurst's formula [10, eq. (16)] for the singlet probability in a RP containing a single group of equivalent nuclei at zero field

$$\langle \hat{P}^{\text{S}} \rangle (t) = \frac{1 + 2I(I+1)\left(1 + \cos\left(\left[I + \frac{1}{2}\right] at\right)\right)}{(2I+1)^2}. \tag{9.21}$$

For a single $I = 1/2$ with hyperfine coupling a, this simplifies to

$$\langle \hat{P}^{\text{S}} \rangle (t) = \frac{5}{8} + \frac{3}{8}\cos at. \tag{9.22}$$

Meanwhile, two equivalent $I = 1/2$ with hyperfine couplings $a/2$ may be treated as an effective $I = 0$ and $I = 0$. Hence,

$$\langle \hat{P}^{\text{S}} \rangle (t) = \frac{1}{4}\left[1 + \frac{5}{3} + \frac{4}{3}\cos\left(\frac{3at}{4}\right)\right] \tag{9.23}$$

$$= \frac{2}{3} + \frac{1}{3}\cos\left(\frac{3at}{4}\right). \tag{9.24}$$

These formulae describe accurately the slow- and fast-hopping limits at zero field in Figure 9.17(a). Hence, the slow hopping limit is equivalent to a one-proton RP with HFC a. Physically, this is quite reasonable because in the slow hopping limit, the unpaired electron spends its entire life in one of the two sites and is oblivious to the hyperfine coupling on the other site. The fast hopping limit is equivalent to a two-proton RP with two equivalent HFCs of $a/2$ each. In general, fast electron hopping between r sites all with hyperfine coupling a is equivalent to having r equivalent nuclei all with hyperfine coupling a/r. Electron hopping is not an efficient means of suppressing the hyperfine interactions in a RP.

9.10 Conclusions and suggestions for further work

In this chapter, we explored in depth the effects of RF fields on RPM product yields for radicals with anisotropic hyperfine tensors. We also introduced a convenient definition for the geometry of a system of simultaneously applied RF and static fields that is suitable for modelling recent behavioural experiments in European robins.

Using this definition and the γ–`COMPUTE` algorithm developed in Chapter 4, we found that "n–0" RPs with no magnetic nuclei in one of the radicals show strong Zeeman resonant effects on their spherical average singlet yield and maximum absolute singlet yield anisotropy. Even in fields as weak as the Earth's, these "n–0" RPs show a Zeeman resonance that behaves in the same manner as would normally be expected at high field. In contrast, RPs with magnetic nuclei in both partners do not, in general, show any Zeeman resonance when the static field is comparable in strength to the geomagnetic field.

Using a RP inspired by the cryptochrome family of proteins, we performed a number of calculations to model the results of behavioural studies in European robins which are summarised in Figures 6.12 and 6.13. This modelling lead us to conclude that the data from the robin behavioural experiments are qualitatively consistent with the hypothesis of RPM-based magnetoreception, providing that the RP involved has (perhaps only effectively) no hyperfine couplings in one radical. In other words, the data are consistent with RPM magnetoreception using an "n–0" or an 'effective "n–0" RP' as its basis.

The physical interpretation of this finding remains to be found. Simple calculations show that electron hopping in Earth-strength fields in the solid state would not abolish the hyperfine couplings in a radical.

Another possibility, which should be investigated, is that the counter-radical may contain many nuclei with equivalent hyperfine couplings. Providing that there were an even number of equivalent nuclei, this group of equivalent nuclei would give rise to a substantial effective $I = 0$ block in the coupled-basis RP spin Hamiltonian. This effective $I = 0$ block would give rise to a Zeeman resonance as described above. Further calculations should be performed to test whether this is indeed the case.

In particular, it is difficult to imagine a molecule containing several nuclei with exactly equivalent anisotropic hyperfine tensors. One would expect the HFTs to differ at least in their orientation depending on the position of the atom in question relative to the molecular frame of the radical. It is not yet known whether, for example, equivalence of the isotropic parts of the hyperfine tensors would be sufficient to produce a Zeeman resonance. This idea could be tested by further numerical modelling calculations.

A more mundane possibility for improvement would be to rewrite the γ–COMPUTE code used in this chapter in a form specialised to making anisotropic calculations. The current γ–COMPUTE code was originally designed to simulate chemical magnetic field effects in isotropic solution for the work in Chapter 4. When calculating anisotropic effects, one performs very similar calculations for each field orientation over an appropriate mesh. One ought, for example, to be able to avoid recalculating the spin Hamiltonian from scratch for every different field orientation. Such code could be used on Oxford's forthcoming new supercomputer in order to greatly expand the range of anisotropic RF simulations in multinuclear RPs. Such optimisations will be necessary if it is to be feasible to average over all three Euler angles routinely.

In Chapter 8 we described briefly ongoing work in Oxford to measure the anisotropic MFEs in a chemical model system: a carotenoid-porphyrin-fullerene (CPC_{60}) triad. The theory for calculating anisotropic MFEs that we have employed in Chapters 7–9 is an extrapolation from the considerable body of results available for isotropic MFEs. There is an urgent need to test the anisotropic MFE theory against experimental results to see whether the approximations and assumptions that perform well for modelling isotropic MFEs continue to serve well in the anisotropic case. When these comparisons have been made for anisotropic static MFEs, it would be instructive also to employ RF fields.

Finally, Ahmad has recently reported MFEs on the germination of the mustard *A. thaliana* [343]. The magnetic-field-dependent processes are known from other work to be regulated by the cryptochrome family of proteins — the same family of proteins that have been proposed as the basis of magnetoreception in birds [106]. Ahmad's

experiments will soon be replicated in Oxford. Assuming that these magnetic field effects can be replicated, *A. thaliana* offers potential for greatly more detailed *in vivo* studies than have been possible with European robins. It may in time be possible to measure and analyse a full "MARY-ν" spectrum for *A. thaliana*. This is an exciting avenue for future work.

Appendix A

Hyperfine coupling data

Radical	a/mT	Nuclei	$\tilde{a}/\mathrm{mT}$	Literature reference
Chrysene-$h_{12}^{\bullet+}$	0.556	2×H	0.934	[210]
	0.265	2×H		
	0.181	2×H		
	0.140	2×H		
	0.070	2×H		
Chrysene-$d_{12}^{\bullet+}$	0.085	2×D	0.234	[210]
	0.041	2×D		
	0.028	2×D		
	0.022	2×D		
	0.011	2×D		
1,2-$DCB^{\bullet-}$	0.413	2×H	0.713	[381]
	0.175	2×N		
	0.042	2×H		
1,3-$DCB^{\bullet-}$	0.829	2×H	1.204	[381]
	0.144	1×H		
	0.102	2×N		
	0.008	1×H		
1,4-$DCB^{\bullet-}$	0.159	4×H	0.525	[381]
	0.181	2×N		
DMA-$h_{11}^{\bullet-}$	0.585	2×H	1.103	[145, NSII/17f - 83Ge1]
	0.515	2×H		
	0.032	1×H		
	0.019	1×N		
DMA-$d_{11}^{\bullet-}$	0.090	2×D	0.278	[145, NSII/17f - 83Ge1]
	0.079	2×D		
	0.005	1×D		
	0.019	1×N		

Radical	a/mT	Nuclei	$\tilde{a}$/mT	Literature reference
$DMA^{\bullet+}$	1.200	6×H	3.472	[145, NSII/17h - 85Ra1]
	1.000	1×N		
	0.500	3×H		
DMA-$h_{11}^{\bullet+}$	1.180	6×H	3.371	[144]
	1.000	1×N		
	0.520	1×H		
	0.170	2×H		
	0.080	2×H		
DMA-$d_{11}^{\bullet+}$	1.000	1×N	1.793	[144]
	0.181	6×D		
	0.080	1×D		
	0.026	2×D		
	0.012	2×D		
Pyrene-$h_{10}^{\bullet-}$	0.481	4×H	1.062	[145, NSII/19d1 - 73Cla1] or [143]
	0.212	4×H		
	0.103	2×H		
Pyrene-$d_{10}^{\bullet-}$	0.074	4×D	0.266	[145, NSII/19d1 - 73Cla1] or [143]
	0.033	4×D		
	0.016	2×D		
Pyrene-$h_{10}^{\bullet+}$	0.540	4×H	1.171	[145, NSII/17h - 80Bu1]
	0.210	4×H		
	0.120	2×H		
Pyrene-$h_{10}^{\bullet+}$	0.538	4×H	1.169	[221]
	0.212	4×H		
	0.118	2×H		
Pyrene-$d_{10}^{\bullet+}$	0.083	4×D	0.293	[221]
	0.033	4×D		
	0.018	2×D		

These hyperfine data were taken from a set collated, with copies of the original literature references, by Wedge [247]. Hyperfine coupling constants for deuterated radicals are estimated from data for the protonated counterparts using the relationship

$$\frac{a_{\text{deuterated}}}{a_{\text{protonated}}} \approx \frac{\gamma_{\text{D}}}{\gamma_{\text{H}}} = 0.1535.$$

This formula assumes that there is no change in molecular geometry or electronic structure on deuteration. In reality, differences in zero-point energy may cause deviations.

Appendix B

Fourier transform definitions

B.1 Fourier transform

Consider an arbitrary function $f(t)$. Its Fourier transform $F(\omega)$ or $\mathscr{F}\{f\}(\omega)$ is defined to be

$$F(\omega) = \sqrt{\frac{|b|}{(2\pi)^{1-a}}} \int_{-\infty}^{\infty} f(t) \mathrm{e}^{\mathrm{i}b\omega t} \, \mathrm{d}t. \tag{B.1}$$

The Fourier integral theorem states that

$$f(t) = \sqrt{\frac{|b|}{(2\pi)^{1+a}}} \int_{-\infty}^{\infty} F(\omega) \mathrm{e}^{-\mathrm{i}b\omega t} \, \mathrm{d}\omega \tag{B.2}$$

provided that the two integrals involved exist [199, 382]. We say that these functions form a Fourier pair, written $f(t) \longleftrightarrow F(\omega)$.

In these definitions, a and b are real numbers which may be chosen at will when defining the Fourier transform. It is unfortunate that there are a wide variety of different definitions in the literature. Derivations in the body of this thesis use the convention that $a = 0$ and $b = 1$. We use the general definitions in this appendix in order to aid implementation of algorithms from the main text using mathematical libraries which make a different choice of a and b.

B.2 Convolution theorem

Theorem: The convolution integral, defined as

$$f(t) \star g(t) \equiv \int_{-\infty}^{\infty} f(\tau) g(t-\tau) \, \mathrm{d}\tau \tag{B.3}$$

has a convenient Fourier transform

$$f(t) \star g(t) \longleftrightarrow \sqrt{\frac{(2\pi)^{1-a}}{|b|}} \, F(\omega) G(\omega). \tag{B.4}$$

Proof.

$$\begin{aligned}
\mathscr{F}\{f(t)\star g(t)\} &= \sqrt{\frac{|b|}{(2\pi)^{1-a}}}\int_{-\infty}^{\infty}\int_{-\infty}^{\infty} f(\tau)g(t-\tau)\,\mathrm{d}\tau \mathrm{e}^{\mathrm{i}b\omega t}\,\mathrm{d}t \\
&= \sqrt{\frac{|b|}{(2\pi)^{1-a}}}\int_{-\infty}^{\infty} f(\tau)\int_{-\infty}^{\infty} g(\sigma)\mathrm{e}^{\mathrm{i}b\omega(\sigma+\tau)}\,\mathrm{d}\sigma\,\mathrm{d}\tau \qquad \text{where } \sigma = t-\tau \\
&= \sqrt{\frac{|b|}{(2\pi)^{1-a}}}\int_{-\infty}^{\infty} f(\tau)\mathrm{e}^{\mathrm{i}b\omega\tau}\int_{-\infty}^{\infty} g(\sigma)\mathrm{e}^{\mathrm{i}b\omega\sigma}\,\mathrm{d}\sigma\,\mathrm{d}\tau \\
&= \sqrt{\frac{|b|}{(2\pi)^{1-a}}}\int_{-\infty}^{\infty} f(\tau)\mathrm{e}^{\mathrm{i}b\omega\tau}\,\mathrm{d}\tau\sqrt{\frac{(2\pi)^{1-a}}{|b|}}G(\omega) \\
&= \sqrt{\frac{(2\pi)^{1-a}}{|b|}}F(\omega)G(\omega). \qquad \square
\end{aligned}$$

Similarly, the Fourier transform of a product of functions is given by

$$f(t)g(t) \longleftrightarrow \sqrt{\frac{|b|}{(2\pi)^{1+a}}}\,F(\omega)\star G(\omega). \tag{B.5}$$

Proof.

$$\begin{aligned}
\mathscr{F}^{-1}\{F(\omega)\star G(\omega)\} &= \sqrt{\frac{|b|}{(2\pi)^{1+a}}}\int_{-\infty}^{\infty}\int_{-\infty}^{\infty} F(\tau)G(\omega-\tau)\,\mathrm{d}\tau\mathrm{e}^{-\mathrm{i}b\omega t}\,\mathrm{d}\omega \\
&= \sqrt{\frac{|b|}{(2\pi)^{1+a}}}\int_{-\infty}^{\infty} F(\tau)\int_{-\infty}^{\infty} G(\sigma)\mathrm{e}^{-\mathrm{i}b(\sigma+\tau)t}\,\mathrm{d}\sigma\,\mathrm{d}\tau
\end{aligned}$$

where $\sigma = \omega - \tau$, implying that

$$\begin{aligned}
\mathscr{F}^{-1}\{F(\omega)\star G(\omega)\} &= \sqrt{\frac{|b|}{(2\pi)^{1+a}}}\int_{-\infty}^{\infty} F(\tau)\mathrm{e}^{-\mathrm{i}b\tau t}\int_{-\infty}^{\infty} G(\sigma)\mathrm{e}^{-\mathrm{i}b\sigma t}\,\mathrm{d}\sigma\,\mathrm{d}\tau \\
&= \sqrt{\frac{|b|}{(2\pi)^{1+a}}}\int_{-\infty}^{\infty} F(\tau)\mathrm{e}^{-\mathrm{i}b\tau t}\,\mathrm{d}\tau\sqrt{\frac{(2\pi)^{1+a}}{|b|}}g(t) \\
&= \sqrt{\frac{(2\pi)^{1+a}}{|b|}}f(t)g(t). \qquad \square
\end{aligned}$$

B.3 Delta function

The Dirac delta "function" $\delta(t)$ is a distribution or functional which is defined by the following integral

$$\int_{-\infty}^{\infty}\delta(x)\phi(x)\,\mathrm{d}x = \phi(0). \tag{B.6}$$

In other words, integration of some test function $\phi(x)$ multiplied by a Delta function gives the value of the test function evaluated at $x = 0$. This operation acts on a function $\phi(x)$ to give a number $\phi(0)$. Such an operator is known as a functional or distribution [382, Appendix I].

The Fourier transform of a Delta function is therefore given by

$$\begin{aligned}\Delta(\omega) &= \sqrt{\frac{|b|}{(2\pi)^{1-a}}}\int_{-\infty}^{\infty}\delta(t)\mathrm{e}^{\mathrm{i}b\omega t}\,\mathrm{d}t \\ &= \sqrt{\frac{|b|}{(2\pi)^{1-a}}}\mathrm{e}^{0} = \sqrt{\frac{|b|}{(2\pi)^{1-a}}}.\end{aligned} \tag{B.7}$$

By taking the inverse Fourier transform of both sides of this expression, we arrive at a very useful alternative definition of the Delta function

$$\begin{aligned}\implies \delta(t) &= \sqrt{\frac{|b|}{(2\pi)^{1+a}}}\int_{-\infty}^{\infty}\sqrt{\frac{|b|}{(2\pi)^{1-a}}}\mathrm{e}^{-\mathrm{i}b\omega t}\,\mathrm{d}\omega \\ &= \frac{|b|}{2\pi}\int_{-\infty}^{\infty}\mathrm{e}^{-\mathrm{i}b\omega t}\,\mathrm{d}\omega\end{aligned} \tag{B.8}$$

B.4 Singlet yield

We recall that under certain assumptions, the singlet yield of a RP reaction may be calculated according to equation (2.1)

$$\Phi_{\mathrm{S}}(B) = \int_{0}^{\infty}\left\langle\hat{P}^{\mathrm{S}}\right\rangle(B,t)f(t)\,\mathrm{d}t.$$

It is often more convenient to transform this expression into an integral in the frequency domain.

We begin by extending the definition of the re-encounter probability function to negative times. Since it is clearly physically impossible for a RP to recombine before it has been created, we set

$$f(t) = 0 \quad \forall \quad t < 0. \tag{B.9}$$

The singlet yield may therefore be written

$$\Phi_{\mathrm{S}}(B) = \int_{-\infty}^{\infty}\left\langle\hat{P}^{\mathrm{S}}\right\rangle(B,t)f(t)\,\mathrm{d}t. \tag{B.10}$$

Applying the convolution theorem and an inverse Fourier transform to the product

$\left\langle \hat{P}^{\mathrm{S}} \right\rangle (B,t) f(t)$, we rewrite this integral as

$$\begin{aligned}
\Phi_{\mathrm{S}}(B) &= \int_{-\infty}^{\infty} \left[\int_{-\infty}^{\infty} \sqrt{\frac{|b|}{(2\pi)^{1+a}}} \left[\sqrt{\frac{|b|}{(2\pi)^{1+a}}} \left\langle \hat{P}^{\mathrm{S}} \right\rangle (B,\omega) \star F(\omega) \right] \mathrm{e}^{-\mathrm{i}b\omega t} \,\mathrm{d}\omega \right] \mathrm{d}t \\
&= \frac{|b|}{(2\pi)^{1+a}} \int_{-\infty}^{\infty} \left[\left\langle \hat{P}^{\mathrm{S}} \right\rangle (B,\omega) \star F(\omega) \right] \left[\int_{-\infty}^{\infty} \mathrm{e}^{-\mathrm{i}b\omega t} \,\mathrm{d}t \right] \mathrm{d}\omega \\
&= \frac{|b|}{(2\pi)^{1+a}} \int_{-\infty}^{\infty} \left[\left\langle \hat{P}^{\mathrm{S}} \right\rangle (B,\omega) \star F(\omega) \right] \frac{2\pi}{|b|} \delta(\omega) \,\mathrm{d}\omega \\
&= \frac{1}{(2\pi)^{a}} \int_{-\infty}^{\infty} \left[\left\langle \hat{P}^{\mathrm{S}} \right\rangle (B,\omega) \star F(\omega) \right] \delta(\omega) \,\mathrm{d}\omega \\
&= \frac{1}{(2\pi)^{a}} \int_{-\infty}^{\infty} \left[\int_{-\infty}^{\infty} \left\langle \hat{P}^{\mathrm{S}} \right\rangle (B,\Omega) F(\omega-\Omega) \,\mathrm{d}\Omega \right] \delta(\omega) \,\mathrm{d}\omega \\
&= \frac{1}{(2\pi)^{a}} \int_{-\infty}^{\infty} \left\langle \hat{P}^{\mathrm{S}} \right\rangle (B,\Omega) F(-\Omega) \,\mathrm{d}\Omega. \qquad \text{(B.11)}
\end{aligned}$$

Finally, since the re-encounter probability is real, *i.e.* $f(t) = f(t)^*$, then $F(\omega) = F(-\omega)^*$ and hence

$$\Phi_{\mathrm{S}}(B) = \frac{1}{(2\pi)^{a}} \int_{-\infty}^{\infty} \left\langle \hat{P}^{\mathrm{S}} \right\rangle (B,\omega) F(\omega)^* \,\mathrm{d}\omega. \qquad \text{(B.12)}$$

Singlet yield is real

Also, since $\left\langle \hat{P}^{\mathrm{S}} \right\rangle (B,t)$ is real, $\left\langle \hat{P}^{\mathrm{S}} \right\rangle (B,\omega) = \left\langle \hat{P}^{\mathrm{S}} \right\rangle (B,-\omega)^*$ and hence

$$\begin{aligned}
\Phi_{\mathrm{S}}^* &= \frac{1}{(2\pi)^{a}} \int_{-\infty}^{\infty} \left\langle \hat{P}^{\mathrm{S}} \right\rangle (B,\omega)^* F(\omega) \,\mathrm{d}\omega \\
&= \frac{1}{(2\pi)^{a}} \int_{-\infty}^{\infty} \left\langle \hat{P}^{\mathrm{S}} \right\rangle (B,-\omega')^* F(-\omega') \,\mathrm{d}\omega', \quad \text{where } \omega' = \omega \\
&= \frac{1}{(2\pi)^{a}} \int_{-\infty}^{\infty} \left\langle \hat{P}^{\mathrm{S}} \right\rangle (B,\omega') F(\omega')^* \,\mathrm{d}\omega' \\
&= \Phi_{\mathrm{S}}. \qquad \text{(B.13)}
\end{aligned}$$

In other words, the singlet yield is real, as it must be physically. This identity sometimes allows the imaginary part of $F(\omega)$ to be neglected, simplifying calculations.

B.5 Summary for $a = 0$, $b = 1$

For convenience, we summarise the above results for the convention used in the main text, *i.e.* when $a = 0$ and $b = 1$. The Fourier transform and its inverse are given by

$$F(\omega) = \sqrt{\frac{1}{2\pi}} \int_{-\infty}^{\infty} f(t) \mathrm{e}^{\mathrm{i}\omega t} \,\mathrm{d}t \qquad \text{(B.14)}$$

$$f(t) = \sqrt{\frac{1}{2\pi}} \int_{-\infty}^{\infty} F(\omega) \mathrm{e}^{-\mathrm{i}\omega t} \,\mathrm{d}\omega. \qquad \text{(B.15)}$$

The convolution theorem gives these Fourier pairs

$$f(t) \star g(t) \longleftrightarrow \sqrt{2\pi}\, F(\omega) G(\omega) \tag{B.16}$$

$$f(t) g(t) \longleftrightarrow \sqrt{\frac{1}{2\pi}}\, F(\omega) \star G(\omega). \tag{B.17}$$

The Dirac delta function may be defined by

$$\delta(t) = \frac{1}{2\pi} \int_{-\infty}^{\infty} \mathrm{e}^{-\mathrm{i}\omega t}\, \mathrm{d}\omega = \frac{1}{2\pi} \int_{-\infty}^{\infty} \mathrm{e}^{\mathrm{i}\omega t}\, \mathrm{d}\omega \tag{B.18}$$

and two related Fourier transforms are

$$\delta(t - t_0) \longleftrightarrow \sqrt{\frac{1}{2\pi}} \mathrm{e}^{\mathrm{i}\omega t_0} \tag{B.19}$$

$$\mathrm{e}^{\mathrm{i}\omega_0 t} \longleftrightarrow \sqrt{2\pi}\delta(\omega + \omega_0). \tag{B.20}$$

The singlet yield is given by

$$\Phi_{\mathrm{S}}(B) = \int_{-\infty}^{\infty} \left\langle \hat{P}^{\mathrm{S}} \right\rangle (B, \omega) F(\omega)^*\, \mathrm{d}\omega. \tag{B.21}$$

B.6 Discrete Fourier transform

The continuous Fourier transform described above is a powerful tool indeed. However, in many areas of application the quantities of interest are not arbitrary continuous functions. For periodic continuous functions, Fourier series decompositions are the appropriate tool. When dealing with sampled, periodic functions — in other words, with quantities described by a list of numbers — the discrete Fourier transform (DFT) is most suitable.

As with the Fourier transform, there is some flexibility in the definitions of the DFT and of its inverse [199]. For ease of presentation, we adopt the convention known as "0-indexing"; in other words, a vector $\boldsymbol{x}$ in $\mathbb{C}^N$ has elements $x_0,\ x_1,\ \ldots,\ x_{N-1}$. Equivalent results for the "1-indexing" convention used in `Matlab` are given in §B.11.

The DFT $\boldsymbol{X}$ of a vector $\boldsymbol{x}$ has elements $X(k)$ given by

$$X(k) = \mathrm{DFT}_k(x) = \sum_{j=0}^{N-1} x(j) \mathrm{e}^{-2\pi \mathrm{i} jk/N} \qquad k = 0, 1, \ldots, N-1. \tag{B.22}$$

The inverse transform (IDFT) is given by

$$x(j) = \mathrm{IDFT}_j(X) = \frac{1}{N} \sum_{k=0}^{N-1} X(k) \mathrm{e}^{2\pi \mathrm{i} jk/N} \qquad j = 0, 1, \ldots, N-1. \tag{B.23}$$

These formulae apply equally well if $X(k)$ and $x(j)$ are taken to be functions with period N, whose values are known at the sampling points, *i.e.* for integer values of k and j.

It should be noted that although these formulae provide a useful definition for the

DFT, they are not suitable for numerical computations. In numerical work, the fast Fourier transform (FFT) algorithm is used to compute the same result much more quickly. High quality libraries are available for this purpose [204].

B.7 Shifted summation

Consider a summation analogous to equation (B.22), but whose limits are shifted by $z \in \mathbb{Z}$, where $0 < z < N$. We may split this sum into two parts:

$$S = \sum_{j=z}^{N+z-1} x(j)\mathrm{e}^{-2\pi \mathrm{i} jk/N} = \sum_{j=z}^{N-1} x(j)\mathrm{e}^{-2\pi \mathrm{i} jk/N} + \sum_{j=N}^{N+z-1} x(j)\mathrm{e}^{-2\pi \mathrm{i} jk/N}.$$

Now, defining $m = j - N$ and since $x(m) = x(m+N) = x(j)$, we write

$$S = \sum_{j=z}^{N-1} x(j)\mathrm{e}^{-2\pi \mathrm{i} jk/N} + \left[\sum_{m=0}^{z-1} x(m)\mathrm{e}^{-2\pi \mathrm{i} mk/N}\right] \mathrm{e}^{-2\pi \mathrm{i} k} = \sum_{j=0}^{N-1} x(j)\mathrm{e}^{-2\pi \mathrm{i} jk/N}.$$

Therefore, by repeated application of this result, it is clear that the DFT summation may be shifted by any $z \in \mathbb{Z}$ without altering the result:

$$X(k) = \mathrm{DFT}_k(x) = \sum_{j=z}^{N+z-1} x(j)\mathrm{e}^{-2\pi \mathrm{i} jk/N}. \tag{B.24}$$

B.8 Discrete convolution theorem

Theorem: The discrete convolution of two sampled functions f and g, with period N, defined as

$$[f \star g](j) \equiv \sum_{m=0}^{N-1} f(m)g(j-m) \tag{B.25}$$

has a convenient discrete Fourier transform

$$f \star g \longleftrightarrow FG. \tag{B.26}$$

Proof.

$$\begin{aligned}\mathrm{DFT}_k(f \star g) &= \sum_{j=0}^{N-1} [f \star g](j)\mathrm{e}^{-2\pi \mathrm{i} jk/N} \\ &= \sum_{j=0}^{N-1} \left[\sum_{m=0}^{N-1} f(m)g(j-m)\right] \mathrm{e}^{-2\pi \mathrm{i} jk/N}.\end{aligned}$$

Swapping the order of summation, and defining $r = j - m$ gives

$$\begin{aligned}\mathrm{DFT}_k\left(f \star g\right) &= \sum_{m=0}^{N-1} f(m) \left[\sum_{r=-m}^{N-1-m} g(r)\mathrm{e}^{-2\pi \mathrm{i} rk/N}\right] \mathrm{e}^{-2\pi \mathrm{i} mk/N} \\ &= \left[\sum_{m=0}^{N-1} f(m)\mathrm{e}^{-2\pi \mathrm{i} mk/N}\right] G(k) \\ &= F(k)G(k). \end{aligned}$$

□

B.9 Discrete correlation theorem

Theorem: The discrete cross-correlation of two sampled functions f and g, with period N, defined as

$$\left[f \diamond g\right](j) \equiv \sum_{m=0}^{N-1} f(m)^* g(j+m) \tag{B.27}$$

has a convenient discrete Fourier transform

$$f \diamond g \longleftrightarrow F^* G. \tag{B.28}$$

Proof.

$$\begin{aligned}\mathrm{DFT}_k\left(f \diamond g\right) &= \sum_{j=0}^{N-1} \left[f \diamond g\right](j)\mathrm{e}^{-2\pi \mathrm{i} jk/N} \\ &= \sum_{j=0}^{N-1} \left[\sum_{m=0}^{N-1} f(m)^* g(j+m)\right] \mathrm{e}^{-2\pi \mathrm{i} jk/N}. \end{aligned}$$

Swapping the order of summation, and defining $r = j + m$ gives

$$\begin{aligned}\mathrm{DFT}_k\left(f \star g\right) &= \sum_{m=0}^{N-1} f(m)^* \left[\sum_{r=m}^{N+m-1} g(r)\mathrm{e}^{-2\pi \mathrm{i} rk/N}\right] \mathrm{e}^{2\pi \mathrm{i} mk/N} \\ &= \left[\sum_{m=0}^{N-1} f(m)\mathrm{e}^{-2\pi \mathrm{i} mk/N}\right]^* G(k) \\ &= F^*(k)G(k). \end{aligned}$$

□

B.10 Sampling theorem

Hitherto, we have discussed the DFT as an entity in its own right. Nevertheless, it is possible to derive the DFT as a special case of the normal continuous Fourier transform. We outline such a proof here and hence demonstrate the number of samples required to completely characterise a periodic, continuous function. This result is the well-known Nyquist sampling theorem.

B.10.1 Fourier Transform of Regularly-Spaced Delta-Functions[1]

What is the Fourier transform of an infinite "[1-D] lattice" of delta-functions? Consider this as the limit of the following finite sum of delta-functions, separated by T in the time domain, as $N \to \infty$

$$\delta_N(t) = \sum_{n=-N}^{N} \delta(t-nT) \quad \longleftrightarrow \quad \Delta_N(\omega) = \frac{1}{2\pi} \sum_{n=-N}^{N} \mathrm{e}^{inT\omega} \qquad T > 0 \quad \text{(B.29)}$$

The right hand side is a Geometric Progression, which we sum

$$\Delta_N(\omega) = \frac{1}{2\pi} \frac{\sin[\omega(N+\frac{1}{2})T]}{\sin[\frac{1}{2}\omega T]} \quad \text{(B.30)}$$

By inspection, $\Delta_N(\omega)$ is periodic in ω with period $\omega_0 = 2\pi/T$. Let us consider just a single period, in the interval $(-\omega_0/2, \omega_0/2)$. To complete the proof, we will show that $\Delta_N(\omega)$ tends to a delta-function in this interval as $N \to \infty$. We write

$$\Delta_\infty(\omega) = \lim_{N\to\infty} \Delta_N(\omega) = \frac{1}{2\pi} \lim_{N\to\infty} \left\{ \frac{\sin[N\omega T]}{\pi\omega T} \right\} \frac{\pi\omega T}{\sin[\frac{1}{2}\omega T]} \quad \text{(B.31)}$$

This limit must be taken as a "generalised limit", within the theory of distributions. Thus we must consider

$$\lim_{N\to\infty} \int_{-\infty}^{\infty} \frac{\sin N\Omega}{\pi\Omega} \phi(\Omega)\,\mathrm{d}\Omega = \int_{-\infty}^{-\varepsilon} + \int_{-\varepsilon}^{\varepsilon} + \int_{\varepsilon}^{\infty} \frac{\sin N\Omega}{\pi\Omega} \phi(\Omega)\,\mathrm{d}\Omega \quad \text{(B.32)}$$

where $\Omega = \omega T$. Since $\phi(\Omega)$ is a member of the class of "test functions" then $\frac{\phi(\Omega)}{\Omega}$ is integrable except at $\Omega = 0$. Thus, by the Riemann-Lebesgue lemma, the first and last terms tend to 0 as $N \to \infty$.

For sufficiently small ε, since $\phi(\Omega)$ is continuous, we may write

$$\int_{-\varepsilon}^{\varepsilon} \frac{\sin N\Omega}{\pi\Omega} \phi(\Omega)\,\mathrm{d}\Omega \approx \phi(0) \int_{-N\varepsilon}^{N\varepsilon} \frac{\sin N\Omega}{\pi\Omega}\,\mathrm{d}\Omega \xrightarrow[N\to\infty]{\text{as}} \phi(0) \int_{-\infty}^{\infty} \frac{\sin N\Omega}{\pi\Omega}\,\mathrm{d}\Omega \quad \text{(B.33)}$$

This is a standard integral, provided $\phi(\Omega)$ is of bounded variation

$$\lim_{N\to\infty} \int_{-\infty}^{\infty} \frac{\sin N\Omega}{\pi\Omega} \phi(\Omega)\,\mathrm{d}\Omega = \phi(0) \int_{-\infty}^{\infty} \frac{\sin N\Omega}{\pi\Omega}\,\mathrm{d}\Omega = \phi(0) \quad \text{(B.34)}$$

Yet this is the definition of the delta-function $\delta(\Omega)$ given in (B.6).
Now, since $\delta(\Omega) = \delta(\omega T) = \frac{1}{T}\delta(\omega)$ we find that

$$\begin{aligned} \delta_\infty(t) \longleftrightarrow \Delta_\infty(\omega) &= \frac{1}{2\pi} \sum_n \frac{1}{T} \delta(\omega - n\omega_0) \frac{\pi\omega T}{\sin[\frac{1}{2}\omega T]} \\ &= \frac{1}{2\pi} \sum_{n=-\infty}^{\infty} \omega_0 \delta(\omega - n\omega_0) \end{aligned} \quad \text{(B.35)}$$

[1] This proof is adapted from [382, p44 and Appendix I].

B.10.2 Fourier Transform of Periodic Functions

It is now simple to show that the Fourier series is a special case of the Fourier transform. Consider a periodic function defined by

$$f(t) = g(t) \star \delta_\infty(t) \qquad \text{where } g(t) = 0 \qquad t < 0, t \geq T \tag{B.36}$$

where $g(t)$ gives the behaviour during a single period $t = [0, T)$ and is zero elsewhere. $g(t)$ may be identified with the "motif" and $\delta_\infty(t)$ with the "lattice".
By the convolution theorem

$$f(t) \longleftrightarrow F(\omega) = 2\pi\, G(\omega)\, \Delta_\infty(\omega) = \sum_n \omega_0 G(n\omega_0)\delta(\omega - n\omega_0) \tag{B.37}$$

where $\omega_0 = 2\pi/T$ as above. Thus, the Fourier transform of a periodic function consists of an infinite series of delta-functions, whose amplitudes are modulated by the Fourier transform of a single period of the function $g(t) \longleftrightarrow G(\omega)$ (multiplied by a scaling factor). This is illustrated in Figure B.1.

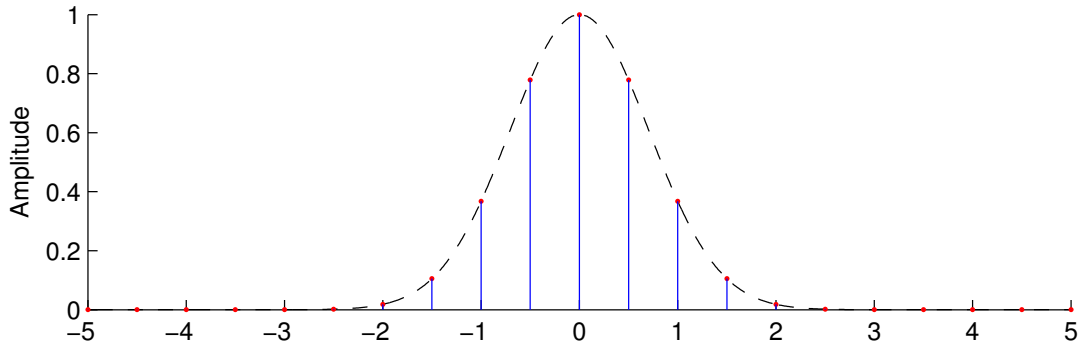

Figure B.1: Fourier transform of a periodic function. The dashed line is $\omega_0 G(\omega)$ and the vertical lines and points represent the Fourier transform $F(\omega)$.

Finally, using the inverse Fourier transform, we may write

$$\begin{aligned} f(t) &= \int_{-\infty}^{\infty} \sum_n \omega_0 G(n\omega_0)\delta(\omega - n\omega_0)\, \mathrm{e}^{-\mathrm{i}\omega t}\, \mathrm{d}\omega \\ &= \sum_n \omega_0 G(n\omega_0)\, \mathrm{e}^{-\mathrm{i}n\omega_0 t} \end{aligned} \tag{B.38}$$

which is the familiar Fourier series expansion.

B.10.3 Fourier Transform of Sampled Periodic Functions[2]

Consider the periodic function $f(t)$ defined in (B.36). However, we are now going to *sample* it at n regular time-intervals per period $T = n\tau$. We write the sampled function as

$$\mathbb{f}(t) = f(t)\, \delta_{\text{sample}} = \left[g(t) \star \delta_{\text{period}}(t)\right] \delta_{\text{sample}}(t) \tag{B.39}$$

[2]This proof is adapted from [199, p94].

where

$$\delta_{\text{sample}} = \sum_{j=-\infty}^{\infty} \delta(t - j\tau) \quad \longleftrightarrow \quad \Delta_{\text{sample}} = \frac{1}{\tau} \sum_{j=-\infty}^{\infty} \delta(\omega - j\frac{2\pi}{\tau}) \tag{B.40}$$

$$\delta_{\text{period}} = \sum_{j=-\infty}^{\infty} \delta(t - jn\tau) \quad \longleftrightarrow \quad \Delta_{\text{period}} = \frac{1}{n\tau} \sum_{j=-\infty}^{\infty} \delta(\omega - j\frac{2\pi}{n\tau}) \tag{B.41}$$

The Fourier transform of this function is

$$\begin{aligned} \mathbb{f}(t) \longleftrightarrow \mathbb{F}(\omega) &= \left[2\pi\, G(\omega)\Delta_{\text{period}}(\omega)\right] \star \Delta_{\text{sample}}(\omega) \\ &= \left[\omega_0 \sum_k G(k\omega_0)\, \delta\left(\omega - k\omega_0\right)\right] \star \frac{n}{T} \sum_j \delta(\omega - jn\omega_0) \end{aligned} \tag{B.42}$$

where $\omega_0 = 2\pi/T$.

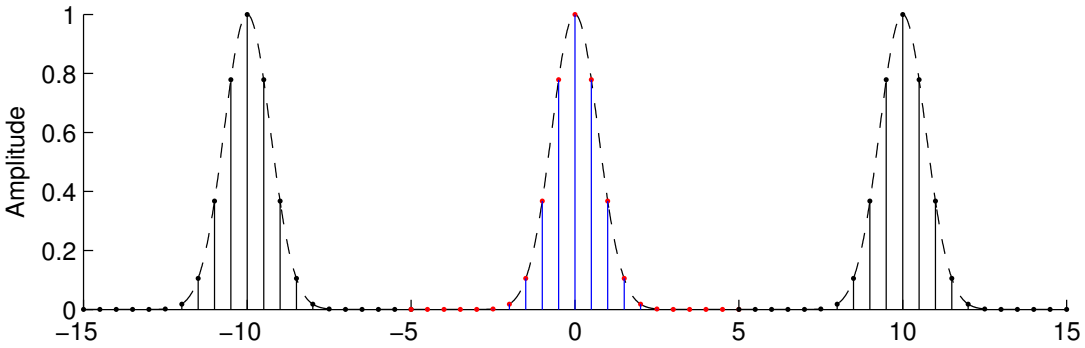

Figure B.2: Fourier transform of a band-limited sampled periodic function. (Parameters: $\tau = 2\pi/10$, $n = 20$, $T = 4\pi$)

Figure B.2 helps us see what is happening. Let us take the terms in (B.42) one at a time.

1. The dashed line shows $\frac{1}{\tau}\frac{1}{n\tau}G(\omega)$, where $G(\omega)$ is the Fourier transform of a single repeat of the periodic function $f(t)$.

2. Of course, $f(t)$ is periodic, not just a single repeat. $\Delta_{\text{period}}(\omega)$ arises from this and means that $G(\omega)$ is sampled at frequencies $\frac{2\pi}{n\tau} = \frac{1}{2}$, as has been shown in the section on Fourier series. This is shown in the colour section around zero frequency.

3. Sampling in the time domain gives rise to the $\Delta_{\text{sample}}(\omega)$ term, which copies the Fourier transform of $f(t)$ at intervals $\frac{2\pi}{\tau} = 10$. The first copies are shown by the black duplicates on the left and right hand sides.

B.10.4 Sampling Theorem

As we can see in Figure B.2, the effect of sampling a function $h(t)$ in the time domain is to convolve the Fourier transform $H(\omega)$ with $\Delta_{\text{sample}}(\omega)$. In other words, it copies

the Fourier transform at regular intervals in frequency. How can we reverse the effects of this time domain sampling?

Let ω_{max} be the maximum frequency component in the Fourier transform $H(\omega)$. Let τ be the sampling rate. Let $\omega_{\text{sample}} = 2\pi/\tau$ be the separation between the delta-functions in Δ_{sample}.

1. $\omega_{\text{sample}} > \omega_{\text{max}}$
   In this case, we can easily reverse the effects of sampling. We simply ignore all the duplicates of the Fourier transform, and only take the part with $|\omega| < \omega_{\text{sample}}$ (appropriately scaled). In this case, we lose no information through sampling.

2. $\omega_{\text{sample}} < \omega_{\text{max}}$
   Now we cannot reverse the effects of sampling. If we adopt the same procedure, we find that the high-frequency "tails" of the neighbouring *black* copies of the Fourier transform overlap the true *coloured* Fourier transform in the centre. Thus, when we take only the part with $|\omega| < \omega_{\text{sample}}$ it appears that the high-frequency parts of the Fourier transform have been "folded back" or "aliased" onto the true Fourier transform. In this case, we have lost information.

B.11 `Matlab` convention

In `Matlab`, vectors use the "1-indexing" convention where a vector $\boldsymbol{x}$ in $\mathbb{C}^N$ has elements $x_1,\ x_2,\ \ldots,\ x_N$. For convenience, we summarise the above results using this convention.

The DFT $\boldsymbol{X}$ of a vector $\boldsymbol{x}$ has elements $X(k)$ given by

$$X(k) = \text{DFT}_k(x) = \sum_{j=1}^{N} x(j)\mathrm{e}^{-2\pi\mathrm{i}(j-1)(k-1)/N} \qquad k = 1,2,\ldots,N. \tag{B.43}$$

The inverse transform (IDFT) is given by

$$x(j) = \text{IDFT}_j(X) = \frac{1}{N}\sum_{k=1}^{N} X(k)\mathrm{e}^{2\pi\mathrm{i}(j-1)(k-1)/N} \qquad j = 1,2,\ldots,N. \tag{B.44}$$

The discrete convolution of two sampled functions f and g, with period N, defined as

$$[f \star g]\,(j) \equiv \sum_{m=1}^{N} f(m)g(j+1-m) \tag{B.45}$$

has a convenient discrete Fourier transform

$$f \star g \longleftrightarrow FG. \tag{B.46}$$

The discrete cross-correlation of two sampled functions f and g, with period N, defined as

$$[f \diamond g]\,(j) \equiv \sum_{m=1}^{N} f(m)^* g(j+m-1) \tag{B.47}$$

has a convenient discrete Fourier transform

$$f \diamond g \longleftrightarrow F^* G. \tag{B.48}$$

Appendix C

Liouville space

C.1 Introduction

Elementary treatments of quantum mechanics [92] are couched in terms of wavefunctions $\psi(\boldsymbol{r},t)$, which depend on time t and on the spatial coordinates $\boldsymbol{r}$ of the system in question. Knowledge of the wavefunction allows any property of that system to be computed. Wavefunctions evolve under the influence of the Hamiltonian $\hat{H}$ according to the Schrödinger equation

$$\mathrm{i}\frac{\partial\psi(\boldsymbol{r},t)}{\partial t} = \hat{H}\psi(\boldsymbol{r},t) \tag{C.1}$$

where we have absorbed $\hbar$ into the Hamiltonian by measuring energy in angular frequency units.

Physically-admissible wavefunctions have the properties necessary to be considered as complex vectors. Using Dirac's notation [383], we write

$$|i\rangle \equiv |\psi_i\rangle \equiv \psi_i(\boldsymbol{r},t). \tag{C.2}$$

Each "ket" $|i\rangle$ has as its dual a "bra" $\langle i| \equiv |i\rangle^\dagger$. Together, these form a Banach space. There is also an inner product

$$\langle i|j\rangle \equiv \int \psi_i(\boldsymbol{r},t)^*\psi_j(\boldsymbol{r},t)\,\mathrm{d}\boldsymbol{r} \tag{C.3}$$

and hence, the wavefunctions form a Hilbert space. Confusingly, this particular Hilbert space is often referred to as "Hilbert space" in magnetic resonance.

In many problems, calculations are simplified still further by writing each wavefunction in terms of a complete orthonormal set of basis kets. In so doing, it becomes possible to reduce any wavefunction to a vector in component form, *i.e.* to a list of numbers. Operators, such as $\hat{H}$, become matrices and the action of an operator on a wavefunction becomes a matrix-vector multiplication. This is the standard "Hilbert space" that we have used for calculations in Chapters 2–5.

In a similar manner, operators in "Hilbert space" may be written in terms of a set of basis operators. For two operators $\hat{A}$ and $\hat{B}$, the quantity $\mathrm{Tr}\left[\hat{A}^\dagger\hat{B}\right]$ behaves such that it may be considered to be an inner product. Thus, the *operators* in the usual QM "Hilbert space" of wavefunctions themselves form another induced Hilbert space,

known as "Liouville space". Some discussion of these points is given in [103, 384].

In order to leave no doubt as to the exact definition of the "Liouville space" quantities used in the main text and for ease of reference, we derive here the appropriate expressions for transforming between the ordinary "Hilbert space" and "Liouville space". Further details may be found in [84, p17ff] and references therein.

C.2 Dirac bracket notation

C.2.1 "Hilbert space" traces

Consider two arbitrary "Hilbert space" states $|\psi\rangle$ and $|\chi\rangle$. Written explicitly, the trace of the operator $|\chi\rangle\langle\psi|$ is

$$\mathrm{Tr}\left[|\chi\rangle\langle\psi|\right] = \sum_k \langle k|\chi\rangle\langle\psi|k\rangle\,.$$

Since the inner products $\langle i|j\rangle$ are just numbers and since $\sum_k |k\rangle\langle k| \equiv 1$

$$\mathrm{Tr}\left[|\chi\rangle\langle\psi|\right] = \sum_k \langle\psi|k\rangle\langle k|\chi\rangle = \langle\psi|\left[\sum_k |k\rangle\langle k|\right]|\chi\rangle = \langle\psi|\chi\rangle\,. \tag{C.4}$$

C.2.2 Liouville kets

Operators in "Hilbert space" form another induced vector space. Let us define a "Liouville space" ket to represent each "Hilbert space" operator

$$|a,b) \equiv |a\rangle\langle b|\,. \tag{C.5}$$

For simplicity, we assume that $|a\rangle, \ldots$ form a complete orthonormal set in "Hilbert space".

C.2.3 Liouville bras and inner product

Having started with a complete orthonormal basis in "Hilbert space", we require that Liouville kets and their duals (Liouville bras) also be orthonormal in the following sense

$$(a,b|c,d) = \delta_{ac}\delta_{bd}. \tag{C.6}$$

To satisfy this requirement, the Liouville bras are defined by

$$(a,b| = |a,b)^\dagger = \mathrm{Tr}\left[(|a\rangle\langle b|)^\dagger \odot\right] = \mathrm{Tr}\left[\,|b\rangle\langle a|\odot\right] \tag{C.7}$$

where $\odot$ indicates the term falling to the right of this bra. We check that this definition is consistent by substituting equations (C.5) and (C.7) into equation (C.6) to give

$$(a,b|c,d) = \mathrm{Tr}\left[\,|b\rangle\langle a|\odot\right]|c\rangle\langle d| = \mathrm{Tr}\left[\,|b\rangle\,\langle a|c\rangle\,\langle d|\right] = \delta_{ac}\,\mathrm{Tr}\left[\,|b\rangle\langle d|\right]. \tag{C.8}$$

Using equation (C.4), $(a,b|c,d) = \delta_{ac}\langle d|b\rangle = \delta_{ac}\delta_{bd}$ as required.

C.2.4 Superoperators

In "Hilbert space", we know that $|a\rangle\langle b|$ represents an operator. Let us expand out the analogous "Liouville space" expression $|a,b)(c,d|$ to give

$$|a,b)(c,d|\odot = \big\{|a\rangle\langle b|\big\}\,\mathrm{Tr}\Big[\,|d\rangle\langle c|\odot\Big] = \big\{|a\rangle\langle b|\big\}\,\langle c|\odot|d\rangle \tag{C.9}$$

$$= |a\rangle\langle c|\odot|d\rangle\langle b|\,. \tag{C.10}$$

In other words, the Liouville superoperator $|a,b)(c,d|$ acting on $\odot$ is equivalent in "Hilbert space" to left-multiplying by the operator $|a\rangle\langle c|$ and right-multiplying by the operator $|d\rangle\langle b|$.

C.3 Matrix representations

Although this "Liouville space" version of Dirac notation is very helpful for performing algebraic manipulations by hand, quantum mechanics is much more easily undertaken on a computer using an equivalent matrix representation. In this case, we identify $|a\rangle\langle b|$ and $|a,b)(c,d|$ respectively as *matrix elements* in the appropriate "Hilbert space" and "Liouville space" matrices.

C.3.1 "Hilbert space" states and operators

The Hilbert space ket $|\psi\rangle$ may be expanded in a complete, orthonormal basis

$$|\psi\rangle = \sum_i \psi_i\,|i\rangle\,, \qquad \text{where } \psi_i = \langle i|\psi\rangle\,. \tag{C.11}$$

Once the basis states $|i\rangle$ are defined, we may write the expansion coefficients as a *column* vector

$$\boldsymbol{\psi} = \begin{pmatrix} \psi_1 \\ \psi_2 \\ \vdots \end{pmatrix}. \tag{C.12}$$

At the same time, an operator $\hat{\Omega}$ may be expanded as

$$\hat{\Omega} = \sum_{i,j} \Omega_{ij}\,|i\rangle\langle j|\,, \qquad \text{where the number } \Omega_{ij} = \langle i|\,\hat{\Omega}\,|j\rangle\,. \tag{C.13}$$

Thus, the action of an operator on a basis state is given by

$$|\chi\rangle = \hat{\Omega}\,|\psi\rangle = \sum_{i,j,k} \Omega_{ij}\psi_k\,|i\rangle\,\langle j|k\rangle \tag{C.14}$$

$$= \sum_{i,j,k} \Omega_{ij}\psi_k\,|i\rangle\,\delta_{jk} \tag{C.15}$$

$$= \sum_{i} \left(\sum_{j} \Omega_{ij}\psi_j \right) |i\rangle\,. \tag{C.16}$$

Thus, the new state $|\chi\rangle$ may be written in vector form as

$$\boldsymbol{\chi} = \begin{pmatrix} \sum_j \Omega_{1j}\psi_j \\ \sum_j \Omega_{2j}\psi_j \\ \vdots \end{pmatrix}. \tag{C.17}$$

This is equivalent to a matrix-vector multiplication if we represent $\hat{\Omega}$ by the matrix

$$\Omega = \begin{pmatrix} \Omega_{11} & \Omega_{12} & \Omega_{13} & \cdots \\ \Omega_{21} & \Omega_{22} & \Omega_{23} & \cdots \\ \vdots & \vdots & \vdots & \end{pmatrix}. \tag{C.18}$$

Notice that we are *not* free to transpose this matrix arbitrarily, it must be in the form given if we wish to represent states by column vectors and the action of an operator as pre-multiplication by a matrix.

C.3.2 "Liouville space" states and operators

Having seen how to form the matrix representation of a "Hilbert space" state and operator, we adopt the same technique in "Liouville space". Consider a Liouville ket $|\Omega)$ (*i.e.* a "Hilbert space" operator). Using equation (C.13) we write

$$|\Omega) = \hat{\Omega} = \sum_{ij} \Omega_{ij}\,|i\rangle\langle j| = \sum_{ij} \Omega_{ij}\,|i,j)\,, \tag{C.19}$$

which we may *flatten* by introducing a new index variable α which counts through all the ij as 11, 12, 13, …, 21, 22, 23, … This amounts to flattening the matrix by placing successive *rows* end-to-end. Such a choice is not unique, but it does give a particularly simple form for the superoperators as Krønecker products of "Hilbert space" operators and is generally adopted. Hence

$$|\Omega) = \sum_{\alpha} \Omega_\alpha\,|\alpha)\,. \tag{C.20}$$

Thus, we may represent $|\Omega)$ by another column vector

$$\mathbf{\Omega} = \begin{pmatrix} \Omega_1 = \Omega_{11} \\ \Omega_2 = \Omega_{12} \\ \Omega_3 = \Omega_{13} \\ \vdots \\ \Omega_{n+1} = \Omega_{21} \\ \Omega_{n+2} = \Omega_{22} \\ \Omega_{n+3} = \Omega_{23} \\ \vdots \end{pmatrix}. \tag{C.21}$$

Similarly, an arbitrary superoperator $\hat{\hat{\Omega}}$ may be decomposed as

$$\hat{\hat{\Omega}} = \sum_{\alpha,\beta} \Omega_{\alpha\beta} \, |\alpha)(\beta| \,, \qquad \text{where the number } \Omega_{\alpha\beta} = (\alpha|\hat{\hat{\Omega}}|\beta) \,. \tag{C.22}$$

By the same reasoning as was used above, we represent this superoperator as a "Liouville space" matrix

$$\hat{\hat{\Omega}} = \begin{pmatrix} \Omega_{(11),(11)} & \Omega_{(11),(12)} & \Omega_{(11),(13)} & \cdots \\ \Omega_{(12),(11)} & \Omega_{(12),(12)} & \Omega_{(12),(13)} & \cdots \\ \vdots & \vdots & \vdots & \end{pmatrix} = \begin{pmatrix} \Omega_{11} & \Omega_{12} & \Omega_{13} & \cdots \\ \Omega_{21} & \Omega_{22} & \Omega_{23} & \cdots \\ \vdots & \vdots & \vdots & \end{pmatrix}, \tag{C.23}$$

which we must also be careful not to transpose inadvertently. Note that a Liouville state and/or superoperator does not *have* to be represented by a direct product basis set as it is here, although in cases where it is not, the connection with the underlying quantum "Hilbert space" becomes less obvious.

C.3.3 Forming superoperator matrices

A superoperator operates as

$$\begin{aligned} \hat{\hat{\Omega}} &= \sum_{a,b,c,d} \Omega_{(ab),(cd)} \, |a,b)(c,d| \\ &= \sum_{a,b,c,d} \Omega_{(ab),(cd)} \, |a\rangle\langle c| \odot \Big[|b\rangle\langle d| \Big]^\dagger . \end{aligned} \tag{C.24}$$

Now, in some cases the numbers $\Omega_{(ab),(cd)}$ will factorise such that

$$\begin{aligned} \hat{\hat{\Omega}} &= \sum_{a,b,c,d} X_{ac} \, (Y_{bd})^* \, |a\rangle\langle c| \odot \Big[|b\rangle\langle d| \Big]^\dagger \\ &= \left[\sum_{a,c} X_{ac} \, |a\rangle\langle c| \right] \odot \left[\sum_{b,d} Y_{bd} \, |b\rangle\langle d| \right]^\dagger = \hat{X} \odot \hat{Y}^\dagger . \end{aligned} \tag{C.25}$$

In such cases, we may identify the superoperator matrix elements as

$$\Omega_{(ab),(cd)} = X_{ac}\left(Y_{bd}\right)^*, \tag{C.26}$$

or, in other words, the "Liouville space" superoperator matrix Ω in such separable cases is given by the following Krønecker (or tensor) product of "Hilbert space" operator matrices X and Y:

$$\hat{X}\odot\hat{Y}^\dagger \iff \Omega = \mathsf{X}\otimes\mathsf{Y}^* \qquad \text{or} \qquad \hat{X}\odot\hat{Y} \iff \Omega = \mathsf{X}\otimes\mathsf{Y}^T. \tag{C.27}$$

C.3.4 "Hilbert space" traces in "Liouville space"

When working with density matrices, we often wish to evaluate expressions of the form $\mathrm{Tr}\left[\hat{A}^\dagger\hat{C}\right]$ where $\hat{A}$ and $\hat{C}$ are Hilbert space operators. Such expressions have a very simple form in "Liouville space" as we demonstrate.

Consider two Liouville states

$$\begin{aligned} |A) &= \sum_{ab} A_{ab}\,|a\rangle\langle b| = \sum_{ab} A_{ab}\,|a,b) \quad \text{and} \\ |C) &= \sum_{cd} C_{cd}\,|c\rangle\langle d| = \sum_{cd} C_{cd}\,|c,d)\,. \end{aligned} \tag{C.28}$$

The "Liouville space" inner product $(A|C)$ may be expanded as follows

$$\begin{aligned} (A|C) &= \sum_{abcd} A^*_{ab}C_{cd}\,(a,b|c,d) \\ &= \sum_{abcd}\left(\hat{A}^\dagger\right)_{ba} C_{cd}\,(a,b|c,d) \end{aligned} \tag{C.29}$$

where $\left(\hat{A}^\dagger\right)_{ba} = \langle b|\hat{A}^\dagger|a\rangle$. Switching to "Hilbert space" using equation (C.8) gives

$$\begin{aligned} (A|C) &= \sum_{bacd}\left(\hat{A}^\dagger\right)_{ba} C_{cd}\,\mathrm{Tr}\left[\,|b\rangle\,\langle a|c\rangle\,\langle d|\right] \\ &= \sum_{bacd}\mathrm{Tr}\left[\left(\hat{A}^\dagger\right)_{ba}|b\rangle\langle a|\,C_{cd}\,|c\rangle\langle d|\right] \\ &= \mathrm{Tr}\left[\left\{\sum_{ba}\left(\hat{A}^\dagger\right)_{ba}|b\rangle\langle a|\right\}\left\{\sum_{cd}C_{cd}\,|c\rangle\langle d|\right\}\right] = \mathrm{Tr}\left[\hat{A}^\dagger\hat{C}\right]. \end{aligned} \tag{C.30}$$

Thus, the "Liouville space" inner product of two vectors $(A|C)$ is equal to the trace of the product of two related operators in "Hilbert space" $\mathrm{Tr}\left[\hat{A}^\dagger\hat{C}\right]$.

C.4 Liouville-von Neumann equation

In the Hilbert space density matrix formalism, the density matrix evolves according to the Liouville-von Neumann equation:

$$\frac{\partial\hat{\rho}(t)}{\partial t} = -\mathrm{i}\left[\hat{H}(t),\hat{\rho}(t)\right] = -\mathrm{i}\left(\hat{H}\hat{\rho}(t)\hat{\mathbb{1}} - \hat{\mathbb{1}}\hat{\rho}(t)\hat{H}\right). \tag{C.31}$$

Transforming to Liouville space using equation (C.25), we find that the density ket $|\hat{\rho}(t))$ evolves under the influence of a superoperator $\hat{\hat{L}}$

$$\frac{\partial\,|\hat{\rho}(t))}{\partial t} = -\mathrm{i}\hat{\hat{L}}\,|\hat{\rho}(t)) \tag{C.32}$$

where the Liouvillian superoperator $\hat{\hat{L}}$ is defined in Hilbert space as

$$\hat{\hat{L}}\odot = \left[\hat{H},\odot\right] = \hat{H}\odot - \odot\hat{H} \tag{C.33}$$

and has a Liouville space matrix representation

$$\mathsf{L} = \mathsf{H}\otimes\mathbb{1} - \mathbb{1}\otimes\mathsf{H}^{\mathrm{T}}. \tag{C.34}$$

Solving equation (C.32), the density ket transforms according to

$$|\hat{\rho}(t)) = \mathrm{e}^{-\mathrm{i}\hat{\hat{L}}t}\,|\hat{\rho}(0)) \tag{C.35}$$

where $|\hat{\rho}(0))$ describes the initial state of the system.

Appendix D

Physical constants

For convenience, physical constants from the 2002 CODATA report [385] are given here. This appendix is adapted from the public domain NIST Standard Reference Database 121 at `http://physics.nist.gov/Constants`. The numbers in parentheses are the one-standard-deviation uncertainty in the last two digits of the given value.

Energy equivalents

$$
\begin{aligned}
(1\ \mathrm{m}^{-1})c &= 299\,792\,458\ \mathrm{Hz} \\
(1\ \mathrm{m}^{-1})hc/k &= 1.438\,7752(25) \times 10^{-2}\ \mathrm{K} \\
(1\ \mathrm{m}^{-1})hc &= 1.239\,841\,91(11) \times 10^{-6}\ \mathrm{eV} \\
(1\ \mathrm{m}^{-1})h/c &= 1.331\,025\,0506(89) \times 10^{-15}\ \mathrm{u} \\
(1\ \mathrm{Hz})/c &= 3.335\,640\,951\ldots \times 10^{-9}\ \mathrm{m}^{-1} \\
(1\ \mathrm{Hz})h/k &= 4.799\,2374(84) \times 10^{-11}\ \mathrm{K} \\
(1\ \mathrm{Hz})h &= 4.135\,667\,43(35) \times 10^{-15}\ \mathrm{eV} \\
(1\ \mathrm{K})k/hc &= 69.503\,56(12)\ \mathrm{m}^{-1} \\
(1\ \mathrm{K})k/h &= 2.083\,6644(36) \times 10^{10}\ \mathrm{Hz} \\
(1\ \mathrm{K})k &= 8.617\,343(15) \times 10^{-5}\ \mathrm{eV} \\
(1\ \mathrm{J}) &= 6.241\,509\,47(53) \times 10^{18}\ \mathrm{eV} \\
(1\ \mathrm{eV}) &= 1.602\,176\,53(14) \times 10^{-19}\ \mathrm{J} \\
(1\ \mathrm{eV})/hc &= 8.065\,544\,45(69) \times 10^{5}\ \mathrm{m}^{-1} \\
(1\ \mathrm{eV})/h &= 2.417\,989\,40(21) \times 10^{14}\ \mathrm{Hz} \\
(1\ \mathrm{eV})/k &= 1.160\,4505(20) \times 10^{4}\ \mathrm{K} \\
(1\ \mathrm{eV})/c^2 &= 1.073\,544\,171(92) \times 10^{-9}\ \mathrm{u} \\
(1\ \mathrm{kg}) &= 6.022\,1415(10) \times 10^{26}\ \mathrm{u} \\
(1\ \mathrm{u}) &= 1.660\,538\,86(28) \times 10^{-27}\ \mathrm{kg} \\
(1\ \mathrm{u})c/h &= 7.513\,006\,608(50) \times 10^{14}\ \mathrm{m}^{-1} \\
(1\ \mathrm{u})c^2 &= 931.494\,043(80) \times 10^{6}\ \mathrm{eV}
\end{aligned}
$$

Constants

Quantity	Symbol	Numerical value	Unit
speed of light in vacuum	c, c_0	299 792 458 (exact)	m s^{-1}
magnetic constant	μ_0	$4\pi \times 10^{-7}$ (exact)	N A^{-2}
		$= 12.566\,370\,614\ldots \times 10^{-7}$	N A^{-2}
electric constant $1/\mu_0 c^2$	ϵ_0	$8.854\,187\,817\ldots \times 10^{-12}$	F m^{-1}
Newtonian constant of gravitation	G	$6.6742(10) \times 10^{-11}$	m^3 kg^{-1} s^{-2}
Planck constant	h	$6.626\,0693(11) \times 10^{-34}$	J s
in eV s		$4.135\,667\,43(35) \times 10^{-15}$	eV s
$h/2\pi$	$\hbar$	$1.054\,571\,68(18) \times 10^{-34}$	J s
in eV s		$6.582\,119\,15(56) \times 10^{-16}$	eV s
elementary charge	e	$1.602\,176\,53(14) \times 10^{-19}$	C
magnetic flux quantum $h/2e$	Φ_0	$2.067\,833\,72(18) \times 10^{-15}$	Wb
Josephson constant $2e/h$	K_J	$483\,597.879(41) \times 10^9$	Hz V^{-1}
von Klitzing constant $h/e^2 = \mu_0 c/2\alpha$	R_K	25 812.807 449(86)	Ω
Bohr magneton $e\hbar/2m_e$	μ_B	$927.400\,949(80) \times 10^{-26}$	J T^{-1}
in eV T^{-1}		$5.788\,381\,804(39) \times 10^{-5}$	eV T^{-1}
nuclear magneton $e\hbar/2m_p$	μ_N	$5.050\,783\,43(43) \times 10^{-27}$	J T^{-1}
in eV T^{-1}		$3.152\,451\,259(21) \times 10^{-8}$	eV T^{-1}
fine-structure constant $e^2/4\pi\epsilon_0\hbar c$	α	$7.297\,352\,568(24) \times 10^{-3}$	
inverse fine-structure constant	α^{-1}	137.035 999 11(46)	
Rydberg constant $\alpha^2 m_e c/2h$	R_∞	10 973 731.568 525(73)	m^{-1}
	$R_\infty c$	$3.289\,841\,960\,360(22) \times 10^{15}$	Hz
energy equivalent in eV	$R_\infty hc$	13.605 6923(12)	eV
Bohr radius $\alpha/4\pi R_\infty = 4\pi\epsilon_0\hbar^2/m_e e^2$	a_0	$0.529\,177\,2108(18) \times 10^{-10}$	m
Hartree energy $e^2/4\pi\epsilon_0 a_0 = 2R_\infty hc = \alpha^2 m_e c^2$	E_h	$4.359\,744\,17(75) \times 10^{-18}$	J
in eV		27.211 3845(23)	eV
electron mass	m_e	$9.109\,3826(16) \times 10^{-31}$	kg
in u		$5.485\,799\,0945(24) \times 10^{-4}$	u
energy equivalent in MeV	$m_e c^2$	0.510 998 918(44)	MeV
electron-muon mass ratio	m_e/m_μ	$4.836\,331\,67(13) \times 10^{-3}$	
electron-proton mass ratio	m_e/m_p	$5.446\,170\,2173(25) \times 10^{-4}$	
electron charge to mass quotient	$-e/m_e$	$-1.758\,820\,12(15) \times 10^{11}$	C kg^{-1}
Compton wavelength $h/m_e c$	λ_C	$2.426\,310\,238(16) \times 10^{-12}$	m
$\lambda_C/2\pi = \alpha a_0 = \alpha^2/4\pi R_\infty$	$\lambda\!\!\!^{-}_C$	$386.159\,2678(26) \times 10^{-15}$	m
classical electron radius $\alpha^2 a_0$	r_e	$2.817\,940\,325(28) \times 10^{-15}$	m
Thomson cross section $(8\pi/3)r_e^2$	σ_e	$0.665\,245\,873(13) \times 10^{-28}$	m^2
electron magnetic moment	μ_e	$-928.476\,412(80) \times 10^{-26}$	J T^{-1}
to Bohr magneton ratio	μ_e/μ_B	−1.001 159 652 1859(38)	
to nuclear magneton ratio	μ_e/μ_N	−1838.281 971 07(85)	
electron magnetic moment anomaly $\lvert\mu_e\rvert/\mu_B - 1$	a_e	$1.159\,652\,1859(38) \times 10^{-3}$	
electron g-factor $-2(1 + a_e)$	g_e	−2.002 319 304 3718(75)	
electron-proton magnetic moment ratio	μ_e/μ_p	−658.210 6862(66)	
muon mass in u	m_μ	0.113 428 9264(30)	u
energy equivalent in MeV	$m_\mu c^2$	105.658 3692(94)	MeV
muon-electron mass ratio	m_μ/m_e	206.768 2838(54)	
muon magnetic moment	μ_μ	$-4.490\,447\,99(40) \times 10^{-26}$	J T^{-1}
to Bohr magneton ratio	μ_μ/μ_B	$-4.841\,970\,45(13) \times 10^{-3}$	
to nuclear magneton ratio	μ_μ/μ_N	−8.890 596 98(23)	
muon magnetic moment anomaly $\lvert\mu_\mu\rvert/(e\hbar/2m_\mu) - 1$	a_μ	$1.165\,919\,81(62) \times 10^{-3}$	

Quantity	Symbol	Numerical value	Unit
muon g-factor $-2(1+a_\mu)$	g_μ	$-2.002\,331\,8396(12)$	
muon-proton magnetic moment ratio	μ_μ/μ_p	$-3.183\,345\,118(89)$	
proton mass	m_p	$1.672\,621\,71(29)\times10^{-27}$	kg
in u		$1.007\,276\,466\,88(13)$	u
energy equivalent in MeV	m_pc^2	938.272 029(80)	MeV
proton-electron mass ratio	m_p/m_e	$1836.152\,672\,61(85)$	
proton magnetic moment	μ_p	$1.410\,606\,71(12)\times10^{-26}$	J T^{-1}
to nuclear magneton ratio	μ_p/μ_N	$2.792\,847\,351(28)$	
proton magnetic shielding correction $1-\mu'_p/\mu_p$ (H_2O, sphere, 25 °C)	σ'_p	$25.689(15)\times10^{-6}$	
proton gyromagnetic ratio $2\mu_p/\hbar$	γ_p	$2.675\,222\,05(23)\times10^{8}$	s^{-1} T^{-1}
	$\gamma_p/2\pi$	42.577 4813(37)	MHz T^{-1}
shielded proton gyromagnetic ratio $2\mu'_p/\hbar$ (H_2O, sphere, 25 °C)	γ'_p	$2.675\,153\,33(23)\times10^{8}$	s^{-1} T^{-1}
	$\gamma'_p/2\pi$	42.576 3875(37)	MHz T^{-1}
neutron mass in u	m_n	$1.008\,664\,915\,60(55)$	u
energy equivalent in MeV	m_nc^2	939.565 360(81)	MeV
neutron-proton mass ratio	m_n/m_p	$1.001\,378\,418\,70(58)$	
neutron magnetic moment	μ_n	$-0.966\,236\,45(24)\times10^{-26}$	J T^{-1}
to nuclear magneton ratio	μ_n/μ_N	$-1.913\,042\,73(45)$	
deuteron mass in u	m_d	$2.013\,553\,212\,70(35)$	u
energy equivalent in MeV	m_dc^2	1875.612 82(16)	MeV
deuteron-proton mass ratio	m_d/m_p	$1.999\,007\,500\,82(41)$	
deuteron magnetic moment	μ_d	$0.433\,073\,482(38)\times10^{-26}$	J T^{-1}
to nuclear magneton ratio	μ_d/μ_N	0.857 438 2329(92)	
helion (^{3}He nucleus) mass in u	m_h	3.014 932 2434(58)	u
energy equivalent in MeV	m_hc^2	2808.391 42(24)	MeV
shielded helion magnetic moment (gas, sphere, 25 °C)	μ'_h	$-1.074\,553\,024(93)\times10^{-26}$	J T^{-1}
to Bohr magneton ratio	μ'_h/μ_B	$-1.158\,671\,474(14)\times10^{-3}$	
to nuclear magneton ratio	μ'_h/μ_N	$-2.127\,497\,723(25)$	
alpha particle mass in u	m_α	$4.001\,506\,179\,149(56)$	u
energy equivalent in MeV	$m_\alpha c^2$	3727.379 17(32)	MeV
Avogadro constant	N_A, L	$6.022\,1415(10)\times10^{23}$	mol^{-1}
atomic mass constant $\frac{1}{12}m(^{12}\mathrm{C})=1$ u	m_u	$1.660\,538\,86(28)\times10^{-27}$	kg
energy equivalent in MeV	m_uc^2	931.494 043(80)	MeV
Faraday constant N_Ae	F	96 485.3383(83)	C mol^{-1}
molar gas constant	R	8.314 472(15)	J mol^{-1} K^{-1}
Boltzmann constant R/N_A	k	$1.380\,6505(24)\times10^{-23}$	J K^{-1}
in eV K^{-1}		$8.617\,343(15)\times10^{-5}$	eV K^{-1}
molar volume of ideal gas RT/p ($T=273.15$ K, $p=101.325$ kPa)	V_m	$22.413\,996(39)\times10^{-3}$	m^3 mol^{-1}
Stefan-Boltzmann constant $\pi^2k^4/60\hbar^3c^2$	σ	$5.670\,400(40)\times10^{-8}$	W m^{-2} K^{-4}
first radiation constant $2\pi hc^2$	c_1	$3.741\,771\,38(64)\times10^{-16}$	W m^2
second radiation constant hc/k	c_2	$1.438\,7752(25)\times10^{-2}$	m K
Wien displacement law constant $b=\lambda_{max}T=c_2/4.965\,114\,231\ldots$	b	$2.897\,7685(51)\times10^{-3}$	m K
Cu x unit: $\lambda(\mathrm{Cu\,K}\alpha_1)/1\,537.400$	xu(Cu Kα_1)	$1.002\,077\,10(29)\times10^{-13}$	m
Mo x unit: $\lambda(\mathrm{Mo\,K}\alpha_1)/707.831$	xu(Mo Kα_1)	$1.002\,099\,66(53)\times10^{-13}$	m

$$\gamma_e = -\frac{|g_e|\,\mu_B}{\hbar} = -1.760\,859\,74(15)\times10^{11}\,\mathrm{rad\,s^{-1}\,T^{-1}}$$

$$\gamma_e/2\pi = -\frac{|g_e|\,\mu_B}{h} = -28.024\,9532(24)\,\mathrm{MHz\,mT^{-1}}$$

Bibliography

[1] Ulrich E. Steiner and Thomas Ulrich. Magnetic field effects in chemical kinetics and related phenomena. *Chem. Rev.*, 89:51–147, 1989.

[2] Hisaharu Hayashi. *Introduction to Dynamic Spin Chemistry: Magnetic Field Effects on Chemical and Biochemical Reactions*, volume 8 of *World Scientific Lecture and Course Notes in Chemistry*. World Scientific, 2004.

[3] K. B. Henbest, K. Maeda, F. Cintolesi, D. Gust, P. J. Hore, and C. R. Timmel. Extremely low magnetic field effects towards a photochemical compass. Poster presented at ESR2007 conference, 2007.

[4] Robert Evans, Christiane R. Timmel, P. J. Hore, and Melanie M. Britton. Magnetic resonance imaging of the manipulation of a chemical wave using an inhomogeneous magnetic field. *JACS*, 128(22):7309–7314, 2006.

[5] Robert Evans, Christiane R. Timmel, P. J. Hore, and Melanie M. Britton. Magnetic resonance imaging of a magnetic field-dependent chemical wave. *Chem. Phys. Lett.*, 297:67–72, 2004.

[6] Hisaharu Hayashi. Advent of spin chemistry. *RIKEN Review*, 44:7–10, 2002.

[7] R. C. Johnson, R. E. Merrifield, P. Avakian, and R. B. Flippen. Effects of magnetic fields on the mutual annihilation of triplet excitons in molecular crystals. *Phys. Rev. Lett.*, 19:285–287, 1967.

[8] R. E. Merrifield. Theory of magnetic field effects on the mutual annihilation of triplet excitons. *J. Chem. Phys.*, 48(9):4318–4319, 1968.

[9] B. Brocklehurst. Formation of excited states by recombining organic ions. *Nature*, 221:921–923, 1969.

[10] Brian Brocklehurst. Spin correlation in the geminate recombination of radical ions in hydrocarbons: Part 1. — theory of the magnetic field effect. *Journal of the Chemical Society, Faraday Transactions 2*, 72:1869–1884, 1976.

[11] Brian Brocklehurst. Spin correlation in the geminate recombination of radical ions in hydrocarbons: Part 2 — time resolved single-photon counting study of the magnetic field effect. *Faraday Discuss. Chem. Soc.*, 63:96–103, 1977.

[12] Joachim Bargon. The discovery of chemically induced dynamic polarization (CIDNP). *Helvetica Chimica Acta*, 89:2082–2102, 2006.

[13] R. Kaptein and J. L. Oosterhoff. Chemically induced dynamic nuclear polarization II (Relation with anomalous ESR spectra). *Chem. Phys. Lett.*, 4(4):195–197, 1969.

[14] G. L. Closs. A mechanism explaining nulcear spin polarizations in radical combination reactions. *JACS*, 91(16):4552–4554, 1969.

[15] Ronald G. Lawler and Glenn T. Evans. Some chemical consequences of magnetic interactions in radical pairs. *Industrie Chimique Belge*, 36(12):1087–1089, 1971.

[16] S. K. Wong and J. K. S. Wan. Photochemically induced dynamic electron spin polarization. The 1,4-naphthosemiquinone radical in 2-propanol. *JACS*, 94(20): 7197–7198, 1972.

[17] P. W. Atkins, I. C. Buchanan, R. C. Gurd, K. A. McLauchlan, and A. F. Simpson. Emission electron spin resonance spectra from free radicals in solution. *J. Chem. Soc. D: Chem. Comm.*, 9:513–514, 1970.

[18] J. Boiden Pedersen and Jack H. Freed. Calculation of magnitudes of chemically induced dynamic electron polarizations. *J. Chem. Phys.*, 57(2):1004–06, January 1972.

[19] J. Boiden Pedersen and Jack H. Freed. Theory of chemically induced dynamic electron polarization. II. *J. Chem. Phys.*, 59(6):2869–85, 1973.

[20] J. Boiden Pedersen and Jack H. Freed. Theory of chemically induced dynamic electron polarization. I. *J. Chem. Phys.*, 58(1):2746–62, 1973.

[21] J. Boiden Pedersen and Jack H. Freed. Some theoretical aspects of chemically induced dynamic nuclear polarization. *J. Chem. Phys.*, 61(4):1517–25, 1974.

[22] J. Boiden Pedersen and Jack H. Freed. Theory of chemically induced dynamic electron polarization. III. Initial triplet polarizations. *J. Chem. Phys.*, 62(5): 1706–1711, 1975.

[23] J. Boiden Pedersen and Jack H. Freed. A hydrodynamic effect on chemically induced dynamic spin polarization. *J. Chem. Phys.*, 62(5):1790–95, 1975.

[24] Klaus Schulten, H. Staerk, A. Weller, H.-J. Werner, and B. Nickel. Magnetic field dependence of the geminate recombination of radical ion pairs in polar solvents. *Zeitschrift für Physikalische Chemie*, 101(1–6):371–390, 1976.

[25] Z. Schulten and K. Schulten. The generation, diffusion, spin motion, and recombination of radical pairs in solution in the nanosecond time domain. *J. Chem. Phys.*, 66(10):4616–4634, 1977.

[26] H.-J. Werner, Z. Schulten, and K. Schulten. Theory of the magnetic field modulated geminate recombination of radical ion pairs in polar solvents: Application to the pyrene–N,N-dimethylaniline system. *J. Chem. Phys.*, 67(2):646–663, July 1977.

[27] Klaus Schulten and Peter G. Wolynes. Semiclassical description of electron spin motion in radicals including the effect of electron hopping. *J. Chem. Phys.*, 68 (7):3292–3297, 1978.

[28] Ernst Walter Knapp and Klaus Schulten. Magnetic field effect on the hyperfine-induced electron spin motion in radicals undergoing diamagnetic-paramagnetic exchange. *J. Chem. Phys.*, 71(4):1878–1883, August 1979.

[29] Klaus Schulten. Magnetic field effects in chemistry and biology. *Festkörper-*

probleme, XXII:61–83, 1982.

[30] P. J. Hore. Spin chemistry. *Mol. Phys.*, 104:1529, 2006.

[31] Martin Goez. An introduction to chemically induced dynamic nuclear polarization. *Concepts in Magnetic Resonance*, 7(1):69–86, 1995.

[32] K. Hun Mok and P. J. Hore. Photo-CIDNP NMR methods for studying protein folding. *Methods*, 34:75–87, 2004.

[33] E. L. Frankevich and S. I. Kubarev. Spectroscopy of reaction-yield detected magnetic resonance. In Richard H. Clarke, editor, *Triplet State ODMR Spectroscopy: Techniques and Applications to Biophysical Systems*, chapter 5, pages 137–183. Wiley-Interscience, New York, 1982.

[34] Mark Sharnoff. ESR-produced modulation of triplet phosphorescence. *J. Chem. Phys.*, 46(8):3263–3264, April 1967.

[35] Jonathan R Woodward, Christiane R Timmel, P J Hore, and Keith A McLauchlan. Low field RYDMR: effects of orthogonal static and oscillating magnetic fields on radical recombination reactions. *Mol. Phys.*, 100(8):1181–1186, 2002.

[36] S. N. Batchelor, K. A. McLauchlan, and I. A. Shkrob. Reaction yield detected magnetic resonance in exciplex systems. I. B_0 and B_1 spectra. *Mol. Phys.*, 75 (3):501–529, 1992.

[37] S.N. Batchelor, K. A. McLauchlan, and I.A. Shkrob. Reaction yield detected magnetic resonance in exciplex systems II. Time resolved and pulse studies. *Mol. Phys.*, 75(3):531–561, 1992.

[38] S. N. Batchelor, K. A. McLauchlan, and I. A. Shkrob. Radical pair phenomena in exciplex and excited radical systems. *Zeitschrift für Physikalische Chemie*, 180:9–31, 1993.

[39] Charles B. Grissom. Magnetic field effects in biology: A survey of possible mechanisms with emphasis on radical-pair recombination. *Chem. Rev.*, 95:3–24, 1995.

[40] J.R. Woodward. Radical pairs in solution. *Progress in Reaction Kinetics and Mechanism*, 27(3):165–207, 2002.

[41] Brian Brocklehurst. Magnetic fields and radical reactions: recent developments and their role in nature. *Chemical Society Reviews*, 31(5):301–311, 2002.

[42] Hisao Murai. Spin-chemical approach to photochemistry: reaction control by spin quantum operation. *Journal of Photochemistry and Photobiology C: Photochemistry Reviews*, 3:183–201, 2003.

[43] Christiane R. Timmel and Kevin B. Henbest. A study of spin chemistry in weak magnetic fields. *Philosophical Transactions of the Royal Society of London A*, 362:2573–2589, 2004.

[44] Saburo Nagakura, Hisaharu Hayashi, and Tohru Azumi. *Dynamic spin chemistry : magnetic controls and spin dynamics of chemical reactions*. Wiley, 1998. ISBN 0471328367.

[45] K. M. Salikhov, Yu. N. Molin, R. Z. Sagdeev, and A. L. Buchachenko. *Spin Polarization and Magnetic Effects in Radical Reactions*, volume 22 of *Studies in*

Physical and Theoretical Chemistry. Elsevier Science Publishers, Amsterdam, 1984. ISBN 044499677X.

[46] Anatoly L. Buchachenko and Eugene L. Frankevich. *Chemical Generation and Reception of Radio- and Microwaves*. VCH Publishers, Inc, 1994. ISBN 1560816309.

[47] F. J. Adrian. Radical pair mechanism of chemically induced magnetic polarisation. In *Chemically Induced Magnetic Polarization*, volume 34 of *NATO Advanced Study Institute: Series C*, pages 77–105. D. Reidel Publishing Company, 1977.

[48] Frank J. Adrian. Role of diffusion-controlled reaction in chemically induced nuclear-spin polarization II. General theory and comparison with experiment. *J. Chem. Phys.*, 54(9):3912–3917, 1971.

[49] Frank J. Adrian. Theory of anomalous electron spin resonance spectra of free radicals in solution. Role of diffusion-controlled separation and reencounter of radical pairs. *J. Chem. Phys.*, 54(9):3918–3923, 1971.

[50] Frank J. Adrian. Role of diffusion-controlled reaction in chemically induced nuclear spin polarization. *J. Chem. Phys.*, 53(8):3374–3375, 1970.

[51] J. B. Pedersen. Diffusional aspects of spin selective reactions; fundamental quantities and relations. In *Spin Chemistry – Spin Polarization and Magnetic Field Effects in Photochemical Reactions*, pages 71 – 89. The Oji International Conference on Spin Chemistry, 1991.

[52] Martin J. Hansen, Anatole A. Neufeld, and Jørgen Boiden Pedersen. Recombination yield of geminate radical pairs in high magnetic fields: general results and application to free diffusion. *Chem. Phys.*, 260(1–2):125–142, 2000.

[53] J.B. Pedersen, M. J. Hansen, A. A. Neufeld, M. Wakasa, and H. Hayashi. A quantitative analysis of recombination data in high magnetic fields. *Mol. Phys.*, 100(9):1349–1354, 2002.

[54] Sharmistha Dutta Choudhury and Samita Basu. Exploring the extent of magnetic field effect on intermolecular photoinduced electron transfer in different organized assemblies. *J. Phys. Chem*, 109A(36):8113–8120, August 2005.

[55] Philip Giles Thomas. *Experimental Studies of the Effects of Magnetic Fields on Radical Recombination Reactions in Vesicular and Micellar Environments*. DPhil thesis, University of Oxford, 2004.

[56] A. A. Neufeld, Martin J. Hansen, and J. Boiden Pedersen. Relaxation induced radical pair recombination in micelles. *Chem. Phys.*, 278(2–3):129–146, 2002.

[57] R. W. Eveson, C. R. Timmel, B. Brocklehurst, P. J. Hore, and K. A. McLauchlan. The effects of weak magnetic fields on radical recombination reactions in micelles. *International Journal of Radiation Biology*, 76(11):1509–1522, 2000.

[58] Keith A. McLauchlan and Steven R. Nattrass. Experimental studies of the spin-correlated radical pair in micellar and microemulsion media; MARY, RYDMR B_0 and RYDMR B_1 spectra. *Mol. Phys.*, 65(6):1483–1503, 1988.

[59] N. N. Lukzen, K. L. Ivanov, V. A. Morozov, R. Z. Sagdeev, D. Kattnig, and

G. Grampp. Chemical polarization of electrons of spin-correlated radical ion pairs in nanotubes. *Doklady Physical Chemistry*, 409(2):233–236, 2006.

[60] M. Justinek, G. Grampp, S. Landgraf, P. J. Hore, and N. N. Lukzen. Electron self-exchange kinetics determined by MARY spectroscopy: Theory and experiment. *JACS*, 126:5635–5646, 2004.

[61] G. Grampp, Martin Justinek, and S. Landgraf. Magnetic field effects on the pyrene–dicyanobenzene system: Determination of electron self-exchange rates by MARY spectroscopy. *Mol. Phys.*, 100(8):1063–1070, April 2002.

[62] M. Justinek, G. Grampp, and S. Landgraf. Determination of electron self-exchange rate constants with MARY spectroscopy: Dependence on the fluorophore. *PCCP*, 4:5550–5553, 2002.

[63] M. K. Bowman, D. E. Budil, G. L. Closs, A. G. Kostka, C. A. Wraight, and J. R. Norris. Magnetic resonance spectroscopy of the primary state, P^F, of bacterial photosynthesis. *PNAS*, 78(6):3305–3307, June 1981.

[64] Wilhelm Lersch, Alexander Ogrodnik, and M. E. Michel-Beyerle. On the influence of microwaves and static magnetic fields on the recombination of radical ions in reaction centers of photosynthetic bacteria. *Zeitschrift für Naturforschung A*, 37a:1454–1456, November 1982.

[65] M. Volk, G. Aumeier, T. Langenbacher, R. Feick, A. Ogrodnik, and M.-E. Michel-Beyerle. Energetics and mechanism of primary charge separation in bacterial photosynthesis. a comparative study on reaction centers of *Rhodobacter sphaeroides* and *Chloroflexus aurantiacus*. *J. Phys. Chem.*, 102B(4):735–751, 1998.

[66] H. Murai, A. Ishigaki, and K. Hirooka. Spin effects on an Alq_3 organic electroluminescence device. *Mol. Phys.*, 104:1727–1731, 2006.

[67] S. A. Wolf, D. D. Awschalom, R. A. Buhrman, J. M. Daughton, and S. von Molnár and. Spintronics: A spin-based electronics vision for the future. *Science*, 294:1488–1495, 2001.

[68] Sir Richard Doll. EMF electromagnetic fields and the risk of cancer. Report of an Advisory Group on Non-ionising Radiation 12:1, National Radiological Protection Board, Chilton, Didcot, Oxon OX11 0RQ, 2001.

[69] M. Havas. Biological effects of non-ionizing electromagnetic energy. *Environmental Reviews*, 8(3):173–253, 2000.

[70] UK Childhood Cancer Study Investigators. Exposure to power-frequency magnetic fields and the risk of childhood cancer. *The Lancet*, 354:1925–1931, 1999.

[71] Sir William Stewart. *Mobile Phones and Health*. Independent Expert Group on Mobile Phones, c/o National Radiological Protection Board, Chilton, Didcot, Oxon, OX11 0RQ, 2000.

[72] International EMF project, 2007. `http://www.who.int/peh-emf/en/`.

[73] W. Wiltschko and F. W. Merkel. Orientierung zugunruhiger Rotkehlchen im statischen Magnetfeld. *Verh. dt. zool. Ges.*, 59:362–367, 1966.

[74] Wolfgang Wiltschko and Roswitha Wiltschko. Magnetic compass of European

robins. *Science*, 176(4030):62–64, 1972.

[75] Roger M. Macklis. Magnetic healing, quackery, and the debate about the health effects of electromagnetic fields. *Annals of Internal Medicine*, 118(5):376–383, 1993.

[76] Peter Atkins. Magnetic field effects. *Chemistry in Britain*, 12:214–218, 1976.

[77] Guy Frija, Jacques Bittoun, Gabriel P. Krestin, and David Norris. European directive on electromagnetic fields. *Eur. Radiol.*, 16:2886–2889, 2006.

[78] John Swanson and Leeka Kheifets. Biophysical mechanisms: A component in the weight of evidence for health effects of power-frequency electric and magnetic fields. *Radiation Research*, 165:470–478, 2006.

[79] Brian Brocklehurst and Keith A. McLauchlan. Free radical mechanism for the effects of environmental electromagnetic fields on biological systems. *International Journal of Radiation Biology*, 69(1):3–24, January 1996.

[80] Keith McLauchlan. Are environmental magnetic fields dangerous? *Physics World*, pages 41–45, January 1992.

[81] Yan Liu, Ruth Edge, Kevin Henbest, Christiane R. Timmel, Peter J. Hore, and Peter Gast. Magnetic field effect on singlet oxygen production in a biochemical system. *Chem. Comm.*, 2:174–176, November 2005.

[82] A. R. Jones, N. S. Scrutton, and J. R. Woodward. Magnetic field effects and radical pair mechanisms in enzymes: A reappraisal of the horseradish peroxidase system. *JACS*, 128(26):8408–8409, 2006.

[83] Claire B. Vink and Jonathan R. Woodward. Effect of a weak magnetic field on the reaction between neutral free radicals in isotropic solution. *JACS*, 126(51): 16730–31, February 2004.

[84] Richard R. Ernst, Geoffrey Bodenhausen, and Alexander Wokaun. *Principles of Nuclear Magnetic Resonance in One and Two Dimensions*. Oxford University Press, 1988.

[85] C. P. Slichter. *Principles of Magnetic Resonance*. Springer-Verlag, third edition, 1990.

[86] Malcolm H. Levitt. *Spin Dynamics: Basics of Nuclear Magnetic Resonance*. Wiley, 2001. ISBN 0471489220.

[87] K. A. McLauchlan and U. E. Steiner. The spin-correlated radical pair as a reaction intermediate. *Mol. Phys.*, 73:241–263, 1991.

[88] Alan D. McNaught and Andrew Wilkinson, editors. *IUPAC Compendium of Chemical Terminology*. IUPAC International Union of Pure and Applied Chem, 1997. ISBN 0865426848. `http://goldbook.iupac.org`.

[89] Keith J. Laidler. A glossary of terms used in chemical kinetics, including reaction dynamics. *Pure and Appl. Chem.*, 68(1):149–192, 1996.

[90] A. Abragam and M. H. L. Pryce. Theory of the nuclear hyperfine structure of paramagnetic resonance spectra in crystals. *Proc. Roy. Soc.*, 205A(1080): 135–153, 1951.

[91] M. H. L. Pryce. A modified perturbation procedure for a problem in paramagnetism. *Proc. Phys. Soc. A*, 63:25–29, 1950.

[92] P.W. Atkins and R.S. Friedman. *Molecular Quantum Mechanics*. Oxford University Press, Oxford, 3rd edition, 1997. ISBN 019855947X.

[93] N. M. Atherton. *Electron Spin Resonance*. Ellis Horwood Limited, 1973. ISBN 0470036001.

[94] M. J. Frisch *et al*. Gaussian 03, Revision C.02, 2003.

[95] F. Neese. ORCA — an ab initio, density functional and semiempirical program package, version 2.5, 2006.

[96] Peter Atkins and Julio de Paula. *Atkins' Physical Chemistry*. Oxford University Press, 7th edition, 2002.

[97] Francesc Illas, Ibério P. R. Moreira, Coen de Graaf, and Vincenzo Barone. Magnetic coupling in biradicals, binuclear complexes and wide-gap insulators: a survey of ab initio wave function and density functional theory approaches. *Theoretical Chemistry Accounts*, 104:265–272, 2000.

[98] Jiro Abe, Tomokatsu Sano, Masaki Kawano, Yuji Ohashi, Michio M. Matsushita, and Tomokazu Iyoda. EPR and density functional studies of light-induced radical pairs in a single crystal of a hexaarylbiimidazolyl derivative. *Angewandte Chemie*, 113(3):600–602, 2001.

[99] Louise E. Sinks, Emily A. Weiss, Jovan M. Giaimo, and Michael R. Wasielewski. Effect of charge delocalization on radical ion pair electronic coupling. *Chem. Phys. Lett.*, 404:244–249, 2005.

[100] Anthony R. O'Dea, Ailsa F. Curtis, Nicholas J. B. Green, Christiane R. Timmel, and P. J. Hore. Influence of dipolar interactions on radical pair recombination reactions subject to weak magnetic fields. *J. Phys. Chem.*, 109A(5):869–873, January 2005.

[101] Richard M. Noyes. A treatment of chemical kinetics with special applicability to diffusion controlled reactions. *J. Chem. Phys.*, 22(8):1349–1359, 1954.

[102] Ryogo Kubo. Stochastic Liouville equations. *Journal of Mathematical Physics*, 4(2):174–183, 1963.

[103] D. Gamliel and H. Levanon. *Stochastic Processes in Magnetic Resonance*. World Scientific Publishing, 1995. ISBN 9789810222277.

[104] Nicola Wagner-Rundell. DPhil thesis, University of Oxford, 2007.

[105] Henrik Mouritsen and Thorsten Ritz. Magnetoreception and its use in bird navigation. *Current Opinion in Neurobiology*, 15:406–414, 2005.

[106] Thorsten Ritz, Salih Adem, and Klaus Schulten. A model for photoreceptor-based magnetoreception in birds. *Biophysical Journal*, 78:707–718, February 2000.

[107] Klaus Schulten, Charles E. Swenberg, and Albert Weller. A biomagnetic sensory mechanism based on magnetic field modulated coherent electron spin motion. *Zeitschrift fuer Physikalische Chemie Neue Folge*, 111:1–5, 1978.

[108] C. R. Timmel, U. Till, B. Brocklehurst, K. A. McLauchlan, and P. J. Hore. Effects of weak magnetic fields on free radical recombination reactions. *Mol. Phys.*, 95(1):71–89, 1998.

[109] S. N. Batchelor, C. W. M. Kay, K. A. McLauchlan, and I. A. Shkrob. Time-resolved and modulation methods in the study of the effects of magnetic fields on the yields of free-radical reactions. *J. Phys. Chem.*, 97:13250–132, 1993.

[110] D. V. Stass, N. N. Lukzen, B. M. Tadjikov, and Yu. N. Molin. Manifestation of quantum coherence upon recombination of radical ion pairs in weak magnetic fields. Systems with non-equivalent nuclei. *Chem. Phys. Lett.*, 233(4):444–450, February 1995.

[111] D. V. Stass, B. M. Tadjikov, and Yu. N. Molin. Manifestation of quantum coherence upon recombination of radical ion pairs in weak magnetic fields. Systems with equivalent nuclei. *Chem. Phys. Lett.*, 235(5–6):511–516, March 1995.

[112] Evgeny V. Kalneus, Dmitri V. Stass, and Yuri A. Grishin. Yoke-free magnetic system for low field studies in magnetically affected reaction yield spectroscopy. *Review of Scientific Instruments*, 76(084102):1–12, 2005.

[113] Vladimir O. Saik, Agnes E. Ostafin, and Sanford Lipsky. Magnetic field effects on recombination fluorescence in liquid iso-octane. *J. Chem. Phys.*, 103(17): 7347–7358, November 1995.

[114] Christopher T. Rodgers, Stuart A. Norman, Kevin B. Henbest, Christiane R. Timmel, and P. J. Hore. A technique for determining the distribution of re-encounters which contribute to magnetic field effects. *JACS*, in press, 2007.

[115] Ulrika Till. *Recombination Kinetics of Radical Pairs*. DPhil thesis, University of Oxford, 1998.

[116] U. Till, C. R. Timmel, B. Brocklehurst, and P. J. Hore. The influence of very small magnetic fields on radical recombination reactions in the limit of slow recombination. *Chem. Phys. Lett.*, 298(1–3):7–14, 1998.

[117] Matlab R2006a, 2006.

[118] C Rodgers. Effects of periodic magnetic fields on radical recombination reactions. Part II thesis, Oxford University, Jun 2003.

[119] Claude Cohen-Tannoudji. *Quantum Mechanics*. John Wiley & Sons Inc, 1977. ISBN 047116433X.

[120] M. E. Rose. *Elementary Theory of Angular Momentum*. Dover Publications Inc., 1995. ISBN 0486684806.

[121] D. M. Brink and G. R. Satchler. *Angular Momentum*. Clarendon Press, 1994. ISBN 0198517599.

[122] D. A. Varshalovich, A. N. Moskalev, and V. K. Khersonskii. *Quantum Theory of Angular Momentum*. World Scientific, 1988. ISBN 9971509962.

[123] John H. Scofield. Frequency-domain description of a lock-in amplifier. *American Journal of Physics*, 62(2):129–133, February 1994.

[124] www.thinkSRS.com. About lock-in amplifiers: Application note 3. Stanford Research Systems, 2004.

[125] Bengt Fornberg. Generation of finite difference formulas on arbitrarily spaced grids. *Mathematics of Computation*, 51:699–706, 1988.

[126] Maple 9, 2003.

[127] Mathematica 5.2, 2005.

[128] Alan L. Andrew and Roger C. E. Tan. Computation of derivatives of repeated eigenvalues and the corresponding eigenvectors of symmetric matrix pencils. *SIAM J. Matrix Anal. Appl.*, 20(1):78–100, 1998.

[129] Roger C. E. Tan, Alan L. Andrew, and Felicia M. L. Hong. Iterative computation of second-order derivatives of eigenvalues and eigenvectors. *Communications in Numerical Methods in Engineering*, 10:1–9, 1994.

[130] Alan L. Andrew, K.-W. Eric Chu, and Peter Lancaster. Derivatives of eigenvalues and eigenvectors of matrix functions. *SIAM J. Matrix Anal. Appl.*, 14(4): 903–926, 1993.

[131] King-Wah Eric Chu. On multiple eigenvalues of matrices depending on several parameters. *SIAM Journal on Numerical Analysis*, 27(5):1368–1385, 1990.

[132] William C. Mills-Curran. Calculation of eigenvector derivatives for structures with repeated eigenvalues. *AIAA Journal*, 26(7):867–871, 1988.

[133] Richard B. Nelson. Simplified calculation of eigenvector derivatives. *AIAA Journal*, 14(9):1201–1205, 1976.

[134] P. Lancaster. On eigenvalues of matrices dependent on a parameter. *Numerische Mathematik*, 6:377–387, 1964.

[135] Alan Andrew. Personal communication. "Re: Computation of the derivatives of repeated eigenvalues...", 2004.

[136] Albert Weller, Hubert Staerk, and Rainer Treichel. Magnetic-field effects on geminate radical-pair recombination. *Faraday Discuss. Chem. Soc.*, 78:271–278, 1984.

[137] George J. Kavarnos and Nicholas J. Turro. Photosensitization by reversible electron transfer: Theories, experimental evidence, and examples. *Chem. Rev.*, 86:401–449, 1986.

[138] George J. Kavarnos. *Fundamentals of photoinduced electron transfer*. VCH, 1993. ISBN 0895737515.

[139] Stuart A. Norman. *Magnetic Field Effects on Radical Pair Reactions*. DPhil thesis, University of Oxford, 2006.

[140] C. A. Hamilton, J. P. Hewitt, Keith A. McLauchlan, and Ulrich E. Steiner. High resolution studies of the effects of magnetic fields on chemical reactions. *Mol. Phys.*, 65:423, 1988.

[141] LabVIEW 6.1, 2002.

[142] A. Weller, F. Nolting, and H. Staerk. A quantitative interpretation of the magnetic field effect on hyperfine-coupling-induced triplet formation from radical ion pairs. *Chem. Phys. Lett.*, 96(1):24–27, March 1983.

[143] R. F. C. Claridge, C. M. Kirk, and B. M. Peake. ^{13}C coupling in the E.S.R.

spectrum of the pyrene anion in tetrahydrafuran. *Aust. J. Chem.*, 26:2055–2058, 1973.

[144] B. G. Pobedimskii, A. L. Buchachenko, and M. B. Neiman. The mechanism of the reactions of peroxides with aromatic amines. *Russian Journal of Physical Chemistry*, 42(6):748–751, 1968.

[145] Hans Landolt and Richard Börnstein. *Landolt-Bornstein physikalisch-chemische Tabellen*. Springer-Verlag, Berlin, sixth edition, 1950.

[146] J. L. Starck, E. Pantin, and F. Murtagh. Deconvolution in astronomy: A review. *Publications of the Astronomical Society of the Pacific*, 114:1051–1069, 2002.

[147] J. A. Högbom. Aperture synthesis with a non-regular distribution of interferometer baselines. *Astron. Astrophys. Suppl.*, 15:417–426, 1974.

[148] A. W. Strong. Maximum entropy imaging with INTEGRAL/SPI data. *Astronomy and Astrophysics*, 411:L127–L129, 2003.

[149] Stig Steenstrup and Steen Hansen. The maximum-entropy method without the positivity constraint - applications to the determination of the distance-distribution function in small-angle scattering. *Journal of Applied Crystallography*, 27:574–580, 1994.

[150] Per Christian Hansen. *Rank-Deficient and Discrete Ill-Posed Problems: Numerical Aspects of Linear Inversion*. SIAM, 1998. ISBN 0898714036.

[151] Per Christian Hansen. Regularization tools: A Matlab package for analysis and solution of discrete ill-posed problems. http://www.imm.dtu.dk/ pch, 2004.

[152] A. N. Tihonov. Solution of incorrectly formulated problems and the regularization method. *Soviet Math Dokl.*, 4:1035–1038, 1963.

[153] Andrey N. Tikhonov and Vasiliy Y. Arsenin. *Solutions of Ill-posed Problems*. Scripta series in mathematics. V. H. Winston & Sons, Washington, D.C., 1977. ISBN 0470991240.

[154] Per Christian Hansen. Analysis of discrete ill-posed problems by means of the L-curve. *SIAM Review*, 34(4):561–580, 1992.

[155] Per Christian Hansen and Dianne Prost O'Leary. The use of the L-curve in the regularization of discrete ill-posed problems. *SIAM J Sci. Comput.*, 14(6): 1487–1503, 1993.

[156] Rasmus Bro and Sijmen de Jong. A fast non-negativity-constrained least squares algorithm. *Journal of Chemometrics*, 11:393–401, 1997.

[157] Charles L. Lawson and Richard J. Hanson. *Solving Least Squares Problems*. Prentice-Hall Inc., Englewood Cliffs, New Jersey, 1974.

[158] Brian Buck and Vincent A. Macaulay, editors. *Maximum Entropy in Action*. Oxford Science Publications. Oxford University Press, 1991. ISBN 0198539630.

[159] Edwin T. Jaynes. Where do we stand on maximum entropy? In Raphael D. Levine and Myron Tribus, editors, *Maximum Entropy Formalism Conference*, pages 15–118. The MIT Press, apr 1978. ISBN 0262120801.

[160] E. T. Jaynes. Information theory and statistical mechanics. *Phys. Rev.*, 106(4):

620–630, 1957.

[161] E. T. Jaynes. Information theory and statistical mechanics. II. *Phys. Rev.*, 108 (2):171–190, 1957.

[162] S.F. Gull and G.J. Daniell. Image reconstruction from incomplete and noisy data. *Nature*, 272:686–690, 1978.

[163] J Skilling and R K Bryan. Maximum entropy image reconstruction: general algorithm. *Mon. Not. R. Astr. Soc.*, 211:111–124, 1984.

[164] P. J. Hore. NMR data processing using the maximum entropy method. *J. Mag. Res.*, 62:561–567, 1985.

[165] Paul J. Flory. *Statistical mechanics of chain molecules*. Interscience Publishers, 1969. ISBN 0470264950.

[166] Eric W. Weisstein. Mathworld, 2007. `http://mathworld.wolfram.com/`.

[167] QUADRULE: quadrature rules, 2007. `http://www.scs.fsu.edu/~burkardt/m_src/quadrule/quadrule.html`.

[168] J. E. T. Penny. *Numerical methods using Matlab*. Prentice Hall; Prentice-Hall International,, 2nd edition, 2000. ISBN 0130126411.

[169] R. Haberkorn. Theory of magnetic field modulation of radical recombination reactions. II. Short time behaviour. *Chem. Phys.*, 24:111–117, 1977.

[170] D. V. Stass. Personal communication. "Re: Low Field Effect", 2006.

[171] Hisao Murai, Shozo Tero-Kubota, and Seigo Yamauchi. *Pulsed and Time-Resolved EPR Studies of Transient Radicals, Radical Pairs and Excited States in Photochemical Systems*, volume 17 of *Electron Paramagnetic Resonance*, chapter 5, pages 130–163. The Royal Society of Chemistry, 2000.

[172] M. K. Bowman, D. E. Budil, G. L. Closs, A. G. Kostka, C. A. Wraight, and J. R. Norris. Magnetic resonance spectroscopy of the primary state, P^F, of bacterial photosynthesis. *PNAS*, 78(6):3305–3307, June 1981.

[173] A. I. Pristupa, V. I. Lesin, and I. A. Krasotkina. Study of solid-surface states by RYDMR spectroscopy. *Chem. Phys. Lett.*, 180(6):569–572, June 1991.

[174] O. A. Anisimov, V. M. Grigoryants, V. K. Molchanov, and Yu. N. Molin. Optical detection of ESR absorption of short-lived ion-radical pairs produced in solution by ionizing radiation. *Chem. Phys. Lett.*, 66(2):265–268, October 1979.

[175] D. V. Stass, J. R. Woodward, C. R. Timmel, P. J. Hore, and K. A. McLauchlan. Radiofrequency magnetic field effects on chemical reaction yields. *Chem. Phys. Lett.*, 329:15–22, October 2000.

[176] J. R. Woodward, R. J. Jackson, C. R. Timmel, P. J. Hore, and K. A. McLauchlan. Resonant radiofrequency magnetic field effects on a chemical reaction. *Chem. Phys. Lett.*, 272:376–382, 1997.

[177] C. R. Timmel and P. J. Hore. Oscillating magnetic field effects on the yields of radical pair reactions. *Chem. Phys. Lett.*, 257:401–408, July 1996.

[178] R. J. Jackson, K. A. McLauchlan, and J. R. Woodward. Resonant radiofrequency effects in spin chemistry. *Chem. Phys. Lett.*, 236:395–401, April 1995.

[179] Christopher T. Rodgers, Kevin B. Henbest, Philipp Kukura, Christiane R. Timmel, and P. J. Hore. Low-field optically detected EPR spectroscopy of transient photoinduced radical pairs. *J. Phys. Chem.*, 109A:5035–5041, 2005.

[180] Kevin B. Henbest, Philipp Kukura, Christopher T. Rodgers, P. J. Hore, and Christiane R. Timmel. Radio frequency magnetic field effects on a radical recombination reaction: A diagnostic test for the radical pair mechanism. *JACS*, 126(26):8102–8103, 2004.

[181] P Kukura. Part II thesis, Oxford University, June 2002.

[182] Christopher J. Wedge. Magnetic field effects on radical recombination reactions. Part II thesis, University of Oxford, 2005.

[183] F. J. Dyson. The radiation theories of Tomonaga, Schwinger, and Feynman. *Phys. Rev.*, 75(3):486–502, 1949.

[184] F. J. Dyson. The S matrix in quantum electrodynamics. *Phys. Rev.*, 75(11): 1736–1755, 1949.

[185] F. Bloch. Dynamical theory of nuclear induction. II. *Phys. Rev.*, 102(1):104–135, 1956.

[186] Anatole Abragam. *The principles of nuclear magnetism*. Oxford: Clarendon Press, 1st paperback edition, 1985. ISBN 019852014X.

[187] P. Hodgkinson and L. Emsley. Numerical simulation of solid-state NMR experiments. *Progress in Nuclear Magnetic Resonance Spectroscopy*, 36:201–239, 2000.

[188] M. Matti Maricq and J. S. Waugh. NMR in rotating solids. *J. Chem. Phys.*, 70 (7):3300–3316, apr 1979.

[189] Mattias Edén. Computer simulations in solid-state NMR. II. Implementations for static and rotating samples. *Concepts in Magnetic Resonance*, 18A(1):1–23, 2003.

[190] Mattias Edén. Computer simulations in solid-state NMR. I. Spin dynamics theory. *Concepts in Magnetic Resonance*, 17A(1):117–154, 2003.

[191] Mattias Edén. Computer simulations in solid-state NMR. III. Powder averaging. *Concepts in Magnetic Resonance*, 18A(1):24–55, 2003.

[192] M. Hohwy, H. Bildsøe, H. J. Jakobsen, and N. C. Nielsen. Efficient spectral simulations in NMR of rotating solids. The γ-COMPUTE algorithm. *J. Mag. Res.*, 136:6–14, 1999.

[193] Malcolm H. Levitt and Mattias Edén. Numerical simulation of periodic nuclear magnetic resonance problems: fast calculation of carousel averages. *Mol. Phys.*, 95(5):879–890, 1998.

[194] Malcolm H. Levitt. Why do spinning sidebands have the same phase? *J. Mag. Res.*, 82(2):427–433, apr 1989.

[195] Thibault Charpentier, Claude Fermon, and Joseph Virlet. Efficient time propagation technique for MAS NMR simulation: Application to quadrupolar nuclei. *J. Mag. Res.*, 132:181–190, 1998.

[196] Thibault Charpentier, Claude Fermon, and Joseph Virlet. Numerical and theoretical analysis of multiquantum magic-angle spinning experiments. *J. Chem. Phys.*, 109(8):3116–3130, 1998.

[197] M. Matti Maricq. Application of average Hamiltonian theory to the NMR of solids. *Phys. Rev.*, 25B:6622–6632, 1982.

[198] A. J. Shaka and James Keeler. Broadband spin decoupling in isotropic liquids. *Progress in Nuclear Magnetic Resonance Spectroscopy*, 19(1):47–129, 1987.

[199] E. Oran Brigham. *The Fast Fourier Transform*. Prentice-Hall, Inc., 1974.

[200] Shangwu Ding and Charles A. McDowell. The equivalence between Floquet formalism and the multi-step approach in computing the evolution operator of a periodical time-dependent Hamiltonian. *Chem. Phys. Lett.*, 288:230–234, 1998.

[201] T. O. Levante, M. Baldus, B. H. Meier, and R. R. Ernst. Formalized quantum mechanical Floquet theory and its application to sample spinning in nuclear magnetic resonanace. *Mol. Phys.*, 86(5):1195–1212, 1995.

[202] Asher Schmidt and Shimon Vega. The Floquet theory of nuclear magnetic resonance spectroscopy of single spins and dipolar coupled spin pairs in rotating solids. *J. Chem. Phys.*, 96(4):2655–2680, 1992.

[203] James W. Cooley and John W. Tukey. An algorithm for the machine calculation of complex Fourier series. *Mathematics of Computation*, 19:297–301, 1965.

[204] Matteo Frigo and Steven G. Johnson. FFTW, 2007. `http://www.fftw.org/`.

[205] MySQL AB. MySQL. `http://www.mysql.com/`.

[206] C. R. Timmel, J. R. Woodward, P. J. Hore, K. A. McLauchlan, and D. V. Stass. A zero-field electron spin resonance spectrometer for the study of transient radical ion pairs. *Measurement Science and Technology*, 12:635–643, 2001.

[207] J. R. Woodward, C. R. Timmel, K. A. McLauchlan, and P. J. Hore. Radio frequency magnetic field effects on electron-hole recombination. *Phys. Rev. Lett.*, 87(7):077602/1–4, 2001.

[208] LabVIEW 7.0 express, 2003.

[209] Christopher W. M. Kay. *Magnetic Field Effects in Chemistry and Biology*. DPhil thesis, University of Oxford, June 1993.

[210] Hiroaki Ohya-Nishiguchi. Both oxidation and reduction of aromatic hydrocarbons by an electrolysis cell designed for low-temperature ESR studies. *Bulletin of the Chemical Society of Japan*, 52(7):2064–2068, 1979.

[211] Philip H. Rieger, Ivan Bernal, William H. Reinmuth, and George K. Fraenkel. Electron spin resonance of electrolytically generated nitrile radicals. *JACS*, 85: 683–693, 1963.

[212] N. M. Atherton. *Principles Of Electron Spin Resonance*. Ellis Horwood and PTR Prentice Hall, 1993.

[213] V. A. Morozov and A. B. Doktorov. Theory of multiquantum optically detected ESR spectra of radical pairs. I. General theory. Resonances in parallel radiofrequency field. *Chem. Phys.*, 153(3):313–331, 1991.

[214] V. A. Morozov and A. B. Doktorov. Theory of multiquantum optically detected ESR spectra of radical pairs. II. Resonances in perpendicular radio-frequency field. *Chem. Phys.*, 153(3):333–350, 1991.

[215] E. G. Bagryanskaya, H. Yashiro, M. Fedin, P. Purtov, and M. D. E. Forbes. Chemically induced multiplet electron–nuclear polarization in zero and low magnetic fields. *J. Phys. Chem.*, 106A(12):2820–2828, 2002.

[216] A. V. Koptyug, V. O. Saik, O. A. Anisimov, and Yu. N. Molin. Spin-locking in concentration-narrowed OD ESR spectra. *Chem. Phys.*, 138:173–178, 1989.

[217] J. R. Norris, M. K. Bowman, D. E. Budil, J. Tang, C. A. Wraight, and G. L. Closs. Magnetic characterization of the primary state of bacterial photosynthesis. *PNAS*, 79(18):5532–5536, September 1982.

[218] Michael R. Wasielewski, James R. Norris, and Michael K. Bowman. Time-domain magnetic resonance studies of short-lived radical pairs in liquid solution. *Faraday Discuss. Chem. Soc.*, 78:279–288, 1984.

[219] W. Lersch and M. E. Michel-Beyerle. Magnetic field effects on the recombination of radical ions in reaction centers of photosynthetic bacteria. *Chem. Phys.*, 78:115–126, 1983.

[220] J. Tang and J. R. Norris. Theoretical calculations of microwave effects on the triplet yield in photosynthetic reaction centers. *Chem. Phys. Lett.*, 94(1):77–80, January 1983.

[221] I. C. Lewis and L. S. Singer. Electron spin resonance of radical cations produced by the oxidation of aromatic hydrocarbons with $SbCl_5$. *J. Chem. Phys.*, 43(8): 2712–2727, October 1965.

[222] O. A. Ponomarev, S. I. Kubarev, I. S. Kubareva, I. P. Susak, and A. S. Shigaev. The recombination of the geminate radical pairs in parallel combined magnetic fields. *Chem. Phys. Lett.*, 388(4–6):231–235, 2004.

[223] Jeff M. Canfield, R. Linn Belford, Peter G. Debrunner, and Klaus Schulten. A perturbation theory treatment of oscillating magnetic fields in the radical pair mechanism. *Chem. Phys.*, 182:1–18, 1994.

[224] J. M. Canfield, R. L. Belford, P. G. Debrunner, and K. Schulten. A perturbation theory treatment of oscillating magnetic fields in the radical pair mechanism. *Chem. Phys.*, 191:347, 1995.

[225] J. M. Canfield, R. L. Belford, P. G. Debrunner, and K. Schulten. A perturbation treatment of oscillating magnetic fields in the radical pair mechanism using the Liouville equation. *Chem. Phys.*, 195:59–69, 1995.

[226] W. Wiltschko. Über den Einfluß statischer Magnetfelder auf die Zugorientierung der Rotkehlchen (*Erithacus rubecula*). *Z. Tierpsychol.*, 25:537–558, 1968.

[227] Roswitha Wiltschko and Wolfgang Wiltschko. Avian navigation: from historical to modern concepts. *Animal Behaviour*, 65:257–272, 2003.

[228] Joseph L. Kirschvink and James L. Gould. Biogenic magnetite as a basis for magnetic field detection in animals. *BioSystems*, 13:181–201, 1981.

[229] Joseph L Kirschvink, Michael M Walker, and Carol E Diebel. Magnetite-based

magnetoreception. *Current Opinion in Neurobiology*, 11:462–467, 2001.

[230] Thorsten Ritz. Personal communication. 2006.

[231] Thorsten Ritz, Peter Thalau, John B. Phillips, Roswitha Wiltschko, and Wolfgang Wiltschko. Resonance effects indicate a radical-pair mechanism for avian magnetic compass. *Nature*, 429:177–180, 2004.

[232] Peter Thalau, Thorsten Ritz, Katrin Stapput, Roswitha Wiltschko, and Wolfgang Wiltschko. Magnetic compass orientation of migratory birds in the presence of a 1.315 MHz oscillating field. *Naturwissenschaften*, 92(2):86–90, February 2005.

[233] Alan Whitaker. The effect of radiofrequency magnetic fields on radical recombination reactions. Part II thesis, University of Oxford, June 2006.

[234] Mattias Edén, Young K Lee, and Malcolm H Levitt. Efficient simulation of periodic problems in NMR. Application to decoupling and rotational resonance. *J. Mag. Res.*, 120:56–71, 1996.

[235] R. Freeman. *A handbook of nuclear magnetic resonance*. Longman, second edition, 1997.

[236] Larry Kevan and Michael K. Bowman, editors. *Modern pulsed and continuous wave electron spin resonance*. John Wiley & Sons, Inc., 1990. ISBN 047150274X.

[237] John A. Weil, James R. Bolton, and John E. Wertz. *Electron Paramagnetic Resonance*. John Wiley & Sons, Inc., 1994. ISBN 0471572349.

[238] I. I. Rabi, N. F. Ramsey, and J. Schwinger. Use of rotating coordinates in magnetic resonance problems. *Reviews of Modern Physics*, 26(2):167–171, April 1954.

[239] R. K. Wangsness and F. Bloch. The dynamical theory of nuclear induction. *Phys. Rev.*, 89(4):728–739, February 1954.

[240] Felix Bloch. Nuclear induction. *Phys. Rev.*, 70(7–8):460–474, October 1946.

[241] F. Bloch and A. Siegert. Magnetic resonance for nonrotating fields. *Phys. Rev.*, 57(6):522–527, March 1940.

[242] Julian Schwinger. On nonadiabatic processes in inhomogeneous fields. *Phys. Rev.*, 51(8):648–651, April 1937.

[243] Y. K. Lee, H. Robert, and D. K. Lathrop. Circular polarization excitation and detection in ^{14}N NQR. *J. Mag. Res.*, 148(2):355–362, February 2001.

[244] J. B. Miller, B. H. Suits, and A. N. Garroway. Circularly polarized RF magnetic fields for spin-1 NQR. *J. Mag. Res.*, 151(2):320–327, August 2001.

[245] M. A. Garstens. Paramagnetic resonance in gases at low fields. *Phys. Rev.*, 93 (6):1228–1231, March 1954.

[246] Martin A. Garstens and Jerome I. Kaplan. Low-field magnetic resonance. *Phys. Rev.*, 99(2), July 1955.

[247] Christopher J. Wedge. Personal communication. 2006.

[248] B. I. Bleaney and B. Bleaney. *Electricity and Magnetism*, volume 1. Oxford University Press, 3rd ed. edition, 1976. ISBN 0198511728.

[249] Tom W. B. Kibble and Frank H. Berkshire. *Classical Mechanics*. Imperial College Press, 5th ed. edition, 2004. ISBN 1860944353.

[250] Martin R. Fuchs, Alexander Schnegg, Martin Plato, Claudia Schulz, Frank Müh, Wolfgang Lubitz, and Klaus Möbius. A high-field/high-frequency heterodyne induction-mode electron paramagnetic resonance spectrometer operating at 360 GHz. *Review of Scientific Instruments*, 70(9):3681–3683, 1999.

[251] Martin R. Fuchs, Alexander Schnegg, Martin Plato, Claudia Schulz, Frank Müh, Wolfgang Lubitz, and Klaus Möbius. The primary donor cation $P^{+\bullet}$ in photosynthetic reaction centers of site-directed mutants of *Rhodobacter sphaeroides*: *g*-tensor shifts revealed by high-field EPR at 360 GHz/12.8 T. *Chem. Phys.*, 294 (3):371–384, 2003.

[252] T. Vaughan, L. DelaBarre, C. Snyder, J. Tian, C. Akgun, D. Shrivastava, W. Liu, C. Olson, G. Adriany, J. Strupp, P. Andersen, A. Gopinath, P.-F. van de Moortele, M. Garwood, and K. Ugurbil. 9.4 T human MRI: Preliminary results. *Magnetic Resonance in Medicine*, 56(6):1274–1282, 2006.

[253] K. Engelhard and H. P. Hollenbach. High-resolution MRI of pancreatic masses with a new circularly polarized body phased-array coil. *Eur. Radiol.*, 7(5):643–648, 1997.

[254] Wilhelm Magnus. On the exponential solution of differential equations for a linear operator. *Communications on Pure and Applied Mathematics*, 7:649–673, 1954.

[255] Daniel Scholz and Michael Weyrauch. A note on the Zassenhaus product formula. *Journal of Mathematical Physics*, 47(033505):1–7, 2006.

[256] Baker-Campbell-Hausdorff formula. Wikipedia, 2006. `http://en.wikipedia.org/wiki/Baker-Campbell-Hausdorff_formula`.

[257] Matthias W. Reinsch. A simple expression for the terms in the Baker-Campbell-Hausdorff series. *Journal of Mathematical Physics*, 41(4):2434–2442, 2000.

[258] Hiroto Kobayashi. Comment on "A simple expression for the terms in the Baker-Campbell-Hausdorff series". *arXiv:math-ph*, 9906010(v1), 1999.

[259] J. D. Franson and Michelle M. Donegan. Perturbation theory for quantum-mechanical observables. *Phys. Rev.*, 65A:052107–1, 2002.

[260] Dragomir Z. Djokovic. An elementary proof of the Baker-Campbell-Hausdorff-Dynkin formula. *Math. Z.*, 143:209–211, 1975.

[261] A. S. Davydov. *Quantum Mechanics*. International series in Natural Philosophy. Pergamon Press, 2nd ed. edition, 1976. ISBN 0080204384.

[262] R. M. Wilcox. Exponential operators and parameter differentiation in quantum physics. *Journal of Mathematical Physics*, 8(4):962–982, 1967.

[263] D. P. Burum. Magnus expansion generator. *Phys. Rev.*, 24B(7):3684–3692, 1981.

[264] S. Klarsfeld and J. A. Oteo. Recursive generation of higher-order terms in the magnus expansion. *Phys. Rev.*, 39A(7):3270–3273, 1989.

[265] Philip Pechukas and John C. Light. On the exponential form of time-

displacement operators in quantum mechanics. *J. Chem. Phys.*, 44(10):3897–3909, 1966.

[266] Ulrich Haeberlen. *High resolution NMR in solids*, volume Supp. 1 of *Advances in Magnetic Resonance*. Academic Press, 1976.

[267] M. Matti Maricq. Spin thermodynamics of periodically time-dependent systems: The quasistationary state and its decay. *Phys. Rev.*, 36B(1):516–528, 1987.

[268] M. Matti Maricq. Thermodynamics for many-body systems evolving under a periodic time-dependent Hamiltonian: Application to pulsed magnetic resonance. *Phys. Rev.*, 31B(1):127–141, 1985.

[269] Jean Margerie and Jean Brossel. Transitions à plusieurs quanta électromagnétiques. *Comptes rendus de l'académie des sciences*, 241:373–375, july 1955.

[270] Jacques Winter. Étude de transitions faisant intervenir plusieurs quanta entre deux niveaux atomiques. *Comptes rendus de l'académie des sciences*, 241: 375–377, 1955.

[271] M P Silverman and F M Pipkin. Interaction of a decaying atom with a linearly polarized oscillating field. *J. Phys. B*, 5:1844–1860, 1972.

[272] K. W. Moehl, E. J. Lous, and A. J. Hoff. Low-power, low-field RYDMAR of the primary radical pair in photosynthesis. *Chem. Phys. Lett.*, 121(1,2):22–27, November 1985.

[273] C. A. Hamilton, K. A. McLauchlan, and K. R. Peterson. J-resonances in MARY and RYDMR spectra from freely-diffusing radical ion pairs. *Chem. Phys. Lett.*, 162(1,2):145–151, October 1989.

[274] Talbot H. Waterman. *Animal navigation*. Scientific American Library, 1989. ISBN 0716750244.

[275] Barrie J Frost and Henrik Mouritsen. The neural mechanisms of long distance animal navigation. *Current Opinion in Neurobiology*, 16:481–488, 2006.

[276] F. Økland, J. Erkinaro, K. Moen, E. Niemelä, P. Fiske, R. S. McKinley, and E. B. Thorstad. Return migration of atlantic salmon in the river tana: phases of migratory behaviour. *J Fish Biol*, 59(4):862–874, 2001.

[277] Thomas P. Quinn, Ian J. Stewart, and Christopher P. Boatright. Experimental evidence of homing to site of incubation by mature sockeye salmon, *oncorhynchus nerka*. *Animal Behaviour*, 72(4):941–949, 2006.

[278] F. A. Urquhart. Found at last: The monarch's winter home. *National Geographic Magazine*, 150:161–173, 1976.

[279] Lincoln P. Brower. Monarch butterfly orientation: missing pieces of a magnificent puzzle. *J. Exp. Biol.*, 199(1):93–103, 1996.

[280] Kenneth J. Lohmann, Shaun D. Cain, Susan A. Dodge, and Catherine M. F. Lohmann. Regional magnetic fields as navigational markers for sea turtles. *Science*, 294(5541):364–366, 2001.

[281] Kenneth J. Lohmann, Catherine M. F. Lohmann, Llewellyn M. Ehrhart, Dean A. Bagley, and Timothy Swing. Animal behaviour: Geomagnetic map used in sea-

turtle navigation. *Nature*, 428:909–910, 2004.

[282] William W. Cochran, Henrik Mouritsen, and Martin Wikelski. Migrating songbirds recalibrate their magnetic compass daily from twilight cues. *Science*, 304: 405–408, 2004.

[283] Henri Weimerskirch, Susanne Åkesson, and David Pinaud. Postnatal dispersal of wandering albatrosses *diomedea exulans*: implications for the conservation of the species. *J. Avian Biology*, 37(1):23–28, 2006.

[284] Collecte Localisation Satellites SA. `https://www.argos-system.org/`.

[285] Julia Stalleicken, Maya Mukhida, Thomas Labhart, Rüdiger Wehner, Barrie Frost, and Henrik Mouritsen. Do monarch butterflies use polarized skylight for migratory orientation? *J. Exp. Biol.*, 208(12):2399–2408, 2005.

[286] Royal Institute of Navigation. Bibliography of peer-reviewed animal navigation research papers. 2005.

[287] R. Wiltschko and W. Wiltschko. *Magnetic orientation in animals*. Springer-Verlag, Berlin, 1995. ISBN 3540592571.

[288] Richard Blakemore. Magnetotactic bacteria. *Science*, 190:377–379, October 1975.

[289] John H. Wang, Shaun D. Cain, and Kenneth J. Lohmann. Identification of magnetically responsive neurons in the marine mollusc *Tritonia diomedea*. *J. Exp. Biol.*, 206:381–388, 2003.

[290] Ad. J. Kalmijn. Electric and magnetic field detection in elasmobranch fishes. *Science*, 218:916–918, November 1982.

[291] Joseph L. Kirschvink, S. Padmanabha, C. Boyce, and J. Oglesby. Measurement of the threshold sensitivity of honeybees to weak, extremely low-frequency magnetic fields. *J. Exp. Biol.*, 200(9):1363–1368, May 1997.

[292] Wolfgang Wiltschko and Roswitha Wiltschko. Magnetic orientation and magnetoreception in birds and other animals. *Journal of Comparative Physiology A*, 191(8):675–693, 2005.

[293] Shaun D. Cain, John H. Wang, and Kenneth J. Lohmann. Immunochemical and electrophysiological analyses of magnetically responsive neurons in the mollusc *Tritonia diomedea*. *Journal of Comparative Physiology A*, 192:235–245, 2006.

[294] P. Semm and R. C. Beason. Responses to small magnetic variations by the trigeminal system of the bobolink. *Brain Research Bulletin*, 25(5):735–740, 1990.

[295] R. Robin Baker. Goal orientation by blindfolded humans after long-distance displacement: Possible involvement of a magnetic sense. *Science*, 210(4469): 555–557, 1980.

[296] G. W. Max Westby and Karen J. Partridge. Human homing: still no evidence despite geomagnetic controls. *J. Exp. Biol.*, 120:325–331, 1986.

[297] Joseph L. Kirschvink, Douglas S. Jones, and Bruce J. MacFadden, editors. *Magnetite biomineralization and magnetoreception in organisms: a new biomagnetism*. Topics in Geobiology. Springer, 1985. ISBN 0306419939.

[298] European robin, 2007. http://en.wikipedia.org/wiki/European_Robin.

[299] Wolfgang Wiltschko and Roswitha Wiltschko. Magnetic orientation in birds. *J. Exp. Biol.*, 199(1):29–38, 1996.

[300] Sönke Johnsen and Kenneth J. Lohmann. The physics and neurobiology of magnetoreception. *Nature Reviews: Neuroscience*, 6:703–712, 2005.

[301] Edward Batschelet. *Circular statistics in biology*. Mathematics in biology. Academic Press, 1981. ISBN 0120810506.

[302] Wolfgang Wiltschko and Roswitha Wiltschko. Magnetic compass orientation in birds and its physiological basis. *Naturwissenschaften*, 89:445–452, 2002.

[303] Mark E. Deutschlander, John B. Phillips, and S. Chris Borland. The case for light-dependent magnetic orientation in animals. *J. Exp. Biol.*, 202:891–908, 1999.

[304] Rachel Muheim, Johan Bäckman, and Susanne Åkesson. Magnetic compass orientation in European robins is dependent on both wavelength and intensity of light. *J. Exp. Biol.*, 205:3845–3856, 2002.

[305] Wolfgang Wiltschko, Joachim Traudt, Onur Güntürkün, Helmut Prior, and Roswitha Wiltschko. Lateralization of magnetic compass orientation in a migratory bird. *Nature*, 419:467–470, 2002.

[306] Henrik Mouritsen, Gesa Feenders, Miriam Liedvogel, and Wiebke Kropp. Migratory birds use head scans to detect the direction of the Earth's magnetic field. *Current Biology*, 14:1946–1949, 2004.

[307] Henrik Mouritsen, Gesa Feenders, Miriam Liedvogel, Kazuhiro Wada, and Erich D. Jarvis. Night-vision brain area in migratory songbirds. *PNAS*, 102 (23):8339–8344, 2005.

[308] Miriam Liedvogel, Gesa Feenders, Kazuhiro Wada, Nikolaus F. Troje, Erich D. Jarvis, and Henrik Mouritsen. Lateralized activation of Cluster N in the brains of migratory songbirds. *European Journal of Neuroscience*, 25(4):1166–1173, 2007.

[309] W. Wiltschko and R. Wiltschko. Migratory orientation of European robins is affected by the wavelength of light as well as by a magnetic pulse. *Journal of Comparative Physiology A*, 177(3):363–369, 1995.

[310] Wolfgang Wiltschko, Katrin Stapput, Peter Thalau, and Roswitha Wiltschko. Avian magnetic compass: fast adjustment to intensities outside the normal functional window. *Naturwissenschaften*, 93(6):300–304, 2006.

[311] William T. Keeton, Timothy S. Larkin, and Donald M. Windsor. Normal fluctuations in the earth's magnetic field influence pigeon orientation. *Journal of Comparative Physiology A*, 95(2):95–103, 1974.

[312] Peter Styles. Personal communication. "Estimate of background RF levels", 2007.

[313] J. M. Canfield, R. L. Belford, and P. G. Debrunner. Calculations of Earth-strength steady and oscillating magnetic field effects in coenzyme B_{12} radical pair systems. *Mol. Phys.*, 89(3):889–930, 1996.

[314] Thorsten Ritz, Peter J. Hore, Christiane R. Timmel, Christopher T. Rodgers, Katrin Stapput, Peter Thalau, Roswitha Wiltschko, and Wolfgang Wiltschko. Key features of the receptor molecule underlying the avian magnetic compass. *For submission to Nature*, 2007.

[315] M. J. M. Leask. A physicochemical mechanism for magnetic field detection by migratory birds and homing pigeons. *Nature*, 267:144–145, 1977.

[316] A. R. Liboff and K. A. Jenrow. New model for the avian magnetic compass. *Bioelectromagnetics*, 21:555–565, 2000.

[317] D. T. Edmonds. A sensitive optically detected magnetic compass for animals. *Proc. Roy. Soc.*, 263B:295–298, 1996.

[318] John C. Montgomery and Michael M. Walker. Orientation and navigation in elasmobranchs: Which way forward? *Environmental Biology of Fishes*, 60: 109–116, 2001.

[319] M.G. Paulin. Electroreception and the compass sense of sharks. *Journal of Theoretical Biology*, 174(3):325–339, 1995.

[320] K. Schulten and A. Windemuth. Model for a physiological magnetic compass. In G. Maret, J. Kiepenheuer, and N. Boccara, editors, *Biophysical effects of steady magnetic fields*, pages 99–106. Springer-Verlag, 1986.

[321] F. Cintolesi, T. Ritz, C. W. M. Kay, C. R. Timmel, and P. J. Hore. Anisotropic recombination of an immobilized photoinduced radical pair in a 50-μT magnetic field: a model avian photomagnetoreceptor. *Chem. Phys.*, 294:385–399, 2003.

[322] C. R. Timmel, F. Cintolesi, B. Brocklehurst, and P. J. Hore. Model calculations of magnetic field effects on the recombination reactions of radicals with anisotropic hyperfine interactions. *Chem. Phys. Lett.*, 334:387–395, 2001.

[323] Steven G. Boxer, Christopher E. D. Chidsey, and Mark G. Roelofs. Magnetic field effects on reaction yields in the solid state: An example from photosynthetic reaction centers. *Ann. Rev. Phys. Chem.*, 34:389–417, 1983.

[324] Steven G. Boxer, Christopher E. D. Chidsey, and Mark G. Roelofs. Dependence of the yield of a radical-pair reaction in the solid state on orientation in a magnetic field. *JACS*, 104:2674–2675, 1982.

[325] Steven G. Boxer, Christopher E. D. Chidsey, and Mark G. Roelofs. Anisotropic magnetic interactions in the primary radical ion-pair of photosynthetic reaction centers. *PNAS*, 79:4632–4636, 1982.

[326] Kiminori Maeda. Personal communication. "Measurements of magnetic field effects in a CPF triad molecule.", 2006.

[327] James C. Weaver, Timothy E. Vaughan, and R. Dean Astumian. Biological sensing of small field differences by magnetically sensitive chemical reactions. *Nature*, 405:707–709, 2000.

[328] A Sancar. Structure and function of DNA photolyase and chryptochrome blue-light photoreceptors. *Chem. Rev.*, 103(6):2203–2238, 2003.

[329] Carrie L. Partch and Aziz Sancar. Photochemistry and photobiology of cryptochrome blue-light photopigments: The search for a photocycle. *Photochem-*

istry and Photobiology, 81:1291–1304, 2005.

[330] L. Hermosilla, P. Calle, J. M. García de la Vega, and C. Sieiro. Density functional theory predictions of isotropic hyperfine coupling constants. *J. Phys. Chem.*, 109A(6), 2005.

[331] Roberta Improta and Vincenzo Barone. Interplay of electronic, environmental, and vibrational effects in determining the hyperfine coupling constants of organic free radicals. *Chem. Rev.*, 104:1231–1253, 2004.

[332] Nadia Rega, Maurizio Cossi, and Vincenzo Barone. Development and validation of reliable quantum mechanical approaches for the study of free radicals in solution. *J. Chem. Phys.*, 105(24):11060–67, 1996.

[333] David C. Young. *Computational chemistry: a practical guide for applying techniques to real world problems*. John Wiley & Sons Inc, 2001. ISBN 0471333689.

[334] Vincenzo Barone. Electronic, vibrational and environmental effects on the hyperfine coupling constants of nitroside radicals. H_2NO as a case study. *Chem. Phys. Lett.*, 262:201–206, 1996.

[335] Carlos Calle and *et al*. Pulse EPR methods for studying chemical and biological samples containing transition metals. *Helvetica Chimica Acta*, 89:2495–2521, 2006.

[336] Henrik Mouritsen, Ulrike Janssen-Bienhold, Miriam Liedvogel, Gesa Feenders, Julia Stalleicken, Petra Dirks, and Reto Weiler. Cryptochromes and neuronal-activity markers colocalize in the retina of migratory birds during magnetic orientation. *PNAS*, 101(39):14294–299, 2004.

[337] Melanie S. Freedman, Robert J. Lucas, Bobby Soni, Malcolm von Schantz, Marta Muñoz, Zoë David-Gray, and Russell Foster. Regulation of mammalian circadian behavior by non-rod, non-cone, ocular photoreceptors. *Science*, 284: 502–504, 1999.

[338] Aziz Sancar. Regulation of the mammalian circadian clock by cryptochrome. *J. Biol. Chem.*, 279(33):34079–82, 2004.

[339] Per-Olof Persson and Gilbert Strang. A simple mesh generator in MATLAB. *SIAM Review*, 46(2):329–345, 2004.

[340] D. W. Alderman, Mark S. Solum, and David M. Grant. Methods for analyzing spectroscopic line shapes. NMR solid powder patterns. *J. Chem. Phys.*, 84(7): 3717–3725, 1986.

[341] Deming Wang and Graeme R. Hanson. A new method for simulating randomly oriented powder spectra in magnetic resonance: The Sydney Opera House (SOPHE) method. *J. Mag. Res.*, 117:1–8, 1995.

[342] Anthony R. Cashmore, Jose A. Jarillo, Ying-Jie Wu, and Dongmei Liu. Cryptochromes: Blue light receptors for plants and animals. *Science*, 284:760–765, 1999.

[343] Margaret Ahmad, Paul Galland, Thorsten Ritz, Roswitha Wiltschko, and Wolfgang Wiltschko. Magnetic intensity affects cryptochrome-dependent responses

in *Arabidopsis thaliana*. *Planta*, 225(3):615–624, 2007.

[344] Yihua Huang, Richard Baxter, Barbara S. Smith, Carrie L. Partch, Christopher L. Colbert, and Johann Deisenhofer. Crystal structure of cryptochrome 3 from *Arabidopsis thaliana* and its implications for photolyase activity. *PNAS*, 103(47):17701–06, 2006.

[345] Chad A. Brautigam, Barbara S. Smith, Zhiquan Ma, Maya Palnitkar, Diana R. Tomchick, Mischa Machius, and Johann Deisenhofer. Structure of the photolyase-like domain of cryptochrome 1 from *Arabidopsis thaliana*. *PNAS*, 101:12142–47, 2004.

[346] S. Crosson and K. Moffat. Structure of a flavin-binding plant photoreceptor domain: insights into light-mediated signal transduction. *PNAS*, 98(6):2995–3000, 2001.

[347] F. Müller. Free flavins: synthesis, chemical and physical properties. In F. Müller, editor, *The Chemistry and Biochemistry of Flavoenzymes*, volume 1, pages 1–71. CRC Press, Boca Raton, 1991.

[348] P. F. Heelis. The photochemistry of flavins. In F. Müller, editor, *The Chemistry and Biochemistry of Flavoenzymes*, volume 1, pages 171–193. CRC Press, Boca Raton, 1991.

[349] Christopher W. M. Kay and Stefan Weber. EPR of radical intermediates in flavoenzymes. *Electron Paramagnetic Resonance*, 18:222–253, 2002.

[350] Yvonne M. Gindt, Esther Vollenbroek, Kristi Westphal, Heather Sackett, Aziz Sancar, and Gerald T. Babcock. Origin of the transient electron paramagnetic resonance signals in DNA photolyase. *Biochemistry*, 38:3857–3866, 1999.

[351] Stefan Weber, Christopher W. M. Kay, Heike Mögling, Klaus Möbius, Kenichi Hitomi, and Takeshi Todo. Photoactivation of the flavin cofactor in *Xenopus laevis* (6–4) photolyase: Observation of a transient tyrosyl radical by time-resolved electron paramagnetic resonance. *PNAS*, 99(3):1319–1322, 2002.

[352] Stefan Weber. Light-driven enzymatic catalysis of DNA repair: a review of recent biophysical studies on photolyase. *Biochimica et Biophysica Acta*, 1707 (1):1–23, 2005.

[353] C. W. M. Kay, H. Mögling, E. Schleicher, K. Hitomi, K. Möbius, T. Todo, A. Bacher, G. Richter, and S. Weber. A comparative time-resolved electron paramagnetic resonance study of the flavin cofactor photoreduction in *Escherichia coli* cyclobutane pyrimidine dimer photolyase and *Xenopus laevis* (6–4) photolyase. In *Flavins and Other Flavoproteins*. Walter De Gruyter Inc, 2002.

[354] Baldissera Giovani, Martin Byrdin, Margaret Ahmad, and Klaus Brettel. Light-induced electron transfer in a cryptochrome blue-light photoreceptor. *Nature Structural Biology*, 10(6):489–490, 2003.

[355] Andrea Möller, Sven Sagasser, Wolfgang Wiltschko, and Bernd Schierwater. Retinal cryptochrome in a migratory passerine bird: a possible transducer for the avian magnetic compass. *Naturwissenschaften*, 91:585–588, 2004.

[356] Alexander Joseph Robinson. The effect of weak magnetic fields on radical reactions: A time-resolved study. Part II thesis, University of Oxford, 2006.

[357] S Kim, A Sancar, C Essenmacher, and GT Babcock. Time-resolved EPR studies with DNA photolyase: Excited-state $FADH^0$ abstracts an electron from Trp-306 to generate $FADH^-$, the catalytically active form of the cofactor. *PNAS*, 90: 8023–8027, 1993.

[358] Stefan Weber, Klaus Möbius, Gerald Richter, and Christopher W. M. Kay. The electronic structure of the flavin cofactor in DNA photolyase. *JACS*, 123:3790–3798, 2001.

[359] Christopher W. M. Kay, Richard Feicht, Kristina Schulz, Peter Sadewater, Aziz Sancar, Adelbert Bacher, Klaus Möbius, Gerald Richter, and Stefan Weber. EPR, ENDOR, and TRIPLE resonance spectroscopy on the neutral flavin radical in *Escherichia coli* DNA photolyase. *Biochemistry*, 38:16740–48, 1999.

[360] R. J. Hulsebosch, J. S. van den Brink, S. A. M. Nieuwenhuis, P. Gast, J. Raap, J. Lugtenburg, and A. J. Hoff. Electronic structure of the neutral tyrosine radical in frozen solution. selective ^{2}H-, ^{13}C-, and ^{17}O-isotope labeling and EPR spectroscopy at 9 and 35 GHz. *JACS*, 119:8685–8694, 1997.

[361] Patrick J. O'Malley and Darryl Ellson. ^{1}H, ^{13}C and ^{17}O isotropic and anisotropic hyperfine coupling prediction for the tyrosyl radical using hybrid density functional methods. *Biochimica et Biophysica Acta*, 1320:65–72, 1997.

[362] Y. Deligiannakis, A. Ivancich, and A.W. Rutherord. 2D-hyperfine sublevel correlation spectroscopy of tyrosyl radicals. *Spectrochimica Acta Part A*, 58:1191–1200, 2002.

[363] F. Lendzian, M. Sahlin, F. MacMillan, R. Bittl, R. Fiege, S. Pötsch, B-M. Stöberg, A. Gräslund, W. Lubitz, and G. Lassmann. Electronic structure of the neutral tryptophan radicals in ribonucleotide reductase studied by EPR and ENDOR spectroscopy. *JACS*, 118:8111–8120, 1996.

[364] Olga Efimova. Personal communication. "Radical pairs with exchange and dipolar interactions", 2007.

[365] George B. Arfken and Hans J. Weber. *Mathematical Methods for Physicists*. Harcourt Academic Press, Fifth (International) edition, 2001. ISBN 0120598264.

[366] J. R. Driscoll and D. M. Healy. Computing fourier transforms and convolutions on the 2-sphere. *Advances in Applied Mathematics*, 15(2):129–250, 1994.

[367] Gilles Burel and Hugues Hénocq. Three-dimensional invariants and their application to object recognition. *Signal Processing*, 45:1–22, 1995.

[368] Thomas Funkhouser, Patrick Min, Michael Kazhdan, Joyce Chen, Alex Halderman, David Dobkin, and David Jacobs. A search engine for 3D models. *ACM Transactions on Graphics*, 22(1):88–105, 2003.

[369] Dietmar Saupe and Dejan V. Vranic. 3D model retrieval with spherical harmonics and moments. In B. Radig and S. Florczyk, editors, *Pattern Recognition: 23rd DAGM Symposium, Munich, Germany, September 12-14, 2001*, volume 2191/2001 of *Lecture Notes in Computer Science*, pages 392–397. Springer, 2001.

[370] D.M. Healy Jr., D. Rockmore, P. J. Kostelec, and Sean S. B. Moore. FFTs

for the 2-sphere — improvements and variations. Technical report, Dept of Mathematics, Dartmouth College, Hanover, NH 03755, 1998.

[371] Peter J. Kostelec and Daniel N. Rockmore. S2kit: A lite version of SpharmonicKit, 2004. http://www.cs.dartmouth.edu/~geelong/sphere.

[372] Ilya Kuprov. Personal communication. "An idea for expansion in terms of spherical harmonics", 2004.

[373] Dingeman J. Wielaard, Michael I. Mishchenko, Andreas Macke, and Barbara E. Carlson. Improved T-matrix computations for large, nonabsorbing and weakly absorbing nonspherical particles and comparison with geometrical-optics approximation. *Applied Optics*, 36(18):4305–4313, 1997.

[374] D A Lavis, B W Southern, and I F Wilde. The inverse of a semi-infinite symmetric banded matrix. *J. Phys. A: Math. Gen.*, 30:7229–7241, 1997.

[375] Victor Eijkhout and Ben Polman. Decay rates of inverses of banded M-matrices that are near to Toeplitz matrices. *Linear Algebra and its Applications*, 109: 247–277, 1988.

[376] Peter J. Kostelec and Daniel N. Rockmore. FFTs on the rotation group. Working Papers Series 03-11-060, Santa Fe Institute, 2003. http://www.santafe.edu/research/publications/workingpapers/03-11-060.pdf.

[377] Darius Kuciauskas, Paul A. Liddell, Ana L. Moore, Thomas A. Moore, and Devens Gust. Magnetic switching of charge separation lifetimes in artificial photosynthetic reaction centers. *JACS*, 120:10880–86, 1998.

[378] Sarah Hall. Anisotropic electron transfer in a CPF triad. Part II thesis, University of Oxford, 2007.

[379] Kefei Wang and Thorsten Ritz. Zeeman resonances for radical-pair reactions in weak static magnetic fields. *Mol. Phys.*, 104:1649–1658, 2006.

[380] S. Trapani and J. Navaza. Calculation of spherical harmonics and Wigner $\mathfrak{D}$-functions by FFT. Applications to fast rotational matching in molecular replacement and implementation into AMoRe. *Acta Cryst.*, A62(4):262–269, 2006.

[381] Philip H. Rieger and George K. Fraenkel. Spin-density distribution in nitrile anion radicals. *J. Chem. Phys.*, 37(12):2795–2810, 1962.

[382] Athanasios Papoulis. *The Fourier Integral and its Applications*. McGraw-Hill, 1962.

[383] P. A. M. Dirac. *The Principles of Quantum Mechanics*. Clarendon Press, 1981. ISBN 9780198520115.

[384] U. Fano. Description of states in quantum mechanics by density matrix and operator techniques. *Reviews of Modern Physics*, 29(1):74–93, 1957.

[385] Peter J. Mohr and Barry N. Taylor. CODATA recommended values of the fundamental physical constants: 2002. *Reviews of Modern Physics*, 77:1–107, 2005.